IntechOpen

Aluminium Alloys, Theory and Applications

Edited by Tibor Kvackaj

ALUMINIUM ALLOYS, THEORY AND APPLICATIONS

Edited by **Tibor Kvačkaj** and **Róbert Bidulský**

Aluminium Alloys, Theory and Applications
http://dx.doi.org/10.5772/576
Edited by Tibor Kvackaj

Contributors

Alfredo Flores, Patiphan Juijerm, Igor Altenberger, Maria Salvador, Vicente Amigó, Mary J. Vergara, Carlos Bloem, Ewald Macha, Dariusz Rozumek, Guozheng Kang, Jun Ding, Yujie Liu, Linda Wu, George Ferguson, Tibor Kvackaj, Jana Bidulska, Robert Kocisko, Robert Bidulsky, Abílio de Jesus, Alfredo Ribeiro, Adinel Gavrus, Henri Francillette, Pedro Vilaça, Telmo G. Santos, Marco Actis Grande, Andrea Gatto, Luca Iuliano, Elena Bassoli, Matteo Pavese, Claudio Badini, Claudia Vega Bolivar, Andrea Antonini, Sara Biamino, Diego Manfredi, Elisa Ambrosio, Paolo Fino, Giuseppe Campanile, Francesco Acerra, Victor Songmene, Riad Khettabi, Imed Zaghbani, Jules Kouam, Abdelhakim Djebara, Jisen Qiao, Shahrum Abdullah, Gilbert Henaff, Grégory Odemer, Bertrand Journet, Kuppuswamy Ramaswamy

Notice

First published in Croatia, 2011 by INTECH d.o.o.
eBook (PDF) Published by IN TECH d.o.o.
Place and year of publication of eBook (PDF): Rijeka, 2019.
IntechOpen is the global imprint of IN TECH d.o.o.
Printed in Croatia

Legal deposit, Croatia: National and University Library in Zagreb

Additional hard and PDF copies can be obtained from orders@intechopen.com

Aluminium Alloys, Theory and Applications
Edited by Tibor Kvackaj

p. cm.

ISBN 978-953-307-244-9

eBook (PDF) ISBN 978-953-51-5974-2

Meet the editors

Professor Tibor Kvačkaj obtained the PhD degree in field of study "Materials Science and Metal Forming" at Faculty of Metallurgy, Technical University in Košice in 1983. He is head of Department of Metals Forming from 1992, chairman of international conference "TherTech-Form" since 1996 and chairman of editorial board of journal "Acta Metallurgica Slovaca". He published as author and co-author more than 350 original scientific works. His scientific fields are theory and technology of plastic deformations of metals, experimental investigations and mathematical simulations of influence of plastic deformation processes on structure formation and properties metal materials, nanostructural formations by SPD, steel research for autobodies.

Dr. Róbert Bidulský obtained PhD in field of study "Material Engineering and Limiting States of Materials" at the Institute of Materials Research of Slovak Academy of Sciences in Kosice in 2003. He is a member of editorial board of journal "Acta Metallurgica Slovaca". He published more than 100 papers and participated in various EC and National projects. Lecturer on the laboratory works on the Training Courses (2007, 2008) under Marie Curie program. He was awarded fellowships for foreign senior researcher at Politecnico di Torino. His scientific work focuses on the materials science (powder metallurgy, SPD) HT processing (sinter hardening), as well physical and mathematical simulation (compressibility, diffusion and material flow phenomena).

Contents

Preface

Aluminium alloy has taken over as the most popular material for structural components in engineering industry included automotive, aerospace and construction industries for several reasons. The most characteristic properties of aluminium are low specific weight and low melting point. In addition, aluminium has excellent corrosion resistance, high strength and stiffness to weight ratio, good formability, weldability, high electrical and heat conductivity. Last but not least, aluminium alloy components are particularly required for environmental, ecological and economical aspects.

The book provides a theoretical and a practical understanding of the metallurgical principles in: severe plastic deformation processes with respect to high strength and ductility achieved on bulk and PM aluminium and aluminium alloys; welding of aluminium, mainly focused on a relatively new technique of friction stir welding as well as welded fatigue behaviour; cyclic deformation behaviour of the aluminium alloys at room and elevated temperature forcefully on the load sequence effects in fatigue crack propagation and crack growth under loading; creep-fatigue crack growth; modelling of precipitation hardening in casting aluminium alloys; an anisotropic behaviour analysis undergoing large plastic deformations; new approaches to reaction kinetics during molten aluminium refining using electron backscatter diffraction; theoretical explanation about number restoration and etching techniques applied to recover the obliterated markings on aluminium and aluminium alloys and information about machining and machinability of aluminium alloys.

Out of all, aluminium alloys offer opportunities in a wide range of applications. The present book enhances in detail the scope and objective of various developmental activities of the aluminium alloys. A lot of research on aluminium alloys has been performed. Currently, the research efforts are connected to the relatively new methodics and processes. We hope that people new to the aluminium alloys investigation will find this book to be of assistance for the industry and university fields enabling them to keep up-to-date with the latest developments in aluminium alloys research.

The editors of this book would like to acknowledge the contribution of all both participants who kindly submitted their chapters and those who want to share their work, and the local organization of the managing the book.

Prof. Tibor Kvačkaj
Technical University of Kosice, Faculty of Metallurgy,
Department of Metals Forming,
Slovakia

Dr. Róbert Bidulský
Politecnico di Torino – Sede di Alessandria,
Italy

Part 1

Severe Plastic Deformation and Modelling

1

Effect of Severe Plastic Deformation on the Properties and Structural Developments of High Purity Al and Al-Cu-Mg-Zr Aluminium Alloy

Tibor Kvačkaj[1], Jana Bidulská[1], Robert Kočiško[1] and Róbert Bidulský[2]
[1]*Technical University of Kosice, Faculty of Metallurgy, Department of Metals Forming*
[2]*Politecnico di Torino – Sede di Alessandria*
[1]*Slovakia*
[2]*Italy*

1. Introduction

Demands of industry producers are to find new forms and facilities for appropriate properties of structural parts suitable for different miscellaneous structural applications in the civil, automotive and aircraft industries. With respect to these facts, aluminium alloys find a wide variety of uses due to their remarkable combination of characteristics such as the low density, the high corrosion resistance, high strength, easy workability and high electrical and heat conductivity.

The traditional process is to obtain the improvement in the mechanical properties of aluminium alloys through the precipitation of a finely dispersed second phase in the matrix. This is accomplished by a solution treatment of the material at a high temperature, followed by quenching. The second phase is then precipitated at room or elevated temperatures. For aluminium alloys this procedure is usually referred to as age hardening and it is also known as precipitation hardening (Michna et al., 2007); (Mondolfo, 1976). Conventional forming methods are ineffective in the achieving of favourable properties area of produced parts, adequate to structural properties; moreover through them only limited levels of structural and strength-plastic characteristics can be obtained. The solution may be non-conventional forming methods (Kvačkaj et al., 2005), (Kvačkaj et al., 2004), (Kvačkaj et al., 2010 a) as well as Severe Plastic Deformation (SPD), such as more preferable are equal channel angular pressing - ECAP, (Valiev & Langdon, 2006), (Valiev et al., 2000) to obtain results structured at the nm level. A combination of high strength and ductility of ultrafine polycrystalline metals, prepared by SPD, is unique and it indeed represents interesting cases from the point of view of mechanical properties (Chuvil'deev et al, 2008); (Zehetbauer et al., 2006); (Han et al., 2005) ;(Ovid'ko, 2005); (Meyers et al., 2006); (Kopylov & Chuvil'deev, 2006); (Zehetbauer & Estrin, 2009). In the past decade, the research focused on to strengthen Al alloys without any ageing treatment, via SPD (Kvačkaj et al., 2010 b).

The finite element method (FEM) is a proven and reliable technique for analyzing various forming processes (Kvačkaj et al., 2007); (Kočiško et al., 2009); (Li et al., 2004); (Leo et al., 2007); (Cerri et al., 2009), (Figueiredo et al., 2006); (Mahallawy et al., 2010); (Yoon & Kim, 2008), in order to analyze the global and local deformation response of the workpiece with

nonlinear conditions of boundary, loading and material properties, to compare the effects of various parameters, and to search for optimum process conditions for a given material (Kim, 2001).
The unique mechanical properties of the ECAPed material are directly affected by plastic deformation. Hence, the understanding the development of strain during processing has a key role for a successful ECAP process. It is well known that the main factors affecting the corner gap formation during ECAP are materials strain hardening and friction. Thus, character of the strained condition and uniformity of plastic flow during ECAP is very sensitive to friction coefficient (Balasundar & Raghu, 2010); (Zhernakov et al., 2001); (Medeiros et al., 2008).
In order to understand various processes like as the workpiece (billet), die design, the friction conditions, etc.; it is essential to combine experimental research with a theoretical analysis of inhomogeneous deformation behaviour in the workpiece during the process.
In addition to the aforementioned properties, the most important factor affecting the mathematical simulation of material is the stress-strain curve (stress-strain curve influences the calculation precision). These data can be derived either from database program or from experimental achieved stress-strain curve. Experimental stress-strain curve can easily be determined by laboratory tests of formability. The most frequently used formability tests are torsion and tension (Pernis et al., 2009); (Kováčová et al., 2010).
Structure investigations by TEM analysis will be useful key to identifications and confirmations the various theories about the material behaviour during the ECAP processing (Dutkiewicz et al., 2009); (Dobatkin et al., 2006); (Lityńska-Dobrzyńska et al., 2010); (Maziarz et al., 2010); (Alexandrov et al., 2005).
The present chapter book focused on the effect of Severe Plastic Deformation on the properties and structural developments of high purity aluminium and Al-Cu-Mg-Zr aluminium alloy.
Former part deals with the high purity aluminium (99,999 % Al) processed by six ECAP passes in room temperature. Influence of strain level, strength, microhardness, plasticity and diameter of grain size in dependence on ECAP passes were investigated. FEM analysis with respect to influence friction coefficient (f=0,01-0,3) and characteristic of deformed materials as such materials with linear and nonlinear strengthening on homogeneity of effective deformations during sample cross section were observed.
Latter part deals with the tensile properties as function of the processing conditions of the Al-Cu-Mg-Zr aluminium alloy. Based on the results above, the tensile properties, hardness and structure development of the Al-Cu-Mg-Zr aluminium alloy along with the numerical simulation are discussed.

2. Experimental conditions

2.1 Experimental conditions for investigation of high purity Al (99,999%Al)

Experimental material was prepared by zonal refining. Structure after producing was heterogeneous with average grain size d_g ~ 650 μm. Mechanical properties before ECAP processing are given in Table 1.
The ECAP process was carried out at room temperature by route C (sample rotation around axis about 180° after each pass) in an ECAP die with channels angle $\Phi = 90°$. The rod-shaped samples (d_0 = 10 mm, l_0 = 80 mm) were extruded twelve ECAP passages at rate of 1 mm·s^{-1}. The deformation forces during ECAP sample processing was measured using tensometric measurement with LabVIEW apparatus.

0,2%YS [MPa]	UTS [MPa]	El. [%]	HV10[-]
36	52	27	24,2

Table 1. Initial mechanical properties of high purity aluminium (99,999 %)

The static tensile test on the short specimens d_0 x l_0 = 5 x 10 mm was performed. Tensile test was done after every second ECAP pass on ZWICK 1387 equipment by standard conditions EN 10002-1. Subsequently, characteristics of the strength (yield strength: YS; ultimate tensile strength: UTS) and elongation (El.) were determined.
The microhardness test was done on polished surface in longitudinal direction of sample after every second ECAP pass on LECO LM 700 AT equipment.
Transmission electron microscopy (TEM) analysis with electron diffraction in longitudinal direction of sample was done on thin foils on Philips CM 20 microscope. The thin foils were prepared using a solution of 5 % HF at a temperature -25 °C and the time 20 - 30 s.
Material flow in ECAP die was investigated. The samples were longitudinal cutting by wire cutter. Cutting surfaces were processing by metallographic grinding and polishing. Polishing surfaces were mechanically marked by square net as is given in Fig. 1. The size of one element was 1 x 1 mm. The samples after marking were again to join together and put in to ECAP unit. Orientation of sample cutting plane was identical with the plane lying in horizontal and vertical cannel axes. One pass in ECAP unit at rate 1 mm·s^{-1} was performed.

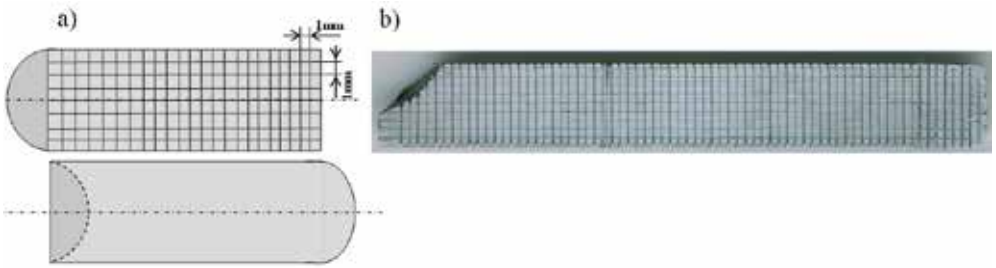

Fig. 1. Sample preparation before ECAP a) scheme of square net implementation on polishing surfaces, b) real Al sample with square net

Simulation of ECAP pass was carried out using the finite element method (FEM) in software DEFORM 2D as considering plane strain conditions (Deform Manual, 2003). Die geometries were directly designed in the software Deform 2D. The parameters were: circle canal of die with diameter, d_0 =10 mm, length, L=100 mm, die with channels angle, Φ = 90°, outer radius, R = 5 mm and inner radius, r = 0 mm. The workpiece dimensions were: diameter, d_0 =10 mm and length, l_0 = 80 mm. The processing rate was constant, v = 1 mm·s^{-1}. Friction was superposed to follow Coulomb's law with friction coefficient f = 0,12. The processing temperature was 20 °C. The theory at the base of FEM implies that at first, the problem has to be divided into little sub problems that are easily to be formulated. There over, they must all be carefully combined and then solved. The manner in which a problem is divided constituents the so called meshing process. Mesh density refers to the size of elements that will be generated within an object boundary. The mesh density is primarily based on the specified total number of elements. Mesh density according to (Kobayashi & Altan, 1989); (Deform Manual, 2003) is defined by the number of nodes per unit length, generally along the edge of the object. The mesh density values specify a mesh density ratio between two regions in the object. Even though the material properties are same, meshing is the most

important factor which will influence the finite element simulation results. The mesh size specifically influences the corner gap formation.
A higher mesh density offers increased accuracy and resolution of geometry, on the other the time required for the computer to solve the problem increases as number of nodes increases. An optimal meshing density has to be chosen according to the geometry and size of object according in (Kvačkaj et al., 2007); (Kočiško et al., 2009); (Li et al., 2004) specimen with diameter d_0 = 10 mm has been decided using 20 elements along the width. Hence, the specimen with diameter d_0 = 10 mm and length l_0 = 80 mm was meshed with 3000 elements, that's to say 28 elements on the specimen diameter, as shown in Fig. 2.

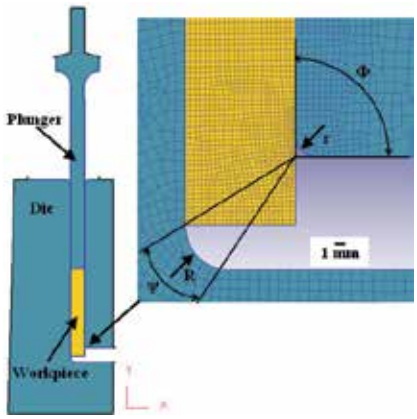

Fig. 2. FEM simulation scheme of ECAP

The finer meshes were built close to the surface in order to better match the geometry of the process, for example in channel areas. Authors (Semiatin et al., 2000) showed that the influence of channel angles of ECAP equipment was influencing the development of effective strain. Thus the highest effective strain is achieved if the angle between channels is 90°.
The tools of ECAP equipment (the die and plunger) were assumed to be elastic materials and they were assigned of tool steel material characteristic, them being much higher than those of deformed material. The specimen was assumed as elasto-plastic object with their material characteristics characterized by stress-strain curve Fig. 3.

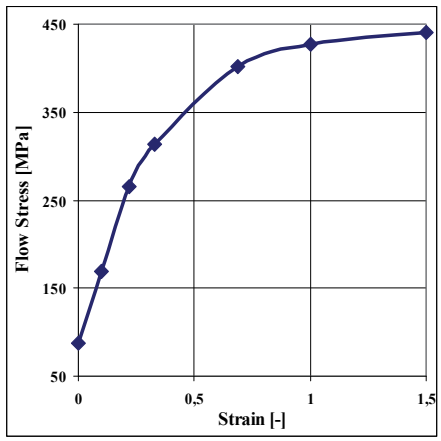

Fig. 3. Stress-strain curve of Al material

2.2 Experimental conditions for investigation of Al-Cu-Mg-Zr aluminium alloy

The material used in this experiment was Al-Cu-Mg-Zr aluminium alloy. The chemical composition is presented in Table 2.

Al	Cu	Mg	Mn	Si	Fe	Zr	Ti
balance	4,32	0,49	0,77	0,68	0,23	0,12	0,03

Table 2. Chemical compositions (wt. %) of investigated aluminium alloys

Hot rolling was carried out by rolling-mill DUO 210 at temperature of 460 °C (as-rolled state). Solution annealing after rolling was performed at temperature of 520 °C (holding time 9 000 s) and cooled to the room temperature by water quenching (quenched state). The quenched specimens (d_0 = 10 mm, l_0 = 70 mm) were subjected to deformation in an ECAP die with channels angle $\Phi = 90°$ at rate of 1 mm·s^{-1} (ECAPed state). The ECAP was realized by hydraulic equipment at room temperature. After one ECAP pass, the specimens were processed to artificial ageing at 100 °C for 720 000 s (ECAPed + aged state).

Tensile specimens were taken after each processing treatments. The tensile testing was done on a FP 100/1 machine with 0,15 mm·min^{-1} cross-head speed (strain rate of 2,5·10^{-4} s^{-1}). Static tensile test on the short specimens d_0 x l_0 = 5 x 10 mm was performed. Subsequently, characteristics of the strength (YS; UTS), El. and Re. were determined.

For optical microscopy, samples were individually mounted, mechanically polished and finally etched at room temperature using a mixture of 2 % HF, 3 % HCl, 5 % HNO_3 and 90 % H_2O (Keller's Reagent).

TEM analysis was performed on thin foils. The foils for TEM were prepared using a solution of 25 % HNO_3 and 75 % CH_3OH at a temperature -30 °C. TEM was conducted at an accelerating voltage of 200 kV.

Additionally, a fractographic study of the fracture surface of the materials after a conventional tensile strength test was carried out using SEM JEOL 7000F.

The numerical simulation of ECAP process was similar as is described in capture 2.1. Only sample length l_0 = 60 mm was changed. The specimen was assumed as elasto-plastic object with their material characteristics characterized by stress-strain curve (Table 3), Young's modulus and thermal properties. Certainly, the simulation conditions of investigated materials were considered so that the bounds of the deformation strain, strain rate and deformation temperature can't lead to loss of accuracy.

Strain [-]	0	0,1	0,2	0,3	1
Database data / stress [MPa]	0	200	233	250	312
Experimental data / stress [MPa]	0	68	144	174	324

Table 3. Stress-strain data of Al-Cu-Mg-Zr aluminium alloy for both conditions

Materials characteristics for both conditions are presented in Table 4.

Hence, mathematical simulations of ECAP process of Al-Cu-Mg-Zr aluminium alloy were realized on the basis of two approaches for stress-strain curve selection: from DEFORM material database and from experimental results. The DEFORM material database contains flow stress data for Al-Cu-Mg-Zr aluminium alloy (Table 3). The flow stress data provided by the material database has a limited range in terms of temperature range and effective strain.

Workpiece		Database	Experimental
Plastic		Flow stress (Table 2)	
Elastic	Young's modulus [MPa]	68900	70000
	Poisson's ratio [-]	0,33	0,33
	thermal expansion [K^{-1}]	$2{,}2 \cdot 10^{-5}$	$2{,}2 \cdot 10^{-5}$
Thermal	thermal conductivity [kW/m·K]	180,2	180,2
	heat capacity [$kJ \cdot kg^{-1} \cdot K^{-1}$]	2,433	2,433
Damage model (Fracture data)		Cockcroft-Latham	

Table 4. Materials characteristics for both investigated specimens

3. Results and discussion

3.1 Experimental results and discussion for high purity Al (99,999%Al)

3.1.1 FEM investigation

The deformed net after 1st ECAP pass is shown in Fig. 4a. Deformed net on sample surfaces was scanning and computer cover by new net for better visualisation as is given on Fig. 4b. Numerical simulations of net deformation in software DEFORM 2D are shown in Fig. 4c.
The intensity of plastic deformation is depended on angle of shearing strain γ. With increased of shearing strain angle is increasing also intensity of plastic deformation. The net deformation of sample is pointing out localization of biggest plastic deformation to top sample part which correspond with inner radius (r) of ECAP channel. The value of this shearing strain angle is γ = 60°. This value is observing up to 2/3 of sample cross section. Started from 2/3 of top to bottom sample part shearing strain angle is rapid decreasing up to level γ = 8°. Reported by authors (Beyerlein et al., 2004); (Stoica et al., 2005) this low level is characterizing by straining way in deformation zone which is more bending as plastic flowing. Mutual comparison of shearing strain angles γ obtained from experiment and numerical simulation reference to high conformity of results. Some difference was observed only in 1/5 bottom sample part where preferable deformation is bending.
The ECAP channel filling by processing material has influence on distribution of effective plastic deformation, which depends on: contact friction, stress – strain (σ-ε) curves characterizing deformed material and geometrical definition of ECAP die (Li et al., 2004). For numerical simulation of 1st ECAP pass geometrical definition of channels was as follow: Φ = 90°, R = 0 mm and r = 0 mm. The influence of friction coefficient in interval f = 0,01 – 0,25 on channels filling was simulated as is shown in Fig.5.
If geometrical definition of channels (Fig. 6) was describe by formula (1) (Oh et al., 2003) that linear graphical dependence shown in Fig. 7 was obtained.

$$\lambda = d_h \cdot \left(1 + \frac{d_h}{d_v}\right) \tag{1}$$

where: λ [-] – index for the outer corner
d_h [mm] – distance between die corner and horizontal contact point of die and workpiece
d_v [mm] – distance between die corner and vertical contact point of die and workpiece

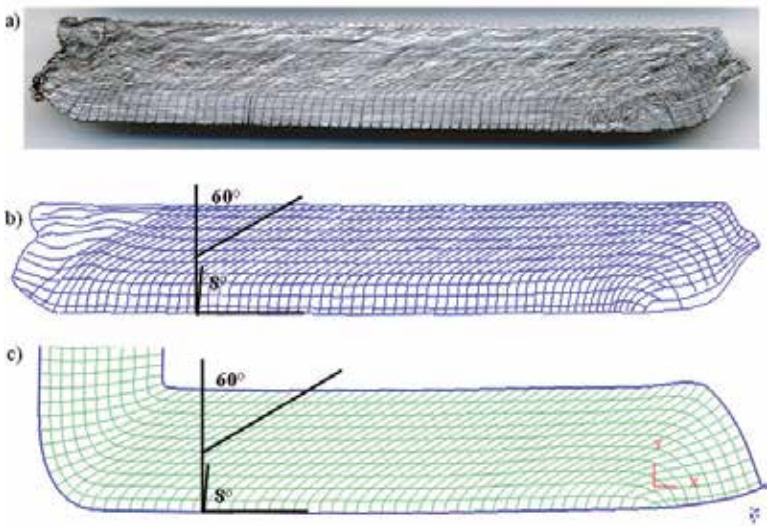

Fig. 4. Deformed net after 1st ECAP pass a) Deformed net on real sample, b) Visualisation deformed net after scanning and computer redrawing with marking of angle of shearing strain γ, c) Deformed net after numerical simulation in DEFORM 2D

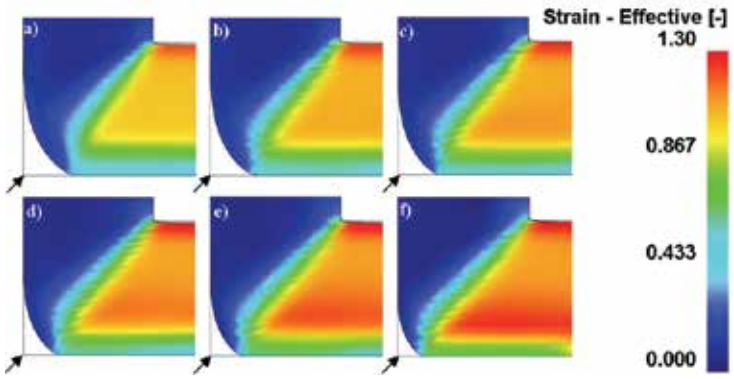

Fig. 5. ECAP channels filling in dependence on friction coefficient: a) f = 0,01; b) f = 0,12; c) f = 0,18; d) f = 0,25; d) f = 0,3 a e) f = 0,35

From graph is resulting that better channels filling by material were obtained when friction coefficient was increased. The numerical simulations confirm biggest localization of effective strain heterogeneity to bottom side of sample as is shown in Fig. 8.

The influence of σ-ε curves characterizing deformed material on channels filling was numerical simulated for σ-ε curves with linear (Fig. 9) and nonlinear (Fig. 10) strengthening. The measurement of lengths d_h and d_v for both type of σ-ε curves are given in Fig. 11, Fig. 12 and dependence of shape index of outer corner on angle of curves inclination is given in Fig. 13. From graphical dependences is resulting negligible influence of σ-ε strengthening type curves (linear and nonlinear strengthening) on channels filling for curve types 1-5. If strengthening curves are approaching to ideal rigid – plastic form with minimal strengthening (types 6-7) so differences in channel filling are observing.

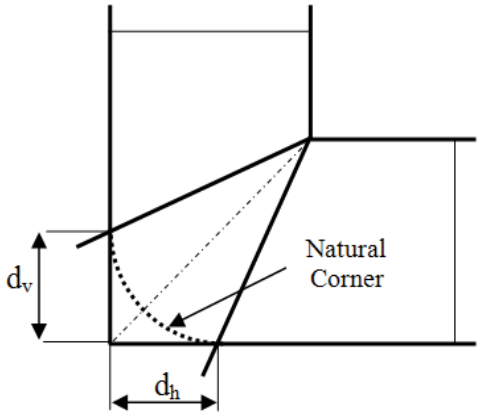

Fig. 6. Geometrical definition of channels

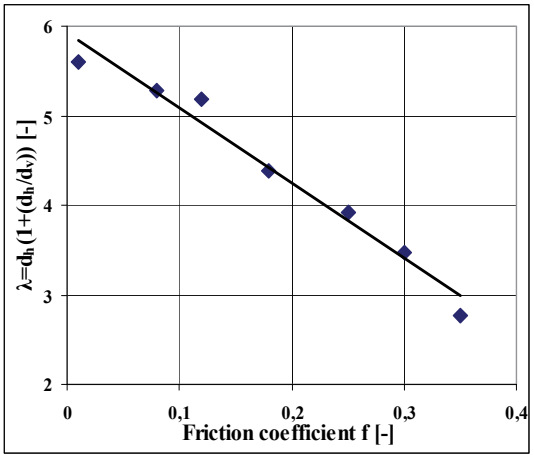

Fig. 7. Dependence of index of outer corner shape on friction coefficient

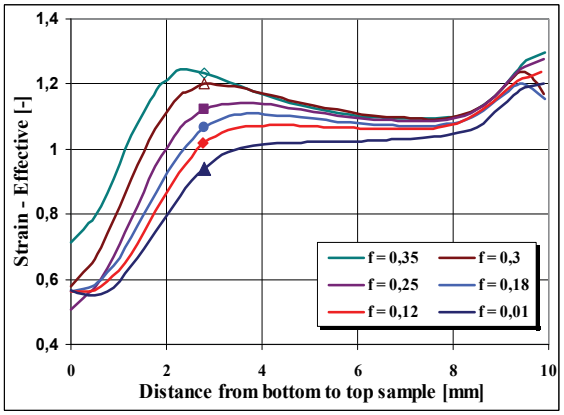

Fig. 8. Distribution of effective strain φ_{ef} in cross section sample on friction coefficient

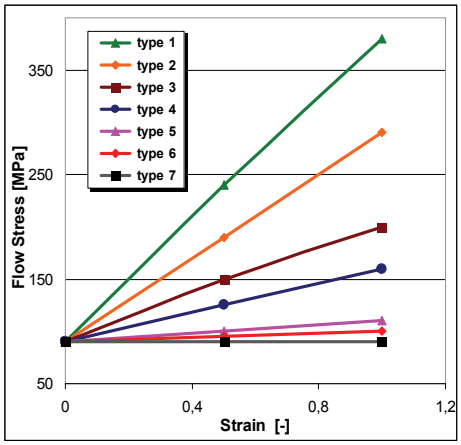

Fig. 9. The σ - ε curves with linear strengthening

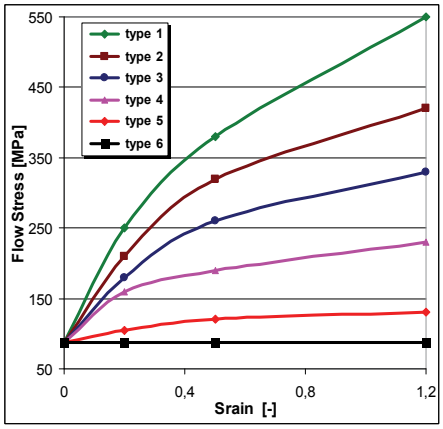

Fig. 10. The σ - ε curves with nonlinear strengthening

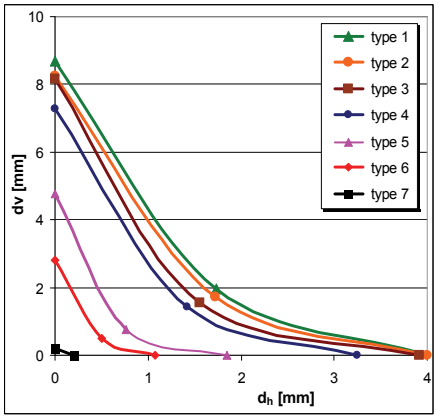

Fig. 11. Effect of σ - ε curves with linear strengthening on the channel outer filling

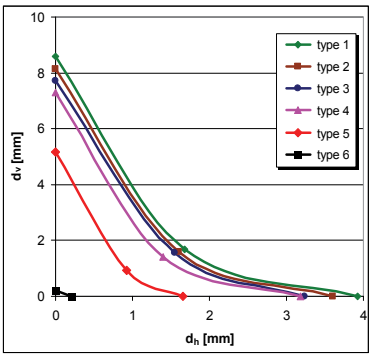

Fig. 12. Effect of σ - ε curves with nonlinear strengthening on the channel outer filling

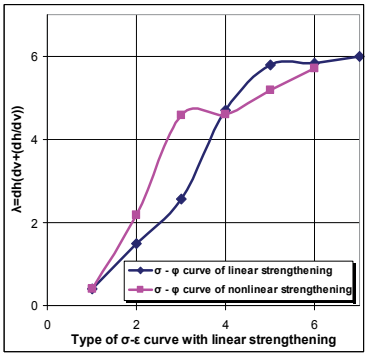

Fig. 13. Dependence of index of outer corner shapes on the type of strengthening curve

3.1.2 Mechanical and structural properties after ECAP

The change of mechanical properties in dependence on number of ECAP passes is shown in Fig. 14. Ultimate tensile strength (UTS) is slightly sensitive on ECAP passes and substructure formation. Yield strength (0,2% YS) is decreasing up to 6th pass where achieved local minimum. From 6th up to 12th pass is growing. Elongation to failure (El.) is inversing to 0,2% YS. Microhardness dependence is given in Fig. 15 from which resulting microhardness growth with an increase of ECAP passes.

TEM analysis was performed on samples after 4th, 6th, 8th and 12th ECAP passes and shown in Fig. 16 - 20.

Initial structure is creating with large polyedric grains (d_g ~ 650 μm) and low dislocation density. Cell substructure with subgrain diameter d_{sg} ~ 2,6 μm was searched after 4th and 6th ECAP passes and are given in Fig. 17, 18. Dislocations are generated with plastic deformation and arranged to dislocation walls, which later transform to subgrains with low or high angles, as it is seeing in Fig. 19. Subgrains are equiaxial with average size d_{sg} ~ 2,2 μm.

Substructure after 12th ECAP pass is equiaxial with low misorientation and average subgrain size d_{sg} ~ 1 μm (Fig. 20). Average subgrain size in dependence to number ECAP passes is given in Fig. 21. The significant substructure refinement was observed after 6th ECAP pass. Yield strength starts to grow also after 6th pass, what coincide with strengthening from grain size refinement after the Hall-Petch equation. Random coarse grains in fine structure matrix were observed after 4th and 12th ECAP pass as shown in Fig. 22.

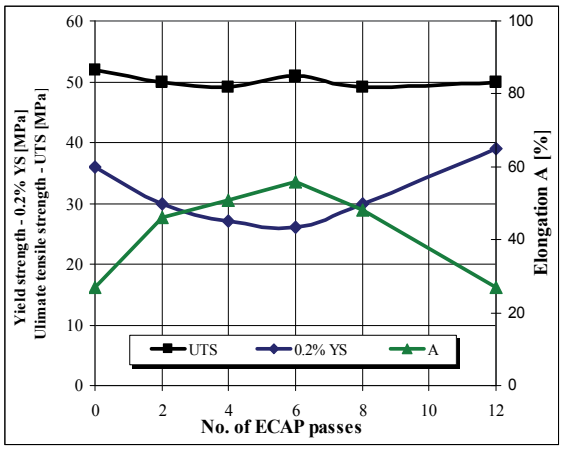

Fig. 14. Development of mechanical properties on ECAP passes

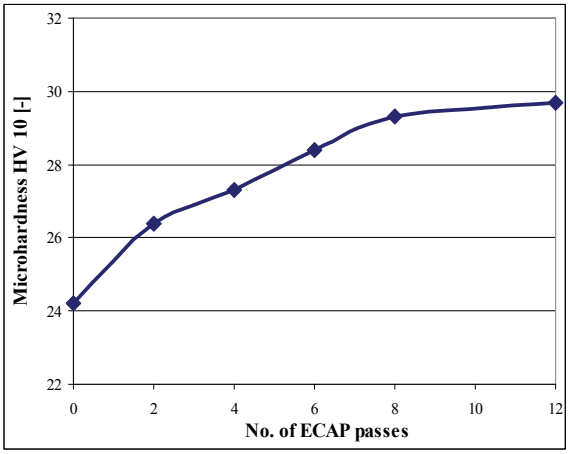

Fig. 15. Microhardness change on ECAP passes

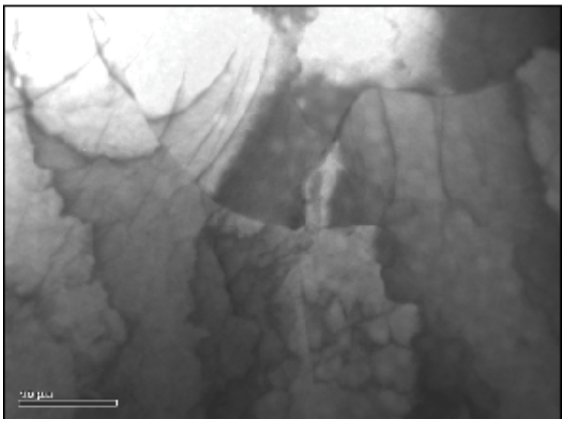

Fig. 16. TEM micrograph before ECAP (d_g ~ 650 μm)

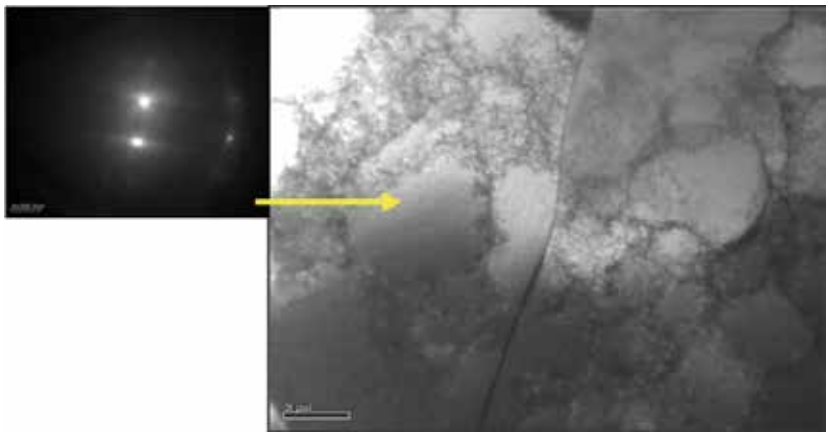

Fig. 17. TEM micrograph after 4th ECAP pass (d_{sg} ~ 2,6 μm)

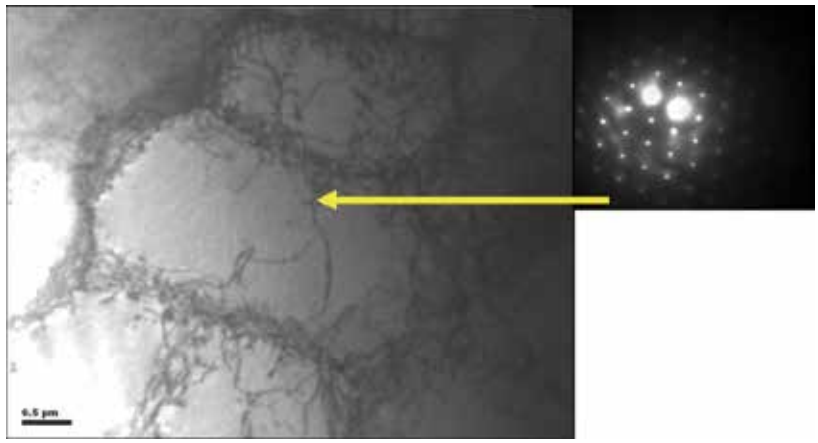

Fig. 18. TEM micrograph after 6th ECAP pass (d_{sg} ~ 2,6 μm)

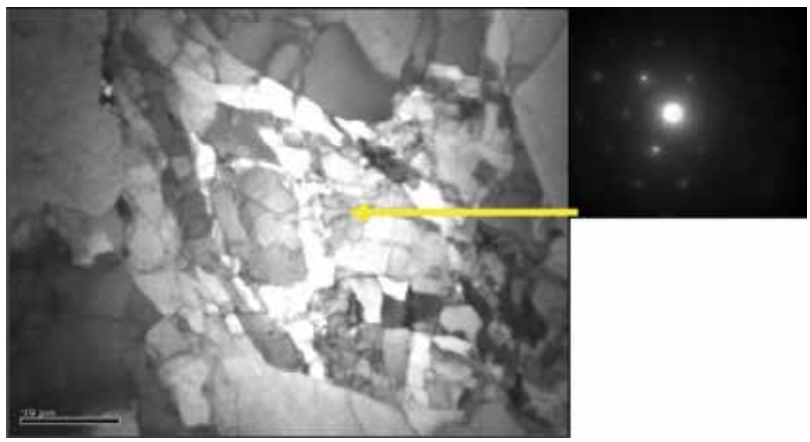

Fig. 19. TEM micrograph after 8th ECAP pass (d_{sg} ~ 2,6 μm)

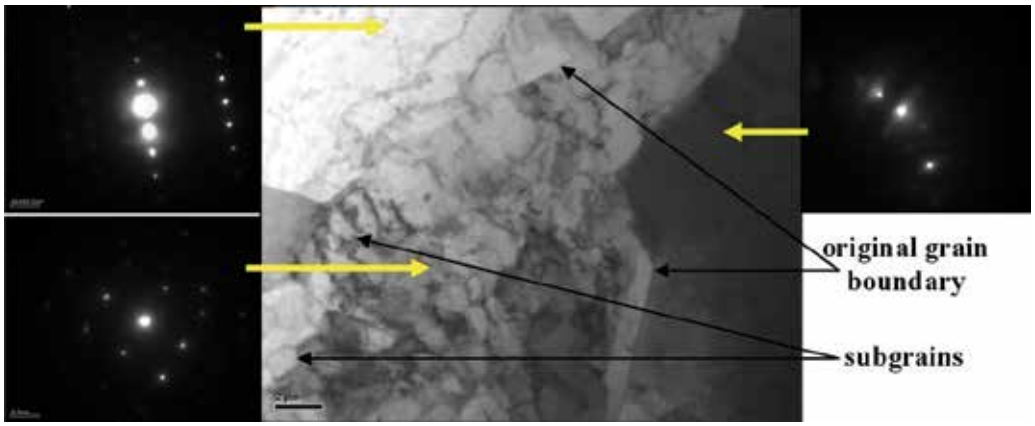

Fig. 20. TEM micrograph after 12th ECAP pass (d_{sg} ~ 0,98 μm)

This anomaly is nucleus of recrystallized subgrain with high angle grain boundary (HAGB). In literature does not exist clear opinion on high purity aluminium recrystallization at room temperature. Dynamic recovery (DR), dynamic recrystallization (DRX), metadynamic recrystallization (MDRX) and static recrystallization (SRX) are possible mechanisms to formation of fine grain structure with SPD at room temperature. Recrystallization of high purity aluminium (99,999%) deformed at room temperature was described (Choi et al., 1994) as DRX and as SRX. Less pure aluminium very slowly recrystallized with comparison of 99,999% pure aluminium (Kim et al., 2003); (Kim et al., 2007). From the literature analysis is resulting intensive sensitivity of aluminium softening (dynamic or static mechanism) in dependence on aluminium purity.

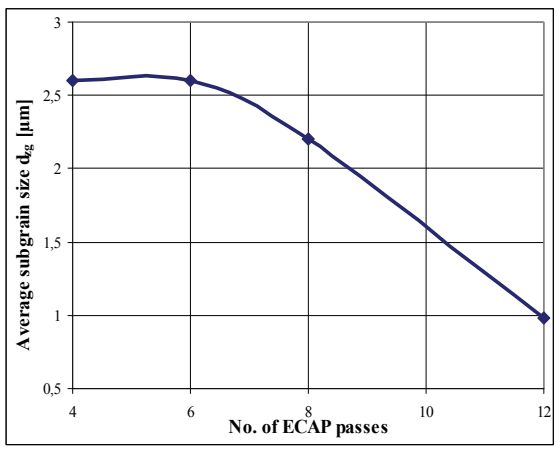

Fig. 21. Grain size change on ECAP passes

The measurement of deformation forces for two material grades (high purity aluminium and oxygen free high conductivity Cu) during ECAP processing were performed by tensometric sensors. The deformation forces were recalculated on deformation stresses and insert to Fig. 23. From graphical dependences are resulting two curve developments. One with decreasing and the other with increasing of deformation stresses. Deformation stress decreasing was observed for aluminium material and increasing for copper material.

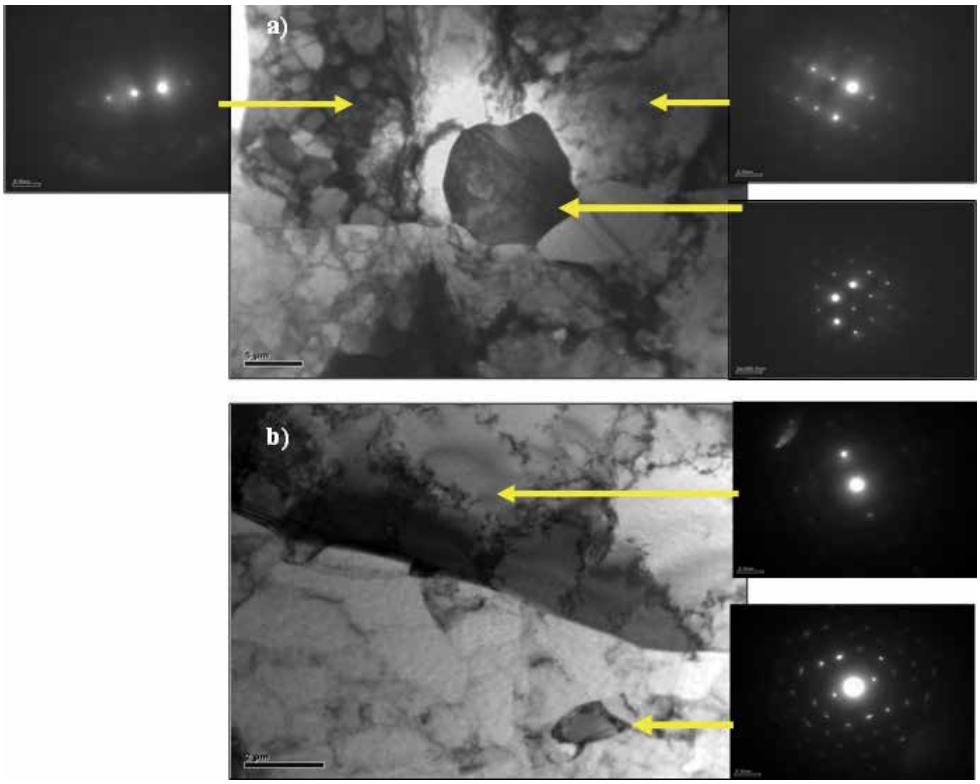

Fig. 22. Recrystallized grains after ECAP processing: a) 4th ECAP pass; b) 12th ECAP pass

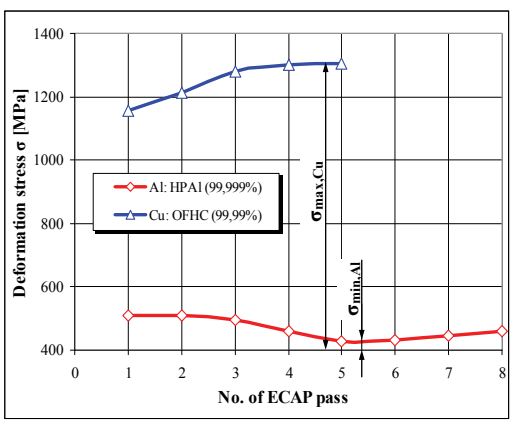

Fig. 23. Dependence of deformation stresses on ECAP passes for different materials

The deformation stress changes with connection of stacking fault energy (SFE) are observed. The high purity aluminium is material with high SFE on level 166 m.J.m^{-2} while OFHC copper is distinguishing with low SFE on level 40 m.J.m^{-2} (Humphreys & Hartherly, 1996); (Neishi et al., 2002).

The materials with high SFE are characterized with dynamic recovery while materials with low SFE by deformation strengthening follow by some kind of recrystallization mechanisms

what have good correlation with observed graphical experimental dependences. Therefore investigated high purity aluminium material is characterized up to 6th ECAP pass with decreasing of deformation stress caused by dynamic recovery and from 6th ECAP pass deformation stress is slightly growing. Similar development of yield strength dependence and inverse dependence of elongation were observed up to 6th and from 6th ECAP passes (Fig. 14). These characteristics dependences from 6th ECAP pass are related on the mechanical strengthening mechanism resulting from refinement of grain size (Fig. 21). On the other side dependence of deformation stress for OFHC copper is growing with the increasing of ECAP passes because of Cu is material with low SFE and mechanical strengthening can be subsequently accompany by some kind of recrystallization process. From Fig. 23 is resulting that ratio between deformation stresses in the 5th ECAP pass ($\sigma_{max,Cu}/\sigma_{min,Al}$) for high purity aluminium and OFHC copper has value 0,33. That means softening mechanisms realized by dynamic recovery was needed only 33% from maximal level of deformation stress occasioning mechanical strengthening which can be subsequently accompanying with possibility of recrystallization process.

3.2 Experimental results and discussion for Al-Cu-Mg-Zr aluminium alloy

3.2.1 Mechanical properties

The stress-strain curves under various processing conditions are plotted in Fig. 24.

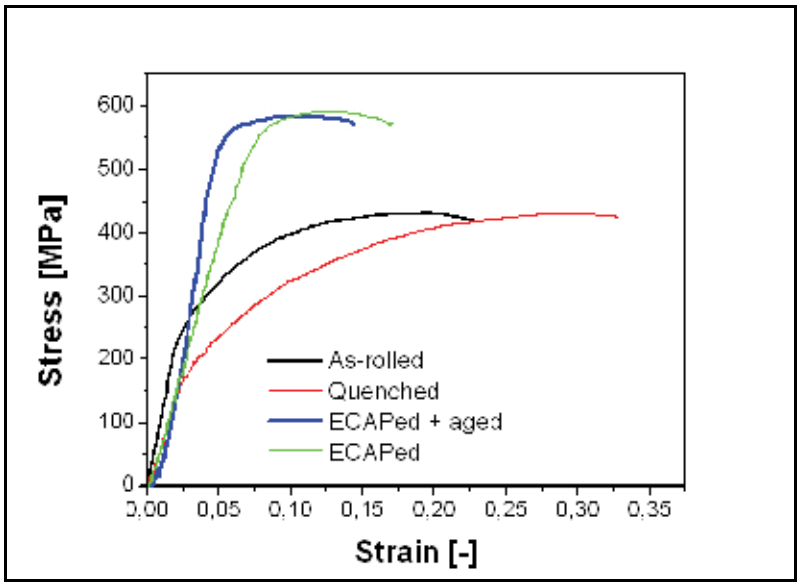

Fig. 24. Stress-strain curves of Al-Cu-Mg-Zr aluminium alloy prepared by different processing conditions

The implementation of SPD via ECAP method caused an increase in materials strength if compared to both systems without application of SPD (as-rolling and quenching). Markedly strengthening of materials after first pass was observed by authors (Vedani et al., 2003); (Cabbibo & Evangelista, 2006); (Kvačkaj et al., 2010). Strengthening of material is caused by grains refinement and strain hardening of solid solution.

The tensile results under various processing conditions are summarized in Table 5.

Processing	Mechanical properties			
	YS [MPa]	UTS [MPa]	El. [%]	Re. [%]
As-rolled	235	381	22,3	27,8
Quenched	157	394	32,8	34,4
ECAPed	511	593	17,1	18,0
ECAPed + aged	515	541	14,4	14,0

Table 5. Mechanical properties of investigated aluminium alloys Al-Cu-Mg-Zr

The difference in the strength values is basically due to the various materials modification. The reason for the increasing of strength and ductility in case of the as-rolled state in comparison to the quenched state was the reduction of strain hardening. The reason for the strength increasing in ECAP was SPD of analyzed alloy, which caused also a sensible decrease of ductility. ECAP increased the strength value approximately 35 % if compared to the as-rolled and quenched alloy. Values of yield strength of approximately 55 % and 70 % separately, of the as-rolled and quenched material were obtained. Overall very good complex mechanical and plastic properties were obtained after ECAP: yield strength of 511 MPa, ultimate tensile strength of 593 MPa, tensile elongation of 17,1 % and reduction in area of 20 %. It is clear that the result of such grains refinement is first of all related to the improvement of mechanical properties; it also increases markedly the density of lattice defects in the solid solution of Al-based alloys and thus accelerates the precipitation process of strengthening particles during the subsequent ageing (Valiev & Langdon, 2006), (Lowe & Valiev, 2000). Finally, present results show that grain refinement by ECAP can lead to a unique combination of strength and ductility. The achieved mechanical properties by ECAP and subsequent treatment can be useful for producing high strength and good ductility in precipitation-hardened alloys.

3.2.2 Fracture and structure investigation

The fracture surfaces analyses of investigated materials showed dominant of transcrystalline ductile fracture. The effect of plastic deformation was revealed in particles cracking for the relevant materials that are typical for aluminium alloys (Nový et al., 2005), (Ovid'ko, 2007); (Nový et al., 2009). During plastic deformation, particles were cracked and/or particles were divided from interphase surface by means of cavity failure systems, which after that exhibited in the formerly dimples, Fig. 25 and Fig. 26.

Detailed fractographical examinations revealed that there were two categories of dimples of transcrystalline ductile fracture: large dimples with average diameter in the range from 5 to 25 μm (arrow in Fig. 27 a), formed by the intermetallic particles on the bases of Fe and Si, which can be to visible by metallography examination (arrow in Fig. 28 b) and small dimples with average diameter in the range from 0,5 to 2,5 μm, formed by submicroscopic and dispersive particles, which were observed by TEM investigation, Fig. 26.

Different average diameters of dimples were obtained for the investigated materials, according to the treatment: as-rolled approximately 10 μm, quenched approximately 9,5 μm, ECAPed approximately 8,5 μm and ECAPed + aged approximately 7,8 μm. The difference between dimples was affected by various processing conditions. For the as-rolled state, the initiator can be identified in the $CuAl_2$ particles, while for the quenched; the role of initiators takes intermetallic particles based of Fe and Si. The SPD via ECAP method caused grains refinement, strain hardening of solid solution and intermetallic deformed particles.

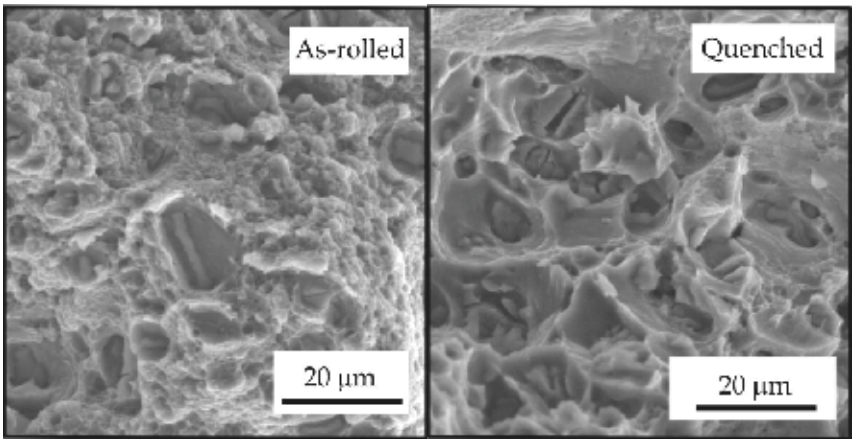

Fig. 25. Transcrystalline ductile fracture as-rolled state and quenched state

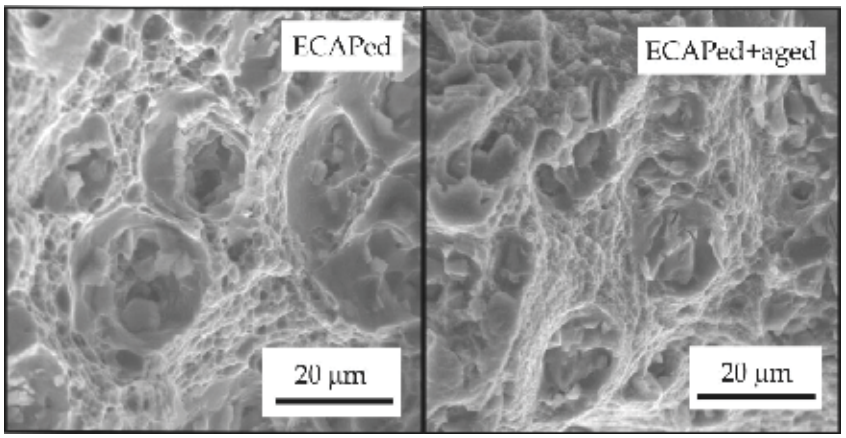

Fig. 26. Transcrystalline ductile fracture ECAPed state, and ECAPed + aged state

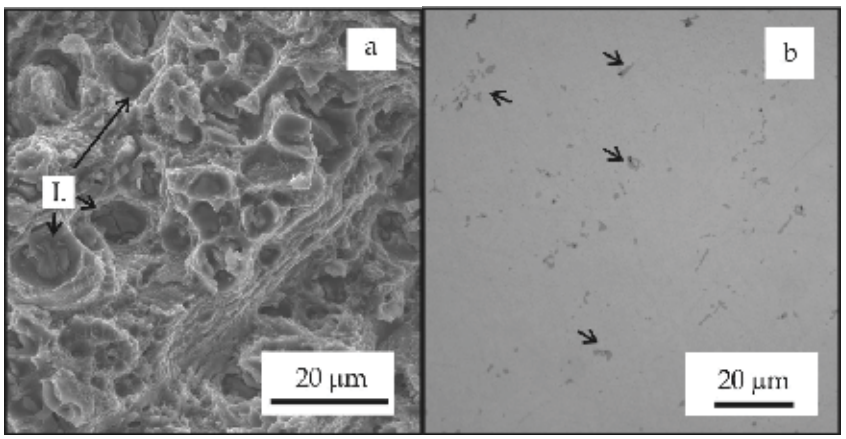

Fig. 27. a, b Intermetallic particles on the base of Fe and Si as a initiators of large dimples

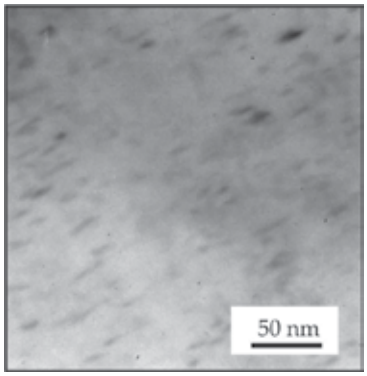

Fig. 28. TEM analyses revealed submicroscopic and dispersive particles as an initiators of small dimples

3.2.3 FEM investigation

Distributions of equivalent plastic deformation after one ECAP pass for both conditions are presented in the Fig. 29.

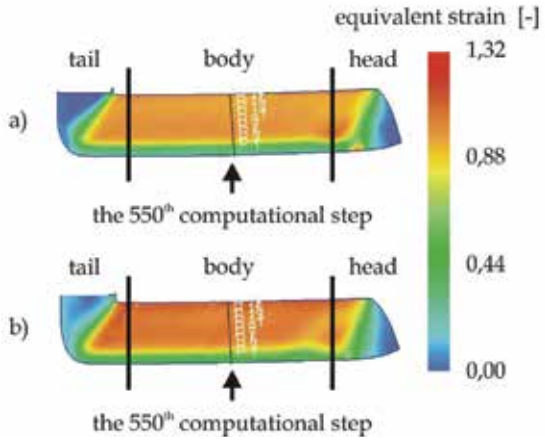

Fig. 29. Distribution of equivalent strain after one ECAP pass at the same forming condition: a) database material, and b) experimental material

Fig. 29 shows, that plastic deformation is non-uniformly distributed along the cross-section and also the length of specimen.

Along the workpiece length is possible to divide the plastic deformation into three deformation areas:

head – non-uniformity of plastic deformation is caused by non-uniformly material flow during junction from vertical to horizontal canal,

body – steady state of plastic deformation,

tail – non-uniformity of plastic deformation is related to the uncompleted pressing of specimen during the exit channel.

Non-uniformity of plastic deformation most be concentrated to the bottom part of the workpiece, in accordance with authors (Kvačkaj et al., 2007); (Kočiško et al., 2009); (Li et al., 2004); (Leo et al., 2007). Due to this fact, the material properties after ECAP are carried out only from body of specimen.

The Fig. 30 illustrates the distribution of equivalent plastic deformation in cross-section part of specimen for the 550th computational step (steady state area of plastic deformation) of both conditions.
Local changes were observed in maximum of curve, where the simulation analysis with database characteristic achieved effective strain value of 1,12 while in simulation analysis with experimental characteristic attained 1,2. The difference represented 7 %. That means the entry data from stress-strain curves did not affect the distribution of plastic deformation intensity in cross-section area of workpiece.

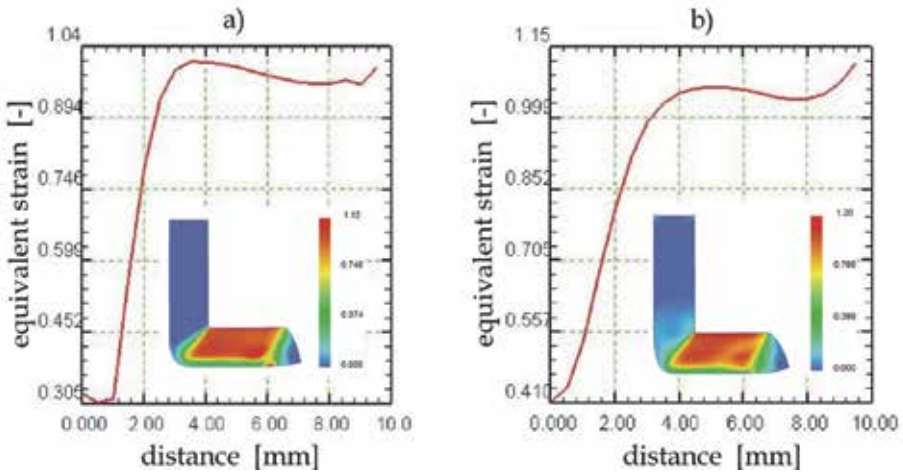

Fig. 30. Distribution of equivalent strain in cross-section part of workpiece in 550th computational step: a) database material, and b) experimental material

Fig. 31 illustrates the distribution of strain rate intensity for both conditions. Strain rate determined the plastic deformation area and/or the plastic deformation zone (PDZ). It can be seen that strain rate is concentrated in the narrow zone – PDZ. In all cases, the plastic deformation zone varies both along the workpiece axis and along the transverse direction from top to bottom as it is confirmed in (Kvačkaj et al., 2007). It is needed to keep in mind that ECAP deformation is generally non-homogeneous, especially when the die is rounded or if conditions lead to a free surface corner gap (Li et al., 2004). However, a disadvantage of the FE studies is that various different combinations like the workpiece, die design, the friction conditions, etc. are applied. All mentioned factors can deeply influence the simulation results and therefore make it difficult to compare results from different studies. Hence, studies for understanding PDZ during the forming process and interpreting the real forming conditions in ECAP process are still lacking.
It can be found from the distribution of strain rate intensity (the 550th computational step in the Fig. 31) that the strain rates are clearly different in case of the database and experimental material; in the inner side of the channel achieved an increase in strain rate about 29 % for experimental material characteristics.
Fig. 32 enables to interpret a temperature development during ECAP process.
Results from Fig. 32 that an increase in temperature during the process, from initial ambient temperature to 35,5 °C for database material and to 46 °C for experimental material. An increase in temperature is connected to heat transformation of plastic deformation part. The temperature of workpiece fail to reach a level of restoration processes for both investigated

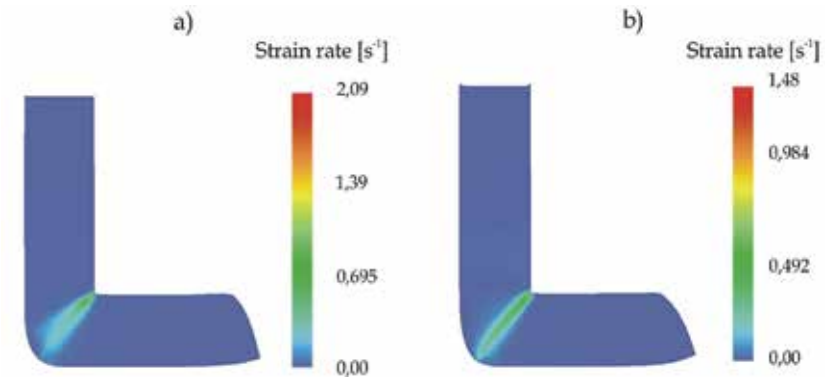

Fig. 31. Distribution of strain rate intensity along to cross-section in 550th computational step: a) database material, and b) experimental material

materials. In simulation to take heat transfer into consideration, for that reason during the ECAP process can to observe a heating of forming tools too. It is important point that temperature of forming tool not allowed to reach a tempering grade. It results from (Kvačkaj et al., 2007) that the significant recovery process can be recognized for temperatures over 300 °C.

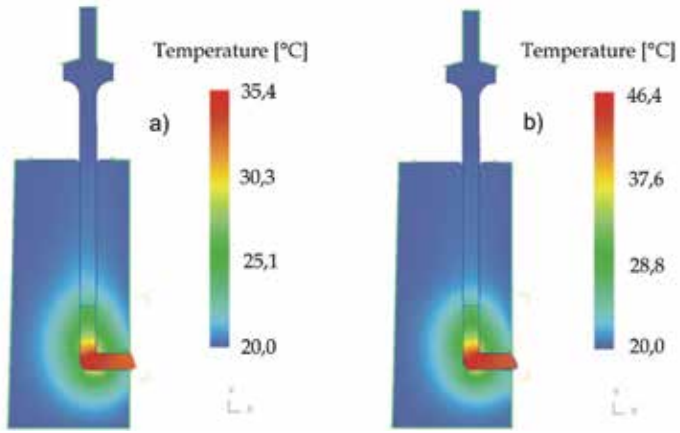

Fig. 32. Temperature development during ECAP process and heating of forming tools: a) database material, and b) experimental material

4. Conclusions

From mathematical simulations of ECAP process by FEM is resulting that the channels filling with material and effective plastic deformations are depends on contact friction, material stress – strain (σ-ε) curves and geometrical definition of ECAP die. Better channels filling by material was observed when friction coefficient was increased. The negligible effect of σ-ε strengthening type curves on channels filling was observed if curves had character rigid – plastic form with linear and nonlinear strengthening. If strengthening curves were approaching to ideal rigid – plastic form with minimal strengthening so differences in channel filling were observed.

The investigation of high purity Al (99,999%Al) material processed by ECAP method refers on slight sensitivity ultimate tensile strength in dependence on ECAP passes. The ultimate

tensile strength was change in interval UTS=49 – 52 MPa. Stronger influence from ECAP passes on yield strength, elongation, microhardness and subgrain diameter was recognized. The values were changed in following intervals: YS=26 – 39 MPa, A=27– 56 %, d_g=650 - 1μm. From the literature analysis is resulting non-uniform opinion on softening mechanisms of high purity Al during or after SPD in ECAP unit. The opinions are recognizing from recovery in dynamic and static regime up to recrystallization in dynamic, metadynamic and static regime. On the essential our results is resulting for high purity Al as material with high stacking fault energy, that softening mechanism up to 6th ECAP pass is dynamic recovery, whereas from 6th ECAP pass the mechanism mechanical strengthening was starting. This supporting viewpoint has good correlation with development of mechanical and substructural properties. On the other side OFHC copper is characterized as material with low stacking fault energy and mechanical strengthening was observed in dependence on ECAP passes. The local dynamic recrystallization grains were observed after 14th ECAP pass. The stress ratio resulting from graphical dependences was $\sigma_{max,Cu}/\sigma_{min,Al}$=0,33, what means that softening mechanisms realized by dynamic recovery needed only 33% from maximal level of deformation stress occasioning mechanical strengthening.
Tensile test results show that, in the stress-strain curves, the stress increased with increasing strain conditions due to severe plastic deformation via ECAP. However, it was observed also that the ECAP exhibited decrease in ductility.
Severe plastic deformation via ECAP may be a very useful process on increasing mechanical properties with only partial decrease and acceptable of ductility. Strengthening of material is caused by grains refinement and strain hardening of solid solution.
Fractographical examinations revealed that there were two categories of dimples of transcrystalline ductile fracture: large dimples, formed by the intermetallic particles and small dimples, formed by submicroscopic and dispersive particles.
The simulation analyses of ECAP process of Al-Cu-Mg-Zr aluminium alloy by means of the commercial two-dimensional finite element code DEFORM shows that in term of prediction individual parameters during forming processing was in the some case (strain rate intensity and temperature) sensible different, providing that material characteristic were given by database or on the basis experimentally determined stress-strain curve. The recorded changes in simulation can be explained to better knowledge of material characteristics from tensile test, by reason that material in them carries the all history of previous technological operations and using a data from program database it needn't exactly to correspond of material selection. In this regard, is necessary to consider in the simulation process to appear from knowledge of material characteristic receives by laboratory test of formability.

5. References

Alexandrov, I. V. , Zhilina, M. V. , Scherbakov, A. V. , Korshunov, A. I. , Nizovtsev, P. N. , Smolyakov, A. A. , Solovyev, V. P. , Beyerlein, I. J. , Valiev, R. Z. (2005). Formation of crystallographic texture during severe plastic deformation. *Archives of Metallurgy and Materials*, Vol. 50, No. 2, (2005) 281-294, ISSN 0860-7052

Balasundar, I. & Raghu, T. (2010). Effect of friction model in numerical analysis of equal channel angular pressing process. *Materials and Design*, Vol. 31, No. 1, (2010) 449-457, ISSN 0261-3069

Beyerlein, I. J. & Tome, C. N. (2004). Analytical modeling of material flow in equal channel angular extrusion (ECAE). *Materials Science and Engineering A*, Vol. 380, No. 1, (2004) 171–190, ISSN 0921-5093

Cabbibo, M. & Evangelista, E. (2006). A TEM study of the combined effect of severe plastic deformation and (Zr), (Sc plus Zr)-containing dispersoids on an Al-Mg-Si alloy. *Journal of Materials Science*, Vol. 41, No. 16, (2006) 5329-5338, ISSN 0022-2461

Cerri, E.; De Marco, P. P. & Leo, P. (2009). FEM and metallurgical analysis of modified 6082 aluminium alloys processed by multipass ECAP: Influence of material properties and different process settings on induced plastic strain. *Journal of Materials Processing Technology*, Vol. 209, No. 3, (2009) 1550-1564, ISSN 0924-0136

Choi, C.; Jeong, J.; Oh, C. & Lee, D. N. (1994). Room temperature recrystallization of 99.999 pct aluminum. *Scripta Metallurgica et Materialia*, Vol. 30, No. 3, (1994) 325-330, ISSN 0956-716X

Chuvil'deev, V. N.; Kopylov, V. I.; Gryaznov, M. Yu.; Sysoev, A. N.; Ovsyannikov B. V. & Flyagin A. A. (2008). Doubling of the strength and plasticity of a commercial aluminum-based alloy (AMg6) processed by equal channel angular pressing. *Doklady Physics*, Vol. 53, No. 11, (2008) 584-587, ISSN 1028-3358

Deform Manual (2003). Scientific Forming Technologies Corporation, version 8.0, Columbus

Dobatkin, S. V.; Zakharov, V. V.; Vinogradov, A. Yu.; Kitagawa, K.; Krasil'nikov, N. A.; Rostova T. D. & Bastarash E. N. (2006). Nanocrystalline structure formation in Al-Mg-Sc alloys during severe plastic deformation. *Russian Metallurgy (Metally)*, Vo. 2006, No 6, (2006) 533-540, ISSN 0036-0295

Dobatkin, S. V. & Sauvage X. (2009). Bulk Nanostructured Multiphase Ferrous and Nonferrous Alloys. In: *Bulk Nanostructured Materials*. Editor(s): Zehetbauer, M. J. & Zhu, Y. T. , 569-603,Wiley-VCH Verlag, ISBN 978-3-52731524-6, Weinheim

Dutkiewicz, J.; Masdeu, F.; Malczewski, P. & Kukuła, A. (2009). Microstructure and properties of α + β brass after ECAP processing. *Archives of Materials Science and Engineering*, Vol. 39, No. 2, (2009) 80-83, ISSN 1897-2764

Han, B. Q.; Lavernia, E. J. & Mohamed, F.A. (2005). Mechanical properties of nanostructured materials. *Reviews on Advanced Materials Science*, Vol. 9, No. 1, (2005) 1-16, ISSN 16065131

Humphreys, F.J. & Hartherly, M. (1995) *Recrystallization and related annealing phenomena*, Pergamon Press, ISBN 13: 9780080418841, Oxford

Figueiredo, R. B.; Pinheiro, I. P.; Aguilar, M. T. P.; Modenesi, P. J. & Cetlin, P. R. (2006). The finite element analysis of equal channel angular pressing (ECAP) considering the strain path dependence of the work hardening of metals. *Journal of Materials Processing Technology*, Vol. 180, No. 1-3, (2006) 30-36, ISSN 0924-0136

Mahallawy, N. E.; Shehata, F. A.; Hameed, M. A. E.; Aal, M. I. A. E. & Kim, H. S. (2010). 3D FEM simulations for the homogeneity of plastic deformation in Al–Cu alloys during ECAP. *Materials Science and Engineering A*, Vol. 527, No. 6, (2010) 1404-1410, ISSN 0921-5093

Maziarz, W.; Dutkiewicz, J.; Lityńska-Dobrzyńska, L.; Santamarta, R. & Cesari, E. (2010). Structure investigations of ferromagnetic Co-Ni-Al alloys obtained by powder metallurgy. *Journal of Microscopy*, Vol. 237, No. 3, (2010) 374-378, ISSN 0022-2720

Medeiros, N.; Lins, J. F. C.; Moreira, L. P. & Gouvêa, J. P. (2008). The role of the friction during the equal channel angular pressing of an IF-steel billet. *Materials Science and Engineering A*, Vol. 489, No. 1-2, (2008) 363-372, ISSN 0921-5093

Meyers, M.A.; Mishra, A. & Benson, D.J. (2006). Mechanical properties of nanocrystalline materials. *Progress in Materials Science*, Vol. 51, No. 4, (2006) 427-556, ISSN 00796425

Michna, Š.; Lukáč I.; et al. (2007). *Aluminium Materials and Technologies from A to Z*, Adin, ISBN 978-80-89244-18-8, Prešov.

Mondolfo, L. F. (1976). *Aluminium Alloys: Structures and Properties*. Butterworth-Heinemann, ISBN 0408706805, Oxford

Neishi, K.; Horita Z. & Langdon, T. G. (2002). Grain refinement of pure nickel using equal-channel angular pressing. *Materials Science and Engineering A*, Vol. 325, No. 1-2, (2002) 54–58, ISSN 0921-5093

Nový, F.; Palček, P. & Chalupová, M. (2005). Failure of Al-alloy AK 4-1c under creep-fatigue interaction conditions. *Kovove Materialy*, Vol. 43, No. 6, (2005) 447-456, ISSN 0023-432X

Nový, F.; Janeček, M. & Král, R. (2009). Microstructure changes in a 2618 alluminium alloy during ageing and creep. *Journal of Alloys and Compounds*, Vol. 487, (2009) 146-151, ISSN 0925-8388

Oh, S.J. & Kang S.B. (2003). Analysis of the billet deformation during equal channel angular pressing; *Materials Science and Engineering A*, Vol. 343, No. 1-2, (2003) 107-115, ISSN 0921-5093

Ovid'ko, I.A. (2005). Superplasticity and ductility of superstrong nanomaterials. *Reviews on Advanced Materials Science*, Vol. 10, No. 2, (2005) 89-104, ISSN 16065131

Ovid'ko, I.A. (2007). Review on the fracture processes in nanocrystalline materials. *Journal of Materials Science*, Vol. 42, No. 5, (2007) 1694-1708, ISSN *0022-2461*

Kim, H. S. (2001). Finite element analysis of equal channel angular pressing using a round corner die. *Materials Science and Engineering A*, Vol. 315, No. 1-2, (2001) 122-128, ISSN 0921-5093

Kim,W. J.; Chung, C. S.; Ma, D. S.; Hong, S. I. & Kim, H. K. Optimization of strength and ductility of 2024 Al by equal channel angular pressing (ECAP) and post-ECAP aging. *Scripta Materialia,*Vol. 49, No. 4, (2003) 333-338, ISSN 1359-6462

Kim, W. J. & Wang, J.Y. (2007). Microstructure of the post-ECAP aging processed 6061 Al alloys. *Materials Science and Engineering A,* Vol. 464, No. 1-2, (2007) 23–27, ISSN 0921-5093

Kobayashi, S.; Oh, S. I. & Altan, T. (1989). *Metal Forming and the Finite-Element Method, 1 ed.*, Oxford University Press, ISBN 978-0-19-504402-7, New York

Kočiško, R.; Kvačkaj, T.; Bidulská, J. & Molnárová, M.: New geometry of ECAP channel. *Acta Metallurgica Slovaca*, Vol. 15, No. 4, (2009) 228-233, ISSN 1335-1532

Kopylov, V. I. & Chuvil'deev, V. N. (2006). The Limit of Grain Refinement during ECAP Deformation. In: Severe Plastic Deformation: Towards Bulk Production of Nanostructured Materials, Burhanettin, S. A. Ed., Nova Science Publishers, 37-58, ISBN 1-59454-508-1, New York

Kováčová, A.; Kvačkaj, T.; Kvačkaj, M.; Pokorný, I.; Bidulská, J.; Tiža J. & Martikán M. (2010). The mechanical properties progress depending on strain rate and load investigation during ecap process. *Acta Metallurgica Slovaca*, Vol. 16, No. 2, (2010) 91-96, ISSN 1335-1532

Kvačkaj, T.; Sokolová, L.; Vlado M.; Vrchovinský V.; Mišičko, R. & Nový, Z. (2004). Influence of pulsation deformations on properties of steel grade Cr18Ni10. *High Temperature Materials and Processes,* Vol. 23, No. 1, (2004) 1-5, ISSN 0334-6455

Kvačkaj, T.; Sokolová, L.; Vlado, M. & Vrchovinský, V. (2005). Influence of deformation temperature and time on the mechanical properties of pulsation deformed stainless steel. *High Temperature Materials and Processes,* Vol. 24, No. 2, (2005) 139-144, ISSN 0334-6455

Kvačkaj, T.; Zemko, M.; Kočiško, R.; Kuskulič, T.; Pokorný, I.; Besterci, M.; Sülleiová, K.; Molnárová, M. & Kováčová, A. (2007). Simulation of ECAP process by finite element method. *Kovove Materialy*, Vol. 45, No. 5, (2007) 249-254, ISSN 0023-432X

Kvačkaj, T.; Kováčová, A.; Kvačkaj, M.; Pokorný, I.; Kočiško, R. & Donič, T. (2010). Influence of strain rate on ultimate tensile stress of coarse-grained and ultrafine-grained copper. *Materials Letters*, Vol. 64, No. 21, (2010 a) 2344-2346, ISSN 0167-577X

Kvačkaj, T.; Bidulská, J.; Fujda, M.; Kočiško, R.; Pokorný, I. & Milkovič, O. (2010). Nanostructure formation and properties in some Al alloys after SPD and heat treatment. *Materials Science Forum*, Vol. 633-634, (2010 b) 273-302, ISSN 0255-5476

Li, S.; Bourke, M. A. M.; Beyerlein, I. J.; Alexander, D. J. & Clausen B. (2004). Finite element analysis of the plastic deformation zone and working load in equal channel angular extrusion. *Materials Science and Engineering A*, Vol. 382, No. 1-2, (2004) 217-236, ISSN 0921-5093

Lityńska-Dobrzyńska, L.; Dutkiewicz, J.; Maziarz, W. & Rogal, ł. (2010). TEM and HRTEM studies of ball milled 6061 aluminium alloy powder with Zr addition. *Journal of Microscopy*, Vol. 237, No. 3, (2010) 506-510, ISSN 0022-2720

Lowe, T. C. & Valiev, R. Z. (2000). *Investigations and Applications of Severe Plastic Deformation,* Kluwer Academic Publishers, ISBN 0-7923-6280-2, Dordrecht, Netherlands

Leo, P.; Cerri, E.; De Marco, P. P. & Roven H. J. (2007). Properties and deformation behaviour of severe plastic deformed aluminium alloys. *Journal of Materials Processing Technology*, Vol. 182, No. 1-3 (2007) 207-214, ISSN 0924-0136

Pernis, R.; Kasala, J. & Bořuta J. (2009). Hot torsion tests of cartridge brass MS70. *Acta Metallurgica Slovaca*, Vol. 15, No. 1, (2009) 5-14, ISSN 1335-1532

Semiatin, S. L.; Delo, D. P. & Shell, E. B. (2000). The effect of material properties and tooling design on deformation and fracture during equal channel angular extrusion. *Acta Materialia*, Vol. 48, No. 8, (2000) 1841-1851, ISSN 1359-6454

Stoica, G.M.; Fielden, D.E.; McDaniels, R.; Liu, Y.; Huang, B.; Liaw, P.K.; Xu, C. & Langdon, T.G. (2005). An analysis of the shear zone for metals deformed by equal-channel angular processing. *Materials Science and Engineering A*, Vol. 410–411, (2005) 239–242, ISSN 0921-5093

Valiev, R. Z.; Islamgaliev, R. K. & Alexandrov I. V. (2000). Bulk nanostructured materials from severe plastic deformation. *Progress in Materials Science,* Vol. 45, No. 2, (2000) 103-189, ISSN 0079-6425

Valiev, R. Z. & Langdon, T. G. (2006). Principles of equal-channel angular pressing as a processing tool for grain refinement. *Progress in Materials Science,* Vol. 51, No. 7, (2006) 881-981, ISSN 0079-6425

Vedani, M.; Bassani, P.; Cabibbo, M. & Evangelista, E. (2003). Experimental aspects related to equal channel angular pressing of a commercial AA6082 alloy. *Metallurgical Science and Technology*, Vol. 21, No. 2, (2003) 3-9, ISSN 0393-6074

Yoon, S. Ch. & Kim, H. S. (2008). Finite element analysis of the effect of the inner corner angle in equal channel angular pressing. *Materials Science and Engineering A*, Vol. 490, No. 1-2, (2008) 438-444, ISSN 0921-5093

Zhernakov, V. S., Budilov, I. N., Raab, G. I., Alexandrov, I. V. & Valiev, R. Z. (2001). A numerical modelling and investigations of flow stress and grain refinement during equal-channel angular pressing. *Scripta Materialia*, Vol. 44, No. 8-9, (2001) 1765-1769, ISSN 1359-6462

Zehetbauer, M. J.; Zeipper L. & Schafler E. (2006). Modelling Mechanical Properties of SPD Materials During and After Severe Plastic Deformation. In: *Nanostructured Materials by High-Pressure Severe Plastic Deformation*, NATO Science Series II: Mathematics, Physics and Chemistry, Vol. 212, Zhu, Y. T & Varyukhin, V., 217-226, DOI: 10.1007/1-4020-3923-9_30

Zehetbauer, M. J. & Estrin, Y. (2009). Modeling of Strength and Strain Hardening of Bulk Nanostructured Materials. In: *Bulk Nanostructured Materials*, Zehetbauer, M. J. & Zhu, Y. T. , 109-136,Wiley-VCH Verlag, ISBN 978-3-52731524-6, Weinheim

2

An Evaluation of Severe Plastic Deformation on the Porosity Characteristics of Powder Metallurgy Aluminium Alloys Al-Mg-Si-Cu-Fe and Al-Zn-Mg-Cu

Róbert Bidulský[1], Marco Actis Grande[1]
Jana Bidulská[2], Róbert Kočiško[2] and Tibor Kvačkaj[2]
[1]*Politecnico di Torino – Sede di Alessandria*
[2]*Technical University of Košice, Faculty of Metallurgy*
Department of Metals Forming
[1]*Italy*
[2]*Slovakia*

1. Introduction

Light weight aluminium alloys, showing excellent workability, high thermal and electrical conductivity, represent a good choice for the powder metallurgy (PM) industry to produce new materials having unique capabilities, not currently available in any other powder metal parts. Moreover the requirement on mechanical properties (i.e. high tensile strength with adequate plasticity) should assure an increasing role for aluminium alloys in the expanding PM market.

Room temperature tensile strengths in aluminium based metal matrix composites (MMC) in excess of 800 MPa have been reported (Guo & Kazama, 1997). However, PM based MMC currently show very limited application, also due to the high costs of production, thus having a low commercial appeal for both producers and end users. The application for aluminium powders is basically in the production of PM parts for structural and non-structural purposes in the transportation and commercial areas. Press and sinter products, blends of aluminium and elemental alloy powders are pressed into intricate configurations and sintered to yield net or near-net shapes. There are two interesting classes of commercial press and sinter aluminium alloys: Al-Mg-Si-Cu and Al-Zn-Mg-Cu-(Si). The first alloy displays moderate strength (the level of tensile strength is 240 MPa) while the latter alloy develops high mechanical properties (the level of tensile strength is 330 MPa) in both the as-sintered and heat-treated conditions. Solid solution strengthening and precipitation hardening can contribute to the higher strength values of the commercial alloys. (Pieczonka et al., 2008) report transverse strength of aluminium-based PM alloys in the range of 400 MPa (Al-Mg-Si-Cu) to 550 MPa (Al-Zn-Mg-Cu).

It's well known (Bidulská et al., 2008 a) that conventional forming methods and heat treatment can determine a limit in the level of strength-plastic characteristics adequate to structural properties. One possible way for achieving higher mechanical properties is

represented by severe plastic deformation (SPD), such as Equal Channel Angular Pressing (ECAP) (Valiev & Langdon, 2006); (Bidulská et al., 2008 b), (Kočiško et al., 2009); (Bidulská et al., 2010 a), as it is further confirmed in (Valiev et al., 2000), (Vinogradov et al., 2002). In the PM area, SPD is a relatively new technological solution for achieving high strength (Lapovok, 2005); (Wu et al., 2008); (Bidulská et al., 2010 b).

Al-Zn-Mg-Cu PM alloys, due to zinc show a poor sintering aid; these alloys do not have a good sintering response either. The high vapour pressure of zinc also gives rise to additional porosity, particularly when elemental powders are used (Lumley & Schaffer, 1998). Al-Zn-Mg-Cu PM alloys have been introduced as elemental powders or rich masteralloys (Neubing & Jangg, 1987); (Miura et al., 1993); (Danninger et al., 1998); (Neubing et al., 2002); (Gradl et al., 2004).

Solid state sintering of aluminium alloys has so far been unsuccessful, mainly due to the stable oxide layers on each particle. The main reason is the relative diffusion rates through the oxide and the aluminium alloys (Schaffer et al., 2001). Some activation is necessary to overcome this barrier and activate the sintering process by effective liquid phase sintering. An essential requirement for effective liquid phase sintering is a wetting liquid. Based on thermodynamically approach, magnesium reacts with aluminium oxide forming spinel, facilitating the disruption of oxide layer and thus wetting by liquid (Ziani & Pelletier, 1999); (Martín et al., 2002); (Martín & Castro, 2003). The reaction may be facilitated during sintering by diffusion of the magnesium through the aluminium matrix and will be accompanied by a change in volume, creating shear stresses in the film, ultimately leading to its break up. This is beneficial to the diffusion, wetting and therefore sintering. Several researches for a suitable design of various aluminium alloys for successful sintering (Martín et al., 2004); (Kim et al., 2004); (Rout et al., 2004); (Schaffer et al., 2001) have been developed. In particular, the effect of copper in the alloys seems to be efficacious and therefore the sintering behaviour of Al-Zn-Mg-Cu alloys needs to be developed properly. Authors (Kehl & Fischmeister, 1980) suggested that the Al–$CuAl_2$ eutectic can wet Al_2O_3 at 873 K. However, magnesium additions to molten aluminium reduce the contact angle sufficiently to produce wetting (Ip et al., 1993); (Liu et al., 1992). The work of adhesion of liquid metals on oxide surfaces increases with the free energy of formation of the metal oxide. It is therefore apparent that the oxide on aluminium is a barrier to sintering and needs to be overcome. Several works analyze the use of sintering additives on enhancing aluminium sinterability (Pieczonka et al., 2008); (Danninger et al., 1998), but few ones concentrated onto the evaluation of the role of porosity (Martín et al., 2004) on sintering behaviour and then on mechanical properties.

Most of the properties of PM materials are strongly related to porosity. Porosity can be used as an indicative parameter to evaluate and control the processes which the components underwent (Salak, 1997). The pores act as crack initiators and due to their presence distribution of stress is inhomogeneous across the cross section and leads to reduction of the effective load bearing area. Both the morphology and distribution of pores have a significant effect on the mechanical behaviour of PM materials. Two types of porosity are typically observed in sintered materials (Salak, 1997): interconnected and isolated porosity. Interconnected porosity has a more pronounced effect on properties than isolated porosity. The effect of porosity on the mechanical properties depends on the following factors (Pietrowski & Biallas, 1998); (Esper & Sonsino, 1994); (Marcu Puscas et al., 2003); (Bidulská et al., 2010 a); (Beiss & Dalgic, 2001):

- the quantity of pores (i.e., the fractional porosity) ;
- their interconnection;

- size;
- morphology;
- distribution;
- chemical composition;
- lubricant;
- die design and
- in terms of sintering:
- atmosphere,
- temperature and
- time.

In order to precisely evaluate the powder behaviour, new approaches are necessary (Hryha et al., 2009); (Mihalikova, 2010), as well as mathematical and computer simulation (Kim, 2002); (Bidulská et al., 2008 c); (Kvačkaj et al., 2007), mainly in the description of densification behaviour after SPD process.

In order to describe the dimensional and morphological porosity characteristics, the dimensional characteristic D_{circle} and the morphological characteristics f_{shape} and f_{circle} have been identified as the most effective parameters. The description of parameters is reported as follows:

- D_{circle} is the diameter of the equivalent circle that has the same area as the metallographic cross-section of the pore.
- f_{shape} and f_{circle} reflect the form of the pores.

The f_{shape} represents pore elongation, while f_{circle} depicts pore profile irregularity. Both parameters range between 0 and 1, being equal to unity for a circular pore. Elongation (elliptical deformation) as well as irregularity of the pore profile results in small values of f_{shape} and f_{circle} approaching 0 for highly elongated ones (Powder Metal Technologies and Applications, 1998); (DeHoff & Aigeltinger, 1970); (Marcu Puscas et al., 2003). Quantitative image analysis of investigated material treats pores as isolated plane two-dimensional objects in solid surroundings (Fig. 1).

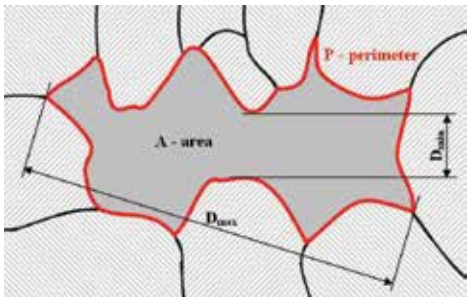

Fig. 1. The base characteristics by quantitative image analysis

The base characteristics are maximum and minimum pore dimensions D_{max} and D_{min}, pore area A, perimeter P and the diameter of the equivalent circle D_{circle}.

2. Experimental conditions

A commercial ready-to-press aluminium based powders (ECKA Alumix 321 and ECKA Alumix 431) were used as materials to be investigated. Formulations of the tested alloys are presented in Table 1 (wt. %).

Alumix 321					
Al	**lubricant**	**Mg**	**Si**	**Cu**	**Fe**
balance	1.50	0.95	0.49	0.21	0.07
Alumix 431					
Al	**lubricant**	**Mg**	**Zn**	**Cu**	**-**
balance	1.0	2.5	5.5	1.6	-

Table 1. Chemical compositions of investigated PM aluminium alloys

Particles size distribution, usually representing the mass percentage retained upon each of series of standard sieves of decreasing size and the percentage passed by the sieve of finest size, was carried out by sieve analyzer according to ISO 4497. The apparent density of powders was determined according to MPIF Standard 04. The tap density of powders was determined according to MPIF Standard 46. Specimens were obtained using a 2000 kN hydraulic press, applying different pressures. Unnotched impact energy specimens 55×10×10 mm^3 (ISO 5754) were prepared. The green compacts were weighed with an accuracy of ± 0.001 g. The dimensions were measured with a micrometer calliper (± 0.01 mm). Specimens were dewaxed in a ventilated furnace (Nabertherm) at 673 K for 3600 s^{-1}. Sintering was carried out in a vacuum furnace (TAV) at 883 K for 1800 s^{-1}, with an applied cooling rate (post sintering) of 6 K/s. The cooling rate was monitored and recorded by means of thermocouples inserted in the central axis and close to the surface of the specimen. In vacuum furnaces, the cooling rate is generally determined by the pressure of the gas (N_2) introduced into the chamber. The SPD processes were dived to two separately steps, first step was ECAP-BP process and second was ECAP process. The set-up of ECAP-BP for the produced PM materials consisted of a vertical entrance channel with a forward pressing plunger and a horizontal exit channel with a back plunger providing a constant back pressure during pressing. The die had a 90° angle with sharp corners and channels of 6×6 mm^2 in the cross section. Specimens were then inserted in the entrance channel with graphite lubrication. A heating device was employed to heat the die to 523 K, which was kept under control to ± 1 K through a thermocouple mounted close to the intersection of the channels. A back pressure of 100 MPa was used. The specimens were ECAPed-BP for 1 pass. The ECAP was realized by hydraulic equipment at room temperature, which makes it possible to produce the maximum force of 1 MN. The die had a 90° angle with sharp corners and channels of diameter 10 mm in the cross section. The specimens were ECAPed for 1 pass.

Optical characterization was carried out on the minimum of 10 different image fields. For determination porosity characteristics were used magnification 100x for specimens prepared pressing and sintering and 500x for ECAPed specimens. Pores were recorded and processed by Leica Qwin image analysis system.

From these primary data a huge variety of secondary quantities can be derived which are used to describe pore size and pore shape. The scatter or deviations from primary data are mostly caused by delaminated specimens that were found in investigated aluminium alloys, mainly in low pressing pressure due to the low green strength or at very high pressing pressure due to the work hardening. The results in this investigation were sorted in number of processing pores in terms of processing conditions; for specimens prepared pressing and

sintering were processed a minimum of 1000 pores and for ECAPed specimens were processed a minimum of 300 pores.
The calculations of both morphological parameters are reported as follows:

$$f_{shape} = \frac{D_{\min}}{D_{\max}} = \frac{a}{b} \quad [-] \tag{1}$$

where:
D_{min} [μm], the parameter representing minimum of Feret diameter;
D_{max} [μm], the parameter representing maximum of Feret diameter;
and

$$f_{circle} = \frac{4 \cdot \pi \cdot A}{P^2} \quad [-] \tag{2}$$

where:
A [μm²], the area of the metallographic cross-section of the pore, as the form

$$A = \pi \cdot a \cdot b \quad \left[\mu m^2\right] \tag{3}$$

P [μm], the perimeter of the metallographic cross-section of the pore, as the form

$$P = \pi \left[1.5 \cdot (a \cdot b) - \sqrt{a \cdot b}\right] \quad [\mu m] \tag{4}$$

3. Results and discussion

3.1 Effect of compacting pressure

The first stage of rigid die compaction is a basic forming technique used in the production of a lot of PM materials. It is primarily uniaxial compaction and the forming operation employs either a mechanical or a hydraulic press. A classical way for the evaluation of the powder compressibility is the relationship between the density or porosity and the applied pressure (Kawakita & Lüdde, 1971); (Panelli & Filho, 2001); (Hryha et al., 2008); (Denny, 2002); (Bidulská et al., 2009); (Bidulský et al., 2008). Different compacting pressures have been applied for the identification of the compressibility behaviour (100, 200, 300, 400, 500, 600 and 700 MPa) and the following compressibility equation (Dudrová et al., 1982); (Dudrová et al., 1983); (Parilák et al., 1983); (Parilák et al., 2004) was used:

$$P = P_0 \cdot \exp\left(-K \cdot p^n\right) \quad [\%] \tag{5}$$

where:
P [%], porosity achieved at an applied pressure p;
P_0 [%], apparent porosity calculated from the value of experimentally estimated apparent density:

$$P_0 = \left[1 - \frac{\rho_a}{\rho_{th}} \cdot 100\right] \quad [\%] \tag{6}$$

p [MPa], applied pressure;
K [-], a parameter related to particle morphology;
n [-], a parameter related to activity of powders to densification by the plastic deformation only.
Using the linear form of equation (5):

$$\ln\left[\ln\left(\frac{P_0}{P}\right)\right] = -\ln K + n \cdot \ln p \tag{7}$$

The parameters K and n can be calculated by linear regression analysis. A linear relationship between the parameters K and n was found and described in (Parilák et al., 2004):

$$\ln K = f(p): \quad \ln K = a - b \cdot n \tag{8}$$

where:
a=1.432;
b=7.6;
correlation coefficient r=0.9665.
The measured characteristics of the as-received aluminium powders are presented in Table 2 and Table 3, where the particle size distribution of both investigated aluminium alloys are reported. It can be seen from the results that the largest fraction of particles for the investigated material is in range of 63 to 100 μm. Particle size distribution of investigated aluminium alloys are presented in Table 2 and Table 3.

Size fraction [μm]	Fraction [%]	St. deviation
200-250	**1.4**	1.6
160-200	**7.3**	0.7
100-160	**28.7**	8.7
63-100	**48.8**	7.3
45-63	**8.8**	3.5
<45	**5**	5

Table 2. Particle size distribution of investigated Al-Mg-Si-Cu-Fe aluminium alloy

Size fraction [μm]	Fraction [%]	St. deviation
200-250	**1**	1.4
160-200	**3.4**	0.9
100-160	**26.2**	8.3
63-100	**31.2**	8.5
45-63	**17.2**	5.3
<45	**21**	7.1

Table 3. Particle size distribution of investigated Al-Zn-Mg-Cu aluminium alloy

Variations in particle size distribution and consequently the uniformity of powder mixes significantly influence the specimens' density and the mechanical properties including strength, wear and fatigue. Therefore, particle size distribution strongly affected apparent and tap density (Table 4). The finer Al-Zn-Mg-Cu alloy achieved 3 times higher tap density than Al-Mg-Si-Cu-Fe alloy. For example, the powders with a higher tap density generally have a lower sintered density than powders of similar size but different shape. The smaller the particles the greater the specific surface of the powder system is. (Powder Metal Technologies and Applications, 1998) suggested that this phenomenon increases the friction between particles and subsequently decreases the apparent density.
Table 4 reports the density properties of the studied systems.

No.	ρ_a [g.cm^{-3}]	ρ_t [g.cm^{-3}]	i [-]	ρ_{th} [g.cm^{-3}]
Al-Mg-Si-Cu-Fe	1.09	1.25	1.15	2.7134
Al-Zn-Mg-Cu	1.10	3.9	1.23	2.7213

Table 4. The fundamental density properties of investigated aluminium alloys

ρ_a is the apparent density, ρ_t is the tap density, i is the ratio ρ_{th} / ρ_a.
Table 5 shows the compressibility behaviour of the investigated systems.

No.	Po [%]	K·10^{-2} [-]	n [-]	p_1 [MPa]	r [-]
Al-Mg-Si-Cu-Fe	59.83	1.57	0.4514	40.5	0.9934
Al-Zn-Mg-Cu	59.58	0.60	0.5822	106.2	0.9994

Table 5. Compressibility parameters of investigated aluminium alloys

p_1 represents the fictive pressure.
According to data listed in Table 5, the compressibility parameter n is related to the activity of powders to densification by the plastic deformation. In case of powders with high plasticity, n is close to 0.5; in case of low plasticity, n is close to 1. The results show excellent trends for both aluminium alloys. Al-Mg-Si-Cu-Fe alloy (n = 0.4514) shows a higher ability to plastically deform than Al-Zn-Mg-Cu alloy (n = 0.5822).
The effect of powder morphology also reflects in the values of the compressibility parameter K, which is lower for Al-Zn-Mg-Cu (K = 0.60·10^{-2}) than for system Al-Mg-Si-Cu-Fe (K = 1.57·10^{-2}). The difference between Al-Mg-Si-Cu-Fe and Al-Zn-Mg-Cu system is connected with the effect of particle geometry (represented by particle size distribution). It is very important to note that the lubrication of aluminium powder during compaction and ejection has to be considered since it has a strong tendency to stick to the tooling (Kehl et al., 1983); (Dudas & Dean, 1969); (Lefebvre et al., 2002).
Fig. 2 and Fig. 3 show the relationship between experimental and calculated data according to the aforementioned equations.
P_1 represents the "work" related to the densification done by particles transient rearrangement (for n=1). Compressibility of the Al-Mg-Si-Cu-Fe alloy is slightly higher than that of the Al-Zn-Mg-Cu alloy, mainly in the area of pressing pressures from 100 to 500 MPa.
The compressibility equation (5) enables to calculate the pressure p_1 needed for achieving almost close to zero porosity, only by particle movements. The results show a shifting from 106.2 MPa (Al-Zn-Mg-Cu) to 40.5 MPa for Al-Mg-Si-Cu-Fe.

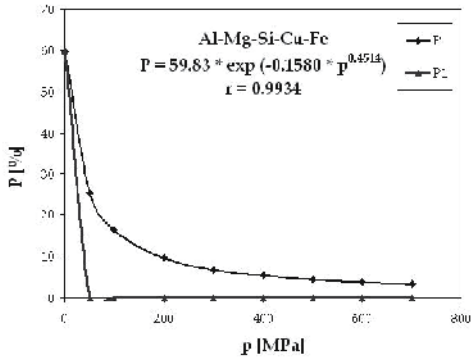

Fig. 2. Compressibility curves of Al-Mg-Si-Cu-Fe aluminium alloy

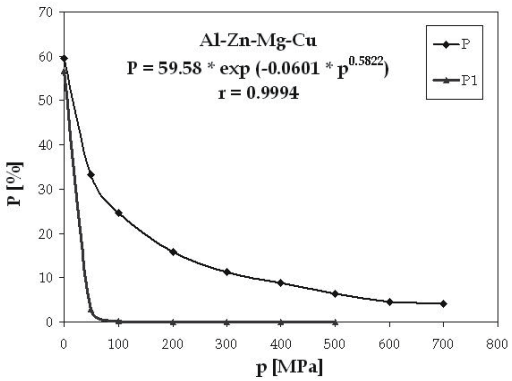

Fig. 3. Compressibility curves of Al-Zn-Mg-Cu alloy

The unetched microstructures after pressing are shown in the following figures.
Fig. 4 presents the typical microstructures for low pressures when the densification of the powder occurs by particle rearrangement (translations and rotations of particles) providing a higher packing coordination. Lower pressure creates high volume of porosity. Using low pressure may lead to edge blunting and porosity agglomeration, consequently a low green strength was found. It is clear visible, mainly in the microstructure of Al-Zn-Mg-Cu alloy.

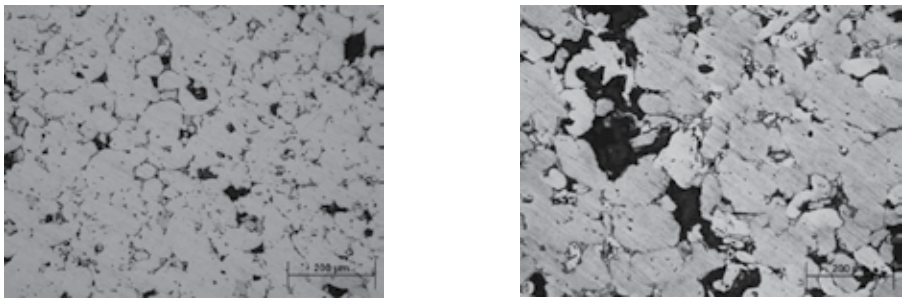

Fig. 4. Microstructure of aluminium alloys at 50 MPa, left - Al-Mg-Si-Cu-Fe, right - Al-Zn-Mg-Cu

After the finishing of particle rearrangement, the elastic and plastic deformation of particles starts through their contacts. Fig. 5 presents the detailed microstructures with small work hardened areas by implication of plastic deformation.

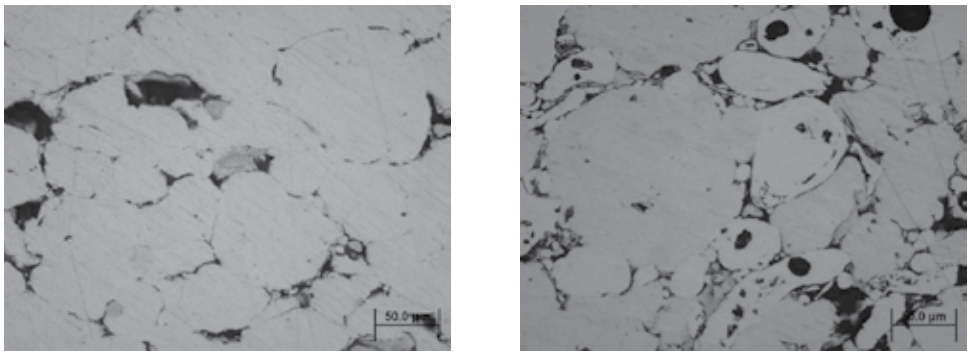

Fig. 5. Microstructure of aluminium alloys at 200 MPa, left - Al-Mg-Si-Cu-Fe, right - Al-Zn-Mg-Cu

Fig. 6 shows that the contact area between the particles increases and particles undergo extensive plastic deformation in both aluminium alloys. During compaction the particles deform following to the formation of solid interfaces at the point or planar particle contacts *„compaction facets*" (Dudrová & Kabátová, 2007), representing areas with elevated free energy. Thus, the potential areas for nucleation and growth of inter-particle necks during the sintering are increased. In terms of compressibility, the pressing pressure of 400 MPa seems to be appropriate for achieving the desirable cold welding.

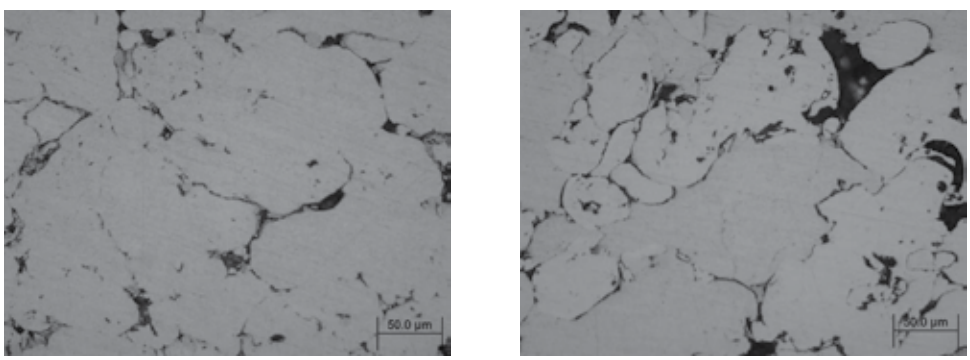

Fig. 6. Microstructure of aluminium alloys at 400 MPa, left - Al-Mg-Si-Cu-Fe, right - Al-Zn-Mg-Cu

The final stages of densification of powder particles under the pressure of 600 MPa are presented in Fig 7 (optical microscopy) and Fig. 8 (scanning electron microscopy).
In a number of materials densified by plastic flow, cusp-shaped pores <1 μm in size have been observed. The radius of material on the pore surface is much smaller than the particle radius. The material surrounding the pore has a shape typical of atomized produced powders (Fig. 9 right). Plastic deformation of powder particles leading to intimate contact between oxide- and/or contamination-free surfaces results in the formation of chemical bonds and adhesion, as confirmed by (Powder Metal Technologies and Applications, 1998).

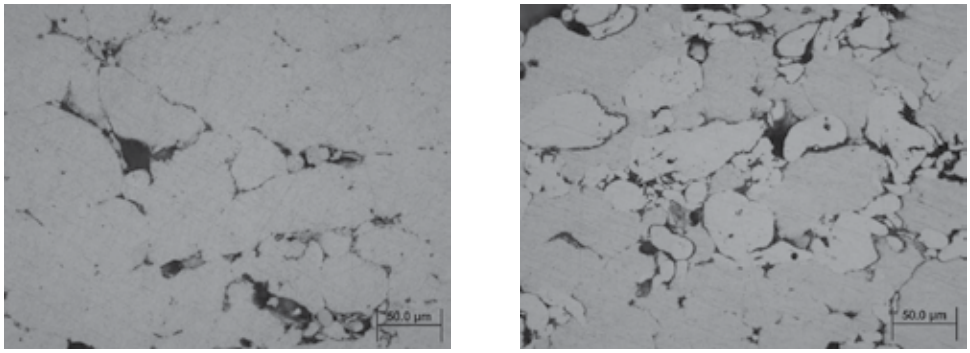

Fig. 7. Microstructure of aluminium alloys at 600 MPa, left - Al-Mg-Si-Cu-Fe, right - Al-Zn-Mg-Cu

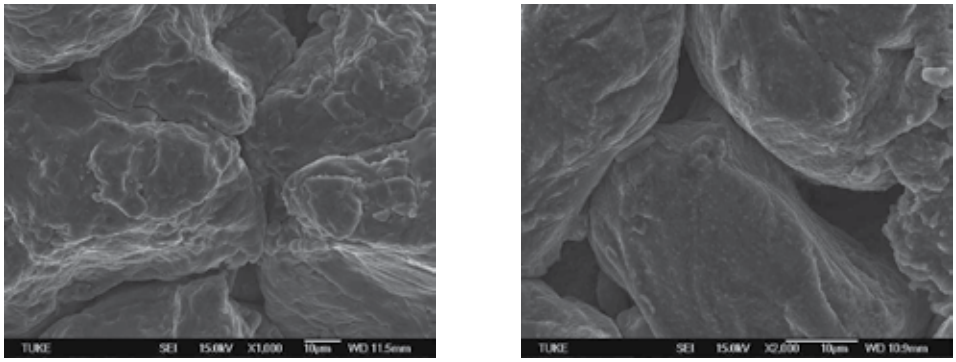

Fig. 8. Microstructure of aluminium alloys at 600 MPa, left - Al-Mg-Si-Cu-Fe, right - Al-Zn-Mg-Cu

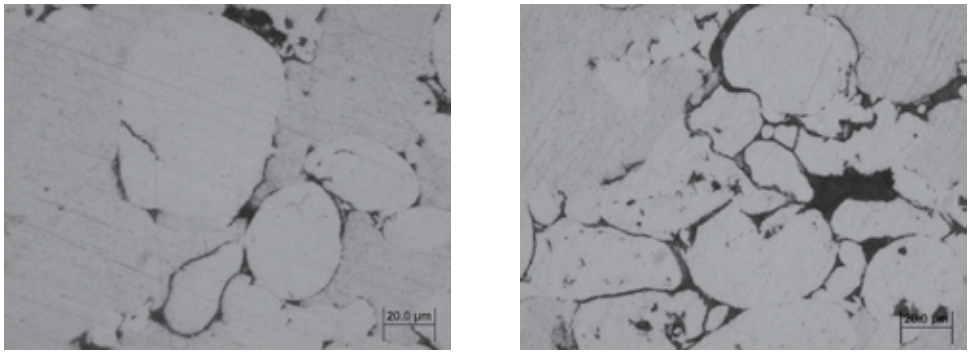

Fig. 9. Microstructure of aluminium alloys at 600 MPa, left, and 700 MPa, right - Al-Zn-Mg-Cu aluminium alloy

It is clear, that the Al-Mg-Si-Cu-Fe has a cold welding development bigger than the Al-Zn-Mg-Cu one. This is confirmed by the results of compressibility behaviour. The pore radius decreases with deformation. Such cusp-shaped pores are less stable under applied pressure than the spherical pores considered by (Powder Metal Technologies and Applications, 1998) formed by diffusional flow. What in principle opposes the closure of cusp-shaped pores is

the increasing surface tension force on the concave surfaces, resulting in LaPlace compressive stresses on these surfaces. At very high pressing pressure delaminated (cracking across the particle, Fig. 9) specimens were failing in the investigated systems; this is basically due to the work hardening effect.

3.2 Effect of sintering process

Consolidation of aluminium alloys by sintering presents a major problem: the oxide layer covering aluminium particles, Fig. 10.

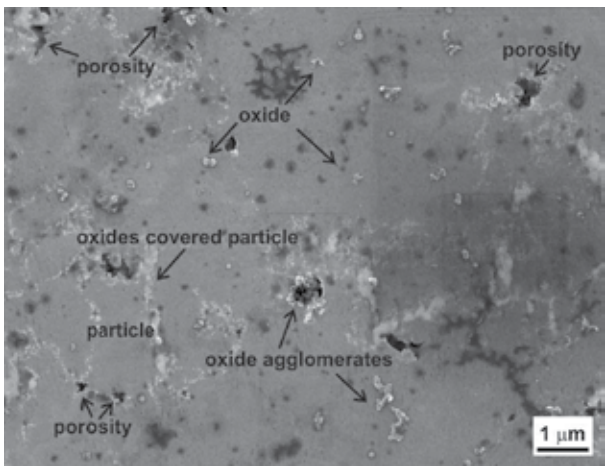

Fig. 10. Oxide layer covering aluminium particles

The oxide thickness is dependent on the temperature at which it is formed and the humidity contents in the atmosphere in which the powders is stored. Schaffer & Hall, 2002, suggested that the oxygen concentration in the nitrogen atmosphere is reduced by the aluminium through a self-gettering mechanism. The outer layers of the porous powder compact serve as a getter for the inner layers such that the oxygen partial pressure is reduced deep within the pore network. Aluminium nitride then forms, either by direct reaction with the metal or by reduction of the oxide layer, and sintering follows according to the equations.

$$Al + N \rightarrow AlN \tag{9}$$

It is highly exothermic: the $\Delta_f H^0_{AlN} = -318\ KJ/mol$. If the temperature rises, as a consequence of the reaction, it will increase the liquid volume, which may enhance sintering (Schaffer et al., 2006). The oxide therefore prevents suitable bonding.

This has been explained in terms of the relative diffusion rates through the oxide and the metal, for metals with stable oxides. It means that, in order to achieve a good sintering response, aluminium alloys have to be modified by additional steps like, for example, severe plastic deformation or, in terms of pre-processing, master alloy powders. Liquid phase sintering of investigated aluminium alloys consists of typical stages. During the heating stage, the penetration of the pressing contacts by the transient liquid eutectic phases results in a pronounced expansion within a rather small temperature range. During further heating, when the solidus temperature for the composition is exceeded, also persistent liquid phase is formed, resulting in fast shrinkage. Depending on the selected heating rate and sintering

temperatures, the ratio solid-liquid varies and also the shrinkage does. The very sensitive solid-liquid equilibrium results in tight requirements for the tolerable temperature interval. It is well-known that for an effective liquid phase sintering, a wetting liquid represents an essential requirement. Authors (Kehl & Fischmeister, 1980) suggested that the Al-$CuAl_2$ eutectic can wet Al_2O_3 at 873 K. However, not even magnesium additions (to melt aluminium) reduce the contact angle sufficiently to produce wetting (Martín et al., 2004); (Danninger, 1987); (Martín & Castro, 2007). This is possibly the main reason why sintering Al-Zn-Mg-Cu and Al-Mg-Si-Cu-Fe aluminium alloys still cannot be considered that easy.
It should be noticed that the investigated microstructures present the regions with alloying elements with high chemical activity, e.g. magnesium and copper, Figs. 11 and 12.
Magnesium is mainly concentrated around the pores and in the necks volume. It appears that the primary porosity inside powder is also relatively permeable. The densification behaviour of powder particles in the examined alloy is complicated due to the large surface area and associated oxide layers. Formation of transient liquid phase, according to (Danninger & Gierl, 2001), enhances homogenization of the alloying element, mainly magnesium and copper, by accelerating material transport through spreading of the melt in the pore network and the pressing contacts and by increasing the diffusional cross-section.

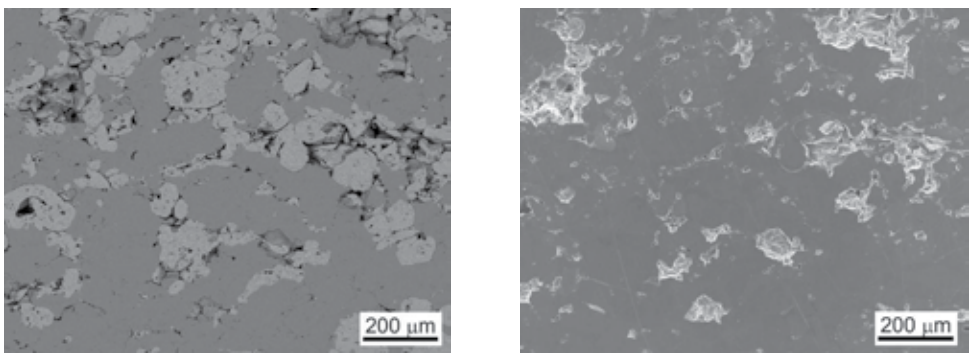

Fig. 11. The typical microstructure for 400 MPa pressed specimens, Al-Zn-Mg-Cu specimens, left SEI and right COMPO

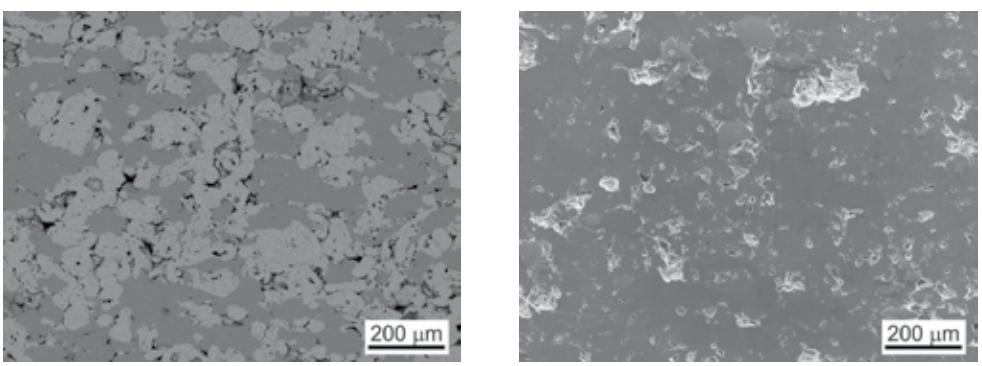

Fig. 12. The typical microstructure for 600 MPa pressed specimens, Al-Zn-Mg-Cu specimens, left SEI and right COMPO

Densification, Ψ, was calculated to determine the amount of shrinkage or swelling during sintering:

$$\Psi = \frac{\rho_s - \rho_g}{\rho_t - \rho_g} \quad [-] \tag{10}$$

where:
ρ_s [g.cm^{-3}], the sintered density
ρ_g [g.cm^{-3}], the green density and
ρ_{th} [g.cm^{-3}], the theoretical density.
The results presented in Table 6 show values of theoretical density in different processing conditions as well as densification behaviour Ψ.

pressure [MPa]	**pressing**	**dewaxing**	**sintering**	**Ψ**	**ECAP**
400	92.48	93.11	92.12	-0.05	98.31
500	92.84	93.30	92.40	-0.06	98.39
600	93.03	92.89	92.82	-0.03	98.64
700	93.19	92.93	93.09	-0.01	98.58

Table 6. Densification behaviour of material as values of theoretical density (%), except Ψ (-).

Considering the first three columns, it can be seen that with increasing pressing pressure, the values of theoretical density increase. It is well-known that aluminium powder would not require much sintering because its relative softness allows very high green densities to be obtained by traditional uniaxial compaction alone; green densities in excess of 90% are typical. Indeed, sintering of aluminium often causes swelling and results in negative densification values (Lumley & Schaffer, 1998).
A high heating rate in transient systems also promotes liquid formation because it limits the time available for dissolution of the additive in the base prior to melting. ECAP process can be sufficient to achieve a good densification. Also, the presence of adsorbed and absorbed gases by the Al particles, as well as water vapour present during vacuum sintering (Showaiter & Youseffi, 2008) would increase the size of the compacts and therefore reducing their sintered density due to volume expansion.
As expected, the sintering brings to the formation of secondary porosity during transient LPS as well as the swelling presented seems to be related to the amount of liquid generated. The formation of secondary pores, according to (Martín et al., 2004); (Danninger, 1987); (Martín & Castro, 2007) is dependent to the previous formation of a liquid able to migrate away from the site of the prior alloying particles. The mix of primary (which still present in studied materials), secondary and residual porosity reveals the mean values of D_{circle} decreased with increasing pressing pressure. As expected, the coarse additive particle sizes leave large residual pores behind. Sintering under vacuum gave rise to the presence of higher pore content and excessive amounts of residual porosity at grain boundaries.
Table 7 shows the values of porosity characteristics for the investigated material processed before ECAP.

pressure [MPa]	D_{circle} [μm]	St. dev.	f_{shape} [μm]	f_{circle}
400	30.64	23.93	0.70	0.92
500	30.20	20.17	0.72	0.93
600	23.64	16.11	0.69	0.92
700	21.27	17.66	0.64	0.89

Table 7. Porosity distribution of studied material before ECAP

The successful densification of elemental powder mixtures by LPS is based on the formation of a combination of transient and permanent liquid phases (Martín et al., 2004); (Danninger, 1987). The LPS, firstly formed, allows the incorporation of alloying elements and therefore leads to swelling of the compacts. Another result of transient liquid phase is the presence of secondary pores. Since the melt spreads into the matrix pores and pressing contacts, it leaves pores behind, the diameter of which is correlated to the size of the original alloy particle.

The subsequently formed permanent liquid phases encourage densification accompanied by the corresponding shrinkage. On the other hand, this swelling-shrinkage sequence leads to distortion and to difficulties for dimensional control of the components.

The origin of compact swelling and the formation of secondary porosity during transient LPS are based on two main causes (Martín et al., 2004); (Schaffer et al., 2001). Firstly, the dissolution of the alloying particles in the metal matrix and secondly, the migration of a wetting liquid, formed from the alloying particles, through pore channels and/or the grain boundaries of the main component, Fig. 13. Both effects lead to the generation of secondary pores.

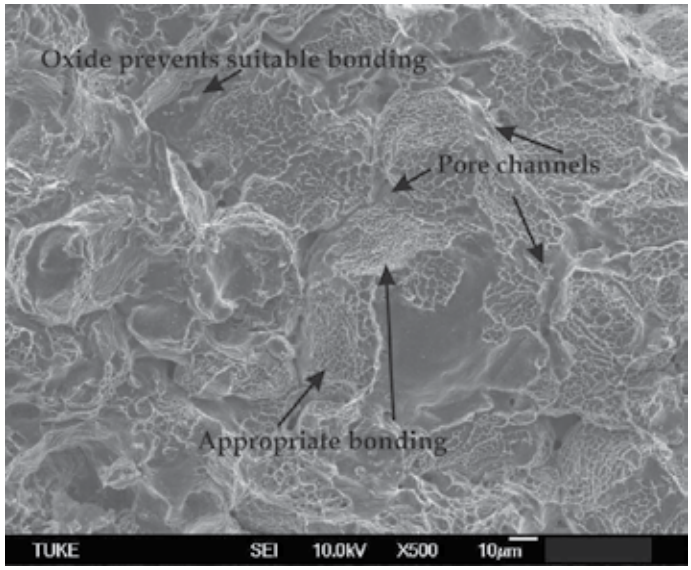

Fig. 13. Consolidation of aluminium alloys by sintering

3.3 Effect of SPD process

Effect of ECAP-BP

The processing way of ECAP-BP differs from ECAP in terms of the adopted temperature, which is settled at 523 K. The results of these investigations are presented in Table 8.

No. and pressure	D_{circle}	f_{shape}	f_{circle}
D, 400 MPa	10.47	0.53	0.25
D, 600 MPa	7.40	0.60	0.25
D+E, 400 MPa	5.75	0.59	0.27
D+E, 600 MPa	4.40	0.58	0.26
D+S+E, 400 MPa	3.18	0.46	0.22
D+S+E, 600 MPa	2.02	0.60	0.25

Table 8. Porosity distribution of studied material after ECAP-BP

Where: D-dewaxing, S-sintering, E-ECAP-BP

As expected, sintering coupled to back pressure tends to shift the distributions towards lower pores size Dcircle and higher values of f_{shape} and f_{circle} since higher-temperature treatments leads to porosity reduction and improving pore morphology. Application of ECAP-BP supported next decreasing of pore size, represented by value of D_{circle}. It can be noted that most of the pores diameter values are in the range from 2 to 10 μm in all specimens, however rarely larger pores with the size up to 45 μm were observed.

It could be expected that this large amount of small pores strongly influences both f_{shape} and f_{circle} considering that small pores reveal preferably circular shape.

The results presented in Table 8 show a value of f_{circle} is in the range from 0.22 to 0.27. It is important to emphasize that f_{circle} depicts only how circular the form of the pore is, and f_{shape} include also how smooth the pore contour is, as it was shown in (Pavanati et al., 2007); the evolution of pores to a smooth contour is more effective than to a circular form during sintering, so the highest value of f_{shape} was registered for sintered and ECAPed specimen. Application of SPD process and sintering causes a decrease of D_{circle} to the minimum value of 2.02 and on the other hand, slightly increase the f_{circle} to maximum value of 0.27. It is interesting that, for both pressing pressure, the parameter D_{circle} has higher values for the initial state (after dewaxing) and the following processing (ECAP-BP and sintering plus ECAP-BP) causes contact areas between particles to increase and, consequently, a decrease in the effective shearing-stresses inside the particles. This condition happens with increasing densification, when the powder particles are plastically deformed and increasingly deformation strengthened. Dewaxing tends to generate larger pores in the microstructure, because of the lower densification attained on the green parts. When back pressure is applied, the stress distribution in deformed specimens causes the powder particles to squeeze together to such an extent that the initially interconnected pores transform to small semi-isolated pores, determining a lower value of parameter D_{circle}. Consequently, ECAP-BP influences the porosity distribution in terms of the severe shear deformation involving and therefore influences the pore morphology which is represented by both parameters of f_{shape} and f_{circle}.

Effect of ECAP

The application of ECAP supported the following decreasing of the pore size, represented by the value of D_{circle}, Table 9.
It can be noted that most of the pores diameter values are under 1 μm. It could be expected that this large amount of small pores (nanoporosity, Fig. 14), strongly influences both f_{shape} and f_{circle} considering that small pores evolve easily to a circular form despite of well-known ability of ECAP to alignment of particles (Lapovok, 2005); (Lapovok et al., 2008).

pressure [MPa]	D_{circle}	St. dev.	f_{shape}	f_{circle}
400	**0.97**	0.45	0.67	0.91
500	**0.90**	0.35	0.65	0.91
600	**0.85**	0.37	0.67	0.91
700	**0.79**	0.34	0.64	0.90

Table 9. Porosity distribution of studied material after ECAP

For the extremely large shear strains imposed by severe plastic deformation processing, even more extensive nucleation of nanopores is expected at grain boundaries or at particle-matrix interfaces (Lapovok et al., 2009). Formation of ultrafine grains during SPD processing increases the total area of grain boundaries and, therefore, the availability of nanopores nucleation sites. An additional effect of the continual grain refinement is an increase in the density of triple junctions that can act as preferred sites for nanopores nucleation. Lapovok et al. (2009) noted that small-angle X-ray scattering experiments on SPD-processed Al and an aluminium alloy carried out by (Betekhtin et al., 2007) provided useful insights in the effect of severe plastic deformation on formation of free volume, as also confirmed by (Divinski et al., 2009); (Ribbe et al., 2009), which was interpreted in terms of nanoporosity.

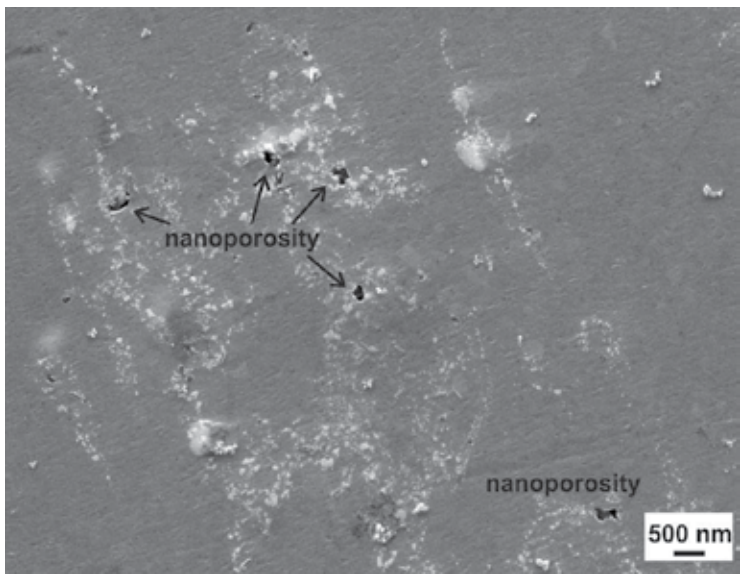

Fig. 14. Nanoporosity present in the studied material

Therefore, structure investigations by TEM (HRTEM) analysis will be useful key to identifications and confirmations the various theories about the material behaviour during the SPD processing (Dutkiewicz et al., 2009); (Lityńska-Dobrzyńska et al., 2010); (Maziarz et al., 2010); (Alexandrov et al., 2005).

4. Conclusion

In terms of compaction. The development of compressibility values with pressing pressure enables to characterize the effect of particles geometry and matrix plasticity on the compaction process. The presented results exhibit a high value of plasticity, as a property related to compressibility, and consequently promising compressibility data in terms of industrial potential applications are obtained.
In terms of sintering. The dissolution of the alloying particles in the metal matrix and therefore, the migration of a wetting liquid (formed from the alloying particles) through pore channels and/or the grain boundaries of the main component (promotes the swelling of compact) and the formation of secondary porosity, mainly at the prior alloying particle sites.
In terms of ECAP-BP. Analysis of presented parameters indicate that sintering coupled to SPD leads to porosity reduction and improving pore morphology. ECAP-BP influences the porosity distribution in terms of the severe shear deformation involved and therefore influences the pore morphology.
In terms of ECAP. The application of SPD, causing stress distribution in deformed specimens, made the powder particles to squeeze together to such an extent that the initially interconnected pores transform to small isolated pores, determining a given value of the parameter D_{circle}.

5. References

Beiss, P. & Dalgic, M. (2001). Structure property relationships in porous sintered steels. *Materials Chemistry and Physics*, Vol. 67, (2001) 37-42, ISSN 0254-0584

Bidulská, J.; Kvačkaj, T.; Bidulský, R. & Actis Grande M. (2008 a). Influence of processing conditions on EN AW 2014 material properties and fracture behavior. *Kovove Materialy*, Vol. 46, No. 6 (2008) 339-344, ISSN 0023-432X

Bidulská, J.; Kvačkaj, T.; Bidulský, R. & Actis Grande M. (2008 b). Effect of Various Processing Conditions on the Tensile Properties and Structural Developments of EN AW 2014 Aluminium Alloy. *High Temperature Materials and Processes*, Vol. 27, No. 3 (2008) 203-207, ISSN 0334-6455

Bidulská, J.; Kočiško, R.; Kvačkaj, T.; Bidulský, R. & Actis Grande, M. (2008 c). Numerical simulation of EN AW 2014 aluminium alloy in ECAP process. *Acta Metallurgica Slovaca*, Vol. 14, No. 3-4 (2008) 342-348, ISSN 1335-1532

Bidulská, J. Kvačkaj, T. Actis Grande, M. & Bidulský, R. (2009). The compressibility behaviour of a new generation of coated metal/ceramic composite powders. *Key Engineering Materials*, Vol. 409 (2009) 362-364, ISSN 1013-9826

Bidulská, J.; Kočiško, R.; Bidulský, R.; Actis Grande M.; Donič T. & Martikán M. (2010 a). Effect of severe plastic deformation on the porosity characteristics of Al-Zn-Mg-Cu PM PM alloy. *Acta Metallurgica Slovaca*, Vo. 16, No. 1 (2010) 4-11, ISSN 1335-1532

Bidulská, J.; Kvačkaj, T.; Bidulský, R.; Actis Grande M.; Donič T. & Martikán M. (2010 b). Influence of ECAP-back pressure on the porosity distribution. *Acta Physica Polonica A*, Vol. 117, No. 5 (2010) 864-868, ISSN 0587-4246

Bidulský, R. Actis Grande, M. Kabátová, M. & Selecká M. (2008). The effect of carbon coating and carbon admixing on the compressibility of Astaloy CrL. *Acta Metallurgica Slovaca*, Vol. 14, No. 3-4 (2008) 349-355, ISSN 1335-1532

Betekhtin, V. I., Kadomtsev, A. G., Sklenicka, V. Saxl, I. (2007). Nanoporosity of fine-crystalline aluminum and an aluminum-based alloy. *Physics of the Solid State*, Vol. 49, No. 10 (2007) 1874–1877, ISSN 1063-7834

Danninger, H. (1987). Secondary porosity in sintered steels and its effects on product quality and consistency. *Powder Metallurgy*, Vol. 30, No. 2 (1987) 103-109, ISSN 0032-5899

Danninger, H.; Neubing, H. C. & Gradl, J. (1998). Sintering of High Strength Al-Zn-Mg-Cu Alloys to Controlled Dimensions. *Proceedings of Powder Metallurgy World Congress*, pp. 272-277, Vol. 5, Granada, 1998, EPMA, Shrewsbury

Danninger, H. & Gierl, Ch. (2001). Processes in PM steel compacts during the initial stages of sintering. *Materials Chemistry and Physics*, Vol. 67 (2001) 49–55, ISSN 0254-0584

DeHoff, R. T. & Aigeltinger, E. H. (1970). Experimental quantitative microscopy with special application to sintering. *Proceedings of Perspectives in Powder Metallurgy*, pp. 81-137, Vol.5, Plenum Press, New York

Denny, P. J. (2002). Compaction equations: a comparison of the Heckel and Kawakita equations. *Powder Technology*, Vol. 127 (2002) 162-172, ISSN 0032-5910

Divinski S. V., Ribbe J., Baither D., Schmitz G., Reglitz G., Rosner H., Sato K., Estrin Y., Wilde G. (2009). Nano- and micro-scale free volume in ultrafine grained Cu-1 wt.%Pb alloy deformed by equal channel angular pressing. *Acta Materialia*, Vol. 57, No. 19 (2009) 5706-5717, ISSN: 1359-6454

Dudas, J. H. & Dean, W. A. (1969). The production of precision aluminum P/M parts. *International Journal of Powder Metallurgy*, Vol. 5, No. 2 (1969) 21–36, ISSN 0888-7462.

Dudrová, E. Parilák, Ľ. Rudnayová, E. & Šlesár, M. (1982). Physico-metallurgical principles of compaction, sintering and their relation with the properties of porous materials. *Proceedings of 6th International Conference on Powder Metallurgy in ČSSR*, pp. 73-83, Part 1, Brno, 1982, DT ČSVTS, Žilina

Dudrová, E. Rudnayová, E. & Parilák, Ľ. (1983). Lisovanie práškových kovov. *Pokroky práškové metalurgie*, Vol. 21, No. 2 (1983) 29-50, ISSN 0322-9769

Dudrová, E. & Kabátová, M. (2007). Microstructural Defects and Properties. *Proceedings of Design and Capabilities of PM Components and Materials. A Residental Training Course for Young Materials/Design Engineers*. pp. 513-535, Vol. 2. Košice, 23.6.-1.7.2007, EPMA

Dutkiewicz, J.; Masdeu, F.; Malczewski, P. & Kukuła, A. (2009). Microstructure and properties of $\alpha + \beta$ brass after ECAP processing. *Archives of Materials Science and Engineering*, Vol. 39, No. 2 (2009) 80-83, ISSN 1897-2764

Esper, F. J. & Sonsino, C. M. (1994). *Fatigue design for PM components: Manual for Design and Production Engineers*, EPMA, ISBN 1-899072-00-4, Shrewsbury

Gradl, J.; Neubing, H. C. & Müller, A. (2004). Improvement in the Sinterability of 7-xxx-based Aluminium Premix. *Proceedings of Euro Powder Metallurgy*, pp. 15-21, Vol. 4, Eds. Danninger, H. & Ratzi, R., Wien, 2004, EPMA, Shrewsbury

Guo, J.Q. & Kazama, N.S. (1997). Mechanical properties of rapidly solidified Al-Ti-Fe, Al-Cu-Fe and Al-Fe-Cu-Ti based alloys extruded from their atomized powders. *Materials Science and Engineering A*, Vol. 232, No. 1-2 (1997) 177-182, ISSN 0921-5093

Hryha, E. Dudrová, E. & Bengtsson, S. (2008). Influence of powder properties on compressibility of prealloyed atomised powders. *Powder Metallurgy*, Vol. 51, No. 4 (2008) 340-342, ISSN 0032-5899

Hryha, E.; Zubko, P.; Dudrová, E.; Pešek, L. & Bengtsson, S. (2009). An application of universal hardness test to metal powder particles. *Journal of Materials Processing Technology*, Vol. 209, No. 5 (2009) 2377-2385, ISSN 0924-0136

Ip, S. W.; Kucharski, M. & Toguri, J. M. (1993). Wetting behaviour of aluminium and aluminium alloys on Al_2O_3 and CaO. *Journal of Materials Science Letters*, Vol. 12, No. 21 (1993) 1699-1702, ISSN 0261-8028

Kawakita, J. & Lüdde, K. H. (1971). Some considerations on powder compression equation. *Powder Technology*, Vol. 4, No. 2 (1971) 61-68, ISSN 0032-5910

Kehl, W. & Fischmeister H. F. (1980). Liquid-phase sintering of Al-Cu compacts. *Powder Metallurgy*, Vol. 23, No. 3 (1980) 113-119, ISSN 0032-5899

Kehl, W.; Bugajska, M. & Fischmeister, H. F. (1983). Internal or die wall lubrication for compaction of Al powders. Powder Metallurgy, Vol. 26, No. 4 (1983) 221-227, ISSN 0032-5899

Kim, H. S. (2002). Finite element analysis of deformation behaviour of metals during equal channel multi-angular pressing. *Materials Science and Engineering A*, Vol. 328, No. 1-2 (2002) 317-323, ISSN 0921-5093

Kim, Y. D.; Min, K. H.; Kang, S. P. & Chang, S.-Y. (2004). PM Lightweight and Porous Materials Effect of Mg Addition on Sintering Characteristic of 7xxx Series Al P/M Alloy. *Proceedings of Euro Powder Metallurgy*, pp. 40-45, Vol. 4, Eds. Danninger, H. & Ratzi, R., Wien, 2004, EPMA, Shrewsbury

Kočiško, R.; Kvačkaj, T.; Bidulská, J. & Molnárová M. (2009). New Geometry of ECAP Channels. *Acta Metallurgica Slovaca*, Vol. 15, No. 4 (2009) 228-233, ISSN 1335-1532

Kvačkaj, T.; Zemko, M.; Kočiško, R.; Kuskulič, T.; Pokorny, I.; Besterci, M.; Sulleiova, K.; Molnarova, M.; Kovačova, A. (2007). Simulation of ECAP process by finite element method. *Kovove Materialy*, Vol. 45, No. 5 (2007) 249-25, ISSN 0023-432X

Lapovok, R.Y. (2005). The role of back-pressure in equal channel angular extrusion. *Journal of Materials Science*, Vol. 40, No. 2 (2005) 341-346, ISSN 0022-2461

Lapovok, R. Y.; Tomus, D. & Muddle B. C. (2008). Low-temperature compaction of Ti-6Al-4V powder using equal channel angular extrusion with back pressure. *Materials Science and Engineering A*, Vol. 490, No. 1-2 (2008) 171-180, ISSN 0921-5093

Lefebvre, L.-P.; Thomas, Y. & White, B. (2002). Effects of lubricants and compacting pressure on the processability and properties of aluminum P/M parts. *Journal of Light Metals*, Vol. 2, No. 4 (2002) 239–246, ISSN 1471-5317

Lityńska-Dobrzyńska, L.; Dutkiewicz, J.; Maziarz, W. & Rogal, Ł. (2010). TEM and HRTEM studies of ball milled 6061 aluminium alloy powder with Zr addition. *Journal of Microscopy*, Vol. 237, No. 3 (2010) 506-510, ISSN 0022-2720

Liu, Y.; He, Z.; Dong, G. & Li, Q. (1992). The effect of cerium on the wettability of Al_2O_3/Al-4.5Cu alloy. *Journal of Materials Science Letters*, Vol. 11, No. 12 (1992) 896-898, ISSN 0261-8028

Lumley, R.N. & Schaffer, G.B. (1998). Precipitation induced densification in a sintered Al–Zn–Mg–Cu alloy. *Scripta Materialia*, Vol. 39, No. 8 (1998) 1089-1094, ISSN 1359-6462

Lumley, R. N. Sercombe, T. B. & Schaffer, G. B. (1999). Surface oxide and the role of magnesium during the sintering of aluminum. *Metallurgical and Materials Transactions A*, Vol. 30, No. 2 (1999) 457-463, ISSN 1073-5623

Marcu Puscas, T.; Signorini, M.; Molinari, A. & Straffelini, G. (2003). Image analysis investigation of the effect of the process variables on the porosity of sintered chromium steels. *Materials Characterization,* Vol. 50, No. 1 (2003) 1-10, ISSN 1044-5803

Martín, J. M.; Gómez-Acebo, T. & Castro, F. (2002). Sintering behaviour and mechanical properties of PM AI-Zn-Mg-Cu alloy containing elemental Mg additions. *Powder Metallurgy*, Vol. 45, No. 2 (2002) 173-180, ISSN 0032-5899

Martín, J. M. & Castro, F. (2003). Alloy development and associated dimensional changes of aluminium alloys during liquid phase sintering. *Materials Science Forum*, Vol. 426-432 (2003) 107-114, ISSN 0255-5476

Martín, J. M.; Navarcorena, B.; Arribas, I.; Gómez-Acebo, T. & Castro, F. (2004). *Dimensional Changes and Secondary Porosity in Liquid Phase Sintered Al Alloys*, *Proceedings of Euro Powder Metallurgy*, pp. 46-53, Vol. 4, Eds. Danninger, H. & Ratzi, R., Wien, 2004, EPMA, Shrewsbury

Martín, J.M. & Castro, F. (2007). Sintering response & microstructural evolution of an Al-Cu-Mg-Si premix. *International Journal of Powder Metallurgy*, Vol. 43, No. 6 (2007) 59-69, ISSN 0888-7462

Maziarz, W.; Dutkiewicz, J.; Lityńska-Dobrzyńska, L.; Santamarta, R. & Cesari, E. (2010). Structure investigations of ferromagnetic Co-Ni-Al alloys obtained by powder metallurgy. *Journal of Microscopy*, Vol. 237, No. 3 (2010) 374-378, ISSN 0022-2720

Mihalikova, M. (2010). Research of strain distribution and strain rate change in the fracture surroundings by the videoextensometric method. *Metalurgija*, Vol. 49, No. 3 (2010) 161-164, ISSN 0543-5846

Miura, S.; Machida, Y.; Hirose, Y. & Yoshimura, R. (1993). The Effects of Varied Alloying Methods on the Properties of Sintered Aluminum Alloys. *Proceedings of Powder Metallurgy World Congress*, pp. 571-574, Japan, 1993, Kyoto, JSPPM

Neubing, H. C. & Jangg, G. (1987). Sintering of aluminum parts: the state-of-the-art. *Metal Powder Report*, Vol. 42, No. 5 (1987) 354-358, ISSN 0026-0657

Neubing, H. C.; Gradl J. & Danninger H. (2002). Sintering and Microstructure of Al-Si PM Components. *Proceedings of Advances in Powder Metallurgy* & *Particulate Materials*, pp. 128-138, Part 13, Eds. Arnhold, V.; Chu, Ch.-L.; Jandeska, W. F. & Sanderow, H. I., 2002, MPIF, Orlando

Parilák, Ľ. Dudrová, E. & Rudnayová, E. (1983). Aproximatívne vyjadrenie lisovacej krivky technických práškových kovov. *Pokroky práškové metalurgie*, Vol. 21, No. 3 (1983) 19-30, ISSN 0322-9769

Parilák, Ľ. Dudrová, E. Bidulský, R. & Kabátová, M. (2004). Quantification of metal powder compressibility in uniaxial compaction. *Proceedings of Euro Powder Metallurgy*, pp. 593-598, Vol. 4, Eds. Danninger, H. & Ratzi, R., Wien, 2004, EPMA, Shrewsbury

Panelli, R. & Filho, F. A. (2001). A study of a new phenomenological compacting equation. *Powder Technology*, Vol. 114, No. 1 (2001) 255-261, ISSN 0032-5910

Pavanati, H. C.; Maliska, A. M.; Klein, A. N. & Muzart, J. L. R. (2007). Comparative study of porosity and pores morphology of unalloyed iron sintered in furnace and plasma reactor. *Materials Research*, Vol. 10, No. 1 (2007) 87-93, ISSN 1516-1439

Pieczonka, T.; Schubert, Th.; Baunack, S. & Kieback B. (2008). Dimensional behaviour of aluminium sintered in different atmospheres. *Materials Science and Engineering A*, Vol. 478, No. 1-2 (2008) 251-256, ISSN 0921-5093

Pietrowski, A. & Biallas, G. (1998). Influence of sintering temperature on pore morphology, microstructure, and fatigue behaviour of MoNiCu alloyed sintered steel. *Powder Metallurgy*, Vol. 41, No. 2 (1998) 109-114, ISSN 0032-5899

Powder Metal Technologies and Applications (1998). Vol. 7, ASM Handbook, ISBN 0-87170-387-4, First printing, December 1998, ASM International, Warrendale

Ribbe, J., Baither D., Schmitz G., Divinski S. V. (2009). Network of Porosity Formed in Ultrafine-Grained Copper Produced by Equal Channel Angular Pressing. *Physical Review Letters*, Vol.102, No. 16 (2009) 165501, ISSN 0031-9007

Rout, S. K.; Veltl, G. & Petzoldt, F. (2004). Effect of Sn additions on Microstructure Evolution in Sintered Aluminium Alloys. *Proceedings of Euro Powder Metallurgy*, pp. 9-14, Vol. 4, Eds. Danninger, H. & Ratzi, R., Wien, 2004, EPMA, Shrewsbury

Salak, A. (1997). *Ferrous Powder Metalurgy*. Cambridge International Science Publishing, ISBN-13: 978-1-898326-03-7, Cambridge

Schaffer, G.B.; Sercombe, T.B. & Lumley, R.N. (2001). Liquid phase sintering of aluminium alloys. *Materials Chemistry and Physics*, Vol. 67, No. 1-3 (2001) 85-91, ISSN 0254-0584

Schaffer, G.B. & Hall, B. J. (2002). The influence of the atmosphere on the sintering of aluminum. *Metallurgical and Materials Transactions A*, Vol. 33, No. 10 (2002) 3279–3284, ISSN 1073-5623

Schaffer, G. B.; Hall, B. J.; Bonner, S. J.; Huo, S. H. & Sercombe, T. B. (2006). The effect of the atmosphere and the role of pore filling on the sintering of aluminium. *Acta Materialia*, Vol. 54 (2006) 131–138, ISSN 1359-6454

Showaiter, N. & Youseffi, M. (2008). Compaction, sintering and mechanical properties of elemental 6061 Al powder with and without sintering aids. *Materials and Design*, Vol. 29, No. 4 (2008), 752–762, ISSN 0261-3069

Valiev, R.Z. , Islamgaliev, R.K. & Alexandrov I.V. (2000). Bulk nanostructured materials from severe plastic deformation. *Progress in Materials Science,*Vol. 45, No. 2 (2000) 103-189, ISSN 0079-6425

Valiev, R.Z. & Langdon, T.G. (2006). Principles of equal-channel angular pressing as a processing tool for grain refinement. *Progress in Materials Science,* Vol. 51, No. 7 (2006) 881-981, ISSN 0079-6425

Vinogradov, A.; Patlan, V. ; Suzuki, Y.; Kitagawa K. & Kopylov, V.I. (2002). Structure and properties of ultra-fine grain Cu-Cr-Zr alloy produced by equal-channel angular pressing. *Acta Materialia*, Vol. 50, No. 7 (2002) 1636-1651, ISSN 1359-6454

Ziani, A. & Pelletier, S. (1999). Supersolidus liquid-phase sintering behavior of degassed 6061 Al powder. *International Journal of Powder Metallurgy*, Vol 35, No. 8 (1999) 49-58, ISSN 0888-7462

Wu, X.; Xu, W. & Xia K. (2008). Pure aluminum with different grain size distributions by consolidation of particles using equal-channel angular pressing with back pressure. *Materials Science and Engineering A*, Vol. 493, No. 1-2 (2008) 241-245, ISSN 0921-5093

3

An Anisotropic Behaviour Analysis of AA2024 Aluminium Alloy Undergoing Large Plastic Deformations

Adinel Gavrus and Henri Francillette
European University of Brittany, National Institute of Applied Sciences, Rennes France

1. Introduction

The mechanical behaviour of metals during real forming processes must be related to their anisotropic properties. Concerning the analysis of the anisotropic behaviour of aluminium alloys this one has been the subject of various studies, generally in the field of sheet forming processes ((Malo *et al.,* 1998), (Lademo *et al.,* 1999)). In the last decades the majority of the fundamentals works search to define the mathematical description of the anisotropy starting from modified quadratic Hill criteria, non-quadratic ones such as Cazacu-Barlat (Cazacu & Barlat, 2001), Banabic (Banabic, 2002) or other sophisticated models synthesized in (Khalfallah, 2004). On the experimental point of view the many researches describe the rolled sheet properties of aluminium alloys (Choi & Barlat, 1999), (Li *et al.,* 2004), (Park, 1999)) and report the anisotropic response during the mechanical deformation from uniaxial tensile tests, wire drawing or simple shear ones ((Fjeldl & Roven , 1996), (Hu *et al.,* 1998), (Lloyd & Kenny, 1980), (Yonn, 2005)). Until now relatively few studies concerns the use of the channel die compression test, where deformation history is close of the principal sheet forming process such as the cold rolling one (Francillette *et al.,* 1998).
In this study an aluminium alloy (AA2024) is analyzed in order to characterize its anisotropy and its mechanical behaviour with this latter mechanical test. In a first part, the microstructure of the material is defined through optical and SEM microscopy, EBSD and X ray measurements. Micro-macro approaches will be used to valid the experimental measurements. Next, mechanical tests mainly the channel die compression one (see Francillette *et al,* 2003) and the tensile one are used in order to determine the macroscopic anisotropic behaviour of the material. A rigorous analytical model, able to describe the large plastic deformation of the material specimen which occurs during these experimental tests, will be developed. The main idea consist to define analytical equations which permits to compute the stress, the plastic strain rate and the cumulated plastic strain corresponding to a parallelepiped material undergoing a channel die upsetting loading. Final formula will be established to compute all the coefficients corresponding to a quadratic Hill criterion. A comparison with the well known computation model corresponding to the tensile test will be made. Next, a more general Hill criterion, taking into account variation of its coefficients with the plastic strain, will be analyzed. Starting from the previous mathematical description, a general methodology, able to identify rigorously all the parameters defining

the laws of variation of the computed quantities with the plastic strain, will be presented. Finally an application for a plan and normal anisotropic formulation, corresponding to AA2024 aluminium alloy rolled plate, will be detailed. A new approach will be then proposed in order to predict the Lankford coefficient values and a validation will be made by a comparison of these ones with those obtained from classical tensile tests.

2. Experimental analysis

Aluminium alloys present specific microstructures according to their chemical composition. These alloys are classified in several series as indicated in Table 1, according to the main elements of their chemical composition.

Series	1000	2000	3000	4000	5000	6000	7000
Composition	Al	Al-Cu	Al-Mn	Al-Si	Al-Mg	Al-Mg-Si	Al-Zn-Mg

Table 1. Chemical composition of aluminium alloys: xxxx series.

They can be shared out in two categories: those which do not present structural hardening (Al, Al-Mn, Al-Mg) and those which present structural hardening (Al-Cu, Al-Mg-Si, Al-Zn-Mg). The different phases which may be present in each series have been reported in (Barralis & Maeder, 2005). The chemical composition strongly favors the presence or not of precipitates during the elaboration process. In this paper anisotropic behaviour of an AA2024 aluminium alloy of 2000 series will be analyzed. Parallelepiped samples were cut out from a starting sheet with a thickness equal to 8.4 mm using the following dimensions: l_0 = 11 mm, w_0 = 10 mm and h_0 = 8.4 mm, where l_0, w_0 and h_0 are the initial length, width and respectively the high of the specimen. The initial rolling, transverse and normal directions of the sheet are defined by RD_0, TD_0 and ND_0. We will call LD, TD and ND the longitudinal, transverse and respectively normal directions corresponding to a channel die device (Fig. 1).

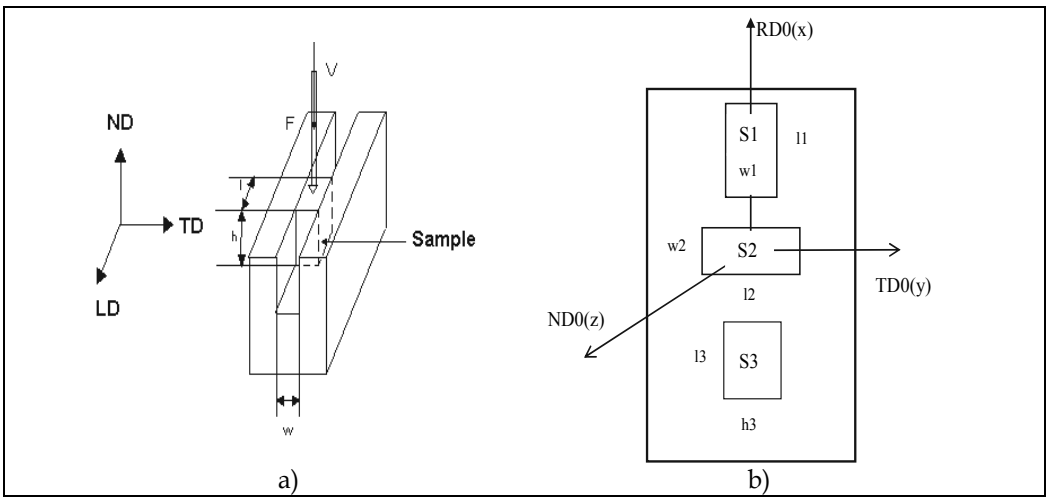

Fig. 1. The channel die compression test: a) device scheme, b) the initial sheet and the cut of the samples (S1, S2 and S3).

For the analysis of the mechanical behaviour of the material, channel die compression tests have been carried for three different specimens. The samples were positioned in the device and cut out from the initial sheet so that:

- LD // RD_0 ; TD // TD_0 ; ND // ND_0 (specimen S_1 and position 1)
- LD // TD_0 ; TD // RD_0 ; ND // ND_0 (specimen S_2 and position 2)
- LD // RD_0 ; TD // ND_0 ; ND // TD_0 (specimen S_3 and position 3)

For the specimen S_3 the following dimensions are chosen: l_0 = 11 mm, w_0 = 8 mm and h_0 = 10 mm. During the mechanical tests the strength is applied along the ND direction with a constant speed V closed to 2.10^{-2} mm/s and the sample is extended along the LD direction without displacement along the TD one. On the other hand, the coefficient of plan anisotropy r(θ) during plastic deformation is also determined starting from the ratio between the measured width reduction and the thickness one and using different orientations of specific tensile specimens cut out from the initial sheet (Banabic, 2000). The angle θ permits to describe the orientation of the specimen with respect to the initial rolling direction and its values chosen in this study are: θ = 0°, 30°, 45°, 60°, 90°. All the specimens were mechanically polished with abrasive paper and a solution with a chemical composition of 64% H_3PO_4, 27% H_2SO_4 and 9% NH_3 was systematically used for surfaces preparation. Different experimental techniques were used for the characterization of the material: optical microscopy, SEM, EBSD and X ray diffraction. The crystallographic textures have been characterized by the measurement of the {111}, {200} and {220} pole figures using the $K\alpha_1$ copper radiation (λ =1.54056). In a next part, the stress-strain curves are determined to highlighting the difference between the mechanical responses of the deformed samples.

3. Preliminary results and comments

In Figure 2, an illustration of the initial microstructure of the AA2024 of this study is presented using optical microscopy (Fig. 2a) and the Scanning Electron Microscope (Fig. 2b).

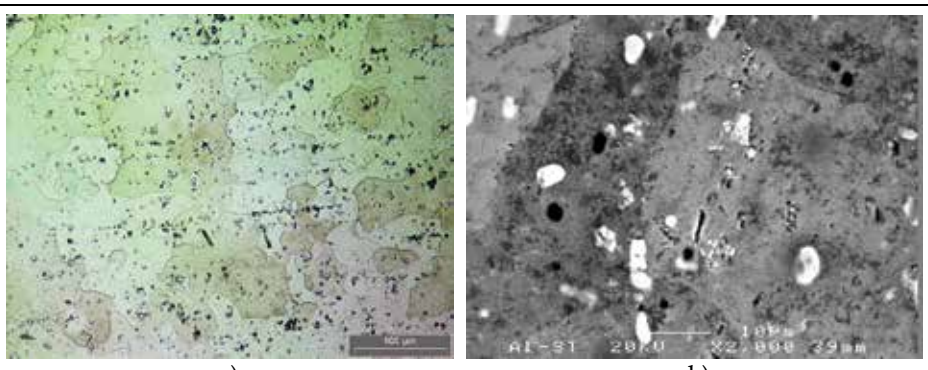

a) b)

Fig. 2. Initial microstructure of the material: a) Optical micrograph, b) SEM characterization - (Al, Cu) precipitates.

It is then possible to see that the size of the grains is not homogeneous: some grains have a size larger than 100 μm and other grains lower than 80 μm. At a finer scale, the observation with the SEM indicates the presence of precipitates (bright points) which are (Al, Cu) precipitates according to EDS analysis. The metallurgical quantities which define the

microstructure of aluminium alloys (gain size, precipitates, dislocations …) are important elements for interpreting the mechanical behaviour. During the elaboration of the material, thermo-mechanical treatments are generally chosen in order to optimize the mechanical properties and the microstructure. Other quantity necessary to understand the mechanical characterization is the crystallographic texture. Deformation, recrystallisation, solidification during thermomechanical processes contribute to the development of this type of texture ((Lücke & Engler, 1990), (Browen, 1990), (Zeng *et al.*, 1994), (Engler, 1994), (Engler, 1995)). To define it for a polycrystalline material, it is necessary to describe the orientation of a particular grain through the Miller indices. For example, in rolling, the (*hkl*)[*uvw*] component corresponds to the (*hkl*) plane parallel to the rolling plane and to the [*uvw*] direction parallel with the rolling direction. The correspondences between the Euler angles and the Miller indices can be found in the literature (Hansen, 1978). For the description of the crystallographic orientation of a particular grain of a textured material, it is necessary to consider a reference system (C_1, C_2, C_3) placed on three characteristic directions of the crystal lattice that are normal to each other, for example <100> directions in cubic metals. Let also consider a sample reference system defined by three directions (X, Y, Z), usually the rolling direction (RD), the transverse direction (TD) and the normal direction to the rolling plane (ND). The description of the crystallite orientation with respect to X, Y, Z is often done by the three Euler angles ϕ_1, ϕ and ϕ_2. At the initial stage, the two coordinate systems are coincidental (X along C_1, Y along C_2 and Z along C_3). The sample system is firstly rotated by a ϕ_1 angle around Z, next, a rotation of ϕ angle is applied around C_1 and, a thirdly, a successive rotation of ϕ_2 around C_3 bring the crystal orientation in its final position, as indicated Figure 3 (Bunge, 1996). Theoretically, ϕ_1 and ϕ_2 may vary from 0° to 360° and ϕ from 0° to 90°. By symmetry, the three angles may be considered between 0° and 90°.

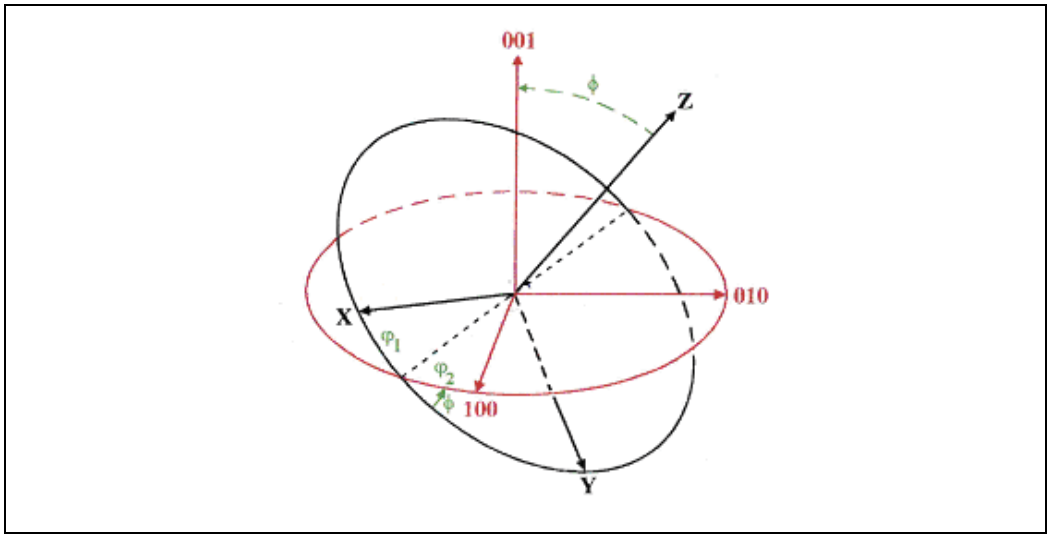

Fig. 3. Definition of the Euler angles.

The matrix transformation which relates the two coordinates systems (X, Y, Z) and (C_1, C_2, C_3) has an expression given by the composition of three elementary rotations:

$$\begin{pmatrix} \cos\phi_1\cos\phi_2 - \sin\phi_1\sin\phi_2\cos\phi & \sin\phi_1\cos\phi_2 + \cos\phi_1\sin\phi_2\cos\phi & \sin\phi_2\sin\phi \\ -\cos\varphi_1\sin\varphi_2 - \sin\phi_1\cos\phi_2\cos\phi & -\sin\phi_1\sin\phi_2 + \cos\phi_1\cos\phi_2\cos\phi & \cos\phi_2\sin\phi \\ \sin\phi_1\sin\phi & -\cos\phi_1\sin\phi & \cos\phi \end{pmatrix} \quad (1)$$

Different techniques may be used for the experimental determination of the crystallographic texture of the material. Among them, one local technique which can afford an orientation mapping of neighbouring grains is the Electron Back Scattering Diffraction (EBSD), in a SEM. Figure 4 presents an example of an experimental diffraction pattern with its indexation.

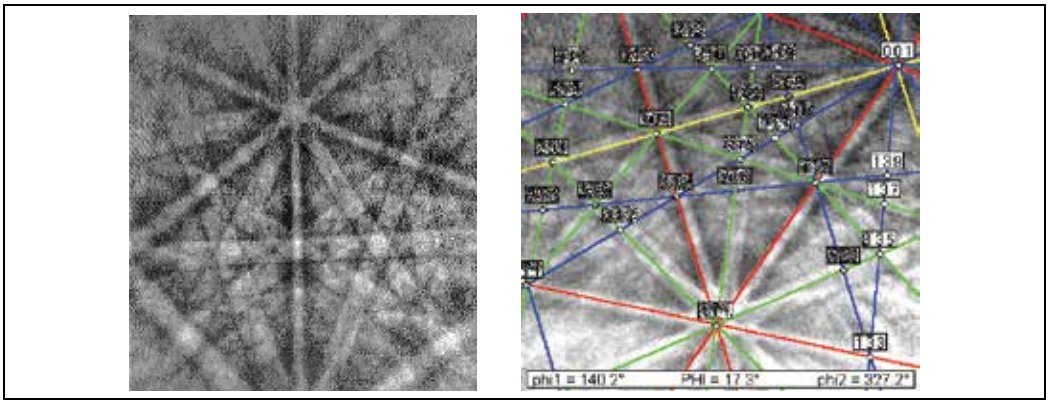

Fig. 4. Example of the diffraction pattern using EBSD technique.

With this technique the individual matrix g expressed by relation (2) are determined for the different particular points. Next, each grain can be compared with its neighbourhood. Figure 5 present then an illustration of a crystallographic experimental determination carried out on the AA2024 alloy using EBSD map determined to precise the neighbouring of the grains necessary for a local characterization of the crystallographic orientations of the starting material (Fig. 5b).

In Fig. 5b the map corresponds to a zone of approximately (200 μm x 570 μm) and the result is consistent with the optical characterization which shows grains greater than the others.

Other possible way to characterize the grain orientations of the material uses X-ray diffraction measurements for the texture determination. Let g be the crystal orientation noted $g = (\phi_1, \phi, \phi_2)$ and dg an infinitesimal range around it. The Orientation Distribution Function (ODF), F(g), is the continuous function which describes the crystallographic texture ((Bunge, 1996), (Bunge & Schwarzer, 1998)). By definition, F(g)dg is the volume fraction of all crystallites for which the g crystal orientation is in the dg range :

$$F(g)dg = dV(g)/V \; ; \; g = (\phi_1, \phi, \phi_2) \quad (2)$$

F(g) is determined from pole figure measurements and background and defocusing corrections.

From the knowledge of ODF complete recalculated poled figures can be determined. As an illustration the crystallographic texture of the aluminium alloy reported in this study have been characterized by the measurement of the {111}, {200}, and {220} pole figures using the

(a)

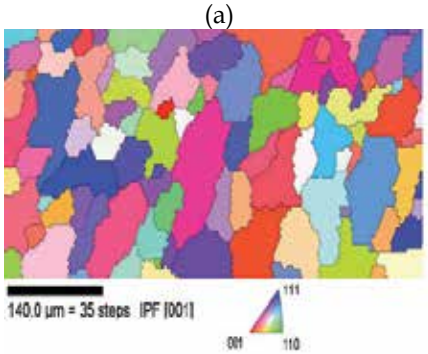

(b)

Fig. 5. Crystallographic characterization of the AA2024 alloy with the EBSD technique in the SEM: (a) the sample surface characterization, (b) crystallographic map of the material.

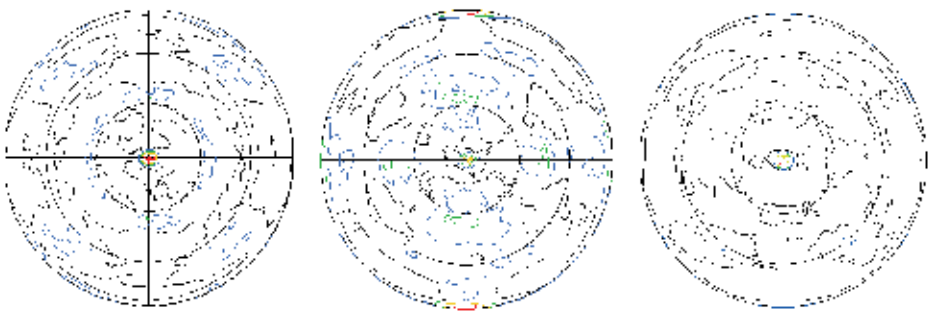

{111}-Max: 3.8 {200}-Max: 3.0 {220}-Max: 4.2

Fig. 6. Initial texture of an AA2024 aluminium alloy: {111}, {200} and {220} recalculated pole figures.

$K_{\alpha 1}$ copper radiation (λ =1.54056 Å). Concerning the initial texture (XR characterization), the {111}, {200} and {220} pole figures corresponding to the initial state of the material are presented in Fig. 6. The recalculated pole figures use the corrections mentioned above.
From these preliminary experimental results it is possible to conclude that the studied material has three principal initial textures and the choice of the three specimen positions is then valid. Moreover these figures are particularly important to determine the evolution of

the orientation of the grains with the plastic deformation. Then the microscopic phenomenon which accompanies the plastic deformation and the stress state in aluminium alloys is the accumulation of dislocations in the material. This contributes to the formation of three-dimensional arrays that depend on strain, strain rate, chemical composition, stacking fault energy, temperature and loading path. The chemical composition is particularly important since for pure aluminium, solute or dispersion strengthened aluminium alloys might exhibit different microstructural features. For instance, pure aluminium is a cell forming material ((Hansen, 1991), (Hansen, 1992), (Lopes *et al.*, 2003)). But Al-Mg is a non cell forming metal ((Hughes, 1992), (Hughes, 1993)). On the other hand, for alloys such as Al-Cu, Al-Mg-Si, Al-Cu-Mg, the description of the microstructure may be more complex because of the presence of alloying elements in solid solution, the precipitates and their interactions with the dislocations (Baudelet *et al.*, 1978). In the mechanical behaviour of these materials, strain hardening is the consequence of the increase of dislocation density which interacts with geometric hardening due to texture change. Generally the grains tend to rotate towards more stable orientations. For aluminium alloys, after hot or cold rolling conditions, the {112}<111> (Copper), {110}<112> (Brass) and {123}<634> (S) orientations are dominant components. The proportions between these different components depend on the rolling conditions and material composition. However, after an annealing treatment, depending on the process conditions, the texture can be nearly isotropic or composed of the following components: {100}<001> (Cube) and {110}<001> (Goss). The positions of important orientations in Euler angle space are listed in the Table 2.

Name	{hkl}	<uvw>	ϕ_1	ϕ	ϕ_2
C	112	111	90	35	45
D	4 4 11	11 11 8	90	27	45
S	123	523	55	37	63
G	011	100	0	45	90
B	011	211	35	45	90
B/G	~011	411	20	45	90

Table 2. The important orientations defined in the Euler angle space (first subspace).

At ambient temperature, the copper type is characteristic for materials with high or intermediate stacking fault energy. On the other hand, the brass type behaviour is characteristic for materials with low stacking fault energy. Important parameters which introduce modifications from one type to texture to and other type are the temperature (particularly for rolling) and the strain rate ((Hu & Cline, 1961), (Hu & Goodman, 1963)). Slip on {111}<110> systems is significant in these alloys and explain the formation of texture. However in the literature there are indications that other slip planes than {111} may be active in fcc alloys. Consequently some authors suggest that non octahedral slip may explain texture formation (Bacroix & Jonas, 1998).

The crystallographic textures of the samples after the plastic deformation are characterized in Fig. 7. This figure pictures the {111}, {200} and {220} pole figures of the AA2024 aluminium alloy after deformation by channel die compression test (specimens S1, S2 and S3). The comparison of the different pole figures indicates that the average orientation of the grains of S_1 and S_2 are similar. This result is consistent with the stress levels measured in the ND direction for these two specimens (614.37 MPa for S1 and 614.05 MPa for S2). Moreover

the measured pole figures seem to be consistent with those determined in aluminium alloys during a cold rolling ((Leacock, 2006), (Huh *et al.*, 2001), (Jin & Lloyd, 2005)).

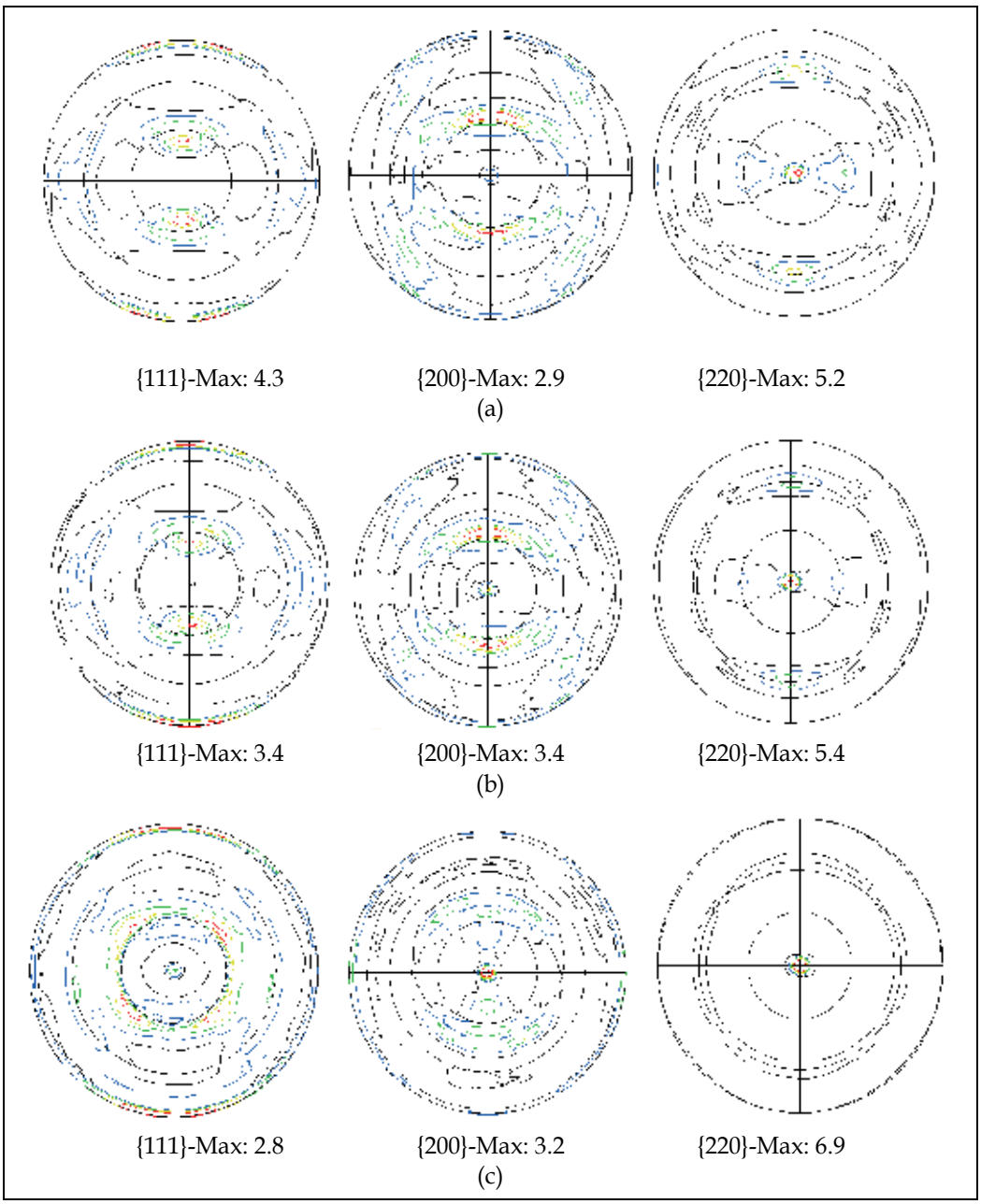

Fig. 7. Experimental textures of the AA2024 alloy after channel die compression tests: {111}, {200} and {220} recalculated pole figures for: (a) LD // RD_0, TD // TD_0, ND // ND_0 (deformed specimen S1), (b) LD // TD_0, TD // RD_0, ND // ND_0 (deformed specimen S2), (c) LD // RD_0, TD // ND_0, ND // TD_0 (deformed specimen S3).

This figure pictures the {111}, {200} and {220} pole figures of the AA2024 aluminium alloy after deformation by channel die compression test (specimens S1, S2 and S3). The comparison of the different pole figures indicates that the average orientation of the grains of S_1 and S_2 are similar. This result is consistent with the stress levels measured in the ND direction for these two specimens (614.37 MPa for S1 and 614.05 MPa for S2). Moreover the measured pole figures seem to be consistent with those determined in aluminium alloys during a cold rolling ((Leacock, 2006), (Huh *et al.*, 2001), (Jin & Lloyd, 2005)).

4. Micro-Macro approach

The mechanical behaviour of aluminium alloys are related to their texture evolutions. Several polycrystalline models have been developed to interpret the experimental observations from the active deformation slip systems. The first one is the Sachs model which assumes the same form for the stress state in each grain (Sachs, 1928). The slip systems are activated when the maximum shear stresses are reached according to the Schmid's law:

$$\sigma_{ij}.m_{ij}^{s} = \tau_c^s \tag{3}$$

where m_{ij}^{s} is the generalized Schmid factor defined by :

$$m_{ij}^{s} = \frac{1}{2}(n_i^s b_j^s + b_i^s n_j^s) \tag{4}$$

Here $\vec{n}^s$ is the unitary slip plane normal of the *s* systems and $\vec{b}^s$ is the unitary slip direction of the system: *s* varies from 1 to 12 for aluminium alloys. With this model, the deformation is different from grain to grain in the polycrystalline material.
On the other hand, the Taylor model considers that the strain tensor is the same in all the grains of the polycrystalline material (Taylor, 1938). Five slip systems are necessary for a prescribed strain increment. The selection of these systems among several possibilities is achieved with the application of the criterion of minimum internal work:

$$\text{Min of } \sum_s \tau_c^s.\dot{\gamma}^s \tag{5}$$

where $\dot{\gamma}^s$ is the shear rate on the active *s* system.
Bishop and Hill (Bishop et al., 1951), (Bishop, 1953)) determined all the possible stress states for five independent slip systems in the five dimensional space of the components of the stress tensor. They used the criterion of the maximum external work to select the appropriated stress state:

$$\text{Max of } \sum \sigma_{ij}\dot{\varepsilon}_{ij} \tag{6}$$

with $\dot{\varepsilon}_{ij}$ given by:

$$\dot{\varepsilon}_{ij} = \sum_s m_{ij}^s \dot{\gamma}^s \tag{7}$$

It can be shown that the Taylor theory and the Bishop-Hill theory are mathematically equivalent. Both criteria (5) and (6) have been shown to lead to the same results. From the

Taylor model, relaxed constraints models have also been developed for more accurate predictions of texture evolutions ((Hirsch & Lücke, 1988)), (Engler *et al.*, 2005), (Molinari *et al.*, 1994)).
More complex models which take into account the active slip systems of the material and the interaction between the grains have been applied to the characterization of anisotropy, notably the viscoplastic self consistent models (VPSC). In their approach, Molinari *et al.* (1994) derived the following interaction law by considering the concept of Homogeneous Equivalent Matrix (HEM) and 1-site approximation:

$$s^g - S = \left(\Gamma^{gg'-1} + A\right) : (\dot{\varepsilon}^g - \dot{E}) \tag{8}$$

where S and $\dot{E}$ are respectively the deviator stress tensor and the strain rate tensor at the macroscopic level. S^g and $\dot{\varepsilon}^g$ represent the same quantities at the grain scale. The interaction tensor Γ between a grain g and its neighbourhood described by g' can be obtained by integration of the symmetric part of the second derive of the Green function. It can take into account the effect of grain shape (spherical or ellipsoidal).
In the model, the microscopic strain rate is calculated using a viscoplastic power law relation:

$$\tau^s = \tau_0^s \left(\frac{\dot{\gamma}^s}{\dot{\gamma}_0^s} \right)^n \tag{9}$$

Then, using (7) it can be written:

$$\dot{\varepsilon}_{ij} = \dot{\gamma}_0 \sum_s m_{ij}^s \left(\frac{s_{kl} m_{kl}}{\tau_0^s} \right)^{\frac{1}{n}} \tag{10}$$

Lebensohn & Tomé (1993) have also developed a VPSC approach to predict the mechanical behaviour of polycrystalline materials. They derived the following interaction relation:

$$\dot{\varepsilon} - \dot{E} = -\tilde{M}(s - S) \tag{11}$$

The tensor $\tilde{M}$ characterizes the interaction between a grain and its neighbourhood.
These micro-macro models have also been used for the determination of the anisotropy of aluminium alloys. They present the advantage to relate the mechanical behaviour of the material to the physical mechanisms of deformation. Some authors have compared experimental measurements of the flow stress and the Lankford coefficient (r-value) with the predictions of the full constraints and relaxed constraints Taylor-Bishop-Hill models ((Kuwabara *et al.*, 2002), (Fjeldly & Roven, 1996)). These comparisons are often carried out for different angles between the tensile axe and the initial rolling direction of the material. Other important application of these models in the characterization of the anisotropy of aluminium alloys is the prediction of the yield loci for different texture components ((Lequeu *et al.*, 1987), (Hu *et al.*, 1998)). In a comparative study Choi and Barlat ((Choi & Barlat, 1999), (Choi *et al.*, 2000)) showed that their experimental results are in better agreement with the VPSC approach than the Taylor one. A complementary analysis of the anisotropy of an AA1050 aluminium sheet has been carried out also by Lopes *et al.* (2003) for

the description of tensile and simple shear stress strain curves with the VPSC model developed by Lebensohn & Tomé (1993). The authors modeled the macroscopic curves by indentifying the parameters describing strain hardening on the slip systems.
From the measurement of the pole figures of the material of this study and the determination of the ODF at the initial stage, the coefficient of anisotropy, obtained from the ratio between the measured width reductions and the high ones, has been calculated with the Taylor FC model and the VPSC developed by Lebensohn and Tomé for different angles between the tensile axis and the specimen. The results are presented in Figure 8.

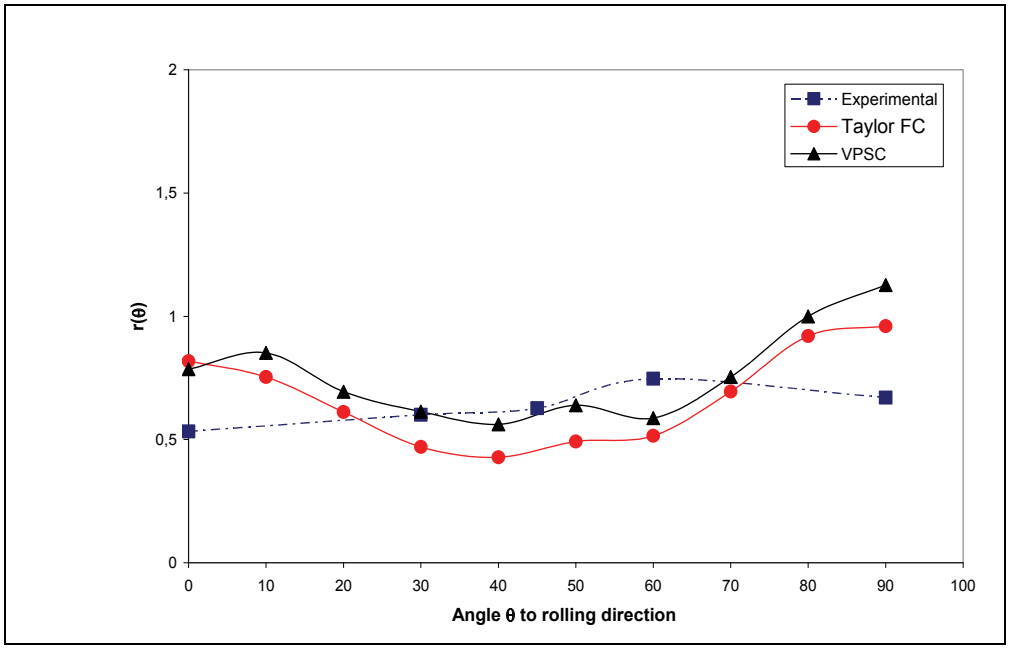

Fig. 8. The coefficient of the anisotropy r(θ) value versus angle θ defining orientation to the initial rolling direction of the starting sheet: experimental and computed values determined with the Taylor FC and the VPSC models.

The two models predict values close to the experimental ones and the differences are relatively low between 20°-70°.

5. Classical analysis of anisotropic behaviour

This paper proposes to analysis the anisotropic behaviour assuming the orthotropic symmetry hypothesis and using the most known quadratic criterion such as the classical Hill one (Hill, 1948) defined by:

$$f([\sigma]) = F(\sigma_{yy} - \sigma_{zz})^2 + G(\sigma_{zz} - \sigma_{xx})^2 + H(\sigma_{xx} - \sigma_{yy})^2 + 2L\sigma_{yz}^2 + 2M\sigma_{zx}^2 + 2N\sigma_{xy}^2 - 1 = 0 \quad (12)$$

According to the basic scientific literature, the Hill coefficients can be defined from simple tensile tests and simple shear ones using the following relationships:

$$F = \frac{1}{2}\left[\frac{1}{\sigma_{0yy}^2}+\frac{1}{\sigma_{0zz}^2}-\frac{1}{\sigma_{0xx}^2}\right], G = \frac{1}{2}\left[\frac{1}{\sigma_{0xx}^2}+\frac{1}{\sigma_{0zz}^2}-\frac{1}{\sigma_{0yy}^2}\right], H = \frac{1}{2}\left[\frac{1}{\sigma_{0yy}^2}+\frac{1}{\sigma_{0xx}^2}-\frac{1}{\sigma_{0zz}^2}\right]$$
$$L = \frac{1}{2\sigma_{0yz}^2}, M = \frac{1}{2\sigma_{0zx}^2}, N = \frac{1}{2\sigma_{0xy}^2} \quad (13)$$

where $\sigma_{0xx}, \sigma_{0yy}, \sigma_{0zz}$ represent the yield stress corresponding to each tensile direction and $\sigma_{0xy}, \sigma_{0yz}, \sigma_{0zx}$ are the critic shear stress.

If a plan anisotropy of the material sheet is assumed, the expression of the coefficient of anisotropy r(θ), expressing the ratio between the width reduction and the thickness one, can be defined analytically by:

$$r(\theta) = \frac{\dot{\varepsilon}_{yy}}{\dot{\varepsilon}_{zz}} = \frac{H + (2N - F - G - 4H)\sin^2(\theta)\cos^2(\theta)}{F\sin^2(\theta) + G\cos^2(\theta)} \quad (14)$$

In this case is possible to estimate the Hill coefficients directly from the measured anisotropic coefficient r(θ) i.e.:

$$r(0) = R = \frac{H}{G}, r(45) = \frac{1}{2}\left(\frac{2N - F - G}{F + G}\right), r(90) = \frac{H}{F}, H = \frac{R}{R+1}\frac{1}{\sigma_{0xx}} \quad (15)$$

Regarding the Fig. 8, the measured values of the plastic strain ratio defined by (14) shows that *r(θ)* increase with the rolling direction θ for most of the experimental points. The greatest measured value is determined for θ = 60°. Values of the coefficient of anisotropy lower than 1 are reported in literature for aluminium alloys ((Leacock, 2006), (Choi *et al.*, 2000), (Choi *et al.*, 2001), (Tong, 2006)). Moreover the variation measured in the study is consistent with the experimental data of Leacock (Leacock, 2006) for an AA2024 alloy. Despite the particular value for the 60°, all the other values are between 0.540 and 0.654. Moreover $\bar{r} = 0.62$, $\Delta r = -0.04$ and it can be concluded that these quantities permits to consider that the plate have a normal anisotropy described by:

$$\sigma_{xx}^2 + \sigma_{yy}^2 - \frac{2R}{R+1}\sigma_{xx}\sigma_{yy} + \frac{2(2R+1)}{R+1}\sigma_{xy}^2 = \frac{R}{H(R+1)} = \sigma_0^2 \quad (16)$$

It is important to note that in all the literature the use of the tensile test and the computation of the anisotropic coefficients are used without the take into account the variation of the yield stress with the plastic deformation. Moreover, because of the striction phenomenon, the tensile test is limited to small plastic deformation (around of 15% for aluminium alloy).

For an anisotropic behaviour analysis corresponding to large plastic deformation conditions, this paper proposes the use the channel die compression experiments. The corresponding stress-strain curves determined from the three different sample positions defined in §2 (according to the three types of observed textures), are presented in Fig. 9.

Using the general law proposed by Gavrus (Gavrus, 1996) and using only influence of the cumulated plastic strain the following expression can be used to fit the above experimental curves:

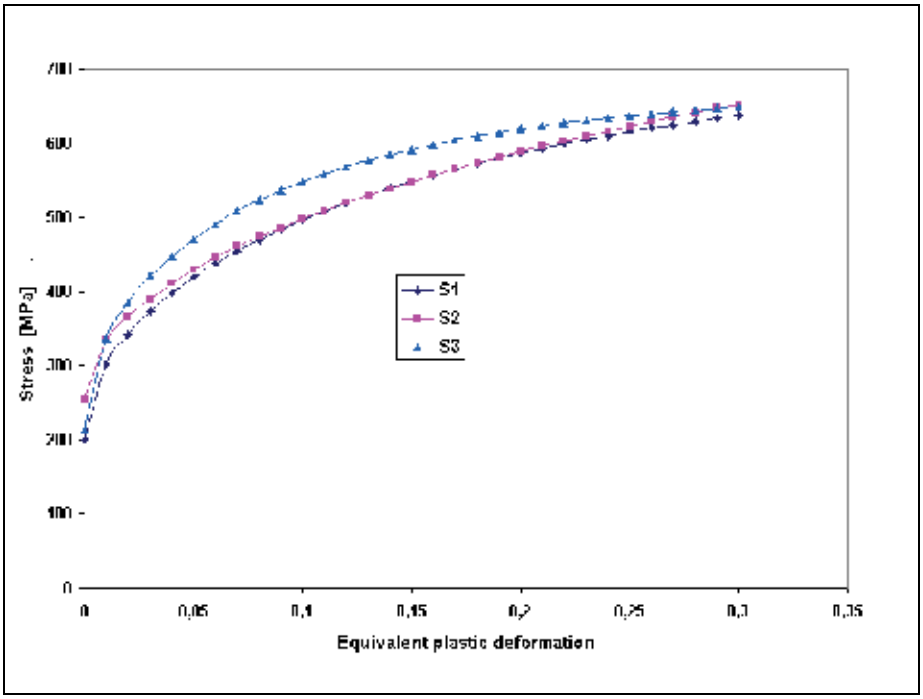

Fig. 9. Experimental stress strain curves of the specimens (S_1, S_2, S_3) deformed by channel die compression.

$$\sigma = \sigma_{00} + \sigma_{pl}\left[1 - \exp(-n\bar{\varepsilon})\right]^{n_a} W + \sigma_{sat}\left[1 - W\right] \quad \text{with} \quad W = \exp\left(-r\bar{\varepsilon}^{s}\right) \tag{17}$$

It have been shown that this formulation is able to describe different shapes of the stress-strain curves and can explain observed physical phenomena such as the hardening, the dynamic recovery, the dynamic softening or the break slope one. It is worth noting that the curves are similar for S_1 and S_2: the stress levels are close to each other in the main part of the plastic deformation. Concerning S_3, the stress levels are more important. For instance, at 15% of the plastic deformation, the normal stress is 548 MPa for S_1, S_2 and 591 MPa for S_3.

6. The analytical model describing the channel die compression test

The main advantage of the channel die compression test is the homogeneity of the plastic deformation caused by the small effect of the friction (if a teflon material is used on the tool-specimen interfaces) and the absence of the shape instability caused by the striction phenomenon (important for the classical tensile test). Consequently an analytical model can be used to compute stress, strain and strain rate tensors. From our knowledge a similar approach has already been mentioned only for tensile tests (Liu *et al.*, 1997) using a phenomenological study of the anisotropic criterion. The present research work proposes a model based on the expression of the classical Hill criterion ((Hill, 1948), (Hill, 1979)) but introducing a variation of the Hill coefficients with a defined cumulated plastic strain. A parameter identification method based on an inverse analysis technique will be used to describe quantitatively the anisotropic model. We note l, w, h the length, width and

respectively the high of the samples during the mechanical test and V the punch compression speed. According to the channel die device axes: X(LD), Y(TD), Z(ND) defined in Fig.1, the kinematics conditions and the incompressibility equation ($\mathrm{div}(\vec{v})=0$) lead to the following form of the velocity vector:

$$\vec{v} = \begin{bmatrix} u(X) \\ 0 \\ w(Z) \end{bmatrix} = \begin{bmatrix} XV/h \\ 0 \\ -ZV/h \end{bmatrix} \tag{18}$$

Consequently we have a diagonal strain rate tensor $\dot{\varepsilon}$ for which the component in the Z direction is equal to -V/h, in the Y direction is equal to 0 and in the X direction is equal to V/h. To take into account the plastic strain history, a deformation tensor can be defined by:

$$\varepsilon = \int_0^t \dot{\varepsilon} dt = \begin{bmatrix} \int_0^t (V/h) d\tau & 0 & 0 \\ 0 & 0 & 0 \\ 0 & 0 & -\int_0^t (V/h) d\tau \end{bmatrix} \tag{19}$$

In a first approximation, an equivalent plastic strain value can be expressed in term of the second invariant of the deformation tensor i.e.:

$$\bar{\varepsilon} = \sqrt{\frac{2}{3}\mathrm{tr}\left(\varepsilon^2\right)} = \sqrt{\frac{2}{3}\left(\varepsilon_{xx}^2 + \varepsilon_{yy}^2 + \varepsilon_{zz}^2\right)} = \frac{2}{\sqrt{3}}\ln\left(\frac{h_0}{h}\right) \tag{20}$$

where h_0 is the initial height of the samples.

Because the deformation along the Y direction is rigorously equal to 0 ($\varepsilon_{yy} = \int_0^t \dot{\varepsilon}_{yy} dt = 0$) we obtain a plane strain deformation. The corresponding stress tensor is also diagonal and has a null component in the X direction (free plastic flow i.e. plan stress conditions):

$$\sigma = \begin{bmatrix} 0 & 0 & 0 \\ 0 & \sigma_{yy} & 0 \\ 0 & 0 & \sigma_{zz} \end{bmatrix} \text{ with } \sigma_{zz} = F/S \tag{21}$$

where $S = lw = (l_0 w_0)h_0/h$ is the area of the real sample surface in contact with the punch and F is the forging load measured in the Z direction.

Starting from this mathematical model of the plan compression experiment, the following expressions of the strain rate tensor and of the stress tensor are obtained for the three sample positions:

a. Position P1 (specimen S1)

$$[\dot{\varepsilon}] = \begin{bmatrix} V/h & 0 & 0 \\ 0 & 0 & 0 \\ 0 & 0 & -V/h \end{bmatrix}; [\sigma] = \begin{bmatrix} \sigma^{(1)}_{LD//RD_0} = 0 & 0 & 0 \\ 0 & \sigma^{(1)}_{TD//TD_0} & 0 \\ 0 & 0 & \sigma^{(1)}_{ND//ND_0} \end{bmatrix}$$

b. Position P2 (specimen S2)

$$[\dot{\varepsilon}]=\begin{bmatrix}0 & 0 & 0\\ 0 & V/h & 0\\ 0 & 0 & -V/h\end{bmatrix};\quad [\sigma]=\begin{bmatrix}\sigma^{(2)}_{TD//RD_0} & 0 & 0\\ 0 & \sigma^{(2)}_{LD//TD_0}=0 & 0\\ 0 & 0 & \sigma^{(2)}_{ND//ND_0}\end{bmatrix} \tag{22}$$

c. Position P3 (specimen S3)

$$[\dot{\varepsilon}]=\begin{bmatrix}V/h & 0 & 0\\ 0 & -V/h & 0\\ 0 & 0 & 0\end{bmatrix};\quad [\sigma]=\begin{bmatrix}\sigma^{(3)}_{LD//RD_0}=0 & 0 & 0\\ 0 & \sigma^{(3)}_{ND//TD_0} & 0\\ 0 & 0 & \sigma^{(3)}_{TD//ND_0}\end{bmatrix}.$$

The index (i) refers to the sample position and all the matrixes are written in the coordinates system of the sheet.

7. The anisotropic behaviour model

For standard materials, using a convex anisotropic yield function *f* expressed in terms of the stress tensor components, the strain rate matrices can be determined from the stress gradient of the convex surface:

$$[\dot{\varepsilon}]=\lambda^{pl}\frac{\partial f}{\partial[\sigma]} \tag{23}$$

where λ^{pl} is the plastic multiplier.
According to the Hill criterion defined in (12), for each strain rate component the following expressions can be written:

$$\begin{aligned}&\dot{\varepsilon}_{xx}=2\lambda^{pl}\left[G(\sigma_{xx}-\sigma_{zz})+H(\sigma_{xx}-\sigma_{yy})\right],\quad \dot{\varepsilon}_{yy}=2\lambda^{pl}\left[F(\sigma_{yy}-\sigma_{zz})+H(\sigma_{yy}-\sigma_{xx})\right]\\ &\dot{\varepsilon}_{zz}=2\lambda^{pl}\left[F(\sigma_{zz}-\sigma_{yy})+G(\sigma_{zz}-\sigma_{xx})\right],\quad \dot{\varepsilon}_{xy}=4\lambda^{pl}N\sigma_{xy},\ \dot{\varepsilon}_{yz}=4\lambda^{pl}L\sigma_{yz},\ \dot{\varepsilon}_{xz}=4\lambda^{pl}M\sigma_{xz}\end{aligned} \tag{24}$$

Using the analytical model detailed in the previous section, for the first position of the specimen (specimen S1) in the channel die compression device, the two equations (22) and (24) lead to:

$$\begin{aligned}&V/h=2\lambda^{pl}\left[-G\sigma^{(1)}_{ND//ND_0}-H\sigma^{(1)}_{TD//TD_0}\right]\\ &0=2\lambda^{pl}\left[F\left(\sigma^{(1)}_{TD//TD_0}-\sigma^{(1)}_{ND//ND_0}\right)+H\sigma^{(1)}_{TD//TD_0}\right]\text{i.e. }\sigma^{(1)}_{TD//TD_0}=\frac{F}{F+H}\sigma^{(1)}_{ND//ND_0}\\ &-V/h=2\lambda_{pl}\left[-F\left(\sigma^{(1)}_{TD//TD_0}-\sigma^{(1)}_{ND//ND_0}\right)+G\sigma^{(1)}_{ND//ND_0}\right]\end{aligned} \tag{25}$$

Then for all the three different positions, combining equations (12), (22), (24) and corresponding (25) ones, the following relationships can be easily obtained:

$$\sigma^{(1)^2}_{ND//ND_0}\left(\frac{FG+FH+GH}{F+H}\right)=1 \text{ for P1}$$

$$\sigma^{(2)^2}_{ND//ND_0}\left(\frac{FG+FH+GH}{G+H}\right)=1 \text{ for P2} \quad (26)$$

$$\sigma^{(3)^2}_{ND//TD_0}\left(\frac{FG+FH+GH}{F+G}\right)=1 \text{ for P3}$$

These three relationships lead to the following expressions of anisotropic criterion coefficients:

$$F=\frac{\alpha}{\alpha\beta+\beta\gamma+\gamma\alpha}\ ;\ G=\frac{\beta}{\alpha\beta+\beta\gamma+\gamma\alpha}\ ;\ H=\frac{\gamma}{\alpha\beta+\beta\gamma+\gamma\alpha} \quad (27)$$

where:

$$\alpha=\frac{1}{2}\left[\sigma^{(1)^2}_{ND//ND_0}+\sigma^{(3)^2}_{ND//TD_0}-\sigma^{(2)^2}_{ND//ND_0}\right],\ \beta=\frac{1}{2}\left[\sigma^{(2)^2}_{ND//ND_0}+\sigma^{(3)^2}_{ND//TD_0}-\sigma^{(1)^2}_{ND//ND_0}\right]$$

and

$$\gamma=\frac{1}{2}\left[\sigma^{(1)^2}_{ND//ND_0}+\sigma^{(2)^2}_{ND//ND_0}-\sigma^{(3)^2}_{ND//TD_0}\right] \quad (28)$$

The parameters *L*, *M*, *N* can be determined from simple shear tests (Liu *et al.,* 1997). Starting from the curves pictures in Fig. 9 and using the phenomenological law (1), the parameters defining the stress components in the ND_0 direction are identified using an inverse analysis technique based on a non-linear regression of a cost function describing in a least squares sense the difference between the experimental points and the predicted ones. The identification results are presented in the Table 3 (here W is chosen equal to 1).

Parameters	S1 (position 1)	S2 (position 2)	S3 (position 3)
σ_{00}	200.	254.	213.
σ_{pl}	538.519	714.260	459.817
n	3.607	1.239	7.563
n_a	0.5	0.5	0.5
Mean error (E_r)	2 %	1.60%	2.60%

Table 3. Identified parameters results obtained for the proposed phenomenological law corresponding to the chosen three positions of the samples (S1, S2 and S3 specimens).

Using the (16) and (17) expressions it is possible to obtain a variation of the Hill coefficients with the defined cumulated plastic strain i.e. $F(\bar{\varepsilon}), G(\bar{\varepsilon})$ and $H(\bar{\varepsilon})$. These evolutions of the Hill coefficients permit to make the classical anisotropic Hill criterion more consistent with the large plastic deformation phenomena which occur during the real forming process and to extend its availability for a large class of metallic materials.

In the particular case of a normal anisotropy, we must have $\frac{dr(\theta)}{d\theta} = 0$. Using formula (4), (16) and (17) it is necessary to have $N=F+2H$ and $F = G$ i.e. $\sigma^{(1)}_{ND//ND_0} = \sigma^{(2)}_{ND//ND_0}$. Or the variation of the stress plotted in Fig. 9 shows that between 10% and 30% of the cumulated plastic strain, this condition is rigorously reached. Then, the corresponding Hill coefficients have the following analytical expressions:

$$F = G = \frac{2}{4\sigma^{(1)2}_{ND//ND_0} - \sigma^{(3)2}_{ND//TD_0}}, \quad H = \frac{2\left[2\sigma^{(1)2}_{ND//ND_0} - \sigma^{(3)2}_{TD//ND_0}\right]}{\sigma^{(3)2}_{ND//TD_0}\left[4\sigma^{(1)2}_{ND//ND_0} - \sigma^{(3)2}_{ND//TD_0}\right]} \tag{29}$$

According to the proved normal anisotropy assumption, for a plan stress hypothesis, the anisotropic criterion in the local (x, y) axes of the plate can be written in the following form:

$$\sigma^2_{xx} + \sigma^2_{yy} - \frac{2r}{r+1}\sigma_{xx}\sigma_{yy} + \frac{2(2r+1)}{r+1}\sigma^2_{xy} = \frac{2r+1}{2(r+1)}\sigma^{(3)2}_{ND//TD_0} = \sigma^2_0 \tag{30}$$

where *r* is named here the Lankford coefficient and can be expressed by:

$$r = r(0) = R = \frac{H}{G} = 2\frac{\sigma^{(1)2}_{ND//ND_0}}{\sigma^{(3)2}_{ND//TD_0}} - 1 \tag{31}$$

With these expressions the dependence of the Lankford coefficient with the cumulated plastic deformation (defined by (20)) can be predicted from the stress-strain curves determined in the previous section. The dependence of the stress components with plastic deformation is given by (17) (see also Table 3). The values predicted by the model are expected to be more realistic when the plastic deformation is relatively low (such as in the case of the tensile test). The result is presented in Fig. 10. For a low plastic deformation (< 5%), it can be seen that the values of *r* are close to 0.57. This value is consistent with the experimental value of *r(0)* =0.54 near determined for θ = 0° (see Fig. 8). The values increase with the plastic deformation: for 25% of deformation, *r* is near 0.9 and the variation is asymptotic to 1 for more large plastic strains. The range of these values is consistent with those mentioned for aluminium alloys [9, 15] and it can be concluded that the proposed model predicts the Lankford coefficient values in accordance with the known anisotropic material properties of AA 2024 alloy. Moreover, the evolution of σ_0 with plastic deformation presented in Fig. 10 shows that the obtained increasing variation is coherent for this material and realistic with other experimental previsions.

8. Conclusions

Channel die compression tests have been carried out for the characterization of the anisotropy of an aluminium alloy undergoing large plastic deformations. Crystallographic evolutions and stress-strain curves show that the material has a specific response according to the normal plane of compression of the specimen. Significant differences are measured

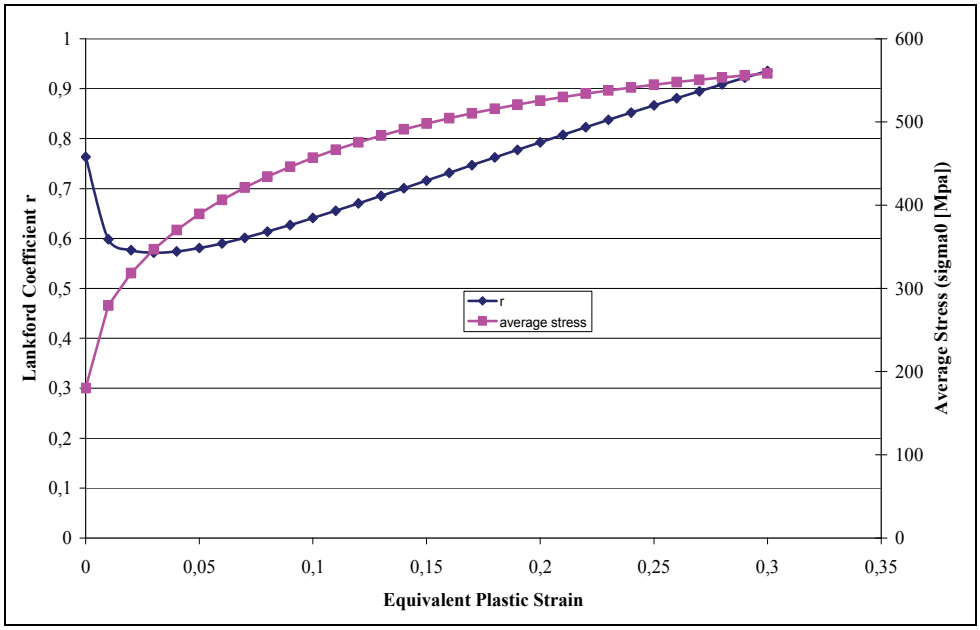

Fig. 10. Prediction of the variation of the Lankford coefficient and of the σ_0 with the equivalent plastic deformation.

when the normal plane is along TD_0 and the longitudinal direction along LD_0. An analytical model, adapted for the channel die compression test, has been proposed in order to describe a Hill criterion. This proposed analysis permits to have an analytical expression of the Hill coefficients and the new idea is here the introduction of its variations with the plastic strain values. The realistic prediction of the Lankford coefficient evolution shows that the obtained values are consistent with values measured for general aluminium alloys. In a future work new 3D anisotropic criteria will be analyzed for plastic solid materials starting from this study and using all the six possible positions of the plate specimen in the channel die compression device.

9. References

Banabic, D.; Bunge, H. –J.; Pöhlandt, K. & Tekkaya, A. E. (2000). *Formability of Metallic Materials: Plastic Anisotropy, Formability Testing, Forming Limits,* Springer-Verlag Berlin and Heidelberg GmbH & Co. K.

Banabic D.; Cazacu, O.; Barlat, F.; Comsa, D. S.; Wagner, S. & Siegert, T. (2002). Description of anisotropic behaviour of AA3103-0 aliminium alloy using two recent yeld criteria, *6th EUROMECH-MECAMAT*, pp. 297-304, Liège, Belgium, 9-12 September 2002, edited by S. Cescotto, C. Teodosiu, A.-M. Habraken, R. Billardon and I. Doghri.

Bacroix, B. & Jonas, J. J. (1998). Proc. ICOTOM 8, pp. 403-421, J.S. Kallend, G. Gottstein (Eds.), Warrendale, The Metallurgical Society.

Barralis J. & Maeder, G. (2005). *Précis de Métallurgie,* Nathan Eds.

Baudelet, B.; Deguen, M.; Felgères, L.; Parnière, P.; Roné-Oustau, F. & Sanz, G. (1978). *Mém. Scient. Revue Métall.,* 75, 409-422.
Bishop, J. F. W. & Hill, R. (1951). *Phil. Mag.,* 42, 414, 1298.
Bishop, J. F. W. (1953). *Phil. Mag.,* 44, 51.
Browen, A. W. (1990). *Mater. Sci. Technol.,* 11, 1058-1071.
Bunge, H. J. (1996). Texture Analysis in materials science, London, Butterworth.
Bunge, H. J. & Schwarzer, R. (1998). Orientation stereology – a new branch of texture studies, *TU Contact* (Clausthal), 2, 67-73.
Cazacu, O. & Barlat, F. (2001). *Mathematics and Mechanics of Solids*, 6, 613-630.
Chin, G. Y. & Mammel, W. L. (1969). *Trans. Metall. Soc. AIME.,* 245, 1211.
Choi, S.-H. & Barlat, F. (1999). Prediction of macroscopic anisotropy in rolled aluminium-lithium sheet, *Scripta Mater.,* 41, 981-987.
Choi, S. H.; Brem, J. C.; Barlat, F. & Oh, K. H.(2000). *Acta mater,* 48, 1853-1863.
Choi, S. H.; Barlat, F. & Liu, J.(2001). *Metallurgical and Materials Transactions A,* 32A, 2239-2247.
Engler, O.; Hecklmann, I.; Rickert, T.; Hirsch, J. & Lücke, K. (1994). *Mater. Sci. Technol.,* 10, 10, 771-781.
Engler, O.; Hirsch, J. & Lücke, K. (1995). *Acta Metall.,* 43, 1, 121-138.
Engler, O.; Crumbach, M. & Li, S. (2005). *Acta Mater.,* 53, 2241-2257.
Fjeldl, A. & Roven,A. (1996). Observations and calculations on mechanical anisotropy and plastic flow of an AlZnMg extrusion, *Acta Mater.*, 44, 9, 3497-3504.
Francillette, H.; Castelnau, O.; Bacroix, B.;J Béchade, J. L.(1998). Experimental and predicted texture evolutions in zirconium alloys deformed in channel die compression, *Mat. Science Forum*, 273-275, 523-528.
Francillette, H.; Gavrus, A. & Lebensohn, R. A.(2003). A constitutive law for the mechanical behaviour of Zr702□, *Journal of Materials Processing Technology,* 142, 43-51.
Gavrus, A.(1996). *Identification automatique des parameters rheologiques par analyse inverse,* PhD Thesis, Ecole des Mines de Paris Eds, France.
Hansen, J.; Pospiech, J. & Lücke, K. (1978), *Tables for textures. Analysis of cubic crystals,* Berlin, Springer.
Hansen, N. (1991). Distributions of glide systems in cell formation metals. In : T. C. Lowe, A. D. Rollett, P. S. Follansbee & G. S. Daehn (Eds), Modelling the Deformation of Crystalline Solids, pp. 37-49, TMS, Warrendale,.
Hansen, N. (1992). *Scr. Metall. Mater.,* 27, 947-950.
Hill, R.(1948). A theory of the yielding and plastic flow of anisotropic metals. *Proc. Roy. Soc. London A,* 193, 281.
Hill, R. (1979). *Math. Proc. Camb. Phil Soc.,* 85.
Hirsch, J. & Lücke, K. (1988). *Acta Metall.,* 36, 2883-2904.
Hu, H. & Cline, R. S. (1961). *J. Appl. Phys.,* 32, 760.
Hu, H. & Goodman, S. R. (1963). *Trans. Metall. Soc. AIME,* 227, 627.
Hu, J.; Ikeda, T. & Murakami, T. (1998). *Journal of Materials Processing Technology,* 73, 49-56.
Hughes, D. A. (1992). *Scr. Metall. Mater.,* 27, 969-974.
Hughes, D. A. (1993). *Scr. Metall. Mater.,* 41, 1421-1430.
Huh, M. Y.; Cho, S. Y. & Engler, O.(2001). Randomization of the annealing texture in aluminium 5182 sheet by cross-rolling, *Materials Sciences and Engineering A,* 315, 35-46.

Jin, H. & Lloyd, D. J.(2005). *Materials Sciences and Engineering A*, 399, 358-367.

Khalffalah, A. (2004). *Identification des lois de comportement élastoplastiques par essais inhomogènes et simulations numériques,* PhD Thesis, Université Tunis El Manar, Tunis.

Kuwabara, T.; Van Bael, A. & Iizuka, E. (2002). *Acta Mater.,* 50, 3717-3729.

Lademo, O.-G.; Hopperstad, O.S. & Langseth, M. (1999). *International Journal of Plasticity*, 15, 191-208.

Leacock, A. G. (2006). *Journal of the Mechanics and Physics of Solids,* 54, 425 –444.

Lebensohn, R. A. & Tomé, C. (1993). *Acta Metall.,* 41, 2611-2624.

Lequeu, Ph.; Gilormini, P.; Montheillet, F.; Bacroix, B. & Jonas, J. J. (1987). *Acta Metall.,* 35, 5, 1159-1174.

Li, Z. J.; Winter, G. & Hansen, N. (2004). Anisotropy of plastic deformation in rolled aluminium, *Mat. Sci. Eng. A*, 387- 389, 199-202.

Liu, C.; Huang Y. & Stout, M. G. (1997). On the asymmetric yield surface of plastically orthotropic materials: a phenomenological study, *Acta Mater,* 45, 6, 2397-2406.

Lopes, A. B.; Barlat, F.; Gracio, J. J.; Ferreira Duarte, J. F. & Rauch, E. F. (2003). *Int. J. Plast. ,* 19,1-22.

Lücke, K. & Engler, O. (1990). *Mater. Sci. Technol.,* 6, 11, 1113-1130.

Lloyd, D. J. & Kenny, D. (1980). The structure and properties of some heavily cold worked aluminium alloys, *Acta Metallurgica*, 28, 639-649.

Malo, K.A.; Hopperstad, O.S. & Lademo, O.G. (1998). J. *of Mat. Processing Technology*, 80-81, 538-544.

Molinari, A.; Canova, G. R. & Ahzi, S. (1994). *Acta Metall. Mater.,* 42, 2453.

Park., J.-J. (1999). Predictions of texture and plastic anisotropy developed by mechanical deformation in aluminium sheet, *Journal of Materials Processing Technology*, 87,146-153.

Sachs, E. (1928). *Z. Ver. Dt. Ing.,* 72, 734.

Taylor, G. I. (1938). *J. Inst. Met.,* 62, 307.

Tong, W. (2006). A plane stress anisotropic plastic flow theory for orthotropic sheet metals, *Int. J. of Plast.,* 22, 497-535.

Yoon, J. W.; Barlat, F.; Gracio, J. J. & Rauch, E. (2005). Anisotropic strain hardening behaviour in simple shear for cube textured aluminium alloy sheets, *International Journal of Plasticity,* 21, 2426-2447.

Zeng, X. H.; Ahmad, M. & Engler, O. (1994). *Mater. Sci. Technol.*, 10, 7, 581-591.

Part 2

Welding Phenomena

4

A Simple Approach to the Study of the Ageing Behaviour of Laser Beam and Friction Stir Welds between Similar and Dissimilar Alloys

Claudio Badini[1], Claudia Milena Vega Bolivar[1], Andrea Antonini[1], Sara Biamino[1], Paolo Fino[1], Diego Giovanni Manfredi[2], Elisa Paola Ambrosio[2], Francesco Acerra[3], Giuseppe Campanile[3] and Matteo Pavese[1]
[1]*Politecnico di Torino, Dipartimento di Scienza dei Materiali e Ingegneria Chimica*
[2]*IIT, Italian Institute of Technology, Center for Space Human Robotics @ PoliTO*
[3]*Alenia Areonautica S.p.A., Materiali e Processi, Italy*

1. Introduction

In recent years, lightweight structures have become more and more important for the transportation industry, since they allows reduction of fuel consumption and thus atmospheric pollution. The most common light metal is aluminium, that has a density close to 2.7 g/cm^3 coupled with interesting mechanical properties. Until 50 years ago, however, aluminium alloys were considered not weldable, due to the formation of aluminium oxide.
Nowadays, the welding of aluminium is a well-known and much studied subject, since welds are often the weak point of a structure. Indeed, aluminium alloys are mainly reinforced by controlled ageing or plastic deformation, so that welds represent an area of the structure where the standard approach for improving mechanical properties is not applicable. On the other side, mechanical fastening or riveting brings to serious problems during application, so that a significant effort has been done to develop low cost and high efficiency joining techniques.
The most used welding techniques are based on the localised melting of the alloys to be joined. The most common are MIG (metal inert gas welding), an arc welding under inert atmosphere with a metal fusible electrode, generally supplied with continuous current at inversed polarity, and TIG (tungsten inert gas welding), that is an arc welding under inert atmosphere with a tungsten electrode, often supplied with alternate current. These techniques avoid the formation of dangerous inclusions, by favouring the oxide removal and protecting the molten metal by inert gas. Oxyfuel and electrical resistance welding are also used, while the most recent techniques use plasma, an electron beam or a laser to induce melting and welding. Recently, friction techniques have gained much support, since they avoid melting of the involved alloys.
General considerations about welding of aluminium alloys must take into account several features of this kind of process. First, aluminium is a good heat conductor, so that localized melting is difficult. Wide deformations and microstructure modifications are observed, since temperature is high even far from the weld. Second, aluminium is oxidised very easily, with

alumina formation. Inclusions in the weld are often obtained, or the formation of oxide films or veils can be observed. Third, gaseous inclusions can be formed during welding, due for instance to the hydrogen solubility in aluminium. With high welding rates (MIG), gases have not the time to go out from the surface of the metal, so that porosity can develop. Hydrogen can be present either in the alloy or in the filler, but alloys are now carefully treated to lower the hydrogen concentration. However surface abrasions can make easier for impurities to enter the metal during working and storage, or hydrogen-rich products can be present on the surface, so that an accurate cleaning of both alloy and filler must be performed before welding. Humidity can be also a clue, since the presence of hydrated metal oxides on the surface can bring to the dissolution of hydrogen during welding. Similarly, the protective gas must not contain impurities, and have a very low dew point. As it happens for many metals, post-weld hot cracking can also occur due to grain growth.

A further difficulty in the welding technology is the requirement, typical for aerospace industry, of joining dissimilar alloys. In aircraft fuselages, for instance, stringers attached to the skin are considered as an important step toward the elimination of mechanically fastened stiffeners; however, this implies the ability of welding together two alloys for example of the 2000 and 7000 series.

In this chapter, two of the most interesting techniques for joining dissimilar alloys are considered: laser beam welding (LBW) and friction stir welding (FSW).

LBW is a melting technique, that uses a source with a high power density (a solid-state or gas laser, rarely a fibre laser) to locally melt a filler wire positioned between the two alloys to be welded. The method is recognized as a rather mature joining technology (Zhao et al. 1999), even if it faces the common drawbacks linked to the fusion welding approach: porosity, hot cracking, low mechanical strength of fusion (FZ) and heat affected zones (HAZ).

To overcome the weaknesses of this technique some care must be taken: a significant attention to the process and to the use of protective atmosphere can reduce hydrogen cracking, occurring grace to the decrease of hydrogen solubility in the fusion zone (FZ). Use of special alloys can reduce solidification cracking (Norman et al. 2003) and the choice of the filler wire can be strategic (Cicala et al., 2005; Braun, 2006). For instance, an Al-12Si alloy can be used with good results, since it avoids the formation of the Mg_2Si phase, that is thought to enhance the solidification cracking susceptibility (Cicala et al., 2005). The control on the process parameter is also extremely important, in particular with dissimilar alloys, and pre- and post-weld treatments can be essential to optimize the weld properties (Braun, 2006; Badini et al., 2009).

Friction stir welding (FSW) was invented at The Welding Institute (UK) in 1991 and is becoming an attractive alternative to conventional bonding techniques for high-performance structural applications in both aerospace and automotive industry. FSW is used mainly with aluminium alloys, even if copper alloys, titanium, steel and magnesium alloys have been welded by this technique. (Mishra & Ma, 2005; Nandan et al., 2008)

The method is based on the production by friction of a thermo-mechanically plasticized zone in the materials to be welded. A rotating tool is put on the contact line between two adjacent metal sheets, and mechanical pressure is applied while the tool is moving along the line of the joint. The tool consists basically in a shoulder and a pin, that from simple cylinders evolved in the last years into more complex shapes (Mishra & Ma, 2005; Thomas et al., 2003; Hirasawa et al., 2010). The tool rotation and applied pressure brings to the movement of matter in the pin zone, with a very complex behaviour. As a result of heat development, plastic deformation and matter movement, a joint is produced with a solid

state process, without the formation of a liquid phase as in more conventional welding techniques. The main parameters of FSW are the tool rotation rate, and the tool transverse speed. The direction of rotation is important for dissimilar alloys welding, where the two sides of the weld, the retreating (tool rotation goes against tool movement along the line of the joint) and the advancing one, correspond to different materials.

FSW shows some advantages over traditional welding techniques involving material melting. First, no added metal is needed, so that many problems related to composition compatibility are overcome, suggesting an easier welding of dissimilar alloys. Second, the total energy consumption of the process is much lower than conventional methods, and there is no need to work with protective gas. Finally, the microstructure of the welds is often very good, with limited porosity, no hot cracking and low residual stresses, that brings to very interesting properties of the joints. However, this method needs expensive equipments and it is easily applicable only for joining plates or components with quite simple geometry, e.g. flat, L and T (Mishra & Ma, 2005).

During FSW, metal flows around the tool, following its rotation, and high temperatures develop. The microstructure of the joint is thus determined by these two phenomena. Metal flow is rather complex and yet poorly understood, and yet is the key parameter to optimize the tool composition and geometry, and FSW parameters (Reynolds, 2000; Reynolds, 2008; Yang et al., 2010). Basically, it was observed that: advancing and retreating sides behaves very differently; the movement occurs both on the plane of the weld but also vertically; the alloys are not always mixed with a regular flow, but random distribution of the two alloys can occur, in particular on the top surface; often, however, alternating shapes (bands, lamellae, onions rings,…) are observed of the two metals, depending in any case on the geometry of the tool. Some authors suggest that FSW can be partially compared to an extrusion process (Krishnan, 2002a; Buffa et al., 2006).

The temperature reached during FSW is rather high, due to the intense plastic deformation occurring around the rotating tool and to the friction between the tool and the welded material (Mendez et al., 2010; Hamilton et al., 2008; Sato et al., 1999; Murr et al., 1998). It is clear that the microstructure of the weld is heavily influenced by these phenomena, in particular concerning grain size, grain boundaries, type, size and shape of precipitates. The microstructure will then influence the mechanical behaviour of the weld. In the central zone of the weld, temperature can reach almost 500 °C, so that dissolution of precipitates can occur. This depends however on the specific alloy, since it is reported both dissolution (Sato et al., 1999) and permanence (Murr et al., 1998) of precipitates in the central part of the weld. In any case, it is rather accepted that the maximum temperature is observed at the centre of the weld, and that there is an isothermal zone positioned under the pin (Mishra & Ma, 2005). As the distance from the weld centre grows, the temperature decreases. It has been suggested (Sato et al., 2002) that the temperature grows with the tool rotation rate, while the heating rate depends on the transverse speed, and that on the advancing side the temperature is slightly higher than on the retreating side.

The combined effect of temperature and tool movement produces a very characteristics microstructure of FSW welds. In the stirred zone, where severe plastic deformation occurs, recrystallization and development of texture can be observed, together with precipitates dissolution and/or coarsening (Kwon et al., 2003; Charit & Mishra, 2003, Sauvage et al., 2008). Three main zones, shown in Figure 1, can be discerned: the nugget, corresponding to the stirred zone; the thermo-mechanically affected zone (TMAZ); the heat-affected zone (HAZ).

Fig. 1. Typical image of a weld obtained by FSW.

The nugget consists generally in a recrystallized zone with small grain size, with a shape that depends on the alloy type, the tool geometry and the processing parameters. Generally the nugget has either the shape of an ellipse or that of a wide glacial valley (Mahoney et al., 1998; Sato et al., 1999, Mishra & Ma, 2005). The microstructure is often characterised by fine equiaxed grains of a few microns size, even if sub-micrometric grains can be obtained by using special tools or by cooling the plate immediately after the weld (Kwon et al., 2003; Su et al., 2003; Benavides et al., 1999). Regarding precipitates in the nugget zone, they can either be dissolved or coarsen, depending on the temperature and the alloy composition.

The TMAZ is a sort of transition zone between the nugget and the base metal (Mahoney et al., 1998). In this case, deformation occurs but not recrystallization, so that elongated grains are observed, with a pattern that follows the metal flow induced by the tool movement. High temperature is also present in this zone, so that precipitates dissolution can be sometimes observed (Sato et al, 1999).

The HAZ is simply a zone of the base metal that suffers high temperature due to the heat generated by plastic deformation in the nugget and TMAZ zones (Sato et al, 1998). The very significant increase of temperature in the HAZ can cause precipitation and/or precipitates coarsening, with a negative effect on the mechanical properties (Jata et al., 2000).

During FSW, due to the complex deformation pattern and to the high temperature gradients, residual stresses develop in the weld. The study of residual stresses suggests that their magnitude is much lower than in the case of traditional fusion welding (Peel et al., 2003; Fratini et al., 2009; Hatamleh et al., 2008). The stresses often presents an M shape, with the maximum stress close to the HAZ. The reason for this behaviour can be found in the fact that recrystallization reduces the extent of residual stresses, that is higher at the interface between the mechanical stressed zone and the heat-affected zone. This can be also due to the strong mechanical restraints needed for FSW (Mishra & Ma, 2005). No very significant differences were observed between the advancing and the retreating side of the weld.

Concerning the mechanical properties of the weld, it is important to consider both precipitation-hardened and solid-solution-hardened aluminium alloys, since hardness and other properties depends heavily on the alloy type. In particular, concerning precipitation-hardened alloys, it is generally observed a region in the centre of the weld where hardness is lower than in the base alloys (Sato et al., 1999). This behaviour has been generally ascribed to the coarsening and/or dissolution of the precipitates due to the high temperatures developed during FSW. Instead, in the case of solid-solution-hardened aluminium alloys, no reduction in hardness is generally observed in the weld (Svensson et al., 2000).

Tensile strength of the welds obtained by FSW has been much studied in the past (Mishra & Ma 2005). This welding method brings to rather high mechanical resistance, if compared with standard fusion welding techniques. In particular it seems that in the nugget the reduction of mechanical properties is not very high, while the weak point of the weld is the interface between TMAZ and HAZ (Mahoney et al., 1998). There, on the retreating side, failure generally occurs. Elongation at fracture generally decrease, because the strain is not anymore uniform along the sample, but is concentrated in the low-resistance zone. A post-

weld aging treatment is needed on the precipitation-hardened alloys, in order to improve yield and ultimate strength, even if complete recovery of the elongation of the base alloys is not generally attained (Sato & Kokawa, 2001; Krishnan, 2002b; Sullivan & Robson, 2008; Malarvizhi & Balasubramanian, 2010).
Regarding fatigue resistance, FSW brings to a reduction of the fatigue strength at 10^7 cycles (Di et al., 2006; Jata et al., 2000, Uematsu, 2009), but this behaviour is believed to be strongly correlated with the bad surface finishing of FSW welds. A surface treatment with removal of a portion of the surface improves the fatigue properties close to those of the base metal. In any case it seems that friction stir welds behave better than those obtained by fusion welding methods.
Fracture toughness of FSW welds has been measured both as significantly higher than that of the base metal (Kroninger & Reynolds, 2002; Mishra & Ma, 2005) and as lower than the base metal (Derry & Robson, 2008). In the first case, this happens both in nugget zone and in HAZ/TMAZ region, even if in this latter case the values are lower than in the nugget. This behaviour is probably due to the presence of a finer microstructure, and finer precipitates, even if other mechanisms can be considered, like the presence of particle free zones (PFZ), the bonding strength between alloy and precipitates, the presence of low energy grain boundaries. In the case of lower toughness than base metal, the precipitate coarsening is the main cause of this phenomenon.
As already pointed out, FSW is a very interesting method for the welding of dissimilar alloys and metals (Mishra & Ma, 2005; Murr, 2010; Dubourg et al., 2010; Kwon et al., 2008; Uzun et al., 2005; Lee et al., 2003). In this case, the study of the welds is more complex, and literature is not univocal about the best approach to the welding treatment. For instance, it is reported that the low-strength alloy must be placed on the retreating side, but also on the advancing, in order to improve the weld strength. The microstructure in the nugget seems to be determined by the retreating side material, and joining two precipitate-hardened alloys brings generally to the failure of the weld in the HAZ, where over-aged precipitates are present. This does not seem to reduce substantially fatigue properties, though.
In any case, the papers already published all suggests that FSW is a very promising technique for joining dissimilar alloys with defect-free welds and good mechanical properties.
One of the main issues that are yet to understand concerning dissimilar alloys welding is the possibility of operating a post-weld heat treatment (PWHT). The current literature suggests that a PWHT is often needed, in particular if the welded alloys are in the O state (Krishnan, 2002b; Malarvizhi & Balasubramanian, 2010; Priya et al., 2009; Chen et al., 2006; Sullivan & Robson, 2008). It is reported though that this kind of treatment can bring to grain growth and properties reduction, so that when aged alloys are welded, there is not yet total agreement on the best strategy to adopt.
In this work, we try to propose a method for the optimization of the post-weld heat treatment on joints of dissimilar alloys. This approach can be applied on any two precipitation-hardened alloys, and consists in the coupling of microscopic observations, Differential Scanning Calorimetry (DSC) analyses and hardness measurements in order to improve the overall performance of the weld, avoiding weak spots in specific locations of the weld.
Depending on the welding technique used, if LBW or FSW, the approach is slightly different, but the basic idea is the same. In LBW the fusion zone consists in the mixture of two or three different alloys, so that the standard treatments for the thermal aging of the base alloys can not be successfully used. By using composition analyses, DSC and microscopic observations, it is possible to determine the best thermal treatment for

increasing the hardness of the weld without incurring in over-ageing of either the base alloys or the weld itself.
In FSW no fusion zone is observed, however many modifications are observed in the HAZ, TMAZ and nugget. Starting from DSC analyses, that suggest the state of precipitates in the specific zones, it is possible to determine the best heat treatment temperature for the weld, and optimize its hardness.
In both cases, two factors are to consider: over-ageing that can occur in the HAZ as a result of the temperature increase during welding; limited increase of hardness in specific weld zones, due to microstructure modifications. It is important to find a compromise between the properties of the base alloys and the properties of the weld, to avoid weak spots in the whole system.

2. Characterization techniques

Samples were taken from the different weld zones by cutting: fusion zone, HAZ and base alloys for LBW; nugget, TMAZ, HAZ and base alloys for FSW.
Vickers or Brinell hardness was measured on polished cross-section of welded specimens, in the different zones of the weld and on base alloys. Microstructure was examined by optical microscopy and scanning electron microscopy. Compositional analysis of the different parts of the cross-section of the specimens was carried out by energy dispersive X-ray spectroscopy. Keller's reagent etching was sometimes used to improve the quality of optical microscopy observations.
Differential Scanning Calorimetry was used in order to identify the thermal phenomena occurring during a temperature scan between ambient temperature and 500 °C, at a heating rate of 20 °C/min and under flowing Ar atmosphere.
Indeed, DSC analysis has been frequently used to investigate the ageing sequence and the precipitation kinetics of several aluminium alloys (Mishra & Ma, 2005; Badini et al., 1990; Badini et al., 1995; Morgeneyer et al., 2006; Jena et al., 1989; Garcia Cordovilla & Louis, 1984; Garcia Cordovilla & Louis, 1991; Papazian, 1982; Genevois et al., 2005). The DSC analysis of solution treated aluminium alloys allows to observe during a temperature scan the precipitation sequence and the dissolution of precipitates. This is possible since the formation of the strengthening phases (GP zones, metastable intermediate precipitates and stable hardening phases) results in exothermal peaks while the precipitates dissolution is an endothermic phenomenon.
In the same manner DSC can be used to asses the state of a partially aged aluminium alloy. For instance, in the case of naturally aged specimens the peak relative to the GP zone formation is missing, and the peak concerning the formation of metastable precipitates is weakened. In the case of artificially aged specimens, both peaks are missing.

3. Results and discussion

The methodology proposed to analyse the behaviour of dissimilar alloys welds and to optimise their post-weld heat treatment (PWHT) is based on different steps:
- analysis of the behaviour of the base alloys;
- analysis of a weld between two parts of the same alloy (optional);
- analysis of the weld between dissimilar alloys;
- DSC analysis of samples taken from different parts of the weld;
- post-weld heat treatment and hardness measurement.

3.1 Laser beam welding

a. **Preparation of the weld**

Regarding LBW method, 2139 alloy and a 7000 series alloy with composition reported in Table 1 were welded. As a filler a 4047 alloy wire with 1 mm diameter was used. The 2139 alloy was furnished in 3.2 mm thick sheets, in the T8 temper (solution heat treated, quenched, cold worked, and aged at 175 °C for 16 h). The 7000 series alloy was used as 2.5 mm thick extrusion, in T4 temper (solution heat treated, quenched, naturally aged).

Alloy	Mean chemical composition (wt. %)									
	Si	Fe	Cu	Mn	Mg	Cr	Ti	Zn	Zr	Ag
2139	0.04	0.06	5.1	0.29	0.43	-	0.05	-	0.014	0.33
7xxx	0.10	0.11	0.61	0.15	3.1	0.15	0.02	10.0	0.10	-
4047	12.0	0.8	0.3	0.15	0.10	-	-	0.2	-	-

Table 1. Mean chemical composition of alloys used for LBW: 2139, 7xxx, 4047.

LBW has been performed using two continuous wave Nd:YAG lasers, with maximum laser power 4 kW and mixed argon and helium as shielding gas. T-shaped specimens were produced, and the chosen process parameters were: welding speed 6 m/min, wire feed rate 4.8 m/min, laser power 3.6 kW. The laser beam was focused on both sides of the contact surface between the two plates, using a 200 mm focusing lens and a 0.6 mm diameter focalized beam. Welded specimens were submitted to various artificial ageing treatments using an oil bath kept at constant temperature.

b. ***Analysis of the behaviour of the base alloys***

In this case the analysis can be either experimental of based on the literature. The composition of the base alloys was already given in Table 1, while the mechanical properties of 7000 and 2139 alloys are reported in Table 2.

Alloy	Ultimate tensile strength (MPa)	Yield strength at 0.2% (MPa)	Fracture elongation (%)	Vickers hardness
2139-T8	480	435	12.5	150
7xxx-T4	660	550	8.9	190

Table 2. Mechanical properties of the alloys welded by laser beam: 2139, 7xxx.

c. ***Analysis of the weld of a single alloy***

In the case of fusion-welded samples this step was not deemed necessary in order to study the weld between dissimilar alloys. In fact, the laser beam welding of two alloys with very different composition, adding a filler wire of a third alloy, brings to a material with a significantly different composition in the melted zone. Generally the weak spot in a LBW weld of a single alloy is between the weld and one of the base alloys, i.e. in the HAZ. However, when dissimilar alloys are considered, the alloy in the weld itself can become the weak spot due to the different composition and the lack of post-weld heat treatment (or due to an incorrect choice of temperature or time).

d. ***Analysis of the weld between dissimilar alloys***

The first step in the analysis of the weld is a microstructure observation. In the case of the weld between 2139 and the 7000 series alloys, a compositional map of the weld is shown in

Figure 2, showing the different zones by their composition: 2139 alloy on the lower part of the image (less zinc), 7xxx alloy on the top (high zinc content) and melted zone in the middle (high silicon content).

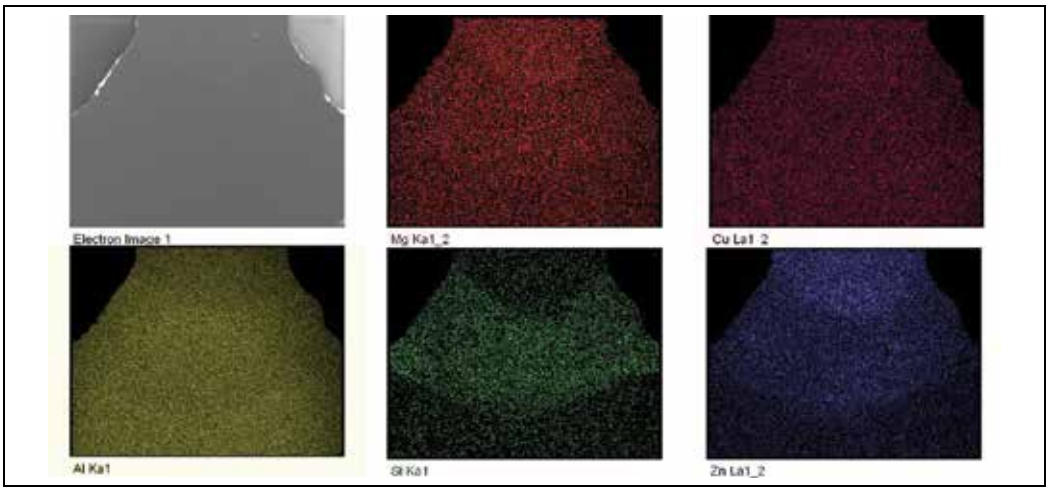

Fig. 2. Elemental map of a laser beam weld between 2139 (low) and 7xxx (high) alloys.

In Figure 3 the microstructure of different parts of the welds is shown. Hot cracks are not observed in the weld, and porosity is rare. The microstructure of 2139 alloy shows almost equiaxed grains, while 7000 series alloy shows the elongated grains typical of extruded structures. In the molten zone a very fine microstructure is observed, with small equiaxed grains. A small fraction of precipitates can be observed at grain boundaries. HAZ zones present a rather sharp transition between base alloy and fusion zone. The precipitates assume partially oriented features.

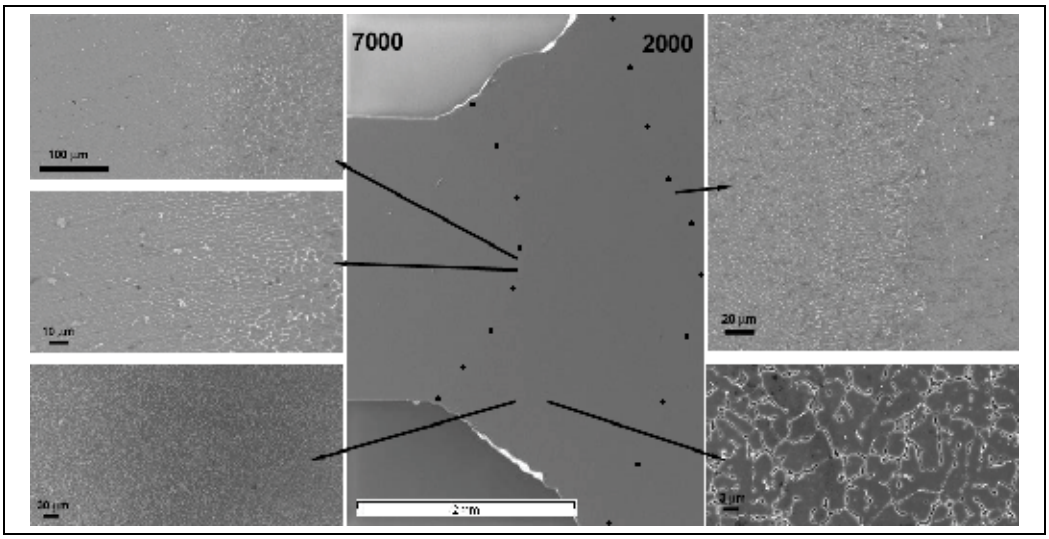

Fig. 3. Microstructure of a laser beam weld between 2139 (right) and 7xxx (left) alloys.

A hardness map of the weld is shown in Figure 4. It is evident that the lowest hardness is observed in the weld zone.

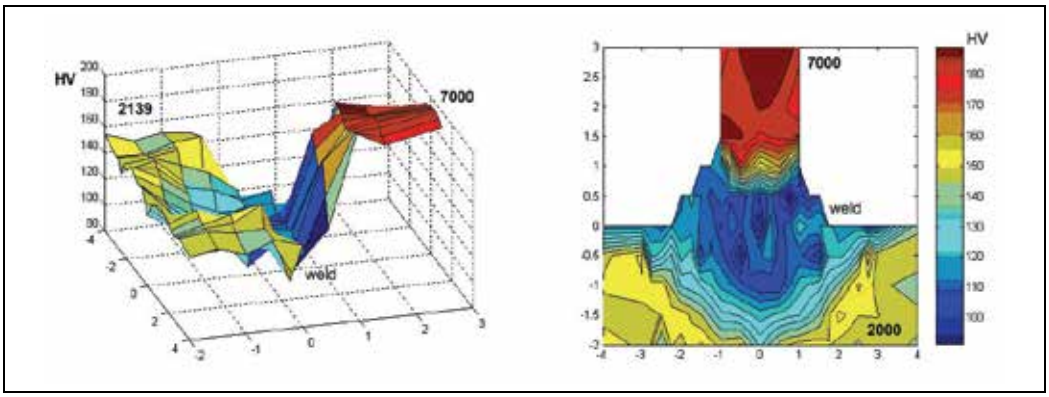

Fig. 4. Hardness map of a laser beam weld between 2139 and 7xxx alloys.

e. DSC analysis of samples taken from different parts of the weld

In the case of LBW, samples were taken from base alloys, from the HAZs, and from the fusion zone. Figure 5 shows the DSC curves for the 7000 series alloy and the fusion zone. The HAZ zones were too small to observe effects by DSC, so that measurements did not reveal further information on the HAZs. The DSC curve of 2139 alloy was flat, due to the fact that this alloy had been already submitted to heat treatment before welding.

The DSC experiments show, in the case of 7000 alloy, a endothermic peak due to precipitates dissolution, starting close to 100 °C, followed by a double exothermic peak, corresponding to the precipitation of intermetallic phases. The onsets of the two peaks are around 160-180 °C and close to 200 °C. A third exothermic peak is observed at higher temperature, close to 250 °C. The fusion zone presents no endothermic signal (due to lack of a significant quantity of precipitates), a small exothermic peak starting at 170 °C and a large exothermic peak starting at 200 °C.

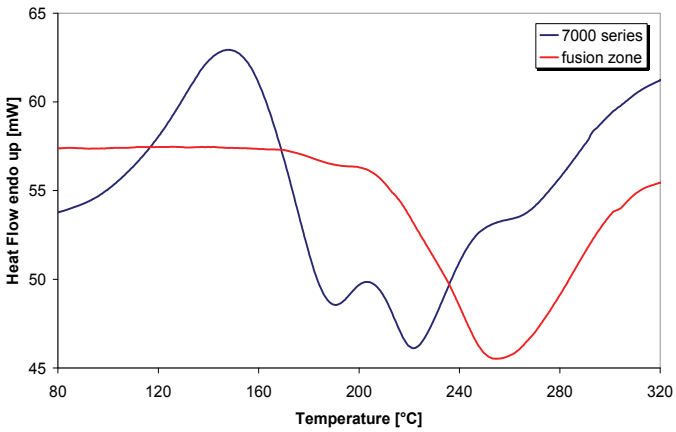

Fig. 5. DSC curves of the 7xxx alloy and of the fusion zone.

From these data a convenient thermal treatment temperature must be chosen. Since ageing must not be carried out too far, to avoid excessive growth of precipitates, the temperature must be kept relatively low. For this reason in this case 170 °C was chosen as the heat treatment temperature. The peak of the fusion zone is starting right around this temperature, so that precipitation of strengthening phases is forecast.

f. Post-weld heat treatment and hardness measurement

A PWHT was performed by varying the time of the heat treatment in the range 0-18 hours, and microhardness measurements were performed on the obtained samples. The results are shown in Figure 6.

While the 2139 alloy maintains a constant hardness during heat treatment, the measurements demonstrates a significant increase in hardness over a limited time range for both 7000 alloy and fusion zone. An excessive permanence at high temperature brought to over-ageing in both zones. The choice of heat treatment time then is limited to 6 to 10 hours. In the former case (6 hours) the weld remains less hardened but the 7000 alloy does not go into over-ageing. In the latter (10 hours) the 7000 alloy becomes slightly over-aged but the weld receives the best hardening treatment.

The approach based on the DSC measurements allowed thus to determine a convenient temperature for heat treatment. A higher temperature would bring to fast over-ageing of the weld, while a lower temperature would not guarantee a sufficient aging to grant the best mechanical properties. This was demonstrated by heat treating the alloys at 140 °C, far from the DSC peaks. Even if the 7xxx alloy showed an increase in hardness during this heat treatment, the weld hardness remained low, suggesting no improvement in its mechanical properties.

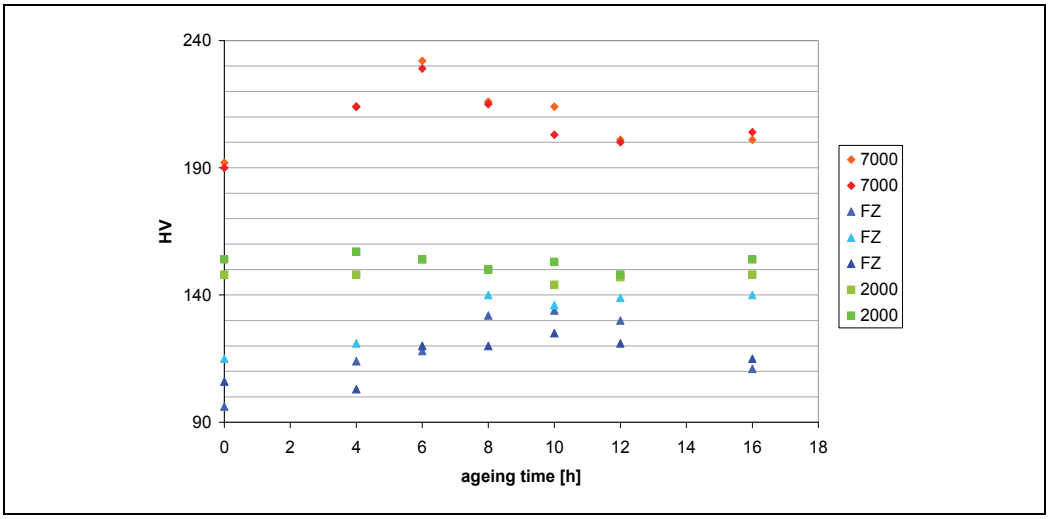

Fig. 6. Hardness of the various parts of the weld after the post-weld heat treatment.

3.2 Friction stir welding

a. Preparation of the weld

Regarding FSW samples, three alloys were used in the form of 3.1 mm thick sheets: 2198 alloy in T3 temper (solution heat treated, quenched, cold worked, and naturally aged), 6013

alloy in T4 temper (solution heat treated, quenched, naturally aged), 7475 alloy in W state (solution heat treated, quenched). The composition of the three alloys is given in Table 3.

Alloy		Si	Fe	Cu	Mn	Mg	Cr	Ti	Zn	Zr	Ag	Li	other
2198	min	0	0	2.9	0	0.25	0	-	0	0.04	0.10	0.80	-
	max	0.08	0.10	3.5	0.50	0.80	0.05	-	0.35	0.18	0.50	1.10	-
7475	min	0	0	1.2	0	1.9	0.18	0	5.2	-	-	-	0
	max	0.1	0.12	1.9	0.06	2.6	0.25	0.06	6.2	-	-	-	0.15
6013	min	0.6	0	0.6	0.2	0.8	0	0	0	-	-	-	0
	max	1.0	0.5	1.1	0.8	1.2	0.1	0.1	0.25	-	-	-	0.15

Table 3. Mean chemical composition of alloys used for FSW: 2198, 7475, 6013.

Two kinds of weld were considered in this work: the first between two 6013 plates; the second between 2198 and 7475 alloys. The welding was performed by using a tool with a nib 3.2 mm long and with 4.7 mm diameter, and a shoulder with diameter of 13.4 mm. A milling machine Rigiva RS 100 was used for welding the sheets in the direction perpendicular to the rolling direction. The work conditions were welding speed from 50 to 200 mm/min, pin rotation speed 830 rpm and tilt angle of the tool 2°.
Welded specimens were submitted to various artificial ageing treatments using an oil bath kept at constant temperature.

b. Analysis of the behaviour of the base alloys

The base alloys are well-known, so that composition and mechanical data were taken from the literature. Mechanical data of the three alloys are given in Table 4.

Alloy	Ultimate tensile strength (MPa)	Yield strength at 0.2% (MPa)	Fracture elongation (%)	Vickers hardness
2198 T3	370	275	15	100
7475 T761	525	460	12	160
6013 T4	320	220	20	100
6013 T6	395	355	12	135

Table 4. Mechanical properties of the alloys welded by laser beam: 2198, 7475, 6013.

The 6013 T4 alloy has been shown to contain Si, GP zones and α(AlFeMnSi) (probably of $(Fe,Mn)_3Si_xAl_{12}$ composition), with the development of Mg_2Si (β'') and $Al_4Cu_2Mg_8Si_7$ (Q') precipitates during ageing at 180 °C (Barbosa et al., 2002; Genkin, 1994). Mg_2Si precipitates are also known to grow from needle-shape to rod-shape and finally to plate-shape (Heinz & Skrotzki, 2002). The passage from T4 to T6 brings to an increase of mechanical performance, in particular of yield strength, that has been motivated with the simultaneous presence of β'' and Q' precipitates. Thus, a typical heat treatment for 6013 alloy is a T6, at 180-190 °C for a few hours.
In 7475 alloy the typical precipitates are $MgZn_2$ (η or η') and $CuMgAl_2$ S phase (Norman et al., 2003). The mechanical data of 7475 alloy were given in the T761 state since it is one of the most common state for this alloy. Moreover, after heat treatment the mechanical properties are heavily altered from those of W state, so that properties of the aged alloys are more interesting for comparison. Heat treatment is generally performed in two steps at around 120 and 180 °C (Li et al., 2007).

The main precipitates in 2198 alloys aged at 155 °C are Al_2CuLi (T1), then Al_3Li (δ') and Al_2CuMg (S'), sometimes Al_2Cu, with formation of small AlLi and Al_3Zr quantities (Cavaliere et al., 2009; Decreus et al., 2010; Chen et al., 2010). Moreover, lithium allows for a reduction of weight (roughly 3% reduction every 1% of Li in the alloy).

c. Analysis of the weld of a 6013 alloy

The case of the welding of 6013 alloy will be considered as an example of the procedure that can be brought out to study the effect of welding on the properties of the alloy. Indeed, there is no real difference between the case of a single alloy weld and that of a dissimilar weld. The image of the 6013-6013 weld is shown in Figure 7.

Fig. 7. Image of the weld between two 6013 alloy plates.

On Figure 8 are presented instead the Brinell and Vickers hardness curves for the weld. It is evident that the lower hardness is present on the retreating side of the weld, at the interface between TMAZ and HAZ.

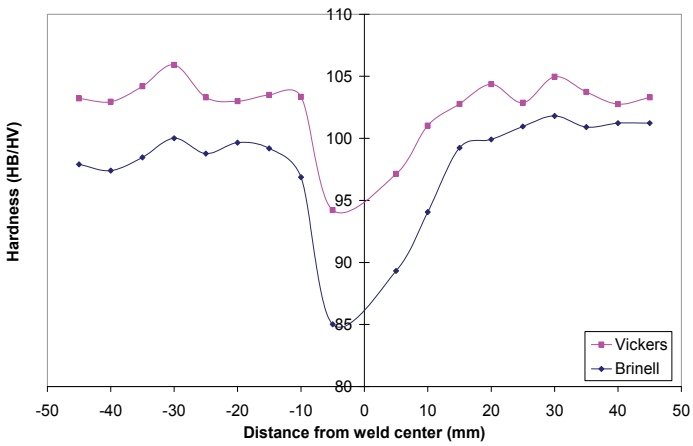

Fig. 8. Brinell and Vickers hardness profiles for a 6013-6013 weld.

On Figure 9 is presented the DSC curves for samples taken at different positions along the weld.

The curves show clearly how at +30 mm and -30 mm from the weld centre the 6013 alloy is in the unmodified T4 state. On heating an endothermic peak is observed typical of GP zones dissolution, around 160 °C, followed by three peaks for the precipitation of strengthening phases. At +10 and -10 mm from the weld centre, only a hint of the endothermic peak is observed, suggesting that GP zones dissolution already took place during the welding treatment, due to the increase of temperature. However the three peaks linked to precipitation are yet observed. At +5 and -5 mm, i.e. very close to the heavily deformed zone, only the exothermic precipitation peaks are observed. There is a small shift of the main

peak toward lower temperature, with the second and third precipitation peaks disappeared or extremely low. In the nugget the main exothermic peak is wider and shifted toward lower temperature. This suggest that in this zone a finer microstructure is present, as confirmed by microscopic observations (Figure 10), and/or higher residual stresses, that brings to an easier precipitation of strengthening phases.

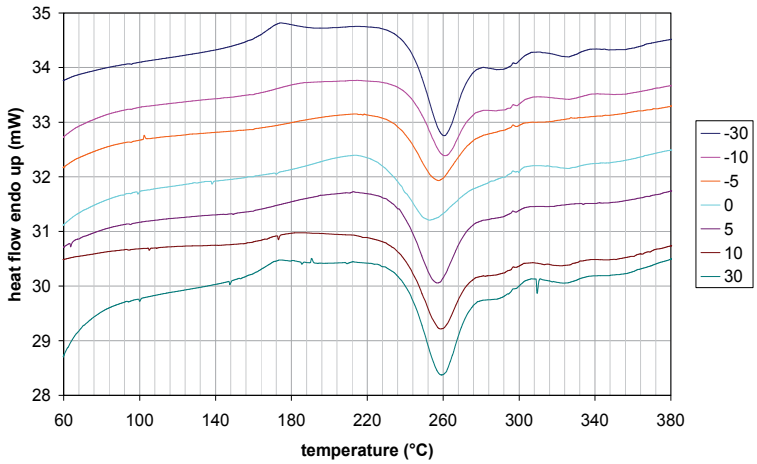

Fig. 9. DSC curves for different parts of a 6013-6013 weld.

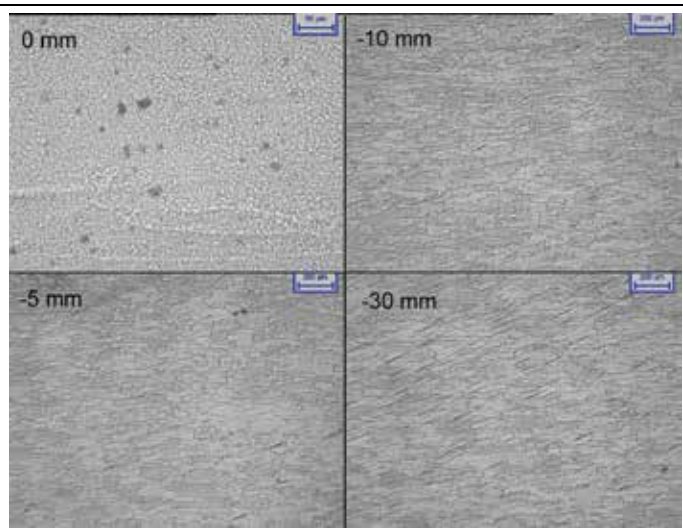

Fig. 10. Microstructure of different parts of a 6013-6013 weld.

DSC analysis thus allows to roughly determine the state of the different parts of the weld, suggesting that for 6013 alloy precipitation must yet occur, so that a significant increase of hardness by PWHT can be obtained. As said before, 6013 alloys are generally heat treated at 180-190 °C for a few hours. The DSC trace shows that these temperature are quite far from

the main precipitation peak, however DSC experiments made on heat treated samples demonstrate that a partial precipitation already occurs, probably with very small β'' and Q' precipitates (Barbosa et al., 2002). Figure 11 shows the DSC curves for welded samples aged at 160 (18 h) and 190 °C (3 h).
It is evident that the intensity of the exothermic peak is much lower than the intensity before heat treatment. This suggests that precipitation occurred during heat treatment. The effect of precipitation can be observed in the hardness curves of Figure 12.

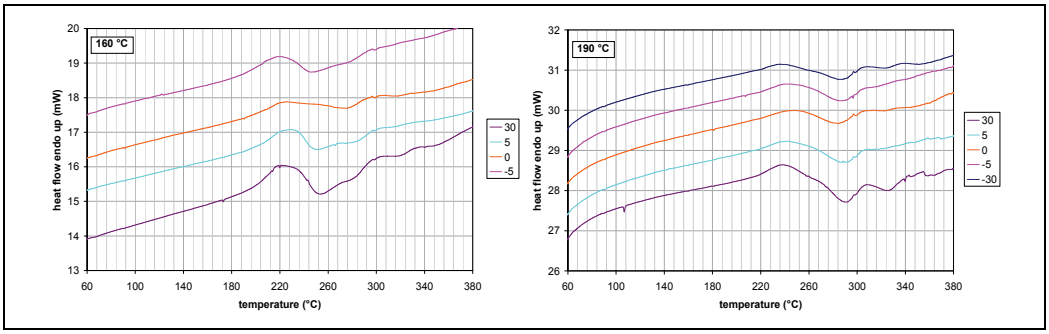

Fig. 11. DSC curves for different parts of a 6013-6013 weld after 160 °C and 190 °C heat treatments.

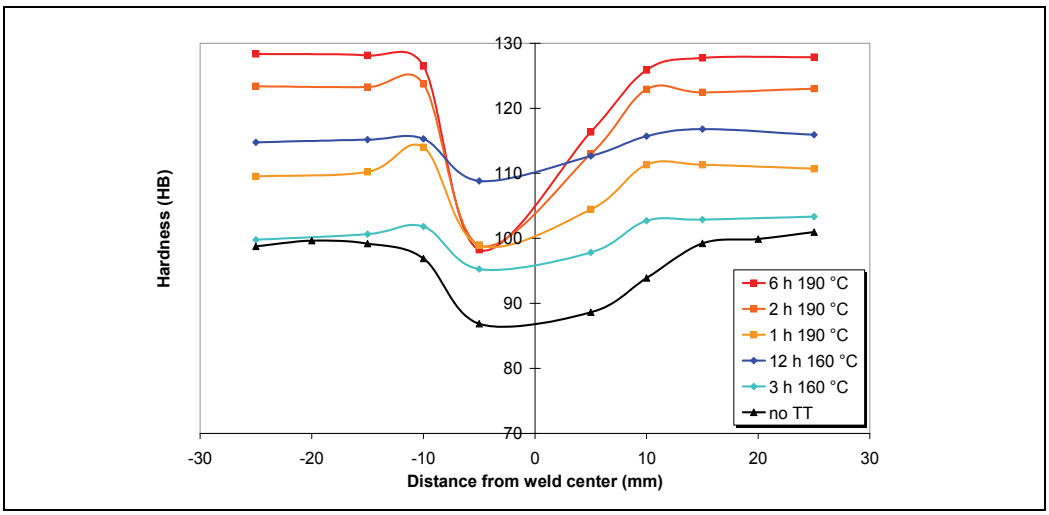

Fig. 12. Hardness profiles for a 6013-6013 weld after 160 °C and 190 °C heat treatments.

Figure 12 shows how the temperature of heat treatment heavily influences the behaviour of both base alloys and weld. Depending on the temperature of the heat treatment, different hardness profiles can be observed. If this heat treatment is kept at low temperature a lower increase of hardness of base alloys occurs, but a larger increase of hardness in the HAZ. If the heat treatment is made at higher temperatures, the precipitates growth prevails and no hardness increase in the weld is observed. In this last conditions, the marked improvement in hardness of the base metals risk to be overcome by the low resistance of the weld zone.

d. Analysis of the weld between dissimilar alloys

The case of welding between 7475 and 2198 will be presented for the welding of dissimilar alloys. An image of the weld is shown in Figure 13.

Fig. 13. Image of the weld between 2198 and 7475 alloy plates.

From the DSC curves of pure 2198 alloy (Figure 14) it can be seen that, passing from T3 state to solubilized one, a less marked exothermic precipitation is observed, and a higher temperature is required for the formation of the strengthening phases. This is probably due to the elimination of cold working effect thanks to the solution heat treatment.
In the case of the dissimilar weld (Figure 15), curves for +30 mm from the weld (retreating side, 7475 alloy) are very similar to curves of the pure 7475 alloy, and the same happens for -30 mm (advancing side, 2198 alloy). The behaviour of the 7475 alloy side is quite constant for samples took on HAZ and TMAZ zones, showing only a smaller peak than the base alloy, linked to a partial precipitation of phases due to the high temperature suffered during welding.

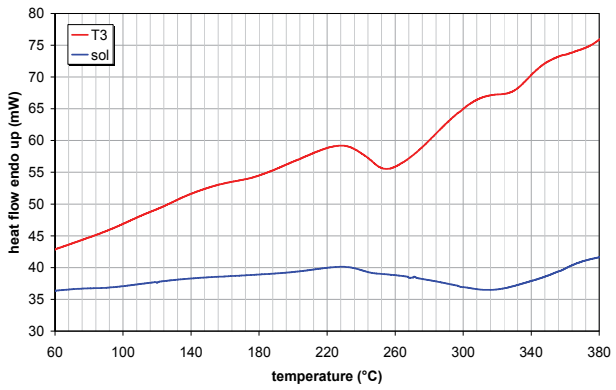

Fig. 14. DSC curves for 2198 alloy.

In the nugget, a behaviour similar to that of the 7475 alloy is observed, with a small precipitation peak. From the 2198 side, the effect of the high temperature developed during the welding is to eliminate the effect of the cold working, so that at -5 mm the curve is similar to the one of solution heat treated 2198 alloy. At -10 mm a peak is yet observed, even if shifted toward higher temperature with respect to the base alloy.
Due to the different approach needed to age the 2198 and the 7475 alloys, different temperatures were tested also for a 2198-2198 weld, in order to understand the effect of temperature on the strengthening mechanism. At low temperature (155 °C) welds need very long times to reach good hardness values, as in the case of 6013 alloy. At high temperature (200 °C) the maximum hardness is reached in 3-4 hours (Figure 16).

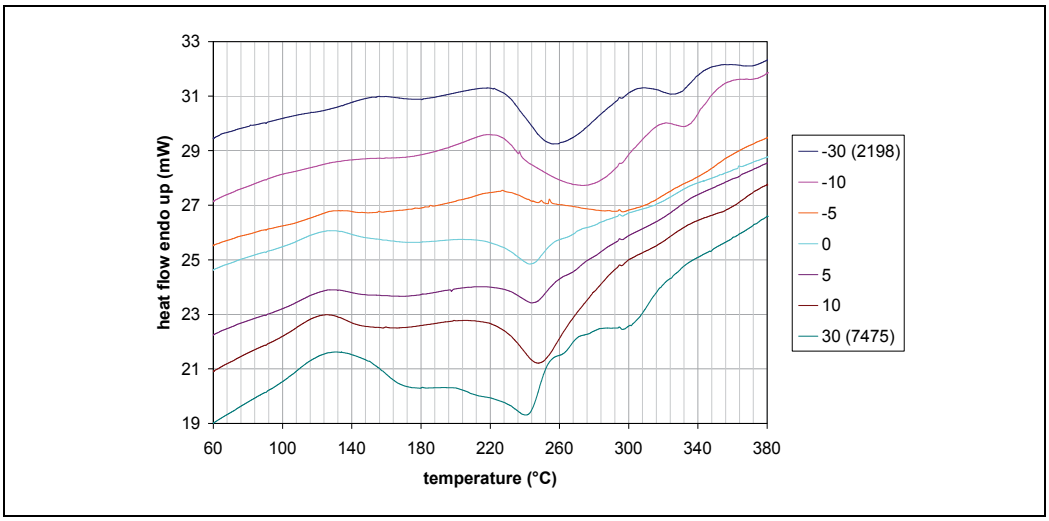

Fig. 15. DSC curves for different parts of a 2198-7475 weld.

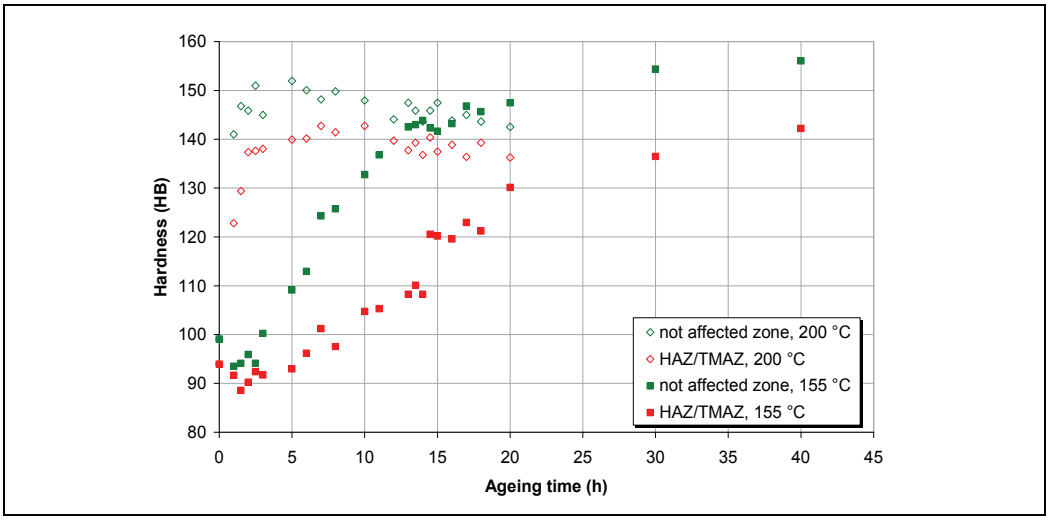

Fig. 16. Hardness curves of different parts of a 2198-2198 weld after 155 °C and 200 °C heat treatments.

The ageing of 7475 alloy is generally realised in a two-step fashion, with a high temperature step at 170-180 °C. The curve showing the behaviour of a 7475-7475 weld is shown in Figure 17.
The risk of over-ageing is rather evident, however it must be stressed that the weak spot in a welded structure is often the weld. For this reason it was chosen to provide an increase of hardness for the 2198 HAZ/TMAZ zone and suffer a small over-ageing of the 7475 alloy. The curve on Figure 18 shows the ageing curve for 2198-7475 weld.

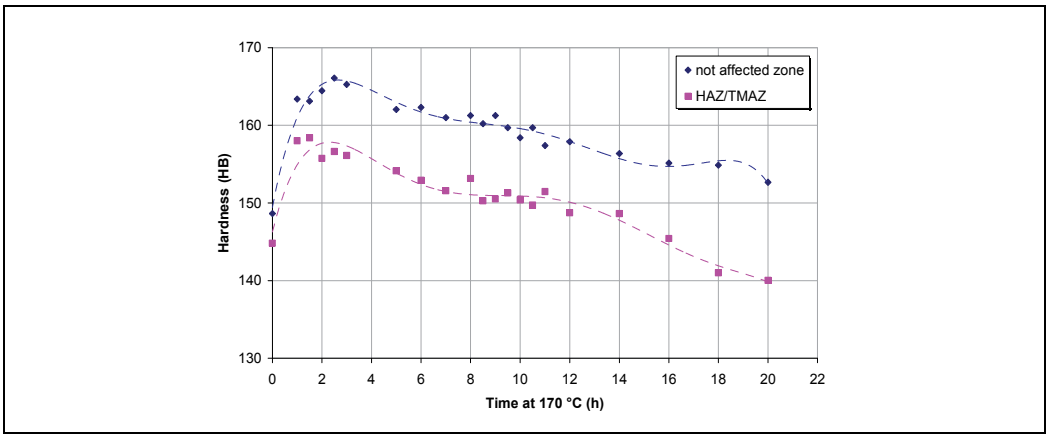

Fig. 17. Hardness curves of different parts of a 7475-7475 weld after heat treatment.

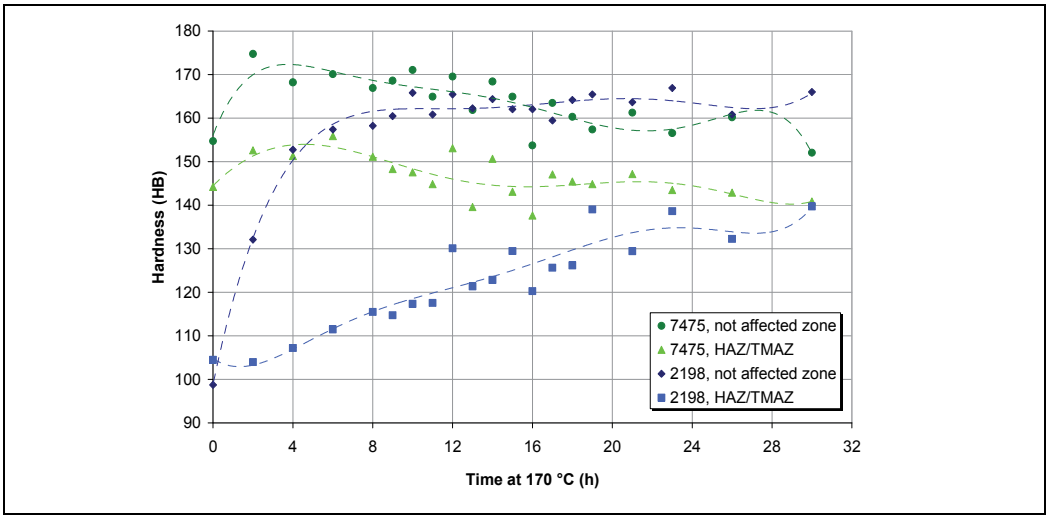

Fig. 18. Hardness curves of different parts of a 2198-7475 weld after heat treatment.

It is evident that while over-ageing is slowly occurring on the base 7475 alloy, precipitation is happening in the weld, with a significant hardening effect, that remains very low in the zone for optimal ageing of the only 7475 alloy.
DSC curves confirm that precipitation occurred, as shown in Figure 19. No significant peak was detected after ageing.
Thus, post welding heat treatments are able to improve mechanical properties of the welds, if the ageing conditions are carefully controlled. The use of the standard ageing treatments used for the base alloys that have been welded not always provide the best results, neither for similar alloys welding nor for dissimilar ones. The control of the PWHT is essential for avoiding weak spots in the weld, that can lower substantially the mechanical properties of the whole welded system.

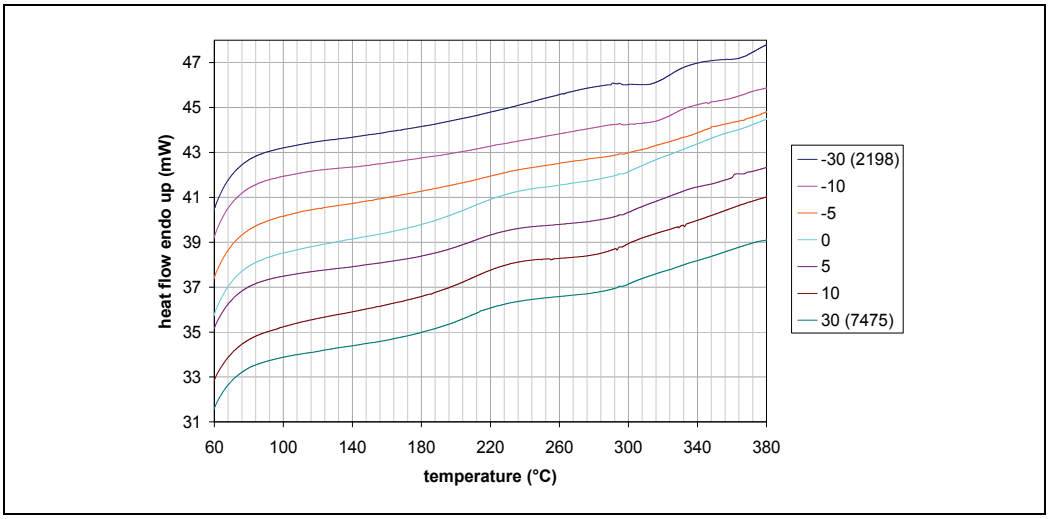

Fig. 19. DSC curves for different parts of a 2198-7475 weld after heat treatment.

4. Conclusion

In this work a method for the study of the ageing behaviour of laser beam or friction stir welds between similar or dissimilar alloys is presented. The approach is based on the DSC study of different parts of the weld. Coupling DSC measurements with literature data, it is possible to choose a convenient heat treatment to optimize the hardness profile of the weld. In most of the cases, a compromise must be found between the improvement of the weld properties and that of the base alloys. A laser beam weld of dissimilar alloys 2139 and 7xxx showed a marked increase in hardness for the weld, at expense of a slight over-ageing of the 7xxx alloy. In the case of the friction stir welding of a 6013-6013 system, a lower temperature than the standard one for the heat treatment of the alloy gives the best results, bringing to a slower yet more uniform hardness increase in the weld. Finally, in a 2198-7475 weld the permanence at high temperature must be carefully regulated: if a short time is chosen, the weld does not harden enough; if too long a time is selected, an important over-ageing of the 7475 alloy occurs.

5. References

Badini, C.; Marino, F. & Tomasi, A. (1990). DSC study of ageing sequence in 6061 aluminum alloy-SiC whiskers composite. *Mater. Chem Phys.*, 25, 1, 57-70, 0254-0584

Badini, C.; Marino, F. & Verné, E. (1995). Calorimetric study on precipitation path in 2024 alloy and its SiC composite. *Mater. Sci. Eng. A*, 191, 1-2, 185-191, 0921-5093

Badini, C., Pavese, M., Fino, P. & Biamino, S. (2009). Laser beam welding of dissimilar aluminium alloys of 2000 and 7000 series: effect of post-welding thermal treatments on T joint strength. *Sci. Technol. Weld. Join.*, 14, 6, 484-492, 1362-1718

Barbosa, C; Rebello, J. M. A.; Acselrad, O.; Dille, J. & Delplancke J.-L. (2002). Identification of precipitates in 6013 aluminum alloy (Al-Mg-Si-Cu). *Z. Metallkd.*, 93, 3, 208-211

Benavides, S.; Li, Y.; Murr, L. E.; Brown, D. & McClure, J. C. (1999). Low-temperature friction stir welding of 2024 aluminium. *Scripta Mater.*, 41, 8, 809-15, 1359-6462

Braun, R. (2006). Nd:YAG laser butt welding of AA6013 using silicon and magnesium containing filler powders. *Mater. Sci. Eng. A*, 426, 1-2, 250-262, 0921-5093

Buffa, G.; Donati, L.; Fratini, L. & Tomesani, L. (2006). Solid state bonding in extrusion and FSW: Process mechanics and analogies. *J. Mater. Process. Technol.*, 177, 1-3, 344-347, 0924-0136

Cavaliere, P.; Cabibbo, M.; Panella, F. & Squillace, A. (2009). 2198 Al–Li plates joined by Friction Stir Welding: Mechanical and microstructural behaviour. *Mater. Des.*, 30, 9, 3622-3631, 0261-3069

Charit, I. & Mishra, R. S. (2003). High strain rate superplasticity in a commercial 2024 Al alloy via friction stir processing. *Mater. Sci. Eng. A*, 359, 1-2, 290-296, 0921-5093

Chen, J.; Madi, Y.; Morgeneyer, T. F. & Besson, J. (2010). Plastic flow and ductile rupture of a 2198 Al–Cu–Li aluminum alloy. *Comput. Mater. Sci.*, in press, DOI: 10.1016/j.commatsci.2010.06.029

Chen, Y. C.; Liu, H. J. & Feng, J. C. (2006). Effect of post-weld heat treatment on the mechanical properties of 2219-O friction stir welded joints. *J. Mater. Sci.*, 41, 1, 297-299, 0022-2461

Cicala, E.; Duffet, G.; Andrzejewski, H.; Grevey, D. & Ignat, S. (2005). Hot cracking in Al-Mg-Si alloy laser welding - Operating parameters and their effects. *Mater. Sci. Eng. A*, 395, 1-2, 1-9, 0921-5093

Decreus, B.; Deschamps, A. & Donnadieu, P. (2010). Understanding the mechanical properties of 2198 Al-Li-Cu alloy in relation with the intra-granular and inter-granular precipitate microstructure. *J. Phys.: Conf. Ser.* 240, 012096, 1742-6596

Derry, C. G. & Robson, J. D. (2008). Characterisation and modelling of toughness in 6013-T6 aerospace aluminium alloy friction stir welds. *Mater. Sci. Eng. A*, 490, 1-2, 328-334, 0921-5093

Di, S.; Yang, X.; Luan, G. & Jian, B. (2006). Comparative study on fatigue properties between AA2024-T4 friction stir welds and base materials. *Mat. Sci. Eng. A*, 435-436, 389-395, 0921-5093

Dubourg, L.; Merati, A. & Jahazi, M. (2010). Process optimisation and mechanical properties of friction stir lap welds of 7075-T6 stringers on 2024-T3 skin. *Mater. Des.*, 31, 7, 3324-3330, 0261-3069

Fratini, L.; Pasta, S. & Reynolds, A. P. (2009). Fatigue crack growth in 2024-T351 friction stir welded joints: Longitudinal residual stress and microstructural effects. *Int. J. Fatigue*, 31, 3, 495-500, 0142-1123

Garcia Cordovilla, C. & Louis, E. (1984). Characterization of the microstructure of a commercial Al-Cu alloy (2011) by differential scanning calorimetry (DSC). *J. Mater. Sci.*, 19, 1, 279-290, 0022-2461

Garcia Cordovilla, C. & Louis, E. (1991). A differential scanning calorimetry investigation of the effects of zinc and copper on solid state reactions in Al-Zn-Mg-Cu alloys. *Mater. Sci. Eng. A*, 132, 1-2, 135-141, 0921-5093

Genevois, C.; Deschamps, A.; Denquin, A. & Doisneau-Cottignies, B. (2005). Quantitative investigation of precipitation and mechanical behaviour for AA2024 friction stir welds. *Acta Mater.*, 53, 8, 2447-2458, 1359-6454

Genkin, J.-M. P. (1994). Corrosion fatigue performance of Alloy 6013-T6. *Master Degree, Massachussets Institute of Technology*, February 1994, MIT, Boston

Hamilton, C.; Dymek, S. & Sommers A. (2008). A thermal model of friction stir welding in aluminum alloys. *Int. J. Mach. Tools Manuf.*, 48, 10, 1120-1130, 0890-6955

Hatamleh, O.; Rivero, I. V. & Maredia, A. (2008). Residual Stresses in Friction-Stir-Welded 2195 and 7075 Aluminum Alloys. *Metall. Mater. Trans. A*, 39, 12, 2867-2874, 1073-5623

Heinz, B. & Skrotzki, B. (2002). Characterization of a Friction-Stir-Welded Aluminum Alloy 6013. *Metall. Mater. Trans. B*, 33, 3, 489-498, 1073-5615

Hirasawa, S.; Badarinarayan, H.; Okamoto K.; Tomimura T. & Kawanami T. (2010). Analysis of effect of tool geometry on plastic flow during friction stir spot welding using particle method. *J. Mater. Process. Technol.*, 210, 11, 1455-1463, 0924-0136

Jata, K. V., Sankaran, K. K. & Ruschau, J. J. (2000). Friction-stir welding effects on microstructure and fatigue of aluminum alloy 7050-T7451. *Metall. Mater. Trans. A*, 31, 9, 2181-2192, 1073-5623

Jena, A. K.; Gupta, A. R. & Chaturvedi, M. C. (1989). A differential scanning calorimetric investigation of precipitation kinetics in the Al-1.53 wt%Cu-0.79wt%Mg alloy. *Acta Metall.*, 37, 3, 885-895

Krishnan, K. N. (2002a). On the formation of onion rings in friction stir welds. *Mater. Sci. Eng. A*, 327, 2, 246-251, 0921-5093

Krishnan, K. N. (2002b). The effect of post weld heat treatment on the properties of 6061 friction stir welded joints. *J. Mater. Sci.*, 37, 3, 473-480, 0022-2461

Kroninger, H. R. & Reynolds, A. P. (2002). R-curve behaviour of friction stir welds in aluminium-lithium alloy 2195. *Fatigue Fract. Eng. Mater. Struct.*, 25, 3, 283-290, 8756-758X

Kwon, Y. J.; Shigematsu, I. & Saito, N. (2003). Mechanical properties of fine-grained aluminum alloy produced by friction stir process. *Scripta Mater.*, 49, 8, 785-789, 1359-6462

Kwon, Y. J.; Shigematsu, I. & Saito N. (2008). Dissimilar friction stir welding between magnesium and aluminum alloys. *Mater. Letters*, 62, 23, 3827-3829, 0167-577X

Lee, W.-B.; Yeon, Y.-M. & Jung, S.-B. (2003). The joint properties of dissimilar formed Al alloys by friction stir welding according to the fixed location of materials. *Scripta Mater.*, 49, 5, 423-428, 1359-6462

Li, H.; Geng, J.; Dong, X.; Wang, C. & Zheng, F. (2007). Effect of Aging on Fracture Toughness and Stress Corrosion Cracking Resistance of Forged 7475 Aluminum Alloy. *J. Wuhan Univ. Technol. Mater. Sci. Ed.*, June 2007, 191-195, 1000-2413

Mahoney, M. W.; Rhodes, C. G.; Flintoff, J. G.; Spurling, R. A. & Bingel, W. H. (1998). Properties of friction-stir-welded 7075 T651 aluminum. *Metall. Mater. Trans. A*, 29, 7, 1955-1964, 1073-5623

Malarvizhi, S. & Balasubramanian, V. (2010). Effects of Welding Processes and Post-Weld Aging Treatment on Fatigue Behavior of AA2219 Aluminium Alloy Joints. *J. Mater. Eng. Perform.*, in press, DOI: 10.1007/s11665-010-9682-5

Mendez, P. F.; Tello, K. E. & Lienert T. J. (2010). Scaling of coupled heat transfer and plastic deformation around the pin in friction stir welding. *Acta Mater.*, 58, 6012-6026, 1359-6454

Mishra, R. S. & Ma, Z. Y. (2005). Friction stir welding and processing. *Mat. Sci. Eng. R*, 50, 1-2, 1-78, 0927-796X

Morgeneyer, T. F.; Starink, M. J. & Sinclair, I. (2006). Experimental analysis of toughness in 6156 Al-alloy sheets for aerospace applications. *Materials Science Forum*, 519-521, Part 2, 1023-1028, 0255-5476

Murr, L. E.; Liu, G. & McClure, J. C. (1998). TEM study of precipitation and related microstructures in friction-stir-welded 6061 aluminum. *J. Mat. Sci.*, 33, 5, 1243-1251, 0022-2461

Murr, L. E. (2010). A Review of FSW Research on Dissimilar Metal and Alloy Systems. *J. Mater. Eng. Perform.*, in press, DOI: 10.1007/s11665-010-9598-0

Nandan, R.; DebRoy, T. & Bhadeshia, H. K. D. H. (2008). Recent advances in friction-stir welding – Process, weldment structure and properties. *Progress Mater. Sci.*, 53, 6, 980-1023, 0079-6425

Norman, A. F.; Hyde, K.; Costello, F.; Thompson, S.; Birley, S. & Prangnell, P. B. (2003). Examination of the effect of Sc on 2000 and 7000 series aluminium alloy castings: For improvements in fusion welding. *Mater. Sci. Eng. A*, 354, 1-2, 188-198, 0921-5093

Papazian, J. M. (1982). Calorimetric studies of precipitation and dissolution kinetics in aluminium alloys 2219 and 7075. *Metall. Trans. A*, 13, 5, 761-769

Peel, M.; Steuwer, A.; Preuss, M. & Withers, P. J. (2003). Microstructure, mechanical properties and residual stresses as a function of welding speed in aluminium AA5083 friction stir welds. *Acta Mater.*, 51, 16, 4791-4801, 1359-6454

Priya, R.; Subramanya Sarma, V. & Prasad Rao, K. (2009). Effect of post weld heat treatment on the microstructure and tensile properties of dissimilar friction stir welded AA 2219 and AA 6061 alloys. *Trans. Indian Inst. Metals*, 62, 1, 11-19, 0019-493X

Reynolds, A. P. (2000). Visualisation of material flow in autogenous friction stir welds . *Sci. Technol. Weld. Join.*, 5, 2, 120-124, 1362-1718

Reynolds, A. P. (2008). Flow visualization and simulation in FSW. Scripta Mater., 58, 5, 338-342, 1359-6462

Sato, Y. S.; Kokawa, H.; Enomoto, M. & Jogan, S. (1999). Microstructural evolution of 6063 aluminum during friction-stir welding. *Metall. Mater. Trans. A*, 30, 9, 2429-2439, 1073-5623

Sato, Y. S & Kokawa, H. (2001). Distribution of tensile property and microstructure in friction stir weld of 6063 aluminum. *Metall. Mater. Trans. A*, 32, 12, 3023-3031, 1073-5623

Sato, Y. S.; Urata, M. & Kokawa, H. (2002). Parameters controlling microstructure and hardness during friction-stir welding of precipitation-hardenable aluminum alloy 6063. *Metall. Mater. Trans. A*, 33, 3, 625-635, 1073-5623

Sauvage, X.; Dèdè, A.; Cabello Muñoz, A. & Huneau B. (2008). Precipitate stability and recrystallisation in the weld nuggets of friction stir welded Al–Mg–Si and Al–Mg–Sc alloys. *Mater. Sci. Eng. A*, 491, 1-2, 364-371, 0921-5093

Su, J. Q.; Nelson, T. W. & Sterling, C. J. (2003). A new route to bulk nanocrystalline materials. *J. Mat. Res.*, 18, 8, 1757-1760, 0884-2914

Sullivan, A. & Robson, J. D. (2008). Microstructural properties of friction stir welded and post-weld heat-treated 7449 aluminium alloy thick plate. *Mater. Sci. Eng. A*, 478, 1-2, 351-360, 0921-5093

Svensson, L. E.; Karlsson, L.; Larsson, H.; Karlsson, B.; Fazzini, M. & Karlsson, J. (2000). Microstructure and mechanical properties of friction stir welded aluminium alloys

with special reference to AA 5083 and AA 6082. *Sci. Technol. Weld. Join.*, 5, 5, 285-296, 1362-1718

Thomas, W. M.; Johnson, K. I. & Wiesner, C. S. (2003). Friction stir welding-recent developments in tool and process technologies. *Adv. Eng. Mater.*, 5, 7, 485-490, 1438-1656

Uematsu, Y.; Tokaji, K.; Shibata, H.; Tozaki, Y. & Ohmune, T. (2009). Fatigue behaviour of friction stir welds without neither welding flash nor flaw in several aluminium alloys. *Int. J. Fatigue*, 31, 10, 1443-1453, 0142-1123

Uzun, H.; Dalle Donne, C.; Argagnotto, A.; Ghidini, T. & Gambaro, C. (2005). Friction stir welding of dissimilar Al 6013-T4 To X5CrNi18-10 stainless steel. *Mater. Design*, 26, 1, 41-46, 0261-3069

Yang, Q.; Mironov, S.; Sato, Y. S. & Okamoto, K. (2010). Material flow during friction stir spot welding. *Mater. Sci. Eng. A*, 527, 16-17, 4389-4398, 0921-5093

Zhao, H.;, White, D. R. & DebRoy, T. (1999). Current Issues and Problems in Laser Welding of Automotive Aluminum Alloys. *Int. Mater. Rev.*, 44, 6, 238-266, 0950-6608

5

Non-Destructive Testing Techniques for Detecting Imperfections in Friction Stir Welds of Aluminium Alloys

Pedro Vilaça[1,2] and Telmo G. Santos[3]
[1]*IDMEC, Instituto de Engenharia Mecânica, Av. Rovisco Pais, 1, 1049-001 Lisboa*
[2]*IST-UTL, Instituto Superior Técnico, Av. Rovisco Pais, 1049-001 Lisboa*
[3]*UNIDEMI, DEMI, Faculdade de Ciências e Tecnologia, UNL, 2829-516 Caparica Portugal*

1. Introduction

The invention of Friction Stir Welding (FSW) (Thomas, 2009) has contributed for a significant push forward in the weldability criteria for many engineering materials and the concept of how they can be mechanically processed in solid state. From the many materials processed by FSW the most remarkable results were obtained for the aluminium and all its alloys including wrought and cast original conditions. The main technological procedures and parameters are presented and most relevant tool features and architecture are established (Vilaça, 2003). Some industrial applications of FSWelds of aluminium alloys are also summarized.

The quality of FSWelds of aluminium and its alloys is easy to reproduce and usually excellent, exceeding for some particular conditions the performance of base materials. Nevertheless, some imperfections can occur. The geometry, location, and microstructural nature of these imperfections will be established and classified for butt and overlap joints, which are the basic geometries enabling the production of all the remaining joint configurations, by combination of the previous. These imperfections bear no resemblance to the imperfections typically found in aluminium fusion welds. Consequently, it is difficult or even impossible, to identify all the FSWelds imperfections with commercially available conventional and advanced non-destructive testing (NDT) techniques. A paradigmatic example is the micro defects located at the root of conventional FSWeld joints with less than 100-50 μm. This state-of-the-art has been revealed as one important drawback preventing a wider transition of FSW to industrial applications, mainly focusing those where the quality standards are highly demanding and pursue the total quality assurance paradigm.

The review of physical fundaments and some technological features of the different NDT concepts is included supporting the presentation of the following content of the present chapter (Santos, 2009).

The assessment of the applicability of the conventional and advanced available NDT techniques to the most relevant FSW imperfections is established. The lack of assertiveness of the available NDT techniques in detecting the FSW joint imperfections are identified emphasizing the importance of the most recent new advances in the NDT technological

field, regarding the support of the industrial production of FSWelds involving aluminium and aluminium alloys.
To solve this lack of technological capacity in detecting non-destructively some imperfections in FSWelds, which may significantly affect the performance of the weld joints, many research and technological development projects are being undertaken and some of the most relevant results are presented in this chapter. The presentation of these new developments starts with the presentation of a system with acronym: QNDT_FSW, which consist of an integrated, on-line, NDT inspection system for FS welds, which employs a data fusion algorithm with fuzzy logic and fuzzy inference functions. It works by analyzing complementary and redundant data acquired from several NDT techniques (ultrasonic, Time of Flight Diffraction (ToFD), and eddy currents) to generate a synergistic effect that is used by the software to improve the confidence of detecting imperfections.
The next NDT development presented is a innovative system consisting of a new patented eddy current (EC) probes; electronic generation, conditioning and signal acquisition; automated mechanized scanning and dedicated NDT software. The new EC probe allows a 3D induced current in the material, and an easy interpretation of the signal based, not on the absolute value, but on a comprehensible perturbation of the signal. The results from an analytical simulation fully agree with the experiments.The experimental results clearly show that this system is able to detect imperfections around 50 μm, which contribute to increase the reliability on NDT of micro imperfections.

2. FSW process fundaments

2.1 General features

Friction stir welding (FSW) is a process for joining workpieces in the solid-phase, using an intermediate non-consumable tool, with a somewhat complex shoulder and probe profile, made of material that is harder than the workpiece material being welded. FSW can be regarded as an autogenous keyhole joining technique without the creation of liquid metal (Thomas et al., 1991).
The rotating tool, is plunged into the weld joint and forced to traverse along the joint line, heating the abutting components by interfacial and internal friction, thus producing a weld joint by extruding, forging and stirring the materials from the workpieces in the vicinity of the tool. The basic principles of the process and some nomenclature are represented in Figure 1.
This machine tool based process is recurrently considered the most important recent development in the welding technology, saving costs and weight for a steadily expanding range of applications of Lightweight Metallic Structures. As evidence of the disruptive character of the FSW process, world-wide research and development centers have chosen this issue has as a primary priority and the many significant advantages of FSW have rapidly been transferred to industry. Initially to the most demanding quality standards industrial applications and more recently spread to a wide range of structural and non-structural components.

2.2 Parameters

One important advantage of FSW is the Total Quality Assurance of results once all the process parameters are correctly established and monitored during the processing. The process parameters are easy to assess because FSW is mostly a mechanical welding process

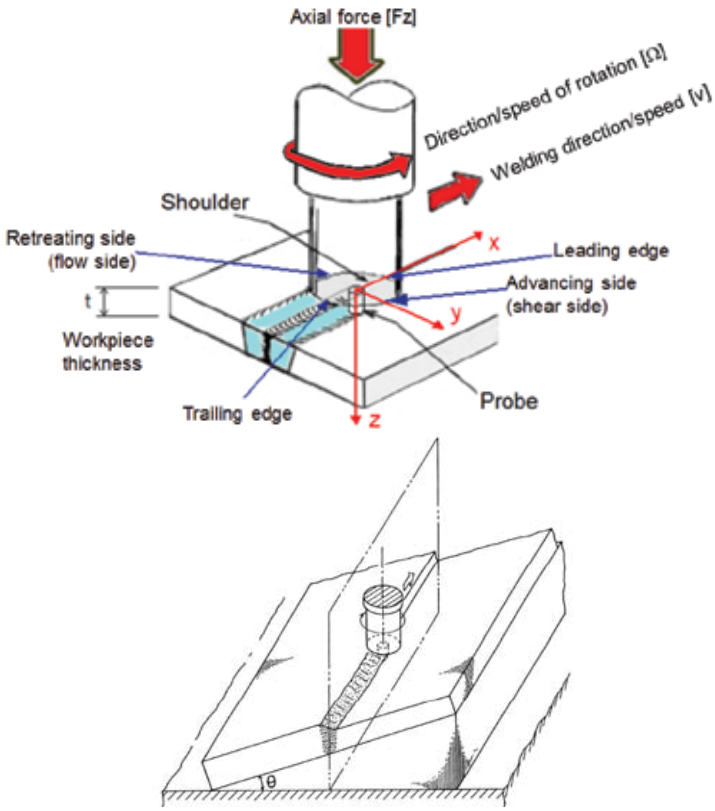

Fig. 1. Representation of some of the main parameters and nomenclature of FSW joints

where the results do not depend on difficult to control conditions, such as, environmental conditions or operator skills.

For achieving the Total Quality Assurance conditions, one important requirement is a strong, stiff machine and clamping system, able to react and apply the necessary load onto the workpiece via the tool, allowing to create and maintain the correct conditions.

In order to optimize the performance of the resultant FSW joint, and considering that the FSW results can be sensitive to variations of some welding parameters, it is important to identify and understand possible interactions between the welding parameters. The main FSW process parameters are the following:

1. FSW tool geometry;
2. Travel speed, v [mm/min];
3. Rotation speed, Ω [rpm];
4. Rotation direction [CW or CCW];
5. Tool rotational axis eccentricity [mm];
6. Vertical downward forging force, F_z [N];
7. Plunge distance of probe bottom to anvil [mm];
8. Plunge speed, [mm/s];
9. Dwell time, [s];
10. Tilt angle, α [°];
11. Concordance angle, θ [°];

12. Start position, (x,y) [mm];
13. End position, (x,y) [mm];
14. FSW control mode during weld [Force/Position];
15. Initial temperature/interpass temperature of welded components.

2.3 FSW tools

The shoulder and probe geometry are the most important feature that influences the final properties of the weld seam.

- Shoulder: outer diameter + shape + features;
- Probe: length +diameter along the length + shape + features;
- Oblique angle between probe axis and tool rotation axis;
- Ratio between static volume and dynamic volume of the probe;
- Tool axis eccentricity relatively to real tool rotation axis.

The most common FSW tools used in industrial applications are the mono-bloc conventional ones, composed by a threaded probe and a shoulder (Figure 2). These tools are limited to single thickness plates, since the probe length cannot be changed.

In laboratorial conditions this tool configurations becomes inadequate, since it is necessary to investigate the influence of different tool geometries (probe and shoulder), or it is necessary welding several plates with different thicknesses. Modular and adjustable tools are needed to meet these requirements. In Figure 3 it is shown a modular FSW tool designed for allowing the adjustment of the probe length by a vertical regulation of a screw. This FSW tool concept also allows the change and combination of different probe and shoulder geometries due to their symmetry (Figure 3 c).

Figure 4 show an alternative design consisting of a modular dual FSW tool with forced cooling.

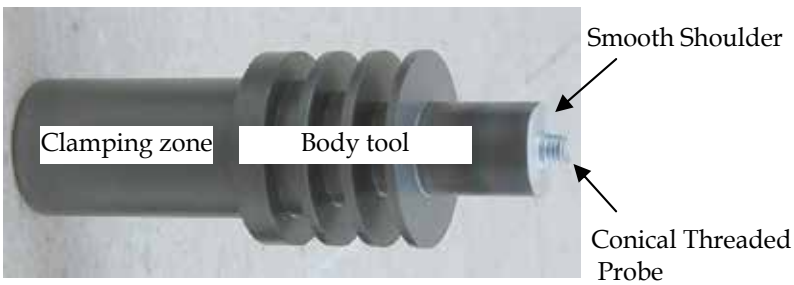

Fig. 2. Conventional FSW mono-bloc tool

A proposed design criterion for producing scrolled shoulders is established in (1) and (2) in polar coordinates. Figure 5, represents the scrolls for different Scroll Pitchs.

$$ScrollPitch \propto \frac{NScr \times v}{\Omega} \tag{1}$$

$$\text{Scroll Position} = \begin{cases} R = R_{shoulder} - \dfrac{ScrollPitch \times \beta \times (R_{shoulder} - R_{\text{int}})}{2\pi} \\ \beta = \left[0.. \dfrac{2\pi}{ScrollPitch} \right] \end{cases} \tag{2}$$

Where:

NScr – Number (integer) of scrolls (this value is set to a maximum of *NScr=4)*;

$R_{shoulder}$ – Exterior radius of the shoulder [mm];

R_{int} – Interior radius of the shoulder [mm];

β – Angle starting with the scroll on the exterior diameter of the shoulder and ending where the scroll ends at the interior radius of the shoulder [rad].

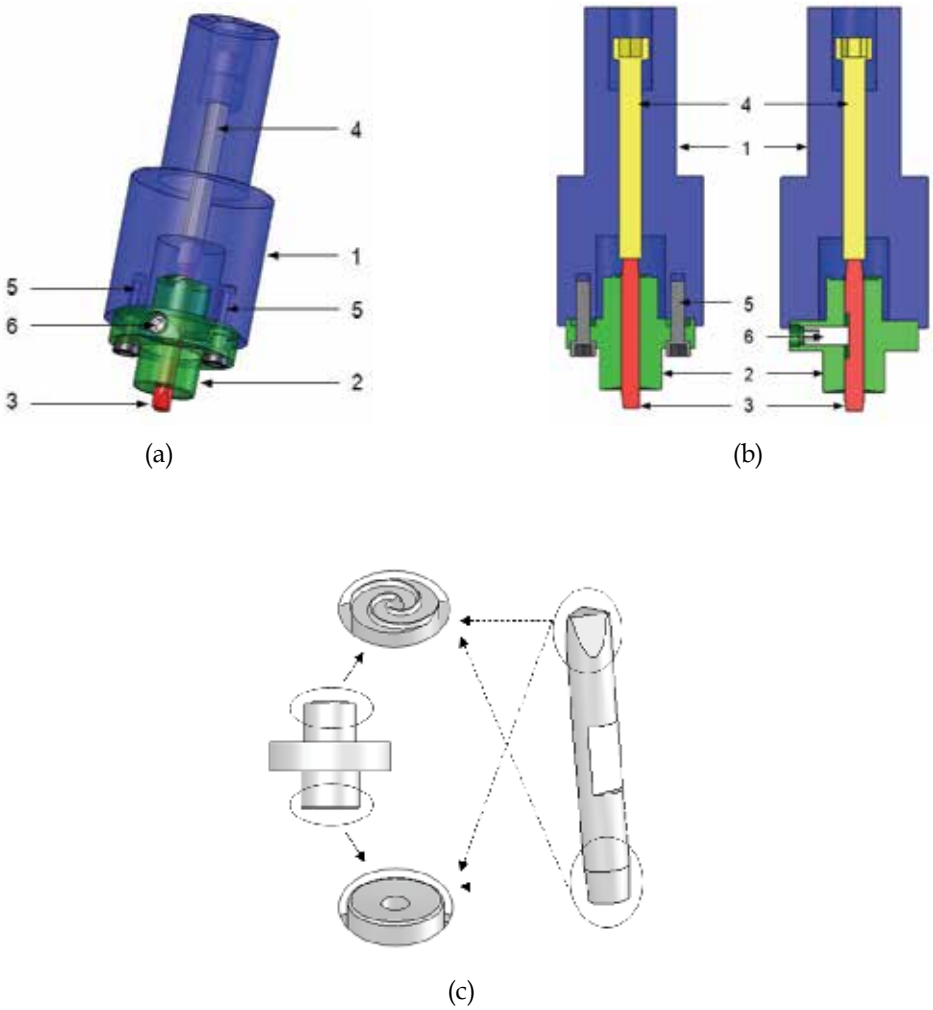

Fig. 3. Modular dual FSW tool. a) 3D view of assembly, b) Cutaway view in two perpendicular planes, c) Detail of geometric duality of the dual basis and probe dual. Nomenclature: main body (1), dual shoulder (2), dual-probe (3), vertical adjustment screw (4), bolts of the dual basis (5), dual screw probe (6).

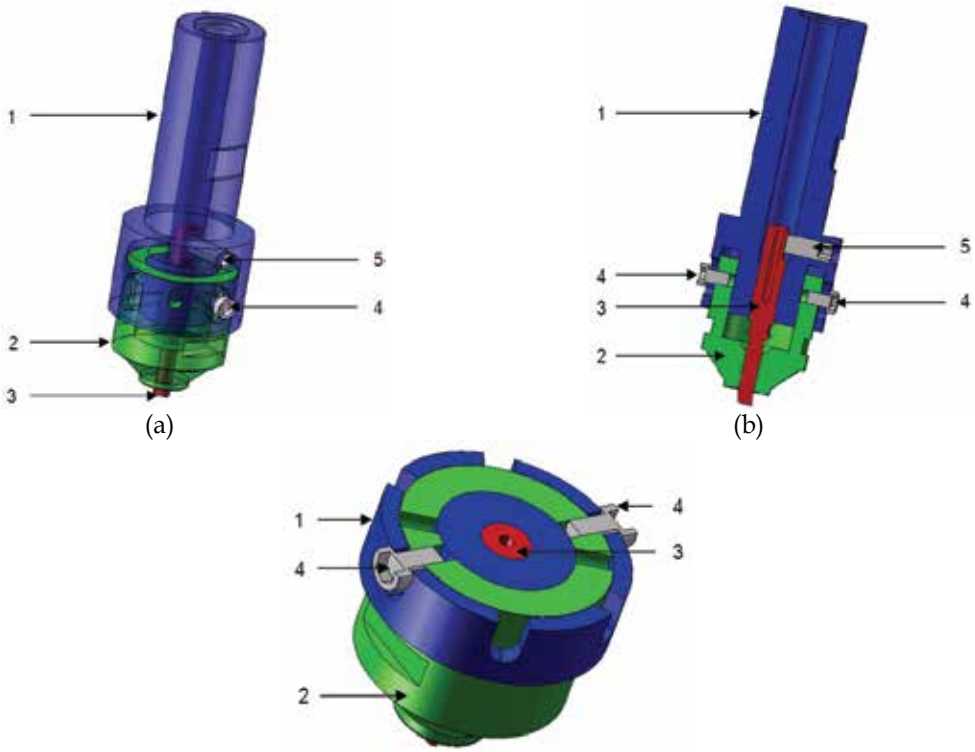

Fig. 4. Modular dual FSW tool with forced cooling.
a) 3D view of assembly, b) Viewed in longitudinal section, c) Viewed in cross section showing in detail the mechanism for adjusting the length of the probe. Nomenclature: tool body (1), built-in base (2), adjustable threaded probe with 1 mm pitch (3) screws to fix the base (4), threaded bolt fastening probe (5).

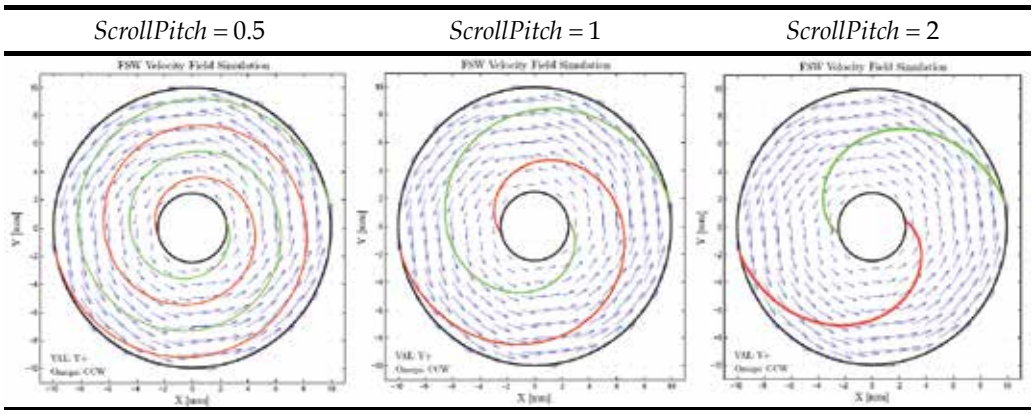

Fig. 5. Graphical representation of planar shoulders with 2 scrolls (spiral striates) for different ScrollPitch = {0.5; 1; 2}. Constant Values: Number of scrolls (striates)=2; R_{ext}=20 mm; R_{int}=5 mm; Ω=800 rpm.

2.4 Typical metallurgical features

During the FSW process, the material undergoes intense plastic deformation at elevated temperature, resulting in generation of fine and equiaxed recrystallized grains. This fine microstructure produces good mechanical properties in friction stir welds (Moreira et al., 2009). Better quality joints are associated with more intense tridimensional material flow pattern.

The typical metallurgical structures present in the processed zone of FS welds are established and classified in Figure 6. Beside the TMAZ central zone, there is the Heat affected Zone (HAZ) and the unaffected parent material or Base Material (BM)

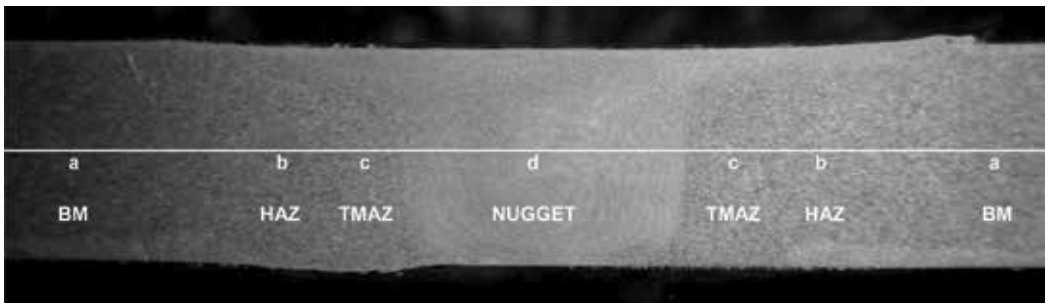

Fig. 6. Generic identification of micrograph locations

The composition of the recrystallised zone of the TMAZ (the nugget) is unchanged from that of the parent material and there is no measurable segregation of alloying elements but grain size varies across the flow contours.

Joining does not involve any use of a filler metal and therefore any lightweight metal and alloy can be joined without concern for the compatibility of the composition, which would be an issue in fusion welding. When desirable, dissimilar lightweight metal alloys and metal matrix composites can be joined with equal ease.

The principal advantages of FSW, being a solid phase process, are low distortion, absence of melt-related imperfections and high joint strength, even in those alloys that are considered non-weldable by conventional fusion techniques.

Furthermore, FSW joints are characterised by the absence of filler induced problems/imperfections. In addition, the hydrogen contents of FSW joints tend to be low, which is important in welding alloys susceptible to hydrogen damage.

3. Production and characterization of FSW samples with and without defects

3.1 Base material, FSW tools and equipment

The materials under study were AA2024-T4 and AA5083-H111 alloys, with 3.8 and 7.0 mm thickness respectively, having the chemical composition presented in Table 1. In Figure 7 it is shown the macrographs of AA2024-T4 in three different views: perpendicular and parallel to the rolling direction, and at surface of the plates.

A conventional milling machine (Figure 8a) and an ESAB LEGIO™ FSW 3UL (Figure 8b) were used to produce FSW in AA5083-H111 and in AA2024-T4, respectively. Several FSW tools geometry was tested to produce different welded conditions with and without defects. Table 3 describes the characteristics of three different FSW shoulders, and Table 4 describes the eight FSW tools tested. These tools are illustrated in Figure 9.

Material	Al	Cr	Cu	Fe	Mg	Mn	Si	Ti	Zn
AA5083-H111	94.5	0.08	0.03	0.33	4.39	0.51	0.12	0.02	0.01
AA2024-T4	93.5	max. 0.1	3.8 – 4.9	max. 0.5	1.2 – 1.8	0.3 – 0.9	max. 0.5	max. 0.15	max. 0.25

Table 2. Chemical composition of base materials as % of weight

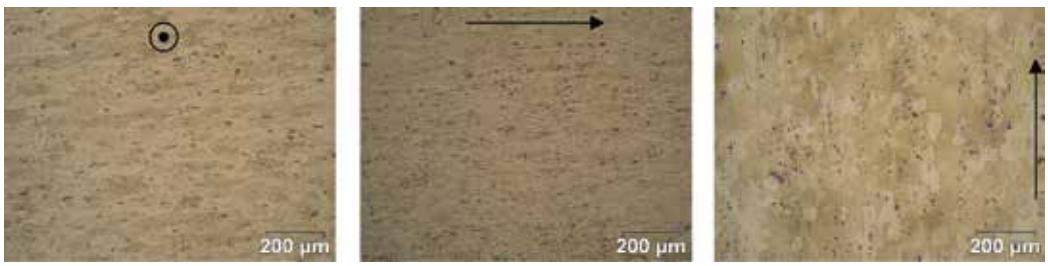

(a) (b) (c)

Fig. 7. Macrographs of AA2024-T4 perpendicular (a) and parallel (b) to the rolling direction, and in surface of the plates (c).

(a) (b)

Fig. 8. FSW equipments used to produce FSW samples. a) Conventional milling machine and the ESAB LEGIO™ FSW 3UL.

Base	$Ø_{exterior}$ [mm]	$Ø_{interior}$ [mm]	Tipo
A	15	5	Non-scrolled concave
B	19	8	Planar with spiral scrolls.and p = 2
C	18	6	Planar with spiral scrolls.and p = 0.5

Table 3. Characteristics of the FSW shoulders

Tool	Base	Probe
# 1	A	cylindrical M5 with 3 flat sided
# 2	B	conical threaded M8 with 3 helicoidal longitudinal channels (Øbase = 8 mm, Øtop = 5 mm)
# 3	B	stepped smooth surface (Øbase = 8 mm, Øtop = 6 mm)
# 4	B	conical smooth surface (Øbase = 8 mm, Øtop = 5 mm)
# 5	B	cylindrical smooth surface, with 4 helicoidally groves at the tip (Øbase = 8 mm, Øtop = 6 mm)
# 6	A	inverted conical smooth surface (Ø middle = 4 mm, Øtop = 5 mm)
# 7	A	conical smooth surface, with 1 helicoidally groves at the tip (Øbase = 8 mm, Øtop = 4 mm)
# 8	C	conical threaded with 3 flat sided (Øbase = 6 mm, Øtop = 5 mm)

Table 4. Characteristics of the FSW tools (shoulders + probes)

Fig. 9. FSW tools used to produce defect and non defect condition on AA2024-T4 and AA5083-H111

3.2 Production and characterization of FSW samples

To test and validate the NDT developed systems, some friction stir welds were produced using the above mentioned aluminium alloys AA2024-T4 and AA5083-H111.

FSW with high defects conditions were initially produced on AA5083-H111, as it shows by transverse macrograph in Figure 10. The non defect condition (Figure 10 a) correspond to a bead on plate weld, and was produced using the FSW tool #1. The high void defect condition (Figure 10 b) also corresponds to a bead on plate weld produced with the FSW

tool #1. The high void and root defect condition (Figure 10 c) was produced using the FSW tool #6. The propose of this welded conditions was to evaluate the applicability of different existent NDT techniques on FSW. This issue will be addressed in section § 4. In addition, this welded conditions was used to calibrate the Quantitative Non Destructive Testing System for FSW (QNDT_FSW) described in § 5.1, in order to compare and classify others FSW with these standard defect conditions.

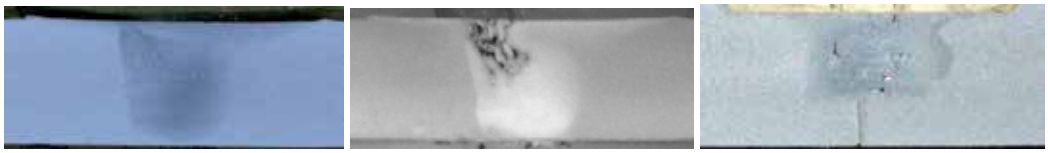

(a) (b) (c)

Fig. 10. FSW produced on AA5083-H111. a) Non defect condition (bead on plate), b) High void defect condition, c) High void and root defect condition

The AA2024-T4 alloy was used to produce three different root defect conditions: Type 0, Type I and Type II (Figure 11). Defect Type 0 is characterized by some residual particles alignment in an intermittent path along ~ 150 µm. This condition is considered a non defective weld. Defect Type I is characterized by a weak or intermittent welding since the materials are in close contact, under severe plastic deformation, but with no chemical or mechanical bond along ~ 50 µm. Defect Type II is characterized by ~ 200 µm non welded zone, followed by particles alignment in an intermittent path. The three different conditions present a consecutive increase of the defect intensity, suitable for a reliability analysis of a NDT system.

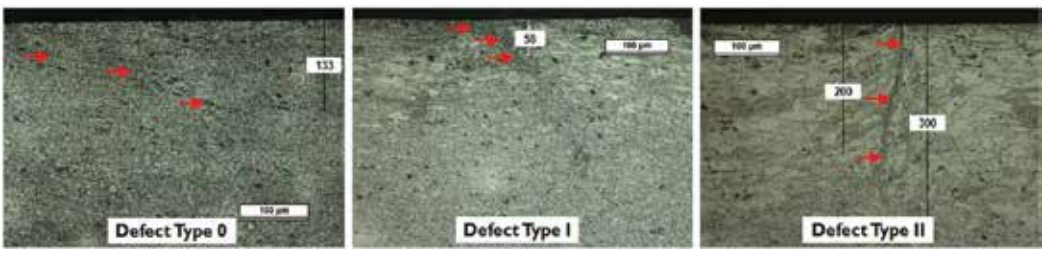

Fig. 11. Transversal macrographs of three different FSW root defects conditions on AA2024-T4 using tool # 2. Defect Type 0: particles alignment, Defect Type I: ≈ 60 µm, Defect Type II: ≈ 200 µm

Other different defects morphology was produced in AA2024-T4 alloy, exploring other FSW tools, in order to correlate the tools geometry and the weld quality of the joints. Figure 12 presents four transversal macrographs of different weld defects conditions produced with different FSW tools. Defect Type III (Figure 12 a) is an internal imperfection type void. Figures 12 a), b) and c) presents a mixed defect weld condition consisting of a root and void defects. These analyses allow concluding that the geometry of the FSW tool #2 produces the best quality welded joints.

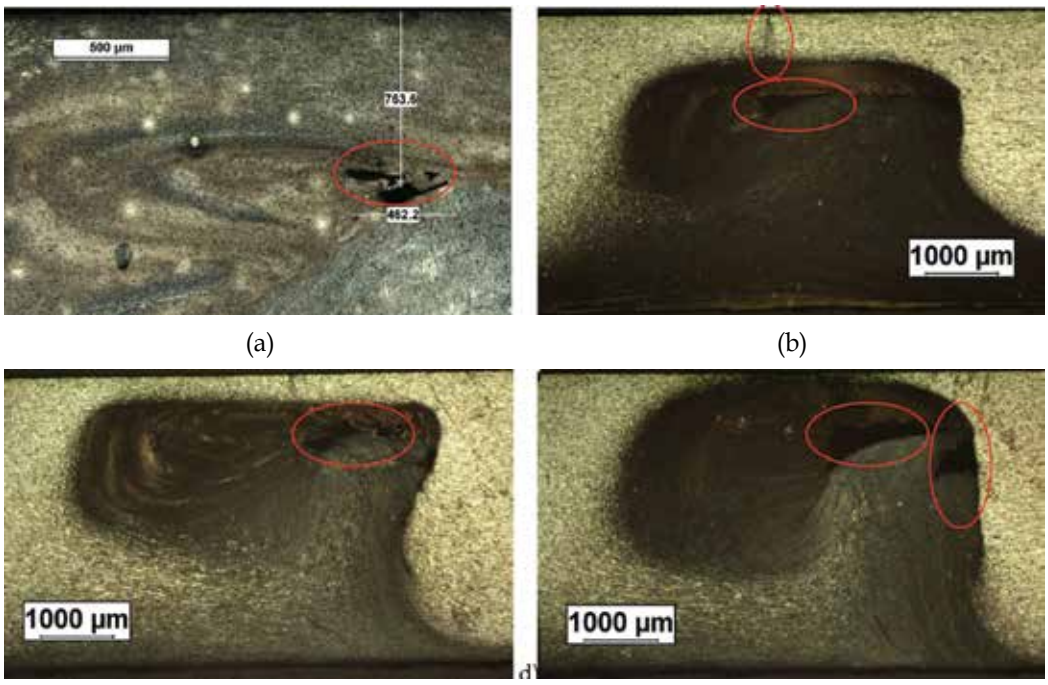

(a) (b)

(c) (d)

Fig. 12. Macrographs of four different FSW void and root defects conditions on AA2024-T4 a) FSW with defect Type III using tool # 2), b) FSW with defect Type M using tool # 4), c) FSW with defect Type M using tool # 6), d) FSW with defect Type M using tool # 7).

3.3 Effects of defects

Fatigue tests were performed on AA2024-T4 in order to evaluate the effects of defects on mechanical behavior of the welded joints. The propose was to identify witch defect condition (Type 0, Type I, Type II and Type III) presents a significantly decrease of fatigue life comparing to the base material.

The fatigue tests are performed on an Instron 8874, with a load cell of 25kN. Stress ratio R is 0.1. The S-N curve results obtained are presented in Figure 13 (Santos et al., 2009). This result leads to conclude about the good mechanical efficiency of the FSW joints with Defect Type 0. In fact, these joints present a mechanical behaviour similar to the base material. Concerning to the other three defect types, all presents a significantly loss of mechanical resistance. Among these different defects, the root defects (Type II) are definitely the ones that show higher loss of mechanical properties under fatigue loading. Those imperfections are thereby the NDT targets defects of FSW. Furthermore, the other type of imperfections (e.g. thickness reduction and flash formation) may be inherent to the process itself and are impossible to be avoided or may be evaluated without need of NDT.

4. Evaluation of the applicability of conventional NDT techniques to FSW

In order to evaluate the applicability of conventional NDT techniques to FSW some experimental tests were performed on above described defects conditions on AA2024 – T4

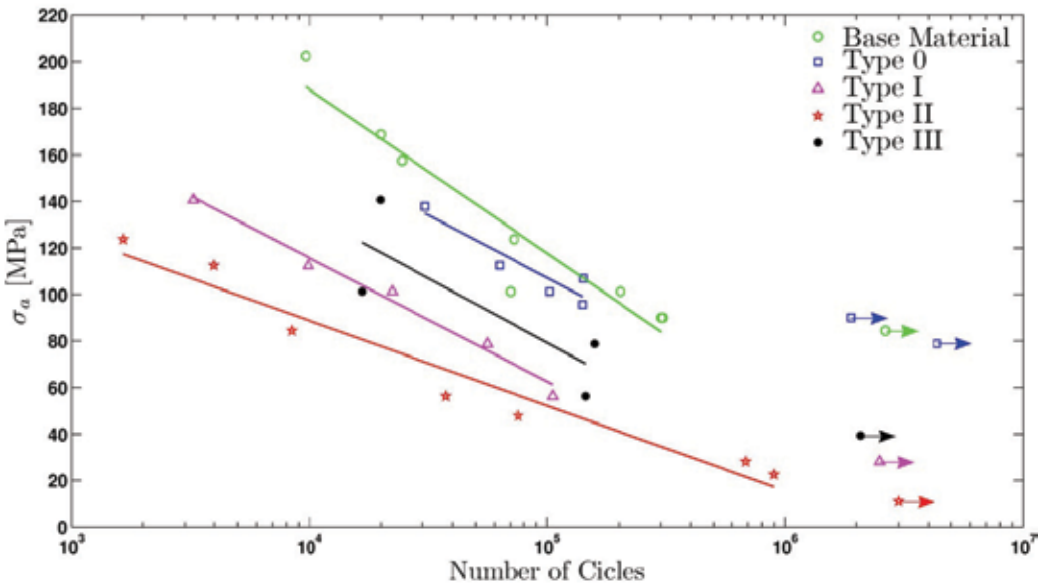

Fig. 13. Fatigue curves for base material and 4 different defect type conditions

and AA5083-H111. The propose is to conclude about the capability of conventional NDT techniques to detect the FSW defects with the morphologies described in section § 3.2.

4.1 Conventional X-ray

The specimens were analyzed using conventional X-Rays, in Scan-Ray® equipment, DOA 300/AC-103 model, rightly calibrated and certificated. AGFA® D4 X-Ray film, an extra fine grain film with very high contrast, and with density value of 2 was used for these trials.

The X-ray parameters were: Intensity: 5mA; Energy: 70 kV; Exposure time: 150 sec; Distance between the source and the film: 800 mm.

The friction stir welds were oriented with the root to the X-ray film in order to avoid image distortion in the cases that the defect at the root was detected. The quality image control and the acquirement of the sensitivity values were done with a pattern behind the sample, in accordance of the standard DIN 54109 and recommended by the International Institute of Welding.

In Figure 14 it is present the X-ray image of specimens produced on AA5083-H111 with high defects type voids and roots similar to the ones presented in Figure 10 a and Figure 10 b). It is possible to observe that booth root and internal defects are visible, since they are very big. However, X-ray NDT technique cannot detect FSW micro root defects whit the morphology described in Figure 11. In Figure 15 and Figure 16 it is presented X-ray image of specimens produced on AA2024-T44 with root defect Type II and void defect Type III, respectively. The acquired image (Figure 15) show that even the biggest root defect (Type II) was not detected. Only defect Type III (void defect) was detected, as it shows in Figure 15.

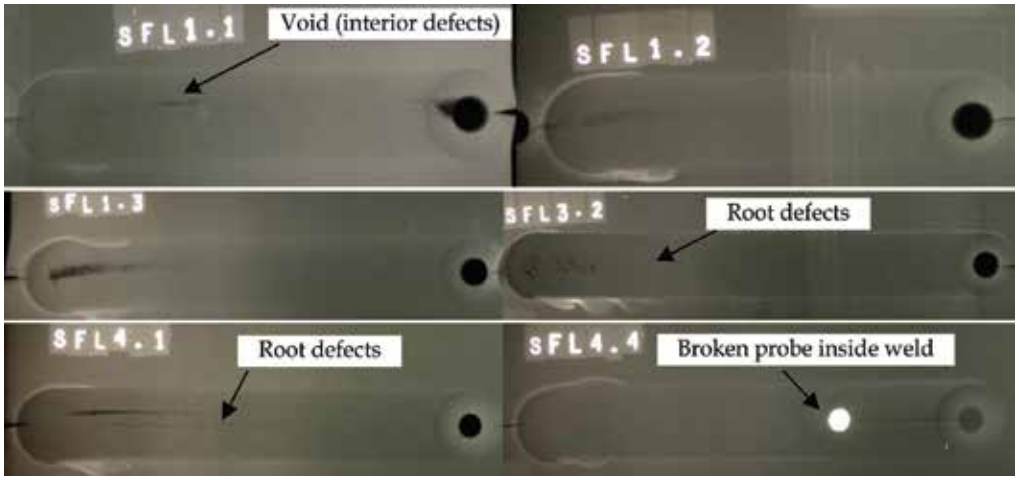

Fig. 14. X-ray image of specimens produced on AA5083-H111 with high voids and roots defects

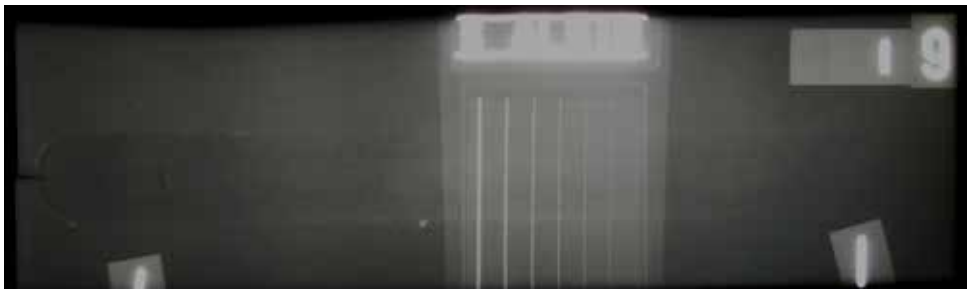

Fig. 15. X-ray image of specimens produced on AA2024-T4 with roots defects Type II

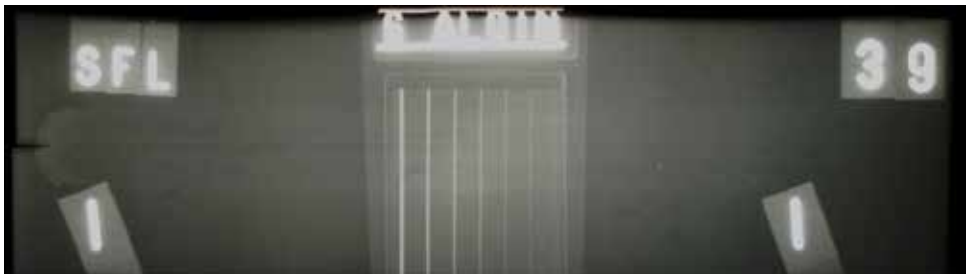

Fig. 16. X-ray image of specimens produced on AA2024-T4 with void defects Type III

4.2 Conventional creping ultra-sound

Creeping ultrasonic inspection was performed with a 4 MHz probe, on both retreating and advancing sides of the weld, where the insonification direction was always perpendicular to the welding direction (Figure 17). Gathering data from both sides of the weld created a redundancy of data, which was analyzed by the data fusion algorithm of the QNDT_FSW described in § 5.1. Creeping inspection was also complemented with data that came from

attenuation measurements. The measurement of the attenuation is performed with an ultrasonic probe working in receiving mode, located at the opposite side of the weld bead in the same insonification plane of the creeping probe. Therefore, in the case of defect, a creeping signal change occurs, increasing at the same time the attenuation. These two simultaneous conditions allowed the QNDT_FSW system to distinguish between signal disturbance and real imperfections.
The results of the NDT creeping ultra-sound on AA5083-H111 presented in Figure 18 show that the high root defects was detected by a signal change, underline by the red boxes. However, once again, the micro root defects presented in AA2024-T4 was not detected.

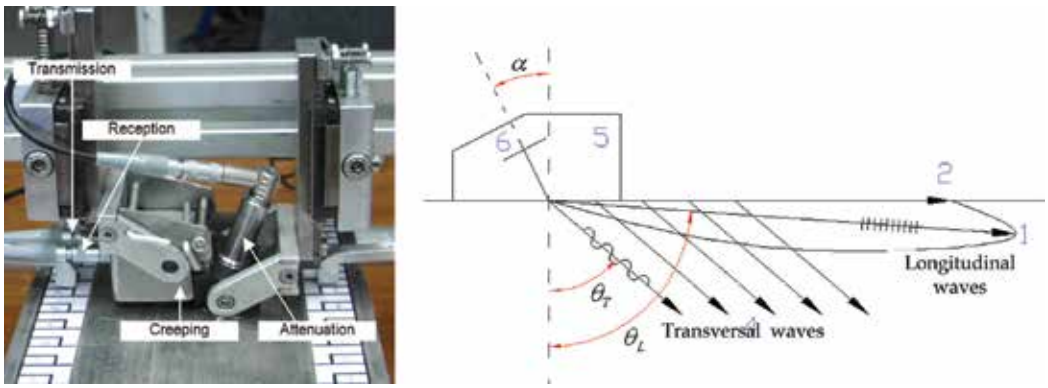

a) b)

Fig. 17. Inspection of FSW with conventional creping ultra-sound.
a) Creeping and attenuation probes displacement, b) Schematic representation of the ultra-sound waves in the material AA6083-H111.

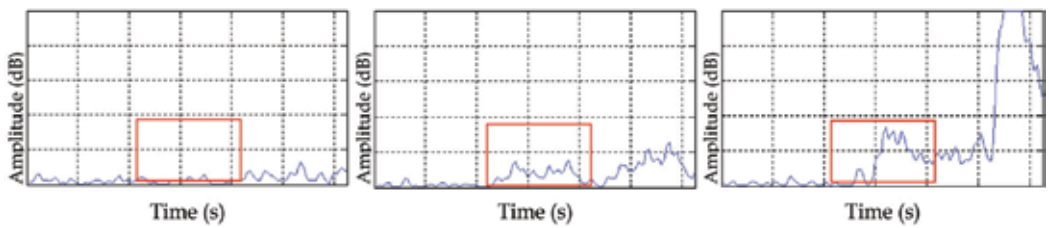

a) b) c)

Fig. 18. Results of the NDT creeping ultra-sound on AA5083-H111.
a) Non defect condition (bead on plate) of Figure 10 a, b) Moderate FSW root defect condition, c) High void and root defect condition of Figure 10 c.

4.3 Time of Flight Diffraction (ToFD)

Time of Flight Diffraction (ToFD) NDT technique was performed with a 15 MHz probes on the same samples described in above section § 4.2. Figure 19 shows the used arrangement of the probes and the motion device. Once again, the results presented in Figure 20 shown that ToFD technique was able to identify high root and void defects in AA5083-H11 samples, by a evident signal change underline by the red boxes. Nevertheless, the micro root defects presented in AA2024-T4 was not detected.

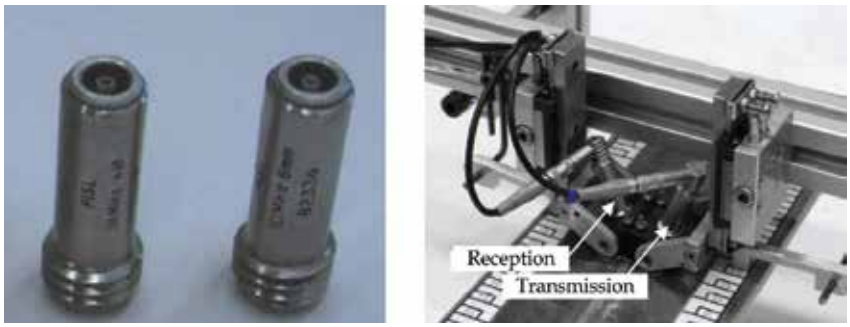

a) b)

Fig. 19. ToFD ultra-sound NDT testing of AA5083-H111.
a) 15 MHz ToFd probes used, b) Arrangement of the probes and motion device.

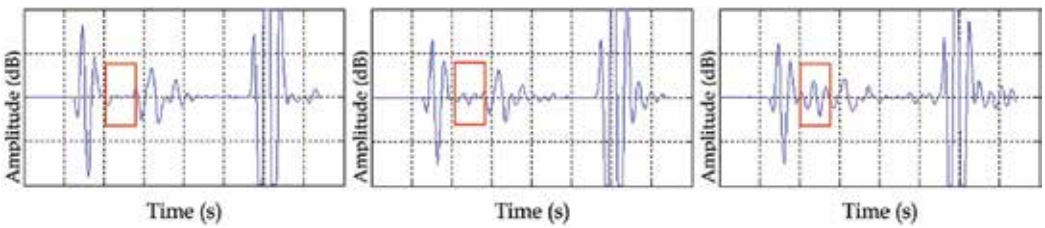

a) b) c)

Fig. 20. Results of the NDT ToFD ultra-sound on AA5083-H111.
a) Non defect condition (bead on plate) of Figure 10 a, b) Moderate FSW root defect condition, c) High void and root defect condition of Figure 10 c.

4.3 Conventional Eddy Current (EC)

The three FSW defect conditions Type 0, Type I and Type II in AA2024-T4, described in Figure 11 (section § 3.2) were inspected by NDT eddy current (EC) technique using a conventional cylindrical helicoidally EC probe.

The signal was acquired from the root side, along a sweep on the transversal direction to the weld joint. The starting point of the tests was set to 25 mm in the retreating side of the weld bead, and 50 mm long segments were characterized in direction to the advancing side, with 250 µm space within each acquisition. In all the acquisitions the real and imaginary part of electrical impedance was measured @ f = 400 kHz.

In Figure 21 it is presented the obtained results S(x) = Abs{Z}. It can be seen that the three curves concerning to the previously defects conditions present a very similar trend between them.

It means that the conventional probes have very low sensitivity to root defects. The reason is that the impedance changes are mainly due to the presence of the FSW weld bead, instead the presence of a defect. In fact the FSW process causes microstructural modifications (Nascimento et al., 2009) material conductivity changes in the bead zone, even without any imperfections. Therefore there is no distinctive signal feature that can allow to distinct between each defect condition. Indeed, the absolute conventional probe can only reproduce the global spreaded increase of conductivity field due to the FSW bead. Such probes are not

able to distinguish small suddenly variations of conductivity, caused by a local micro root defect as those tested (Santos et al., 2009). These results illustrate the difficulty of NDT of FSW when using conventional EC probes.

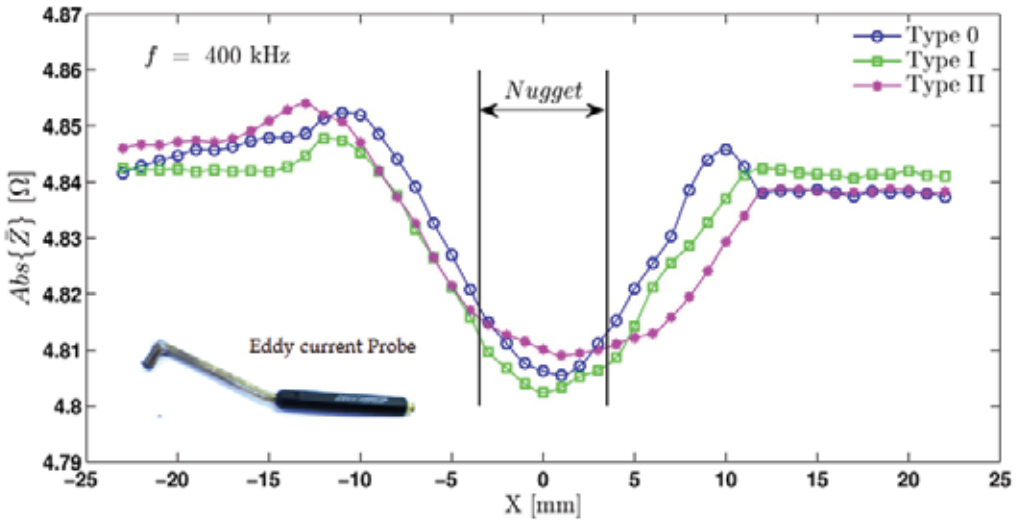

Fig. 21. Results for the NDT inspection of FSW joints with defect Types 0, I and II @ f = 400 kHz using a conventional cylindrical helicoidally EC probe.

5. Recent advances in NDT for FSW of aluminium alloys

5.1 QNDT_FSW: Inspection system for FS welds based on data fusion

The Quantitative Non Destructive Testing for FSW (QNDT_FSW) is an integrated, on-line system. It employs a data fusion algorithm to improve the confidence of inspection based on Relative Operating Characteristics (ROC) and Probability of Detection (PoD). The complementary and redundant data acquired from several NDT techniques generate a synergistic effect, which is the main advantage of the present approach. The data fusion algorithm uses fuzzy logic and fuzzy interference functions to mingle the data from several NDT techniques.

The QNDT_FSW system incorporates three, distinct NDT techniques. They include a 4 MHz creeping ultrasonic probe, a 15 MHz Time of Flight Diffraction (ToFD) probe, a 20 kHz eddy current probe, and a 2 MHz eddy current probe. These techniques were selected to detect, as much as possible, the position and diversity of imperfections in FS welds (Santos et al., 2008).

Among the several FSW trials performed to validate and implement the QNDT_FSW system, one application samples are presented. The results of testing the QNDT_FSW system are presented in terms of equivalent imperfection indices called the Root Imperfection Index (RII) and the Internal Imperfection Index (III). These imperfection indices were calculated with fusion inference functions and represent the data fusion result for all of the above mentioned NDT techniques. Figure 22 illustrates algorithm to calculate IRD and III.

An imperfection index equal to 100 % means a high-imperfection weld section, similar to the high-imperfection weld standard of the Figure 10 b and c). An imperfection index equal to 0 % means an imperfection-free weld section, similar to imperfection-free weld standards of the Figure 10 a).

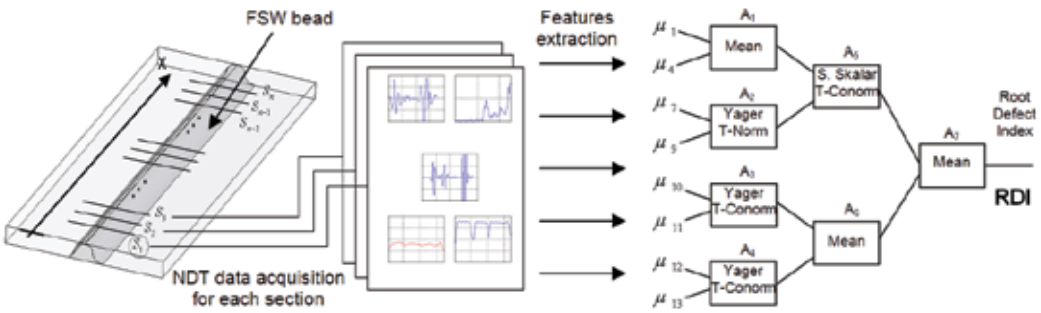

Fig. 22. Schematic representation of the algorithm to calculate IRD and III

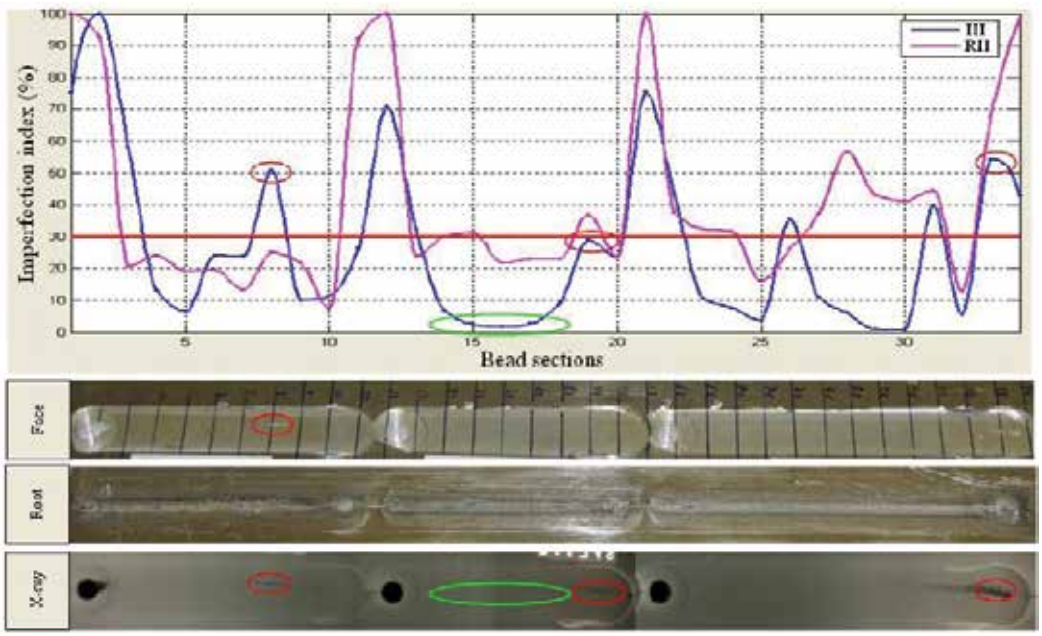

Fig. 23. RII and III for three consecutive welds on AA5083-H111

Figure 22 presents the results of applying the QNDT_FSW system to three different FSW trials on AA5083-H111. The trials were performed with a probe length of 6.8 mm, a tilt angle of 2º, and a rotation speed of 710 rpm. The difference between these 3 trials was a change in the travel speed. In section 11 to section 1, the travel speed was 160 mm/min; from section

21 to section 12, the travel speed was 224 mm/min; and from section 34 to section 22, the travel speed was 320 mm/min. Based on a comparison (Figure 23) of the RII and III results with the macroscopic, visual, and radiographic test results, the following conclusions were made:

- The exit holes located at sections 1, 12 and 22 were detected by both imperfection indices;
- In section 8, the III revealed a cavity, which was corroborated by radiographic testing and visual inspection as the cavity breaks the surface of the workpiece. Moreover, the RII was not affected, which confirmed the independence of both imperfection indices;
- Sections 14 to 18 present a very low III, which was corroborated by radiographic testing. RII was able to detect small, root imperfections, as confirmed by metallographic cross-sections of the weld. Emphasis should be given to the fact that in these sections, radiographic testing cannot detect a root imperfection;
- For the 3 FSW trials, the RII increased as the travel speed increased. This behaviour was expected because the probe length was 0.2 mm shorter than the plate thickness. This created a small root imperfection that increased with increased in size as the travel speed increased.

The proposed equivalent defect indices for evaluating the significance of root (RII) and internal (III) imperfections show that the results accurately predicted the quality of the weld. In fact, combining the data from several NDT processes is an improvement, when compared to interpreting the individual results of each NDT process, due to the synergistic effect of the data fusion algorithm.

5.2 Eddy current IOnic probe

In order to improve the reliability in FSW non-destructive inspection a new NDT EC system with a special designed probe was developed and tested in AA2024-T4 FSW defects conditions. The EC probe allows a 3D induced eddy currents in the material; deeper penetration; independence of the deviation between the probe and the material surface; and easy interpretation of the output signal based on a comprehensible qualitative change.

The so called IOnic (Rosado et al., 2010) probe is constituted by one excitation filament, in the middle of two sensitive planar coils, in a symmetric configuration (Figure 24). Due to this layout the operation of the IOnic probe is based on an integration effect along each sensitive coil, and simultaneous, on a differential effect between the two coils. The probe was manufactured on 1.6 mm dual layer FR4 PCB subtract with an external diameter of 11 mm. The two sensitive coils are formed by tracks of 100 µm width separated by same dimension gaps.

The IOnic probe has some other advantages when compared to the conventional eddy currents probes: i) precision differential based operation resulting on high sensibility and superior lift-off immunity; ii) improved contact with test material by being planar, leading to deeper eddy currents penetration in test material; iii) the straight eddy currents induced in the material near the driver trace can be taken as advantage to evaluate materials where the flaws tend to follow a specific orientation; iv) allow the inspection of the material borders as long as the symmetry axis remains perpendicular to it; v) can be implemented in flexible substrates easily adaptable to non-planar and complex geometry surfaces.

The eddy current NDT System for FSW includes further dedicated components, namely: i) electronic devices for signal generation, conditioning and conversion, ii) automated mechanized scanning, and iv) dedicated software, shown in Figure 25.
The IOnic Probe was applied on AA2024-T4 defects condition Type 0, Type I and Type III described before in Figure 10. The data $S(x) = Im\{\bar{U}out/\bar{I}\}$ was acquired from the root side, along a sweep on the transversal direction to the weld joint, with the excitation filament of the probe parallel to weld joint. The inspection was perform @ f = 50 kHz, f = 100 kHz and f = 250 kHz. The imaginary part of the three types of defects at these frequencies is shown in Figure 26.

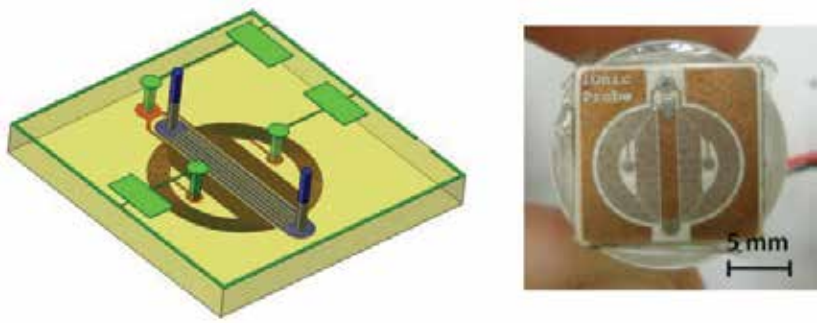

Fig. 24. The IOnic Probe prototype.

Fig. 25. NDT system overview: laboratory apparatus for inspecting FS welds: the mechanical support system device and the computational data acquisition device.

As FSW process causes material conductivity changes, even without imperfections, the weld bead is responsible for the large curve on the imaginary part. The presence of imperfections creates a small perturbation observed on the middle of the joint, highlighted in red. This small perturbation observed at the middle of the joint concerns to the suddenly decrease of conductivity due to the local root defect of each defect condition. Notice that there is a very good proportionality between the defect dimension and the observed perturbation on the imaginary part Im{Ūout/Ī}. These results show that IOnic probe is able to identify the three different types of defect conditions produced in AA2024-T4 aluminum alloy.

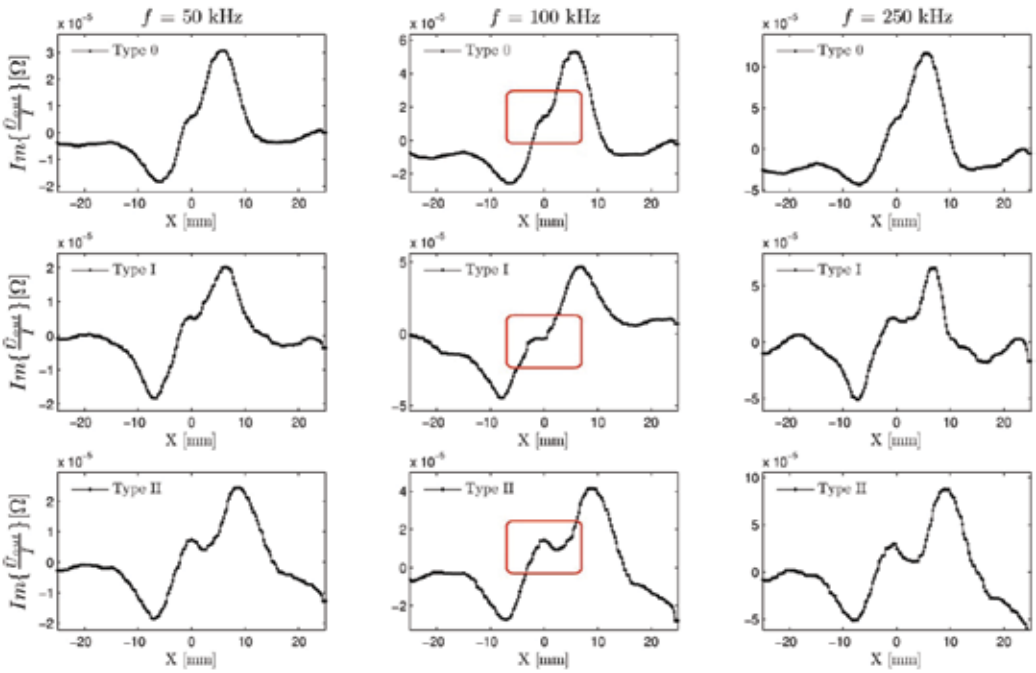

Fig. 26. Results of IOnic Probe for the FSW joints with defect types 0, I and II @ f = 50 kHz, f = 100 kHz and f = 250 kHz.

6. Conclusion

From the present work the following conclusions can be drawn:
Micro root defects in friction stir welds as the lack of penetration or kissing bond are defects endorsed by failures in the process parameters that can occur in industrial applications. These defects weaken the structural fatigue strength that in critical structural are not tolerated. In this way, effective and reliable nondestructive techniques are required for the detection of these flaws.
The geometry, location and microstructural nature of the FSW defects, which bore no resemblance with defects typical of fusion welding of aluminium alloys, lead to very difficulties in identification when using the common NDT techniques.

Conventional NDT techniques such as creeping ultrasound, ToFD, X-ray or axis-symmetry eddy current probes are not able to detect the typical FSW micro root defects with depth below 200 μm.

A NDT integrated data fusion system for FSW named QNDT_FSW was presented. Equivalent defective indexes are proposed for evaluating the relevance of the root (RDI) and internal (IDI) defects. The data fusion algorithm for NDT of FSW, based on fuzzy logic and fuzzy inference functions disclosed a general powerful data fusion NDT approach. Combining the data from several NDT processes is an improvement, when compared to interpreting the individual results of each NDT process, due to the synergistic effect of the data fusion algorithm.

The experiments shown that the IOnic Probe is able to identify different levels of FSW micro root defects by a qualitative perturbation of the output signal. It was also shown that exist a good proportionality between the defects size and this signal perturbation.

7. Acknowledgements

The authors would like to acknowledge Fundação para Ciência e Tecnologia (FCT) for its financial support via project POCTI/EME/60990/2004

8. References

Moreira, P. M. G. P., T. Santos, S. M. O. Tavares, V. Richter – Trummer, P. Vilaça, P. M. S. T. de Castro, (2009), Mechanical and metallurgical characterization of friction stir welding joints of AA6061 – T6 with AA6082 – T6, Materials and Design (ISSN: 0261-3069); Vol. 30, Issue 1, pp.180 – 187;

Nascimento, F., T. Santos, P. Vilaça, R.M. Miranda, L. Quintino, (2009), Microstructural modification and ductility enhancement of surfaces modified by FSP in aluminium alloys. International Journal of Materials Science and Engineering: A (Structural Materials: Properties, Microstructure and Processing). Vol. 506, N.º 1 – 2, pp. 16 – 22,. DOI:10.1016/j.msea.2009.01.008.

Rosado, Luís, Telmo G. Santos, Moisés Piedade, Pedro Ramos, Pedro Vilaça, (2010) Advanced technique for non-destructive testing of friction stir welding of metals, Measurement (ISSN: 0263-2241); doi:10.1016/j.physletb.2003.10.071

Santos, T., P. Vilaça, L. Quintino, (2008), Developments in NDT for Detecting Imperfections in Friction Stir Welds in Aluminium Alloys. Welding in the World (ISSN 0043 – 2288), Journal of the International Institute of Welding (IIW), Vol. 52, N.º 9 – 10, pp.30 – 37;

Santos, Telmo, Pedro Vilaça, Luísa Quintino, (2009), Computational Tools For Modeling FSW and An Improved Tool for NDT, Welding in the World (ISSN: 0043 – 2288), Journal of the International Institute of Welding (IIW), (IIW-1978-08 (ex-doc. III-1507r1-08), Vol. 53, N.º 5/6;

Thomas W M, Nicholas E D, Needham J C, Murch M G, Temple-Smith P, and Dawes C J (1991) Improvements relating to friction stir welding. US Patent No. 5,460,317.

Thomas Wayne M. (2009). PhD thesis: *An Investigation and Study into Friction stir Welding of Ferrous-Based Material*, University of Bolton.

Vilaça, P, (2003). PhD thesis: Fundamentos do Processo de Soldadura por Fricção Linear - Análise Experimental e Modelação Analítica, Instituto Superior Técnico, Technical University of Lisbon.

6

Aluminium 7020 Alloy and Its Welding Fatigue Behaviour

Carlos Bloem[1], Maria Salvador[2], Vicente Amigó[2] and Mary Vergara[1]
[1]*Universidad de Los Andes*
[2]*Universidad Politécnica de Valencia*
[1]*Venezuela*
[2]*España*

1. Introduction

Since Alfred Wilm discovered the aluminium alloys hardening precipitation phenomena at the begining of the last century (Polmear 1996), the use of aluminium alloys has increased, owing their advantages against corrosion and good strength weight ratio.
The Aluminium Zinc Magnesium ternary alloys are getting more relevance every day. These alloys are commonly called Al-Zn-Mg. In this family the most used are the AA7005 and AA 7020, which are nearly the same alloys. Although the most remarkable difference between them is the slightly better mechanical behaviour of the 7020 one after welding.
The ageing development of these alloys follows a simple precipitation phenomena summarized as:

$$\alpha_{ss} \rightarrow \alpha_1 + GP \rightarrow \alpha_2 + \eta' \rightarrow \alpha_{eq} + \eta$$

Some investigators propose a transitional step on the Guinier Preston (GPs) evolution that gives the response to the natural ageing as:

$$\alpha_{ss} \rightarrow \alpha_1 + GP_{round} \rightarrow \alpha_2 + GP_{ordered} \rightarrow \alpha_3 + \eta' \rightarrow \alpha_4 + \eta \rightarrow \alpha_4 + T$$

The calorimetric study of the natural ageing evolution shows that there is no difference on the heat exchange of η' and η. So, the GPs evolution is the responsible of strengthening of the alloy.
The mechanical properties of AA7020 are evaluated and the exponential evolution is advisable, due to natural ageing.
The fatigue behaviour of AA7020 natural aged shows a typical Aluminium Wohler pattern. From this curve a mathematical model is proposed.
Welded aluminium:
Riveted and welded aluminium structures are getting more relevance every day.
Heat treatable alloys as the 7XXX, 2XXX, and 6XXX are vulnerable to critical changes in the Heat Affected Zone (HAZ) due to the heat input during welding. For this reason an extensive study of the HAZ is done.
This chapter attempts to describe the changes happening during the welding process of AA7020.

A concise study of the HAZ by Differential Scanning Calorimetry (DSC) and Transmission Electron Microscopy (TEM) is presented. Likewise a fatigue study is done.
The fatigue pattern of the welded joints looks like parent metal with a significant decrease of its strength. From this data, a mathematical model for the fatigue behaviour of the welded joint is developed.

2. Ageing (Heat treatment)

Aluminium Zinc Magnesium ternary alloys are widely used in medium and large structures. Some of these structures are assembled as factory received with no importance on the alloy heat treatment condition.
The thermal state of the heat treatable aluminium alloys confers important changes to their performance so it is real of importance to take care of it.
Thermal state means how the second phases are precipitated into the aluminium matrix.
The elementary thermal states are usually designated by the letter T followed by a number as described below: (alubook, 2010)

T1: Cooled from an elevated temperature shaping process and naturally aged to a substantially stable condition.
T2: Cooled from an elevated temperature shaping process, cold worked and naturally aged to a substantially stable condition.
T3: Solution heat-treated, cold worked and then naturally aged to a substantially stable condition.
T4: Solution heat-treated and naturally aged to a substantially stable condition.
T5: Cooled from an elevated temperature shaping process and then artificially aged.
T6: Solution heat-treated and then artificially aged.
T7: Solution heat-treated and over aged stabilised.
T8: Solution heat-treated, cold worked and then artificially aged.
T9: Solution heat-treated, artificially aged and then cold worked.

Commercial plates come normally on the T5 or T6 state, but when it is necessary a solution treatment is done. Then, within a few days plates become as stronger as T6. This process is discussed in the next chapter. The microstructural evolution of the alloy is of course the main factor of the mechanical properties enhancement. Such aspect is one of the principal goals of this chapter.
Natural ageing, as artificial ageing is the precipitation of the second metastable phases. Certainly, natural ageing requires more time to evolve the precipitation phenomena. This delay is the response to the slower diffusion process due to the lower temperature.
The basic precipitation process is proposed by many authors as:

$$\alpha_{ss} \rightarrow \alpha_1 + GP \rightarrow \alpha_2 + \eta' \rightarrow \alpha_3 + \eta \rightarrow \alpha_{eq} + T$$

However, as discussed onwards, there is a transitional step on GP evolution as follows:

$$\alpha_{ss} \rightarrow \alpha_1 + GP_{round} \rightarrow \alpha_2 + GP_{ordered} \rightarrow \alpha_3 + \eta' \rightarrow \alpha_4 + \eta \rightarrow \alpha_{eq} + T$$

The importance of precipitates evolution is due they are the responsible of strength increase, but only the precipitates that are coherent with aluminium matrix, as seen on figure 1 b) because they block the dislocation movement. On the other hand the precipitates that are not coherent with the matrix are nearly like a void in the dislocation passage.

Figure 1 shows schematically how a solute stays a) dissolved in a solid solution, b) forming a second phase that is coherent with the matrix crystalline structure or c) a precipitate that is not coherent with the structure.

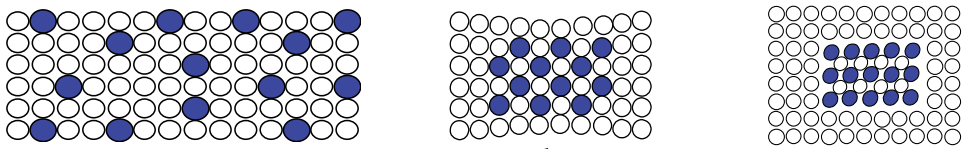

Fig. 1. Diagram of the different states of the solute into the matrix a) supersaturated solution b) precipitate coherent with the matrix c) precipitate incoherent.

It is essential to mention that a precipitate that is not coherent with the aluminium matrix is nearly the same as a filled void, likely as a hole. So the dislocations passes easily through the cavity.

Some second phases are semi-coherent meaning that is coherent in some latices and incoherent in others.

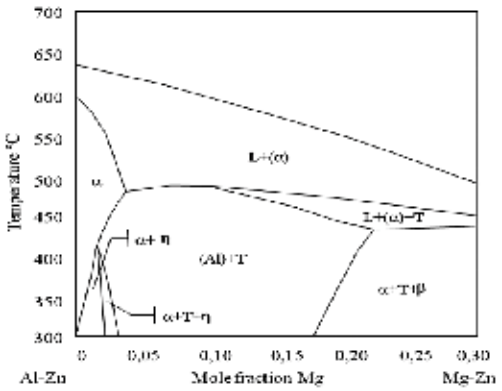

Fig. 2. Isopleth of the Al-5%Zn-Mg alloy

The ternary equilibrium diagram of an Al-Zn-Mg alloy was determined initially by Körser and improved by Mondolfo (Polmear 1996). Nowadays, articles about this diagram still continue explaining, the behaviours, precipitation sequences, temperatures and energies of formation and dissolution of second metastable phases and new heat treatments (Polmear 1996, Schiller et al., 2006, Soto et al., 2007)

Observing the isopleths of the alloy, figure 2 shows that there are two phases; the binary $MgZn_2$ generally called η and the most stable the ternary $Mg_3Zn_3Al_2$ called **T**. Obviously, there are more intermediate phases between them as mentioned in the precipitation sequence.

The second phases that appear due to its commonly alloying elements in the commercial Al-Zn-Mg alloys are written in table 1.

Because the precipitation process drives the alloy hardening, it is essential to know it

When the solute precipitates in a special manner, the second phases can rise the strength of the alloy more than three times than the quenched condition, the aim of the investigators is to develop heat and or thermo-mechanical treatments that increase the strength.

Element	Designation	Phase
Mg	**η, T**	$MgZn_2$, $(AlZn)_{49}Mg_{32}$, Al_3Mg_2,$Al_{12}Mg_{17}$
Si	β	Mg_2Si
Fe		$FeAl_3$,$(FeCr)_3SiAl_{12}$
Mn		$(FeMn)Al_6$
Cu	**α, S**	Solid Solution, Al_2CuMg
Cr		$(FeCr)_3SiAl_{12}$
Zr		Solution inside of $(FeMn)Al_6$

Table 1. Commonly second phases found in 7XXX series.

It is necessary start from a supersaturated solid solution to reach a satisfactory hardening after a heat treatment. Heat treatments precipitate the excess of solute in the solid solution as second phases, which generally are metastable. The precipitation goal is that the precipitates must be coherent with the aluminium solid solution.
Precipitation is analogue to solidification. It requires a nucleation and a growth process, on which the alloy goes to a lower thermodynamic state. This equilibrium can be accelerated or damped by mechanical or thermal barriers.
Notwithstanding the ageing treatment, there are many thermo-mechanical treatments, which improve the strengths achieved with only ageing.

3. Natural ageing

3.1 Precipitation evolution

The precipitation evolution of the alloy gives it better mechanical properties. At low temperature (room temperature) 18 ~ 22° C, natural ageing evolves slowly. So, in few weeks natural ageing reaches strength values as its artificial counterpart. This difference in time is due to the lower diffusion rate.
Table 2 shows the evolution in the first stages of the common mechanical properties, where an increase of strength is advisable, while ductility remains nearly the same.

Ageing time (h)	$\sigma_{0,2\%}$ (MPa)	σ_{Max} (MPa)	Elongation (%)
Inmediate	141.2	256.3	19.47
1 day	192.5	320.4	18.31
4 days	214.6	349.8	18.99
8 days	224.2	365.8	18.25
11 days	226.8	374.2	18.29
21 days	240.9	386.8	17.84
48 days	241.1	395.9	25.38
90 days	249.8	408.9	18.93
18 months	266.7	421.2	16.94

Table 2. Static mechanical properties evolution of AA7020 due to natural ageing.

As shown on table 2, the mechanical properties evolution is important within the first fifteen days. Then, up to 40 ~ 45 days, the increase in strength is quite significant. After this time,

the ageing process slows down. Nevertheless, the elongation remains nearly the same through the whole ageing time.

To evaluate the ageing evolution, a differential scanning calorimetry test is done. Samples are compared to pure 99,998% aluminium. The heating rate is performed a controlled Ar atmosphere at 20°C per minute. As seen in figure 3, the peaks and valleys represent exothermic and endothermic processes, respectively.

The valleys (endothermic curves) from 60 to 190 ~ 200°C reveal a dissolution of the more immature GPs precipitate. The exothermic peaks between 200 to 300°C are the η' and η precipitations, and the peaks from 300 to 360°C are mixture of sub peaks due to the dissolution of all metastable phases as suggested by (Donoso E. 1985).

To minimize any thermal or inertial distortion on the zone of interest, the thermal analyses are done from -20 to 520°C.

Figure 3 shows the thermal evolution of the second phases between 60° to 410°C.

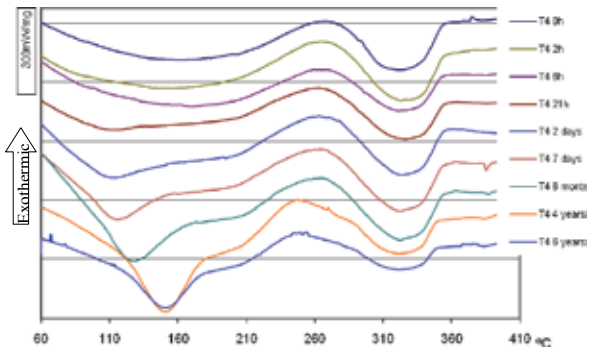

Fig. 3. Thermal evolution of natural ageing precipitation of an AA 7020 alloy.

In the first stages of the precipitation, up to four hours, the precipitate dissolution shows a definitely slow response. In the curve corresponding to 6 hours, there is a slight endothermic peak that can be noticed finishing around 93°C. It is the clear response to small clusters or GP_{Round} dissolutions. On the other hand, observing the 21-hour curve, there are two followed endothermic peaks ending at 90 and 125°C, respectively. Those peaks clearly denote that there are two different dissolution processes and two different precipitates, corroborating the existence of two GPs phases.

From this ageing time and forward, the dissolution peaks show a more stable process due to the increase on the beginning and ending temperatures.

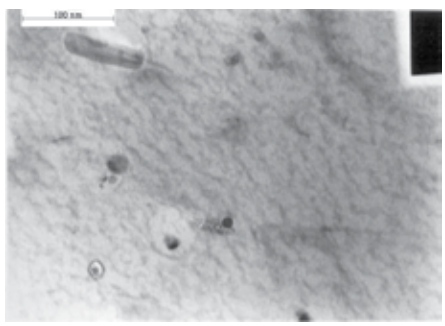

Fig. 4. Rounded GPs on a matrix of aluminium T4 at 25 hours of natural ageing 100,000 X

Figure 4 shows how the GPs evolve after 25 hours of natural ageing. Note the GPs are smaller than 11 nm.
Another point of interest is that through the whole 6 years of ageing process the endothermic and exothermic peaks from 200 to 410°C remain steady. Analyzing the energies in the thermograms, it can be concluded that there are no changes through the ageing process. It obviously construe that in natural ageing the GPs is the only responsible of the alloy hardening increase, because there is no change in the evolution of the zones corresponding to η′ and η.

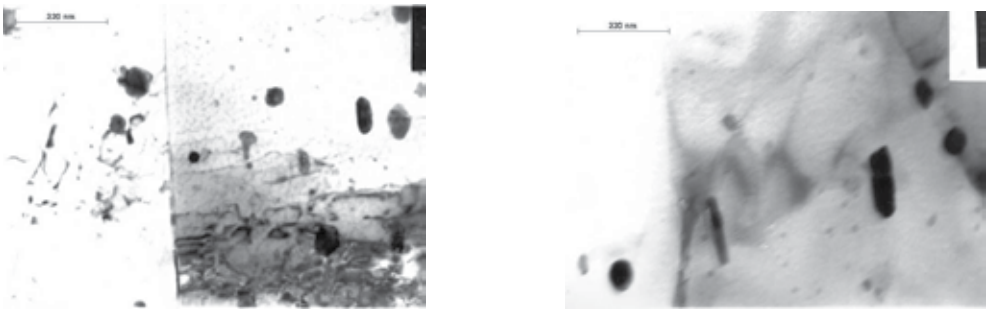

a) b)

Fig. 5. Precipitation evolution after 90 a) 180 b) days of natural ageing 46,400X

Figure 5 shows how the precipitation evolves. In part *a* of the figure, "coarse" precipitates outshine over the tiny GPs, and in part *b,* Some GPs become bigger than the ones at 90 days. There is relevant to mention that there are no noticeable precipitation free zones (PFZ) surrounding the precipitates in the natural ageing.

3.2 Artificial ageing

Artificial ageing is the most common commercial procedure. The precipitation process is governed by a temperature controlled diffusion process, where the higher the temperature, the faster the atoms move. Special care must be taken on the temperature selection; otherwise, a "burnt" of the alloy can happened.
(Robinson & Tanner et al., 2006, Jiang et al., 2008) and others have found great importance on the quenching rate of Al-Zn-Mg alloys. However, in the case of the AA7020 alloy, the results plotted in figures 6 *a* and *b* show no relevance on the mechanical properties. The largest difference in hardening is less than 2.5%. This can be attributed to the low Cu content of the alloy.

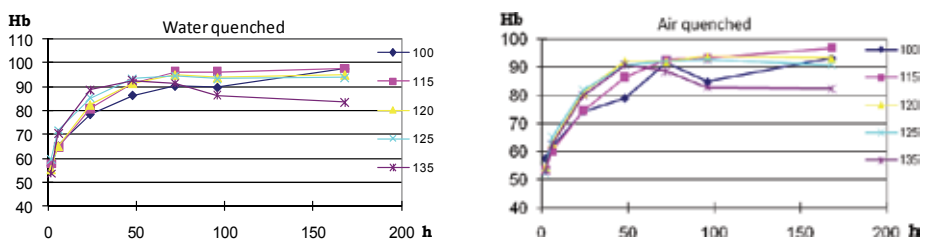

a) b)

Fig. 6. a, b shows how quenching rate and temperature influences on time and hardness.

Temperature plays an important role on hardening evolution. However, in the first 48 hours (industrial interest) and the range from 120 to 135°C, the highest values of hardening are achieved with both quenching rates. For temperatures above 125°C, the heat treatments cause alloy overageing after 48 hours.
AA 7020 alloys are nearly insensitive to the quenching rate. Nevertheless, it has been found that water quenching make the aloy more unalterable to overageing.

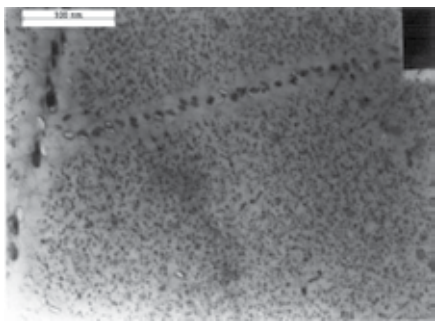

Fig. 7. Aspect of the microstructure after artificial ageing of the AA7020. 100,000X

To ensure no overageing and to reach the more stable thermodynamic condition after the artificial heat treatment, it is required a solubilisation heat treatment, then quench, preferably in water, and finally ageing at 122°C for 48 hours.
The microstructure in the artificial ageing differs of that in the natural ageing. Figure 7 shows a profuse precipitation when the alloy is artificially aged; however, a slightly precipitation free zone also appears in the subgrain boundaries where aligned beads precipitate.

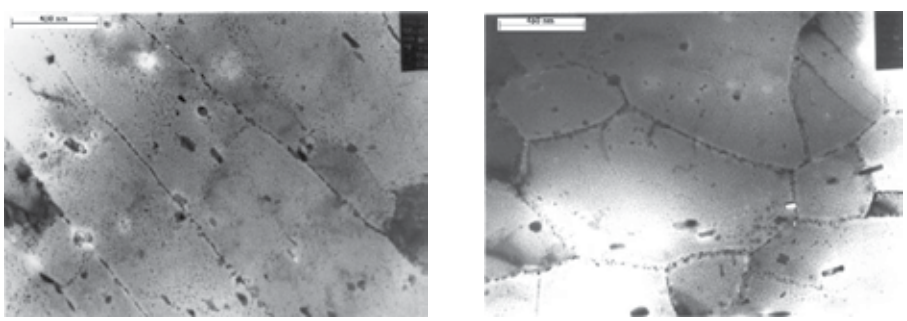

a) b)

Fig. 8. Differences between the microstructures of AA7020 alloys in T6 a) as delivered and b) after a solution heat treatment TEM 21,500X

In figure 8, a comparison of two micrographs from the alloy in T6; one as-received and the other after a solution heat treatment. Figures 8 a) and b) show the typical texture after lamination, and the equiaxed microstructure after grains recrystallization due to the solution heat treatment, respectively. Certainly, some anisotropy still remains in the as-received material due to the outstretched grains.
Although the precipitation levels for both states are nearly the same, the precipitation of the η′ follows the lamination direction in the case of the as-received alloy and a heterogeneous direction in the solubilised one.

4. Fatigue behaviour

Unlike steel, aluminium has no fatigue limit. The fatigue (Wöhler) curve for aluminium follows an exponential pattern, as observed in figure 4.
The fatigue tests are conducted at various stress levels up to fracture in a four-point bending machine. These results are validated with the data obtained from (Gatto F. and Morri E. 1979)
These tests are performed using different plates and time of ageing. The fatigue tests are conducted at room temperature in a not fully reversed loading cycle R=-0.1 and frequencies between 3 to 5 Hz.

4.1 Natural ageing fatigue behaviour

Figure 9 shows different fatigue curves for various time of ageing. It is notorious that the ageing time plays an important role in the mechanical properties of the alloy. From the plot, it is advisable that as time of ageing increase, the fatigue resistance decreases considerably at high cycle levels.
The Wöhler curves have a vital importance in mechanical design when fatigue behaviour must be taken into account for engineers.
Curves represented in figure 9 are plotted from the mathematical model discussed in the next paragraph.
The natural ageing evolution of AA7020 shows a contradictory behaviour. The fatigue limit decreases as ageing time evolves, becoming nearly steady after 3 months. This phenomenon is corroborated by the precipitation evolution, as observed in the DSC curves of figure 3. These calorimetric curves show that most of the solute precipitated into GPs; the only difference is the GPs stability reached over time.
The drawback of the fatigue strength decrease is associated to the lower degree of crack propagation resistance caused by the solute distribution and cluster precipitates acting as a brittle phase.
Plasticity is nearly the same in the whole range of ageing time. It is reasonable to suppose that clusters are able to obstruct dislocation movement, but they cannot support high stresses at crack tips. This phenomenon is associated to the residual stresses development when precipitation occurs due to, for example, misalignments, crystalline structure disparity and atomic size differences.

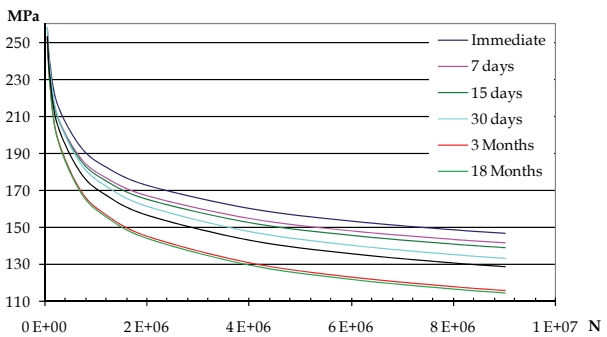

Fig. 9. Fatigue curves of AA7020 at different times of natural ageing.

4.2 Artificial ageing (T6) fatigue behaviour

The fatigue behaviour on high cycles of T6 state shows a slightly better performance than the T4 state with a 30-day or larger natural ageing. It can be attributed to a higher stability and size of the precipitates, which certainly can support better the stresses in front of the crack tip. The T6 fatigue behaviour in high cycles can be up to 10% better than the T4 state. Without any posterior heat input (i.e., welding or grinding), the T6 plates are better than the T4 ones for fatigue loading.

The modelled Wöhler curve and experimental data of the AA7020 T6 is plotted in figure 10.

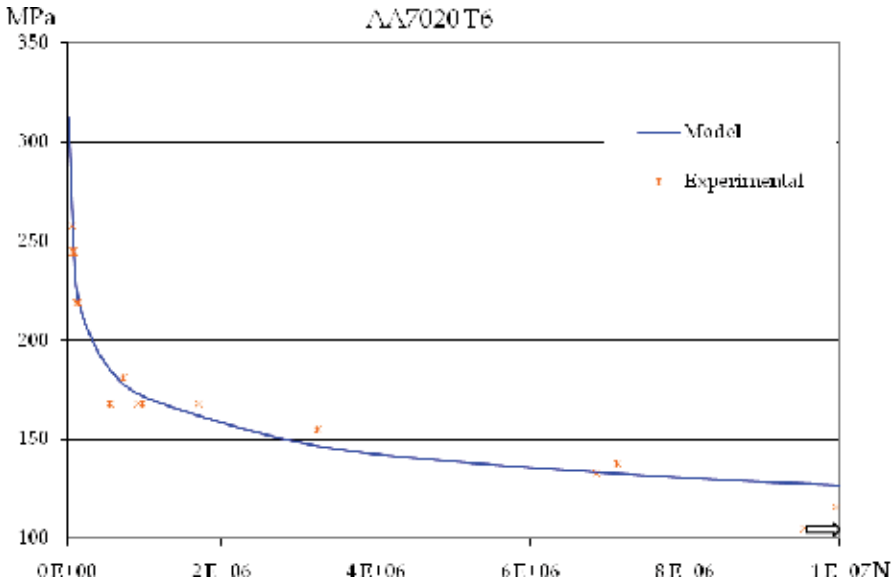

Fig. 10. Fatigue curve of the AA7020 T6

4.3 Mathematical model of fatigue behaviour

The fatigue behaviour of the AA7020 for different thermal states is collected, drawn, and analyzed. Using a least squares approach, a numerical model is found from the experimental data. The best data fit is an exponential equation, written as:

$$\sigma_{(N)} = \sigma_0 * e^{-k*\ln(N)} \quad (1)$$

Where:

- $\sigma_{(N)}$ means the stress at which the piece would fail in N number of cycles.
- σ_0 is a "theoretical" value at which the piece fails in zero cycles.
- k represents the damping parameter.
- N is the number of cycles

The correlation factor and deviation are satisfactory, as summarized in table 3. Some curves obtained from the model are drawn in figures 9 and 10.

The difference between the σ_0 and the real σ_{max} can be attributed to the multiple tiny plasticization processes occurring in front of the crack tip while opening and closing during each cycle.

The model, and correlation factors as well as the standard deviation are written in table 3.

Ageing	σ_0	K	ρ^2	Std dev
T6	1034.0	0.1300	0.9436	0.003400
T4 $_{immediate}$	839.3	0.1090	0.9335	0.000572
T4 $_{30\ days}$	1084.7	0.1318	0.9838	0.001243
T4 $_{180\ days}$	1275.3	0.1500	0.9705	0.001527
T4 $_{540\ days}$	1308.2	0.1519	0.9974	0.001766

Table 3 Model factors.

This model describes the alloy fatigue behaviour for the selection of ageing times used. However, a new correlation is found to approximate σ_0 as a function of the ageing time and the corresponding yield stress.
The new σ_0 model does not require a time evaluation.
The new model could be expressed as follows:

$$\sigma_{(N)} = \sigma_y * (4.389 + 0.0759 * Ln(t)) * e^{-k * ln(N)} \quad (2)$$

Where:

- $\sigma_{(N)}$ means the stress at which the piece would fail in N number of cycles.
- σ_y is the yield stress at that time (t) of ageing.
- t is the time of ageing.
- k represents the damping parameter (from table 3).

This model fits the data with a significant accuracy, being the worst ρ^2 equal to 0.9818.
This model can be used as a basis for design, but it does not substitute the real fatigue behaviour of the alloy.

5. Aluminium welding

Welding is the process where two pieces of metal are melted with the aid of electrical, Fuel or frictional power; in other words it means the joint of two pieces of metal through a real metal crystalline blend. To create a crystalline bond, for instance, in a frictional stir welding, it is required to reach the adequate temperature to allow atom migration.
In whatever welding process, a heat input is required; so, in the surrounding welded area there is a Heat Affected Zone (HAZ), even for non-heat-treatable alloys. In the HAZ, microstructure is affected by grain coarsening, second phase dissolving, grain boundary re-precipitating, retrogressioning, and texture killing.
The best welding process should melt the faces to be joined without heating. Although it is not possible, it is necessary a better understanding of both the alloy and HAZ.
Additionally, Al-Zn-Mg alloy weldings have another nuisance called the white zone. The white zone, which occurs only in Al-Zn-Mg alloys, is a narrow area adjacent to the welding pool in the parent metal, with a likely precipitation free zone.
In age hardenable alloys, there are some special considerations to enhance their post welded resistances: Some of the factors are the joint design, parent-metal metallurgical state, toe or bulge configuration, gas shield, power source, and filler metal.
The weldability of Al-Zn-Mg alloys has some interesting details. Alloys with Cu+Zn+Mg content higher than 9% are poorly welded, between 6 and 8% are fairly welded but sensitive to stress corrosion cracking, and lower than 6% are good welded. (Mondolfo 1976)

For the same welding conditions, pulsed gas metal arc welding represents a better choice than the direct current counterpart due to its higher penetration.
Pulsed arc permit a better control on metal deposition, heat transfer, and arc stability, allowing welding on thinner plates.
The pulse frequency and duration affect considerably the post welded microstructure (Potluri et al., 1996).
Gas metal arc welding (GMAW) allows welding many plate thicknesses; however, to avoid the lack of fusion in large thicknesses, it is recommended piece preheating from 50 to 100°C
The welding procedure, parameters, and conditions are the commonly used in industrial applications.
The welding procedure used by the authors is Pulsed arc GMAW with the following parameters: Argon/Helium 75/25, filler metal AA5356, 20.5 ~ 21.5 Volts, 135 ~ 144 Amp., and travel speeds 520~530 mm/min first pass and 380 ~ 390 mm/min second pass.

5.1 Findings and analysis of the welded joint

To study the dilution of the base metal into the welding pool, a quantitative analyses using Energy-Dispersive X-rays (EDX) in a Scanning electron microscope is carried out. An EDX microanalysis of the W-B.M is plotted in figure 12.

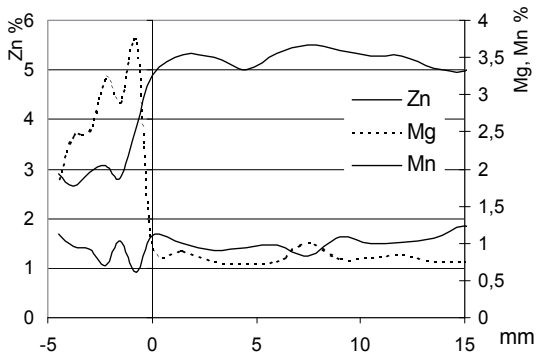

Fig. 12. EDX analysis of welded joint.

Figure 12 reveals that there is not volatilization of the alloys during the welding process, corroborating (Gomez de Salazar et al., 1998) work. Likewise, it can be seen from the same figure that there is a significant dilution of the base metal into the weld, reaching a zinc content of nearly half the one in the parent metal.
This zinc content generates a new alloy of the Al-Zn-Mg, which is corroborated by the appearance of the T precipitates $(Al,Zn)_{49}Mg_{32}$ found in the samples.
A microhardness profile of a welding joint through the HAZ is shown on figure 13
There is no evidence that the microhardness loss in the HAZ is due to a variation in the alloy contents as seen on figure 12. The microhardness defeat is attributed to a precipitation phenomenon.
The zones of possible failure, agree with the failure zones in axial and fatigue tested samples. In the microhardness profile of figure 13, five valleys appear displaying a decrease in hardness and revealing a HAZ of 24~26 mm from the fusion line. These five areas correspond to:

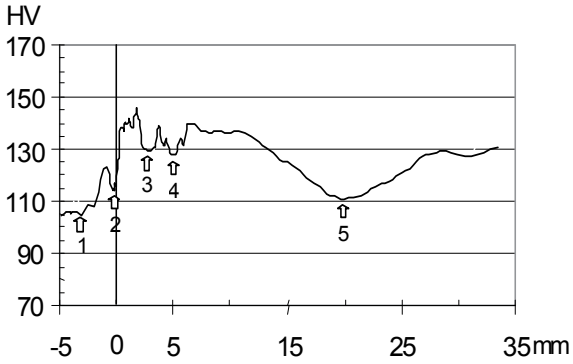

Fig. 13. Microhardness profile of welded joint and its possible failure zones.

1. The centre of the weld pool. This zone shows a decrease in hardness in the second pass welded pool of up to 40%. A much lower hardness decrease is advisable in the first pass welded pool. The hardness decrease is due to the lower alloying content of the filler metal. In the first pass, the lower hardness loss can be attributed to the thermal effects of the second pass heat input, which promotes the dissolution, diffusion and precipitation of second hardener phases, as reported by (Malin V. 1995). During the welding process, there is a dilution of the B.M into the weld. The dissolution generates a new Al-Zn-Mg-Mn alloy, as confirmed by the different analyses.
2. An adjacent zone to the interface weld pool base metal. The zone is around 0.2~1.0 mm from the interface and shows a hardness decrease of up to 34 %. This hardness decrease is the response of the internal stresses between the interface of the finer equiaxed and the large dendritic crystals. Moreover, the different cooling rates can also generate some internal stresses.
3. A zone close to the interface welded pool-base metal and in the parent metal side (HAZ). This area appears at 0.5~3 mm from the interface with a hardness reduction of up to 22 %. This area, attributed to the white zones, seems to grow further away as higher the heat input is.
4. A HAZ detected area, usually confused macroscopically with the previous discussed one. The identified zone is about 1.5 ~ 5 mm from the fusion border, but after the previous discussed one and, like the previous one, shows the same loss of hardness and also grows further away as higher the heat input is.
5. A detected zone of loss in hardness of up to 25% in the HAZ. The closest and the furthest areas can be 15 and 25 mm from the fusion line, respectively. This area is located where many authors consider a non HAZ.

It is common to find that there are three possible zones of fracture; the centre of the weld, the interface welded pool-base metal and the end surrounding of the HAZ, as reported by (Malin 1995). The non accurate zone identification can be understood due to the narrow zone where areas 2, 3 and 4 are in the weld.

To understand the mechanical behaviour, a calorimetric study of welded HAZ is performed up to 28 mm from the fusion zone, as seen on figure 14. Furthermore, a DSC running of the base metal is included to clarify the discussion.

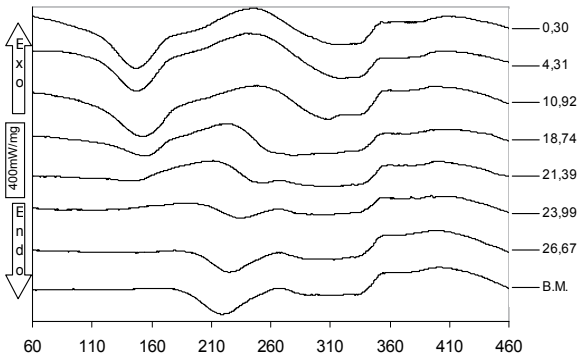

Fig. 14. DSC through a welded joint HAZ.

The calorimetric analyses reveal important details on how the precipitates evolve through the HAZ.

The analysis of the curves in figure 14 shows the presence of three peaks; one exothermic (formation) and two dissolution (endothermic) peaks. The lowest temperature (endothermic) valley corresponds to the dissolution of GPs. The first exothermic peak represents the precipitation of η', and the second valley corresponds to the dissolution of η. The GPs dissolution energy and temperature evolution are graphed in figure 15.

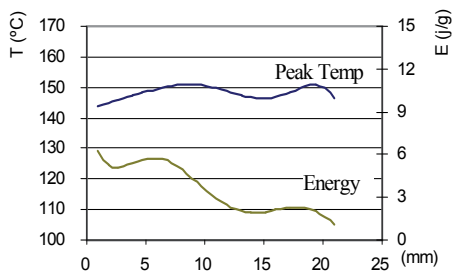

Fig. 15. Evolution of the dissolution energy and on set temperature of GPs

The evolution of the peak temperatures shows a smooth pattern, as seen in figure 14 and 15. These temperatures correspond to those referenced by researchers as (Donoso 1985, Ryum 1975).

DSC is a powerful technique for the assessment of the microestructural changes and evolution, as observed in figure 14. The evolution of the dissolution energy of the GPs shows how a total or partial dissolution of the precipitates occurs up to 12 mm. The BM has a low GP dissolution energy and does not show a formation peak, meaning that all of the alloying elements are precipitated. However, after welding, important peaks of GPs dissolution appear up to 12~15 mm.

It is important to highlight that beyond 29 mm a non HAZ is reached, as seen on figure 14. The calorimetric curves become similar to the BM curve in zones near the 30 mm from the fusion zone meaning that a non HAZ was reached.

The discussion about the dissolution and precipitation is held on the temperatures below 350°C, where the hardening precipitates GPs, η', and η evolves.

Observing the curves near the Weld-base metal interface, a GPs dissolution occurs. Considering that this zone is so close to the heat input, there is enough energy to dissolve all the precipitates during welding, and generate some precipitates during cooling.
(Ryum 1975) proposes that the precipitates at the beginning of the HAZ are just GPs and T. However, the thermogram reveals an important amount of η and η', and the micrography shows the presence of at least two precipitate morphologies, corroborating the calorimetric findings.
The zone at 3 mm reveals a slightly disposition to round the spheroids, and rod-like precipitates seem to be thicker than previous ones.
This can be explained as a function of the temperature and time reached during welding.
If temperature is high enough to dissolve all the precipitates, but not long enough to allow diffusion process of the alloying elements, the precipitation on those rich alloying zones should be promote.
This corroborates Ryum's (1975) findings and is in accordance with the slight decrease on GPs energy shown in the thermograms. These rich alloying zones precipitate faster because the initial stages of the precipitation process are controlled by an interface reaction of Mg and Zn. Before welding, the initial plate state plays an important role in the final properties, due to the state of the precipitates after and before welding. Depending on the thermal state, the most thermodynamically stable plates will turn into dissolved, but with solute rich zones. On the other hand, less stable ones will dissolve precipitates and spread the solute easily. The different behaviour between both states changes completely the strength evolution.
At the 17~19 mm zone, the thermoscan reveals that from 250 to 360°C appears a joined double peak of η'and η dissolutions, denoting the existence of both precipitates.
Microhardness begins to increase at this zone, which can be attributed to the existence of both precipitates with particle sizes of ~6 nm when the Orowan mechanism begins to operate (Donoso E. 1985). On the other hand, at the 24 mm zone, the finest precipitates appear smaller than they were in the zone discussed previously. This remarkable aspect can be attributed to a real agglomeration of the alloying elements into the η' metastable phase, corresponding to the increase of the dissolution energy observed in the diagram.
The η' dissolution temperature would be lower as far the zone is from the fusion line, meaning that more unstable is that precipitate, and lower are the amount of GPs. Therefore, it can be concluded that all the alloying elements are in η' form with a tendency to transform into η (Donoso E . 1985).
At the 29 mm zone, a non HAZ is detected by DSC or microhardness response, meaning that a non affected zone is finally reached. It implies that the HAZ goes further that commonly is thought.

5.2 Mechanical behaviour of aluminium welded

As discussed above, the strength performance of aluminium welds decrease substantially,
Nevertheless, there are some factors that diminish such strength loss. Leaving the toe as a reinforced zone, an increase of static strength occurs. Authors such as (Zivkovic & Anzulovic 2005) have investigated the importance of the welded surface finish. Unfortunately, many of these studies are done under laboratory conditions; i.e. untreated or mirror-like surfaces.
This section exposes the findings of welding behaviour with the commonly used industrial surface treatments after welding. A typical industrial surface treatment is seen in figure 16

a b

Fig. 16. Toe finish, a) toe emery eliminated, b) bulge emery smoothing.

The static mechanical properties are shown in table 4. From the table it is noted that mechanical properties of smoothed toe welds are nearly 25 % better than those of eliminated bulge welds; it is logic due to the larger cross sectional area.
The toe eliminated welds strength is lower than the bulge smoothed one. This strength difference is attributed to the microporosity of the weld pool, the worst mechanical properties of the filler metal, and the thinner cross-sectional area.
Tested samples are analyzed and microporosities are measured in the interface of parent metal-weld pools.
Microporosities are nearly spherical. It is probably because of the hydrogen separation while welding pools solidify. With a mean size of 30 ~ 50 μm, this porosity is not detected by XR non destructive tests. Although porosity affects fatigue performance, surface finishing becomes a vital parameter; notwithstanding, finishing is not a relevant factor in static strength.

Bulge condition	σ_y MPa	σ_{Max} MPa
Eliminated toe	248.3	273.6
Smothed bulge	268.6	349.8

Table 4. Static mechanical response of welded AA7020 as toe finish.

Testing under industrial conditions is becoming more relevant each day.
In order to reproduce the real industrial conditions, the samples are welded and then just grinding with an emery to remove the toe or to smooth the toe.
The fatigue behaviour of both eliminated and smoothed bulge is observed in figure 17,
The welded fatigue strength is lower than the parent metal one; although, both strengths have the same pattern and behaviour.
Figure 17 shows that the total and partial bulge removal do not affect significantly the fatigue behaviour. However, when compared to bulge removal, toe elimination gives a higher dispersion and slightly better behaviour (~3%) in the high cycle zone (>2*10^6 cycles).
It is in clear disagreeing with most of the bibliographic findings. Obviously, these dissimilarities are due to the differences in the surface roughness.
The toe dihedral angle gives an important stress concentration, which is reduced or eliminated when the toe weld is emery smoothed.
The second phases play an important role on the mechanical properties. During welding, such precipitates trial dissolution, precipitation, retrogression ageing, and overageing processes. It is advisable that the thermal state before welding plays also an important role.
Some studies are done to evaluate thermal state influence on the parent metal before welding. The thermal states selected are T6 and T4 with a 30-day natural ageing.
To evaluate the evolution of the HAZ, microhardness profiles are done and represented in figure 18.

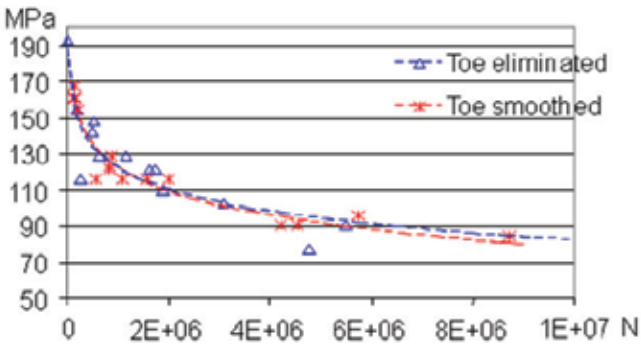

Fig. 17. Fatigue behaviour of AA7020 welding as a function of toe configuration.

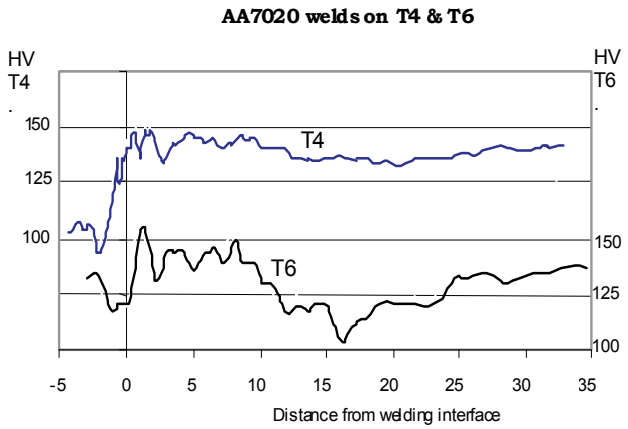

Fig. 18. Microhardness profiles on welded plates on previous T4 and T6 thermal state.

As seen in figure 18, there are some differences on the hardness behaviour. (Malin 1995, Den Ouden et al., 1999) quoted that welds of T6 plates show typical HAZ with three clearly defined areas; total dissolution and ageing, partial dissolution precipitation and overageing; for this reason, the T6 microhardness profile in figure 18 shows such kind of pattern, on the other hand, the T4 profile shows a more steady configuration because there is only dissolution and ageing through the HAZ.
The static strengths are shown in table 5

Thermal state	σ_0	σ_{Max}
T6	244,0	265,3
T4	253,3	308,9

Table 5. Static strengths of AA7020 aluminium welded in T4 and T6

As presented in table 5, there is a significant diminution of strength after welding. However, it is less notorious in welds of T4 plates, corroborateing microhardness findings.
The microscopic precipitation evolution through the HAZ of both welding states is shown in figures 18 to 21.

As seen in figure 18 a) and b), there are some noticeable differences. Coarse precipitates in welds of T6 plates seem to be bigger than those in the welds of T4 plates. Additionally, the T4 welds show profuse tiny precipitates over the whole matrix. This finding corroborates the microhardness profile, where the lost of microhardness through the HAZ is lower in T4 welds.

The micrographs in figure 19 show the differences between the welds of both T6 and T4 states. Through the matrix of T6 welds, there is a heterogeneity on precipitate sizes and a lack of tiny precipitates; while in the matrix of T4 welds, there is a more uniform size of the coarse precipitates and a extended small precipitates.

In the welds of T6 plates, microhardness in the 10~13 mm zone starts to decrease considerably. On other hand, in the welds of T4 plates, microhardness does not decrease considerably; it can be intuitively understood due to the influence of the precipitations seen in figure 19 b).

In the welded zone of T6 plates, dissolution, retrogression, and ageing processes are present (Den Ouden et al., 1999). In the T4 case, just a dissolution and precipitation processes occur because of an incipient precipitation state.

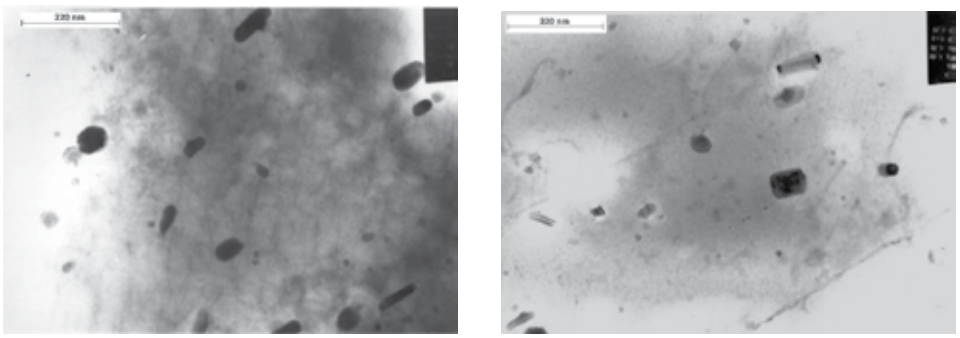

a b

Fig. 18. TEM micrograph of AA7020 welded 46400X a) T6 at 1.9 mm from the fusion zone b) T4 at 1.5 mm from the fusion zone.

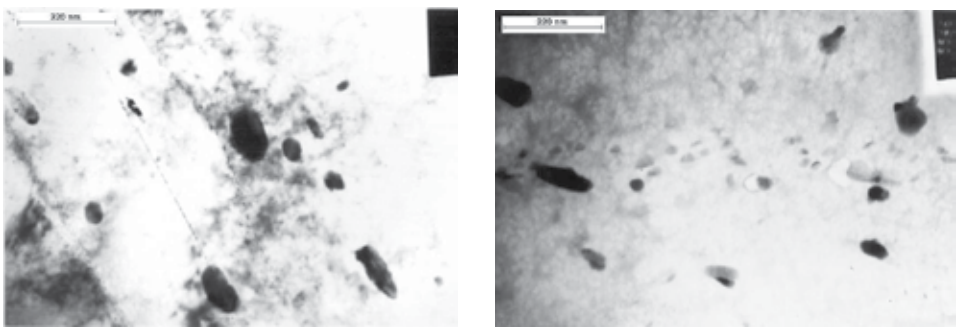

a) b)

Fig. 19. TEM micrograph of AA7020 welded 46400X a) T6 at 10.8 mm from the fusion zone b) T4 at 12.5 mm from the fusion zone.

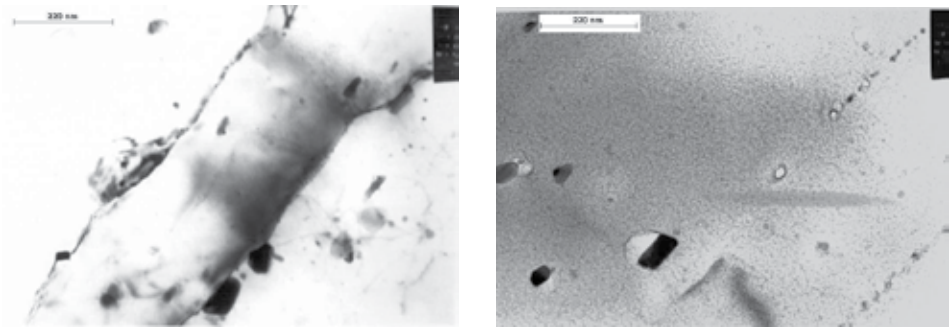

a) b)

Fig. 20. TEM micrograph of AA7020 welded 46400X a) T6 at 15.1 mm from the fusion zone b) T4 at 14.7 mm from the fusion zone.

Figure 20 shows, for the 15 mm zone of the T6 welds, large heterogeneities on precipitates are present. On the other hand, in the T4 welds, it is observed profuse tiny precipitates over the whole matrix. Another aspect to highlight is the appearance of subgrain structures and aligned bead precipitations along the subgrain borders, as seen in figures 20 a) and b).
Figures 20 b) and 21 b) demonstrate how vacancies (dislocations, in our case) play an important role in the precipitation processes and dislocations create subgrain crystalline defects. In the subgrain borders, precipitations are enhanced.

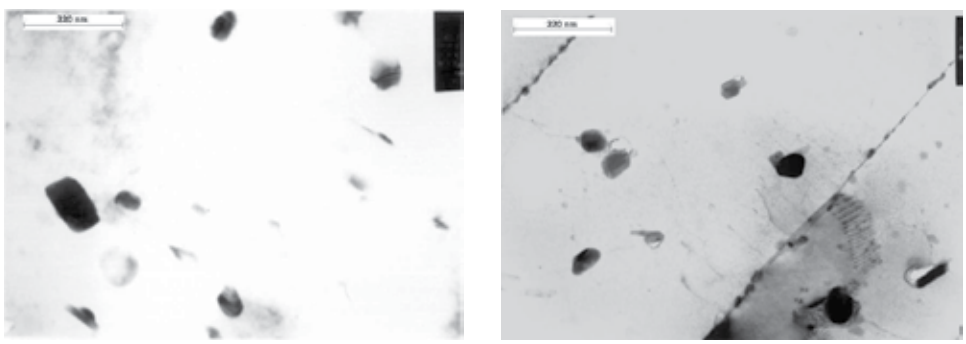

a) b)

Fig. 21. TEM micrograph of AA7020 welded 46400X a) T6 at 17.9 mm from the fusion zone b) T4 at 16.9 mm from the fusion zone.

Figure 21 a) and b) show the differences between both T6 and T4 microstructures, respectively
In the T6 weld shows coarser precipitates and a lack of tiny ones. In the case of T4 welds, it is shown evidences of fine precipitates through the matrix.
The fatigue behaviour in figure 22 shows a better performance on T4 welds; as expected because of its precipitate homogeneity.

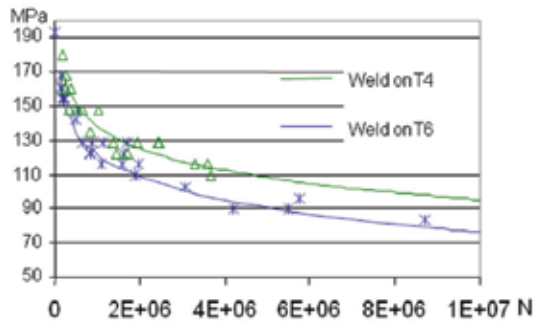

Fig. 22. Fatigue behaviour of AA7020 welding as a function of parent metal's thermal state.

5.3 AA7020 welded fatigue behaviour mathematical model

The following mathematical model for the fatigue behaviour of T4 and T6 welded plates is proposed.

$$\sigma_{(N)}=\sigma_y*(K_1+(3.005*K_2*K_3))*e^{-(k_3/a)*\ln(N)} \quad (3)$$

Where:
$\sigma_{(N)}$ is the fatigue strength for the number of cycles (N)
σ_y is the yield point.
K1 is the constant of thermal state of the parent metal.
K2 is the damping coefficient associated to the thermal state of parent metal.
K3 is the toe improvement factor.
a is the factor that involves the welding procedure in this case is 14.309

K1	Parent metal T6	- 3.0
	Parent metal T4	- 2.05
K2	Parent metal T6	1.0
	Parent metal T4	0.85
K3	Toe eliminated	1.636
	Toe smoothed	1.48

Table 6. Factor of the AA7020 welded fatigue model.

The general AA7020 welded fatigue model (3) with the factors in table 6 fits quite good the experimental data.

6. Conclusion

The further studies over the engineering materials, the better understanding of it. It allows us to understand its nature and exploit its potential usability.
There are enough evidences, as presented in figure 3, that there is a precipitate precursor before the GPs, with stability under the 95°C.
Due to the precipitation evolution evaluated up to 6 years of natural ageing, there is adequate data to conclude that the only responsible of strength increase due to ageing is the GPs instead of the normally thought η'.

Although the definition of T6 is solution heat treatment and then artificial aged, commercial plates on T6 still preserve part of their lamination texture. Therefore, special care must be taken when such plates are used in applications involving strength and fatigue.
The best balance between time and strength in artificial ageing for AA7020 alloys is the temperature of 122°C for 48 hours.
AA7020 alloys are low in cupper and do not exhibit real sensitive to quench severity in the T6 heat treatments. Nevertheless, water quenching delays overageing.
Three different models were proposed for mechanical response under fatigue loading conditions. These models fit quite well the experimental data and should be used just for preliminary designs.
The authors wish to thanks the microscopy service of the Universidad Politecnica de Valencia and Dr Jose A. Alvarado for his help reviewing this manuscript.

7. References

Alubook. (July 2010) http://www.alu-info.dk/html/alulib/modul/albook40.htm,

Den Ouden T. Ma (1999) Softening behaviour of Al-Zn-Mg alloys due to welding *Material science and engineering* A266, 1999, pp198-204

Donoso, E. (1985) Calorimetric study of the dissolution of Guinier-Preston Zones and n' Phase in Al-4,5at%Zn-1.75at%Mg. *Material Science and engineering*, vol 74, pp 39-46

Gatto, F., Morri, D.(1979) Fatigue behaviour of some welded joints of aluminium alloys. Ed Novara. Italy.

Gomez de Salazar, J.M, A. Ureña, E. Villauriz, S. Manzanedo E I. Barrena. (1998) Soldadura TIG y MIG de las aleaciones de aluminio 6061 y 7020. Estudios microestructurales y de propiedades mecanicas. *Revista Metalurgia*. vol, 34 pp 276, 280

Jiang-hai, Y.;, Sheng-dan, L.; Xin-ming, Z. and Xiao-yan, Z. (2008) Effect of Two-Step Ageing on Microstructure and Properties of 7150 Aluminium Alloy *Chinese Journal of Rare Metals* Volume 15, Number 2, 153-158

Malin V. (1995) Study of the metallurgical phenomena in the HAZ of 6061-T6 Aluminium welded joints *Welding research supplement* pp 305-318

Mondolfo, L.F.(1976) *Aluminium Alloys: Structure and Properties*. Ed. Butterworths, London-Boston.

Polmear, I. J. (1996) Recent developments in light alloys Overview *Materials Transactions JIM*, Vol 37, Nº 1, pp12, 31

Potluri N. Gosh P.Gupta P., and Srikanth R. Y. (1996) Studies on weld metal *Welding journal* Vol 74 1996 pp 64

Robinson, J. S.; Tanner, D. A. (2006) The Influence of Aluminium Alloy Quench Sensitivity on the Magnitude of Heat Treatment Induced Residual Stress Journal Materials Science Forum (Volumes 524 - 525) Residual Stresses VII pp. 305-310

Ryum, N. (1975) Precipitation kinetics in an Al-Zn-Mg alloy". *Zeitschrift fur Metalkunde*. Vol 64. Pp 338 343

Schiller, I.; Gubicza, J.; Kovács, Zs.; Chinh, N. Q.; and Illy, J. (2006) Precipitation and mechanical roperties of supersaturated Al-Zn-Mg alloys processed by severe plastic deformation *Materials Science Forum* Vols. 519-21 pp. 835-840

Soto, J. L.; Campillo, B.; Juarez-Islas, J.A. (2007) Prediction of Microstructure and distribution of Solute in Al-Zn-Mg Non-Dilute Alloys *Materials Science Forum* (Volume 560) Advanced Structural Materials III PP 73-78

Zivkovic, D. & Anzulovic, B. (2005) The fatigue of 5083 aluminium alloy welds with the shot-peened crater hot-cracks *Materials and. Design*. 26 n°3 pp 247-250.

7

Fatigue Behaviour of Welded Joints Made of 6061-T651 Aluminium Alloy

Alfredo S. Ribeiro and Abílio M.P. de Jesus
UCVE, IDMEC-Pólo FEUP
School of Sciences and Technology, University of Trás-os-Montes and Alto Douro
Portugal

1. Introduction

The purpose of this chapter is to present the main results of an investigation concerning the assessment of the fatigue behaviour of welded joints made of the 6061-T651 aluminium alloy. The 6061 aluminium alloy is one of the most common aluminium alloys for heavy-duty structures requiring good corrosion resistance, truck and marine components, railroad cars, furniture, tank fittings, general structures, high pressure applications, wire products and pipelines. Many of these applications involves variable loading, which makes very relevant the study of the fatigue behaviour of this aluminium allow. In particular, the study of the fatigue behaviour of welded joints is of primordial importance since welds are intensively used for structural applications. The proposed investigation focuses in four types of welded joints, made from 12 mm thick aluminium plates, namely one butt welded joint and three types of fillet joints: T-fillet joint without load transfer, a load-carrying fillet cruciform joint and a longitudinal stiffener fillet joint.

Traditionally, the fatigue assessment of welded joints, including those made of aluminium alloys, is based on the so-called S-N approach (Maddox, 1991). This approach, which is included in main structural design codes of practice, adopts a classification system for details, and proposes for each fatigue class an experimental-based S-N curve, which relates the applied stress range (e.g. nominal, structural, geometric) with the total fatigue life. Alternatively to this S-N approach, the Fracture Mechanics has been proposed to assess the fatigue life of the welded joints. It is very often claimed that welded joints have inherent crack-like defects introduced by the welding process itself. Therefore, the fatigue life of the welded joints may be regarded as a propagation process of those defects. A relation between the Fracture Mechanics and the S-N approaches is usually assumed. The slope of the S-N curves is generally understood to be equal to the exponent of the power relation governing the fatigue crack propagation rates of fatigue cracks.

More recently, the local approaches to fatigue have gaining added interest in the analysis of welded joints (Radaj et al., 2009). In general, such approaches are based on a local damage definition (e.g. notch stresses or strains) which makes these approaches more adequate to model local damage such as the fatigue crack initiation. In this sense, the Fracture Mechanics can be used to complement the local approaches, since the first allows the computation of the number of cycles to propagate an initial crack until final failure of the component.

The present research seeks to understand the significance of the fatigue crack initiation, evaluated using a local strain-life approach, on the total fatigue life estimation for four types

of welded joints made of 6061-T651 aluminium alloy. The Fracture Mechanics is also applied to assess the fatigue crack propagation, in order to allow a comparison with the crack initiation predictions and also with the global S-N data, made available for the welded joints by means of constant amplitude fatigue tests.
In the section 2 of the chapter, the 6061-T651 aluminium alloy is described. Then, on section 3 the basic fatigue properties of the material are presented. The strain-life fatigue data as well as the fatigue crack propagation data of the 6061-T651 aluminium alloy (base material) are presented. Also, the fatigue crack propagation data is presented for the welded and heat affected materials. On section 4, the fatigue S-N data obtained for the welded details is presented. Section 5 is devoted to the fatigue modelling of the welded details. Finally, on section 6, the conclusions of the research are presented.

2. The 6061-T651 aluminium alloy

This research was conducted on an AlMgSi aluminium alloy: the 6061-T651 aluminium alloy. The 6061-T651 alloy is a precipitation hardening aluminium alloy, containing Magnesium and Silicon as its major alloying elements. The T651 treatment corresponds to stress-relieved stretch and artificially aging. The typical chemical composition of the 6061-T651 aluminium alloy is shown in Table 1. The high Magnesium content is responsible for the high corrosion resistance and good weldability. The proportions of Magnesium and Silicon available are favourable to the formation of Magnesium Silicide (Mg_2Si). The material used in this research was delivered in the form of 12 mm and 24 mm thick plates. This alloy is perhaps one of the most versatile of heat treatable aluminium alloys. It has good mechanical properties. It is one of the most common aluminium alloys for general purpose applications. It was developed for applications involving moderate strength, good

Si	**Fe**	**Cu**	**Mn**	**Mg**	**Cr**
0.69	0.29	0.297	0.113	0.94	0.248
Zn	**Ti**	**B**	**Zr**	**Pb**	**Ti+Zr**
0.15	0.019	0.0021	0.001	0.02	0.02

Table 1. Chemical composition of the 6061-T651 aluminium alloy (weight %)

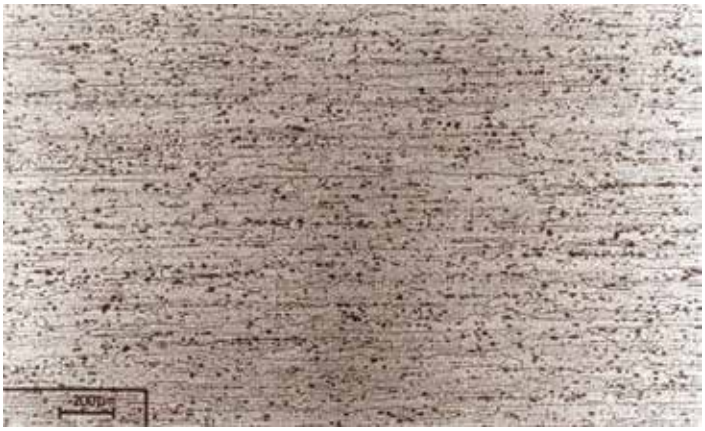

Fig. 1. Microstructure of the 6061-T651 aluminium alloy according the rolling direction

formability and weldability. Because of such desirable properties, this alloy is used in civilian and militaries industries. Figure 1 illustrates a typical microstructure of the aluminium alloy evaluated along the rolling or longitudinal direction. It is visible the stretched grains due to the rolling process. Also, a dispersed second phase typical of deformed and heat treated wrought aluminium alloys is observed.

3. Fatigue behaviour of the 6061-T651 aluminium alloy

3.1 Strain-life fatigue relations

Strain-life fatigue results, derived using smooth specimens, are usually applied to model the macroscopic fatigue crack initiation. An initiation criteria based on a 0.25 mm depth crack is commonly used by some authors (De Jesus, 2004). One important strain-life relation was proposed by Coffin (1954) and Manson (1954), which relates the plastic strain amplitude, $\Delta\varepsilon_p/2$, with the number of reversals to crack initiation, $2N_f$:

$$\frac{\Delta\varepsilon_p}{2} = \varepsilon'_f (2N_f)^c \tag{1}$$

where ε'_f and c are, respectively, the fatigue ductility coefficient and fatigue ductility exponent. The Coffin-Manson relation, which is valid for low-cycle fatigue, can be extended to high-cycle fatigue domains using the relation proposed by Basquin (1910). The latter relates the elastic strain amplitude, $\Delta\varepsilon_e/2$, with the number of reversals to failure, $2N_f$:

$$\frac{\Delta\varepsilon_e}{2} = \frac{\sigma'_f}{E}(2N_f)^b \tag{2}$$

where σ'_f is the fatigue strength coefficient, b is the fatigue strength exponent and E is the Young's modulus. The number of reversals corresponding to the transition between low- and high-cycle fatigue regimes is characterised by total strain amplitude composed by equal components of elastic and plastic strain amplitudes. Lives below this transition value are dictated by ductility properties; lives above this transition value are dictated by strength properties. Morrow (1965) suggested the superposition of Equations (1) and (2), resulting in a more general equation, valid for low- and high-cycle fatigue regimes:

$$\frac{\Delta\varepsilon}{2} = \frac{\Delta\varepsilon_e}{2} + \frac{\Delta\varepsilon_p}{2} = \frac{\sigma'_f}{E}(2N_f)^b + \varepsilon'_f (2N_f)^c \tag{3}$$

Equation (3) may be changed to account for mean stress effects, resulting:

$$\frac{\Delta\varepsilon}{2} = \frac{\sigma'_f - \sigma_m}{E}(2N_f)^b + \varepsilon'_f (2N_f)^c \tag{4}$$

where σ_m stands for the mean stress. The application of Equations (3) and (4) requires the knowledge of the stabilized strain amplitude, $\Delta\varepsilon/2$, at the point of interest of the structure. The computation of the strain amplitude requires the prior knowledge of the cyclic curve of the material, which relates the stabilized strain and stress amplitudes. The cyclic curve is usually represented using the Ramberg-Osgood relation (Ramberg & Osgood, 1943):

$$\frac{\Delta\varepsilon}{2}=\frac{\Delta\sigma}{2E}+\left(\frac{\Delta\sigma}{2k'}\right)^{1/n'} \tag{5}$$

where k' is the cyclic hardening coefficient and n' is the cyclic hardening exponent. Equation (5) may also be used to describe the hysteresis loops branches if the material shows Masing behaviour. In these cases, the hysteresis loops results from the magnification of the cyclic stress-strain curve by a scale factor of two.

3.2 Experimental strain-life data

Eight smooth specimens were tested under strain controlled conditions in order to identify the strain-life and cyclic elastoplastic behaviour of the 6061-T651 aluminium alloy. The geometry and dimensions of the specimens are represented in Figure 2 and are in agreement with the recommendations of ASTM E606 (ASTM, 1998). After machining, the specimen surfaces were mechanically polished. The experiments were carried out in a close-loop servohydraulic test machine, with 100 kN load capacity. A sinusoidal waveform was used as command signal. The fatigue tests were conducted with constant strain amplitudes, at room temperature, in air. The longitudinal strain was measured using a longitudinal extensometer with a base length equal to 12.5 mm and limit displacements of ±2.5 mm. The specimens were cyclic loaded under strain control with symmetrical push-pull loading, with a nominal strain ratio, $R_\varepsilon=-1$. The nominal strain rate $d\varepsilon/dt$ was kept constant in all specimens at the value $8\times10^{-3}s^{-1}$ in order to avoid any influence of the strain rate on the hysteresis loop shape. The cyclic stress-strain curves were determined using the method of one specimen for each imposed strain level. The stable hysteresis loop was defined as the hysteresis loop for 50% of the fatigue life. The specimens were tested with imposed strain ranges between 0.9% and 3.5%. The monotonic stress-strain curves were also experimentally determined for comparison purposes.

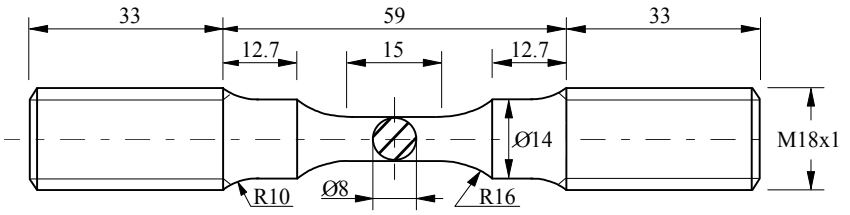

Fig. 2. Geometry and dimensions of the specimens used in the strain-controlled fatigue tests (dimensions in mm)

The monotonic strength and elastic properties of the 6061-T651 aluminium alloy are presented in Table 2. Table 2 also includes the properties obtained by Moreira et al. (2008), for the 6061-T6 aluminium alloy, and by Borrego et al. (2004), for the 6082-T6 aluminium alloy, for comparison purposes. In general, the three materials show comparable properties. However, a detailed comparison reveals that the 6082-T6 alloy presents better monotonic strength with slightly lower ductility than the 6061-T651 aluminium alloy. This may be due to the fact that the 6082 aluminium alloy exhibits higher Silicon (1.05) and Manganese contents (0.68) than the 6061 aluminium alloy (Ribeiro et al., 2009). The 6061-T6 aluminium alloy shows slightly higher strength properties and very similar ductility properties than the

6061-T651 aluminium alloy. The T6 treatment does not include any stress relieve by stretch as performed by the T651 treatment.

Properties	6061-T651	6061-T6	6082-T6
Tensile strength, σ_{UTS} (MPa)	290-317	310-342	330
Yield strength, $\sigma_{0.2\%}$ (MPa)	242-279	276-306.3	307
Elongation, ε_r (%)	10.0-15.8	12.0-17.1	9
Young modulus, E (GPa)	68.0	68.5-68.9	70

Table 2. Monotonic strength and elastic properties of the 6061-T651, 6061-T6 and 6082-T6 aluminium alloys

Figure 3 shows the cyclic behaviour of the 6061-T651 aluminium alloy, namely the stabilized stress amplitude is plotted against the corresponding strain amplitude. The 6061-T651 aluminium alloy, despite not presenting a significant cyclic hardening, it shows some hardening for strain amplitudes above 1%. Cyclic softening is verified for strain amplitudes bellow 1.0%. Figure 4 compares the cyclic and monotonic curves of the material, which further validates the previous observations. Figure 5 plots the stabilized stress amplitude against the plastic strain amplitude. It is verified that both parameters follows a power relation as described by the non-linear term of the Ramberg-Osgood relation (Equation (5)). Figure 6 presents the total strain amplitude versus life curve obtained from the superposition of the elastic and plastic strain amplitude versus life curves. The number of reversals of transition, $2N_T$, verified for 6061-T651 aluminium alloy was 969 reversals. The

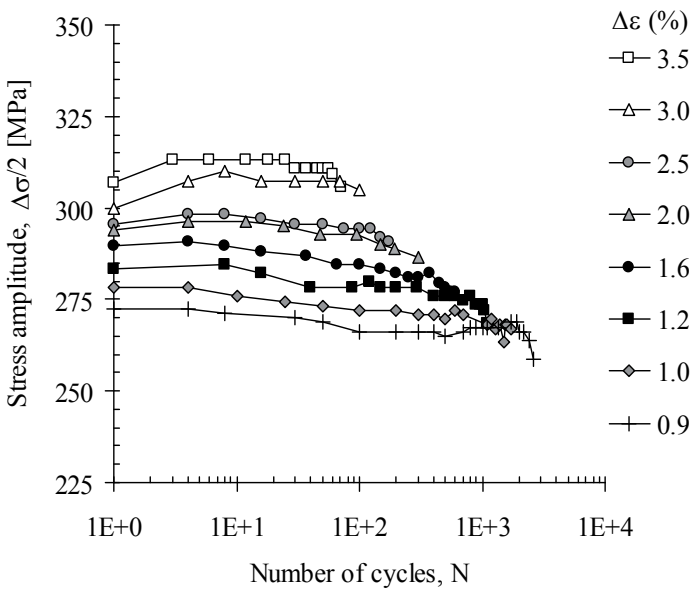

Fig. 3. Stress amplitude versus number of cycles from fully-reversed strain-controlled tests obtained for the 6061-T651 aluminium alloy

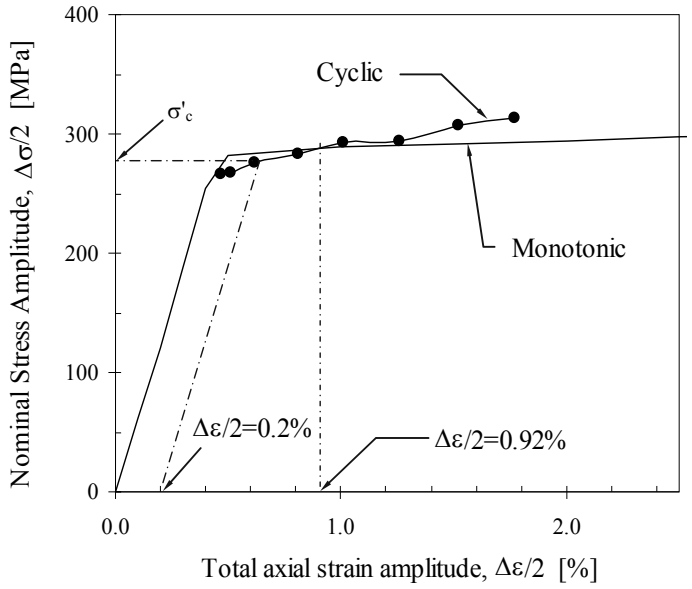

Fig. 4. Comparison of monotonic and cyclic stress-strain curves of the 6061-T651 aluminium alloy

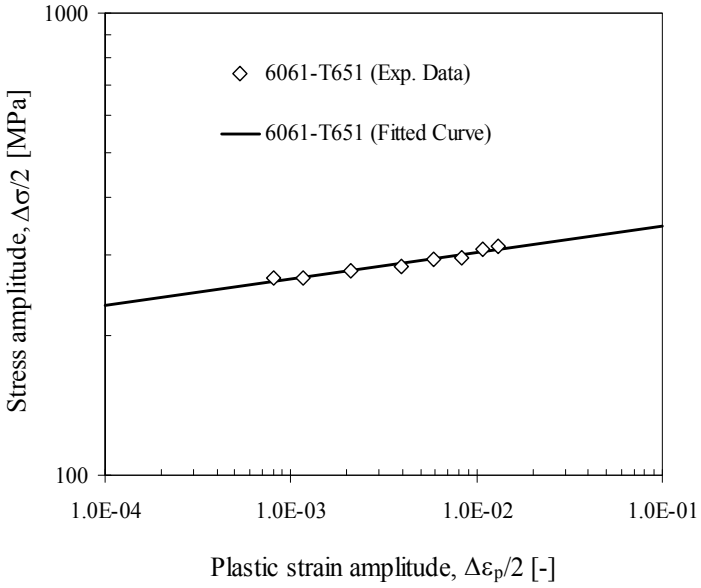

Fig. 5. Cyclic curve of the 6061-T651 aluminium alloy

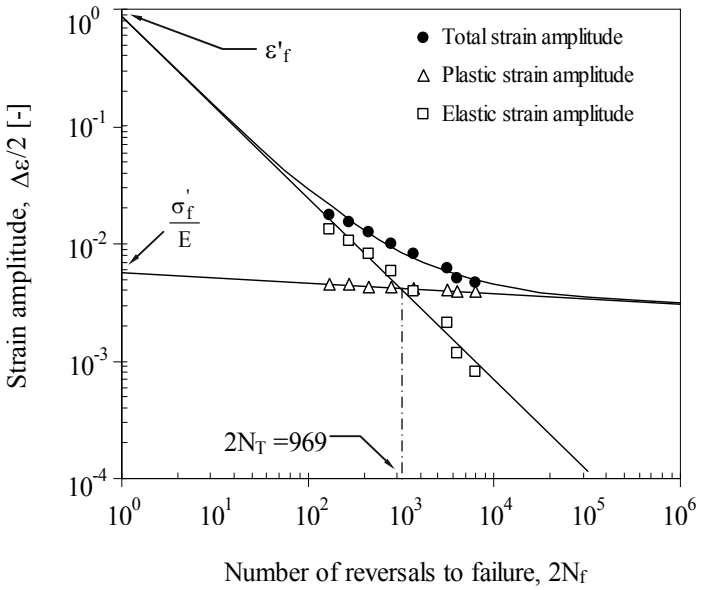

Fig. 6. Strain-life data of the 6061-T651 aluminium alloy

Properties	6061-T651	6061-T6	6082-T6
Fatigue strength coefficient, σ'_f [MPa]	394	383	487
Fatigue strength exponent, b	-0.045	-0.053	-0.07
Fatigue ductility coefficient, ε'_f (-)	0.634	0.207	0.209
Fatigue ductility exponent, c	-0.723	-0.628	-0.593
Cyclic strain hardening coef., k' [MPa]	404	-	444
Cyclic strain hardening exponent, n'	0.062	0.089	0.064

Table 3. Strain-life and cyclic properties of the 6061-T651, 6061-T6 and 6082-T6 aluminium alloys

fatigue ductility and strength properties of the alloy were derived from results shown in Figure 6. Table 3 summarizes the fatigue properties of the 6061-T651 aluminium alloy as well as the cyclic elastoplastic constants. Also, the properties obtained by Borrego et al. (2004), for the 6062-T6 aluminium alloy, and Chung & Abel (1988), for the 6061-T6 aluminium alloy, are included for comparison purposes. The 6061-T651 aluminium alloy shows significantly higher fatigue ductility than the other aluminium alloys.

3.3 Fatigue crack propagation relations

The evaluation of the fatigue crack propagation rates has been a subject of intense research. The Linear Elastic Fracture Mechanics (LEFM) has been the most appropriate methodology to describe the propagation of fatigue cracks. The LEFM is based on the hypothesis that the

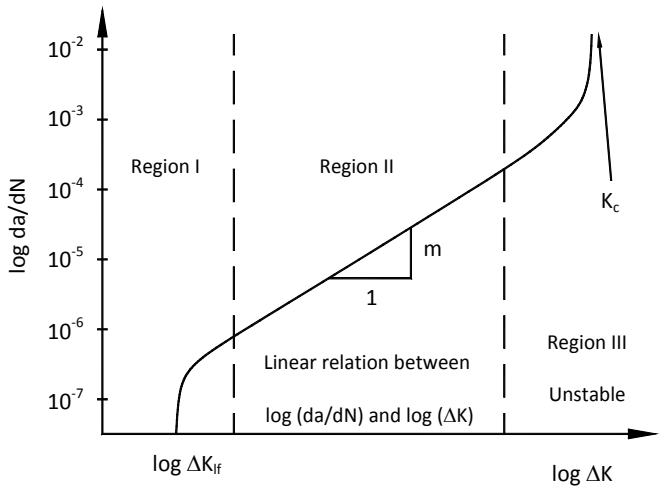

Fig. 7. Schematic representation of the relation between da / dN and ΔK

stress intensity factor is the mechanical parameter that controls the stress range at the crack tip. The typical fatigue crack propagation data is presented in the form of fatigue crack propagation rates versus stress intensity factor range diagrams. A typical diagram is illustrated in Figure 7. The da / dN versus ΔK curves are usually derived, for the majority of high strength materials, for crack propagation rates ranging between 10^{-7} and 10^{-2} mm/cycle. The diagram illustrates three different propagation regions, usually designated by regions I, II and III. In the region I, the propagation rate depends essentially on the stress intensity factor. In this region there exists a ΔK value below which no propagation is verified, or if propagation exists the propagation rate is below 10^{-7} mm/cycle. This value of the stress intensity factor range is denominated propagation threshold and it is represented by ΔK_{If}. In the region II, a linear relation between $\log(da / dN)$ and $\log(\Delta K)$ is observed. Region III appears when the maximum value of the stress intensity factor approaches the fracture toughness of the material, K_{Ic} or K_c. This region is characterized by an acceleration of the crack propagation rate that leads to an unstable propagation of the crack and consequently to the final rupture. The region III is not well defined for materials experiencing excessive ductility. For these materials the development of gross plastic deformations is observed in region III which invalidates the application of the LEFM, since the basic hypothesis of the LEFM are violated.

A great number of fatigue crack propagation laws have been proposed in literature, however the most used and simple relation was proposed by Paris & Erdogan (1963):

$$\frac{da}{dN} = C\Delta K^m \tag{6}$$

where da / dN is the fatigue crack propagation rate, $\Delta K = K_{\max} - K_{\min}$ represents the range of the stress intensity factor and C and m are materials constants. This relation describes the region II of fatigue crack propagation. The number of cycles to propagate a crack from an initial size, a_i, to a final size, a_f, may be computed integrating the fatigue crack propagation law. In the case of the Paris's law, this integration may be written in the following form:

$$N = \frac{1}{C}\int_{a_i}^{a_f}\frac{da}{\Delta K^m} = \frac{1}{C}\frac{1}{\Delta\sigma^m}\int_{a_i}^{a_f}\frac{da}{\left(Y\sqrt{\pi a}\right)^m} \tag{7}$$

Equation (7) may be used to compute the number of cycles to failure if a_f corresponds to the critical crack size, leading to failure.

3.4 Fatigue crack propagation data

In order to determine the fatigue crack propagation curves, Compact Tension (CT) specimens were used. This specimen geometry presents, in relation to the alternative Centre Crack Tension geometry (CCT), the advantage of providing a larger number of readings with a smaller material volume requirement. The specimens were cut from a 24 mm thick plate of 6061-T651 aluminium alloy, containing a butt welded joint made from both sides using the MIG welding process. The filler material used in the welding process was the AlMg-5356. Due to material limitations, specimens with thickness B=10 mm and nominal width W=50 mm were used. These dimensions are according to the recommendations of the ASTM E647 standard (ASTM, 2000). Figure 8 illustrates the locations in the aluminium plate from where the specimens were extracted. Specimens containing base material (BM), heat affected zone (HAZ) and welded material (WEL) were cut from the plate. This extraction process was planned in agreement with the recommendations included in the standard. The specimens were tested in a servohydraulic machine, rated to 100 kN, applying a sinusoidal waveform with 15 Hz. The crack length was measured on both faces of the specimen, using two magnifying eyeglasses. The resolution of the measuring device was 0.01 mm.

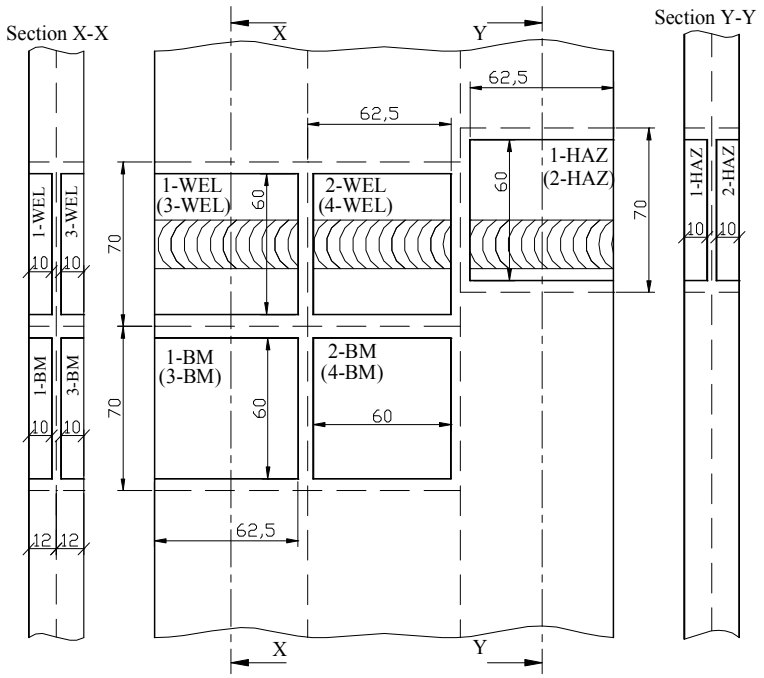

Fig. 8. Locations of the CT specimens at the welded plate (dimensions in mm)

In order to obtain the da/dN versus ΔK curves it is necessary to find an appropriate expression to evaluate ΔK. The ASTM E647 standard (ASTM, 2000) proposes the following formulation of ΔK, for the CT geometry:

$$\Delta K = \Delta\sigma \cdot f\left(\frac{a}{W}\right) \tag{8}$$

where $f(a/W)$ is the compliance function that is specified in the standard and $\Delta\sigma$ is the applied stress range. For the CT geometry $\Delta\sigma$ assumes the following form:

$$\Delta\sigma = \frac{\Delta P}{B \cdot W^{1/2}} \tag{9}$$

where ΔP is the applied load range, B and W define, respectively, the thickness and the nominal width of the specimen.

Table 4 summarizes the experimental program carried out in order to derive the da/dN versus ΔK for the base material, heat affected zone, and welded material. The stress ratios tested were R=0.1 and R=0.5. The frequency of the tests, f, was 15 Hz. The table also includes the maximum and minimum loads of the test. It was verified that for some tests, namely for tests performed with welded material, the crack deviates from the ideal shape, namely a divergence between the crack on the two faces of the specimen was verified. This phenomenon can be explained by the following factors: misalignments, asymmetrical disposition of the welding or existence of inclusions, oxides or porosities in the welding.

Specimen	**Material**	***R***	***f*** **[Hz]**	F_{max} **[N]**	F_{min} **[N]**
2 - BM	Material Base	0.1	15	3676.8	367.6
3 - BM		0.5	15	8372.7	4186.3
1 - WEL	Welded Material	0.1	15	3231.0	323.1
3 - WEL		0.1	15	3600.0	360.0
2 - WEL		0.5	15	6205.5	3102.7
1 - HAZ	HAZ	0.1	15	29652	296.52
2 - HAZ		0.5	15	4688.2	2344.1

Table 4. Crack propagation experimental program

The evaluation of the fatigue crack propagation rates was made through the seven point polynomial incremental method as proposed in the ASTM E647 standard (ASTM, 2000). Figures 9 to 11 represent the da/dN versus ΔK curves for the base material, welded material and heat affected zone and for stress ratios R=0.1 and R=0.5. The results correspond to the region II, region of validity of the Paris's law. Figures 12 and 13 compare the propagation curves for the three tested materials, respectively for R=0.1 and R=0.5. It can be concluded that the propagation rates increase with the increase of R. This influence is more significant for low values of ΔK. R influences the crack propagation curves for the three materials but its influence is more significant for the base material. The HAZ shows low sensitivity to the stress ratio. It can be observed that HAZ presents the greatest propagation

rates for R=0.1. The propagation rates of the welded material present intermediate values between HAZ and the base material. Tests conducted with R=0.5 do not show significant differences in the propagation rates for the three materials. The factors that justify these results are several, such as the elevated levels of residual stresses at the crack tip, the effect of the stress ratio, the yield stress and the grain size that is distinct for the three materials. The parameters of the Paris's law are listed in the Table 5 for the three materials and for the two stress ratios, R=0.1 and R=0.5. The determination coefficients, R^2, obtained for the adjusted curves are significant.

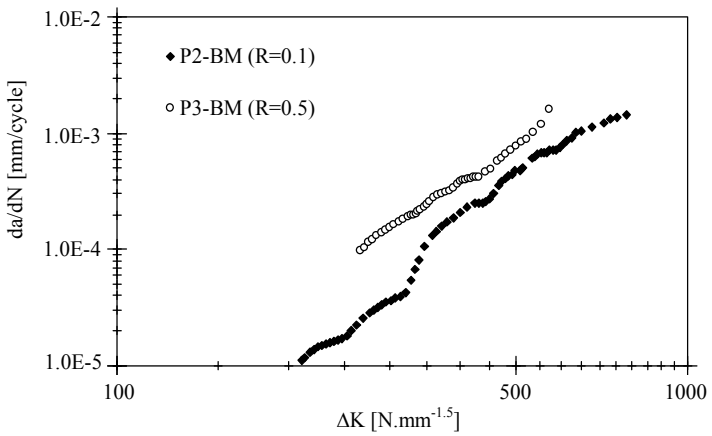

Fig. 9. Fatigue crack propagation rates for the base material

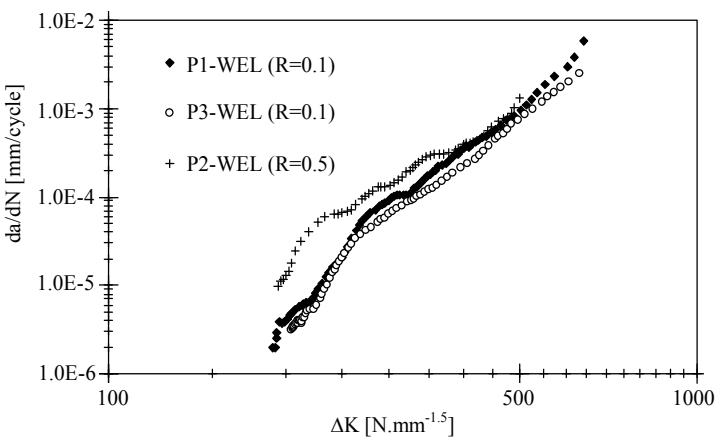

Fig. 10. Fatigue crack propagation rates for the welded material

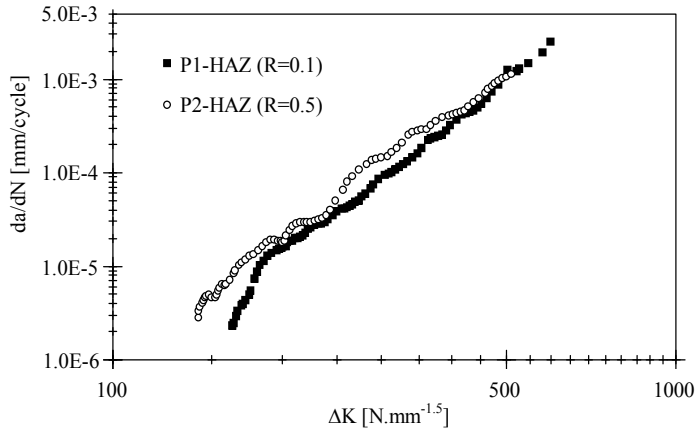

Fig. 11. Fatigue crack propagation rates for the heat affected material

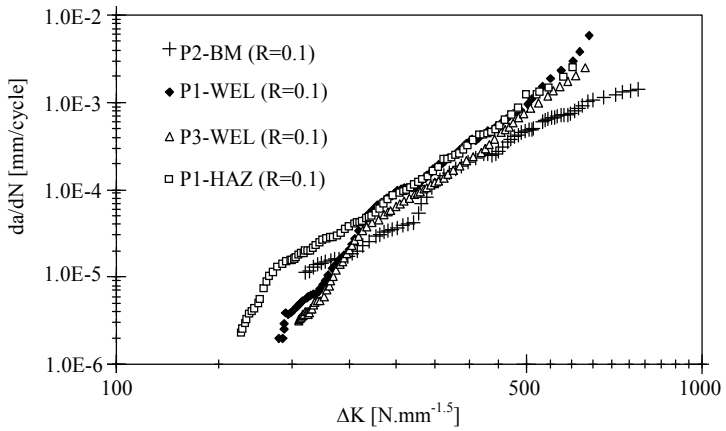

Fig. 12. Comparison of fatigue crack propagation rates for R=0.1

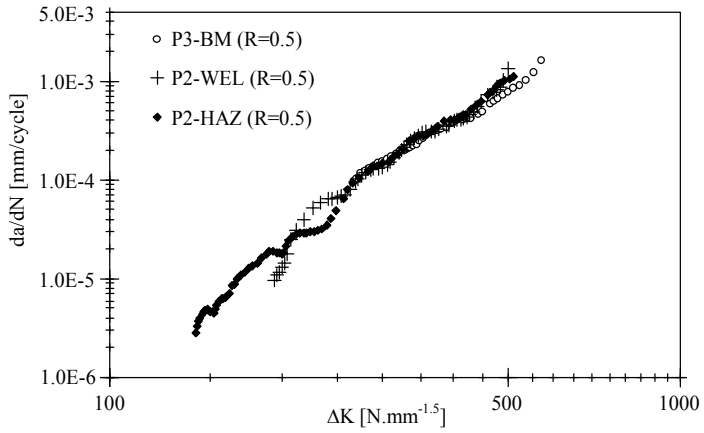

Fig. 13. Comparison of fatigue crack propagation rates for R=0.5

Material	R	$da/dN = C\Delta K^m$			R^2
		C^*	C^{**}	m	
BM	0.1	1.9199E-15	3.7086E-12	4.1908	0.9822
BM	0.5	1.2863E-12	9.8151E-11	3.2547	0.9912
WEL	0.1	6.5017E-20	6.7761E-14	6.0120	0.9731
WEL	0.5	1.9094E-15	6.7566E-12	4.3657	0.9639
HAZ	0.1	1.1363E-16	1.7580E-12	4.7932	0.9863
HAZ	0.5	8.7433E-16	4.8669E-12	4.4972	0.9930
BM	0.1;0.5	1.3790E-14	1.0619E-11	3.9242	0.8592
WEL	0.1;0.5	4.5939E-19	1.6769E-13	5.7082	0.9249
HAZ	0.1;0.5	5.4406E-16	3.6208E-12	4.5489	0.9770
BM; WEL; HAZ	0.1	3.2668E-17	8.3120E-13	4.9371	0.9314
BM; WEL; HAZ	0.5	2.0587E-15	6.7596E-12	4.3444	0.9835
BM; WEL; HAZ	0.1; 0.5	2.6567E-16	2.2733E-12	4.6217	0.9039

*da/dN (mm/cycle) and ΔK (N.mm-1.5)
**da/dN (m/cycle) and ΔK (MPa.m0.5)

Table 5. Constants of Paris's law of the tested materials

4. Fatigue behaviour of welded joints made of 6061-T651 aluminium alloy

The proposed investigation focused in four types of welded joints, made from 12 mm thick aluminium plates of 6061-T651 aluminium alloy, namely one butt welded joint and three types of fillet joints (see Figure 14). As described in Figure 14, detail 1 corresponds to a butt welded joint; detail 2 corresponds to a T-fillet joint without load transfer; detail 3 corresponds to a load-carrying fillet cruciform joint and finally, detail 4 is a longitudinal stiffener fillet joint. Welds were performed with the manual MIG process with Al Mg-5356 filler material (ϕ1.6 mm) and Argon + 0.0275% NO gas protection (17 litres/min). The butt welded joint was prepared with a V-chamfer. For the fillet welds, no chamfer was required. The butt welded joint was made using two weld passes; each fillet of the fillet joints was made using a single weld pass. Details 1 to 3 were subjected to a pos-welding alignment using a 4-Point bending system. No stress relieve was used after the alignment procedure. Detail 4 was tested in as-welded condition.

For each type of geometry, a test series was prepared and tested under constant amplitude fatigue loading conditions, in order to derive the respective S-N curves. The tests were carried out on a MTS servohydraulic machine, rated to 250 kN. Remote load control was adopted in the fatigue tests, under a sinusoidal waveform. A load ratio equal to 0.1 was adopted. Figure 15 represents the experimental S-N data obtained for each welded detail, using the nominal/remote stress range as a damage parameter. Small corrections were introduced into the theoretical remote stress range, using the information from strain measurements carried out on a sample of specimens.

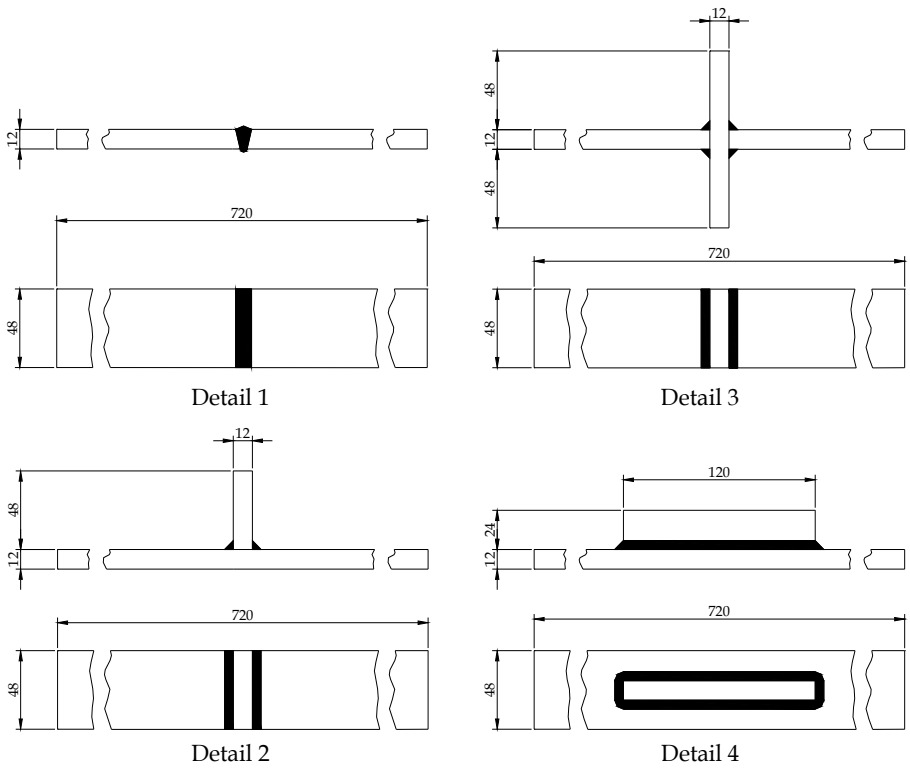

Fig. 14. Welded joints made of 6061-T651 aluminium alloy (dimensions in mm)

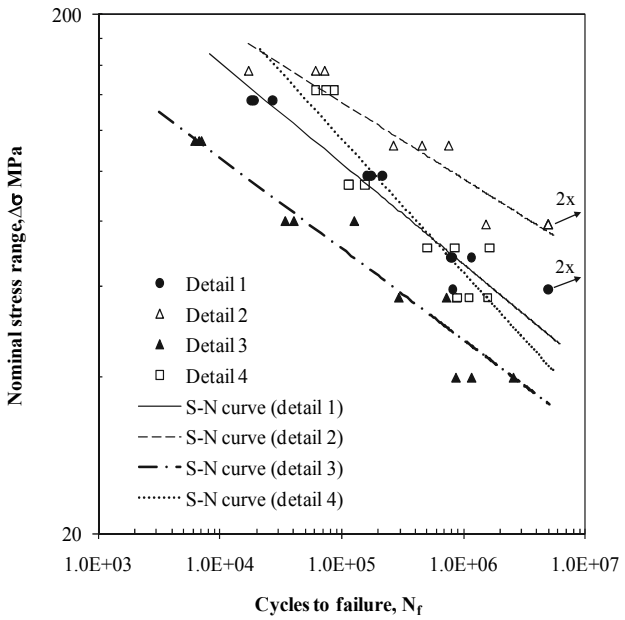

Fig. 15. S-N fatigue data from the welded specimens

The usual way to express the S-N fatigue data is to use a power relation that is often expressed in one of the following ways:

$$\Delta\sigma^m N_f = C \tag{10}$$

$$\Delta\sigma = A N_f{}^{\alpha} \tag{11}$$

where m, C, A and α are constants. Table 6 summarizes the constants for each test series obtained using linear regression analysis. The determination coefficients are also included in the table. Relative high determination coefficients are observed. S-N curves derived for the details 1 to 3 are rather parallel. The detail 4 shows a significantly distinct slope. The detail 2 shows the highest fatigue resistance; conversely, detail 3 – the load-carrying T-fillet cruciform joint- shows the lowest fatigue resistance.

Welded details	S-N parameters				R^2
	A	α	C	m	
1	969.530	-0.194	2.305E+15	5.144	0.953
2	739.863	-0.147	2.913E+19	6.784	0.844
3	535.373	-0.176	3.371E+15	5.691	0.926
4	2216.671	-0.257	1.054e+13	3.892	0.848

Table 6. Parameters of the S-N data of the welded details

5. Fatigue modelling of welded joints

5.1 Description of the model

The fatigue life of a structural component can be assumed as a contribution of two complementary fatigue processes, namely the crack initiation and the macroscopic crack propagation, as:

$$N_f = N_i + N_p \tag{12}$$

where N_f is the total fatigue life, N_i is the number of cycles to initiate a macroscopic crack, and N_p is the number of cycles to propagate the crack until final failure. Generally, is it assumed that the fatigue behaviour of welds is governed by a crack propagation fatigue process, since the welding process may introduce initial defects. The validity of this assumption is analysed in this study for four types of welded joints made of 6061-T651 aluminium alloy. Both crack initiation and crack propagation phases are computed and compared with the experimental available S-N data.

The computation of the crack initiation phase will be carried out using the local approaches to fatigue based on the strain-life relations, such as the Morrow's equation (see Equations (3) and (4)). The number of cycles required to propagate the crack will be computed using the LEFM approach, based on Paris's equation (refer to Equations (6) and (7)). The material properties required to perform the referred computations were already presented in the previous sections.

The application of the strain-life relations to compute the crack initiation requires the elastoplastic strain amplitudes at the critical locations, namely at the potential sites for crack initiation. These locations are characterized by a high stress concentration factor, corresponding many times to the notch roots (e.g. weld toes). The elastoplastic strain amplitudes may be calculated using the Neuber's approach (Neuber, 1961):

$$\Delta\sigma \cdot \Delta\varepsilon = k_t^2 \Delta\sigma_{nom} \cdot \Delta\varepsilon_{nom} \tag{13}$$

where $\Delta\sigma$ and $\Delta\varepsilon$ are the total local elastoplastic stress and strain ranges, $\Delta\sigma_{nom}$ and $\Delta\varepsilon_{nom}$ are the nominal stress and strain ranges and k_t is the elastic stress concentration factor. Equation (13) can be used together with the Ramberg-Osgood equation (Equation (5)). Since Equation (13) stands for cyclic loading, some authors replace the elastic stress concentration factor by the fatigue reduction factor, k_f. However, the elastic concentration factor is an upper bound of the fatigue reduction factor. Therefore, in this research, the following conservative assumption is made:

$$k_f = k_t \tag{14}$$

The elastic stress concentration factors for the welded details may be computed based on numerical methods (e.g. FEM), experimental or analytical methods. Ribeiro (1993, 2001) suggested for the welded joints under investigation the elastic stress concentration factors listed in Table 7, based on both finite element analysis and available analytical formulae. The stress concentration factors characterize the stress intensification at the weld toes for details 1, 2 and 4; for detail 3, k_t characterizes the stress intensification at the weld root. Figure 16 shows the potential cracking sites for the investigated details, confirmed by the experimental program.

Welded details	Elastic stress concentration factor, k_t
1	3.50
2	2.60
3	7.24
4	4.43

Table 7. Elastic stress concentration factors

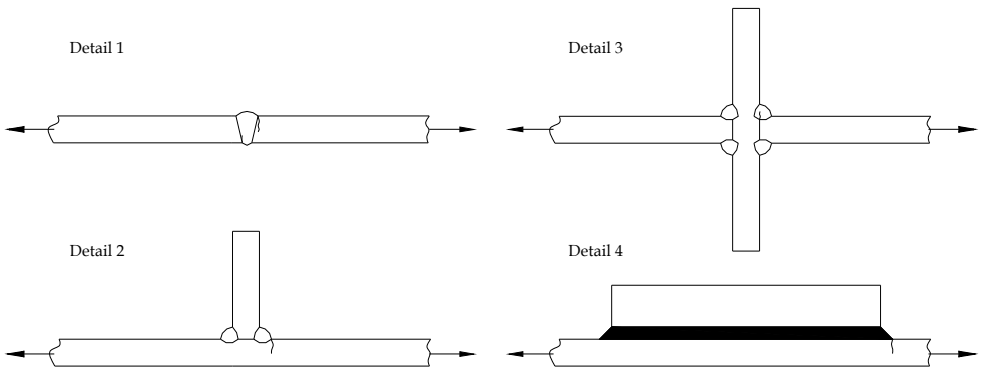

Fig. 16. Potential cracking locations at the investigated welded details

In what concerns the simulation of the fatigue crack propagation, initial defects of 0.25 mm were assumed corresponding to the initiation period. Cracks propagating from the weld toes, perpendicularly to the loading, are assumed for details 1, 2 and 4. For detail 3, a crack propagating from the weld root, perpendicularly to the loading, is assumed (see Figure 16). Constant depth cracks were assumed for details 1 and 3. For details 2 and 4 semi-elliptical cracks were assumed to propagate from the weld toes. In these latter cases, an initial circular crack with a radius equal to 0.25 mm was assumed and Equations (6) and (7) have to be applied twice, namely at both semi-axis endpoints. However, the crack increments are dependent to each other, in order to guarantee the compatibility in the number of propagation cycles, resulting:

$$\frac{da}{dc} = \left(\frac{\Delta K_a}{\Delta K_c} \right)^m \tag{15}$$

where da is the crack increment at the plate surface, dc is the crack increment at the deepest point of the crack front, ΔK_a and ΔK_c are, respectively, the stress intensity factor ranges at the surface and deepest crack front points and m is the Paris's law parameter. The integration of the Paris's law may be easily carried out assuming discrete increments of the crack, for which the stress intensity factors are assumed constant. In order to integrate the Paris's law, the formulations of the stress intensity factors are required. Solutions available in the literature were adopted in this study (Snijder & Dijkstra, 1989). The crack was propagated until it reached 11.8 mm depth (any detail) or 48 mm width for details 2 and 4. Finally, the crack propagation properties presented in section 3.4 were used to simulate the crack propagation period for the welded details. In particular, the properties for R=0.1 were used. For details 1 and 3 the crack propagation data obtained for the welded material was used; for details 2 and 4 the properties obtained for the heat affected material were applied.

5.2 Fatigue predictions

Figures 17 to 20 present the predictions of the fatigue lives for the investigated welded details, made of 6061-T651 aluminium alloy, taking into account the crack initiation and crack propagation phases. Three S-N curves are represented, one corresponding to the fatigue crack initiation, the other corresponding to the fatigue crack propagation and finally the third corresponding to the total fatigue life. Also, the experimental data is included in the graphs for comparison purposes. The analysis of the results reveals that there is a close relation between the fatigue strength and the elastic stress concentration factor. The welded details with higher fatigue resistance show lower elastic stress concentration factors at the critical locations of the welds. The global predictions are in good agreement with the experimental results.

The comparison of the crack initiation based S-N curves with the average experimental data, allows the following comments:

- Crack initiation if significant for butt welded joints, representing about 37% of the total fatigue life for stress ranges equal of higher than 98 MPa.
- For the T-fillet joint without load transfer, the crack initiation is significant representing about 50% of the total fatigue life, for the stress range of 156 MPa. For stress ranges bellow 79 MPa, the crack initiation was about 5×10^6 cycles.

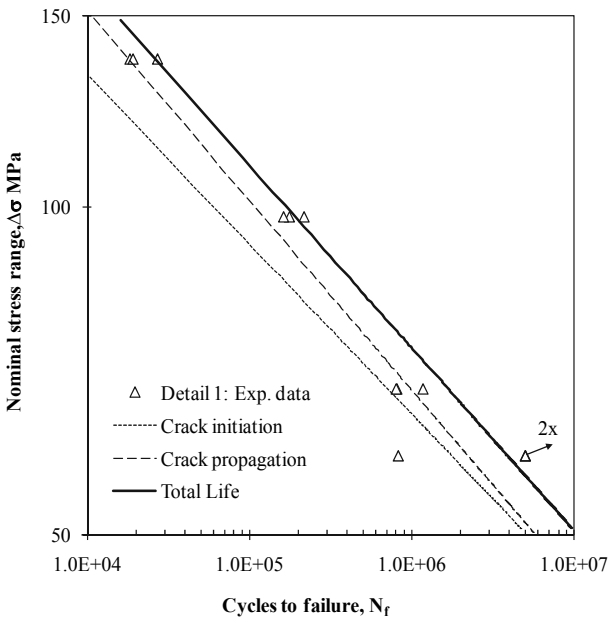

Fig. 17. Fatigue life predictions for the butt welded joint: detail 1

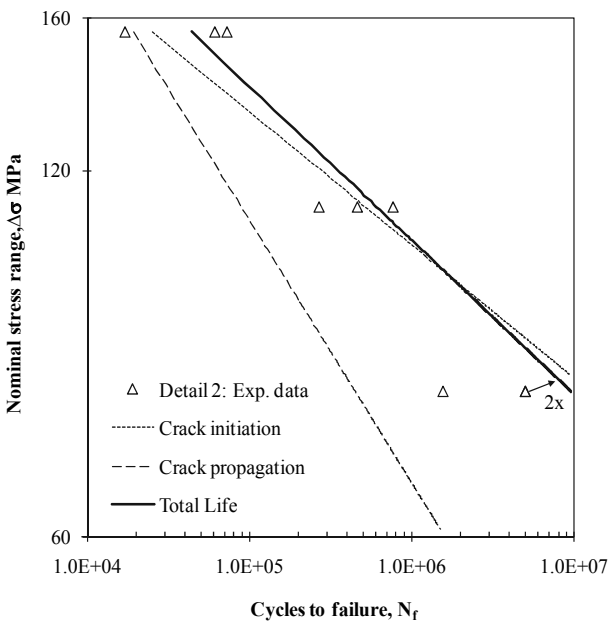

Fig. 18. Fatigue life predictions for the T-fillet joint without load transfer: detail 2

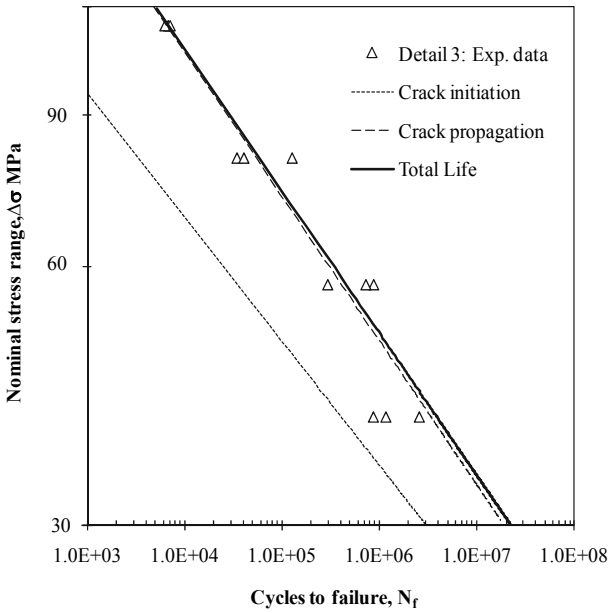

Fig. 19. Fatigue life predictions for the load-carrying fillet cruciform joint: detail 3

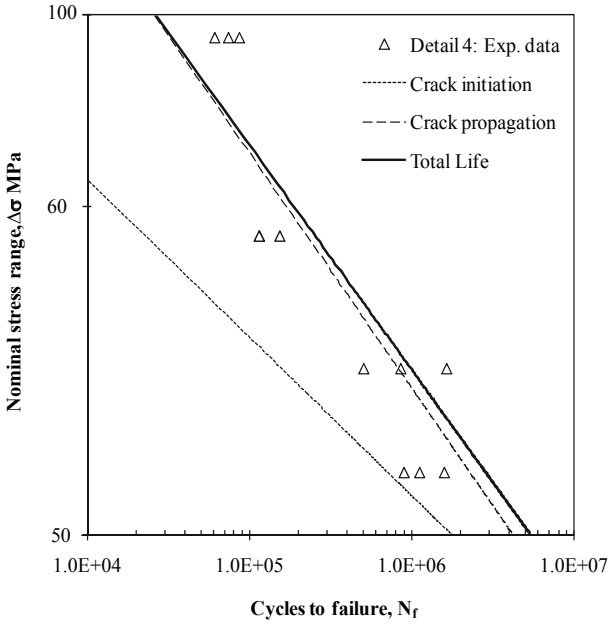

Fig. 20. Fatigue predictions for the longitudinal stiffener fillet joint: detail 4

- For the load-carrying fillet cruciform joint, the crack initiation is almost negligible, since it represents 3.5% to 6.5% of the total life for the stress ranges from 57 MPa to 114 MPa. For a stress range of 40 MPa, the importance of the crack initiation increases to about 36% of the total fatigue life.
- For the longitudinal stiffener fillet joint, crack initiation represented about 2.2% of the experimental fatigue life for the stress range of 143 MPa. The importance of the crack initiation phase increases for stress ranges between 94 and 71 MPa reaching, respectively, values of 11 to 20% of the total fatigue life.

The above comments allow the following conclusions:

- For welded joints characterized by high stress concentration factors and for high stress ranges, the initiation period is negligible. For low stress range levels, the crack initiation becomes more important.
- For welded joints characterized by low stress concentration factors, the crack initiation is meaningful, for both low and high stress ranges.

From the above discussion, it is recommended to neglect the crack initiation for the welded joints with high stress concentration factors, when loaded under high stress levels. For these cases, the crack propagation from an initial crack of 0.25 mm, leads to consistent predictions.

6. Conclusion

The fatigue life of four types of welded joints, made of 6061-T651 aluminium alloy, was predicted using a two phase model, namely to account separately for crack initiation and crack propagation phases. While the strain-life relations were used to compute the crack initiation, the LEFM was used as a base for crack propagation modelling. The required basic materials properties required for the model application were derived by means of strain-controlled fatigue tests of smooth specimens, as well as by means of fatigue crack propagation tests.

A globally satisfactory agreement between the predictions and the experimental fatigue S-N data was observed for the welded details. A 0.25 mm depth crack demonstrated to be an appropriate crack initiation criterion. The analysis of the results revealed that the crack initiation may be significant, at least for welded joints with relative lower stress concentrations and low to moderate loads. In these cases, the classical predictions based exclusively on the crack propagation, may be excessively conservative.

The proposed two-stage fatigue predicting model can be further improved in the future. Namely, residual stresses effects should be accounted at least in the local elastoplastic analysis, concerning the fatigue crack initiation prediction. The strain-life properties were only derived for the base material. However, a more accurate analysis may be performed if these properties would be derived for the welded or heat affected materials. Finally, the crack initiation criterion, which has been established on an empirical basis, requires a more fundamental definition.

7. References

ASTM (1998). ASTM E606: Standard Practice for Strain-Controlled Fatigue Testing, In: *Annual Book of ASTM Standards*, Vol. 03.01, American Society for Testing and Materials: ASTM, West Conshohocken, PA.

ASTM (2000). ASTM E647: Standard Test Method for Measurement of Fatigue Crack Growth Rates, In: *Annual Book of ASTM Standards*, Vol. 03.01, American Society for Testing and Materials: ASTM, West Conshohocken, PA.

Basquin, O.H. (1910). The Exponential Law of Endurance Tests. *ASTM*, Vol. 10, 625-630.

Borrego, L.P.; Abreu, L.M.; Costa, J.M. & Ferreira, J.M. (2004). Analysis of Low Cycle Fatigue in AlMgSi Aluminium Alloys. *Engineering Failure Analysis*, Vol. 11, 715-725.

Chung, Y.S. & Abel, A. (1988). Low Cycle Fatigue of Some Aluminum Alloys. In: *Low Cycle Fatigue*, ASTM STP 942, H. D. Solomon, G. R. Halford, L. R. Kaisand, and B. N. Leis, (Ed.), 94-106, American Society for Testing and Materials, Philadelphia, PA.

Coffin, L.F. (1954). A study of the effects of the cyclic thermal stresses on a ductile metal. *Translations of the ASME*, Vol. 76, 931-950.

De Jesus, A.M.P. (2004). *Validação de Procedimentos de Cálculo à Fadiga de Reservatórios sob Pressão*, PhD. Thesis, Universidade de Trás-os-Montes and Alto Douro, Portugal.

Maddox, S. J. (1991). *Fatigue strength of welded structures*, Second Edition, Woodhead Publishing, ISBN 978-1855730137, UK.

Manson, S.S. (1954). Behaviour of materials under conditions of thermal stress. *Technical Report No. 2933*, National Advisory Committee for Aeronautics.

Moreira, P.M.G.P.; de Jesus, A.M.P.; Ribeiro, A.S. & de Castro, P.M.S.T. (2008). Fatigue crack growth in friction stir welds of 6082-T6 and 6061-T6 aluminium alloys: A comparison. *Theoretical and Applied Fracture Mechanics*, Vol. 50, 81–91.

Morrow, J.D. (1965). Cyclic Plastic Strain Energy and Fatigue of Metals. *Int. Friction Damping and Cyclic Plasticity*, ASTM STP 378, 45-87.

Neuber, H. (1961). Theory of Stress Concentration for Shear-Strained Prismatical Bodies with Arbitrary Nonlinear Stress-Strain Law. *Translations of the ASME: Journal of Applied Mechanics*, Vol. 28, 544-550.

Paris, P.C & Erdogan, F. (1963). A critical analysis of crack propagation laws. *Journal basic Engineering Trans. ASME*, 528–534.

Radaj, D.; Sonsino, C. M. & Fricke, W. (2009). Recent developments in local concepts of fatigue assessment of welded joints. *International Journal of Fatigue*, Vol. 31, 2–11.

Ramberg, W. & Osgood, W.R. (1943). Description of stress-strain curves by three parameters, *Technical Report No. 902*, National Advisory Committee for Aeronautics.

Ribeiro, A.S. (1993). *Efeito da Fase de Iniciação na Previsão do Comportamento à Fadiga de Estruturas Soldadas*, PhD. Thesis, Universidade de Trás-os-Montes and Alto Douro, Portugal.

Ribeiro, A.S. (2001). *Estimativa da vida à fadiga de juntas soldadas. Propriedades de Resistência Mecânica da Liga de Alumínio Al 6061-T651*, Série Técnica-Científica, Ciências Aplicadas, Universidade de Trás-os-Montes e Alto Douro, ISBN 972-669-283-0, Vila Real, Portugal.

Ribeiro, A.S.; Borrego, L.P.; De Jesus, A.M.P. & Costa, J.D.M. (2009). Comparison of the low-cycle fatigue properties between the 6082-t6 and 6061-t651 aluminium alloys, *Proceedings of the 20th International Congress of Mechanical Engineering*, Gramado, RS, Brasil, November, 2009, ABCM.

Snijder, H.H. & Dijkstra, O.D. (1989). *Stress intensity factors for cracks in welded structures and containment systems*, TNO Report BI-88-128, TNO Institute for Building Materials and Structures, The Netherlands.

8

Inhomogeneous Material Modelling and Characterization for Aluminium Alloys and Welded Joints

Jisen QIAO and Wenyan WANG
College of Materials Science and Engineering, Lanzhou University of Technology
P.R China

1. Introduction

Structure functions are decided by the material properties which made of it. Material modelling and characterization are important to crashworthiness of automobile. Some times right material parameters are the key to the models which describe large deformation and failure behaviours of car body. Therefore aimed at the dynamic behaviours of aluminium alloy in certain crashing state with high strain rate, triaxiality, and damage initialization etc., large work has been done in this field including component and full scare crashing tests, which cost a lot. However, the result is not satisfied. Detail information about the crashing is hard to obtained from the experiments because of the high rate and limited time of deformation (in some specific cases, the strain rate is over $2X10^2$). Simulation is an effective method to extend the experimental data for complete models of crashworthiness.

In certain degree, the precision of simulation is depended on the authority of material parameters of modelling. Large deformation during crashing is an complicated process including various stages of elastic deformation, plastic deformation, damage initialization, evolution and failure. Strain rate, anisotropy and stress state make effects on this process. How do these factors exactly work? Still so many questions are left in this field. Smooth tension tests combined with simulation were carried out for material modelling and characterization of aluminium alloy AW 6061 (Blauel & Su, 2002; Sun, 2003). Static and dynamic response of typical aluminium alloy components is predicted successfully by using G-T-N damage mode for FEM simulation. The damage model explains the ductile fracture of the aluminium and its initiation and evolution by mechanism of growth of voids that could be applied in industry. Dynamical loading was established by using explicit solver of FEM code (Franck & Bruno, 2001). This model takes elastic flow and anisotropic into account. Thereby this could be used to predict situation of damage and fracture of materials with obvious texture deformation such as extruded aluminium alloys in circumstances of dynamic loading with large deformation. Another contribution of Frank's research is to develop iterative algorithm which has an experiment combined with numerical simulation to achieve optimizing parameters in material characterization. This algorithm uses data from notch tensile as the basic input to derive parameters of G-T-N damage model, and revise these parameters by FEM calculation in consider of anisotropic influence. Eventually, the result of numerical simulation fit with experiments. In comparing with other method of

material characterization, this could avoid a great amount of experiment expenses, and improving the efficiency of modelling.
Meanwhile, the inhomogeneous deformation and failure of welded joints and components have become a key problem for crashworthiness of light automobile. There is much dissimilarity in mechanical behaviour between welded and un-welded metal, evaluation of the mechanical properties of welded joint has become a hot topic in the research world. Material modelling and characterization for aluminium alloy welded joints are focused in this chapter.
Joint strength was evaluated as a function of strength mismatch factors and the geometric size of HAZ (Zhu et al., 2004). The author used FEM analysis of tensile specimens in comparison with test results to study the stress distribution in tension plate samples. Finally, Zhu identified an analytical approach to predict tensile strength of mismatch joints for pipeline steel. Asif Husain, Sehgal D k, et al. Another inverse finite element procedure was developed by carrying out with the commercial FE code, such as ABAQUS to determine constitutive tensile behaviour of homogeneous materials (Asif et al., 2004). More experimental research results have been reported by other scholars (Campitelli et al., 2004; Hankin et al, 1998). A series of analytical equations based on a force-distribution assumption were formulated to describe mechanical properties of a tailor blank welded by a CO2 laser (B.Y. Ghoo et al., 2001). Actually, the results demonstrate the average mechanical property of welds and HAZ, which can not precisely describe the effect of micro zone on the general mechanical behaviour of a joint. It is necessary to develop experimental techniques and analytical methods in order to quantitatively evaluate the material mechanical heterogeneity.
In this chapter, an inverse finite element procedure is developed and executed using the ABAQUS computer code for the determination of the constitutive tensile behavior of welded metals. The proposed inverse technique is based on the small punch shearing law. The validation of numerical modeling is identified compared with uniaxial tensile tests.

2. Material modelling and characterization for basic aluminium alloy under static and dynamic loading

2.1 Experiment procedure

2.1.1 General idea

Alminium alloy 5052H34 and 6063T6 are widely used for welded structure of car body because of their remarkable performance in welding as well as forming process. In actual collision, these structures would mostly have large plastic deformation before failure. Therefore, it's not enough for material characterization only testing yield and ultimate strength, more work should be done in work hardening, anisotropic and facture features of initiated damage. As for specific aluminium alloy, the welded structure is fixed, however the work temperature and loading condition varies with the actual impact process. In accordance with the actual impact condition, various tensile tests under static and dynamic loading are carried out for aluminium alloy. The experiments were divided into five groups, which are smooth tensile, notch tensile, double notch tensile, Iosipescu shear test, and dynamic tensile test. Serial number of the test specimens and experiment condition are show in Table.1, sizes of the specimens are show in Fig.1, the specimens are cut from original plate, the distribution of all the specimens on plate can be seen on Fig 2.

Test Style	Cross section (mm^2)	Gauge Length（mm）	Sample No.	Load Speed (mm/s)	Strain Rate s^{-1}
Smooth Tensile	2.897×5.037	10	PT1-UT-S1Q	0.01	Static
	2.894×5.042	10	PT1-UT-S2Q	0.01	Static
	2.889×5.029	10	PT1-UT-S3Q	0.01	Static
	2.889×5.029	10	PT1-UT-S1L	0.01	Static
	2.885×5.025	10	PT1-UT-S2L	0.01	Static
	2.893×5.031	10	PT1-UT-S3L	0.01	Static
Notch Tensile	2.889×5.025	10	PT1-UNT-S1Q	0.01	Static
	2.892×5.033	10	PT1-UNT-S2Q	0.01	Static
	2.889×5.030	10	PT1-UNT-S3Q	0.01	Static
Double Notch Tensile	2.787×5.123	10	PT1-DNT-S1Q	0.01	Static
	2.789×5.132	10	PT1-DNT-S2Q	0.01	Static
	2.785×5.134	10	PT1-DNT-S3Q	0.01	Static
	2.788×5.128	10	PT1-DNT-S1L	0.01	Static
	2.787×5.133	10	PT1-DNT-S2L	0.01	Static
	2.791×5.128	10	PT1-DNT-S3L	0.01	Static
Iosipescu Shear Test	2.796×4.029	10	PT1-PSC-S1L	0.01	Static
	2.792×4.031	10	PT1-PSC-S2L	0.01	Static
	2.795×4.034	10	PT1-PSC-S3L	0.01	Static
	2.794×4.033	10	PT1-PSC-S1Q	0.01	Static
	2.793×4.032	10	PT1-PSC-S2Q	0.01	Static
	2.792×4.034	10	PT1-PSC-S3Q	0.01	Static
Dynamic Tensile	2.892×5.038	10	PT1-UT-D1Q	1.7×10^3	143
	2.888×5.036	10	PT1-UT-D2Q	1.7×10^3	143
	2.883×4.997	10	PT1-UT-D3Q	1.7×10^3	143
	2.892×5.035	10	PT1-UT-D4Q	1.7×10^3	143
	2.888×5.033	10	PT1-UT-D5Q	1.7×10^3	143
	2.883×4.995	10	PT1-UT-D6Q	1.7×10^3	143

Table. 1. Various tests for material modelling

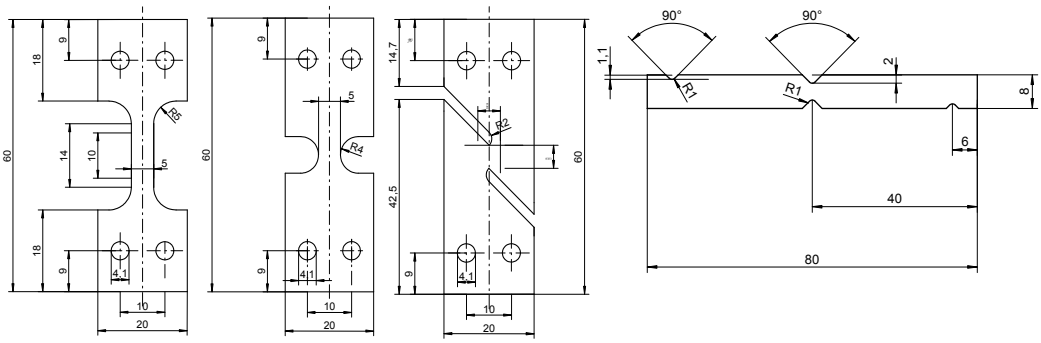

Fig. 1. Sample size for different tensile and shear tests
(a) smooth tensile, (b) notch tensile, (c) double notch tensile, (d) Isoipescu shear

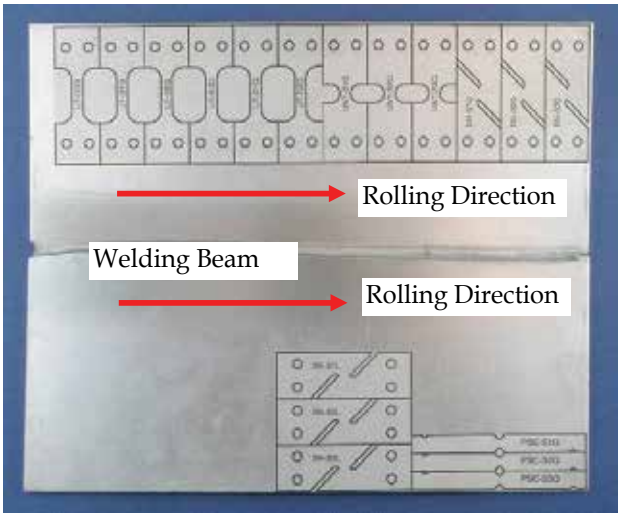

Fig. 2. Distribution of test samples on original plate

Taking PT1-UT-S1Q as an example, the meaning of serial codes can be expressed as followings:
PT1-Project No.; UT-Uniaxial tensile; UNT-Notch tensile; DNT-Double notch tensile; PSC-Isoipescu shear; S1Q-Static transverse sample 1; D2L –Dynamic longitude sample 2

2.1.2 Static uniaxial tensile test

Uniaxial smooth tensile test is one of the basic mechanical tests. The primary aim of this test is to measure the true stress-strain curve and fracture strain. In order to provide with material property for next numerical simulation, so as to expand the scale of the test data, obtain practical data as much as possible; the experiment adopted two sets of equipments. one is the strength-displacement detect system, which uses extend-measurement displacement, also loading sensor to measure load, which is owned by Instron 1886 tensile test machine. Another set of machine is optical deformation measure system, including static camera, digital transition card and following image processing software and diagram

calculation software. The system is equipped with two sets of digital camera; the shooting angle is perpendicular to front side and lateral side of the specimens. Therefore it could detect changes in width and thickness direction immediately when the specimen is in the tensile process, with dynamic image detecting to acquire changes in specimen section, so we could calculate the minimum section size Ai, according to the formulation to calculate the actual stress, strain in tensile process, which could get stress-strain relation of the tensile specimens after necking. In this research two sets of equipments were introduced to work collaboratively. One is normal mechanical test system, another is optical measurement system. The common mechanical testing system is mainly responsible for recording of whole course loading detection and elastic deformation and partial ductile deformation (before maximum loading), while the optical detecting system aim at recording of detection of elastic and ductile(before fracture) deformation.

From Fig. 3, it can be seen that the true strain of aluminium alloy 5052H34 is 0.096 correspond to static maximum tensile load at room temperature, and fracture strain ε_f is 0.73 at this time. These data segment is undetectable by using ordinary tensile experiment, and there will be severe error in the coming up numerical simulation. By contrast, segment data after necking can be repaired if optical detecting system is used, and the maximum true strain can be measured up to 0.561. The measure problem of stress-strain curve can be fixed by linear interpolation. Comparison of Curves of specific materials and precision of numerical simulation will be discussed in this chapter in related diagrams.

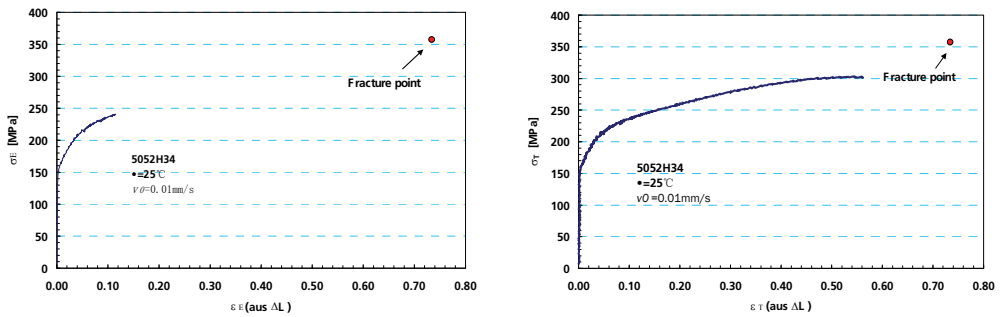

(a) (b)

Fig. 3. Comparison of true strain stress curve tested by different devices.
(a) tested by mechanical machine, (b) tested by optical inspection system

2.1.3 Results

1. Strain and stress curves

The true strain stress curves obtained by two sets of different detecting systems can be shown in Fig.3. The optical deformation testing system is better than the mechanical system for data collection. However the complexity and costs of this optical system is relatively higher.

2. Material characterization of anisotropic and stress state

Specimen of smooth tensile test is cut from the plate with longitude and transverse direction. The engineering strain stress curves can be seen in Fig.4. Result shows that longitude yield stress is 22Mpa higher than that of transverse. Ultimate strength is 26MPa difference between two directions, which demonstrates particular anisotropic. The size and

distribution of grains is regular from further research in microstructure. First of all, grain size of the surface is larger than centre (Fig.5). Secondly, there is certain grain orientation in the centre of the material because of a rolling process (Fig.6). Grains were extended in the axis along the rolling direction, which caused grain refinement along the thickness direction during rolling process. In the following anneal and artificial aging, there are certain preferred orientation in the refined grains after grain growth or recrystallization, and these factors lead material with certain anisotropic.

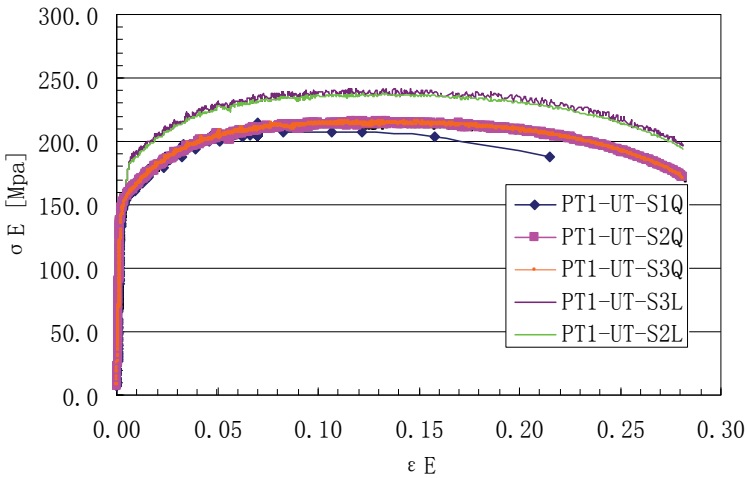

Fig. 4. Strain stress curves for longitude and transverses direction

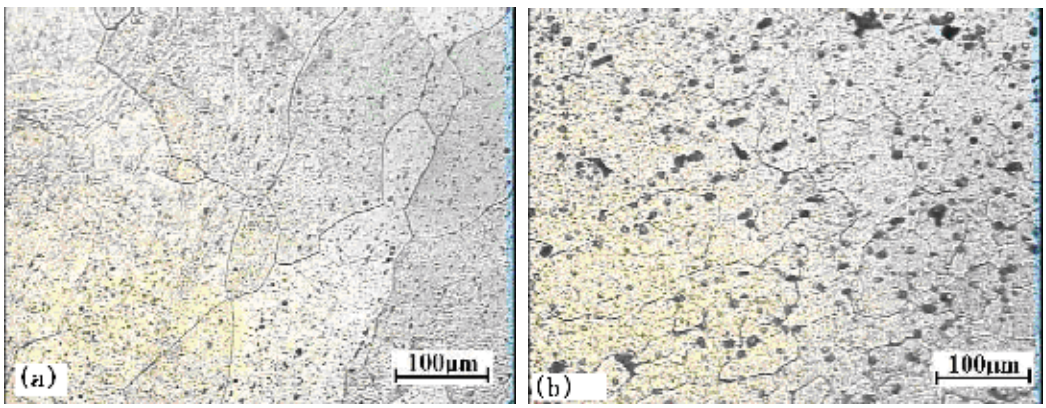

Fig. 5. Microstructure comparison between surface and centre area
(a) Surface (b) centre area

Fig.7 compares smooth tensile test with notch tensile test, the notch radius is 4mm, the test showed that the deformation resistance increased at notch condition. With the same deformation, load of smooth test is lower. Triaxiality is bigger at the foot of notch under geometry restraint. In the simple tensile process, larger additional stress derived from the thickness and width direction, and then tri-axis tensile stress formed. Effective shear stress or equivalent Mises stress that ductile deformation needed decreased, which would lead to

ductile difficulty. From the microcosmic aspect, minish the, stress triaxiality of increased with notch radius reducing; stress concentration increased at the foot of the notch, ductility decreased, and fracture strain decreased too. The yield strain of the notch specimen is 4.19%,which is only 35% of the engineering strain of smooth tensile specimen. From the experiment analysis, it's clear that stress condition is not related to yielding obviously, but it matters badly to losing effectiveness of fracture.

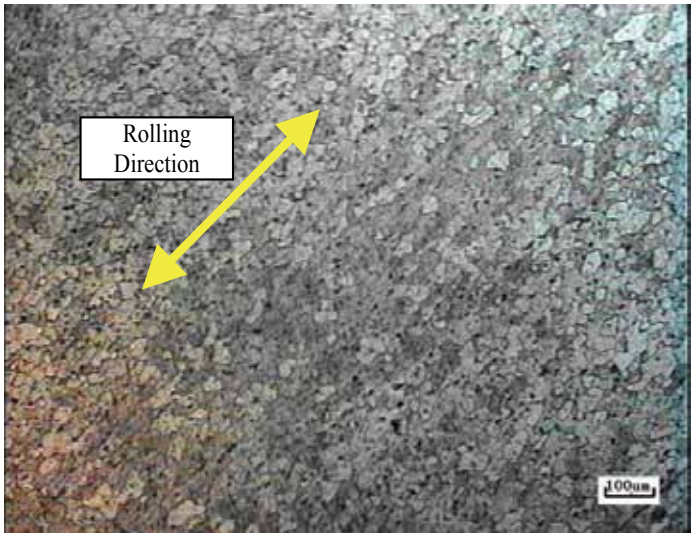

Fig. 6. Microstructure of rolling plate 5052H34

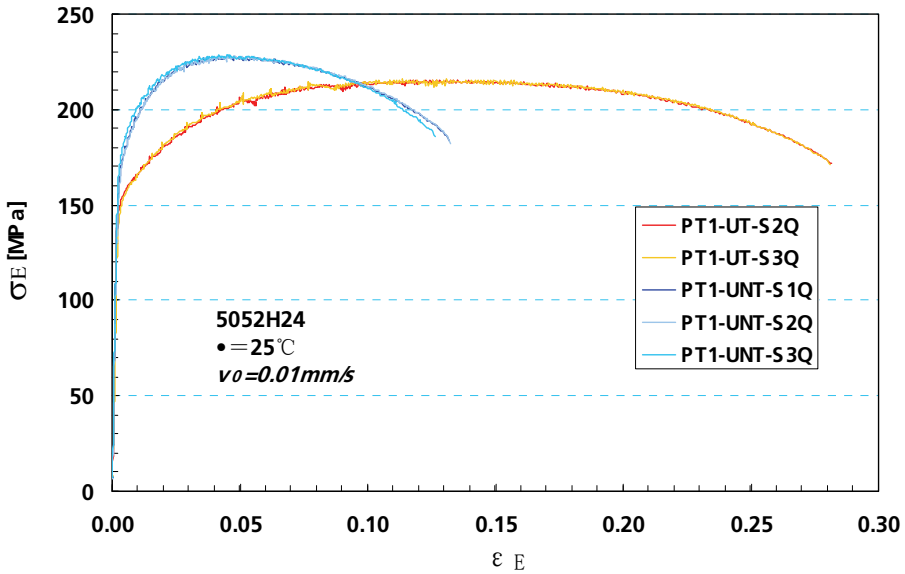

Fig. 7. Strain stress curves of smooth tensile and notch tensile

2.1.4 Dynamic tensile test

1. **Experiment equipment and measurement principle**

Most of the transportation accidents happened at the velocity of 50Km per hour, the impact kinetic energy of mid-weight car can be up to 150KJ. And the strain rate of these similar impact accidents is about $100s^{-1}$, but the limitation of local strain rate is within $1X10^{-3}$. Mostly, the strain of dynamic test is in the scale of $102\sim103s^{-1}$ on the basis of safe impact design. Currently, the applied test equipments are as follows:

a. Falling weight device

Different heights of falling hammer acquire various kinetic energy, experiment data are collected and processed by using signal processing device. Advantages of such devices are simple structure, easy operation and low costing. It fits impact tests of the level of 10m/s. Previously, there have been such devices such as Qsinghua University; State Key Laboratory of Automotive Safety and Energy and Haribin institute of technology throughout the nation.

b. Ejection experiment devices

There are vertical type and horizontal type, it gains great speed by exploded high energy balloon, the specimens are fastened on data acquisition board with piezoelectric sensor, specimens are impacted with hammer loaded with different masses, while record the impact process with high-speed camera. Advanced digital shooting technology can acquire video image of 10000 frames per second, and the frequency of impact data reach up to 200kHz.At present, all the advance institute are capable of this test, such as Cambridge, Kaiserslautern University and Fraunhofer IWM mechanical institute ,who use this device to test impact responses of components.

c. Improved Hopkinson draw(press) poles test devices

This method is first proposed in 1914, it's the earliest method of testing transient state pulse stress. lately, many researchers changed and developed this method, in which the improved discreet Hopkinson draw poles by Koisky is the most typical one, that has become major testing tool of dynamic property of material. This kind of experiment is taken in metallic large deformation dynamic mechanism response of strain rate within $102\sim104s^{-1}$.

The key point of Hopkinson's testing technology is to assure that separate the stress wave effect with dynamic buckling effect within the impact load. Therefore, the incidence pole and test pole of the test device are designed to be longer, in order to separate the influence from reflex waves of press pole, so the equipment would take much space. On the other hand, due to the strict restriction of specimen size, which could make sure ductile stress wave in the component take small proportion in structure buckling response time, compress stress is well distributed in components. Key physical qualities need to be determined in this experiment are as follows:

Input response of impact load

Response, value and distribution of structural load

Response, value and distribution of structural displacement

Strain rate of material, the key formula are as follows:

Process of impacting load

$$P(t) = A_I E \varepsilon_I(t) \tag{1}$$

Course of input and output loading response of components

$$F_{input}(t) = A_I E\left[\varepsilon_I(t) + \varepsilon_R(t)\right] \tag{2}$$

$$F_{output}(t) = A_0 E\varepsilon_I(t) \tag{3}$$

Course of input and output displacement response of components

$$S_{input}(t) = C_0 \int_0^t [\varepsilon_I(t) - \varepsilon_R(t)]dt \tag{4}$$

$$S_{output}(t) = C_0 \int_0^t \varepsilon_I(t)dt \tag{5}$$

A1 and A0 represent section surface of input pole and output pole superlatively, E represents elastic modulus; $\varepsilon_I(t)$ is course of input strain and$\varepsilon_R(t)$ is the course of response strain.

Since the disadvantages of complexity and bulky of Hopkinson's test device, many researcher have improved it in recent years (Nicholas et al., 1982). One case is to replace impact devices to concussive bullet shoot by high-pressure gas gun, which reduced the size of device greatly and the flexibility increased as well. This innovation made dynamic impacting tests popular.

d. The improved ejection test device in this research

Considering the effectiveness and convenience of dynamic tensile experiment, making full use of previous equipment, a new particular type of dynamic tensile device-Instron VHS dynamic tensile test machine in Fig.8 was used in this research. Components of such experiment system can be show in Fig.9, including three significant part.

1. Executive part of loading. Pneumatic chuck is the key part, Fig.10 shows the prepare condition of the part before testing, the upper is tied on the fixture, well the below is connected with following system. When the below fixture of testing machine reaches certain speed downside driven by high-energy gas, follow up system would fasten fixed part of the specimen below, which could make the down fixture move along with specimen below synchronously.

2. Zimmer laser-transient displacement high speed photography and force testing part. When lower clip tied up with specimen to move downward synchronously, this would trigger the laser sensor at the same time, and then turn on the high-speed camera, which would record deformation and displacement of the specimen with the scale distance. Sampling frequency of shooting is 2500fps. Analyze relationship between displacement and time of scale boundary by means of later digital image processing. Comparison of calculation error and data of local foil gauge is smaller than 5%.Measurement of tensile load via acceleration sensor to multiply instantaneous acceleration by quality to get changes of system dynamic load. Formula 3.6 shows the calculation in details

$$P(t) = M[g + a(t)] \tag{6}$$

Where P (t) is instantaneous tensile load represents movable chuck component is acceleration, a (t) is instantaneous acceleration. Accordingly, whole deformation energy and impact energy can be derived by integral calculus of compounded load-displacement.

3. Data collection system. It includes digital oscillograph, later treatment part of computer. Digitalize the amplified signal, with filtering waves; lastly, digital documents will be stored in computer. The filtering process adopted high-frequency filtering circuit and spine fit smoothing technique of ultimate data. The advantages is that sorting of wave characteristics can be artificially controlled, in accordance with various experiment condition to choose filter function, which can avoid data distortion inn filtering by means of adjusting smoothness. Common spline function is demonstrated in formula 7

$$f_t^{'} = \frac{1}{32}(5f_{i-1} + 22f_i + 5f_{i+1}) \tag{7}$$

f_{i-1}, f_i, f_{i+1}, represent function value of i-1, i and i+1. f'_t represent the function value after t times filtering, this function can be iterated endlessly till the result is satisfied.

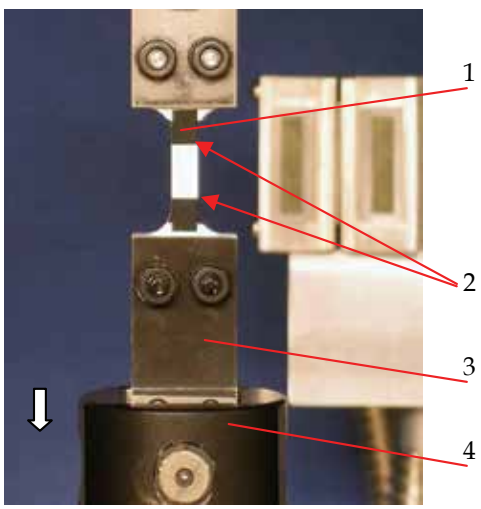

Fig. 8. Dynamic tensile test
1 sample, 2 fixture boundary, 3 fixture, 4 cross head

e. Size of specimen and initial conditions

Specimen size is as same as the static tensile one; orientation of specimens is perpendicular to rolling directions. Install foil gauges symmetrically on two sides of the specimen within the measure scale before experiment, so as to adjust twist error in dynamic tensile test. Meanwhile print glisten glue of light colour in the centre of test zone, which is used to high-speed photography. Finally fix the whole specimen in the tensile fixture, and adjust laser trigger.

2. **Experiment result**

Relationship among engineering strain, initial tensile velocity and scale distance in dynamic tensile test can be demonstrated as

$$\dot{\varepsilon}_{nom} = v_0 / L_c \tag{8}$$

In this experiment, it's certain that initial velocity of fixture v_0 is 1.7m/s, scale distance is 10.08mm. Average strain rate is 169s-1, according to formula 8 at tensile condition. Fig. 9 shows the curve of load-displacement at dynamic tensile condition. Fig. 10 demonstrates the relationship among engineer-stress, strain and true stress-strain.Fig.11 shows the comparison between dynamic load and static true stress.

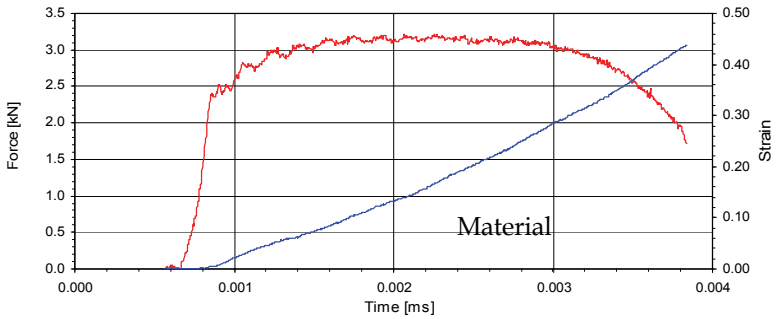

Fig. 9. Load and displacement curve

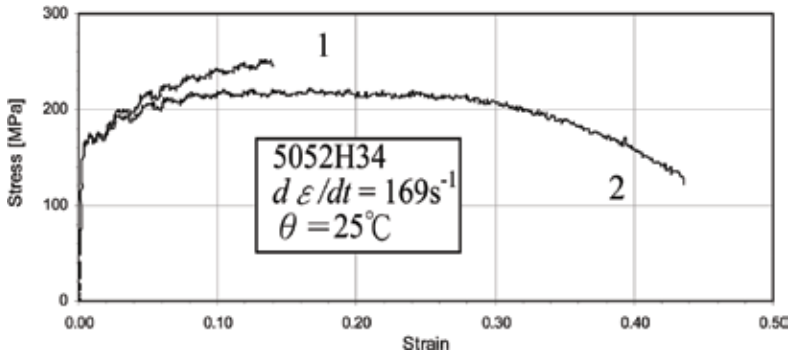

Fig. 10. 5052H34 strain stress curves
1 true strain and stress, 2 engineering strain and stress

Fig.12 is the comparison of engineer stress-strain measured by static notch tensile, smooth tensile and dynamic load smooth tensile test.Fig.13 shows that static and dynamic strength of material and plasticity index vary with strain rate. The data imply the slight improvement of the aluminium alloy strength with the strain rate increase from dynamic to static tensile, by contrast, the fracture strain increase by 60%, shrinkage of section increase by 18%, which means the ductility is enhanced. High-speed deformation is done in short time in dynamic loading test, a lot of heat is generated and unable to consume, so it could be treat as a non-exchange heat process with the outside. So temperature of local material would rise dramatically, mechanism response of material has become a heat-stress coupling problem. On the basis of document, as for Al-Mg-Si alloys, work hardening and dynamic softening are concurrence under condition of large strain rate, they are paradoxical on the affection of mechanism property. In the process of elastic deformation, crossing, propagation and accumulation of dislocation lead to networks of dislocation, which caused work hardening, the higher the strain rate is, the larger resistance of slip movement of dislocation will be.

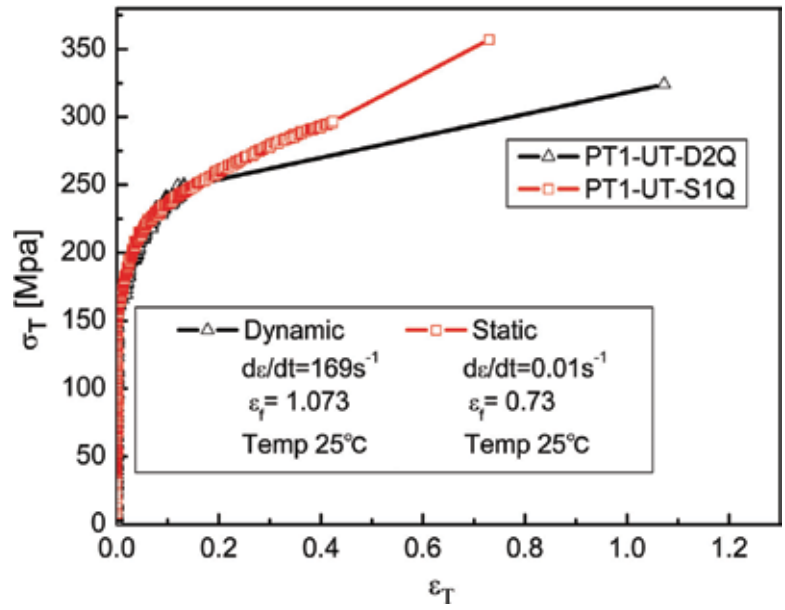

Fig. 11. Dynamic and static true stress and strain curves

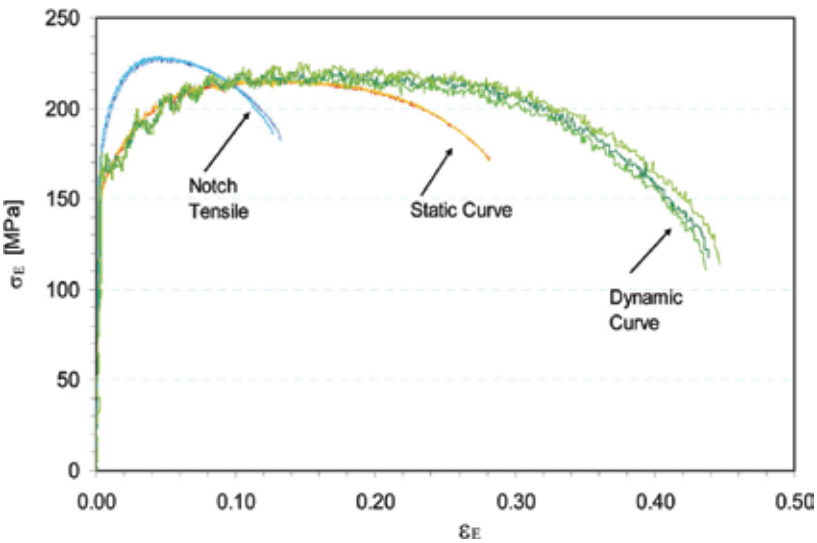

Fig. 12. Effects of stress state and strain rate on material flow property

Material deforms in the way of twin crystal, yield stress and flow stress grows with the increase of strain rate. But, as for aluminium alloys, R.Mignogna.etc found that the strain rate sensitivity is lower at temperature index is smaller than 0.1, so yield stress would improve slightly with the increase of strain rate. Comparing with the 6063 aluminium alloy, data of stress-strain rate hit off with our result (Fig.13).With the temperature increasing, strain sensitivity grows significantly. When the temperature surpasses half of the melting point, m values between 0.1 and 0.2.

All in all, notch sensitivity of aluminium alloy 5052H34 is strong. With stress triaxiality grows, the plasticity decrease. However, dynamic and static tensile test prove that material strength at room temperature is not sensitive with strain rate, but sensitively grow with increasing of ductile strain rate, which has close association with dynamic softening in thermal isolation process. We need to fully consider affection of temperature to plastic flow in constitutive model of material. Temperature's influence on flow stress will be discussed in detail in up coming chapters.

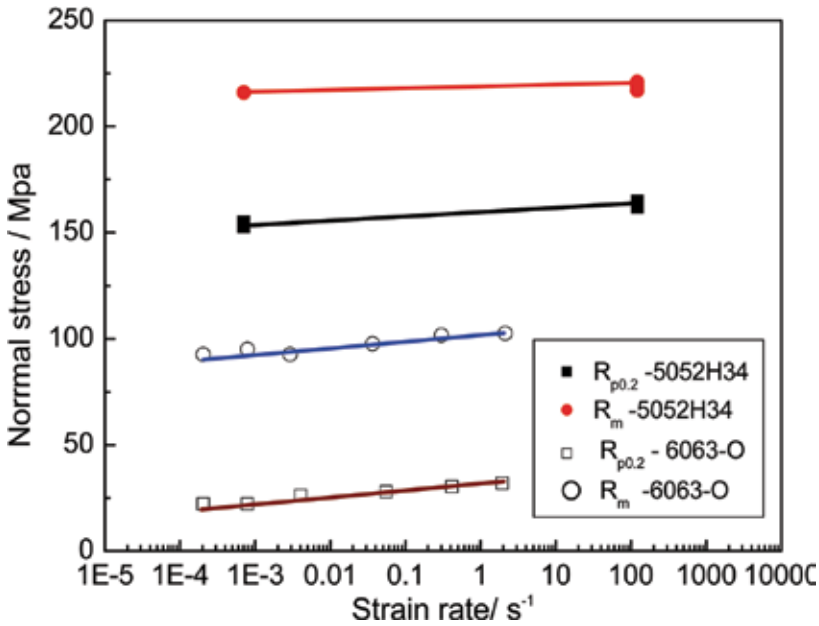

Fig. 13. Relationship between strength and strain rate

2.2 Shear test

2.2.1 Introduction of shear test.

Shear damage is one of the most common failure in car crashes. Especially, the thin-walled components such as buffing tubes and frameworks, etc. Shearing, buckling and tearing always happen in crashes. So, how to use simple and effective method to research shear deformation and failure detail, acquire characterization of key materials that really matter to whole characterization and model-building.

Previously, shear test such as twisting, quasi-static punching and Iosipescu shear test have been widely accomplished throughout the world. Precision and effectiveness of these tests have been confirmed by numerous application, but it still proved its limitations. Generally, Iosipescu and twisting tests are used in static experiments, and can hardly expand to dynamic shear research of high strain rate. In this case, we are trying to design a kind of new double notch shear test and method, which could be adopted in static and dynamic shear validation. So as to confirm effect of this new type of shear test, we used Iosipescu test as a reference to analyze the advantages and disadvantages of this double notch test.

2.2.2 Specimen size and experiment equipment

1. **Double notch shear test**

In this experiment, we designed a kind of tensile specimen to test failure process and shear damage of plate materials.Fig.14 shows the appearance and sizes of specimen. Notching at two parallel sides of the specimen, notch angle with the neutral axis is 45 degree. The design of other geometry parameters is identical with normal tensile specimen. Fix the specimen on tensile test machine during experiment, the minimum available section is the plane between two notch tips, where would occur yielding very first at tensile process, and then shear deformation develop in the direction of tensile axis till facture.

In order to observe the deformation between two notches during tensile process, draw the grid lines on main deformation zone before experiment. Record the process of deformation by digital shooting system, while output the data of load and displacement within scale distance. Fig.15 (a) shows the control panel of the experiment and (b) shows test device.

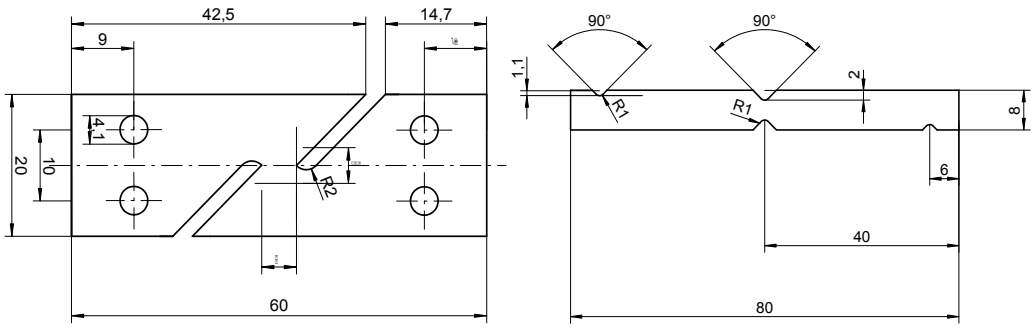

Fig. 14. Sample sizes for shearing test
(a) Double notch tensile test, (b) Iosipescu shearing test

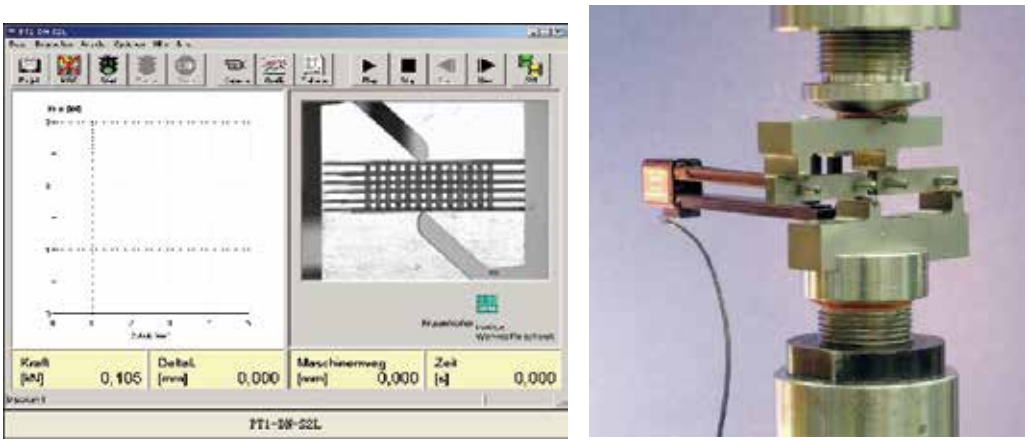

Fig. 15. Shearing test devices
(a) Interface of monitoring system for double notch tensile test
(b) Equipments for shearing test

2. Iosipescu shear experiment

Fig.14 (b) shows the specimen size,Fig.15(b) is the experiment device. The specimen is fixed on test machine with four rigid cylinders. With up chuck pushing downward, specimen would be damaged and shear deformed. According to force analysis, theoretically, shear place should locate on the vertical surface of the specimen's central symmetrical axis. Local deformation can be measured by strain gauge, meanwhile record the process by digital photography.

Under static condition, the loading rate of double notch test and Iosipecu test is 0.001m/s.Type of testing machine: Instron material tensile testing machine.

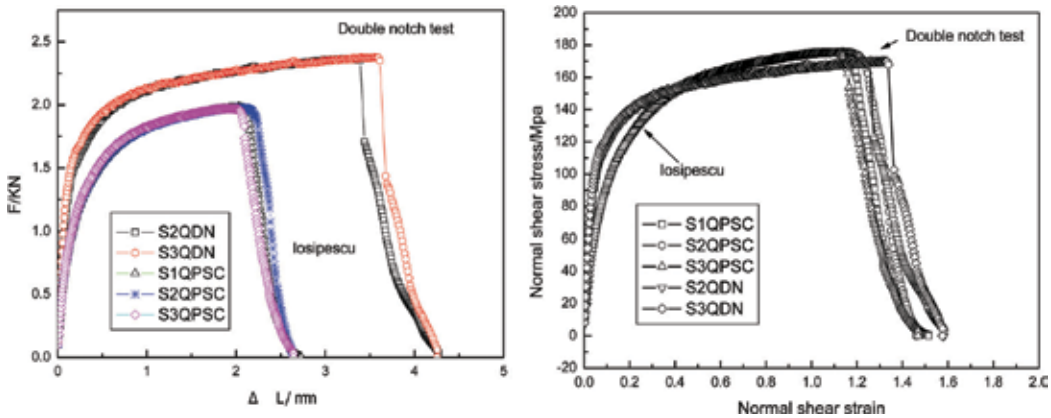

Fig. 16. Displacement and load curves for double notch tensile and Iosipescu shearing test

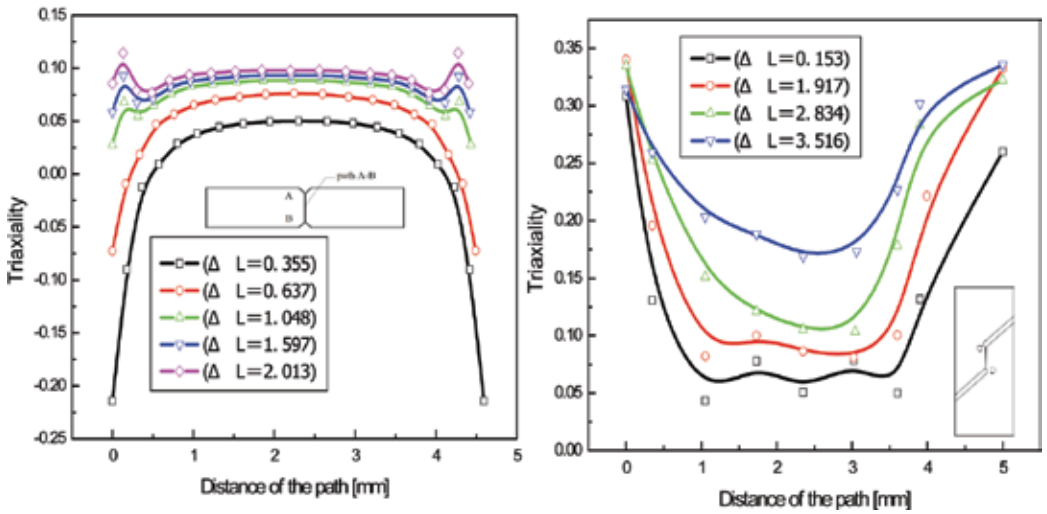

(a) (b)

Fig. 17. Comparison of triaxiality for Iosipescu and double notch tensile
(a) Iosipescu shearing test, (b) double notch tensile test

3. **Test results**

The displacement and load curves of shear tests are shown in Fig. 16. When deformation is small than 0.5, the strain stress curve of double notch tensile test is higher than Iosipescu; when the deformation is larger than 0.5, the curve of Iosipescu exceeded that of double notch tensile. The maxim stress of double notch tensile test is 169.8MPa as well as 175.6MPa of Iosipescu. The difference is 3.3%. The fracture strain is 1.28 for double notch tensile and 1.6 for Iosipescu. The difference is 9.3%. In a general view, the results of two experiments have good agreement with each other, which means the double notch tensile test is comparable for a standard shearing test.

Fig.17 shows the evolution of triaxiality during deformation for double notch tensile test and Iosipescu shearing test. It can be seen from the results that average value of triaxiality about DNT (double notch tensile) is from 0.1 to 0.3, mean while, the triaxiality changed from 0.05 to 0.15 for Iosipescu shearing test.

Fig. 18 shows the distribution of stress state and concentration for the two kinds of tests.

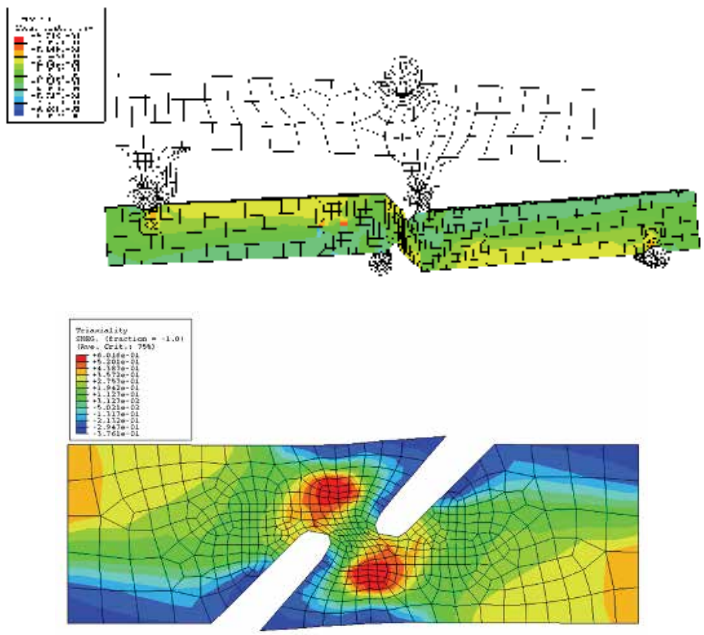

Fig. 18. The distribution of triaxiality for Iosipescu and double notch tensile test

3. Inhomogeneous deformation and damage modelling for aluminium alloy welded joints

3.1 Experiment procedure

The small punch test (SPT) has been used by numerous researchers to test mechanical properties of various materials, especially for steel, copper, magnesium and aluminium. The test programme and experimental setup are described in great detail in related reference (Asif et al., 2004). Based on the general idea of SPT, a small punch-shearing test setup was established for this study. In brief, it consists of a thin sheet specimen with the thickness of 2mm, specimen holder, shear punch, punch die, and fixture.

There are two types of specimens used in this study. One is made of homogeneous materials, such as Al alloy 6063. The other is made of inhomogeneous materials such as a sheet butt joints welded by TIG. The specimens were shaped 24mm×50mm rectangular pieces. The surfaces of the specimen are mechanically polished by emery paper (grain size 320) to obtain the desired thickness (i.e. 2 mm thick) in each case. Fig.19 shows the schematic diagram for the small punch test experimental setup.
A special rigid punch of 1.5 mm diameter with a flat tip was designed for small punch test. The offset of the diameter is less than ±0.03mm. In order to concentrate the punch plastic deformation below the punch area, a small clearance between punch and dies was left during punch test. The clearance was identified by equation 1.

$$z = mt \tag{9}$$

Where z is the maximum clearance between punch and dies, m is correlative coefficient. For aluminium alloy m, it is equal to 0.06, and t is thickness of the specimen. For example, for the aluminium alloy 6063 sheet specimen, if the thickness is 2mm, Z is 0.12mm. Therefore, considering the accuracy of punch, geometrical dimension of the punch die would be less than 1.77mm.
Specimen holders and lower dies were included in a homocentric structure, which keeps the upper holder precisely fitting the lower die. Rectangularly shaped specimen was placed into the lower die, and was fixed by four screw bolts. Miniature specimens are carried out at room temperature and static condition using an instron testing machine. The loading speed of punch was 0.5mm/min. For each case, at least three punch specimens were tested to ensure the stability of results.

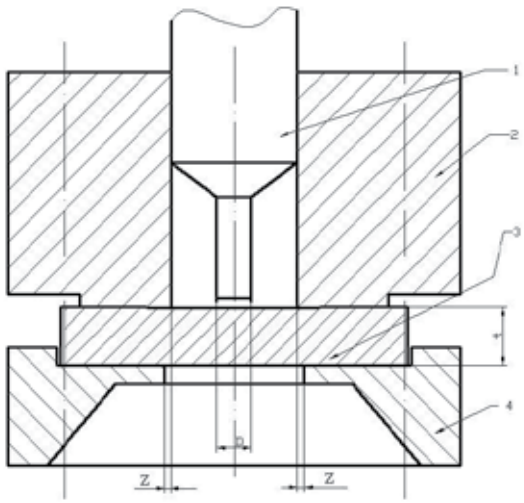

Fig. 19. Experimental setup of the STP
1. punch, 2. holder, 3. sheet specimen, 4. die

Three types of homogenous materials: copper; Al alloy 5052; and Al alloy 6063 T5 were tested by the small punch test setup. Their displacement vs. punch force curves are shown in Fig. 20. During the punch process, the specimen had experienced three specific deformation stages. First, elastic deformation, then plastic deformation and finally a

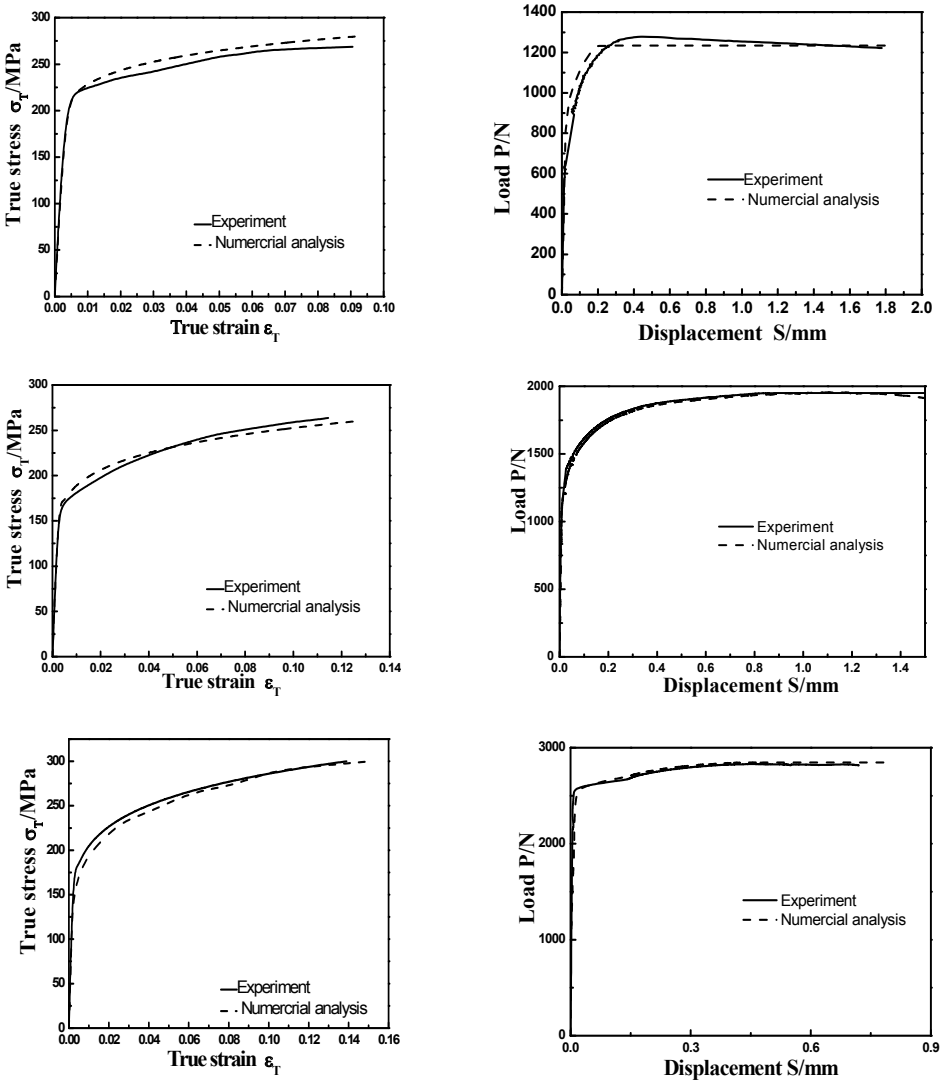

Fig. 20. True strain-stress and load-displacement curves of SPT

fracture. The specimen surface was subjected to a composition of shear force, friction force, and pure pressure.

3.2 Inverse finite element procedure

For this study, the inverse FE procedure was tried to identify the true strain stress curve of unknown materials. The experimental load-displacement curve is used as an input in linear, step by step, iterative process of FEM for comparison. The outputs of this inverse procedure are: the modulus of elasticity of the unknown material; true stress vs. true plastic strain curve, starting from yield stress and corresponding zero plastic strain. The pictorial algorithm is shown in Fig. 21 and the iterative process is expressed as follows:

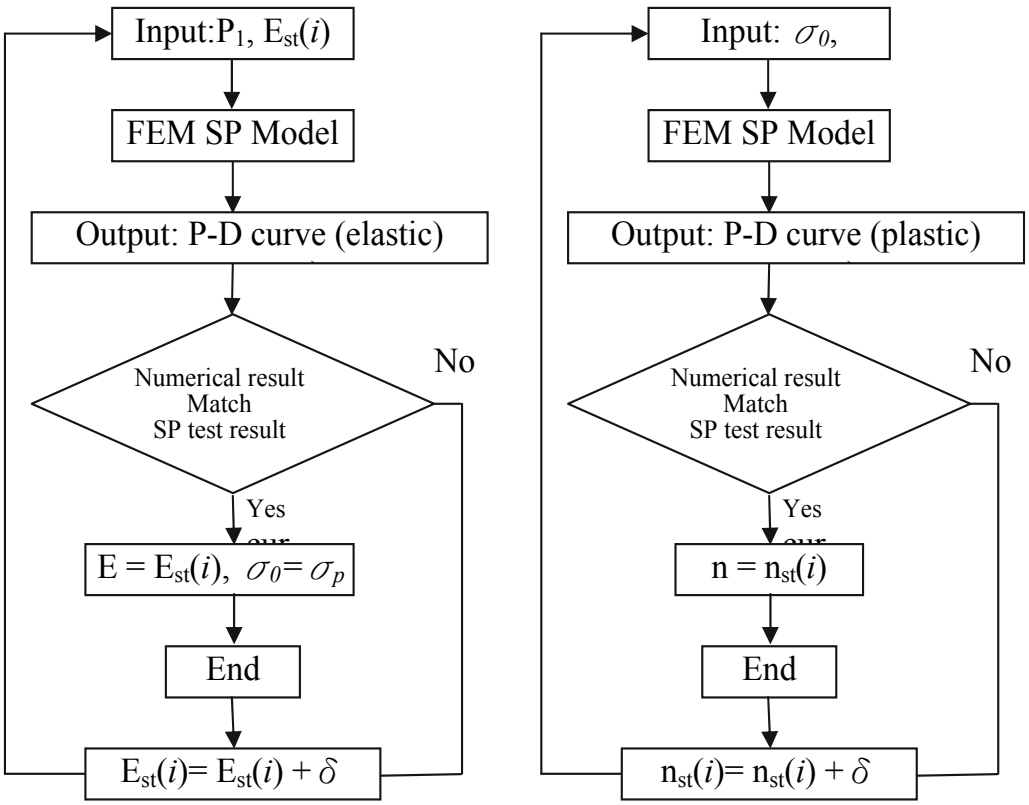

(a) Elastic part (b) Plastic part

Fig. 21. Diagram of inversed FE procedure from SPT

1. the small punch experimental load *vs.* displacement curve is divided into two parts. One is the elastic linear segment. The other part is nor linear elastic-plastic segment, which can be expressed by the exponent function of Eq. (2).
2. for the iterative process of the elastic segment, the inputs are punch load P1 (elastic peak load) and an assumed starting value of modulus of elasticity E_{st}. The outputs are punch load *vs.* displacement curve which try to match the actual experimental load-displacement curve by increasing or decreasing E_{st} during each iteration step (value of δ). The final value of E_{st} should be equal to modulus of elasticity E of the material and maximum equivalent von-Mises stress of the specimen equal to the yield stress of the material.
3. for the iterative process of the elastic-plastic segment, the true stress and strain can be expressed as equation (10).

$$\sigma = \frac{\sigma_0}{\varepsilon_0^n}\varepsilon^n \tag{10}$$

Where the σ, ε are true stress and strain; σ_0, ε0 are yield stress and yield strain, which has been from the previous step (2); n is the hard coefficient. During this nonlinear segment, the inputs are σ_0, experimental maxim punch load P_k and assumed hard coefficient n_{st}. The outputs are punch load *vs.* displacement curve which was matched to that of experimental data by changing the value of n_{st} . the final value of n_{st} would be equal to the hard coefficient n of the material.

4. after the iterative calculation, the mechanical property of the unknown material can be described by material parameters of elasticity modulus E, yield stress and strain σ_0, ε0, and hard coefficient n.

3.3 Validation of material modeling and discussion

3.3.1 Mechanical behavior determination for homogeneous materials

Fig. 20 shows the comparison between true stress-strain curves obtained from the uniaxial tensile test and those of predicted results using inverse FE arithmetic for SPT specimens of three different materials. The results show that numerical models agree well with the experiment data.

3.3.2 Case of material modeling for butt welded joint

In a welded joint, the microstructure, grain size and mechanical properties are quite different in each specific zone such as HAZ, weld, and base metal. Considering the mechanical heterogeneity the butt joint was divided into ten micro-portions from base metal to welded metal (see Fig. 22) according to the hardness distribution as showed in Fig. 23. Accurate mechanical tension behavior of each micro-portion was obtained by the inverse finite element procedure (Fig. 24). Finally a uniaxial tension numerical model was set up according to the experimental condition. Material properties obtained from the inverse FE procedure were assigned to the specific micro zones. General tensile mechanical behavior was calculated by the ABAQUS finite element code. The simulated and experimental strain-stress curves are presented in Fig.25. The simulation results are in good agreement with thoses of experiments, which means that the mechanical properties obtained from the sp test and inverse FE procedure are believable.

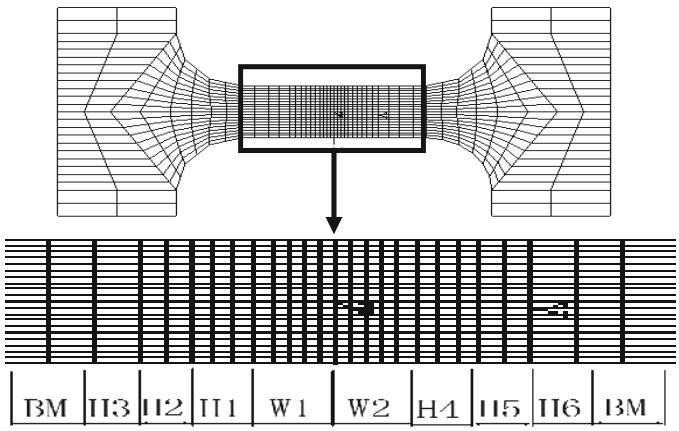

Fig. 22. Micro-portions distribution of butt joint

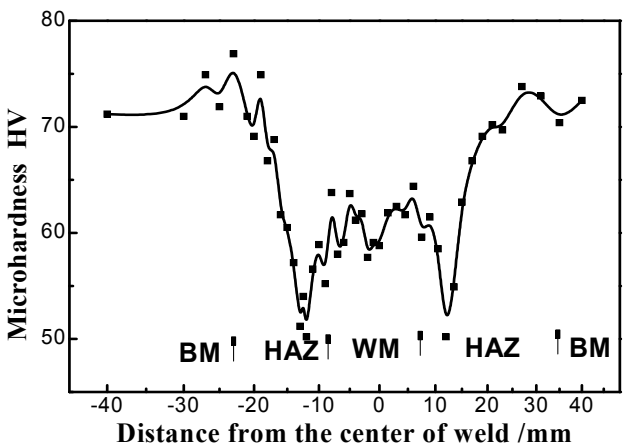

Fig. 23. Hardness distribution of butt joint (6063T5)

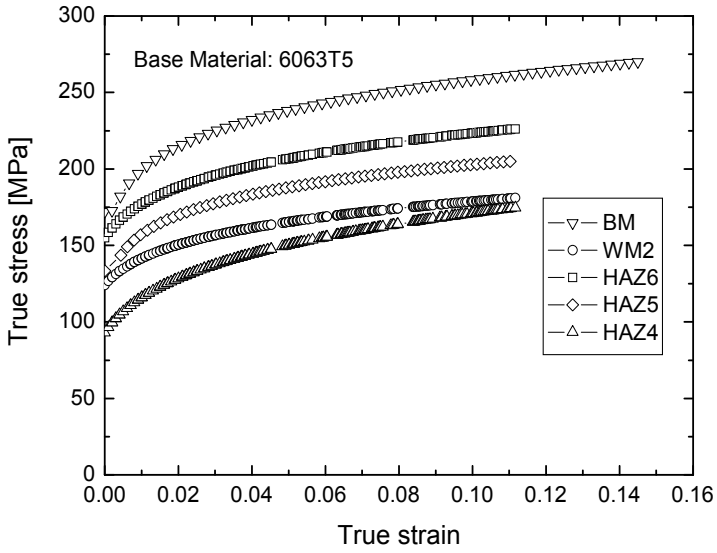

Fig. 24. Uniaxial tensile behavior of different micro zones of joint (6063T5)

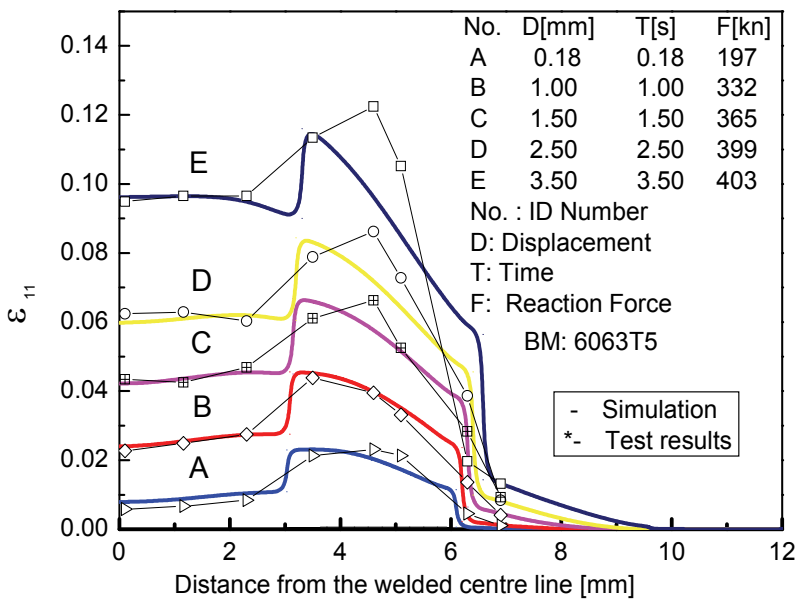

Fig. 25. Evaluation of Inhomogeneous deformation of a welded joint

4. Conclusions

In the current work, aimed at aluminium alloy 5052H34 and 6063T6, material characterization and modelling have been carried out. Material plastic deformation and damage initialization and evolution were studied under static and dynamic loading with different stress state and strain rate.

In addition that, a new experiment double notch tensile was expressed with related evaluating standard and sample size as well. The test precision was discussed with Iosipescu shearing test by using experimental and numerical data. Results show that the double notch tensile test is a suitable measurement for mater mechanical behaviour driven by shear stress. It can be used not only for static loading but also for dynamic impacting. Combined with Iosipescu shear test, uniaxial tensile and notch tensile test, strain stress relationship and damage parameters were obtained for the two kinds of aluminium alloy.

For the inhomogeneous deformation and damage of welded joints, an inverse FE algorithm based on a SPT experiment was represented for determination of constitutive behaviour of an unknown material. A numerical simulation of SPT to identify the accurate material parameters was carried out. The inverse FE procedure was tested and validated on a case of a butt joint of aluminium alloy 6063T5. The welded joint was divided into ten micro zones along the tension axis. Localized mechanical properties were assigned to the specific sections of joint. Finally the global mechanical behaviour of welded joint was simulated by a numerical model. The numerical tensile load-displacement curve agrees well with the experimental results.

5. Acknowledgments

This work was substantially supported by The Nature Science Foundation of China (Project No.51065016), and Foundation of Science and Technology of Gansu Province (Project No. 0702GKDJ009). The author wish to thank Fraunhofer Institut Werkstoffmechanik for their support during testing of mechanical behavior.

6. References

Asif Husain, Sehgal D K, Pandey R K. An inverse finite element procedure for the determination of constitutive tensile behavior of materials using miniature specimen, Computational Material Science, 2004 (31): 84-92

Blauel J.G, Sommer. Crashtests and numerical simulation of welded aluminium component with defects. In: 3rd international symposium “Passive safety of rail vehicles”. Berlin, 2002，57－61

Campitelli E, Spa¨tig P, Hoffelner W. Assessment of the constitutive properties from small ball punch test: experiment and modeling, Journal of Nuclear Materials, 2004 (335) : 366-378

Sun D-Z, Silk Sommer. Characterization and modeling of material damage under crash loading. In: 21st CAD-FEM Users’Meeting. Berlin,2003,98-103

Franck Lauro, Bruno Bennani. Identification of the damage parameters for anisotropic materials by inverse technique: application to an aluminium.Journal of Materials Processing Technology.2001,118(3):472-477

Ghoo B Y, Keum Y. Evaluation of the mechanical properties of welded metal in tailored steel sheet welded by co2 laser, Journal of Materials Processing Technology, 2001 (113) : 692-698

Hankin G, Toloczko M B, Hamilton M L, et al. Validation of the shear punch-tensile correlation technique using irradiated materials, Journal of Nuclear Materials, 1998 (258) : 1651-1656

Johann Georg Blauel, Wolfgang Bosshme. Material characterization for crash simulation. In: CrashMat 2002.2. Berlin,2002,46-50

Nicholas T. Material behavior at high strain rates. Impact Dynamics. New York : John Wiley & Sons, 1982

Zhu Liang, Chen Jianhong. The stress distributions and strength of the welded joints with mechanical heterogeneity. Proceedings of the International Conference on Heterogeneous Materials Mechanics, China Chongqing, 2004:18-24

Part 3

Fatigue, Fracture and Cyclic Deformation Behaviour

9

Cyclic Deformation Behaviour and Its Optimization at Elevated Temperature

Patiphan Juijerm[1] and Igor Altenberger[2]
[1]*Department of Materials Engineering, Kasetsart University*
[2]*WIELAND-WERKE AG, Central Laboratory, Research & Development*
[1]*Thailand*
[2]*Germany*

1. Introduction

Recently, low-weight components are particularly required for environmental, ecological and economical aspects. Therefore, light-weight metals/alloys are frequently mentioned and selected for many applications where low density and high strength to weight ratios are an important consideration. Consequently, development and improvement in the field of light-weight alloys can be seen continuously for advanced applications in automotive as well as aerospace industries, where many applications involved about elevated temperature are increase. One of the most important light-weight metals is aluminium and its alloys which possess many attractive characteristics including excellent corrosion resistance in most environments, reflectivity, high strength and stiffness to weight ratio, good formability, weldability and recycling potential. Certainly, these advantageous properties make them ideal candidates to replace heavier materials (steel or copper) for several industries. Therefore, mechanical behaviour of aluminium alloys becomes more and more important, especially under cyclic loading at room and elevated temperature due to failures occurring in machinery components are almost entirely fatigue failures. Accordingly, cyclic deformation behaviour of aluminium alloys was investigated and also improved by well-known mechanical surface treatments, e.g. shot peening, deep rolling and laser shock peening. Deep rolling is one of the most well-known mechanical surface treatment methods and exhibits a great depth of near-surface work hardening state and compressive residual stresses serving to inhibit or retard fatigue crack initiation as well as crack growth (Scholtes, 1997; Wagner, 1999; Schulze 2005). However, the outstanding benefits of the deep rolling treatment are insecure under high-loading and/or elevated temperature conditions due to occurring relaxation of near-surface macroscopic compressive residual stresses as well as work hardening states. In this case, a detrimental effect on the fatigue lifetime can be expected, particularly in smooth, soft and mechanically surface treated materials, such as deep rolled aluminium alloys because their fatigue lifetime depends significantly on the stability of near-surface compressive residual stresses as well as work hardening states (Altenberger, 2003). Therefore, the main purpose of this research is to investigate systematically the cyclic deformation behavior of the deep rolled aluminium alloys at room and elevated temperature. Wrought aluminium alloys AA5083 and AA6110 were selected

and investigated in this research representing typical non-precipitation-hardenable and precipitation-hardenable aluminium alloys, respectively. The precipitation-hardened aluminium wrought alloy AA6110 (Al-Mg-Si-Cu) was heat treated to the as quenched, under-, peak- and over-aged conditions. The cyclic deformation as well as fatigue behavior have been investigated systematically at room and elevated temperature. The effects of static/dynamic precipitation occurring during fatigue at elevated temperatures was analyzed and discussed by means of the cyclic deformation and s/n curves. To optimize the fatigue behavior and performance, deep rolling was performed a room temperature. Residual stresses and work hardening states near the surface of the deep rolled condition were characterized by X-ray diffraction methods. Depth profiles of residual stresses, full width at half maximum (FWHM) values of the X-ray diffraction peaks and microhardness near the surface of the deep rolled conditions are presented. The cyclic deformation behavior and s/n curves of deep rolled specimens have been investigated by stress-controlled fatigue tests at room and elevated temperatures up to 250 °C and compared to the non deep rolled condition as a reference. The effect of deep rolling on the fatigue lifetime and residual stresses under high-loading and/or elevated-temperature conditions will be discussed.

2. Materials and experimental procedure

The aluminium wrought alloy AA5083 was delivered as warm rolled sheet with a thickness of 15 mm. The chemical composition of this alloy is 0.4% Si, 0.4% Fe, 0.1% Cu, 0.4–1% Mn, 4.5% Mg, 0.05–0.25% Cr, 0.25% Zn, 0.15% Ti and Al balance (all values in wt%). The aluminium wrought alloy AA6110 was delivered as extruded bars with a diameter of 34 mm. The chemical composition of this alloy is 0.86 Si, 0.19 Fe, 0.45 Cu, 0.46 Mn, 0.78 Mg, 0.17 Cr, 0.02 Zn, 0.01 Ti and Al balance (all values in wt%). Aluminium alloy AA6110 specimens were solution heat treated in an argon atmosphere furnace at 525 °C for 30 minutes followed by water quenching to room temperature. Quenched specimens were aged immediately at 160 °C for 1, 12 and 168 hours (1 week), which will be designated as under-, peak- and over-aged, respectively in the following discussion. Important mechanical properties of investigated aluminium alloys are given in table 1. Cylindrical specimens with a diameter of 7 mm and a gauge length of 15 mm were prepared. The loading direction during fatigue investigations corresponds to the extrusion direction of the bar or sheet. For deep rolling, a hydraulic rolling device with a 6.6 mm spherical rolling element and a pressure of 100 bar (80 bar for the as-quenched condition) was applied at room temperature. Tension-compression fatigue tests were conducted with a servohydaulical testing device under stress control without mean stress (R = -1) and with a test frequency of 5 Hz. Strain was measured using capacitative extensometers. Residual stress depth profiles were determined by successive electrolytical material removal using the classical $\sin^2\Psi$-method with Cu-Kα radiation at the {333}-planes and $½\ s_2 = 19.77 \times 10^{-5}\ mm^2/N$ as elastic constant. Near-surface work hardening was characterized by the full width at half maximum (FWHM) values of the X-ray diffraction peaks and by microhardness measurements. All residual stresses and FWHM-values were measured in longitudinal direction of the specimens. No stress correction was carried out after electrolytical material removal of surface layers.

	Ageing parameter	Hardness [HV]	$\sigma_{0.2}$ [MPa]	UTS [MPa]	Elongation [%]
AA5083	–	90	185	295	19
as-quenched AA6110	–	84	155	302	33
under-aged AA6110	160 °C, 1 hour	125	292	400	28
peak-aged AA6110	160 °C, 12 hours	139	425	455	22
over-aged AA6110	160 °C, 168 hours	120	393	413	24

Table 1. Some mechanical properties of aluminium alloys AA5083 and AA6110

3. Cyclic deformation behaviour at room temperature

The fatigue lifetimes at room temperature of aluminium alloys AA5083 and AA6110 in different ageing treatments are shown as non-statistically evaluated s/n-curves in Fig. 1. Due to quite similar hardnesses of the under-, peak- and over-aged conditions, no significant differences in fatigue lifetime between under-, peak- and over-aged AA6110 at room temperature are seen. Obviously, for these investigations of AA6110, if the hardness is significantly lower as in the as-quenched condition, fatigue lifetimes are lower when compared with aged conditions in low cycle fatigue regime. Although fatigue lifetime of the under-, peak- and over-aged conditions show no significant differences, their cyclic deformation behaviour was distinctly different because of the different size and structure of precipitates within the matrix. Cyclic deformation behaviour of aluminium alloys is associated by dislocation-precipitation and/or dislocation-dislocation interaction during cyclic deformation (Srivatsan & Coyne, 1986; Srivatsan, 1991). The AA5083 and as-quenched AA6110 contain mainly solute atoms (no effective precipitates are assumed). Consequently, cyclic hardening indicating increasing dislocation densities and dislocation-dislocation interaction during cyclic deformation was observed at room temperature as shown in Fig. 2. The under-aged AA6110 exhibited also cyclic hardening during fatigue tests at room temperature. It can be mentioned that dislocation densities increased and dislocation-dislocation interactions occurred in the under-aged AA6110, although precipitates β´´ in the under-aged AA6110 could be expected. However, these precipitates in the under-aged AA6110 were possibly so small and not fully effective. Consequently, for impeding dislocation movement, dislocations could still move easier through the precipitates as well as strain fields induced by remained solute atoms or atomic clusters and then dislocation-dislocation interactions occurred during cyclic deformation. On the other hand, if the major precipitates β´´ in AA6110 alloy are ordered, coherent, semi-coherent and effective within the aluminium matrix, the to-and-fro motion of dislocations during cyclic deformation through the ordered precipitates causes a mechanical local disordering or scrambling of the atoms in the precipitates. The structure of the precipitates becomes disordered and degraded. The hardening due to ordering is lost, therefore cyclic softening is observed in the peak- and over-aged AA6110 as depicted in Fig. 3. The analogous cyclic hardening as well

as cyclic softening mechanism of precipitation-hardened aluminium alloys was also reported in (Srivatsan & Coyne, 1986; Srivatsan, 1991). In general, the stress amplitude does not strongly affect the shape of the cyclic deformation curve, i.e. the AA5083, as-quenched and under-aged AA6110 exhibit still cyclic hardening and the peak- and over-aged AA6110 show cyclic softening. However, an increase of plastic strain amplitudes during fatigue tests at room temperature was measured with increasing stress amplitude, consequently, fatigue lifetimes decreased taking into account the Coffin-Manson law (Manson, 1966; Coffin, 1954).

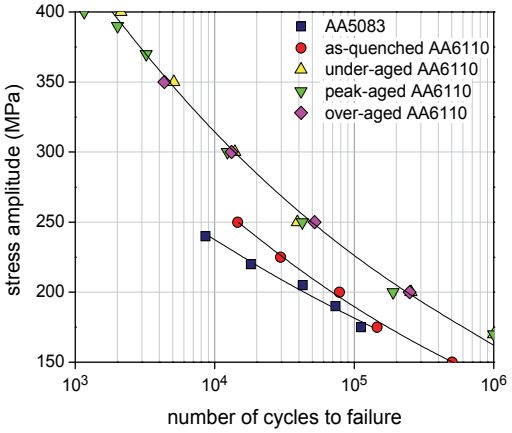

Fig. 1. Non-statistically evaluated s/n-curves of AA5083 and differently aged AA6110 at room temperature

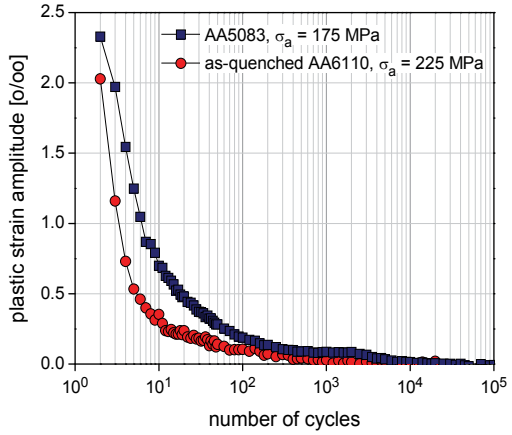

Fig. 2. Cyclic deformation curves of AA5083 and as-quenched AA6110 at an applied stress amplitude of 175 and 225 MPa, respectively

4. Cyclic deformation behaviour at elevated temperature

Fatigue lifetimes of the AA5083 and AA6110 usually decreased with increasing test temperature due to an increase of plastic strain amplitudes of cyclic deformation curves with increasing test temperature (at the same stress amplitude). It could be attributed to easy glide, climb and cross slip of edge and screw dislocations at elevated temperatures.

Non-statistically evaluated s/n-curves of peak-aged AA6110 at elevated temperatures are presented in Fig. 4 as an example. As expected, an increasing test temperature shifts s/n-curves to lower fatigue strength as well as lifetime. The fatigue lifetime of the peak-aged condition at room temperature at an applied stress amplitude of 250 MPa is about 42,500 cycles, whereas for the same applied stress amplitude at a temperature of 250 °C, it is reduced to only roughly 5,500 cycles. Normally, fatigue lifetimes decrease with increasing temperature, however during fatigue tests in the temperature range 100–200 °C the static/dynamic precipitation occurs and affects more or less the fatigue lifetimes of the as-quenched AA6110 as shown in Fig. 5. The fatigue lifetime at room temperature of the as-quenched condition for an applied stress amplitude of 225 MPa is about 30,000 cycles, whereas at a test temperature of 100 °C for the same applied stress amplitude, the fatigue lifetime increases to approximately 50,000 cycles. But for a test temperature of 250 °C, lower fatigue lifetimes of approximately 12,000 cycles were measured. Therefore, the fatigue

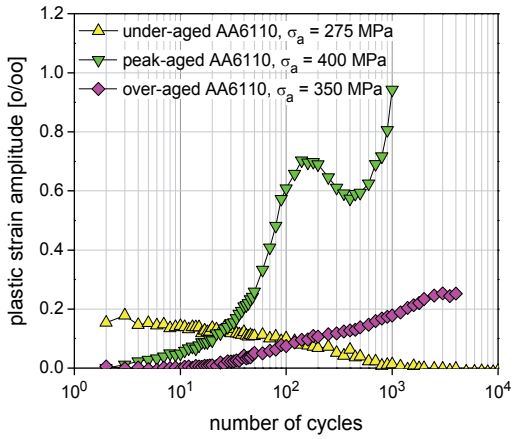

Fig. 3. Cyclic deformation curves of under-, peak- and over-aged AA6110 at an applied stress amplitude of 275, 400 and 350 MPa, respectively

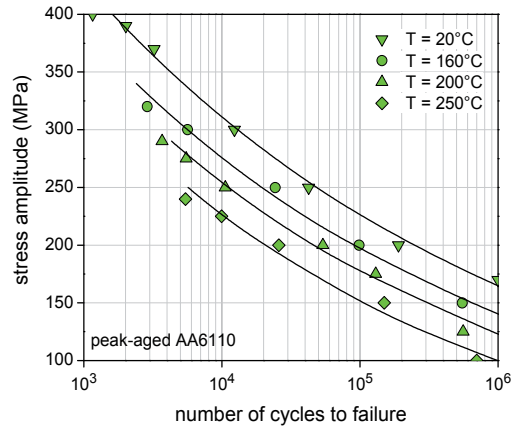

Fig. 4. Non-statistically evaluated s/n-curves of peak-aged AA6110 for different test temperatures

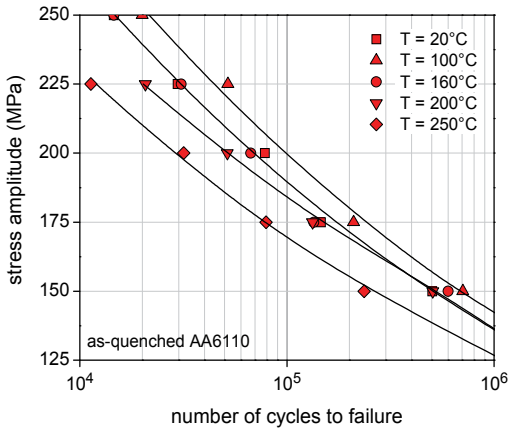

Fig. 5. Non-statistically evaluated s/n-curves of as-quenched AA6110 for different test temperatures

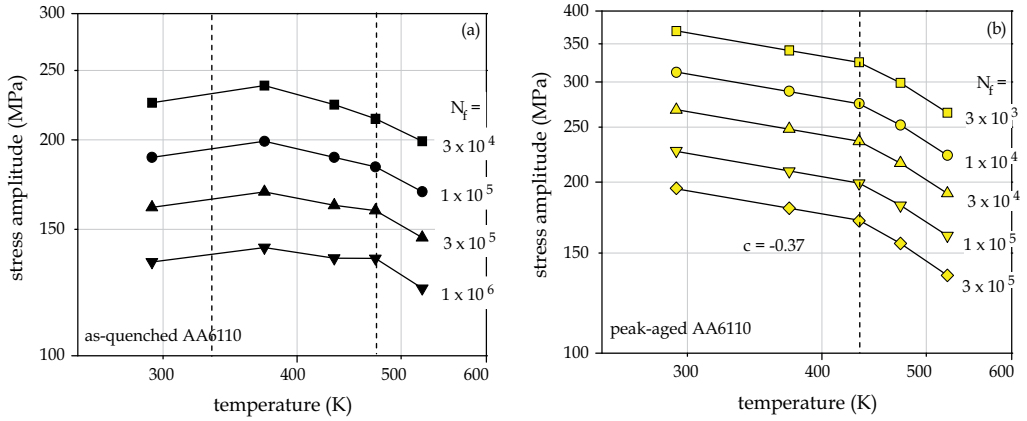

Fig. 6. Temperature dependence of stress amplitudes in a bi-logarithmic scale of (a) as-quenched and (b) peak-aged AA6110

behavior at elevated temperature of the as-quenched and peak-aged AA6110 is meaningful and ought to be analyzed in more details. For elevated temperature, if log-log scales and Kelvin temperature are used, the Basquin equation can be generalized to the following form (Kohout, 2000).

$$\sigma_a = a^* N_f^b T^c \tag{1}$$

where a* is a materials constant which differs from the constant a in equation (1), c is also a materials constant, named the temperature sensitivity parameter and can be defined by the equation.

$$c = \left.\frac{\partial \log \sigma_a}{\partial \log T}\right|_{N_f = const.} \tag{2}$$

From equation (2), the temperature dependence of stress amplitude was plotted in a bi-logarithmic scale for a given number of cycles to failure (3 x 10^3, 10^4, 3 x 10^4, 10^5 and 3 x 10^5) of the as-quenched AA6110 in Fig. 6a. Stress amplitudes for given numbers of cycles increase at a test temperature of 100 °C and then slightly decrease with increasing test temperature up to approximately 200 °C. It can be attributed to the effect of static/dynamic precipitates on the fatigue lifetimes of the as-quenched AA6110 at elevated temperatures. Consequently, a materials constant c of the polished as-quenched AA6110 for fatigue tests at elevated temperatures can not be determined using equation (2). On the other hand, for the peak- and over-aged AA6110, two important aspects were detected: firstly, the experimental results can be fitted by equation (2) for test temperatures lower than about 160–200 °C; secondly, the decrease in stress amplitude as well as fatigue strength at temperatures of 200 and particularly 250 °C (see Fig. 6b) indicates that creep probably begins to play a dominant role at these temperatures. Cyclic creep can be described by monitoring positive mean strains during stress-controlled fatigue test. Therefore, mean strains during fatigue tests were measured and plotted for different test temperatures in Fig. 7 which depicts values of mean strains during fatigue tests of the peak-aged AA6110 at an applied stress amplitude of 300 MPa for different test temperatures as an example. Clearly, for test temperatures less than 160 °C, no significant mean strains during fatigue tests of the polished peak-aged AA6110 were observed. Whereas at a test temperature of 200 °C at a similar applied stress amplitude of 300 MPa, positive mean strains were measured during fatigue test. Moreover, these mean strains became more and more pronounced with increasing number of cycles. Elevated temperature affects not only on the fatigue lifetime, but also on the cyclic deformation curves of aluminium alloy AA6110. The as-quenched AA6110 exhibits cyclic hardening during fatigue tests at elevated temperature up to 250 °C at a number of cycles to failure of about 10,000 cycles (duration about 1 hour). It can be probably said that the static/dynamic precipitates of the as-quenched AA6110 were not fully effective during this investigation in spite of a relatively high temperature of 250 °C (but relatively short investigated period). Thus, dislocations could still move easier through the precipitates as well as strain fields induced by remaining solute atoms or clusters and then dislocation-dislocation interactions occurred during cyclic deformation. Cyclic deformation curves of

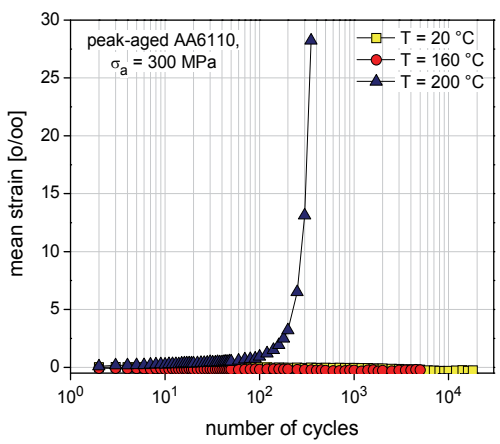

Fig. 7. Mean strains during fatigue tests of peak-aged AA6110 at a stress amplitude of 300 MPa for different test temperatures

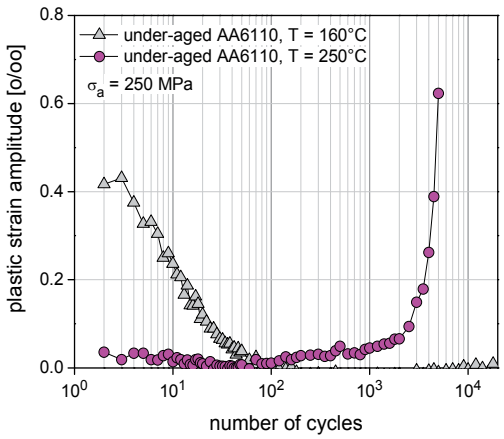

Fig. 8. Cyclic deformation curves of under-aged AA6110 at a stress amplitude of 250 MPa for test temperatures of 160 and 250 °C

the under-aged condition during fatigue tests at elevated temperature up to 200 °C show also a similar behavior. However, a change of cyclic deformation curve of the under-aged AA6110 from cyclic hardening at test temperatures less than 200 °C to cyclic softening at a test temperature of 250 °C was observed as shown in Fig. 8. It possibly indicates that during fatigue tests at a test temperature of 250 °C, precipitates of the under-aged AA6110 were altered to be more effective in size and coherent as well as semi-coherent within the aluminium matrix. Then, during cyclic deformation, dislocations moved to-and-fro through the coherent/semi-coherent precipitates causing a mechanical local disordering or scrambling of the atoms in the precipitates. The structure of the precipitates became disordered and degraded. The hardening due to ordering was lost, and consequently cyclic softening was observed for this situation. For the peak- and over-aged AA6110, cyclic softening still occurred during fatigue tests at test temperatures up to 250 °C and their plastic strain amplitudes during fatigue tests increased with increasing test temperature.

5. Effects of deep rolling on cyclic deformation behaviour

Important affecting factors on the cyclic deformation behaviour of the aluminium alloys AA5083 and AA6110 have been considered and discussed, e.g. influence of precipitation, stress amplitude and temperature. However, for the deep rolled condition, additional factors as surface smoothening, near-surface compressive residual stresses, work hardening states and increased hardness values (see in Figs. 9–10 as examples) induced by deep rolling affect significantly the cyclic deformation behaviour. These beneficial effects of the deep rolling treatment enhance the fatigue lifetime of aluminium alloys due to they serve to inhibit or retard fatigue crack initiation as well as fatigue crack growth (Scholtes, 1997; Wagner, 1999; Schulze 2005). Lower plastic strain amplitude of the deep rolled condition was normally observed during fatigue tests at a given temperature (see in Fig. 11 as an example). Hence, a fatigue lifetime enhancement should be expected taking into account the Coffin-Manson law. Non-statistically evaluated s/n-curves of deep rolled AA5083 and AA6110 at room temperature are presented in Fig. 12. At elevated temperature, the fatigue lifetimes as well as strengths of the deep rolled AA5083 and differently aged AA6110

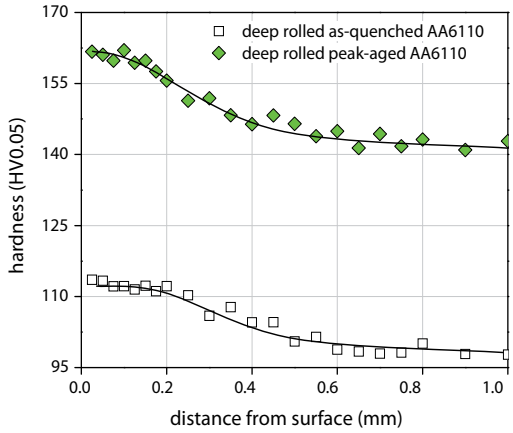

Fig. 9. Near surface hardness values of the deep rolled as-quenched and peak-aged AA6110

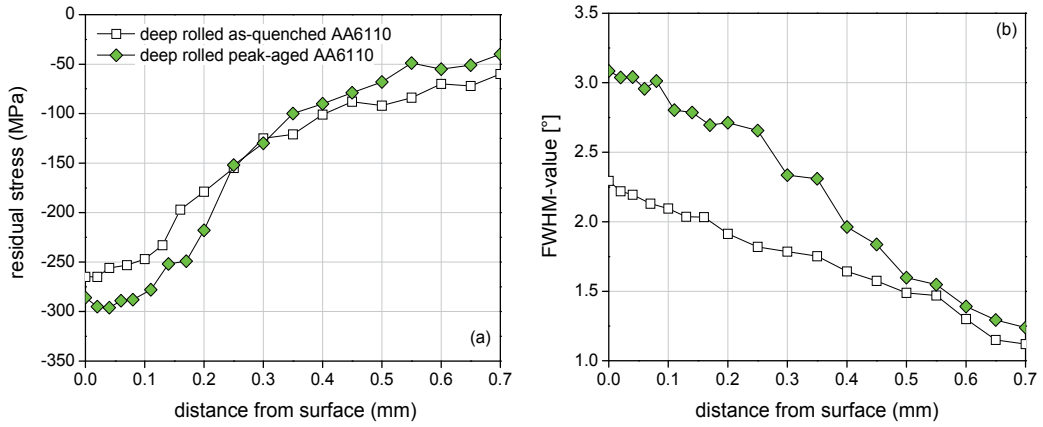

Fig. 10. Depth-profiles of near-surface (a) compressive residual stresses and (b) FWHM-values of the deep rolled as-quenched and peak-aged AA6110

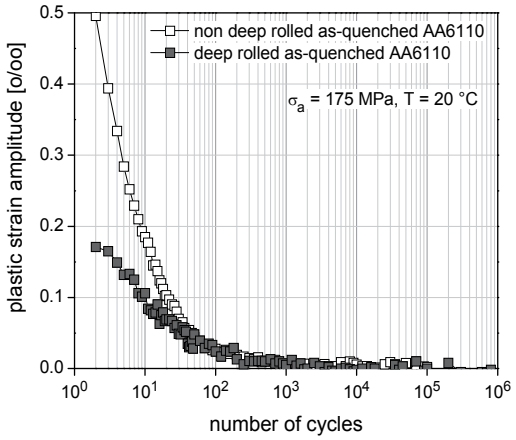

Fig. 11. Cyclic deformation curves of the non- and deep rolled as-quenched AA6110 at stress amplitude of 175 MPa at room temperature

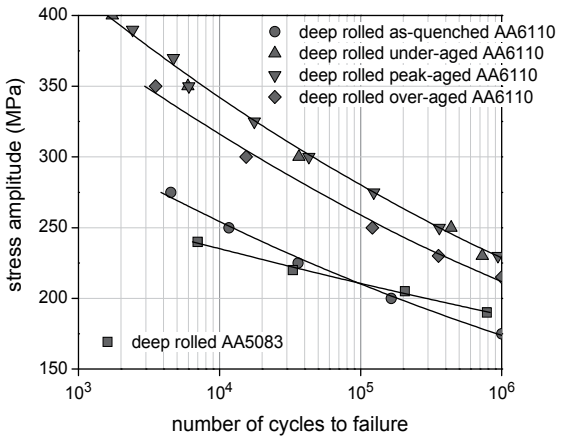

Fig. 12. Non-statistically evaluated s/n-curves of deep rolled AA5083 and differently aged AA6110 at room temperature

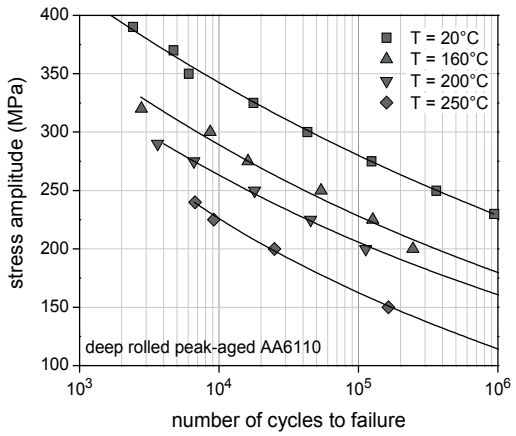

Fig. 13. Non-statistically evaluated s/n-curves of deep rolled peak-aged AA6110 for different test temperatures

decreased undoubtedly under cyclic loading as shown an example in Fig. 13 depicting non-statistically evaluated s/n curves of deep rolled peak-aged AA6110 for different test temperatures. It indicates that the fatigue lifetimes of the deep rolled aluminium alloys depend strongly on the state of near surface compressive residual stresses and work hardening. At elevated temperature, dislocations can glide, climb as well as cross slip easier including high diffusion rates at elevated temperature. Consequently, residual stress relaxation is more and more pronounced for this loading situation. Moreover, a more complicated situation can be expected for the deep rolled as-quenched and under-aged AA6110, where occurring static/dynamic precipitation and residual stress relaxation took place simultaneously during elevated temperature fatigue tests. The competition between occurring static/dynamic precipitates which can enhance the fatigue life and residual stress relaxation phenomena which normally deteriorate the fatigue lifetime of the deep rolled condition should be analyzed and discussed. Equation (2) was used again to analyze the temperature sensitivity parameter, c. The temperature dependence of stress amplitude was

plotted in a bi-logarithmic scale for a given number of cycles to failure of the deep rolled as-quenched and peak aged AA6110 as presented in Figs. 14a and 14b. The materials constants c of the deep rolled as-quenched AA6110 of -0.22 was detected although static/dynamic precipitation occurred during fatigue tests at elevated temperatures. For the deep rolled peak-aged AA6110 (see Fig 14b), the materials constant c (c = -0.50) can be determined. It indicates that the fatigue lifetimes of the deep rolled condition are dominated by the effects of the residual stress relaxation and not by the effects of static/dynamic precipitation for the deep rolled as-quenched AA6110. As compared to the non deep rolled condition, fatigue lifetime enhancement through deep rolling was observed certainly but only for all low and intermediate applied stress amplitudes for given test temperatures. It is possible that near-surface compressive residual stresses as well as work hardening states relax significantly under relatively high loading and/or elevated temperature (Löhe & Vöhringer, 2002). Consequently, deep rolling becomes probably ineffective under severe loading conditions. To simplify this state, s/n-curves at test temperatures of 20 and 160 °C of the non deep rolled

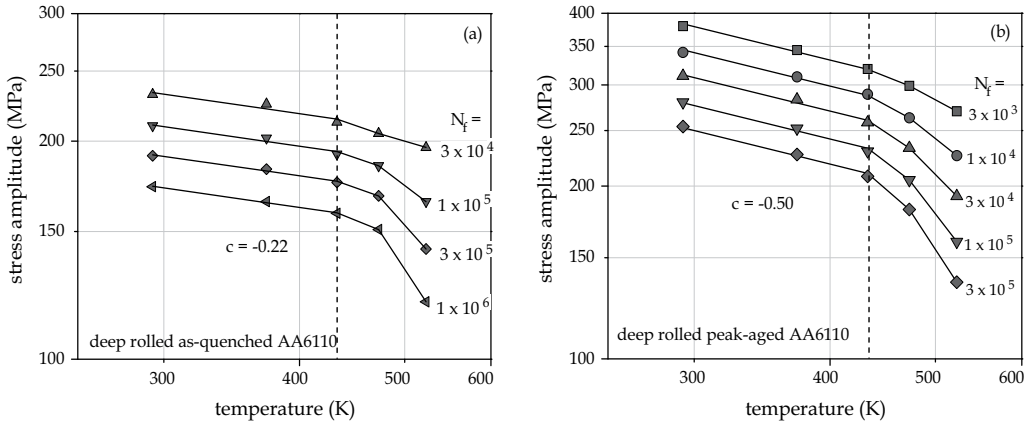

Fig. 14. Temperature dependence of stress amplitudes in a bi-logarithmic scale of deep rolled (a) as-quenched and (b) peak-aged AA6110

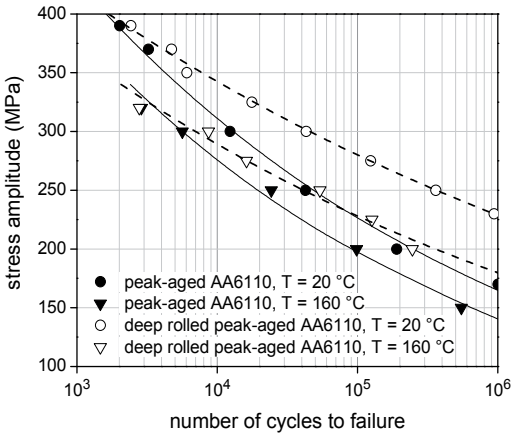

Fig. 15. Non-statistically evaluated s/n curves of non- and deep rolled peak-aged AA6110 for test temperatures of 20 and 160 °C

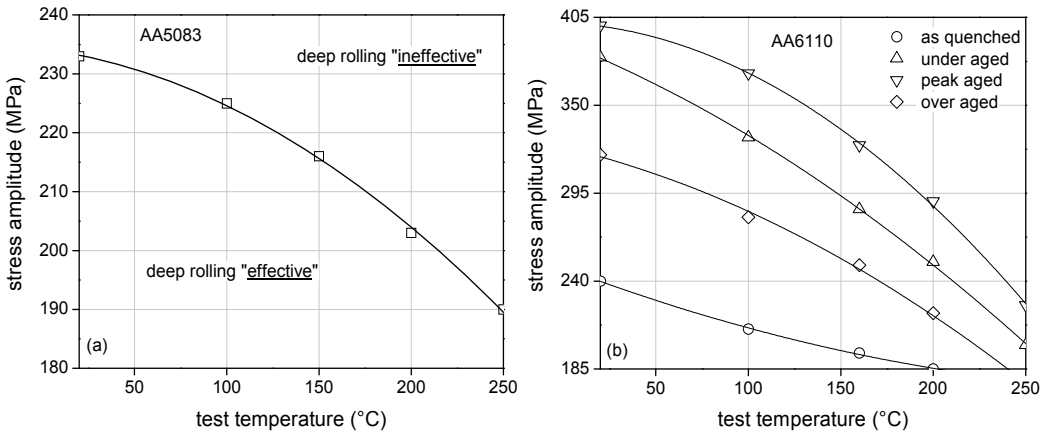

Fig. 16. Effective boundary lines of deep rolling treatment of (a) AA5083, (b) differently aged AA6110 plots as a function of stress amplitude and test temperature

and deep rolled peak-aged AA6110 were plotted in one diagram as an example in Fig. 15. For AA5083 and other differently aged AA6110, analogous diagrams were found also. Relaxation of residual stresses as well as work hardening states during cyclic loading at room and elevated temperatures may be a cause for the different effectiveness of deep rolling. From Fig. 15, intersection points between s/n-curves of the non deep rolled and deep rolled conditions for each test temperatures can be seen. Therefore, all intersection points were summarized and plotted in stress amplitude-temperature diagrams for AA5083 and different aged AA6110 as shown in Figs 16a and b.

6. Residual stress stability

Hitherto, it can be mentioned that too high stress amplitudes and temperatures are certainly the main detrimental effects on the fatigue lifetime of deep rolled aluminium alloys. This implies that at certain (very high) stress amplitude for a given (very high) test temperature, deep rolling becomes ineffective due to the near surface residual stresses and work hardening states were relaxed as well as unstable. Fatigue lifetimes of the non- and deep rolled conditions were plotted and compared in one diagram to illustrate the effectiveness of the deep rolling as shown in Fig. 17. Residual stresses and work hardening states (FWHM-values) were measured during fatigue tests. Several test conditions which were located both in the regions where deep rolling is effective and ineffective (see Figs. 16a and b) were investigated as shown in table 2. It was seen obviously that the fatigue lifetimes of the deep rolled conditions which deep rolling is ineffective were not improved as compared to the non deep rolled condition. The stability as well as instability of compressive residual stresses and work hardening states can be seen clearly when their values before and after fatigue tests were plotted in one diagram in Figs. 18a and b. From Figs 17, 18a and b, a correlation between the effectiveness of deep rolling and the stability of compressive residual stresses as well as work hardening states is obvious. The deep rolling treatment can enhance the fatigue lifetime of aluminium alloys although residual stresses relaxed

significantly up to about 70% (see Figs. 17 and 18a). On the other hand, the effectiveness of deep rolling depends strongly on the stability of near-surface work hardening represented by the FWHM-value. If FWHM-values decrease more than about 5%, deep rolling becomes ineffective (see Figs. 17 and 18b). Therefore, it can be concluded that the near-surface work hardening state is the major factor influencing the fatigue lifetime of the deep rolled aluminium alloys. Deep rolling can enhance the fatigue lifetime of aluminium alloys AA5083 and differently aged AA6110 through the stability of work hardening states. A possible explanation for this behaviour is that the fatigue damage is primarily crack initiation and thus work hardening controlled for deep rolled aluminium alloys.

Number	Alloy	Condition	Test temperature (°C)	σ_a (MPa)	Cycles
1	AA5083	as received	20	205	100,000**
2*	AA5083	as received	20	240	2,500**
3	AA6110	as-quenched	160	150	1,000
4*	AA6110	as-quenched	160	250	1,000
5	AA6110	under-aged	20	250	175,000**
6	AA6110	under-aged	20	350	3,000**
7*	AA6110	under-aged	20	400	400**
8	AA6110	under-aged	200	175	1,000
9*	AA6110	under-aged	200	300	1,000
10	AA6110	peak-aged	20	250	150,000**
11	AA6110	peak-aged	20	300	20,000**
12	AA6110	peak-aged	20	350	3,500**
13*	AA6110	peak-aged	20	400	250**
14	AA6110	peak-aged	160	200	1,000
15	AA6110	peak-aged	160	300	1,000
16*	AA6110	peak-aged	200	300	100
17	AA6110	over-aged	20	250	50,000**
18*	AA6110	over-aged	20	350	1,000**
19	AA6110	over-aged	160	200	1,000
20*	AA6110	over-aged	160	290	1,000

* deep rolling is ineffective, ** at half the number of cycles to failure

Table 2. Test conditions for residual stress and work hardening stability and effectiveness of deep rolling treatment investigations

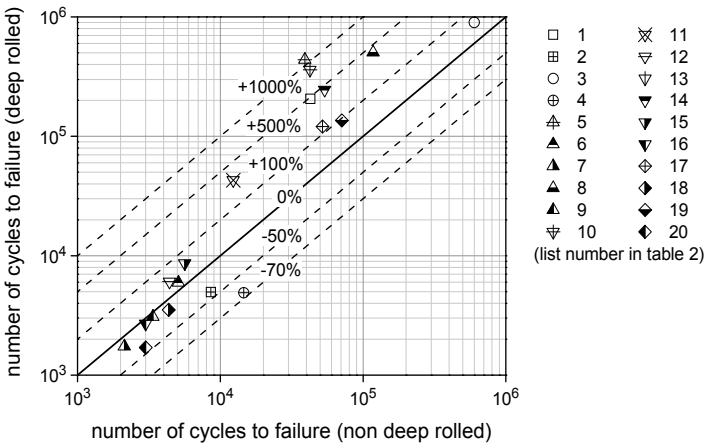

Fig. 17. Effectiveness of deep rolling treatment for several test conditions (in table 2)

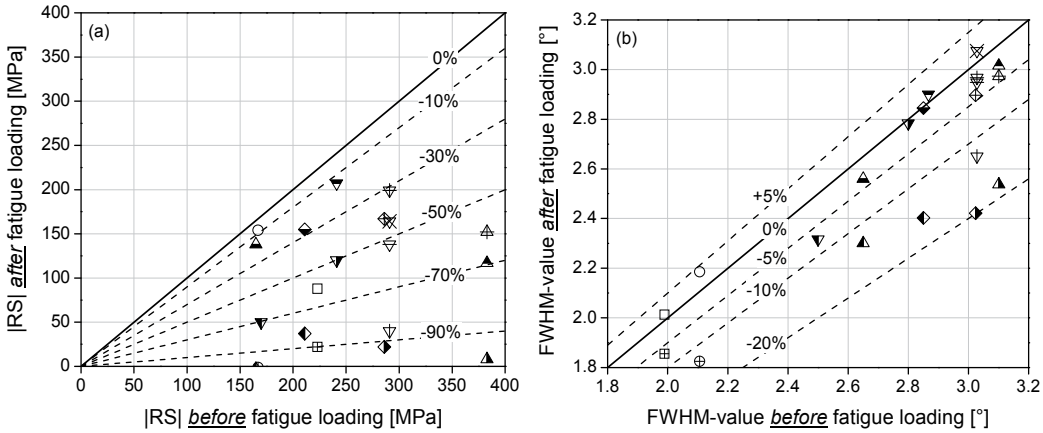

Fig. 18. Relaxation of (a) residual stresses and (b) work hardening states (FWHM values) for several test conditions (in table 2)

7. Acknowledgements

The authors would like to express sincere thanks to the German Science Foundation (DFG) and to the Faculty of Engineering, Kasetsart University, Thailand, for financial support for Dr.-Ing. I. Altenberger and Dr.-Ing. P. Juijerm, respectively.

8. Conclusion

The cyclic deformation behavior of aluminium alloys AA5083 and differently aged AA6110 at room and elevated temperature under stress control has been successfully investigated

and discussed. The effects of deep rolling on cyclic deformation behavior has been systematically studied and clarified both at room and elevated temperatures as compared to the non deep rolled condition as a reference. Residual stress as well as work hardening stability has been investigated. From this research, the conclusions can be addressed as presented below

1. Fatigue lifetimes of the non- and deep rolled conditions depend strongly on stress amplitude and temperature. Their fatigue lives decrease with increasing stress amplitude and/or temperature. An exception was found for the as-quenched AA6110, where a slight increase of fatigue life at a test temperature of 100°C was observed due to occurring static/dynamic precipitation during investigations.
2. The cyclic deformation behaviour of aluminium alloys AA5083 and AA6110 are governed by dislocation-dislocation and/or dislocation-precipitation interactions during cyclic loading. Aluminium alloys AA5083, as-quenched and under-aged AA6110 exhibit cyclic hardening due to increasing dislocation and dislocation-dislocation interactions during cyclic loading, whereas peak- and over-aged AA6110 show cyclic softening due to the to-and-fro motion of dislocations through the ordered precipitates during cyclic deformation causing a mechanical local disordering or scrambling of the atoms in the precipitates, leading to a loss of hardening (Srivatsan & Coyne, 1986; Srivatsan, 1991).
3. Deep rolling enhances fatigue lifetimes of aluminium alloys AA5083 and differently aged AA6110 efficiently at applied stress amplitudes below a threshold stress amplitude at a given temperature where the near-surface work hardening states are unaltered and remain essentially constant, whereas compressive residual stress relax substantially during fatigue loading. On the other hand, above a threshold stress amplitude at a given temperature, deep rolling has no beneficial effect on the fatigue behavior of AA5083 and AA6110. This is a consequence of unstable near-surface work hardening states.

9. References

Altenberger, I. (2003). Alternative mechanical surface treatments: microstructures, residual stresses and fatigue behavior, In: *Shot Peening*, Wagner, L., (Ed.), pages 421-434, Wiley-VCH, ISBN 3527305378, Weinheim.

Coffin, L.F., (1997). A study of the effects of cyclic thermal stresses on a ductile metal, *Trans ASME* 76, pages 931-950.

Kohout, J., (2000). Temperature dependence of stress-lifetime fatigue curves, *Fatigue & Fracture of Engineering Materials & Structures*, Vol. 23, No. 12, pages 969-977.

Löhe, D., Vöhringer, O. (2002). Stability of Residual Stresses, In: *ASM International Handbook of Residual stress and Deformation of Steel*, Totten, G., Howes, M., & Inoue, T. (Ed.), pages 54-69, ASM International, ISBN 0-87170-729-2, USA.

Manson, S.S., (1966). *Thermal stress and low cycle fatigue*, McGraw-Hill, New York.

Scholtes, B. (1997). Assessment of residual stresses, In: *Structural and Residual Stress Analysis by Nondestructive Methods*, Hauk, V. (Ed.), pages 590-636, Elsevier, ISBN 978-0-444-82476-9, Amsterdam.

Schulze, V., (2005). *Modern Mechanical Surface Treatment*, Wiley-VCH, Weinheim.

Srivatsan, T.S. & Coyne, E.J., Jr, (1986). Cyclic stress response and deformation behavior of precipitation-hardened aluminium-lithium alloys, *International Journal of Fatigue*, Vol. 8, No. 4, pages 201-208.

Srivatsan, T.S., (1991) The low-cycle fatigue and cyclic fracture behaviour of 7150 aluminium alloy, *International Journal of Fatigue*, Vol. 13, No. 4, pages 313-321.

Wagner, L., (1999). Mechanical surface treatments on titanium, aluminum and magnesium alloys, *Materials Science and Engineering: A*, Vol. 263, No. 2, pages 210-216.

10

Summary on Uniaxial Ratchetting of 6061-T6 Aluminium Alloy

Guozheng Kang, Jun Ding and Yujie Liu
Department of Applied Mechanics and Engineering, Southwest Jiaotong University
China

1. Introduction

Aluminium alloys are currently being used as major structure components in automobiles, high-speed railway vehicles and aircrafts, which are often subjected to a cyclic loading. It is necessary to predict their cyclic responses as accurately as possible by constructing new constitutive models before the strength, fatigue life and safety of structure components can be assessed reasonably. During asymmetrical stress-controlled cyclic loading, a cyclic accumulation of inelastic deformation, i.e., ratchetting will occur in the materials. The ratchetting is an important factor which should be carefully considered in the assessment of fatigue failure and safety of structures, and has been extensively studied for three decades by many researchers as reviewed by Ohno (1990; 1997), Bari and Hassan (2002), Kang (2008), and Chaboche (2008). The existing work shows that the cyclic softening/hardening feature of materials, and the loading level, history, path, rate, and waveform, as well as ambient temperature have great effect on the ratchetting behaviour of materials. Based on the experimental observations, some phenomenological cyclic elasto-plastic and viscoplastic constitutive models have been constructed to describe the uniaxial and multiaxial ratchetting of metal materials. The established models are mainly obtained by extending the nonlinear kinematic hardening rules originally developed by Armstrong and Frederick (1966) and revised by Chaboche (1991), Ohno and Wang (1993a; 1993b), Jiang and Sehitoglu (1996), Abdel-Karim and Ohno (2000), Kang et al (2003), Chen and Jiao (2004), Kan et al (2007), and Kang et al (2009) and so on. However, most of the researches concerned the ratchetting behaviours of stainless steels and other carbon steels. A few papers addressed the ratchetting behaviours of aluminium and its alloys, e.g., the papers published by Chen and Abel (1996), Yang et al (1998), Hu et al (1999), and Ding et al (2008) for 2014-T6, pure aluminium, 7050-T7451, and LY12-CZ aluminium alloys, respectively. Such results show that the ratchetting behaviours of aluminium alloys also differ greatly from different types of the alloys. Recently, the authors have also accomplished some experimental and theoretical researches for the uniaxial time-dependent ratchetting behaviour of 6061-T6 alloy at room and high temperatures, and its ratchetting-fatigue interaction (Ding et al, 2007; Kang et al, 2008; Ding et al, 2010) and obtained some significant conclusions which are very useful to realize the ratchetting behaviours of aluminium alloys and predict them accurately in the future work.

Therefore, in this Chapter, some experimental and theoretical results about the uniaxial ratchetting and ratchetting-fatigue interaction of 6061-T6 aluminium alloy are provided to

demonstrate our attempt to launch more comprehensive research about the ratchetting behaviour of aluminium alloys in the future. Based on the detailed tests, the dependences of uniaxial ratchetting of the alloy on the stress level, stress rate, peak stress hold and ambient temperature are investigated, and then a new cyclic constitutive model is proposed to describe the ratchetting of aluminium alloy reasonably. In the proposed model, a new kinematic hardening rule is employed to represent the time-dependence of ratchetting behaviour of aluminium alloy at room and high temperatures.

2. Experimental procedure

As-received 6061-T6 aluminium alloy is used as the experimental material in our researches, as discussed in Ding et al (2007), Kang et al (2008), and Ding et al (2010). The chemical composition of the alloy in mass percentage is: Cu, 0.15-0.40%; Si, 0.4-0.8%; Fe, 0.7%; Mn, 0.15%; Mg, 0.8-1.2%; Zn, 0.25%; Cr, 0.04-0.35%; Ti, 0.15%; Al, remained. Cylindrical specimens are manufactured directly from the as-received 6061-T6 bars. The specimens for the tests at room temperature have gauge length of 10 mm and cross-section diameter of 6 mm; while those for the tests at high temperature have gauge length of 30 mm and cross-section diameter of 6 mm. All the tests are performed in MTS-809-25kN machine with a temperature controlling system of MTS653. The experimental procedure and data are controlled and collected by TestStar system attached to the test machine, respectively. The specimens are investigated under the uniaxial strain- and stress-controlled cyclic loading tests (simplified as uniaxial cyclic straining and stressing, respectively) at the strain rate of $2\times10^{-3}\cdot s^{-1}$ and stress rate of 100 $MPa\cdot s^{-1}$, respectively, except for the cases specified. The tests are performed at room temperature and 150˚C. In some cases, the specimens are tested till the fracture occurs, in order to investigate the ratchetting-fatigue interaction of the alloy. To demonstrate the ratchetting behaviour of 6061-T6 aluminium alloy more clearly, the curves of ratchetting strain vs number of cycles are illustrated in the figures in the next section, based on the following definition of uniaxial ratchetting strain ε_r:

$$\varepsilon_r=(\varepsilon_{max}+\varepsilon_{min})/2 \quad (1)$$

Where ε_{max} and ε_{min} are the maximum and minimum axial strains measured after each cycle, respectively.

3. Experimental results

3.1 Uniaxial time-dependent ratchetting behaviour

At first, 6061-T6 aluminium alloy is tested under monotonic tension and uniaxial strain-controlled cyclic loading to realize some basic performances of the alloy and determine the loading conditions for the uniaxial ratchetting tests discussed in the next section. Fig. 1 shows the results of monotonic tension obtained at different strain rates and at room temperature and 150˚C. It is seen from Fig. 1 that the alloy presents apparent rate-dependent deformation during the monotonic tension, and the tensile stress-strain curve of the alloy is higher at faster strain rate. However, the degrees of rate-dependence for the alloy at room temperature and 150˚C are almost the same, which can be concluded by comparing the results shown in Fig. 1a and Fig. 1b.

Fig. 2 gives the results of responded stress amplitude evolving with increasing number of cycles under the uniaxial cyclic straining with applied strain amplitude of 0.6% and with or

without peak/valley strain hold. And Fig. 3 shows the results in the cyclic straining with only peak strain hold and at 150˚C, where the applied strain amplitude is also 0.6%.

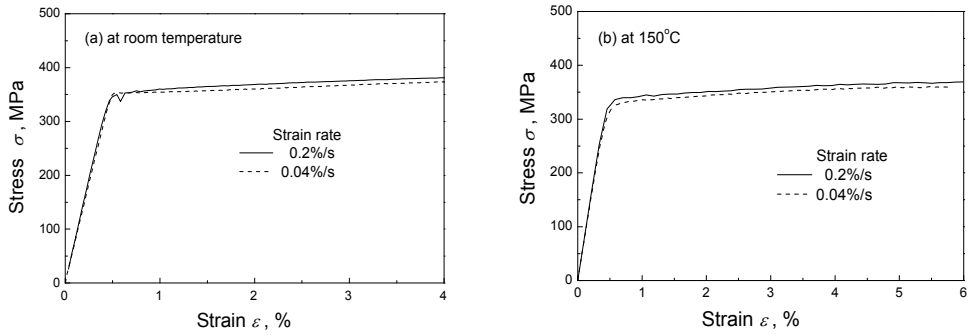

Fig. 1. Tensile stress-strain curves of the alloy at different strain rates: (a) at room temperature; (b) at 150˚C. (Originally from Ding et al. (2007))

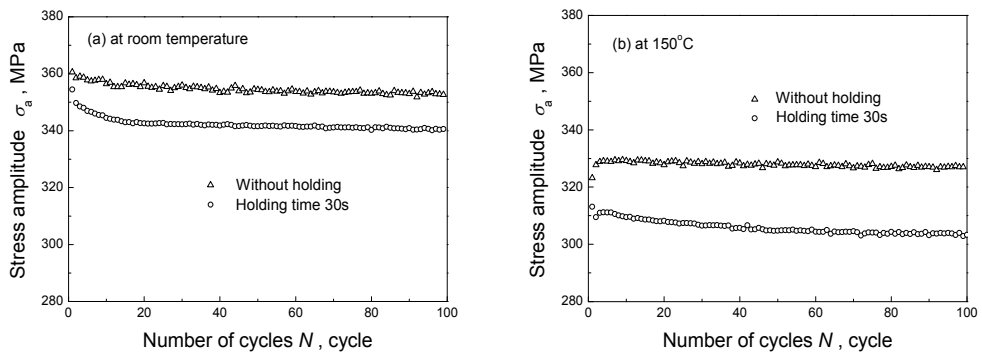

Fig. 2. Curves of responded stress amplitude vs number of cycles for the alloy during the cyclic straining with or without peak/valley strain hold: (a) at room temperature; (b) at 150˚C. (Originally from Ding et al. (2007))

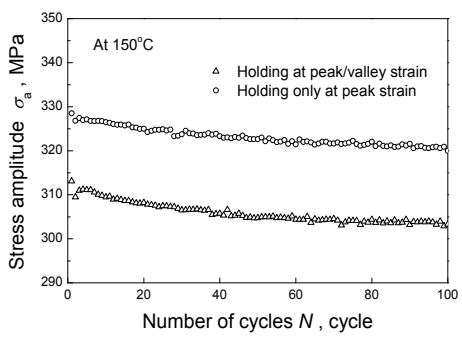

Fig. 3. Curves of responded stress amplitude vs number of cycles for the alloy during the cyclic straining with only peak strain hold and at 150˚C. (Originally from Ding et al. (2007))

It is shown that the as-received 6061-T6 aluminium alloy presents apparent cyclic softening feature at room temperature and 150˚C, and the responded stress amplitude continuously decreases with the increasing number of cycles. Also, the cyclic softening behaviour of the alloy is time-dependent, and the curves of responded stress amplitude vs number of cycles without any peak/valley strain hold are higher than those with certain peak/valley strain hold, as shown in Fig. 2a and 2b. Moreover, the responded stress amplitude of the alloy during the cyclic straining with only peak strain hold is also higher than that with peak/valley strain hold, as shown in Fig. 3. The decreased responded stress amplitude during the cyclic straining with peak/valley strain hold is caused by the stress relaxation occurred in the peak and/or valley strain hold due to the viscosity of the alloy. It should be noted from Fig. 2 that during the strain-controlled cyclic loading, the time-dependent cyclic softening feature of the alloy is more remarkable at 150˚C than that at room temperature, which is different from the rate-dependent feature presented in the monotonic tensions with different strain rates. It implies that the viscosity of the alloy is more remarkable at 150˚C than at room temperature.

Then the alloy is tested under the uniaxial asymmetrical stress-controlled cyclic loading with different applied stresses and at constant stress rate. The uniaxial ratchetting of 6061-T6 aluminium alloy and its dependence on the applied stress level and loading history are observed at room temperature and 150˚C. The results are shown in Fig. 4 to Fig. 6.

It is concluded from the figures that: (1) Ratchetting occurs progressively in the alloy during the asymmetrical uniaxial cyclic stressing at room temperature and 150˚C. The ratchetting strain increases with the increasing number of cycles, but the ratchetting strain rate (e.g., the increment of ratchetting strain after each cycle) decreases gradually during the cyclic stressing, as shown Fig. 4 and Fig. 5. It should be noted that the exception illustrated in Fig. 5 and occurred in the loading case of 30±300MPa (i.e., the applied mean stress is 30 MPa, and stress amplitude is 300 MPa), i.e., the increasing ratchetting strain rate after 60 cycles is mainly caused by the fluctuation of temperature during the test at 150˚C. (2) The ratchetting of the alloy depends on the applied stress level, and the ratchetting strain increases with the increasing mean stress and stress amplitude. The evolution of ratchetting behaviour of the alloy at room temperature is similar to that at 150˚C, as shown Fig. 4 and Fig. 5. (3) The ratchetting of the alloy also depends on the loading history, and the previous cyclic stressing with higher stress level can restrain the occurrence of ratchetting in the alloy in the sequent cyclic stressing with lower stress level, as shown in Fig. 6 for the multi-stepped cyclic loading of 20±340MPa (200c) → 30±340MPa (200c) → 20±340MPa (100c). (4) After certain cycles, a stable evolution of ratchetting with a constant ratchetting strain rate is reached due to the cyclic softening feature of 6061-T6 aluminium alloy and no shakedown of ratchetting occurs. This is different from that of stainless steels commented by Kang (2008), where a quasi-shakedown of ratchetting occurs due to the cyclic hardening feature of stainless steels.

Finally, the alloy is tested under the uniaxial asymmetrical stress-controlled cyclic loading at different stress rates and with or without peak stress hold, respectively. The uniaxial time-dependent ratchetting of 6061-T6 aluminium alloy is observed at room temperature (loading case of 30±340MPa) and 150˚C (loading case of 30±300MPa). The results are shown in Fig. 7 and Fig. 8. It is concluded from the figures that the ratchetting of the alloy presents apparent time-dependence. The values of ratchetting strain produced during the cyclic stressing at lower stress rate and with certain peak stress hold are much larger than those at higher stress rate and without peak stress hold, respectively, both at room temperature and 150˚C. Furthermore, the ratchetting strain increases remarkably with the increasing hold time at peak stress point.

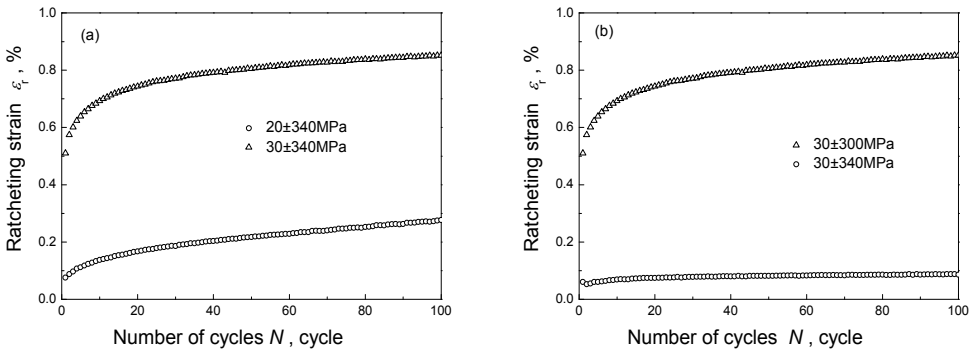

Fig. 4. Ratchetting of the alloy at room temperature: (a) with various mean stresses; (b) with various stress amplitudes. (Originally from Ding et al. (2007))

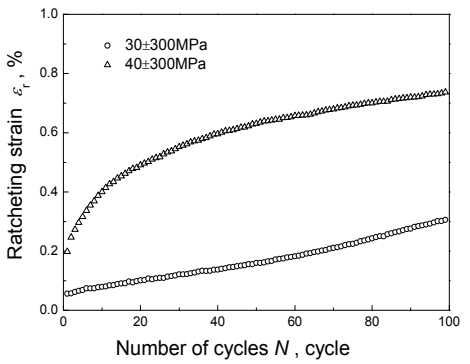

Fig. 5. Ratchetting of the alloy with various mean stresses and at 150˚C. (Originally from Ding et al. (2007))

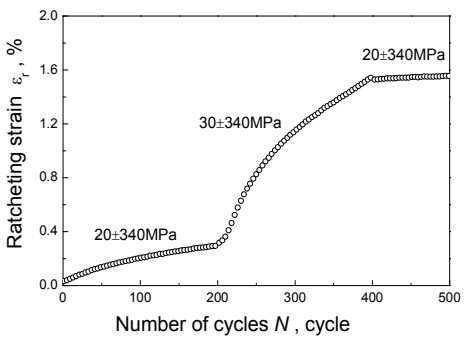

Fig. 6. Ratchetting of the alloy with multi-stepped stress levels at room temperature. (Originally from Ding et al. (2007))

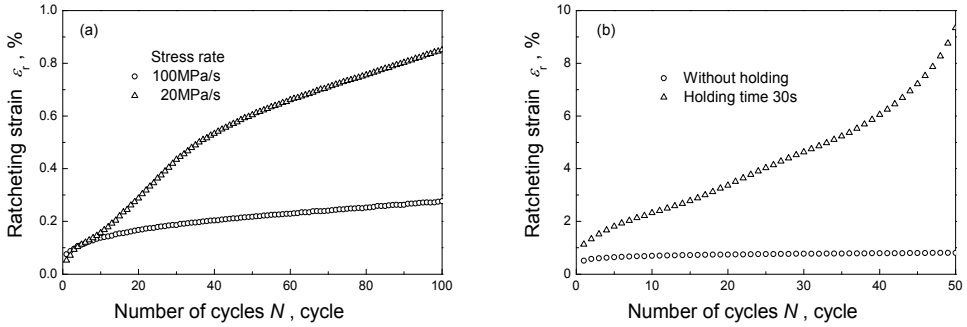

Fig. 7. Time-dependent ratchetting of the alloy at room temperature (30±340MPa): (a) at two stress rates; (b) with or without peak stress hold. (Originally from Ding et al. (2007))

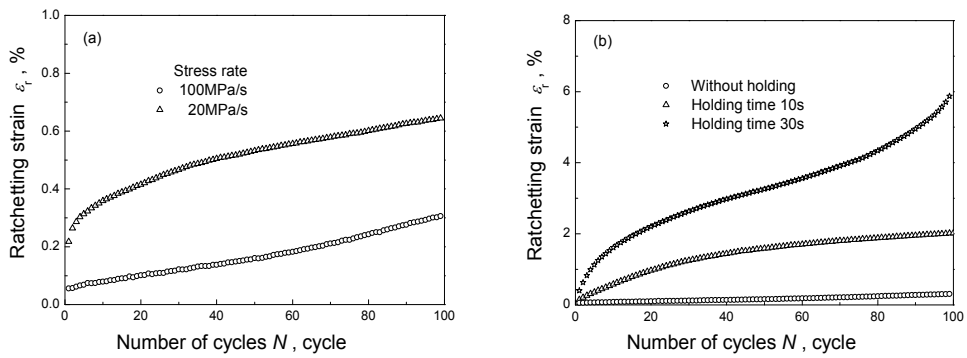

Fig. 8. Time-dependent ratchetting of the alloy at 150˚C (30±300MPa): (a) at two stress rates; (b) with or without peak stress hold. (Originally from Ding et al. (2007))

Similar to that of SS304 stainless steel observed by Kang et al. (2006), the time-dependent ratchetting of 6061-T6 aluminium alloy is also caused by the viscosity of the alloy, and the creep deformation occurred during the peak stress hold and the cyclic stressing at lower stress rate results in the increase of total ratchetting strain, which should be reasonably considered when the time-dependent ratchetting is theoretically modelled.

3.2 Ratchetting-fatigue interaction

In the former subsection, only the ratchetting behaviour of 6061-T6 aluminium alloy is discussed within relatively fewer numbers of cycles, i.e., fewer than 200 cycles. The effect of fatigue damage on the cyclic responses of the alloy has not been involved. In this subsection, the whole-life ratchetting of the alloy is investigated by the cyclic stressing tests till the fracture of the alloy occurs, in order to reveal the ratchetting-fatigue interaction of the alloy at room temperature.

At first, the whole-life ratchetting of the alloy is investigated by the tests with various stress levels (where, the mean stress is 20MPa, and the stress amplitudes are 320, 325 and 330MPa, respectively; the stress rate is 200MPa·s^{-1}). The results obtained at room temperature are shown in Fig. 9.

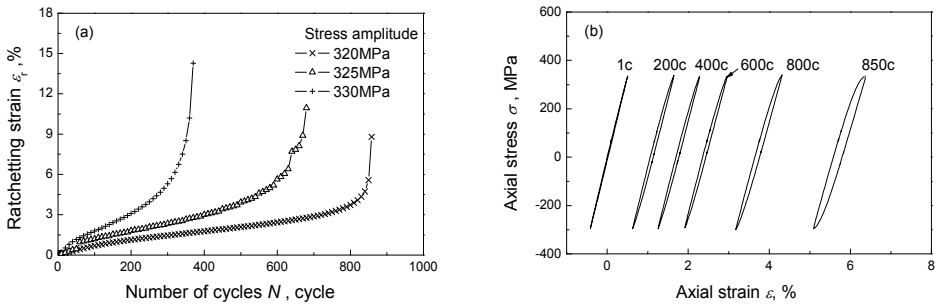

Fig. 9. Whole-life ratchetting of the alloy at room temperature: (a) curves of ratchetting strain vs number of cycles with various stress amplitudes; (b) hysteresis loops obtained in the stress cycling with 20±320MPa. (Originally from Kang et al. (2008))

It is concluded from Fig. 9 that the whole-life ratchetting evolution of 6061-T6 aluminium alloy during uniaxial cyclic stressing can be divided into three stages with respect to the variation of ratchetting strain rate, i.e., the first stage with decreasing ratchetting strain rate, second stage with an almost constant ratchetting strain rate and the third stage with quickly increasing ratchetting strain rate, as shown in Fig. 9a. Very large ratchetting strain is caused in the alloy by the stress cycling with non-zero mean stress after certain cycles, even if the initial ratchetting strain produced in the first beginning of cyclic loading is very small since the applied maximum stress is very close to the yielding strength of the alloy (i.e., about 350MPa). The re-acceleration of ratchetting deformation in the third stage of ratchetting evolution is mainly caused by the apparent fatigue damage after certain cycles and the cyclic softening feature of the alloy. It is also concluded that the increase of stress amplitude speeds up the evolution of whole-life ratchetting, the first and second stages are ended and the third stage appears more quickly, and then the material fractures within fewer cycles. It implies that the fatigue life also depends upon the applied stress amplitude, and is remarkably shortened by the increase of stress amplitude; simultaneously, the fatigue damage accelerates the evolution of ratchetting, and causes the quick occurrence of the third stage of ratchetting evolution as shown in Fig. 9a. From Fig. 9b, it is seen that the hysteresis loops gradually change from nearly linear type to apparent nonlinear ones and will become fatter and fatter during the stress cycling due to the cyclic softening feature of the alloy and the fatigue damage caused by the cyclic loading after certain number of cycles.

Secondly, the whole-life ratchetting of the alloy is observed in the tests at varied stress rate and with or without peak and/or valley stress hold, and the time-dependent ratchetting-fatigue interaction is discussed. The results at room temperature are shown in Fig. 10. Two kinds of loading charts are employed in the tests: one is composed of the tension and compression parts (simplified as T and C in Fig. 10a, respectively) at identical stress rate, which is signed as Type I; while the other is composed of the tension and compression parts at different stress rates, which is signed as Type II.

It is seen from Fig. 10a (loading case: 20±330MPa) that the evolution of whole-life ratchetting at lower stress rate is faster than that at faster stress rate in the stress cycling with the Type I loading chart, and the alloy fails within fewer cycles, even if the magnitude of final ratchetting strain at lower stress rate is lower. In the stress cycling with the Type II loading

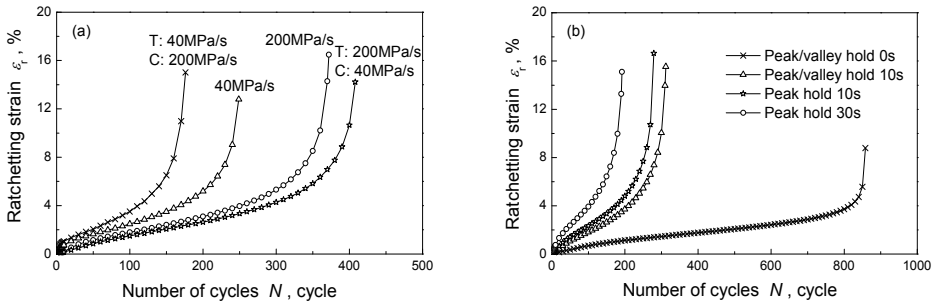

Fig. 10. Time-dependent whole-life ratchetting at room temperature: (a) at different stress rates; (b) with different hold-times at peak (/valley) stress point. (Originally from Kang et al. (2008))

chart, the evolution of ratchetting is much quicker for the case at lower stress rate in the tension part than that at quicker stress rate in the tension part, which also results in a shorter fatigue life. It is concluded that the evolution of whole-life ratchetting and fatigue life of 6061-T6 aluminium alloy depends greatly on the stress rate and its loading sequence.

The peak/valley stress hold also influences greatly the evolution of whole-life ratchetting and fatigue life of the alloy as shown in Fig. 10b. The evolution of whole-life ratchetting is accelerated and then the fatigue life is shortened by the peak or peak/valley stress hold, which becomes more remarkable when the hold time is longer. It is mainly caused by the creep strain produced during the peak stress hold. It is also shown that the fatigue life of alloy is shorter in the stress cycling with only peak stress hold than that with peak/valley stress hold. The reason is straightforward, since the stress at valley point is compressive.

To illustrate further the effect of creep deformation on the ratchetting-fatigue interaction, the alloy is tested in the stress cycling interrupted by a peak stress hold after every 50 cycles at room temperature. It is seen from Fig. 11 (loading case: 20±325MPa) that the evolution of whole-life ratchetting is accelerated and the fatigue life is shortened greatly by such stress hold, and both of them become more remarkable if the hold time is longer, even if the final ratchetting strain is almost the same for the cases with hold times of 120 and 60 seconds. It should be noted from the experimental results that the total creep strain produced at all the

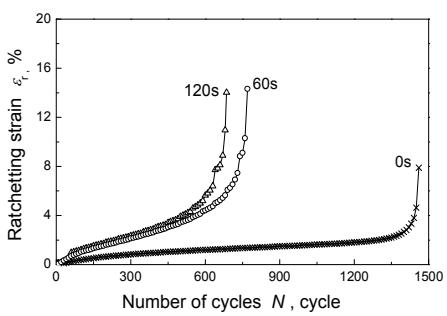

Fig. 11. Time-dependent whole-life ratchetting in interrupted stress cycling with different hold-times. (Originally from Kang et al. (2008))

interrupting peak stress holds is less than 1.0%.Therefore, the difference of final ratchetting strain between the cases with or without interrupting peak stress hold is not mainly caused by the creep strain produced during the hold. However, such small amount of creep strain causes the great increase of ratchetting strain and decrease of fatigue life. It implies that the additional creep is very detrimental to the fatigue life of the alloy in the stress cycling.

4. Time-dependent constitutive model

As commented by Kan et al. (2007), a good candidate for modelling the time-dependent ratchetting of the materials is the nonlinear kinematic hardening rule with a static recovery term. Therefore, the Kang-Kan model (Kan et al., 2007) is extended to predict the uniaxial time-dependent ratchetting of cyclic softening materials by employing a new combined nonlinear kinematic hardening rule (i.e., combination of the A-F model (Armstrong and Frederick, 1966) and Ohno-Wang model II (Ohno and Wang, 1993a)) with a static recovery term and introducing an additional nonlinear isotropic hardening rule to capture the effect of cyclic softening feature on the ratchetting (Ding et al., 2010). The developed model (Ding et al., 2010) is outlined in this chapter as follows

4.1 Main equations

In the framework of infinitesimal visco-plasticity, it is assumed that the total strain can be divided additively into elastic and inelastic strains for the isothermal case. The main equations of the proposed visco-plastic constitutive model are the same as those of the Kang-Kan model (Kan et al., 2007) and listed as follows:

$$\boldsymbol{\varepsilon} = \boldsymbol{\varepsilon}^{e} + \boldsymbol{\varepsilon}^{in} \tag{2}$$

$$\boldsymbol{\varepsilon}^{e} = \mathbf{D}^{-1} : \boldsymbol{\sigma} \tag{3}$$

$$\dot{\boldsymbol{\varepsilon}}^{in} = \sqrt{\frac{3}{2}} \left\langle \frac{F_y}{K} \right\rangle^{n} \frac{\mathbf{S} - \boldsymbol{\alpha}}{\|\mathbf{S} - \boldsymbol{\alpha}\|} \tag{4}$$

$$F_y = \sqrt{1.5(\mathbf{S} - \boldsymbol{\alpha}) : (\mathbf{S} - \boldsymbol{\alpha})} - Q \tag{5}$$

Where $\boldsymbol{\varepsilon}$, $\boldsymbol{\varepsilon}^{e}$, $\boldsymbol{\varepsilon}^{in}$ and $\dot{\boldsymbol{\varepsilon}}^{in}$ are second-ordered total strain, elastic strain, inelastic strain and inelastic strain rate tensors, respectively; $\mathbf{D}$ is the fourth-ordered elasticity tensor; K and n are temperature-dependent material parameters representing the viscosity of the material at different temperatures; $\mathbf{S}$, $\boldsymbol{\alpha}$ and Q represent deviatoric stress, back stress and isotropic deformation resistance, respectively. Hereafter, bold capital Roman alphabet represents fourth-ordered tensor, and other bold letters denote second-ordered tensors. The symbol $\langle\cdot\rangle$ denotes Macaulay bracket and means that: as $x \le 0$, $\langle x \rangle = 0$; as $x > 0$, $\langle x \rangle = x$.

4.2 Kinematic hardening rule

The non-linear kinematic hardening rule employed in the Kang-Kan model (Kan et al., 2007) is modified as a combination of the A-F model (Armstrong and Frederick, 1966) and Ohno-Wang model II (Ohno and Wang, 1993a) to describe the continuously decreasing ratchetting strain rate within certain cycles reasonably, i.e.,

$$\boldsymbol{\alpha} = \sum_{k=1}^{M} \boldsymbol{\alpha}^{(k)} \tag{6}$$

where $\boldsymbol{\alpha}$ is total back stress tensor and is divided into M components denoted as $\boldsymbol{\alpha}^{(k)}$ (k=1, 2, …, M). The evolution equation of each back stress component is expressed as:

$$\dot{\boldsymbol{\alpha}}^{(k)} = \zeta^{(k)} \left\{ \frac{2}{3} r^{(k)} \dot{\boldsymbol{\varepsilon}}^{in} - \mu^{(k)} \boldsymbol{\alpha}^{(k)} \dot{p} - \left(\frac{\bar{\alpha}^{(k)}}{r^{(k)}} \right)^{m} \left\langle \dot{\boldsymbol{\varepsilon}}^{in} : \mathbf{K}^{(k)} - \mu^{(k)} \dot{p} \right\rangle \boldsymbol{\alpha}^{(k)} \right\} - \chi^{(k)} (\bar{\alpha}^{(k)})^{\beta(k)-1} \boldsymbol{\alpha}^{(k)} \tag{7}$$

Where, $\zeta^{(k)}$ and $r^{(k)}$ are temperature-dependent material parameters; (:) indicates the inner product between second-ordered tensors; $\mathbf{K}^{(k)} = \dfrac{\boldsymbol{\alpha}^{(k)}}{\bar{\alpha}^{(k)}}$ represents the orientation of back stress component, where $\bar{\alpha}^{(k)} = (\frac{3}{2} \boldsymbol{\alpha}^{(k)} : \boldsymbol{\alpha}^{(k)})^{1/2}$ is the magnitude of each back stress component; $\dot{p} = (\frac{2}{3} \dot{\boldsymbol{\varepsilon}}^{in} : \dot{\boldsymbol{\varepsilon}}^{in})$ is the accumulated inelastic strain rate. $\mu^{(k)}$ is called as ratchetting parameter and is assumed to be identical for all the back stress components, i.e., $\mu^{(k)} = \mu$. It is also assumed that μ is a temperature-dependent material parameter and can be determined by trial-and-error method from one of the uniaxial ratchetting results. The static recovery term $-\chi^{(k)} (\bar{\alpha}^{(k)})^{\beta(k)-1} \boldsymbol{\alpha}^{(k)}$ is used to represent the static recovery effect of the alloy produced during the peak/valley stress hold. For simplicity, it is assumed that $\chi^{(k)} = \chi$ and $\beta(k) = \beta$. The parameters χ and β control the degree of static recovery occurred during the peak stress hold and are temperature-dependent.

4.3 Isotropic hardening rule

To describe the effect of cyclic softening feature on the ratchetting of the alloy, a nonlinear isotropic hardening rule is adopted in the work, i.e., for the isothermal case

$$\dot{Q} = \gamma (Q_{sa} - Q) \dot{p} \tag{8}$$

where, Q_{sa} is the saturated isotropic deformation resistance of the material presented in a specific cyclic loading and is assumed as a constant for simplicity. In Eq. (8), if $Q_{sa}<Q_0$, a decreasing isotropic deformation resistance Q is modelled, which means that the material presents a cyclic softening feature during the cyclic loading. However, if we set that $Q_{sa}>Q_0$ as done in the previous work (Kan et al., 2007), the cyclic hardening feature of SS304 stainless steel can be modelled by Eq. (8). Also, if $Q_{sa}=Q_0$, Eq. (8) represents a cyclic stable feature, which is suitable for some materials such as U71Mn rail steel (Kang, 2004). The parameter γ controls the evolution rate of isotropic deformation resistance Q. The Q_{sa} and γ are both temperature-dependent.

5. Simulations and discussion

5.1 Determination of material parameters

The material parameters used in the proposed constitutive model can be determined from the experimental results as follows: (1) The material parameters $\zeta^{(k)}$ and $r^{(k)}$ are determined

directly from the stress-plastic strain curves of monotonic tension at moderate strain rate (e.g., 0.2%·s^{-1}) by using the method described in Kang et al. (2002). (2) The material constants K and n are determined by fitting the monotonic tensile stress-strain curves at several strain rates and at room or elevated temperature. (3) Q_{sa} is determined from one of uniaxial symmetrical strain-controlled cyclic experiments with moderate strain amplitude (e.g., 0.7%) and at moderate strain rate (e.g., 0.2%·s^{-1}). (4) μ and m are obtained by trial-and-error method from one of uniaxial ratchetting results. (5) χ and β are determined from the cyclic stress-strain curves with peak/valley stress hold by trials-and-errors method at certain temperature. Besides, M=8 is used in order to simulate the ratchetting more accurately, as Kan et al (Kan et al., 2007) did. All the parameters used in the model are listed in Table 1.

Room temperature	M=8, Q_0=260MPa, K=90MPa, n=13, μ=0.01, v=0.33, E=76GPa, m=10, Q_{sa}=255MPa, γ=4; $\xi^{(1)}$=10000, $\xi^{(2)}$=2083, $\xi^{(3)}$=649, $\xi^{(4)}$=359.7, $\xi^{(5)}$=207, $\xi^{(6)}$=101, $\xi^{(7)}$=50.8, $\xi^{(8)}$=25; $r^{(1)}$=2.51, $r^{(2)}$=25.8, $r^{(3)}$=4.39, $r^{(4)}$=2.3, $r^{(5)}$=1.68, $r^{(6)}$=3.94, $r^{(7)}$=3.92, $r^{(8)}$=22.66(MPa); χ=7.9e-10MPa^{-1}, β=3.5.
150°C	M=8，Q_0=230MPa, K=80MPa, n=10, μ=0.005, v=0.33, E=75.6GPa, m=13, Q_{sa}=225MPa, γ=3; $\xi^{(1)}$=6666, $\xi^{(2)}$=2016, $\xi^{(3)}$=909, $\xi^{(4)}$=333, $\xi^{(5)}$=147, $\xi^{(6)}$=74.6, $\xi^{(7)}$=32.5, $\xi^{(8)}$=18.2; $r^{(1)}$=21.78, $r^{(2)}$= 23.84, $r^{(3)}$=17.16, $r^{(4)}$=1.11, $r^{(5)}$=5.07, $r^{(6)}$=1.93, $r^{(7)}$=12.08, $r^{(8)}$=16.38(MPa); χ=1.2e-10MPa^{-1}, β=3.

Table 1. Material parameters used in the proposed model

It should be noted that except for the parameters χ and β, other parameters used in the proposed model are determined from the experimental results obtained without any peak/valley stress/strain hold, where the effect of static recovery term can be ignored for simplicity.

5.2 Simulations and discussion

At first, it is seen from Fig. 12 that the monotonic tensile stress-strain responses of the alloy at two different strain rates are simulated by the proposed model well. However, since the static recovery term is neglected when the material parameters (except for χ and β) are determined from the monotonic tensile experiments, the simulated stress-strain responses by the proposed model with static recovery term are somewhat lower than the experimental ones in some cases.

Secondly, the cyclic stress-strain responses of the 6061-T6 aluminium alloy presented under the uniaxial strain-controlled cyclic loading with or without peak and valley strain holds are also simulated by the proposed model at two described temperatures. The results in Fig. 13 show that: (1) The cyclic softening feature is predicted reasonably by the model due to the employment of a nonlinear isotropic hardening rule describing the cyclic softening behaviour at two prescribed temperatures; (2) The effect of peak/valley strain holds on the responded stress amplitude is described reasonably by the model due to its kinematic hardening rule with a static recovery term.

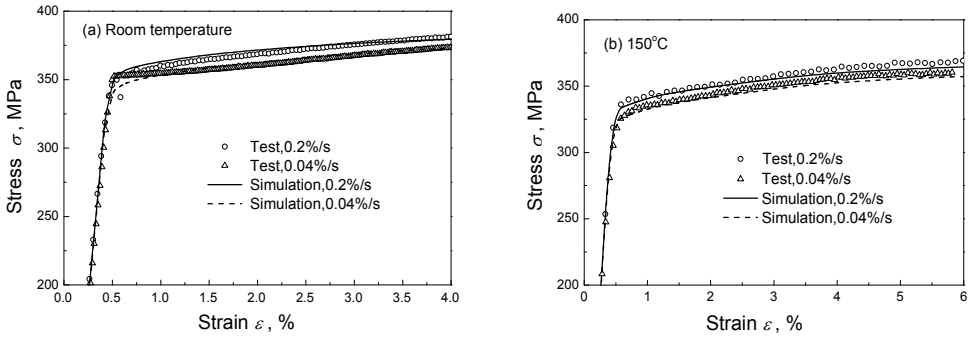

Fig. 12. Experimental and simulated results of monotonic tensile stress-strain curves of 6061-T6 aluminium alloy at two strain rates: (a) at room temperature; (b) at 150°C. (Originally from Ding et al. (2010))

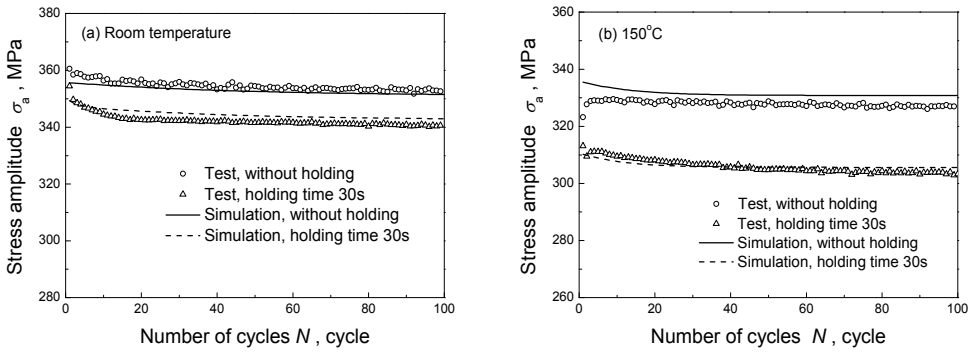

Fig. 13. Experimental and simulated results of responded stress amplitude vs. number of cycles for 6061-T6 aluminium alloy in the uniaxial symmetrical strain-controlled cyclic loading with strain amplitude of 0.6% and varied hold-time at peak and valley strains: (a) at room temperature; (b) at 150°C. (Originally from Ding et al. (2010))

Finally, the time-dependent ratchetting of 6061-T6 aluminium alloy is simulated by the proposed model, and the simulated results for different loading cases are shown in Fig. 14 to Fig. 17.

It is concluded from the figures that: (1) The effects of applied mean stress and stress amplitude on the uniaxial ratchetting of the alloy are reasonably described by the proposed model at room temperature and 150°C, as shown in Fig. 14 and Fig. 15. (2) The time-dependent ratchetting behaviours of the alloy presented at different stress rates and with or without peak stress holds are well predicted by the proposed model as shown in Fig. 16 and Fig. 17, due to the addition of the static recovery term into the nonlinear kinematic hardening rule.

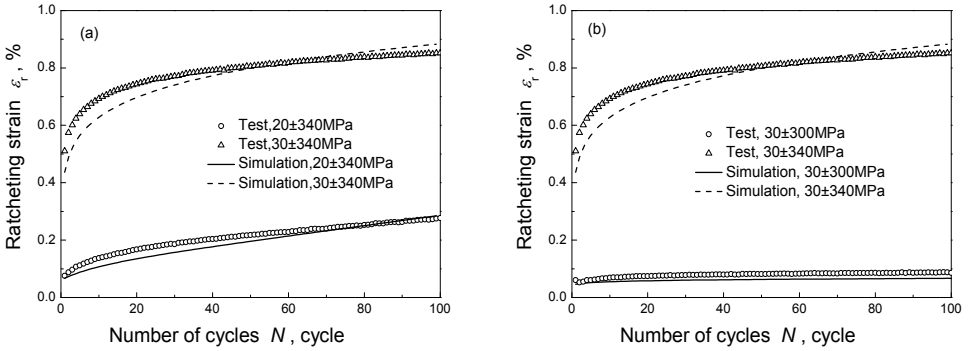

Fig. 14. Experimental and simulated results of uniaxial ratcheting for 6061-T6 aluminium alloy at room temperature (stress rate 100MPa·s^{-1}): (a) with different mean stresses; (b) with different stress amplitudes. (Originally from Ding et al. (2010))

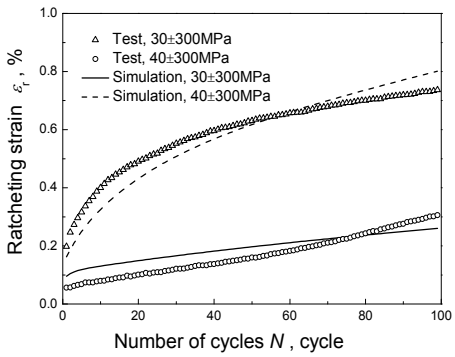

Fig. 15. Experimental and simulated results of uniaxial ratcheting for 6061-T6 aluminium alloy at 150°C and with different mean stresses (stress rate 100MPa·s^{-1}). (Originally from Ding et al. (2010))

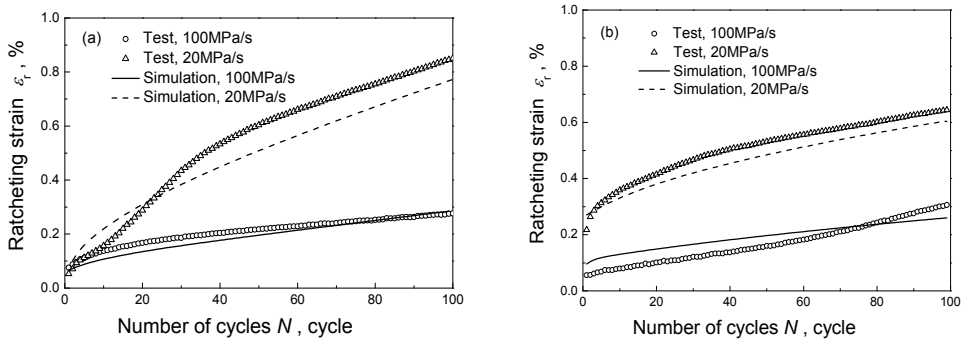

Fig. 16. Experimental and simulated results of time-dependent ratchetting for 6061-T6 aluminium alloy at two stress rates: (a) 20±340MPa, at room temperature; (b) 30±300MPa, at 150°C. (Originally from Ding et al. (2010))

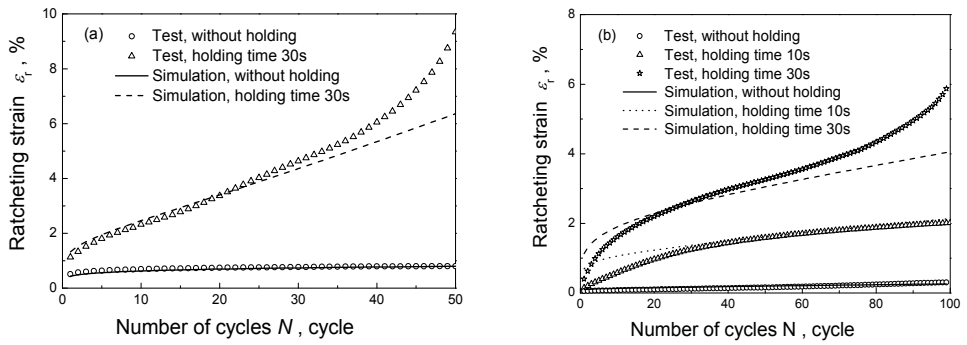

Fig. 17. Experimental and simulated results of time-dependent ratchetting of 6061-T6 aluminium alloy with different hold-times at peak stress (stress rate 100MPa·s^{-1}): (a) 30±340MPa, at room temperature; (b) 30±300MPa, at 150°C. (Originally from Ding et al. (2010))

From the simulated results shown in Fig. 14 to Fig. 17, it can be obtained that the decreasing ratchetting strain rate with the increasing number of cycles observed in the experimental results of 6061-T6 aluminium alloy within certain cycles is simulated reasonably by the proposed model employing the nonlinear kinematic hardening rule combining A-F model and Ohno-Wang model II. The decreasing rate of ratchetting strain is reasonably described by the power function $\left(\frac{\bar{\alpha}^{(k)}}{r^{(k)}}\right)^m$ used in the proposed model, while the Heaviside function $H(f^{(k)})$ used in the Kang-Kan model (Kan et al. 2007) just can provide a constant rate of ratchetting strain.

It should be noted that in the cases with peak stress hold for 30s at room temperature and 150°C, the experimental phenomenon that the ratchetting strain rate re-increases quickly with the increasing number of cycles after certain cycles as shown in Fig. 17a and 17b cannot be precisely predicted by the proposed model. As mentioned in Section 3, the re-acceleration of ratchetting deformation in these cases is mainly caused by the interaction of cyclic softening feature and fatigue damage after certain cycles. However, the proposed model neglects the evolution of fatigue damage and its effect on the ratchetting of the alloy. Therefore, although the cyclic softening feature of the alloy has been reasonably considered in the proposed model as shown in Fig. 13, the model cannot provide a precise simulation to the re-acceleration of ratchetting strain rate as shown in Fig. 17. The constitutive model

considering the interaction of ratchetting and fatigue damage will be discussed in the future work for 6061-T6 aluminium alloy in the framework of finite deformation, because the final ratchetting strains in some cases are much larger than 10% as shown in Figs. 9 to 11. Furthermore, only the uniaxial time-dependent ratchetting of 6061-T6 aluminium alloy is discussed in this work with the assumption of isothermal deformation. The multiaxial time-dependent ratchetting and that in the non-isothermal case have not been considered yet. It is concluded in Kang et al. (2006) that the multiaxial time-dependent ratchetting is affected by the obvious non-proportionally additional hardening under multiaxial cyclic loading. So the non-proportionality should be considered in the model describing the multiaxial time-dependent ratchetting, which is now in progress and will be discussed in future work.

6. Conclusions and future research

Based on the works done by Ding et al. (2007), Kang et al. (2008) and Ding et al. (2010), the following conclusions are summarized for the cyclic deformation of 6061-T6 aluminium alloy at room and high temperatures: (1) The 6061-T6 aluminium alloy presents apparent cyclic softening feature, and the cyclic softening feature is time-dependent at room and high temperatures, i.e., the responded stress amplitude decreases with the increasing holding time during the cyclic straining with peak/valley strain hold. (2) Ratchetting occurs in the alloy remarkably during the cyclic stressing with non-zero mean stress. The ratchetting greatly depends on the current stress level and its loading history. The ratchetting strain increases with the increasing of applied mean stress or stress amplitude, and the previous cyclic stressing with higher stress level restrains the occurrence of ratchetting in the sequent cyclic stressing with lower stress level. (3) The ratchetting of the alloy presents remarkable time-dependence at room and high temperatures. The ratchetting strain produced during the cyclic stressing at lower stress rate or with certain peak stress hold is much higher that that at higher stress rate and without peak stress hold. The time-dependent ratchetting of the alloy is mainly caused by the creep deformation produced during the peak stress hold or at lower stress rate due to its viscosity at room and high temperatures. (4) The whole-life ratchetting evolution of the alloy at room temperature can be divided into three stages, i.e., the first stage with decreasing ratchetting strain rate, second stage with an almost constant rate and the third stage with quickly increasing rate. As a result, the fatigue life is shortened by the quicker ratchetting evolution. The creep strain produced during the peak/valley stress hold and at lower stress rate accelerates the evolution of ratchetting and shortens the low-cycle fatigue life of the alloy. (5) Based on the experimental results of time-dependent ratchetting for 6061-T6 aluminium alloy at room temperature and 150°C, a new unified visco-plastic constitutive model is proposed to predict the uniaxial time-dependent ratchetting by extending the Kang-Kan model (Kan et al., 2007). The extended kinematic hardening rule is based on the combination of the A-F model and Ohno-Wang model II, rather than that of the A-F model and Ohno-Wang model I in Kan et al. (2007), to obtain a continuously decreasing ratchetting strain rate. Comparing with the experimental results shows that the proposed model provides a good simulation to the time-dependent cyclic deformation behaviour of 6061-T6 aluminium alloy at room temperature and 150°C, including the uniaxial time-dependent ratchetting.

As a preliminary study on the ratchetting of aluminium alloys, as summarized in this chapter, the authors only perform an experimental observation on the uniaxial ratchetting and ratchetting-fatigue interaction of 6061-T6 aluminium alloy and their time-dependence, and construct a new unified visco-plastic cyclic constitutive model to describe the uniaxial time-dependent ratchetting of the alloy. Much more effort is needed to investigate the ratchetting and ratchetting-fatigue interaction of aluminium alloys in the future, especially on the topics listed as follows: (1) Experimental observation of multiaxial ratchetting and ratchetting-fatigue interaction of aluminium alloys at room and high temperatures; (2) Constitutive model of multiaxial time-dependent ratchetting; (3) Damage-coupled constitutive model and fatigue failure model of ratchetting-fatigue interaction; (4) finite element implementation of newly developed cyclic constitutive model and numerical simulation to the cyclic deformation of structure components made from aluminium alloys; (5) Micro-mechanism of ratchetting behaviour of aluminium alloys and micro-mechanism-based constitutive model.

7. Acknowledgement

The work was financially supported by National Natural Science Foundation of China (No. 10772153) and the project of "973" with contract number of 2007CB714704. AvH Foundation and Prof. O.T. Bruhns are also appreciated for their support to G.Z. Kang's staying in Germany (2009-2010) as an AvH Experienced Research Fellow.

8. References

Abdel-Karim, M. & Ohno, N. (2000). Kinematic hardening model suitable for ratchetting with steady-state, *International Journal of Plasticity*, Vol. 16, No. 2, 225-240.

Armstrong, P. & Frederick, C. (1966). A mathematical representation of multiaxial Bauschinger effect, *CEGB report rd/b/n731*, Berkely Nuclear Laboratories, Berkely, UK.

Bari, S. & Hassan, T. (2002). An advancement in cyclic plasticity modeling for multiaxial ratchetting simulation, *International Journal of Plasticity*, Vol. 18, No. 5, 873-894.

Chaboche, J. (1991). On some modifications of kinematic hardening to improve the description of ratchetting effects, *International Journal of Plasticity*, Vol. 7, No. 7, 661-678.

Chaboche, J. (2008). A review of some plasticity and viscoplasticity constitutive theories, *International Journal of Plasticity*, Vol. 24, No. 9, 1642-1693.

Chen, X. & Abel, A. (1996). A two-surface model describing ratchetting behaviours and transient hardening under nonproportional loading, *Acta Mechanica Sinica*, Vol. 12, No. 4, 368-376.

Chen, X. & Jiao, R. (2004). Modified kinematic hardening rule for multiaxial ratchetting prediction, *International Journal of Plasticity*, Vol. 20, No. 5, 871-898.

Ding, J., Kang, G., Liu, Y. & Wang, H. (2007). Uniaxial time-dependent cyclic deformation of 6061-T6 aluminium alloy, *The Chinese Journal of Nonferrous Metals*, Vol. 17, No. 12, 1993-1998. (in Chinese)

Ding, J., Kang, G., Liu, Y. & Wang, H. (2008). Study on the uniaxial cyclic deformation of LY12CZ aluminium alloy and its time-dependence, *Acta Aeronautica et Astronautica Sinica*, Vol. 29, No. 1, 70-74. (in Chinese)

Ding, J., Kang, G., Kan, Q. & Liu, Y. (2010). Constitutive model for time-dependent ratcheting behavior of 6061-T6 aluminium alloy, *Computational Materials Science*, 2010, to be submitted.

Hu, W., Wang, C. & Barter, S. (1999). Analysis of cyclic mean stress relaxation and strain ratchetting behaviour of aluminium 7050, *DSTO-RR-0153*, Aeronautical and Maritime Research Laboratory, Victoria, Australia.

Jiang, Y. & Sehitoglu, H. (1996). Modeling of cyclic ratchetting plasticity, *ASME Journal of Applied Mechanics*, Vol. 63, No. 3, 720-733.

Kan, Q., Kang, G. & Zhang, J. (2007). Uniaxial time-dependent ratchetting: visco-plastic model and finite element application, *Theoretical and Applied Fracture Mechanics*, Vol. 47, No. 2, 133-144.

Kang, G. (2004). A visco-plastic constitutive model for ratchetting of cyclically stable materials and its finite element implementation, *Mechanics of Materials*, Vol. 36, No. 4, 299-312.

Kang, G. (2008). Ratchetting: Recent progresses in phenomenon observation, constitutive modelling and application, *International Journal of Fatigue*, Vol. 30, No. 10, 1448-1472.

Kang, G., Gao, Q. & Yang X. (2002). A visco-plastic constitutive model incorporated with cyclic hardening for uniaxial/multiaxial ratchetting of SS304 stainless steel at room temperature, *Mechanics of Materials*, Vol. 34, No. 9, 521-531.

Kang, G., Kan, Q., Zhang, J. & Sun, Y. (2006). Time-dependent ratchetting experiments of SS304 stainless steel, *International Journal of Plasticity*, Vol. 22, No. 5, 858-894.

Kang, G., Liu, Y. & Ding, J. (2008). Experimental study on time-dependent ratcheting-fatigue interaction of T6-6061Al alloy, *Proceedings of FM2008*, pp. 287-291, Hangzhou, October, 2008, East China University of Science and Technology Press, Shanghai, China.

Kang, G., Liu, Y., Ding, J. & Gao, Q. (2009). Uniaxial ratcheting and fatigue failure of tempered 42CrMo steel: Damage evolution and damage-coupled visco-plastic constitutive model, *International Journal of Plasticity*, Vol. 25, No. 5, 838-860.

Kang, G., Ohno N. & Nebu, A. (2003). Constitutive modeling of strain-range-dependent cyclic hardening, *International Journal of Plasticity*, Vol. 19, No. 10, 1801-1819.

Ohno, N. (1990). Recent topics in constitutive modeling of cyclic plasticity and visco-plasticity, *Applied Mechanics Review*, Vol. 43, No. 11, 283-295.

Ohno, N. (1997). Recent progress in constitutive modelling for ratchetting, *Material Science Research International*, Vol. 3, No. 1, 1-10.

Ohno, N. & Wang, J. (1993a). Kinematic hardening rules with critical state of dynamic recovery: I. Formulation and basic features for ratchetting behavior, *International Journal of Plasticity*, Vol. 9, No. 3, 375-389.

Ohno, N. & Wang, J. (1993b). Kinematic hardening rules with critical state of dynamic recovery: II. Application to experiments of ratchetting behavior, *International Journal of Plasticity*, Vol. 9, No. 3, 390-403.

Yang, X., Gao, Q., Cai, L. & Xiang, Y. (1998). An experimental study on the ratchetting behaviour of pure aluminium under uniaxial cyclic stressing, *Acta Mechanica Solida Sinica*, Vol. 19, No. 2, 134-137.

11

Crack Growth in AlCu4Mg1 Alloy under Combined Cyclic Bending and Torsion

Dariusz Rozumek and Ewald Macha
Opole University of Technology
Poland

1. Introduction

Aluminium and its alloys are the materials tested for many years and frequently used for the elements of fatigue loading. The most characteristic properties of aluminum are low weight (3 times less than iron) and low melting point (about 2.5 times smaller than the iron). In addition, aluminum has good corrosion resistance properties by creating a thin and tight (passive) layer of Al_2O_3. Therefore, aluminum alloys are widely used in the construction of airplanes, vehicles, transport equipment, machinery or parts of building structures. All technical alloys are divided into two groups: alloys for plastic working and foundry alloys. The boundary between them is determined by the maximum content of an additional component dissolved in the solid solution at the eutectic temperature. The appearing eutectic adversely affects the technological properties of the alloy (reduced susceptibility to plastic working). As for aluminum alloys subjected to plastic working and heat treatment in order to their hardening, duralumin is most widely applied. These alloys are usually subjected to heat treatment consisting of annealing, saturating or ageing. In the paper (Kocańda & Kozubowski, 1974) the authors studied the influence of microstructure on the alloy PA6 on appearance of fatigue microcracks. It was noted the presence of gas microbubbles, and precipitations of secondary phases. It was found that gas microbubbles are the source of fatigue microcracks. Döring et al. (2006) presented the test results described by the ΔJ-integral range, obtained under non-proportional loading including the crack closure. The test results obtained under tension with torsion for three materials (two steels and one aluminium alloy) were analysed. Different loading paths were applied (circle, ellipse, octant, square and cross). Fatigue crack growth behavior (Chung & Yang, 2003) in Al 6061-T6 thick aluminium plate with composite material patch was studied. Five inclined crack plates repaired with patch were tested. Crack branching at the threshold level and crack closing can be described (Pokluda, 2004) with the local approach including the ratio of the grain size to the plastic zone size. At that level of the crack development there are three mixed-cracking modes before the crack front, even in the case of mode I only, visible outside the tested element. Three materials were tested (steel, aluminium alloy and titanium alloy).
The aim of this chapter is the presentation of static and cyclic properties of aluminum alloy AlCu4Mg1 and to present the test results of fatigue crack growth in plane notched specimens under bending and proportional bending with torsion.

2. Experimental procedure

2.1 Material and specimens

AlCu4Mg1 aluminium alloy included in the standard EN AW- 2024 and PN-92/H-93667 was subjected to tests. The tested material belongs to a group of medium-alloy duralumins. Beams of such a shape are used, among others, as torsion bars in cars (Renault), trucks and tanks (attachment of springs), and intermediate beams for gas and oil wells. The AlCu4Mg1 aluminium alloys with copper and magnesium, i.e. duralumin, belong to the alloys of high strength properties. They contain a solid solution α and numerous precipitations of phases Al_3Mg_2, $CuAl_2$ and triple S-phase (Al_2CuMg), and dark precipitations of the phase containing Fe: $Fe_3Si_2Al_{12}$, occurring mainly at grain boundaries of phase α. Precipitations of these phases strongly influence strength and hardness of AlCu4Mg1 alloy, especially precipitations at the phase boundaries reduce plastic properties. Cracks of the specimens made of aluminium alloys of phase α structure occur on the slip plane $\{111\}$ under the shear stress independent on spatial orientation of the grain. Figure 1 shows a microstructure of AlCu4Mg1 aluminium alloy that consists of lighter α grains with darker phases $CuAl_2$ and Al_2CuMg. The microstructure is characterized by a bands grains according to the plastic treatment direction: elongated grains of the phase α are to 50 μm in width and the minor phase $CuAl_2$ and Al_2CuMg diameter from 5 to 10 μm.

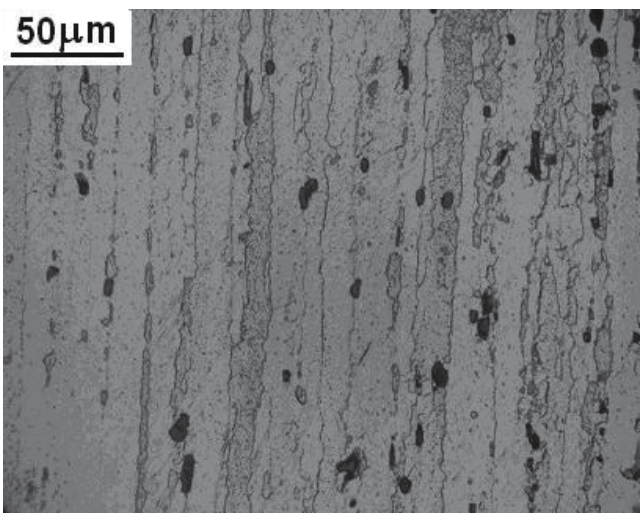

Fig. 1. Microstructure of AlCu4Mg1 aluminium alloy, magnification 500x

Specimens with rectangular cross-sections for bending (area 60 mm²) and bending with torsion (area 64 mm²) and dimensions: length l = 110 (90) mm, height w = 16 (10) mm and thickness g = 4 (8) mm were tested (see Fig. 2). Each specimen had an external unilateral notch with depth 2 mm and radius ρ = 0.2 mm. The notches in the specimens were cut with a milling cutter and their surfaces were polished after grinding. Chemical composition and some mechanical properties of the tested aluminium alloy are given in Tables 1 and 2.

The critical value of the integral for AlCu4Mg1 aluminium alloy is J_{Ic} = 0.026 MPa·m (ASTM E1820-99). Strain-based fatigue curves are shown in Fig. 3, where elastic and plastic components are given too. As usual, such curves have been described by a linear law in a

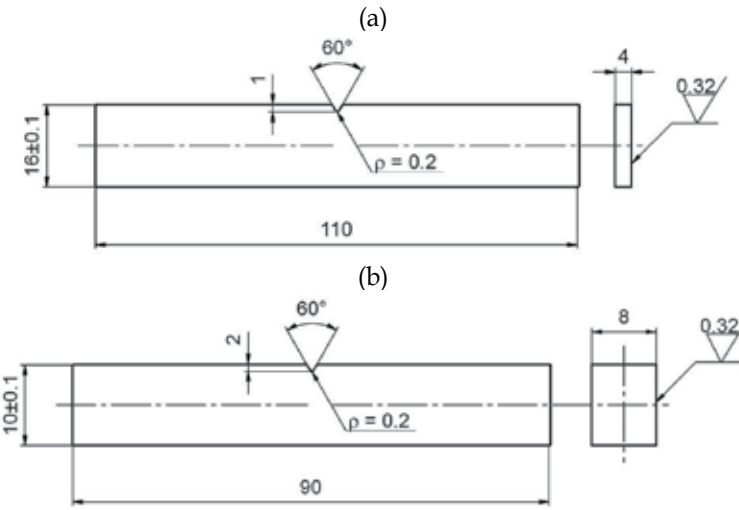

Fig. 2. Shape and dimensions of specimen, dimensions in mm for: (a) bending, (b) bending with torsion

Cu	Mn	Zn	Mg	Fe	Cr	Si	Ti	Al
4.15	0.65	0.50	0.69	0.70	0.10	0.45	0.20	bal.

Table 1. Chemical composition of the AlCu4Mg1 aluminium alloy (in wt %)

σ_y MPa	σ_u MPa	E GPa	ν
382	480	72	0.32

Table 2. Monotonic quasi-static tension properties of the AlCu4Mg1 aluminium alloy

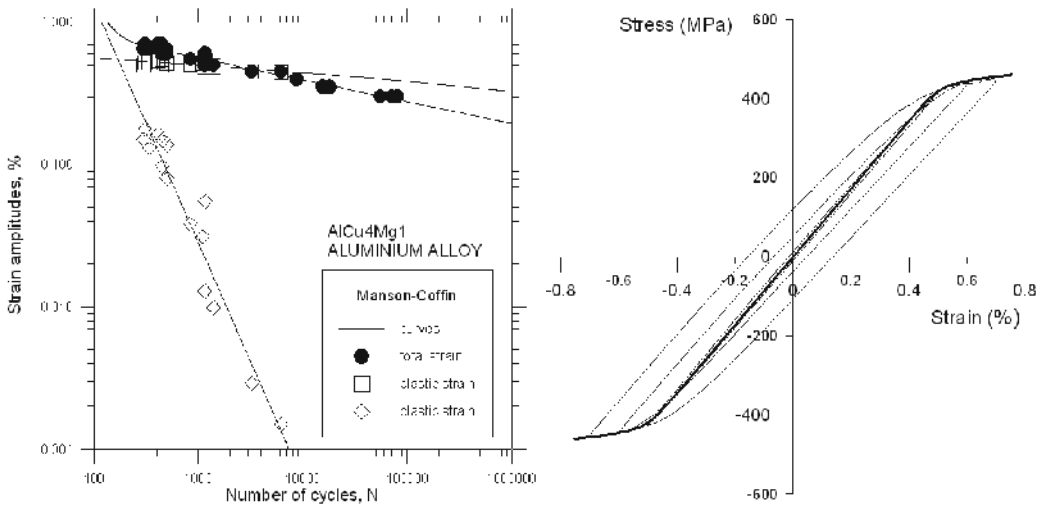

Fig. 3. Fatigue curves under strain control and some stabilized hysteresis loops of AlCu4Mg1 aluminium alloy

log-log diagram, as suggested by the Manson-Coffin model. In the same figures, some stabilised hystheresis loops are displayed too. Coefficients of the Ramberg-Osgood equation describing the cyclic strain curve under tension-compression conditions with R = - 1 for AlCu4Mg1 aluminium alloy are the following (Rozumek, 2005): the cyclic strength coefficient K′, the cyclic strain hardening exponent n′, fatigue strength coefficient σ_f', fatigue ductility coefficient ε_f', fatigue strength exponent b, fatigue ductility exponent c (Table 3). After the analysis of axial cyclic stress–strain curves, it was concluded that AlCu4Mg1 aluminium alloy is cyclically hardening material during fatigue tests.
The static and cyclic properties for AlCu4Mg1 aluminium alloy were obtained from the tests done at the laboratory of Department of Mechanics and Machine Design, Opole University of Technology, Poland.

K′ MPa	n′	σ_f' MPa	ε_f'	b	c
563	0.033	605	0.105	-0.051	-0.858

Table 3. Fatigue properties of the AlCu4Mg1 aluminium alloy

2.2 Fatigue testing

Fatigue tests were performed in the low cycle fatigue (LCF) and high cycle fatigue regimes (HCF) under the load ratio R = M_{min} / M_{max} = - 1, - 0.5, 0. The tests were carried out under controlled loading from the crack occurrence to the specimen fracture. Starting point of crack initiation at notch root was observed on side of the specimen. The tests were performed on a fatigue test stand MZGS-100 (Rozumek & Macha, 2006) where the ratio of torsion moment to bending moment was $M_T(t)$ / $M_B(t)$ = tanα, where α = 30°, 45° and 60° (Fig. 4) and loading frequency was 29 Hz. The total moment $\overline{M}(t)=\overline{M}_T(t)+\overline{M}_B(t)$ was

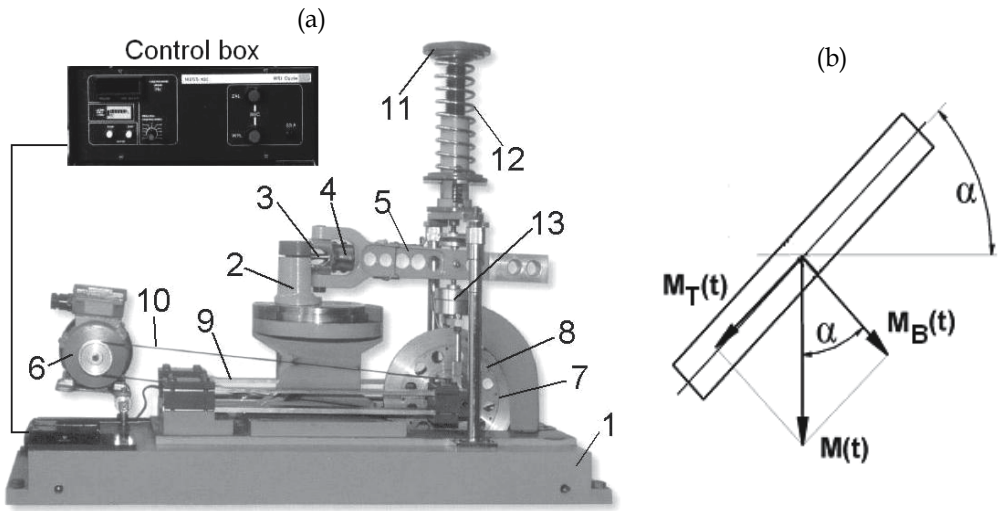

Fig. 4. Fatigue test stand MZGS-100 (a) and loading of the specimen (b)
where: 1 – bed, 2 – rotational head with a holder, 3 - specimen, 4 - holder, 5 - lever (effective length = 0.2 m), 6 - motor, 7 – rotating disk, 8 - unbalanced mass, 9 – flat springs, 10 – driving belt, 11 – spring actuator, 12 - spring, 13 – hydraulic connector.

generated by forces on the arms 0.2 m in length. When $\alpha = 0°$ we have pure bending; for $\alpha = 90°$ we obtain pure torsion. Shearing force on a fatigue test stand MZGS-100 coming from bending takes very small values, below 2% of the maximum moment. The fatigue test stand MZGS-100 (Fig. 4a) consist of power unit, control unit and loading unit. Loading unit consists of cyclic and static loading. Cyclic loading is obtained by vertical movements of the lever. Static loading is obtained by a spring pressure. Crack development was observed on the specimen surface with the optical method. The fatigue crack increments were measured with a digital micrometer located in the portable microscope with magnification of 25 times and accuracy of 0.01 mm. At the same time, a number of loading cycles N was written down. Under bending with torsion, dimension "a" of the crack growth was defined as increments of length and angle α_1 (Fig. 12) of the crack measured on the specimen side surface.

2.3 Microstructure and fatigue crack path in AlCu4Mg1

Fig. 5 shows the surface of the specimen made of AlCu4Mg1 aluminium alloy, tested under loading $M_a = 15.6$ N·m corresponding to the nominal stress amplitude to the crack initiation $\sigma_a = 104$ MPa and the stress ratio $R = - 0.5$ after $N_f = 49000$ cycles. Different magnifications were selected in such a way that they present a path of the main crack, about 3 mm in length. Fig. 5b presents the final history of the crack about 250 μm in length, cut off from Fig. 5a and magnified in order to analyse the crack development. In AlCu4Mg1 aluminium alloy transcrystalline microcracks can be seen in grains of phase α, in the axial section of the specimen (see Fig. 5b). The main characteristics of long cracks development is their regularity of propagation and orientation. There are no short cracks, some or several μm in length, deflecting from the main crack, which we can observe, for example, in titanium alloys.

The forming faults from the main crack can be seen, which run according to directions of phases Al_2CuMg (almost perpendicularly to the loading applied), and next they go into the phase α. On the fractures we can observe usually transcrystalline cracks through grains of the phase α, but also cracks along the grain boundaries can be noticed. The main cracks developed on the planes of maximum shear stresses. In the considered material we have mixed cracking, i.e. brittle and plastic. In Fig. 5b we can observe both kinds of cracking near the main crack, i.e. pits of different size, typical for plastic cracking, and cracks along the grain boundaries typical for brittle fractures.

2.4 Stress distribution

If the specimen is both bended by moment M_B and twisted by moment M_T (Fig. 4b), then in a given rectangular cross-section normal stresses form under the influence of bending and the shear stresses result from torsion (Rozumek & Macha, 2009). The normal stresses change from zero in the neutral axis to the maximum value $\sigma_a = \frac{6M_B}{gw^2}$ in the extreme fibres (σ_{max}) (Fig. 6). Shear stresses occur changing from zero in the specimen axis to the maximum value $\tau_a = \frac{M_T}{k_1 wg^2}$ ($k_1 = 0.208$ – ratio of the height to the thickness of specimen) in the most distant points of specimen's shorter side (τ_{max}) (Fig. 6).

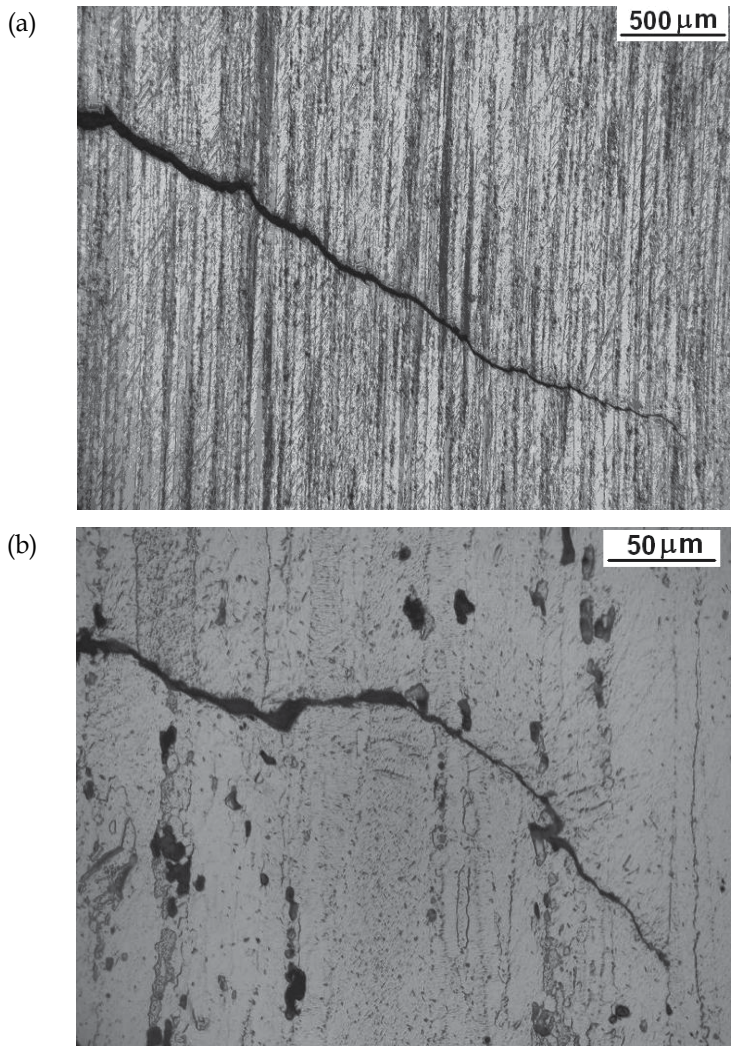

Fig. 5. The fatigue crack path in the AlCu4Mg1 under bending: (a) magnification 50x, (b) magnification 500x

De Saint-Venant worked on the problem of stress distribution under torsion. He found that stresses were equal to zero inside and in the corners of the bar, and they were the biggest in the centers of square sides (longer sides of the rectangle). In the specimen under torsion, cross-sections do not remain plane but are subjected to deformation or the so-called deplanation. If torsion is unfree (as in the presented case), then shear and normal stresses occur induced by torsion. In the presented case, the normal stresses were about three times bigger than shear stresses (due to the occurrence of the notch in the plane of their action). Under simultaneous action of the two moments, M_B and M_T, the most dangerous stress state forms in the planes most distant from both the neutral axes of the specimen (Fig. 6 - σ_{max}). The stress intensity factors can be expressed as: for mode I, $K_I = Y_1\sigma_a\sqrt{\pi a}$ and for mode III, $K_{III} = Y_3\tau_a\sqrt{\pi a}$.

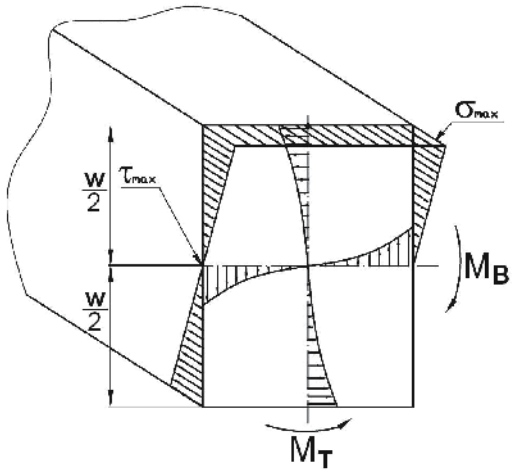

Fig. 6. Distribution of normal and shear stresses in the specimen subjected to bending with torsion (Rozumek & Marciniak, 2010)

2.5 ΔJ parameter criterion

In the case of mixed mode I and III, the range of the equivalent parameter ΔJ was assumed as the sum of ΔJ_I and ΔJ_{III}

$$\Delta J = \Delta J_{eq} = \Delta J_I + \Delta J_{III} . \tag{1}$$

The ΔJ-integral range for mode I and mode III is calculated from (Rozumek, 2005)

$$\Delta J_I = \left(1-\nu^2\right)\Delta K_I^2 / E + \pi Y_1^2 a\left(\Delta\sigma\Delta\varepsilon_p / \sqrt{n'}\right), \tag{2}$$

$$\Delta J_{III} = (1+\nu)\Delta K_{III}^2 / E + \pi Y_3^2 a\left(\Delta\tau\Delta\gamma_p / \sqrt{n'}\right), \tag{3}$$

where the first term of Eqs. (2) and (3) concerns the linear-elastic range, and the other term refers to the elastic-plastic range, a – crack length, E – Young's modulus, ν - Poisson's ratio, Δσ, Δτ - ranges of stresses under bending and torsion in the near crack tip, respectively, $\Delta\varepsilon_p$, $\Delta\gamma_p$ – ranges of plastic strains under bending and torsion in the near crack tip, respectively. The stress intensity factors ranges ΔK_I for mode I and ΔK_{III} for mode III were calculated from

$$\Delta K_I = Y_1 \Delta\sigma \cos^2\alpha\sqrt{\pi a} , \tag{4}$$

$$\Delta K_{III} = Y_3 \Delta\sigma \sin\alpha\cos\alpha\sqrt{\pi a} , \tag{5}$$

according to (Harris, 1967) and (Chell & Girvan, 1978), for mode I and mode III the correction coefficients are

$$Y_1(a/w) = 5/\sqrt{20 - 13(a/w) - 7(a/w)^2} , \tag{6}$$

$$Y_3(a/w) = \sqrt{(2w/a)\tan(\pi a/(2w))} . \tag{7}$$

3. Experimental results and discussion

3.1 Finite and boundary element model

Stresses and strains in the elastic-plastic ranges were calculated with use of the finite element method (FRANC2D software) for bending and the boundary element method (FRANC3D software) for bending with torsion. A specimen model was built and divided into finite elements with the use of CASCA graphic processor, which was integrated with FRANC2D software. Each of these areas was covered with a net of finite elements. Fig. 7a shows the division of the area around the crack into finite elements. In the model, six-nodal triangular elements were applied; the triangles were of different dimensions. The geometrical model of the specimen was created using OSM software, with the boundary element mesh generated in the FRANC3D software. The programs include the nonlinear physical Ramberg-Osgood curve of cyclic strain of the material tested. It was decided that calculations would be based on incremental elastic-plastic analysis including the kinematic model of material hardening. Having made the specimen outline, segments were divided and closed areas were defined. A boundary element mesh was put on each area. The programs design the mesh automatically. The calculations were performed for a two-dimensional and three-dimensional models of the notched specimens. Figure 7b shows division of the notch region into boundary elements. The model shown in Fig. 7b includes ten-node elements being tetrahedral (the model including 1354 triangular elements). Loading values assumed for calculations were the same as those applied in the experiments. Magnitude and shapes of boundary elements depend on division of intervals closing a given area. The greatest mesh concentration occurs in the area of the crack development (Fig. 7).

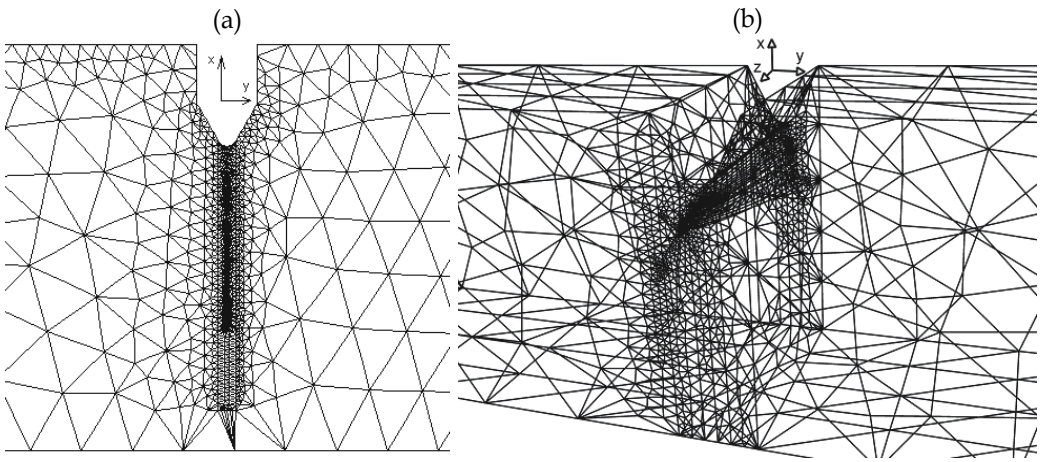

Fig. 7. Division of the notch region into finite and boundary elements in the software (a) FRANC2D, (b) FRANC3D

Next, one end of the specimen is restrained (thus taking away the degrees of freedom from the nodes of specimen model) and it is fixed in direction of axes x, y and z. In order to perform numerical calculations, it is necessary to introduce material data (such as the yield point, Young's modulus, Poisson's ratio, temperature, material density, critical value – for example, J_{Ic} integral) into the FRANC3D software.

3.2 Bending

Each series of specimens made of AlCu4Mg1 aluminium alloy was subjected to cyclic bending by the constant amplitude moment M_a = 15.64 N·m (which corresponded to the nominal amplitude of normal stresses σ_a = 104 MPa before the crack initiation) and different load ratio R = - 1, - 0.5, 0 (different mean bending moment M_m = 0, 5.21, 15.64 N·m). The test results were shown as graphs of the crack length "a" versus the number of cycles N and crack growth rate da/dN versus the ΔJ parameter. ΔJ was compared with the ΔK stress intensity factor range. The theoretical stress concentration factor in the specimen K_t = 4.29, was estimated with use of the model (Thum et al., 1960). From the fatigue crack length "a" versus number of cycles N curves reported in Fig. 8, it appears that after changing the load ratio R from - 1 to 0, fatigue life decreases. The tests were conducted under constant amplitude loading for three different values M_{max}. During the tests the lengths of fatigue cracks were measured and the current number of cycles was recorded. Basing on these measurements graphs were made "a" versus number of cycles N, which were used for calculating the fatigue crack growth rate. Graphs of the fatigue crack growth rate da/dN versus ΔJ parameter for the material tested under three load ratios R are shown on a binary logarithmic system in Fig. 9.

The test results presented in Fig. 9 were approximated with the empirical formula (Rozumek, 2005)

$$\frac{da}{dN} = \frac{B\left(\frac{\Delta J}{J_0}\right)^n}{(1-R)^2 J_{Ic} - \Delta J}, \tag{8}$$

where ΔJ = J (Δσ) - range of J parameter, B and n – coefficients determined experimentally, R - load ratio, $J_0 = 1\,\mathrm{MPa}\cdot\mathrm{m}$ - per unit value introduced to simplify the confounded coefficient unit B.

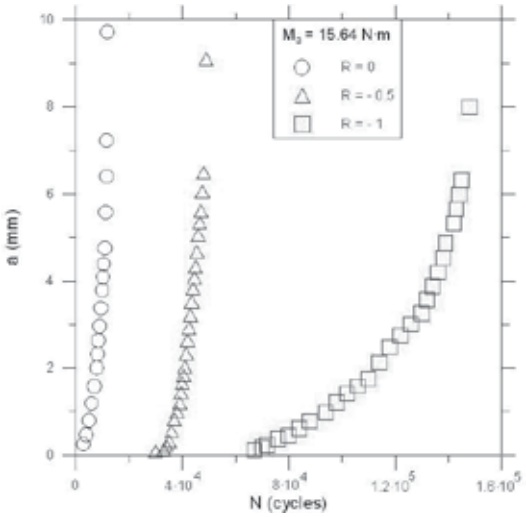

Fig. 8. Fatigue crack length versus number of cycles under bending

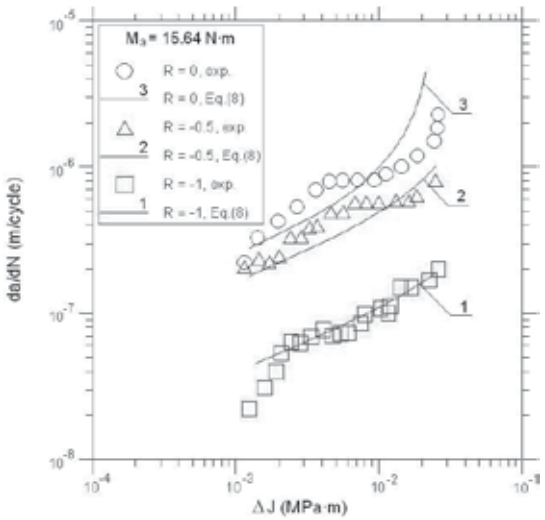

Fig. 9. Comparison of the experimental results with calculated ones according to Eq. (8)

It has been observed that in Fig. 9 (graphs 1, 2, 3), the change of the load ratio R from – 1 to 0 is accompanied by an increase in the fatigue crack growth rate. From the graphs it appears Fig. 9 that influence of the loading mean value on the crack growth rate in the AlCu4Mg1 alloy is significant. For example, from Fig. 9 it appears that while changing the value of the load ratio from R = - 1 to R = 0, a nine fold increase in fatigue crack growth rate has been noticed for $\Delta J = 3 \cdot 10^{-3}$ MPa·m. The empirical coefficients B and n occurring in Eq. (8) were calculated with the least square method and they were shown in Table 4. It means that B and n are not dependent on a kind of the material only. The test results for cyclic bending include the error not exceeding 20% at the significance level $\alpha = 0.05$ for the correlation coefficients r_w given in Table 4. The correlation coefficients take high values in all the considered cases and it means that there is a significant correlation of the test results and the assumed empirical formula (8). Table 4 also contains coefficients of the multiple correlation r_w applied in Eq. (8) and expressed by equation (Rozumek & Macha, 2006)

$$r_w = \sqrt{\frac{r_{y1}^2 + r_{y2}^2 - 2r_{y1}r_{y2}r_{12}}{1 - r_{12}^2}}, \tag{9}$$

where r_{12}, r_{y1}, r_{y2} – coefficients of cross correlation.

Fig.	Graphs	B $\mathrm{MPa \cdot m^2/cycle}$	n	r_w
9	1	$1.04 \cdot 10^{-7}$	0.51	0.96
9	2	$9.49 \cdot 10^{-8}$	0.28	0.97
9	3	$8.11 \cdot 10^{-8}$	0.30	0.94

Table 4. Coefficients B and n in Eq. (8) and correlation coefficients r_w for the curves shown in Fig. 9

Calculating ΔJ parameter, we can find that there is a functional relation between the loading range, the elastic-plastic strain range, the crack tip opening displacement and the crack length. High values of correlation coefficients show that all these factors were approximately included. Above a certain value of ΔJ parameter, the fatigue crack growth rate increases rapidly without further increase of loading. Such behaviour is connected with an unstable crack growth rate in the final stage of specimen life. In this period the stress drop can be observed as plasticization increases. Application of the ΔJ parameter is reasonable in the case of elastic-plastic materials and those with yield stress. An analysis of correlation of ΔJ and ΔK parameters was carried out to show that the ΔJ parameter is more advisable than ΔK. Therefore the following equation was used:

$$\Delta J^* = \frac{\Delta K^2}{E}, \tag{10}$$

where stress intensity factor range ΔK calculated from $\Delta K = K_{max} - K_{min} = Y_1 \Delta\sigma\sqrt{\pi a}$ and $\Delta\sigma = \sigma_{max} - \sigma_{min}$ stress range and $\Delta\sigma = 2\sigma$ for R = - 1, Y_1 - correction coefficient including finite of the specimen dimensions for mode I applied in Eq. (6).

In the linearly-elastic range, the ΔJ* parameter calculated from Eq. (10) were compared with the results obtained from to tests. The relative error was below 5%. Figure 10 shows the relation between the parameters ΔJ* and ΔJ for three load ratios R. A good linear relation (in the double logarithmic system) between these two parameters in the case of the fatigue crack growth rate for the tested material was observed. In the AlCu4Mg1 alloy and bending, this occurs for ΔJ < $4 \cdot 10^{-3}$ MP·m (Fig. 10). This means that in this test range under controlled loading, the parameter ΔJ plays a similar role to the parameter ΔK up to the moment when plastic strain occurs. When plastic strains increase, we can find an increasing difference between ΔJ* and ΔJ. The difference results from the fact that the parameter ΔJ* does not include plastic strains. At the final stage of specimen life, when ΔJ parameter approaches the

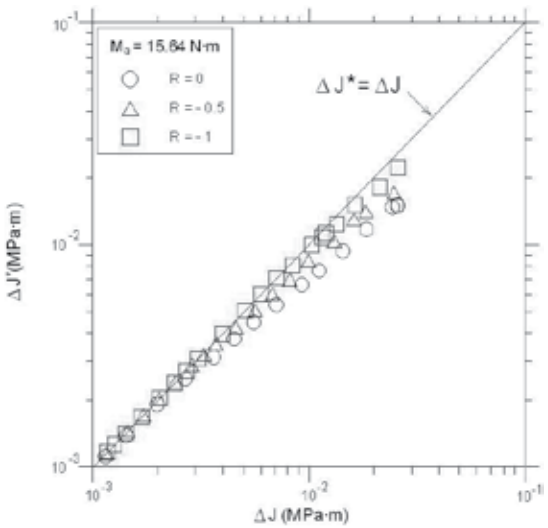

Fig. 10. The relationship between ΔJ* and ΔJ for bending

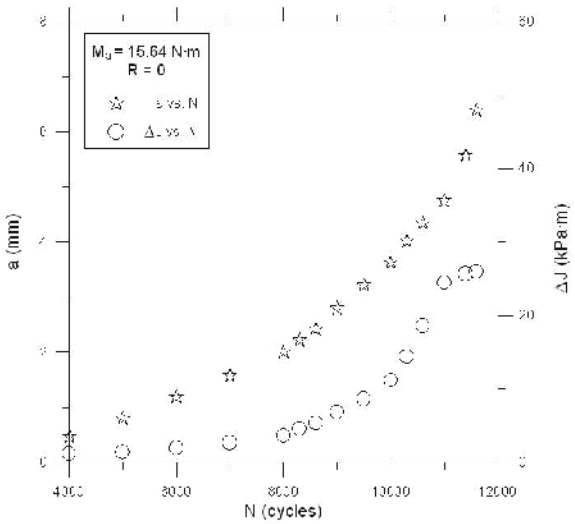

Fig. 11. Variation with cycles of crack length and ΔJ for bending and R = 0

critical value of J_{Ic}, the crack growth rate increases rapidly (Fig. 10, R = 0) and leads to the material failure. For example in Fig. 11 (AlCu4Mg1 aluminium alloy and R = 0) fatigue crack growth "a" versus the number of cycles N and ΔJ parameter versus the number of cycles N are shown in the linear system. In this figure we can observe fatigue crack growth since the beginning of the propagation until the specimen failure. In Fig. 11 the graph ΔJ versus N also shows that ΔJ parameter increases with the number of cycles until reaching 11000 cycles, then the graph stabilises (it becomes almost constant).

3.3 Bending with torsion

The chapter contains the fatigue crack growth test results obtained under proportional bending with torsion (Rozumek, 2009). The tests were performed on a fatigue test stand MZGS-100 (Fig. 4a), where the ratio of torsion moment to bending moment was $M_T(t)/M_B(t) = \tan\alpha$, where $\alpha = 30°$, 45° and 60° (Fig. 4b). Unilaterally restrained specimens were subjected to cyclic bending with torsion (mixed mode I+III) with the constant amplitude of moment M_a = 7.92 N·m and load ratio $R = M_{min} / M_{max}$ = - 1, - 0.5, 0 (for three different values M_{max} = 7.92, 10.56, 15.84 N·m), which corresponded to the nominal amplitude of normal stresses σ_a = 80.36, 65.63 and 46.41 MPa ($\sigma_{max} = K_t\sigma_a$ = 302.15, 246.77, 174.50 MPa) and the nominal amplitude of shear stresses τ_a = 37.18, 52.58 and 64.39 MPa before the crack initiation. The theoretical stress concentration factor in the specimen under bending K_t = 3.76, was estimated with use of the model (Thum et al., 1960). During experimental tests fatigue cracks lengths and angles α_1 (Fig. 12) were measured and number of cycles were registered. Next, on the basis of experimental results in the range of linear-elastic, the range of ΔK parameter was analytically calculated for mode I and mode III loading. Stresses and strains calculations in linear-elastic and elastic-plastic were made with use of numerical method (FRANC3D software). Measurement of the crack length were made on both sides of the specimens. At one side, the cracks were a little greater than at the other side. For calculations of the ΔJ parameters, greater cracks are assumed because they mainly influence the specimen failure. Also the stress fields are greater at one side of the specimen. During

the tests on the observed reproducibility of the test specimens. Fig. 12 shows an example of the crack path under proportional bending with torsion for $\alpha = 45°$.

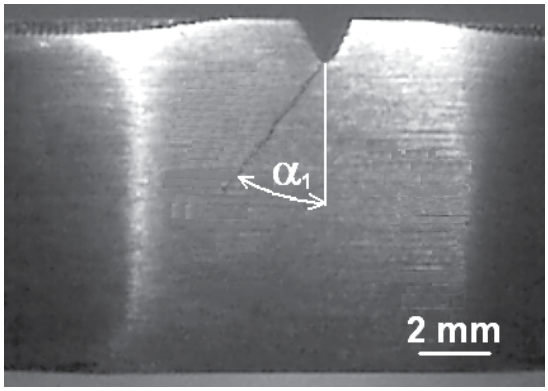

Fig. 12. Crack path in specimen under proportional bending with torsion for R = - 1 and $\alpha = 45°$

Figures 13, 14 and 15 present results of fatigue crack length versus the number of cycles for mixed mode I+III and $\alpha = 30°$, 45° and 60°, respectively.
From the graphs in Figs. 13, 14, 15 it appears that changes of the angle α from 30° to 60° are accompanied by decrease of fatigue life of the specimens for the load ratio R = - 1, - 0.5, 0. as well as after changing the load ratio from - 1 to 0, fatigue life decreases. Figures 16, 18 and 20 for load ratio R = - 1, - 0.5, 0 show fatigue crack growth rates da/dN versus ΔJ parameter for pure mode I and pure mode III and three the ratio of torsion moment to bending moment ($\alpha = 30°$, 45° and 60°). The ΔJ parameter for pure mode I and pure mode III was calculated from Eqs. (2) – (7). Next, Figs. 17, 19, 21 present the results according to equation (1) for mixed mode I+III loading.

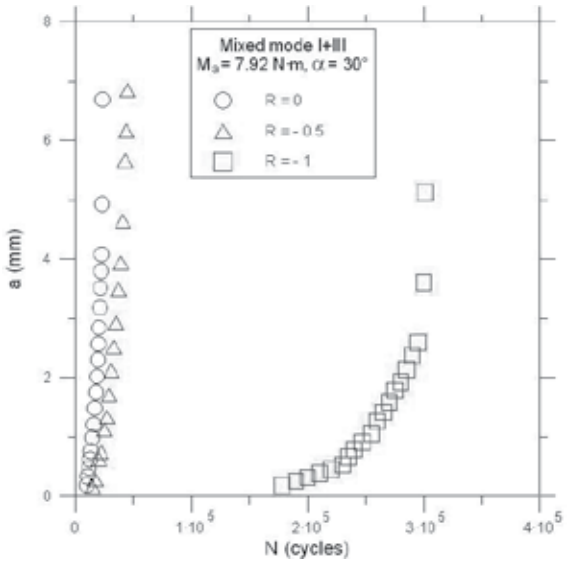

Fig. 13. Fatigue crack length versus number of cycles under mixed mode I+III loading for $\alpha = 30°$

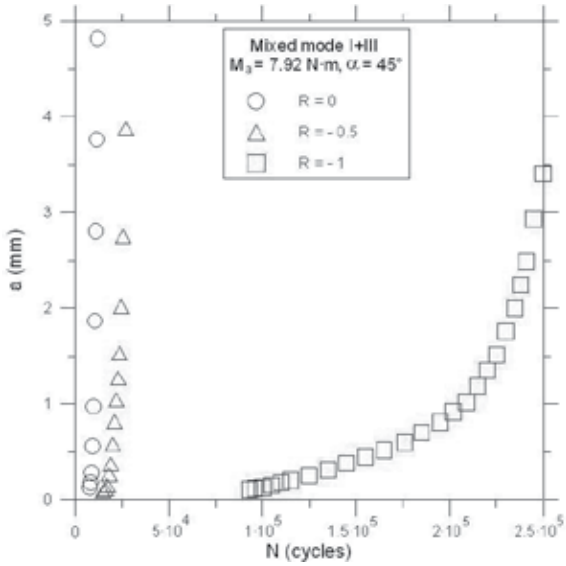

Fig. 14. Fatigue crack length versus number of cycles under mixed mode I+III loading for $\alpha = 45°$

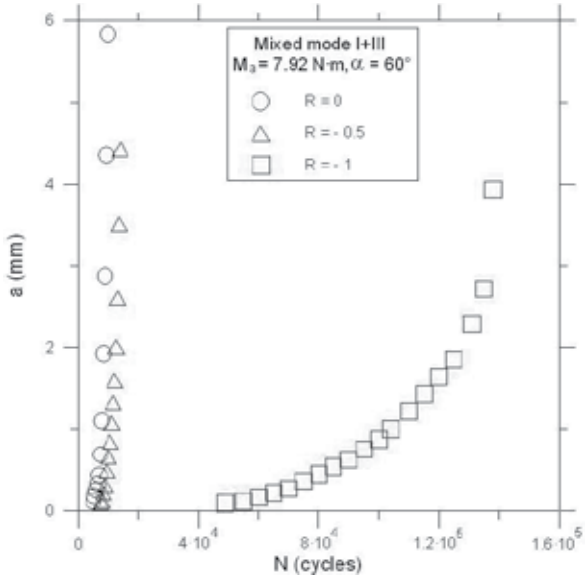

Fig. 15. Fatigue crack length versus number of cycles under mixed mode I+III loading for $\alpha = 60°$

From Figs. 16 – 21 it appears that the fatigue crack growth rate increases when we increase α from 30° to 60° and load ratio R from – 1 to 0 in the AlCu4Mg1 aluminium alloy. Moreover (Figs. 16, 18, 20), the fatigue crack growth rate is higher for mode III than for mode I for the same value of ΔJ and load ratio R = - 0.5, 0. It was found that for R = - 1 and $\alpha = 30°$ (Fig. 16) the crack growth rate was higher for mode III than for mode I in the case of the same value of ΔJ; for R = - 1 and $\alpha = 60°$ (Fig. 20) a higher rate is observed for mode I.

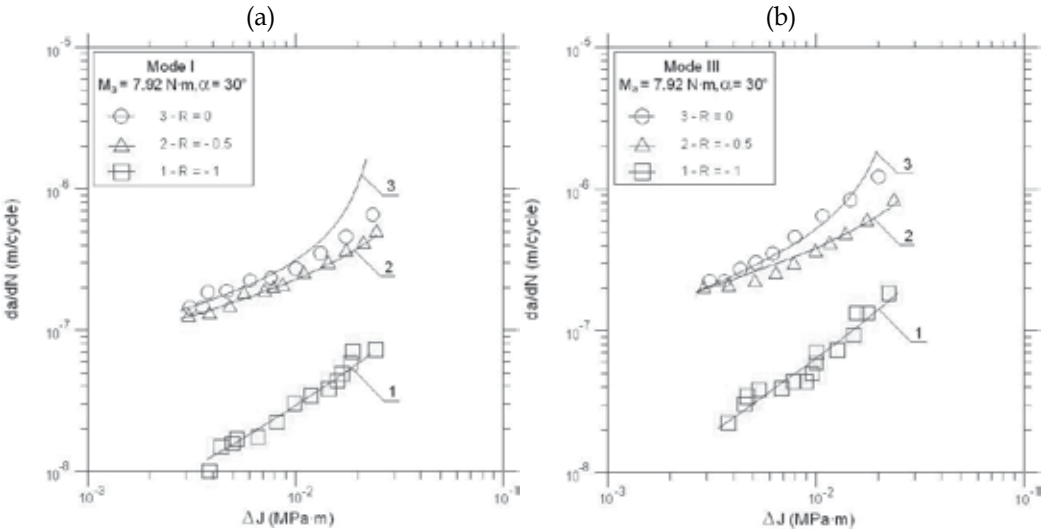

Fig. 16. Comparison of the experimental results with calculated ones according to Eq. (8) for $\alpha = 30°$ and: (a) mode I, (b) mode III

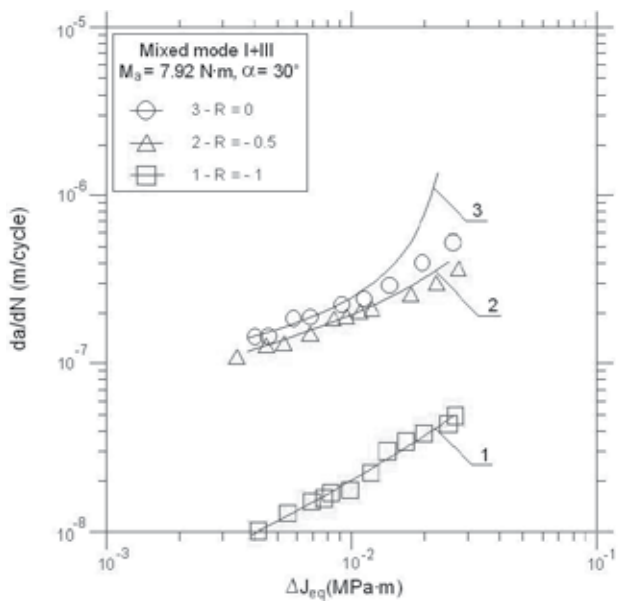

Fig. 17. Comparison of the experimental results with calculated ones according to Eq. (8) for $\alpha = 30°$ and mixed mode I+ III

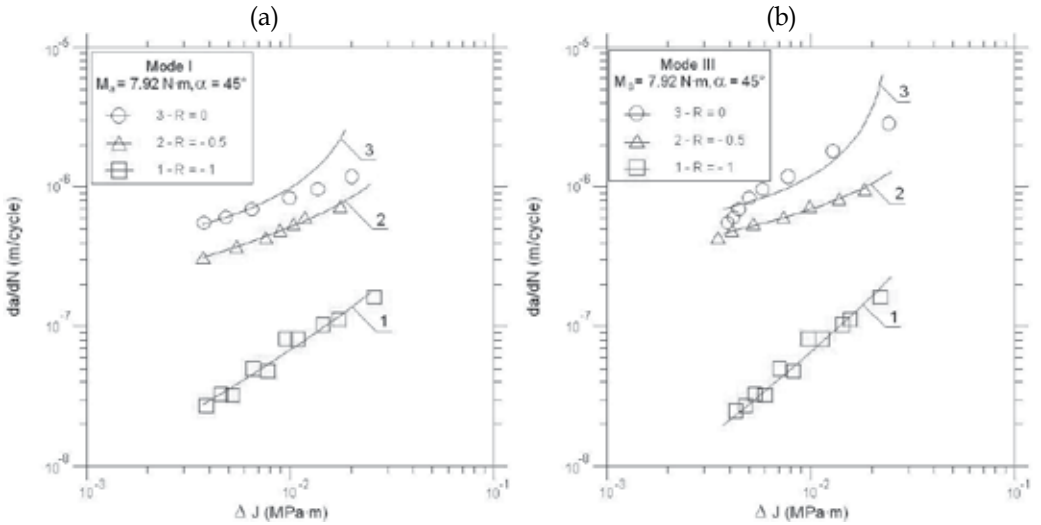

Fig. 18. Comparison of the experimental results with calculated ones according to Eq. (8) for $\alpha = 45°$ and: (a) mode I, (b) mode III

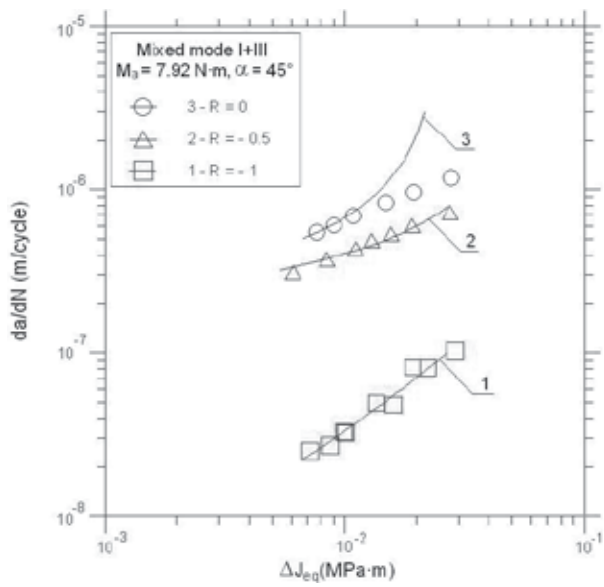

Fig. 19. Comparison of the experimental results with calculated ones according to Eq. (8) for $\alpha = 45°$ and mixed mode I+ III

For R = - 1 and α = 45° (Fig. 18), a higher crack growth rate was found for mode I to da/dN = $8 \cdot 10^{-8}$ m/cycle above that value mode III was dominating together with increase of the material plasticity. This behaviour is due to the decrease of normal stresses and increasing shear stresses. The test results presented in Figs. 16 - 21 were described with the empirical formula (8). Eq. (8) is valid for mode I and mode III as well as for mixed mode I+III loading.

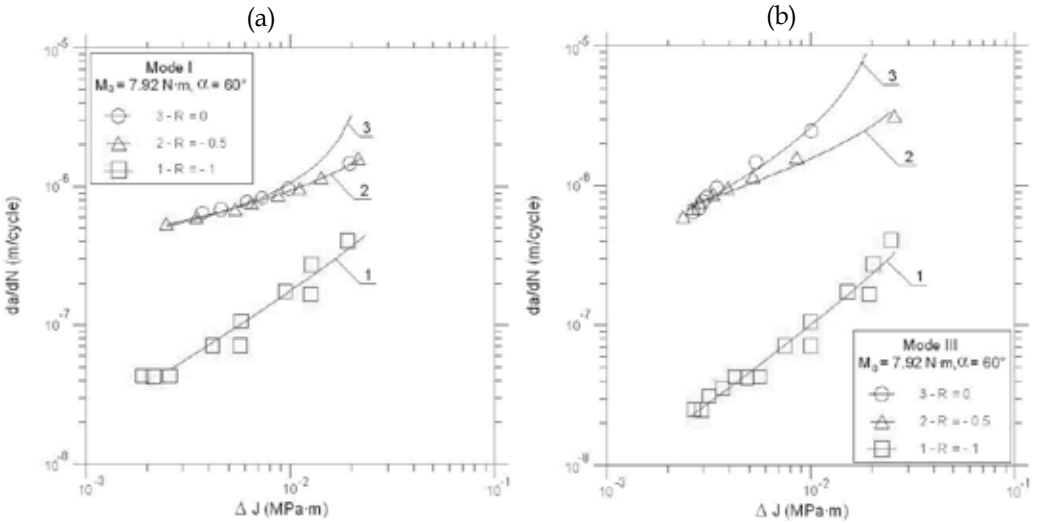

Fig. 20. Comparison of the experimental results with calculated ones according to Eq. (8) for α = 60° and: (a) mode I, (b) mode III

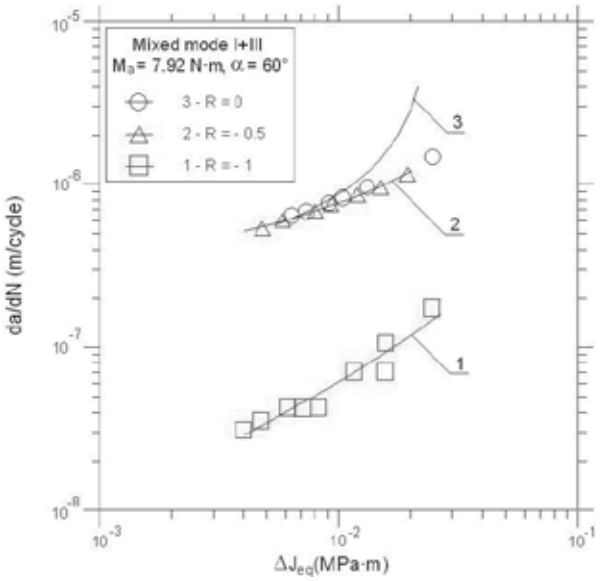

Fig. 21. Comparison of the experimental results with calculated ones according to Eq. (8) for α = 60° and mixed mode I+ III

The applied empirical formula (8) including ΔJ parameter gives good results in the description of fatigue crack growth rate. Surfaces of fatigue fractures were analysed (magnification 13x) in order to determine directions of the normal stress (mode I) and the shear stress (mode III). In the cases of mixed mode I+III and $\alpha = 30°$, 45° and 60°, principal directions of stresses change their positions. During tests under bending with torsion (Fig. 12) and $\alpha = 30°$, the fatigue crack growth proceeded at the average angle $\alpha_1 = 25°$, and under $\alpha = 45°$ - at the angle $\alpha_1 = 33° - 37°$, and under $\alpha = 60°$ - at the angle $\alpha_1 = 40° - 43°$ to the cross section of the specimens.

The empirical coefficients B and n occurring in Eq. (8) were calculated with the least square method and they were shown in Table 5. The coefficients take different values for pure bending and pure torsion. It means that B and n are not dependent on a kind of the material only. The test results for cyclic bending with torsion include the error not exceeding 20% at the significance level $\alpha = 0.05$ for the correlation coefficients r_w given in Table 5.

Figs.	Graphs	B $\frac{MPa \cdot m^2}{cycle}$	n	r_w
16a	1	$1.46 \cdot 10^{-7}$	0.86	0.99
	2	$0.73 \cdot 10^{-7}$	0.40	0.99
	3	$0.31 \cdot 10^{-7}$	0.35	0.99
16b	1	$5.52 \cdot 10^{-7}$	0.98	0.98
	2	$1.35 \cdot 10^{-7}$	0.43	0.99
	3	$0.80 \cdot 10^{-7}$	0.49	0.99
17	1	$0.56 \cdot 10^{-7}$	0.73	0.99
	2	$0.62 \cdot 10^{-7}$	0.40	0.99
	3	$0.15 \cdot 10^{-7}$	0.24	0.98
18a	1	$3.23 \cdot 10^{-7}$	0.85	0.99
	2	$1.42 \cdot 10^{-7}$	0.38	0.99
	3	$0.57 \cdot 10^{-7}$	0.28	0.98
18b	1	$1.35 \cdot 10^{-6}$	1.17	0.99
	2	$1.22 \cdot 10^{-7}$	0.28	0.99
	3	$0.50 \cdot 10^{-7}$	0.21	0.97
19	1	$2.23 \cdot 10^{-7}$	0.93	0.98
	2	$0.58 \cdot 10^{-7}$	0.23	0.99
	3	$0.41 \cdot 10^{-7}$	0.29	0.98
20a	1	$1.10 \cdot 10^{-6}$	0.91	0.98
	2	$1.88 \cdot 10^{-7}$	0.31	0.99
	3	$0.51 \cdot 10^{-7}$	0.24	0.99
20b	1	$1.20 \cdot 10^{-6}$	1.05	0.98
	2	$6.22 \cdot 10^{-7}$	0.46	0.99
	3	$1.08 \cdot 10^{-6}$	0.71	0.99
21	1	$2.03 \cdot 10^{-7}$	0.77	0.98
	2	$1.59 \cdot 10^{-7}$	0.32	0.99
	3	$0.57 \cdot 10^{-7}$	0.31	0.98

Table 5. Coefficients B and n in Eq. (8) and correlation coefficients r_w for the curves shown in Figs. 16 - 21

The test results indicate that the ΔJ parameter concept may be applied to fatigue problems in linear-elastic or nonlinear elastic-plastic fracture mechanics. The trends described in the chapter were confirmed for various loads and three load ratios. Because of its properties the ΔJ parameter may appear the main energetic criterion for fatigue crack growth characterizing the crack tip strain field for cyclic loading. Directions of future research will focus on fatigue cracks growth under non-proportional and random loads.

4. Conclusion

The presented results of the fatigue crack growth rate in AlCu4Mg1 aluminium alloy subjected to cyclic bending and proportional bending with torsion loading under different load ratio allow to formulate the following conclusions:

1. On the specimen fractures we can observe usually transcrystalline cracks through grains of the phase α, but also cracks along the grain boundaries can be noticed.
2. It has been shown that the applied parameter ΔJ as compared with the parameter ΔK for different load ratios R is better for description of fatigue crack growth rate.
3. Increase of the angle α determining a ratio of the torsional moment to the bending moment and load ratio causes increase of the fatigue crack growth rate.
4. In the case of separation of the mixed mode I+III loading into the pure mode I and mode III, for α = 30°, 45°, 60° and R = - 0.5, 0 the fatigue crack growth rate is higher for mode III compared with mode I under the same value ΔJ.

5. Acknowledgements

This work was supported by the National Centre for Research and Development, Contract No. N R03 0065 06.

6. References

ASTM E1820-99, (1999). Standard test method for measurement of fracture toughness, *Annual Book of American Society for Testing and Materials Standards*, Vol. 03.01, ISBN 0-8031-2712-X, Philadelphia

Chell, G.G. & Girvan, E. (1978). An experimental technique for fast fracture testing in mixed mode, Int. J. Fracture, Vol. 14, No. 2, pp. R81-R84

Chung, K.H. & Yang, W.H. (2003). Mixed mode fatigue crack growth in aluminium plates with composite patches, *Int. J. of Fatigue,* Vol. 25, No. 4, pp. 325-333, ISSN 0142-1123

Döring, R.; Hoffmeyer, J.; Seeger, T. & Vormwald, M. (2006). Short fatigue crack growth nonproportional multiaxial elastic-plastic strains, *Int. J. of Fatigue,* Vol. 28, No. 9, pp. 972-982, ISSN 0142-1123

Harris, D.O. (1967). Stress intensity factors for hollow circumferentially notched round bars, *Journal Bas. Engng.*, Vol. 89, No. 49, pp. 121-126

Kocańda, S. & Kozubowski, J. (1974). Ermudungsbruche von ausscheidungen in aluminiumlegierungen, *Zeitschrift f. Metallkunde* 6, s. 453-456

Pokluda, A. J. (2004). Intrinsic thresholds of long fatigue cracks, *Proceedings of XX Symposium Fatigue and Fracture Mechanics*, pp. 327-337, ISBN 83-89334-06-2, Bydgoszcz-Pieczyska, April 2004, Akademia Techniczno-Rolnicza, Pieczyska

Rozumek, D. (2005). Fatigue crack growth rate in aluminium alloy including mixed mode I and III, *Journal of Theoretical and Applied Mechanics*, Vol. 43, No. 4, pp. 731-743, ISSN 1429-2955

Rozumek, D. (2005). J-integral in description of fatigue crack growth rate, *The Archive of Mechanical Engineering*, Vol. LII, No. 1, pp. 51-62, ISSN 0004-0738

Rozumek, D. (2009). Mixed mode fatigue cracks of constructional materials, Studies and Monographs No. 241, Opole University of Technology, ISSN 1429-6063, Opole, (in Polish)

Rozumek, D. & Macha, E. (2006). A description of fatigue crack growth in elastic-plastic materials under proportional bending with torsion, Opole University of Technology, ISBN 83-88492-08-X, Opole, (in Polish)

Rozumek, D. & Macha, E. (2009). J-integral in the description of fatigue crack growth rate induced by different ratios of torsion to bending loading in AlCu4Mg1, *Materialwissenschaft und Werkstofftechnik*, Vol. 40, No. 10, pp. 743-749, ISSN 1521-4052

Rozumek, D. & Marciniak, Z. (2010). Fatigue crack growth of specimens with rectangular cross-sections under out-of-phase bending and torsional loading, *Proceedings of the XV International Colloquium Mechanical Fatigue of Metals (XV-ICMFM)*, pp. 45-45 and CD, ps 8, ISBN 978-83-60691-83-0, Opole, September 2010, Opole University of Technology, Opole

Thum, A.; Petersen, C. & Swenson, O. (1960). Verformung, Spannung und Kerbwirkung, *VDI*, Düesseldorf

12

Fatigue Crack Growth Simulation of Aluminium Alloy under Cyclic Sequence Effects

S. Abdullah, S. M. Beden and A. K. Ariffin
Department of Mechanical and Materials Engineering
Universiti Kebangsaan Malaysia
Malaysia

1. Introduction

During service time machine and component failures may occur, that cause the structure breakdown. This generally yields enormous economical costs and sometimes in worst-case scenarios evens the death of human beings. Frequently such damage events originate from misconstructions, manufacturing and material failures, inappropriate fatigue strength calculations, overloads or other problems during service time or maintenance. Beginning from already existing or newly originating flaws, often extended fatigue crack growth (FCG) occurs due to service loads. Finally, the functional capability of structures and components is lost with the already mentioned consequences. In case of existing damage events, it is of major importance to fundamentally analyse them in order to obtain valuable information on structural improvements. Therefore, the knowledge about the real global and local loadings, the relevant material parameters and the initiation and growth of cracks under various general loading situations is essential. By fracture mechanics the development of FCG processes than can be reconstructed. So it is possible to improve the strength optimised and fracture safe design of structures and components. This goal can ideally be achieved by a composition of numerical and experimental simulations.

FCG in structure components, which is subjected to variable amplitude (VA) loading, is a complex subject. Studying of FCG rate and fatigue life calculation under the spectrum loading is vital in life prediction of engineering structures at higher reliability. The ability to understand and predict fatigue life remains a key technical factor in maintaining aircraft fleets, which are required to safely operate up to their design lives, and sometimes beyond. The load spectra applied to this aircraft are complex and highly variable, and experience has shown that traditional fatigue prediction tools do not always perform well in calculating the lives of modern, highly optimised airframes.

The main aim of this chapter is to address how two characterise the load sequence effects in fatigue crack propagation under VA loading and to select appropriate model from the large number of FCG models with validation of it. Thus, a fatigue life under various load spectra, which was predicted, based on the Austen, modified Forman and NASGRO models. This article analyses FCG under random loading using experimental results taken from literature on the subject and from growth simulations carried out based on different FCG models. These models are validated with the literature-based FCG test data in 2024-T3 aluminium alloys under spectrum loadings. This work summarises recent FCG models that appear to

be capable of producing more accurate fatigue life predictions using those loadings. With the consideration of the load cycle interactions, Load cycle interactions can have a significant effect in FCG under VA loading. Finally, the results show a good agreement in the behaviour with small differences in fatigue life compare to the test data and the previous literatures.

2. Literature review

Fatigue performance of structures is greatly affected by the presence of stress raisers such as fastener holes, manufacturing errors, corrosion pits, and maintenance damage, which serve nucleation sites for fatigue cracking. During service, sub-critical cracks nucleate from these sites and grow until catastrophic failure (unstable crack growth) takes place when the crack length reaches critical dimension. From economic point of view a costly component cannot be retired from service simply on detecting a fatigue crack. Hence, reliable estimation of fatigue crack propagation and residual life prediction are essential so that the component can timely service or replaced. VA loading involves load interaction effects and significantly affects the FCG and consequently, the fatigue life leading to either retardation (an overload tensile in nature) or acceleration (an under load compressive in nature) or reduction in retardation (an overload followed by an under load).

Nowadays, the study of FCG rate and fatigue life calculation under the spectrum loading is very important for the reliable life prediction of engineering structures. A number of load interaction models have been developed to correlate FCG rates and predict crack growth under VA loading over the past three decades. It is difficult to model all the parameters influence FCG correctly due to the random nature of VA loading. It overloads are known to retard crack growth, while under loads accelerate crack growth relative to the background rate. These interactions, which are highly dependent upon the loading sequence, make the prediction of fatigue life under VA loading more complex than under constant amplitude (CA) loading. The prediction of life is a challenging job for the engineering community because of two reasons. Firstly, it involves a robust integration scheme; secondly, no single universal method is available as far as the different load interaction mechanisms are concerned.

Many models have been developed to predict the fatigue lives of components subjected to VA loadings [James & Petrson, 1997; Paris, et al., 1999; Sadananda & Vasndern, 1999; Taheri, et al., 2003]. These models can be generally divided into global analysis and cycle-by-cycle analysis (see Fig.1). In particular, the global analysis concept predicts the FCG, considering the average of the applied loading cycles, while the cycle-by-cycle analysis evaluates the crack growth for each load cycle and determines the crack growth life by accumulation. The cycle-by-cycle analysis can be performed with or without involving the interaction effects, i.e. the effect of a load cycle on the crack growth in later cycles. A well-known interaction effect is caused by an overload on crack growth in the subsequent load cycle. The models that take interaction effects into account can be divided into three main categories namely yield zone models, crack closure models and strip yield models [Murthy, et al., 2004].

The earliest of these are based on calculations of the yield zone size ahead of the crack tip, and they are still widely used in many applications and research. The Wheeler model [1972] and Willenborg et al. model [1971], for example, both fall into this category. The Willenborg model, on the other hand, does not incorporate any empirical parameters, but it uses the material yield stress to give a plastic zone size [Corbly & Packman, 1973; Rudd & Engle, 1981; Chang, et al., 1981]. The amount of retardation is determined as a function of the stress

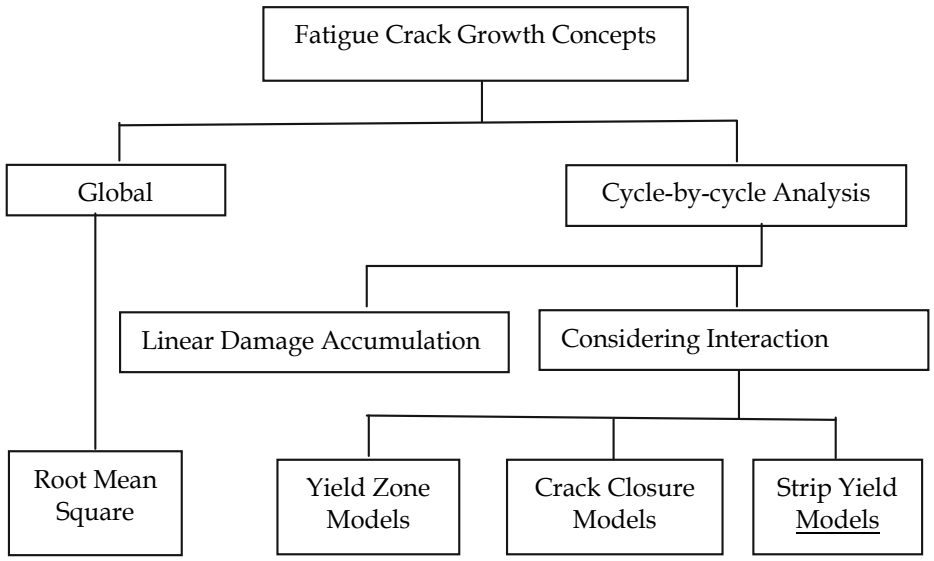

Fig. 1. Classification of the fatigue crack growth concepts

intensity factor necessary to cancel the effect of the overload plastic zone. The model computes an effective stress intensity factor that is being reduced by the compressive residual stress. However, the Willenborg model was found to be not reliable for predicting the overload retardation [Taheri, et al., 2003].

The second main category of retardation models, known as the crack closure models, is based on Elber's experimental observation [Elber, 1971], which used to model crack growth rates under VA loadings [Schijve, 1981; Newman, 1984; Ray & Patanker, 2001a; Ray & Patanker, 2001b]. As a result of the tensile plastic deformation left in the wake of a fatigue crack, a partial closure of the crack faces occurs during part of a fatigue load cycle. Since crack propagation can only occur during the time for which the crack is fully open, the formation of crack closure reduces the range of the applied stress that is effective for crack propagation. In addition, the magnitude of stress required for the crack to be fully open, i.e., the crack opening stress, depends on the previous load history. As a crack propagates through an overload plastic zone, the residual stresses in the zone increase the load required to open the crack and cause crack growth retardation. Thus, the use of the crack closure models required the crack opening stress to be determined throughout the load history. This is accomplished either by direct experimental measurements [Kim & Song, 1994; Dominguez, et al., 1999; Jono, et al., 1999] or by finite element computations [Lee, 2003; Sander & Richard, 2005; Ljustell & Nilsson, 2005]. However, the major drawback to using crack closure models is that measuring the crack opening stress under VA loading is very difficult and the magnitude and the precision might depend on the measuring techniques, while the finite element analysis for computing the crack opening stress is often complicated and relatively time consuming. More recent proposals include combinations of the Wheeler model with the Newman crack closure model [Huang, et al., 2005a] and model based on the strain energy density factor [Huang, et al., 2005b]. The most advance category is the strip yield models, which are based on the Dugdale model [Newman 1981]. The Dugdale model was used to estimate the size of the plastic zone at the tip of the crack. Dug- dale assumes that yielding occurs in a narrow strip ahead of the crack tip.

Each of these models has its own capabilities and limitations as discussed in several literatures [Sadananda, et al., 1999; Kujawski, 2003; Murthy, et al., 2004]. Because of the complexity, large ambiguities and disagreements, and also lack of proper understanding of the mechanism of retardation, no fundamental and universally accepted model is available that would include all the mechanisms and could be applied to all materials.
With respect to the continuity information between this study and the available literature, the purpose of this work is two characterise the effects of load sequence on fatigue crack propagation under the spectrum loading. For that reason, a feasible study towards the crack propagation model under various spectra loading has been carried out based on the Austen, modified Forman and NASGRO models. These models are compared to FASTRN and AFGROW codes as well as test data under various VA and spectrum loading from previous literature. One of the aims of the analysis is to show the effect of using different FCG models with various load sequences. Every single FCG model developed so far attempts to correlate the crack growth information with different crack driving forces and several other parameters to predict the residual fatigue life. In the present work, the FCG rate has been correlated with crack length by correlations with the high percentage of a correction factor.

3. Fatigue crack growth models

The reason for building FCG models is to link theoretical ideas with the observed data. Modelling of FCG rate data has enhanced the ability to create damage tolerant design philosophies [Kassim, et al., 2008]. The influence of the mean stress is probably the most significant, and it usually results in closely spaced lines parallel to each other. Region I, which is shown in Fig. 2, represents the early development of a fatigue crack and the crack growth rate, for which da/dN is typically in the order 10^{-6} mm/cycle or smaller of the test data results from ASTM E647 [2002]. This region is extremely sensitive, and it is largely influenced by the microstructure features of the material such as grain size, the mean stress of the applied load. The most important feature of this region is the existence of a stress intensity factor range below which fatigue crack should not propagate. This value is defined as the FCG threshold and is represented by the symbol K_{th}. The limitation of the Paris law is that it is only capable of describing data in region II. If the data exhibits a threshold (region I) or an accelerated growth (region III) Paris law cannot adequately describe these regions. Region III represents the FCG at the very high rate, $da/dN > 10^{-3}$ mm/cycle due to rapid and unstable crack growth just prior to final failure. The da/dN versus ΔK curve becomes steep and asymptotically approaches the fracture toughness K_c for the material.
The common approach for FCG analysis is to describe the data using a deferential equation, which is referred to as a FCG law or model. Modelling of FCG data has enhanced the ability to create damage tolerant design philosophies. Paris and Erdogan [1963] proposed the most important and popular work. In fact, they were the first to correlate FCG with the fracture mechanic's parameters (K_{min} and K_{max}), and describe the loading conditions in the region of the crack front. In addition, they also observed a linear relationship between the FCG rate (da/dN) and ΔK, when plotted on a log–log scale. Consequently, Paris and Erdogan [1963] proposed the power law relationship, as follows:

$$\frac{da}{dN} = C\Delta K^n \tag{1}$$

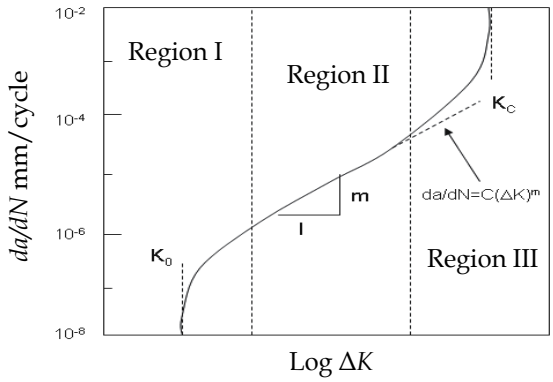

Fig. 2. Typical *da/dN* versus *dK* curve

where *C* and *n* are the material parameters that are determined experimentally. The Paris–Erdogan equation does not consider: (a) the effect of the stress ratio, (b) the existence of fatigue threshold, and (c) the accelerated FCG rate when the maximum stress intensity factor (K_{max}) approaches the material fracture toughness (K_c). Moreover, it does not adequately describe the region, I or III FCG rates, and it tends to overestimate region I, but underestimates region III FCG rates. Although the Paris–Erdogan equation is a simplification of a very complex phenomenon, it is still very popular on the account of significant engineering interest.

It is practically impossible to discuss every available model because of their large number in the literature. Therefore, the remainder of this section discusses about the models which are rather promising and/or commonly used. The fact that all used different FCG models reconfirms the fact that there is no standard methodology used to perform the FCG life predictions for structures under random loading.

The main goal of the crack propagation models is to relate the material damage to the cyclic loads applied. However, due to the number and complexity of the mechanisms involved in this problem, there are probably as many equations as there are researchers in the field. Though many models have been developed, none of them enjoys universal acceptance. In more specific, each model can only account for one or several phenomenological factors. Moreover, the applicability of each model varies from case to case, there is no general agreement among the researchers to select any FCG model in relation to the concept of fatigue crack behaviour [Kujawski, 2001; Hamam, et al., 2007; Richard, et al., 2008; Mohanty, et al., 2009]. Hence, three different models, namely, the Austen, modified Forman and NASGRO models, were selected in this study. Each model has its own capabilities and limitations as discussed in several literatures [Sadanada & Vasndevan, 1999; Murthy, et al., 2004; Mohanty, et al., 2009], which they belong to three categories. These models take into account the main properties, such as the crack closure, plane stress and plain strain, threshold, mean stress and region III. A comparison of the three models is shown in Table 1.

3.1 The austen model

The Austen growth model [nCode, 2003] is known as the implicitly model threshold and it is expressed in the following equation:

$$da / dN = C.(\Delta K_{eff})^n \tag{2}$$

Property	Models		
	Austen	Modified Forman	NASGRO
Crack closure	✓		✓
Plain strain	✓		✓
Plain stress	✓		✓
Threshold		✓	✓
Mean stress effect (R-ratio)		✓	✓
Region III		✓	✓

Table 1. A comparison between the three FCG models

Where, $\Delta K_{eff} = \Delta K_{max,eff} - \Delta K_{min,eff}$, $K_{max,eff} = K_{max} + K_{SF}$, $K_{min,eff} = \max(K_{min}, K_{CL})$, and K_{SF} is defined as the modification for static fracture and K_{CL} is known as the stress intensity at the crack closure. Furthermore, Austen modelled the onset of fast fracture using the following expression:

$$K_{SF} = \frac{K_{\max}}{K_{1C} - K_{\max}} \tag{3}$$

Austen also took into account the threshold and short cracks by applying a crack closure stress K_{CL} which is expressed as follows:

$$K_{CL} = K_{\max} - K_{\max}\sqrt{\frac{a + I_o}{a}} + \frac{\Delta K_{th}}{1 - R} \tag{4}$$

I_o is the smallest crack size that will propagate and is given by:

$$I_o = \frac{1}{\pi(\frac{K_{th}}{\Delta\sigma_o})^2} \tag{5}$$

where, $\Delta\sigma_o$ is the un-notched fatigue strength and ΔK_{th} is the threshold stress intensity.
The threshold stress intensity is expressed as a bilinear function of the mean stress and the Austen model does not possess any explicit mean stress correction. Austen argued the irrelevance of this and attributed it to a manifestation of crack closure and retardation.

3.2 The modified forman model

Although Walker improved the Paris model by taking account of the stress ratio, neither of the models could account for the instability of the crack growth when the stress intensity factor approaches its critical value [Forman, 1972]. However, Forman improved the Walker model by suggesting a new model which is capable of describing Region III of the fatigue rate curve and includes the stress ratio effect. The Forman model is therefore given by the following mathematical relationship:

$$\frac{da}{dN} = \frac{C_F(\Delta K)^{m_y}}{(1-R)K_C - \Delta K} = \frac{C_F(\Delta K)^{m_y}}{(1-R)(K_C - K_{\max})} \tag{6}$$

where, *Kc* is the fracture toughness for the material and thickness of interest. Eq. (6) indicates that as K_{max} approaches *Kc & da/dN* tends to infinity. Therefore, the Forman equation is capable of representing stable intermediate growth (region II) and the accelerated growth rates (region III). The Forman equation is capable of representing data for various stress ratios by computing the following quantity for each data point, i.e.:

$$Q = \frac{da}{dN}\left[(1-R)K_C - \Delta K\right] \tag{7}$$

If the various ΔK and R combinations fall together on a straight line on a log-log plot of Q versus ΔK, the Forman equation is applicable and may therefore be used. Comparing Eqs. (6 and 7), the Forman equation can be represented as:

$$Q = C_F\left(\Delta K\right)^{m_y} \tag{8}$$

A more simplified model, which does not include crack closure effects, is given by the following Forman equation:

$$\frac{da}{dN} = \frac{C(\Delta K)^n}{(1-\frac{\Delta K}{(1-R)K_c})^q} \tag{9}$$

for $0 \leq R < 1$

Forman proposed its modified model [Carlson & Kardomateas, 1996; Kassim, et al., 2006] as:

$$\frac{da}{dN} = \frac{C(1-R)^m \Delta K^n (\Delta K - \Delta K_{th})^p}{((1-R)K_c - \Delta K)^q} \tag{10}$$

Certain values of the exponents *m*, *p*, and *q* of Eq. (10) give other forms of the crack growth equation, as indicated in Table 2.

Exponent value	FCG Model
$m = p = q = 0$	Paris
m = p= 0 , q =1	Forman
$P = q = 0$, $m = (mw\text{-}1)n$	Walker

Table 2. Exponent values for crack growth laws

The Forman equation is capable of representing data of various stress ratios for regions II and III. Further modifications of the Forman's expression to represent regions I, II and III have been accomplished by including the threshold stress intensity parameter, ΔK. Thus, Hartman and Schijve [1970] proposed the following equation which is the continuation of Forman's work:

$$\frac{da}{dN} = \frac{C_{HS}(\Delta K - \Delta K_{th})^{m_{HS}}}{(1-R)K_C - \Delta K} \tag{11}$$

Another version of the Forman equation is given as follows:

$$\frac{da}{dN} = \frac{C_{MOD}(\Delta K)^{m_{MOD}}(\Delta K - \Delta K_{th})^{0.5}}{(1-R)K_C - \Delta K} \tag{12}$$

Both Eqs. (11 and 12) produce a sigmoid shaped curve; in this case, an asymptote does not only occur as K_{max} approaches, K_c, but it also occurs when ΔK approaches ΔK_{th}. One disadvantage of using these equations is that the value of ΔK_{th} is sensitive to R and a specific value of this parameter in the equation is generally needed for any given R value [Dowling, 1993]. In addition, the correct value of K_c for the given thickness should be used. Technically, the FCG rate *da/dN* can be described, for instance, by the modified Forman-Mettu equation [Richard, et al., 2008]:

$$\frac{da}{dN} = C\left[\left(\frac{1-f}{1-R}\right)\Delta K_{eq}\right]^n \frac{\left(1-\frac{\Delta K_{th}}{\Delta K_{eq}}\right)^p}{\left(1-\frac{K_{\max}}{K_C}\right)^q} \tag{13}$$

In this equation, *C, n, p* and *q* are the material parameters, whereas $R = R_{min} / R_{max}$ or $R = K_{min}/K_{max}$ is the *R*-ratio of the load and *f* denotes the crack opening function [Forman & Mettu, 1992; Sandar & Richard, 2006]. Despite the fact that the influence of single loading change events likes over or blocks loads which are well-known [Sandar & Richard, 2006], extensive research for the arbitrary VA loadings is still necessary not only for the amplitude, but also the direction of the load (Mixed-Mode-loading) changes.

3.3 The NASGRO model

The Willenborg model is based on the yield zone concept. Meanwhile, retardation is accounted for the tensile overloads by a reduction in SIF and truncating the minimum effective SIF at zero. In this method, both the effective SIF and apparent SIF are the same and this method is effective in computing the crack growth only when the crack growth equation contains the stress ratio *R*. However, this method is not applicable for overloads as it does not predict acceleration which is caused by compressive overloads or underloads as well as the combination of both.

Another related development has lead NASGRO to extend the generalized Willenborg model [Forman, 1972; Maymon, 2005; Kassim, et al., 2008] by taking into account the reduction of retardation due to underloads. The NASGRO equation represents the most comprehensive growth law formulation comprising the mean stress effect, threshold, the honest of fast fracture and crack closure [nCode, 2003]. The NASGRO formula is expressed as:

$$\frac{da}{dN} = \frac{C(\Delta K_{eff})^m}{(1-R_{eff})K_C - \Delta K_{eff}} \tag{14}$$

where

$$\Delta K_{eff} = (K_{\max})_{eff} - (\Delta K_{\min})_{eff} \tag{15}$$

$$K_{\max,eff} = K_{\max} - K_{red} \tag{16}$$

$$K_{\min,eff} = \max\left\{\left(K_{\min} - K_{red}\right),0\right\}, \text{ for } K_{\min} > 0 \tag{17}$$

$$= K_{\min} \text{ for } K_{\min} \le 0$$

$$K_{red} = \phi\left[(K_{OL})_{\max}\left[1-\left(\frac{a_n - a_{OL}}{\gamma P_{ol}}\right)\right]^{1/2} - K_{\max}\right] \tag{18}$$

$$\phi = 2.523\phi_o / (1.0 + 3.5(2.5 - R_{U)})0.6), \quad R_U < 0.25$$

$$= 1.0 \qquad R_U \ge 0.25$$

$$R_U = \sigma_{UL} / \sigma_{\max,OL}, \qquad \phi_O = 0.2 \qquad to \qquad 0.8$$

$$K_{\min,eff} = \max\left\{\left(K_{\min} - K_{red}\right),0\right\},$$

$$K_{\max} = \frac{\Delta K}{(1-R)}$$

and ΔK is the stress intensity factor (depends on the stress, crack length, geometry factor), ΔK_{th} is the threshold stress intensity range, K_c is the critical stress intensity factor, C, n, p and q are the empirically derived coefficients from the measured data. The other parameters, such as the crack tip opening function f, are determined using the following formulation:

$$f = \begin{vmatrix} \max\left\{(R),\left(A_0 + A_1.R + A_2.R^2 + A_3.R^3\right)\right\} \\ if\ (R \ge 0) \\ A_0 + A_1.R \quad if \quad (-2 \le R < 0) \\ A_0 - 2.A_1 \quad if \quad (R < -2) \end{vmatrix} \tag{19}$$

where

$$\begin{aligned} A_0 &= \left(0.825 - 0.34\alpha + 0.05\alpha^2\right)\left[\cos\left(\pi SR/2\right)\right]^{1/\alpha} \\ A_1 &= \left(0.415 - 0.071\alpha\right)SR \\ A_2 &= 1 - A_0 - A_1 - A_3 \\ A_3 &= 2.A_0 + A_1 - 1 \end{aligned} \tag{20}$$

α is the plain stress/strain constraint factor and SR is the ratio of the maximum applied stress to the flow stress. These values are all empirically derived. Meanwhile, the threshold stress intensity is obtained from the following equation:

$$\Delta K_{th} = \frac{\Delta K_o(\sqrt{\frac{a}{a+a_o}})}{\left[\frac{(1-R)}{(1-A_o)(1-R)}\right]^{1+C_{th}R}} \tag{21}$$

where, ΔK_o is the threshold stress intensity range at R = 0 obtained from the test results, a is the crack length, a_o is the intrinsic crack length given as the constant, and C_{th} is the threshold coefficient obtained from the test results.

3.4 The FASTRAN model

The crack-growth relation used in FASTRAN was:

$$\frac{da}{dN} = \frac{C_i(\Delta K_{eff})^{n_i}}{[1-(\frac{K_{\max}}{K_{Ie}})^q]} \tag{22}$$

where Ci and ni are the coefficient and power for each linear segment, K_{max} is the maximum stress-intensity factor, K_{Ie} is the elastic fracture toughness (which is, generally, a function of crack length, specimen width, and specimen type), and q was set to 2. The table-lookup form is used because many materials, especially aluminum alloys, show sharp changes in the crack-growth-rate curves at unique values of rates. These sharp changes have been associated with monotonic and cyclic-plastic-zone sizes, grain sizes, and environments [Yoder, et al., 1982]. The Functional relations for geometry factors (F (a, w)) are given in the FASTRAN manual [Newman, 1992] as:

$$F(a,w) = \sqrt{\sec\left(\left\{\pi/2\right\}\left\{a/w\right\}\right)} \tag{23}$$

3.5 The AFGROW model

AFGROW model is the Walker equation with Willenborg retardation model [Ray & Patankar, 2001b], which is a cycle-by-cycle structural crack growth fracture mechanics computer program developed at the Air Vehicles Directorate of the United States Air Force Research Laboratory (AFRL), and is widely used to predict the fatigue life of components [Harter, 2003].

4. Simulation and experiments

For many years, fatigue analysis has been thought of as following the logic as illustrated in Fig. 3. In this overview, the three main input parameters, namely geometry, material and loading, are regarded to have similar functions. These parameters seem to be the main input to any software for modelling and simulation. The details of these inputs are as follows:
In this application centre-cracked specimen geometry described in ASTM E647 [2002] is used with a width of 229 mm, thickness of 4.1 mm and 610 mm in length, while the initial crack size is 12.7 mm, for which E = 71750 MPa. Aluminium alloys are widely used in the design of many engineering application, due to their good mechanical properties and low densities. The chemical composition and mechanical and fatigue properties of this material

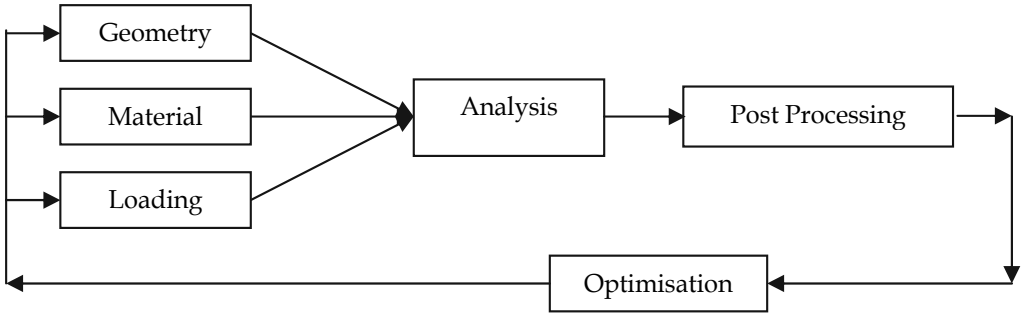

Fig. 3. A conventional schematic flow of the fatigue analysis process (the general durability process)

are shown in Table 3 and Table 4, respectively [ASM Handbook, 1985; 1990; ASM Metal Refrence, 1993].

Components and structures that are subjected to quite diverse load histories, their histories may be rather simple and repetitive and at the other extreme, they may be completely random. The cycle-by-cycle analysis can be performed with or without involving the interaction effects, i.e. the effect of a load cycle on crack growth in later cycles.

Component	Wt%	Component	Wt%
Al	90.7-94.7	Cr	Max. 0.1
Cu	3.8-4.9	Fe	Max. 0.5
Mg	1.2-1.8	Mn	0.3-0.9
Si	Max. 0.5	Ti	Max. 0.15
Zn	Max. 0.25	Other, each	Max. 0.05
Other, total	Max. 0.15		

Table 3. Chemical composition of aluminium alloy 2024 T3

Titles	Symbols	Values
Yield Stress (MPa)	σ_y	345
Ultimate Tensile Strength (MPa)	σ_u	483
Plane Strain Fracture Toughness (MPa.√m)	K_{1C}	36.262
Plane Stress Fracture Toughness (MPa √m)	K_{1D}	72.524
Part Through Fracture Toughness (MPa √m)	K_{1E}	50.547
Forman Exponent	m_y	3.284
Forman Co-efficient (m/MPa(m^1/2)^(n-1)	C	1.5451×10^{-10}
NASGRO Exponent	p	0.5
NASGRO Exponent	q	1
Modulus of Elasticity (GPa)	E	71.75
Fatigue Strength coefficient (MPa)	f	130
Elongation at Break (%)		18

Table 4. Mechanical and fatigue properties of aluminium alloy 2024 T3

The programmable and VA load histories given by Ray and Patanker [2001b] and Huang et al.[2005b] are used in this analysis with different load sequences from high to low or low to high shown in Fig. 4 (load cases 1 to 5). These types of loading represent the load sequencing and spectrum loading in most of the application. To account load ranges and mean of the used load history, the rainflow counting method was then used. In this overview, as mentioned before, the three main input parameters are geometry, material and loading. The process proceeds by selection of the FCG model to show the behaviour of the geometry. The results of the previous process predict the fatigue life and FCG rate. At each cycle, to get a new result it is possible to change any of the factors (FCG model, geometry, material, loading and stress ratio), which mean the ability to make a new prediction. The detail flow of such process is shown in Fig. 5.

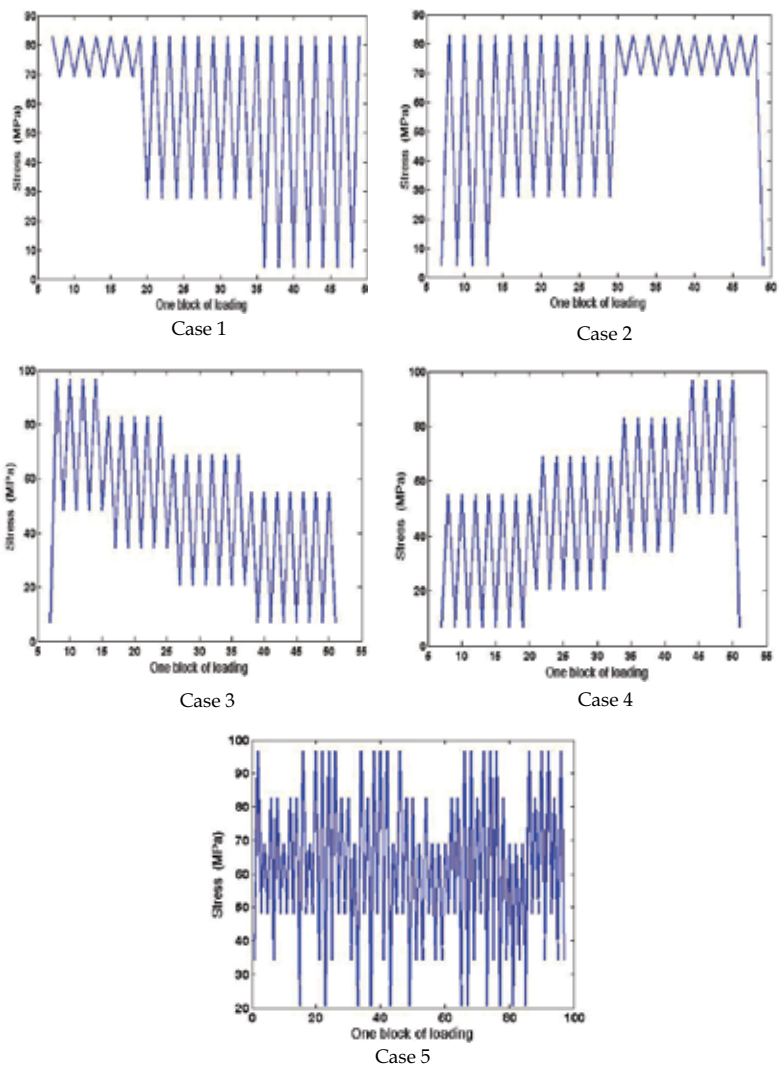

Fig. 4. Display of load histories with different sequences

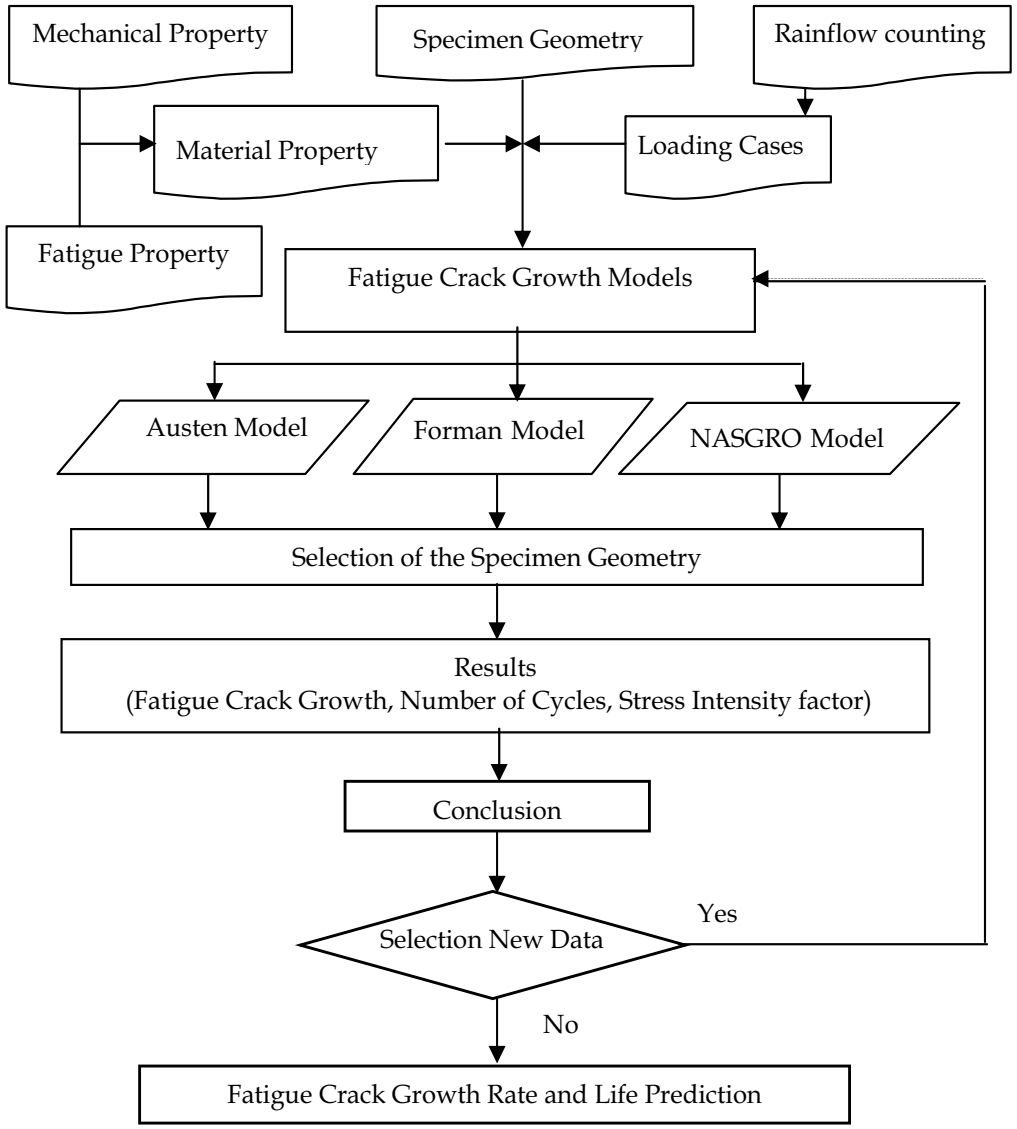

Fig. 5. Flow chart of the simulation process

5. Results and discussion

Many engineering structures are subjected to random loading in service and the fatigue life will be affected by load sequence. However, for design purposes it is particularly difficult to generate an algorithm to quantify these sequence effects on fatigue crack propagation, due to the number and to the complexity of the mechanisms involved in this problem [Kujawski, 2001]. The presence of interaction effects is always altering the crack growth rate under the application of VA loading. For correctly predicting the crack growth under VA loading, it is necessary to involve the interaction effects while developing the prediction models as a part of cycle-by-cycle analysis using different models. Hence, one of the purposes of this research

is to address how two characters the effect of VA loading in fatigue crack propagation. Despite the extensive work on crack growth, there is still a need for a satisfactory and generally applicable method to predict the fatigue crack propagation to consider various effects. In the current investigation, systematic crack growth predictions were conducted on an aluminium alloy. Several existing models were evaluated critically based on the experimental results [Richard, et al., 2008]. Thus, the fatigue crack propagation models under VA loading are presented in this section based on the Austen, modified Forman and NASGRO models. For demonstrating the validation of these models predictions are compared with test data, FASTRN and AFGROW codes given in Ray and Patanker [2001b]. Figs. 6 and 7 exhibit the results of the comparisons under two types of block loading, one with decreasing the minimum stresses (load case 1) and the other with increasing them (load case 2). The changes of a stress ratio related to changing of minimum stress with a constant maximum stress. The data predicted using the Austen, modified Forman and NASGRO models are compared with those models performed by previous literatures [Ray & Patanker, 2001b; Huang, et al., 2005a; Huang, et al., 2005b].

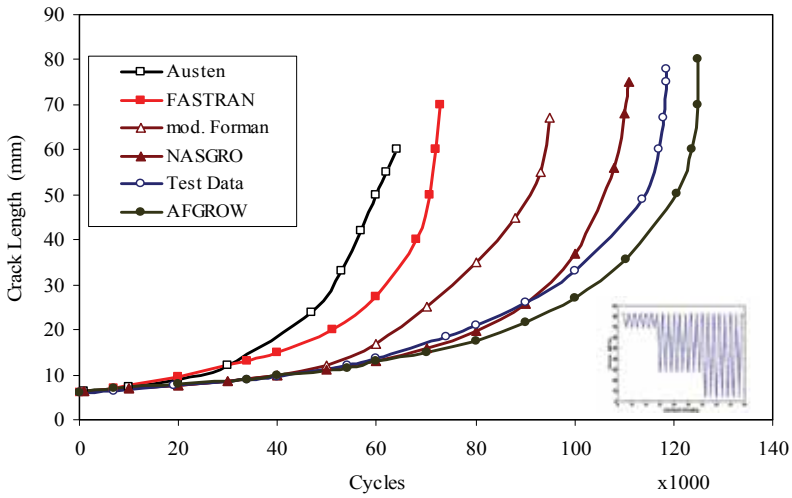

Fig. 6. Comparison of fatigue crack growth with different FCG models under load case 1

The maximum differences in life predicting for the load cases for all models are 40% as a maximum compared to the test data. The lowest life has been found using the Austen prediction model, while NASGRO gave the maximum and the others are in between both the Austen and the NASGRO models. Moreover, the fatigue life predicted under the load case 2 is higher than the case 1. The results show clearly the effect of changeable stress ratio and the first block is more effective than others, in other words, the sequence of the loads. The results indicate that, when the first value of R is high, it is clearly reduce the life, although this value will be decreased later. In the load cases when the stress ratio is low in the first block of the load, it has less effect, although its value will be increased later.

The effects of load sequence can be shown clearly in Fig. 8, which represent the comparison between these load cases based on test data and NASGRO model. The maximum difference in the test data is 8%, while in NASGRO model is 25%. These differences mainly due to the effects of load ratios for each load case.

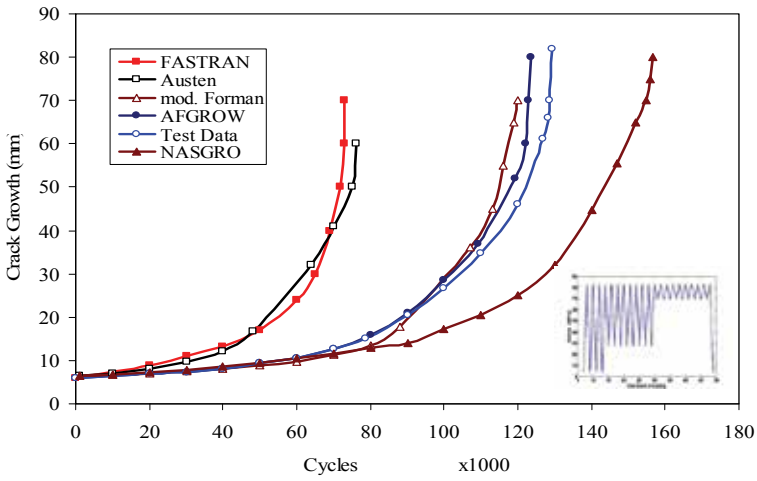

Fig. 7. Comparison of fatigue crack growth with different FCG models under load case 2

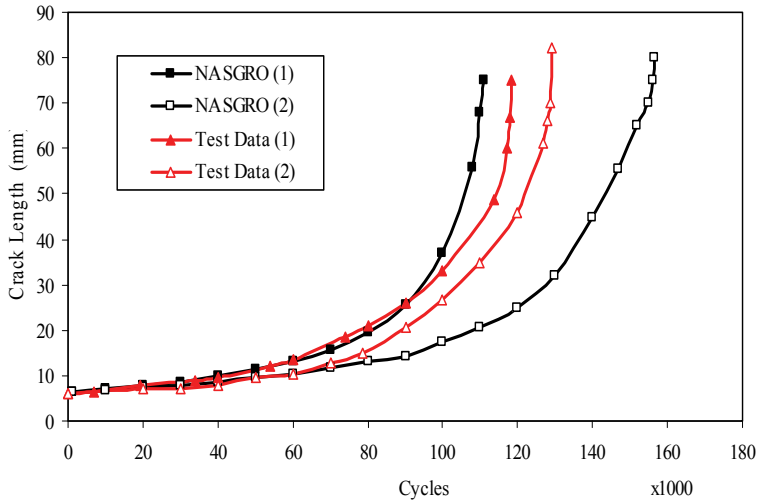

Fig. 8. Comparison of fatigue crack growth of test data and NASGRO model under load cases 1 and 2

From previous results mentioned in Figs. 6 and 7, it is possible to draw the FCG rate curve relating to crack length as shown in Fig. 9. The power equation gave a correction factor of 97.8% for load case 1 and 99.5% for load case 2. The two equations indicate that the rate of crack versus crack length approximately same with small difference in linear relationship.
Tests on SM520B steel using CCT test specimens under four different variable amplitude block loading spectra were reported by Yamadaa et al. [2000] and presented in Fig. 10, while Pell et al. [2004] reported on Aluminum alloy by the same indication. Fig. 10 again reveals a near linear relationship between *da/dN* and the crack length, which introduce the same conclusion presented by this research (Fig. 9).

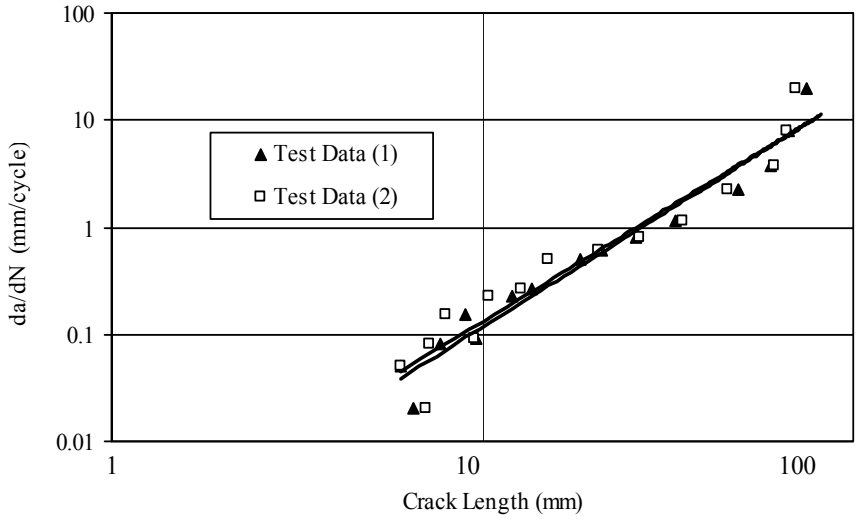

Fig. 9. Fatigue crack growth rate versus crack length of test data under load cases 1 and 2

For the load cases 3 and 4, the stress ratios are changeable either in a decreasing way (case 3) or increasing (case 4) due to the changes in both stresses (maximum and minimum), which differ from the cases 1 and 2. The results in Figs. 11 and 12 show good agreement to the predicted life for all models with a difference range from 17% to 30% related to experimental results for the two load cases (3 and 4), except the results of the Austen model, which are less by more than 50% for the load case 3 compared to load case 4.

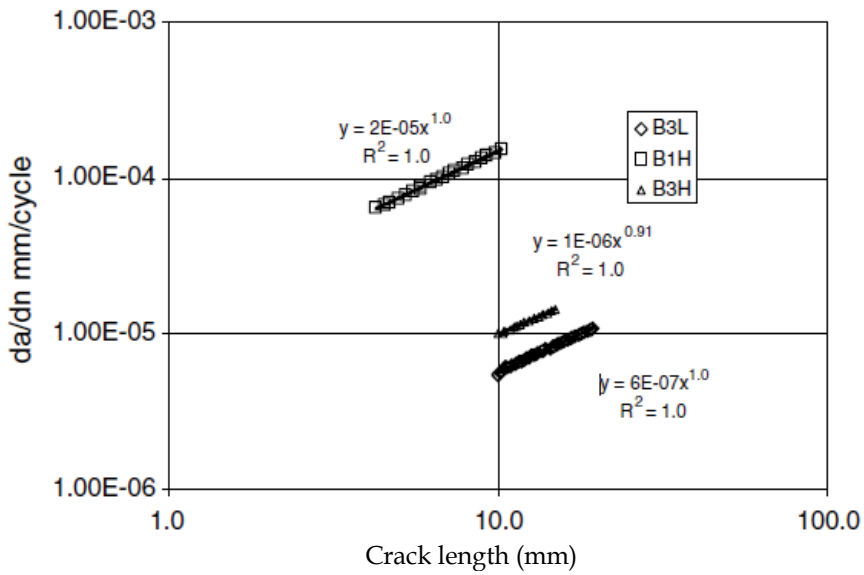

Fig. 10. Fatigue crack growth versus crack length for SM520B steel using CCT specimens adapted from Yamadaa et al., [2000]

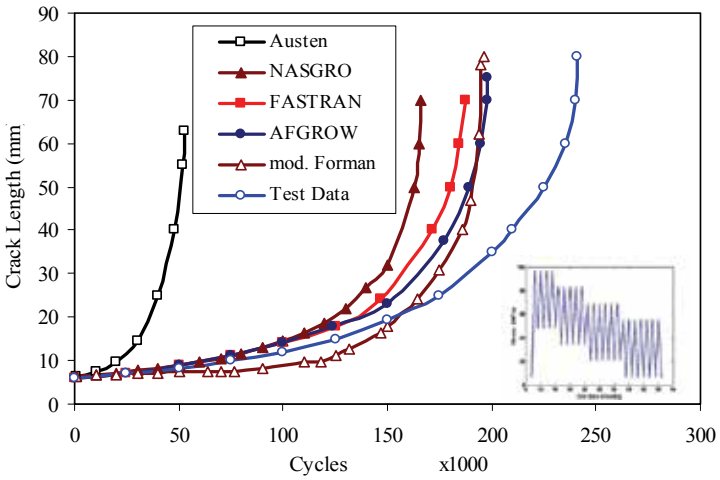

Fig. 11. Comparison of fatigue crack growth with different FCG models under load case 3

The comparison of test data and results predicted based on the NASGRO model for the two load cases (load cases 3 and 4) are shown in Fig. 13. The life predicted based on NASGRO model is 168 x 10^3 cycles, while for load case 4 is 160 x 10^3 cycles. The difference between the lives based on test data is 9%. These differences are due to the different load ratios and load sequence effects for the load cases.

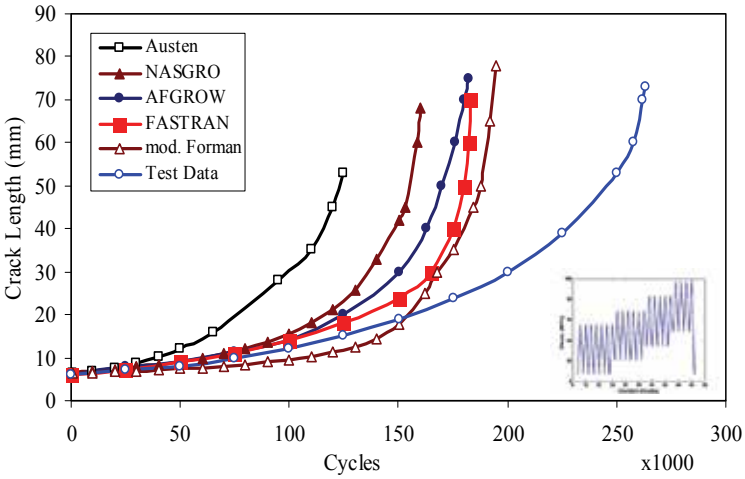

Fig. 12. Comparison of fatigue crack growth with different FCG models under load case 4

The FCG rate versus the crack length for the two load cases 3 and 4 shown in Fig. 14. The two power equations are approximately same (da/dN= 0.0019 $(a)^{1.6328}$) and the correction factor for these cases is 97.8%. This relation is a linear, which is in a good agreement with results published in literature [Molent, et al., 2006]. The crack growth results obtained by Roach [2002] as part of the FAA Aging Aircraft program are analysed in Fig. 15. We again

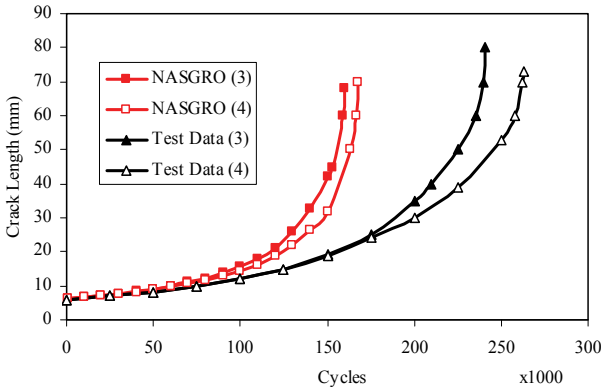

Fig. 13. Comparison of fatigue crack growth of test data and NASGRO model under load cases 3 and 4

see that there is a near linear relationship between the apparent growth rate and the crack length [Baker, 2002]. Although, the differences in the types of specimens and load magnitudes, it showed the same behaviour.

For the random loading case, i.e. case 5, the results show a good agreement of AFGROW model with experiment values and 10% difference with the modified Forman and NASGRO models, while for the FASTRAN and the Austen models are 30% and 50%, respectively. These results are clearly shown in Fig. 16. The correlation between the FCG rate and crack length for this load case is (da/dN = 0.0387 (a)$^{1.0051}$) and the correction factor is 98%, which shown in Fig. 17 in a linear relationship. The linear relationship between crack growth rate and crack length is in a good agreement in behaviour with the further test results illustrated and presented by Brot and Matias [2002]

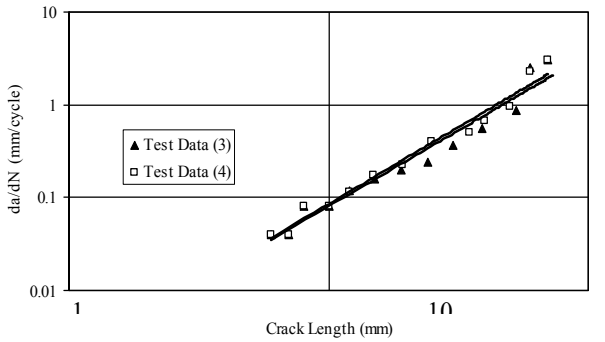

Fig. 14. Comparison of fatigue crack growth rate versus crack length of test data under load case 3 and 4

The above results indicates that, using VA loading in practice, the fatigue life is often affected by load or cycle sequences, although, the values of the load are same for each block. Neglecting the cyclic interaction effects in fatigue calculations lead to inaccurate life predictions [Kassim, et al., 2008]. These load cases, the load ranging from 4.14 to 82.8 MPa for the first two cases, while for the second two cases ranged from 6.9 to 96.6 MPa.

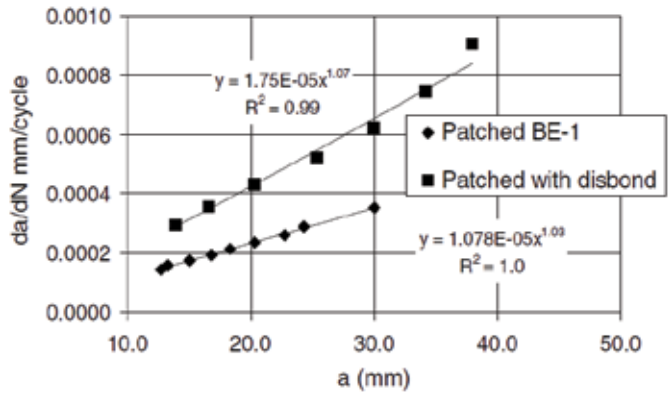

Fig. 15. Fatigue crack growth versus crack length in Al 2024-T3 adapted from Roach et al. [2002]

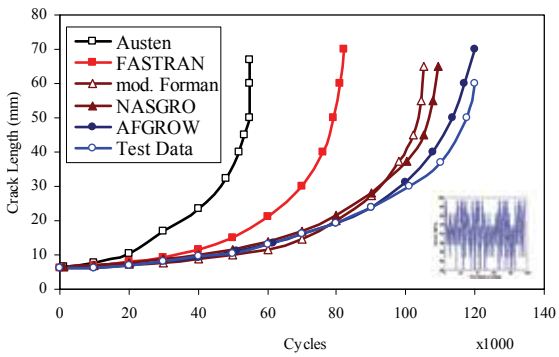

Fig. 16. Comparison of fatigue crack growth with different FCG models under load case 5

With reference to load cases 1 and 2, the changing in *R* ratio due to changing in the minimum stresses only, while for the load cases 3 and 4 the changes due to variability of both maximum and minimum stresses. For these cases (1, 2, 3 and 4) the results indicate that the value of stress ratio in the first block of the load had much effect on the crack growth. From the overall findings, therefore, the effect of load sequences on the fatigue life prediction is necessary to involve the interaction effects and neglecting the sequences effect lead to inaccurate results.

6. Conclusions

The application of multiple over and under loads can interact with each other, and as a result they could either accelerate or decelerate the overall crack growth retardation depending on the frequency of the overload. Three different models namely, the Austen, modified Forman and NASGRO have been used to predict the fatigue life on centre-cracked 2024-T3 aluminium alloy specimens under several program loadings. The load spectra and the schematic comparisons of predicted values with test data and those of FASTRN and AFGROW codes are compared. All the findings obtained from the comparisons with the five different program loadings agree with some discrepancies relating to the test data. It is

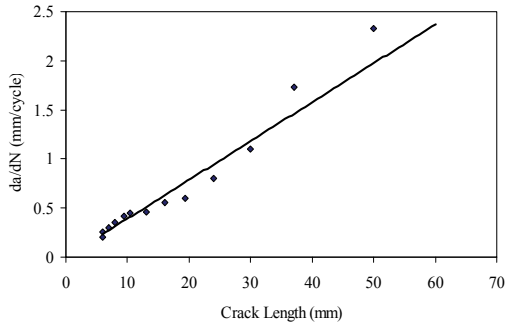

Fig. 17. Fatigue crack growth rate versus crack length of test data under load case 5

obvious that neglecting the effect of load sequence in fatigue calculations under VA loading can lead to inaccurate life predictions.

This work reveals that under the spectrum loading; there is a near linear relationship between the fatigue crack growth rate and the crack length when plotted on a log–log scale. These findings offer the potential to assess the effect on durability of an increase in the loading level due to different load ratios.

Finally, the present models have been proving applicable to crack propagation under VA loading with different approaches and the NASGRO model is the most proper model for VA loading fatigue life prediction.

7. References

ASM Metals Handbook. (1985). *Howard E. Boyer and Timothy L. Gall, Eds., American Society for Metals, Materials Park, OH.*

ASM Metals Handbook. (1990). *Properties and Selection: Nonferrous Alloys and Special-Purpose Materials,* Vol., 2. ASM International 10th Ed.

ASM Metals Reference Book. (1993). Michael, Bauccio, Ed. *ASM International, Materials Park*, 3rd edition, OH.

ASTM Standard E647-00. (2002). Standard test method for measurement of fatigue crack growth rates. *Annual book of ASTM Standards*, Vol., 03.01. ASTM International.

Baker, AA. (2002). Boron epoxy patching efficiency studies. *In: Baker A, Rose LRF, Jones R, editors. Advances in the bonded composite repair of metallic aircraft structure*. London: Elsevier Applied Science Publishers.

Brot, A. & Matias, C. (2002). An evaluation of several retardation models for crack growth prediction under spectrum loading. In*: Proceedings of the USAF aircraft structural integrity program conference*, 10 December. Savannah, Georgia.

Chang, JB.; Szamossi, M. & Liu, KW. (1981). Random spectrum fatigue crack life predictions with or without considering load interactions. In:Chang JB, Hudson CM, editors. *Methods and models for predicting fatigue crack growth under random loading*. ASTM STP, Vol.., 748. American Society for Testing and Materials, p. 1151–32.

Corbly, DM. & Packman, PF. (1973). On the influence of single and multiple peak overloads on fatigue crack propagation in 7075-T6511 aluminium*. Engineering Fracture Mechanics,* Vol., 5, p. 479–497.

Dominguez, J.; Zapatero, J. & Moreno, B. (1999). A statistical model for fatigue crack growth under random loads including retardation effects. *Engineering Fracture Mechannics,* Vol., 62, p. 351–369.

Elber, W. (1971*). The significance of fatigue cracks closure. In: Damage tolerance in aircraft structures.* ASTM STP, Vol.., 486. American Society for Testing and Materials, p. 230–242.

Forman, RG. (1972). Study of fatigue crack initiation from flaws using fracture mechanics theory. *Engineering Fracture Mechanics,* Vol., 4, No., 2, p. 333-345.

Harter, JA. (2003). AFGROW *users guide and technical manual,* Air Vehicles Directorate, Air Force Research Laboratory OH, AFRL-VA-WPTR; June.

Huang, XP.; Cui, WC. & Leng, JX. (2005a). A model of fatigue crack growth under various load spectra. In*: Proc of Sih GC,* 7th Int. conf of MESO, August 1th–4th, Montreal, Canada, p. 303–308.

Huang, XP.; Zhang, JB.; Cui, WC. & Leng, JX. (2005b). Fatigue cracks growth with overload under spectrum loading. *Theoretical and Applied Fracture Mechanics,* Vol., 44, p. 105–115.

James, MN. & Paterson, AE. (1997). Fatigue performance of 6261-T6 aluminium alloys – constant and variable amplitude loading of parent plate and welded specimens. *International Journal of Fatigue,* Vol., 19, p. S109–18.

Jono, M.; Sugeta, A. & Uematsu, Y. (1999). Fatigue crack growth and crack closure behavior of ti-6al-4v alloy under variable amplitude loadings. In: McClung RC, Newman Jr JC, editors. *Advances in fatigue crack closure measurement and analysis.* ASTM STP, Vol.., 1343. West Conshohocken (PA): American Society for Testing and Materials, p. 265–284.

Kassim, S., Al-Rubaie; Emerson, KL.; Barroso, L. & Godefroid, B. (2008). Statically modelling of fatigue crack growth rate in ore-strained 7475-T7351 aluminium alloys. *Materials Science and Engineering,* Vol., A486, p. 585-595.

Kujawski, D. (2001). A new $(DK+K_{max})^2$ driving force parameter for crack growth in aluminum alloys. *International Journal of Fatigue,* Vol., 23, p. 733–740.

Kim, CY. & Song, JH. (1994). Fatigue crack closure and growth behavior under random loading. *Engineering Fracture Mechanics,* Vol., 49, No., 1, p. 105–120.

Lee, CF. (2003). EndoFEM integrated methodology of fatigue crack propagation with overloaded delay retardation. *The Chinese Journal of Mechanics* – Series A, Vol., 19, No., 2, p. 327–335.

Ljustell, P. & Nilsson, F. (2005). Variable amplitude cracks growth in notched specimens. *Engineering Fracture Mechanics*, Vol., 72, p. 2703–2720.

Mohanty, JR.; Verma, BB. & Ray, PK. (2009). Prediction of fatigue crack growth and residual life using an exponential model: Part II (mode-I overload induced retardation) *International Journal of Fatigue*, Vol., 31, p. 425–432.

Murthy, ARC.; Palani, GS. & Iyer, NR. (2004). State-of-the-art review on fatigue crack growth analysis under variable amplitude loading. IE (I) J-CV, Vol., 85, p.118–29.

NASA. (2000). *Fatigue crack growth computer program.* ''NASGRO", version 3.0 –reference manual.

nCode. (2003). *User guide manual.* ICE-FLOW cracks growth.

Newman, Jr.; Phillips, EP. & Everett, RA. (1981). Fatigue analyses under constant and variable amplitude loading using small-crack theory. *NASA/TM-1999-209329, ARL-TR.*

Newman, Jr. (1984). *A crack opening stress equation for fatigue crack growth. International Journal of Fracture,* Vol., 24, p. R131–135.

Newman, JC. (1992). *FASTRAN-II A fatigue crack growth structural analysis program*, NASA Technical Memorandum 104159, Langley Research Centre, Hampton, VA 23665.

Paris, PC.; Erdogan, F. (1963). A Critical Analysis of Crack Propagation Laws. *Journal of Basic Engineering; Transaction*, American Society of Mechanical Engineers, Series D, Vol., 85, p. 528-534.

Paris, PC.; Tada, H. & Donald, JK. (1999). Service load fatigue damage – a historical perspective. *International Journal of Fatigue,* Vol., 21, p. S35–46.

Pell, RA.; Molent, L. & Green, AJ. (2004). Fractographical comparison of F/A-18 aluminium alloy 7050–T7451 bulkhead representative coupons tested under two fatigue load spectra at several stress levels. *DSTO-TR-1547. Melbourne, Australia*. February.

Piascik, RS. & Gangloff, RP. (1993). Environmental fatigue of an Al–Li–Cu alloy: part II microscopic hydrogen cracking processes. *Metall Trans*, Vol., 24, p. A:2751–2762.

Ray, A. & Patanker, P. (2001a). Fatigue crack growth under variable amplitude loading: Part I – Model formulation in state space setting. *Applied Mathematical Modelling*, Vol., 25, p. 979–994.

Ray, A. & Patanker, R. (2001b). Fatigue crack growth under variable-amplitude loading: Part II-Code development and model validation. *Applied Mathematical Modelling*, Vol., 25, p. 995–1013.

Roach, D. (2002). Damage tolerance assessment of bonded composite doubler repairs for commercial aircraft applications. *In: Baker A, Rose LRF, Jones R, editors. Advances in the bonded composite repair of metallic aircraft structure.* London: Elsevier Applied Science Publishers.

Rudd, JL. & Engle, Jr. (1981). Crack growth behaviour of centre-cracked panels under random spectrum loading. In: Chang JB, Hudson CM, editors. *Methods and models for predicting fatigue crack growth under random loading. ASTM STP, vol. 748*. American Society for Testing and Materials, p. 103–114.

Sadananda, K. & Vasudevan, AK. (1999). Analysis of overloads effects and related phenomena. *International Journal of Fatigue*, Vol ., 21, p. S233–46.

Sander, M. & Richard, HA. (2005). Finite element analysis of fatigue crack growth with interspersed mode I and mixed mode overloads. *International Journal of Fatigue,* Vol., 27, p. 905–913.

Schijve, J. (1981). Some formulas for the crack opening stress level. *Engineering Fracture Mechannics,* Vol., 14, p. 461–465.

Taheri, F.; Trask, D. & Pegg, N. (2003). Experimental and analytical investigation of fatigue characteristics of 350WT steel under constant and variable amplitude loadings. *Journal of Marine Structure*, Vol., 16, p. 69–91.

Tianwen, Zhao; Jixi, Zhang & Yanyao, Jiang. (2008). A study of fatigue crack growth of 7075-T651-aluminum alloy. *International Journal of Fatigue,* Vol., 30, p. 1196-1180.

Voorwald, HJC. & Torres, MAS. (1991). Modeling of fatigue crack growth following overloads. *International Journal of Fatigue, Vol.*,13, No., 5, p. 423–427.

Wheeler, OE. (1972). Spectrum loading and crack growth. *Journal of Basic Engineering, Trans ASME, Ser D,* Vol., 94, No., 1, p. 181–186.

Willenborg, JD.; Engle, RM. & Wood, HA. (1971). A crack growth retardation model using an effective stress concept. *Report AFFEL-TM-71-1-FBR, Dayton (OH): Air Force Flight Dynamics Laboratory,* Wright–Patterson Air Force Base.

Yoder, GR.; Cooley, LA. & Crooker, TW. (1982). On microstructural control on near-threshold fatigue crack growth in 7000-series aluminum alloys. *Scr Metall,* Vol.., 16, p.1021–1025.

13

Creep and Creep-Fatigue Crack Growth in Aluminium Alloys

Gilbert Hénaff[1], Grégory Odemer[2] and Bertrand Journet[3]
[1]*Institut Pprime, UPR 3346 CNRS – ENSMA – Université de Poitiers*
[2]*Cirimat, Ensiacet, Toulouse*
[3]*EADS IW, Suresnes*
France

1. Introduction

Due to the low melting point of aluminium and its consequences on microstructural stability and mechanical resistance, aluminium alloys are generally not considered for applications that have to withstand elevated temperatures in service. However, in some very specific instances where the temperature is not too high, aluminium alloys can present a unique solution. In addition, for such applications, the damage tolerance assessment can be a key issue and data as well as predictive models of propagation life are needed to meet the requirements. This is the case for fuselage panels for civil transport aircraft: a cruise speed of Mach 2.05 induces a maximum temperature of the fuselage skin of 130°C. Concorde, the first supersonic civil transport aircraft, was originally designed to sustain 7000 flights, i.e. 15000 hours. The fuselage design was conducted by considering creep deformation of the 2618A aluminium alloy used for fuselage skin on one hand, and the fatigue resistance of this alloy on the other hand. However, as the damage tolerance philosophy was not mature at that time, life predictions were mainly based on safe life concepts, without specific consideration of crack growth. More recently, a future supersonic aircraft was designed to sustain a total of 20000 flights, i.e. 60000 hours at almost the same elevated temperature (130°C). In this design the fuselage skin was still be made of aluminium alloy. In addition, this structure had to meet damage tolerance requirements, which requires reliable fatigue crack growth models. Such models should account for the physical mechanisms that affect crack growth at elevated temperature, including creep damage. However, issues related to creep-fatigue interactions during crack growth have not been extensively studied so far in aluminium alloys. One can however find some information in (Kaufman et al., 1976; Bensussan et al., 1984; Bensussan et al., 1988; Jata et al., 1994). With this respect, the present chapter presents an overview of the creep crack growth and creep-fatigue crack growth resistance of a precipitation-hardened aluminium 2650 T6 alloy, which is precisely the alloy selected for this type of application. More precisely, it reports on investigations that have been carried out to identify the mechanisms that would control possible creep-fatigue interactions in the 2650 T6 aluminium alloy and to evaluate the conservatism of the cumulative damage rule. With this aim, crack growth data have been established not only under creep-fatigue loading, but also under fatigue and creep loading. Most of the tests were carried out in the 100-175°C temperature range in laboratory air. Some additional tests were carried out in

vacuum in order to evaluate the effect of environment on these processes. The Creep Crack Growth (CCG) behaviour of the 2650 T6 aluminium alloy is first presented. Similarly, the Fatigue Crack Growth (FCG) behaviour is examined at room temperature and elevated temperatures. Finally, the Creep-Fatigue Crack Growth (CFCG) is studied by means of low frequency signals with different waveshapes. The analysis of creep-fatigue mechanisms is supported by quantitative fracture surface observations by scanning electron microscopy. Finally the ability of simple cumulative rules to correctly account for the CFCG behaviour is examined and discussed.

2. Material and experimental techniques

2.1 Material

The 2650 alloy is a copper-magnesium aluminium alloy, provided in the form of sheets (thickness: 2.5 and 5mm). The chemical composition is given in Table 1.

Analysis	Si	Fe	Cu	Mn	Mg	Cr	Ni	Zn	Ti	Zr
Min	0.36	0.08	2.60	0.32	1.50				0.08	
Expected	0.40	0.11	2.70	0.35	1.60				0.10	
Max	0.44	0.13	2.80	0.38	1.70	0.04	0.03	0.10	0.12	0.03

Table 1. Chemical composition of the 2650 aluminium alloy.

T(°C)	σ_Y(MPa) L	σ_Y(MPa) LT
20°C	421	411
100°C	394	386
130°C	375	371

Table 2. Yield strength σ_y as a function of temperature for two orientations (data from EADS IW).

The CCG, FCG and CFCG resistance of this alloy is investigated after T6 artificial ageing treatment (192°C for 21 hours) resulting into a fully recrystallised microstructure with an average grain size of 40µm in the rolling plane. The precipitation hardening of this alloy has been studied by Majimel et al. (Majimel et al., 2002; Majimel et al., 2002). For this composition, the precipitation hardening system is Al-S (Al_2CuMg). Besides, results of hardness and tensile tests carried out on specimens aged 20000 hours at 175°C and 30000 hours at 100°C and 130°C respectively have shown no significant decay in mechanical properties with respect to those measured without prior ageing treatment, suggesting that bulk ageing effects during long-time crack growth experiments at elevated temperatures can be neglected (Odemer, 2005).

2.2 Testing

CCG, FCG and CFCG testing were performed on CT specimens (W=32mm) of 5 mm thickness in the L-T orientation. The crack length was monitored by means of the potential

drop technique for the three types of test. For CCG tests, the samples were precracked by fatigue at room temperature. The initial value of K at the beginning of the creep test was higher than the value of K_{max} achieved at the end of the fatigue precracking in order to avoid a possible interaction between the fatigue precracking zone and the creep zone. CCG tests were carried out using dead-weight lever-type creep machines to apply a constant load. FCG and CFCG were conducted under a constant load ratio R=0.5on a servohydraulic machine equipped with a furnace. The same load ratio was used during tests in vacuum. These tests were carried out on a servo-hydraulic machine equipped with a furnace and a chamber operating at a residual pressure of about 10^{-7} mbar. Crack closure measurements were performed by means of a capacitive displacement sensor. A triangular waveform loading with frequencies of 20Hz and 0.05Hz was used for fatigue tests. The 0.05Hz fatigue tests present the same loading increase/decrease times (10s) that trapezoidal waveform loading tests applied for creep-fatigue conditions and different hold-time durations (30, 300, 1500 and 3000 seconds) have been considered for CFCG tests.

3. Crack growth results and analysis

3.1 Creep crack growth

First, it is worth noticing that during CCG experiments, crack extension was not detected immediately after application of the load. The time during which no crack advance is measured is called incubation time and noticed t_i. Its value was experimentally determined as the time required to obtain a 1mV variation in the potential drop, as proposed by Bensussan (Bensussan et al., 1988), which corresponds to a crack advance of about 0,05mm. The t_i values obtained at different loads at 130°C are given in the table 2. This time can be interpreted as the time necessary to accumulate a critical amount of creep damage at the precrack tip to initiate propagation. According to Vitek (Vitek, 1977) this crack initiation would be governed by a critical value of the crack opening displacement. Ewing (Ewing, 1978) and Riedel (Riedel, 1977) using a modified Dugdale model, suggest that at high stresses: $t_i \propto K_i^{-2n}$, where n is the creep power law exponent. However the data obtained in the present study obey to the following law: $t_i \propto K_i^{-2}$, which means that the n exponent value is different from that derived from creep experiments. This discrepancy between theory and experimental results may be partly accounted for by the fact that the experimental incubation time may also include a propagation stage where the CCG rate is so slow that it cannot be detected by the potential drop method (Bensussan, Maas et al., 1988).

Incubation time (h)	K-level (MPa x $m^{1/2}$)
192	20
96	29
72	33

Table 2. Incubation time as a function of the initial stress intensity factor K_i at 130°C.

The influence of temperature on the CCG resistance of the 2650 alloy is shown in Figure 1 . Three domains, schematically represented in Figure 2, can be distinguished on CCG curves, regardless of temperature:

- a first domain where, just after incubation, Creep Crack Growth Rates (CCGRs) rapidly increases with K values; it was shown that, for a given temperature, the behaviour in this domain is also affected by initial load level (Odemer et al., 2006).
- a domain, corresponding with intermediate K values, where, except at 100°C, CCGRs obeys a fourth power law dependence with respect to K ($\frac{da}{dt} \propto K^4$); it is interesting to note that a similar power-law is predicted by theoretical models (see (Sadananda, 1978; Vitek, 1978));
- finally a third domain, characterised by a pronounced CCGR enhancement, corresponds with K values close to the critical value for fracture.

The values of the exponents noticed in the stage II and stage III, as the K and $\frac{da}{dt}$ range concerned, are given in table 3.

T (°C)	$[K_2]$ (MPa x $m^{1/2}$)	$[da/dt]_2$ (m/s)	β_2	$[K_3]$ (MPa x $m^{1/2}$)	$[da/dt]_3$ (m/s)	β_3
100	29-47	5.10^{-10}-3.10^{-8}	8,47	47-52	5.10^{-8}-$3x10^{-7}$	22,36
130	22-35,5	10^{-9}-6.10^{-9}	3,88	35,5-47,5	6.10^{-9}-1.10^{-7}	10,17
160	16-31	2.10^{-9}-3.10^{-8}	4,04	35-50	5.10^{-8}-10^{-6}	8,33
175	19-42	2.10^{-8}-5.10^{-7}	4,08	42-52	5.10^{-7}-2.10^{-6}	8,03

Table 3. Values of the CCG power law exponents (cf. Figure 2) exponents in the steady state regime at different temperatures.

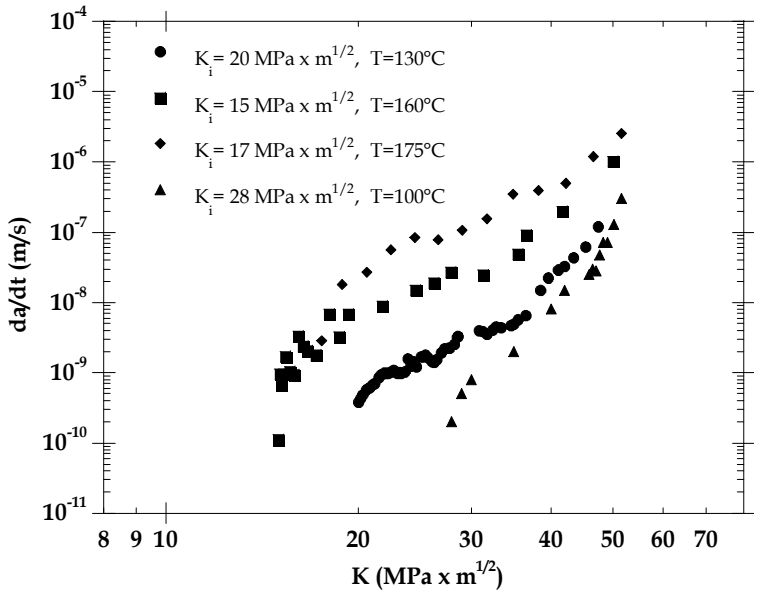

Fig. 1. Influence of temperature on CCG rates in the 2650 T6 alloy.

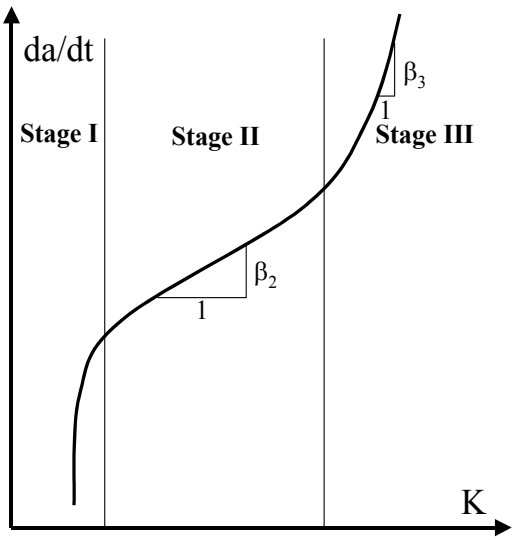

Fig. 2. Schematic representation of CCG curve.

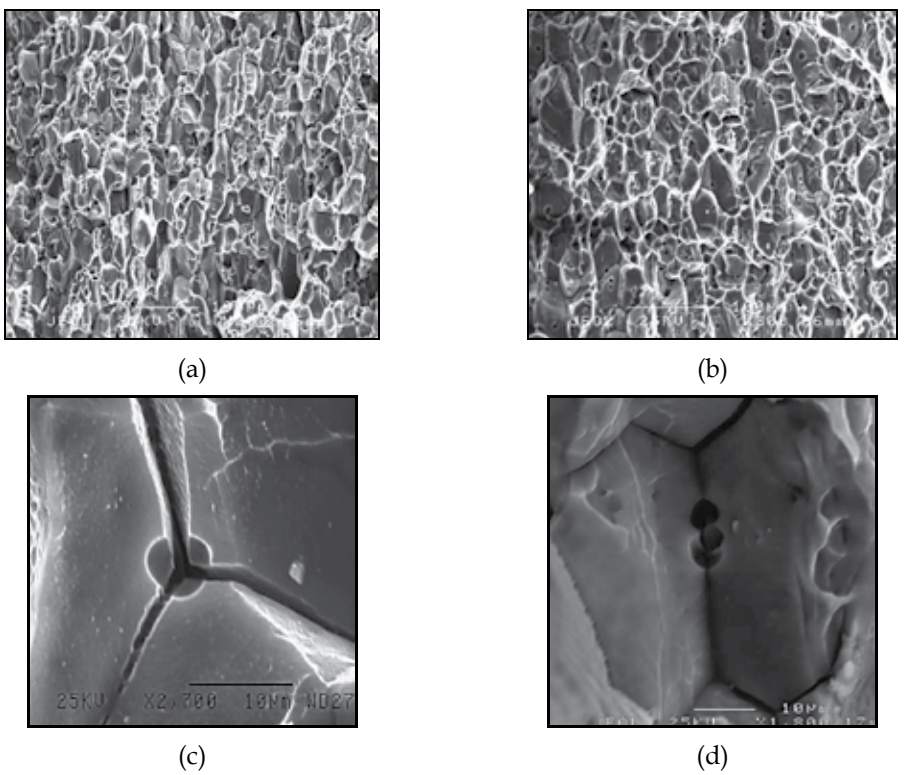

Fig. 3. Fracture surfaces produced during CCG (a) intergranular fracture (K=22 MPa x $m^{1/2}$, 175°C), (b) Intergranular and ductile rupture (K=44 MPa x $m^{1/2}$, 175°C); (c) Cavities nucleation at triple boundaries; (d) Coalescence of cavities.

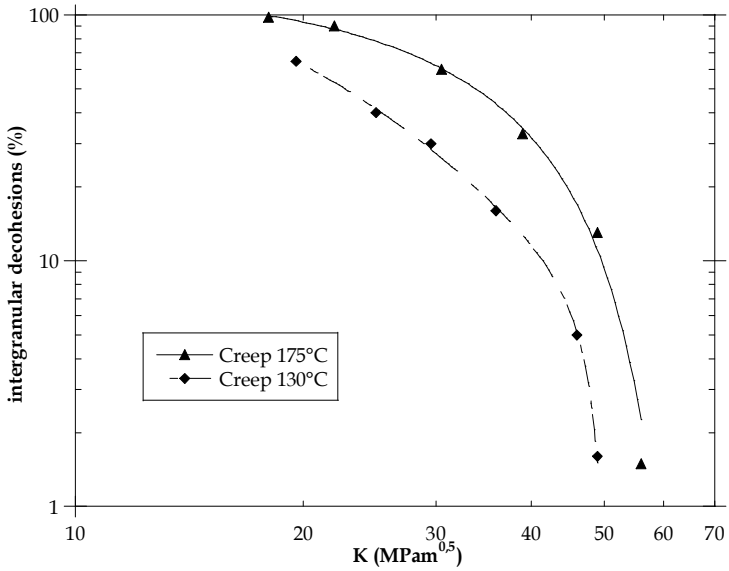

Fig. 4. Evolution of the intergranular decohesions during creep crack growth.

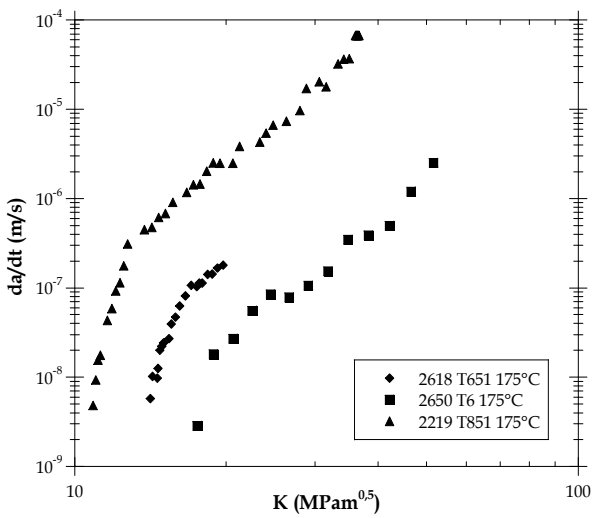

Fig. 7. Creep crack growth resistance of the 2650 T6, 2618 T651 (Leng, 1995) and 2219 T851 (Bensussan et al., 1984) alloys.

It can be seen that the CCG resistance is slightly affected by temperature in the range 100-130°C, except in the low K value domain. The temperature effect is more pronounced in the range 130-160°C and seems to saturate between 160°C and 175°C. This influence of temperature is consistent with results previously obtained on 2219 (Bensussan et al., 1984) and 2618 (Leng, 1995) alloys. However the second regime is larger at higher temperatures, although initial load may also account for this discrepancy. CCG fracture surfaces exhibit two characteristic failure modes, namely an intergranular fracture mode prevailing in the

slow growth rate regime (Figure 3 a) and a mixture of intergranular and ductile fractures which develops when approaching failure (Figure 3 b). The intergranular mode occurs by cavitation. The cavities nucleate at triple grain boundaries (Figure 3 c) or on precipitates along grain boundaries (Figure 3 d). This cavitation process is promoted at elevated temperature, as confirmed by quantitative measurements of the area percentage occupied by interganular facets (Hénaff et al., 2010) presented in Figure 4.
The comparison presented in Figure 7 of the creep crack growth resistance of the 2650 T6 alloy and the resistance of 2618 T651 (Leng, 1995) and 2219 T851 (Bensussan et al., 1984) aluminium alloys at 175°C indicates a superior resistance of the 2650 T6 alloy, at least at his temperature. However an ageing effect cannot be excluded at this temperature (175°C) which is close to the heat-treatment temperature (192°C for 21h) of the 2650 alloy. However such an effect when exists would be beneficial to crack growth resistance.

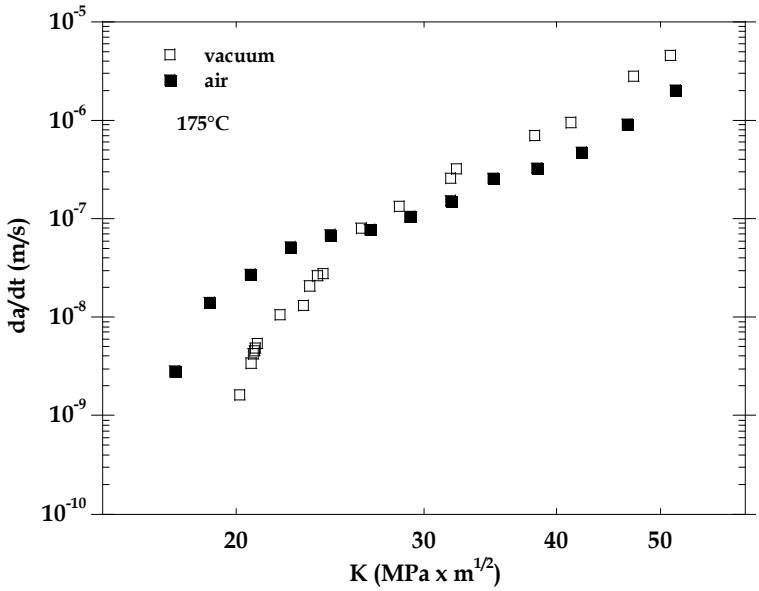

Fig. 5. CCG behaviour in air and in vacuum of the 2650 T6 alloy at 175°C.

In order to investigate possible environmental effects on crack growth, CCG rates obtained in air and in vacuum at 175°C are compared in Figure 5. It can be seen that CCG rates are nearly identical over the entire explored range. The difference noticed at low K values is difficult to analyse since it was shown that, for a given environment, the behaviour is influenced by initial load levels (Odemer et al., 2006). At high K values CCG rates in vacuum are slightly higher than those observed in air, as observed by Leng (Leng, 1995) on a 2618 alloy. However, apart from these small discrepancies, one can consider that the CCG resistance of the 2650 alloy is almost unaffected by environmental effects. However, as noticed by (Kaufman et al., 1976), this results demonstrates that stable crack growth under static load in air in not due to a stress corrosion cracking process which might also result into intergranular cracking (Menan and Hénaff, 2009).

3.2 Fatigue and Creep-fatigue crack growth

Figure 6 compares FCG rates measured at 20°C, 130°C and 175°C for load frequencies of 20Hz and 0.05Hz. At the load ratio considered, namely R=0.5, no crack closure effect was detected, regardless of temperature. Actually, even at R=0.1, crack closure effects are limited in this material (Odemer, 2005). It can be seen that temperature has almost no influence on FCG rates, and that frequency has only a slight influence on FCG rates in the 20-0.05Hz frequency range at 175°C. However, this slight deleterious effect is accompanied by a change in fracture surfaces, with a sharp increase in the surface fraction of intergranular decohesions similar to those observed during CCG, as shown in Figure 8. This effect, both on growth rates and fracture surfaces, suggests that, at low frequency, creep damage can occur during cyclic loading. In order to get further insights into this damage process occurring at elevated temperature, a hold time was introduced at the maximum load of the triangular loading. Figure 9 compares CFCG measured at 175°C for a 10s-0s-10s triangular loading and a 10s-300s-10s trapezoidal loading. A deleterious influence of hold-time on crack growth rates is noticed, more particularly in the 8 MPa x $m^{1/2}$- 40 MPa x $m^{1/2}$ K_{max} range. Therefore, different hold-time durations (0s, 30 s, 300s, and 1500s) have been considered in order to evaluate the creep damage effect as a function of hold-time only for loadings at R=0.5 (Odemer et al., 2006). The results obtained at 175°C are presented in Figure 10. It can be noticed that CFCG rates significantly increase as hold-time duration increases, indicating a significant contribution of creep damage to crack advance. A similar influence of hold time, although less pronounced, is also observed at 130°C. CFCG rates measured at 130°C and 175°C for the same hold-time duration, namely 300s, are compared in Figure 11. The hold time effect is more pronounced at 175°C, since it was shown that the FCG behaviour is only slightly affected by temperature (Figure 6).

A typical CFCG fracture surface is presented in Figure 12 a. The main observation is that, for a selected K value, CFCG fracture surfaces are not fundamentally different from those

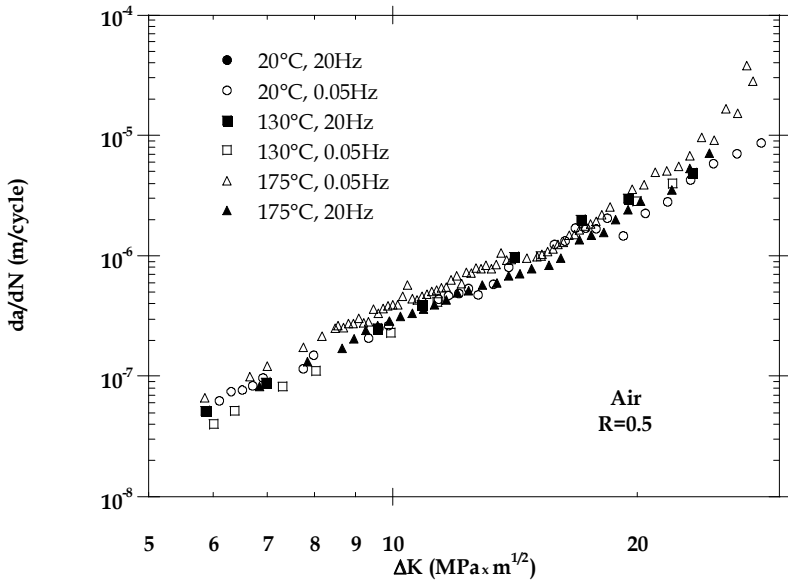

Fig. 6. Fatigue crack growth rates vs. ΔK at 20°C, 130°C and 175°C in air.

produced during FCG at 0.05Hz (10s-0s-10s). However the introduction of a hold-time at maximum load results into a higher percentage of intergranular decohesions. Additionally, as during CCG, the intergranular fracture seems to be controlled by cavitation (Figure 12 b). The same statement still holds at 130°C, although the amount of intergranular fracture is lower for a fixed loading condition. Additional testing using different waveshape signals (saw-tooth, triangle) indicate that it is the load period, and not the waveshape, that governs the crack growth enhancement during creep-fatigue, as shown in Figure 13. Indeed, CFCG rates obtained under saw-tooth signals, with a rapid or a slow loading rate, are identical to those obtained under trapezoidal waveshape with the same frequency. This suggests that there is no interaction between the additional damage process taking place at elevated temeprature and the cyclic damage, conversely to what can be observed in corrosion-fatigue (Menan and Hénaff, 2009). With this respect, CFCG rates are plotted as a function of load period for selected values of K_{max} at R=0.5, at 130°C and 175°C in Figure 14a and Figure 14b respectively. The linear dependence in the right-hand part of these diagrams suggests that the time-dependent damage is governed by hold-time above a critical value of period T_c, which is dependent on temperature. Hence it is found that $T_c \approx 50s$ at 175°C, while $T_c \approx 320s$ at 130°C. A similar influence of frequency has been observed in 2219-T851 (Bensussan et al., 1984) and 8009 aluminium alloys (Jata et al., 1994).

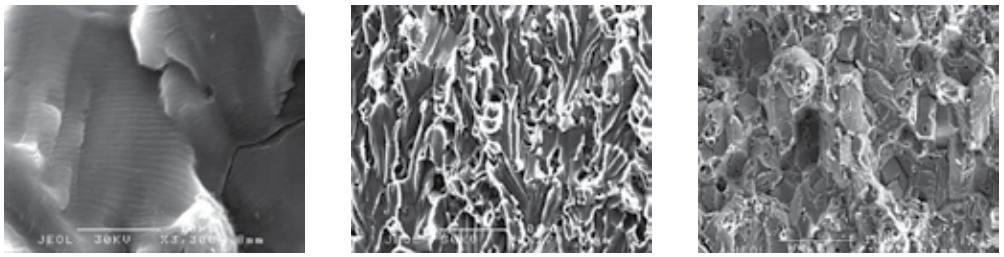

(a) (b) (c)

Fig. 7. Fracture surfaces produced during fatigue crack growth in the 2650 T6 alloy (a) at ΔK=9 MPa x $m^{1/2}$, 20°C, 20 Hz, (b) at ΔK=9 MPa x $m^{1/2}$, 130°C, 20 Hz and (c) at ΔK=7 MPa x $m^{1/2}$, 175°C, 0.05Hz.

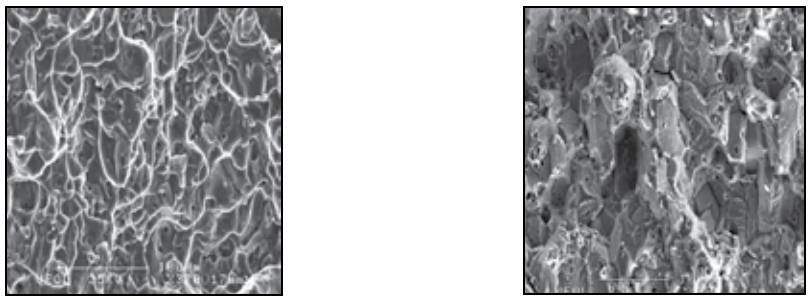

(a) (b)

Fig. 8. Fractures surfaces obtained at 0.05Hz (a) 130°C, da/dN=1x10^{-7} m/cycle, (b) 175°C, da/dN=1x10^{-7} m/cycle.

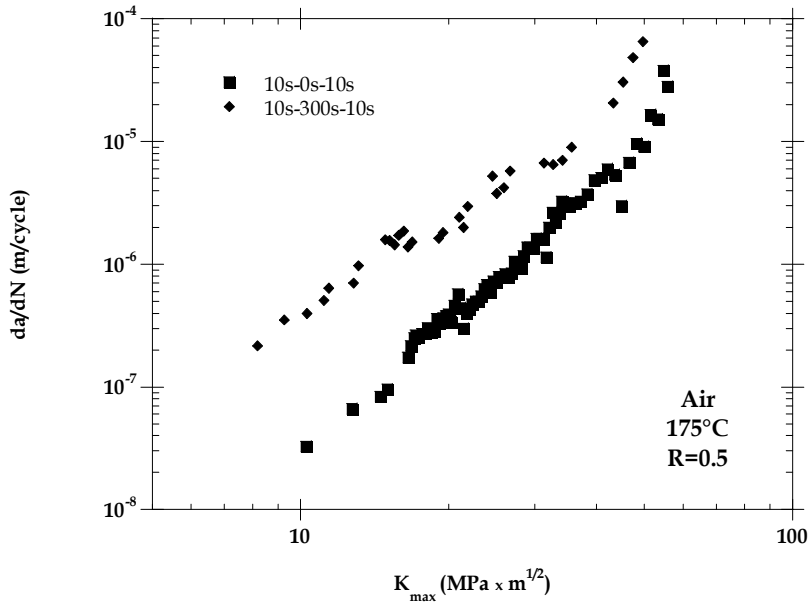

Fig. 9. FCG and CFCG rates vs. K_{max} (175°C) in air.

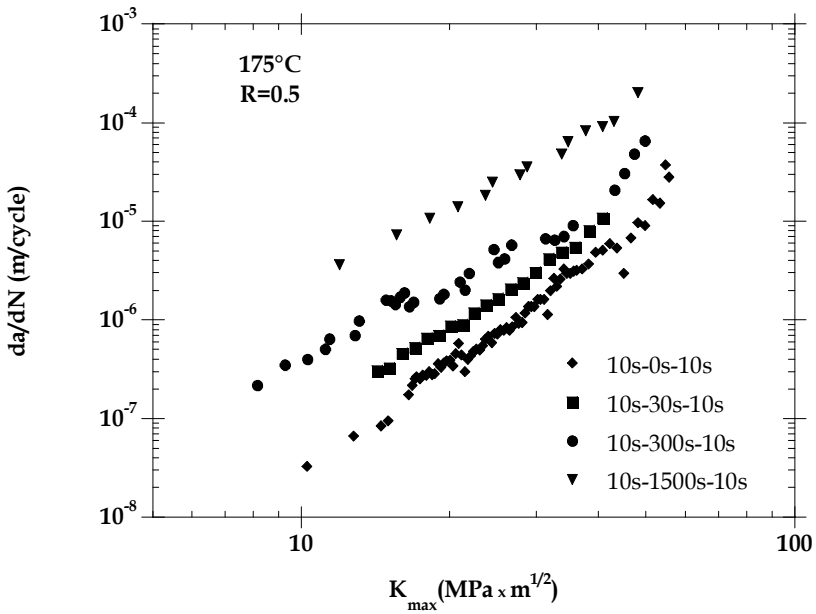

Fig. 10. Effect of the hold-time duration on the CFCG rates at 175°C in air.

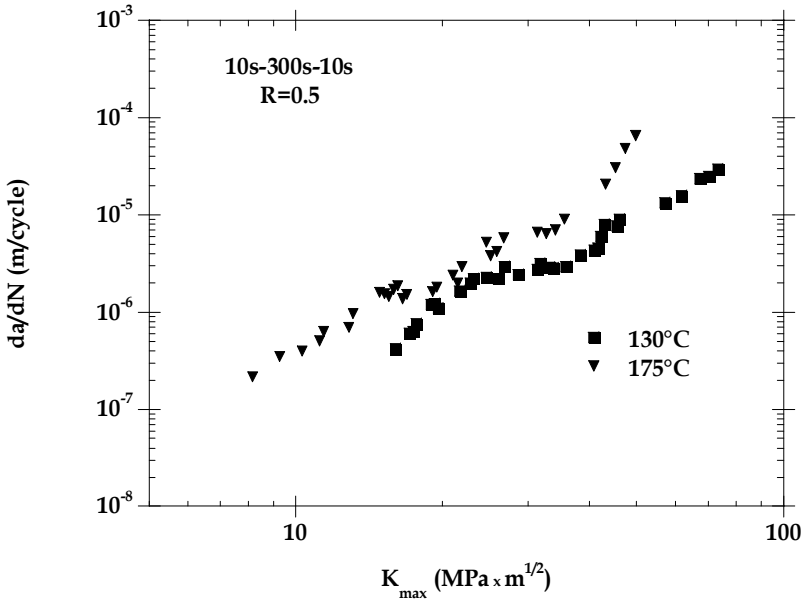

Fig. 11. Influence of temperature on CFCG rates for a 300s hold-time in air.

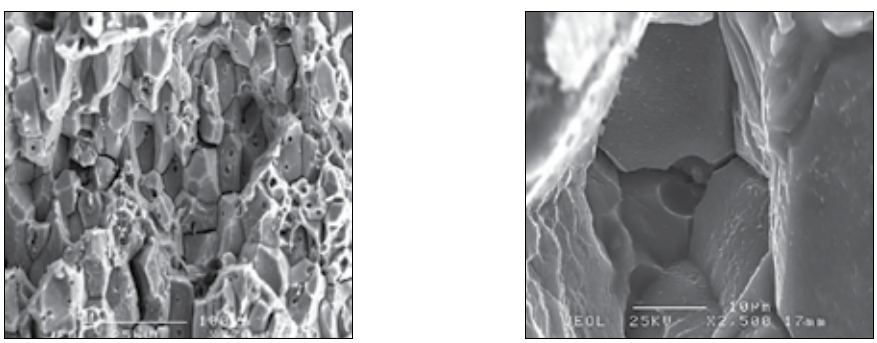

(a) (b)

Fig. 12. CFCG fracture surfaces in air (a) intergranular decohesions (K_{max}= 23 MPa x $m^{1/2}$, da/dN = 2x10^{-5} m/cycle, 10s-1500s-10s, 175°C); (b) cavitation at triple grain boundary (K_{max}= 30 MPa x $m^{1/2}$, da/dN = 2x10^{-6} m/cycle, 10s-300s-10s, 175°C).

In order to analyse the observed crack growth enhancement quantitative measurements of the area fraction occupied by intergranular facets have been performed for different loading conditions (Hénaff et al., 2010). The results obtained under trapezoidal wave shape signals at 130°C and 175°C are presented in Figure 16 a and Figure 16 b, respectively, as a function of hold time. It can be noticed that, for a selected temperature, the longer the hold time, the higher the amount of intergranular facets, especially at low K values. Nevertheless, even for hold times as high as 3000s, the amount of intergranular facets never exceeds the amount obtained during CCG at the same K or K_{max} value for a fixed temperature. Besides, for a given hold time value, the percentage of intergranular facets is higher at 175°C than at

130°C. Therefore a relationship between the amount of intergranular decohesions and the crack growth enhancement induced by creep damage with respect to fatigue at high frequency can be established.

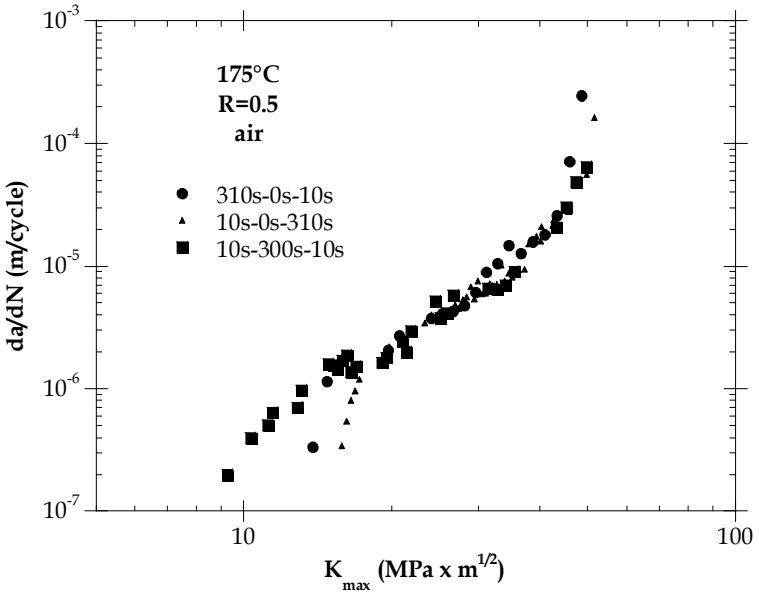

Fig. 13. CFCG rates for 3 different waveshapes of same period (320s) at 175°C in air.

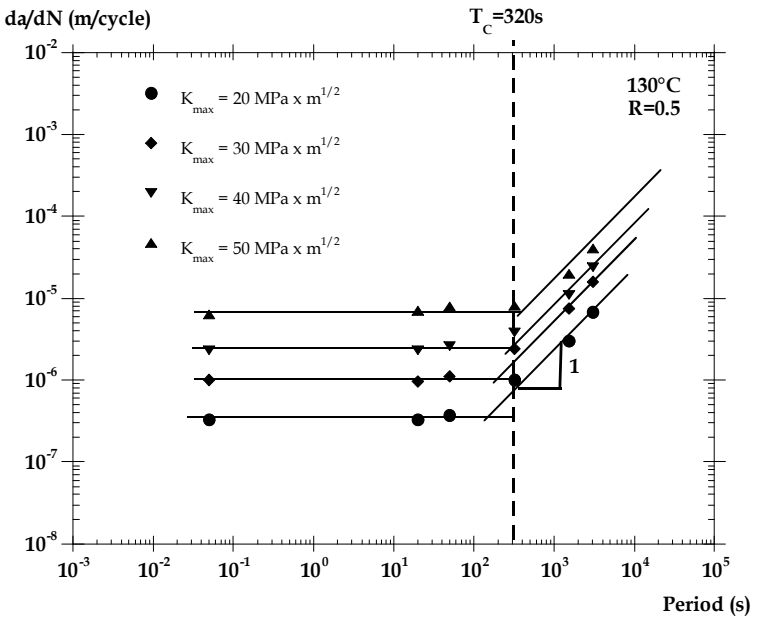

(a)

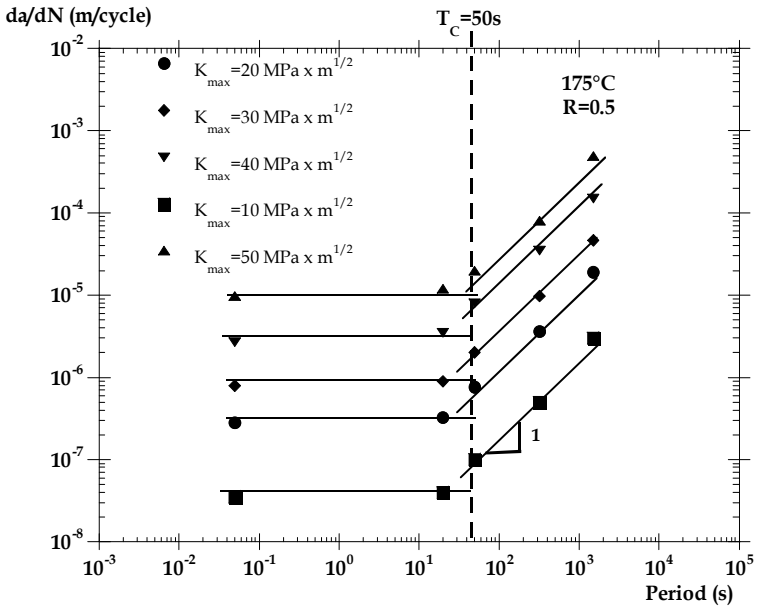

(b)

Fig. 14. CFCG rates as a function of load period in air at 130°C (a) and 175°C (b).

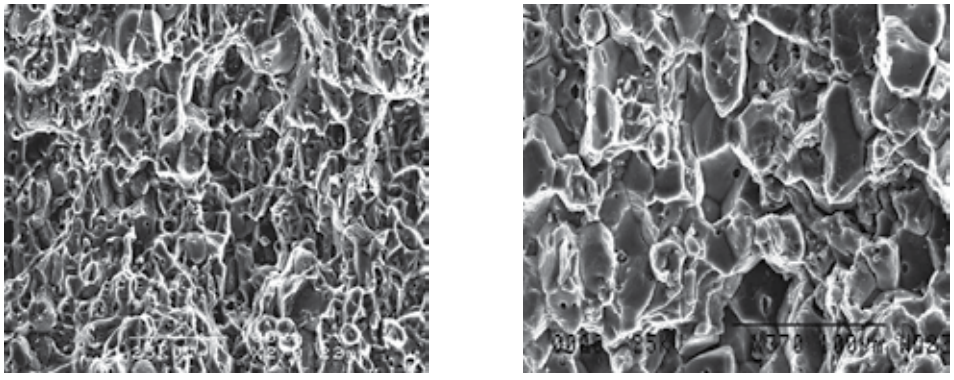

(a) (b)

Fig. 15. Influence of environment on fracture surfaces in CFCG at 175°C (a) air (b) vacuum(trapezoidal signal, 10s-300s-10s, K_{max}=20MPa x $m^{1/2}$).

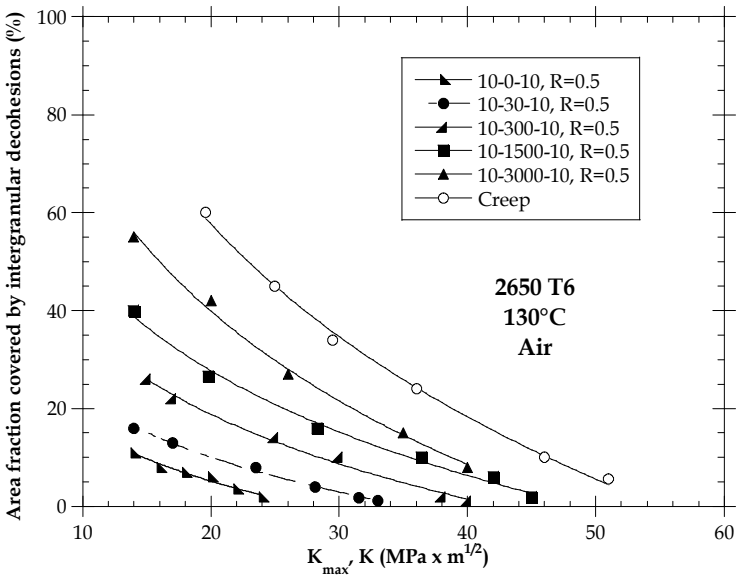

(a)

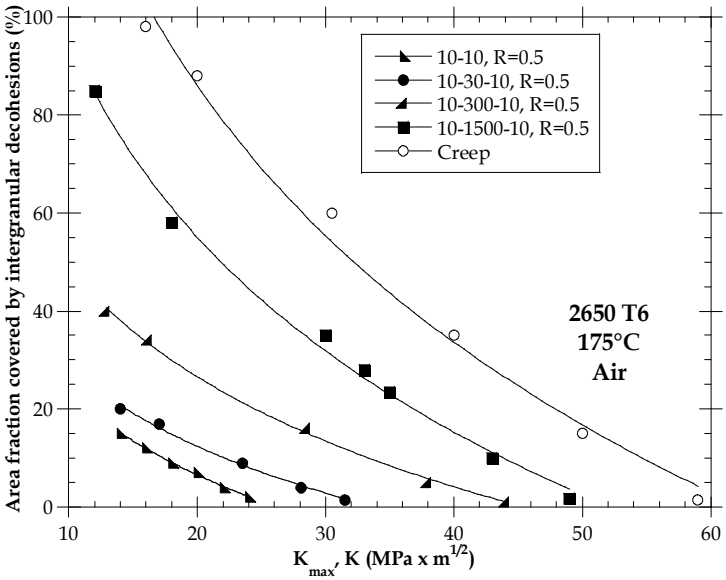

(b)

Fig. 16. Percentage of area covered by intergranular decohesions as a function of maximum stress intensity factor for different loading cases (a) at 130°C; (b) at 175°C.

3.3 Influence of environment

The same experiments have been conducted in vacuum, mainly at 175°C, in order to evaluate the intensity of environmental effects on CGCG. With this respect, the results reported in Figure 17 indicate that, at high frequency (20Hz), FCGR in air are about fourfold higher than in vacuum. This enhancement can be mainly attributed to a surface adsorption effect (Hénaff et al., 1995), although the role of temperature on desorption may need to be more thoroughly analysed. However, while frequency has almost no influence on FCGRs in air at both temperatures as in vacuum at room temperature, a significant enhancement is observed at low frequency (0.05Hz) in vacuum at 175°C, suggesting that creep–fatigue effects may take place. The results of additional testing under creep-fatigue loading, typically trapezoidal load signals with hold time at the maximum load, are reported in Figure 18 using the same type of graph as in Figure 14. As observed in air, above a critical value of the period T_c, CFCG rates are proportional to the load period T. However, it should be noticed that the value of T_c determined in vacuum is lower than in air at the same temperature (Odemer, 2005). This might be accounted for by the enhanced FCGR in air as compared to vacuum which would induce a higher fatigue damage, so that a longer time is required to achieve higher cavitation-induced damage. Consistently, CCG and CFCG fracture modes in the 2650 alloy are characterised by a significant amount of intergranular decohesions induced by diffusion-controlled cavitation, regardless of environment as shown in Figure 15, for a trapezoidal 10s-300s-10s signal at 175°C. For a fixed K value it seems that the fraction of intergranular fracture is lower in air than in vacuum. This is confirmed by the quantitative measurements presented in Figure 19 which indicates that, for a selected K value, the percentage of fracture surface occupied by intergranular decohesions is higher in vacuum than in air. These observations suggest that the contribution of creep damage to the

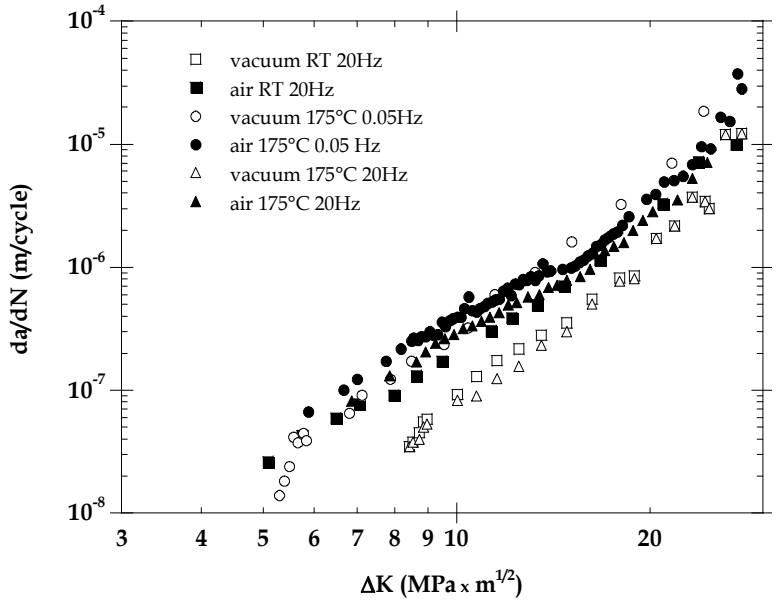

Fig. 17. FCG behaviour of the 2650 T6 alloy in air and in vacuum at 25°C and 175°C for two loading frequencies.

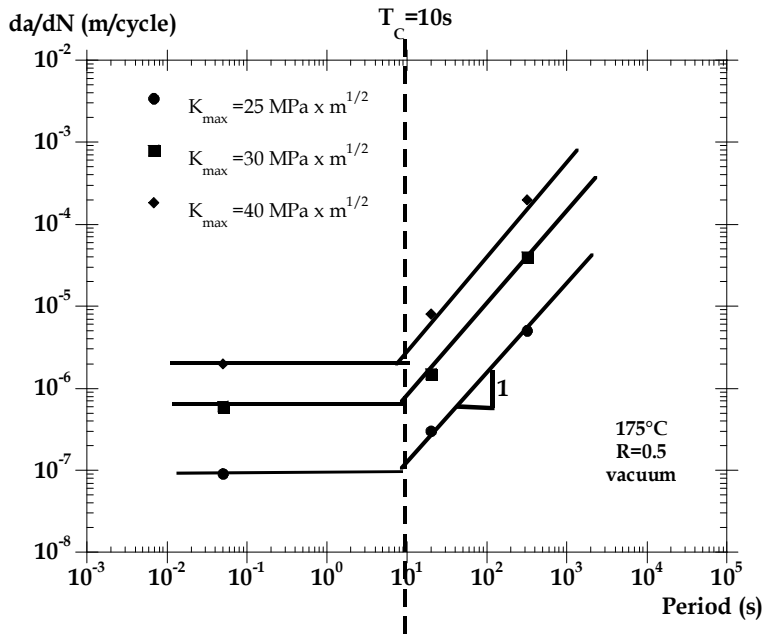

Fig. 18. CFCG rates as a function of the loading period for selected K_{max} values at 175°C in vacuum.

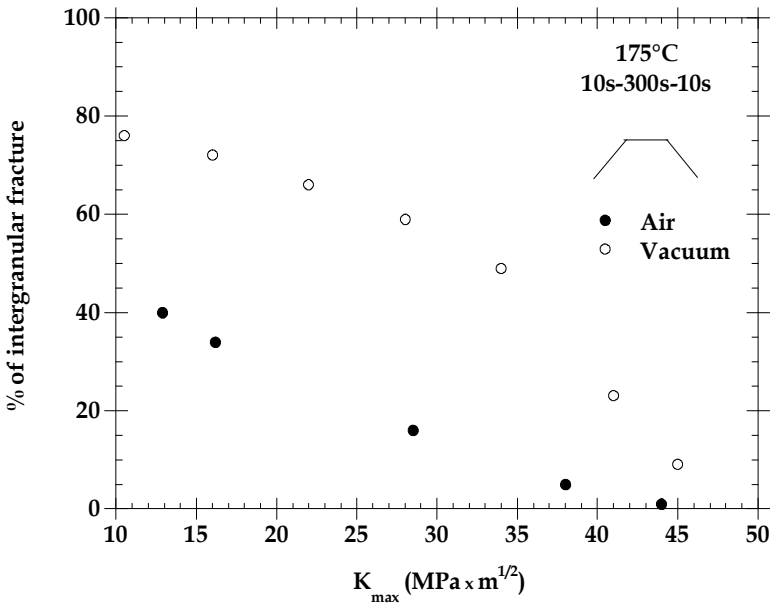

Fig. 19. Percentage of intergranular fracture mode during CFCG as a function of K_{max} in air and in vacuum at 175°C for a 10s-300s-10s trapezoidal signal.

total crack growth is lower in air than in inert environment for a fixed K_{max} value, which consistent with CFCG rates results. They furthermore suggests that interactions between creep, fatigue and environmental exposure reduce the contribution of cavitation-induced intergranular fracture (Hénaff et al., 2007).

4. Predictions of Creep-fatigue Crack Growth Rates

The predictions of CFCGRs may be carried out using a simple cumulative rule. The basic assumption in such a case is that, for a fixed K value, the cyclic damage and the creep damage, each characterised by a crack growth increment, can be linearly added. Thus the crack growth increment per cycle is estimated as follows:

$$\left(\frac{da}{dN}\right)_{CFCG} = \left(\frac{da}{dN}\right)_{FCG} + T \times \left(\frac{da}{dt}\right)_{CCG} \quad (1)$$

where:

- T is the load period;
- $\left(\frac{da}{dN}\right)_{CFCG}$ represents the total crack growth rate in a creep-fatigue cycle;
- $\left(\frac{da}{dN}\right)_{FCG}$ denotes the crack growth rate induced by cyclic loading (typically under triangular waveform loading at high frequency) and determined by the □K value:
- $\left(\frac{da}{dt}\right)_{CCG}$ is the crack growth contribution due to creep and derived from the CCG curve at the selected temperature using a value of K averaged over the cycle duration (for low frequency this average value is very close to K_{max}).

The comparison between predictions and experimental data indicates that such a cumulative rule can correctly predict CFGR in vacuum for the data available in most of the conditions investigated, namely in the 100°C-175°C and for Kmax values ranging between temperature range. An example of comparison is presented in Figure 20 a. However it should be noticed that the agreement observed at low ΔK is obtained by extrapolating the 4^{th} power law dependence towards this low value. This suggests that the first domain observed at low K values on CCG curves and dependent on initial loading conditions might not be relevant in the CFCG conditions examined here.

The same prediction procedure has been applied to the crack growth behaviour in air. An example is presented in Figure 20 b. It can be seen that at low K values the predictions underestimates CFCGRs and overestimates at high K values. The results at low K values could also be improved by extrapolating the 4^{th} power law to this regime. Anyway, the longer the hold-time, the larger the discrepancy between predictions and experimental results. An alternative procedure based on experimental observations is thus proposed in the following (Hénaff et al., 2008).

Figure 14 and Figure 18 clearly indicate that above a critical value of the load period T_c, CFCGRs are proportional to the load period, regardless of temperature and environment, suggesting that a Time-Dependent Crack Growth (TDCG) process takes place. In air however the results of cumulative damage rule predictions indicate that this TDCG process

might be different from the CCG process. On the basis of these observations, CFCG behaviour can be described using an empirical law accounting for cyclic and time-dependent damage and expressed as follows:

$$\left(\frac{da}{dN}\right)_{CFCG} = \left(\frac{da}{dN}\right)_{FCG} + (T - T_c) \times \left(\frac{da}{dt}\right)_{TDCG} \quad \text{for} \quad T > T_c \,,$$

where $\left(\frac{da}{dN}\right)_{FCG}$ and $\left(\frac{da}{dt}\right)_{TDCG}$ denotes the fatigue crack growth and the time-dependent crack growth (TDCG) rate, respectively. A power-law of the same form than that used for CCG has been identified for the TDCG regime during CFCG. The values of the coefficient and exponent are identified using the data from right-hand side of the diagrams presented in Figure 14 and Figure 18, and compared to those identified for CCG. The values of the parameters for CCG and TDCG are compared in Table 3.

Environment	Temperature	Critical period T_c (s)	Time-dependent crack growth	
Air	175°C	50	TDCG	$\frac{da}{dt} = 1 \times 10^{-12} \left(K_{\max}\right)^{3,1}$
			CCG	$\frac{da}{dt} = 1.2 \times 10^{-13} \left(K_{\max}\right)^{4}$
Air	130°C	320	TDCG	$\frac{da}{dt} = 9.6 \times 10^{-12} \left(K_{\max}\right)^{1.8}$
			CCG	$\frac{da}{dt} = 4.0 \times 10^{-15} \left(K_{\max}\right)^{4}$
Vacuum	175°C	10	TDCG	$\frac{da}{dt} = 9.6 \times 10^{-14} \left(K_{\max}\right)^{4.1}$
			CCG	$\frac{da}{dt} = 9.8 \times 10^{-14} \left(K_{\max}\right)^{4.1}$

Table 3. Critical values of loading period, time dependent crack growth law and creep crack growth law as a function of environment and temperature.

The corresponding curves are compared for air and vacuum at 175°C in Figure 21 and in air at 130°C and 175°C and Figure 22. It can be seen that, while TDCG in vacuum is extremely close to the CCG law at 175°C, TDCG in air is slower than CCG and the K dependence is weaker (n<4) than during CCG. This, in relation with the differences noticed in the fraction of intergranular facets (Figure 19) suggests that an interaction between fatigue damage, creep damage and environmental exposure takes place at the crack tip during propagation in air. This interaction would partly inhibit the cavitation process leading to intergranular fracture. The effect of this complex interaction is indeed beneficial at 175°C since TDCG is slower than CCG for a given K value, as shown in Figure 21, and therefore needs to be specifically determined. The situation at 130°C is perhaps more complex. The CCG curve in vacuum has not been determined at this temperature. However it can be considered that, as observed at 175°C, this curve is not basically modified by environment. Figure 22 indicates

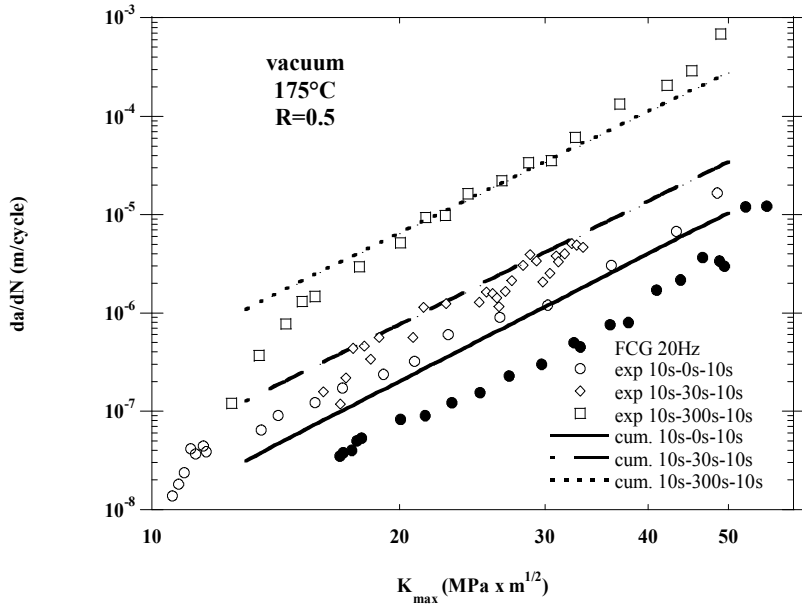

(a)

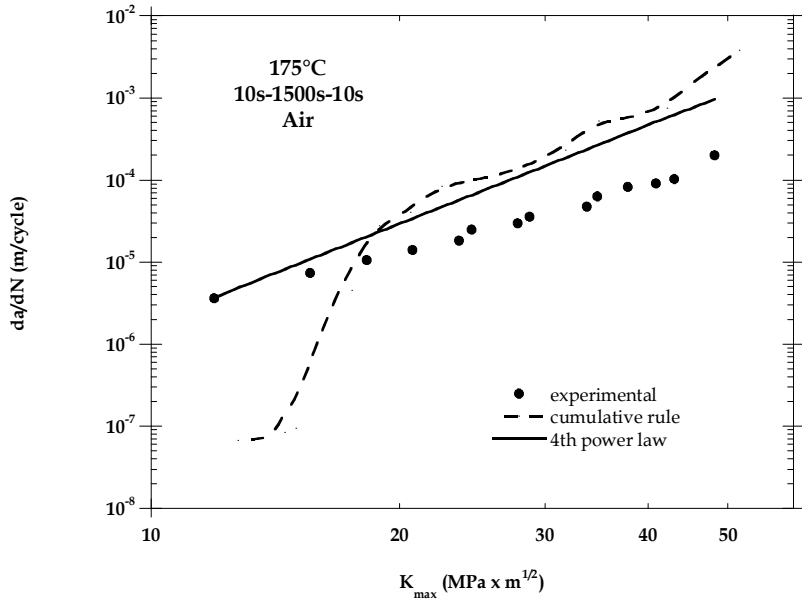

(b)

Fig. 20. Comparison of experimental results and cumulative rule predictions at 175°C (a) in vacuum (b) in air.

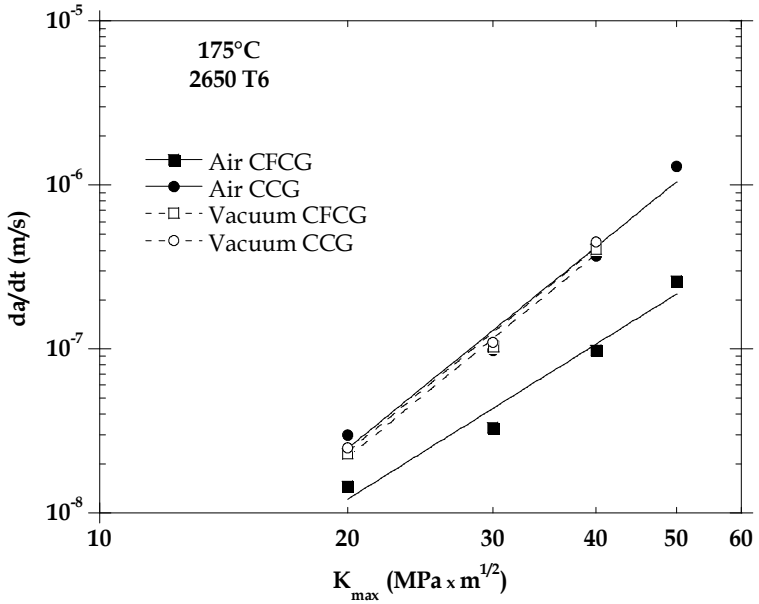

Fig. 21. TDCG and CCG behaviour of the 2650 T6 alloy in air and in vacuum at 175°C.

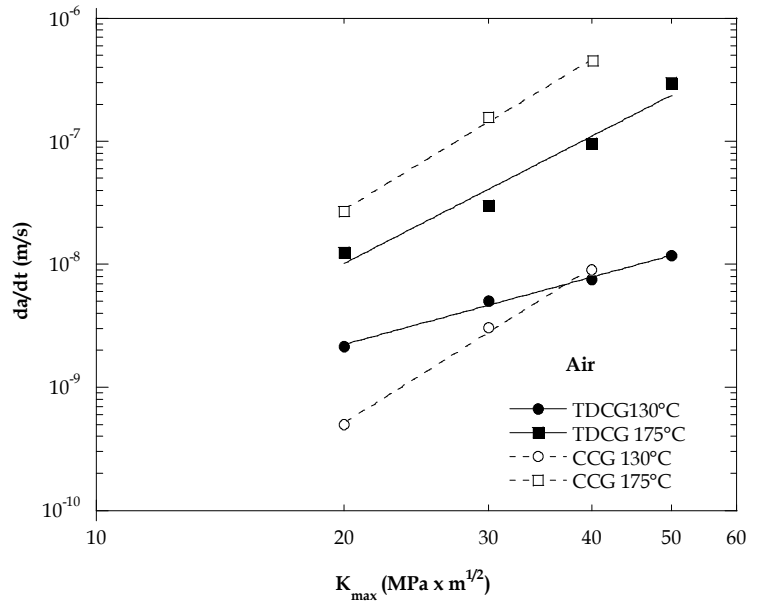

Fig. 22. TDCG and CCG behaviour in air at 130°C and 175°C.

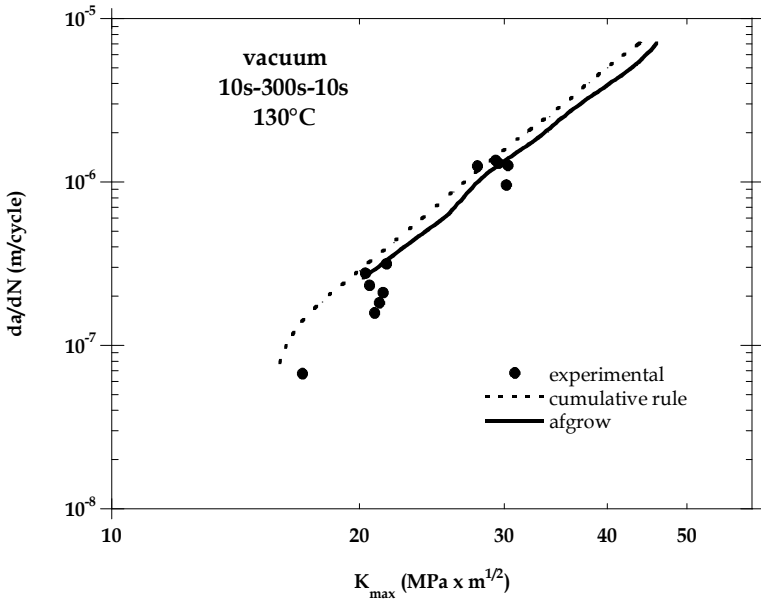

Fig. 23. Comparison of experimental data and predictions obtained using a cumulative damage rule and the time-dependent crack growth option of the AFGROW software for a 10s-300s-10s signal at 130°C in vacuum.

that the TDCG in air at low K_{max} values is actually more rapid than CCG. This may indicate that at this temperature environment may rather promote the creep damage under CFCG. However the mechanisms responsible for this type of behaviour need clarification.
Nevertheless the main interest of the approach proposed here is that the TDCG law could be identified for a fixed temperature at moderate values of frequency for selected values of stress intensity factor. This procedure would allow significant reductions in test duration and cost. In addition it can be easily implemented into software packages for crack growth predictions such as AFGROW (Harter, 2006). An example of calculation produced using the "time–dependent crack growth" option of AFGROW is compared in to experimental results and predictions obtained by the cumulative rule for a 10s-300s-10s trapezoidal signal in vacuum at 130°C. The CCG or the TDCG can be introduced in order to calculate crack growth life of more complex cracked structural elements. An assessment of the ability of this approach to account for the behaviour at extremely low but realistic frequency is however required. This point is under current investigation.

5. Summary and conclusions

In this chapter, the creep and creep-fatigue crack growth behaviour of a precipitation-hardened 2650 T6 aluminium alloy has been reviewed.
First, stable crack growth induced by creep has been characterised in the 100°C-175°C range. While temperature enhances creep crack growth rates in this range, this enhancement is particularly pronounced in the 130-160°C range and seems to saturate above 160°C. Creep crack growth is controlled by cavitation-induced intergranular fracture. Environment does not seem to affect CCG.

The fatigue crack growth behaviour at high frequency is almost unaffected by temperature in the range 25°C-175°C. However a deleterious influence of hold-time introduced at the maximum load and/or low frequency on crack growth rates under cyclic loading is observed in the 130°C-175°C temperature range in air and in vacuum. This effect is characterised by a significant contribution of intergranular fracture mode similar to that observed during creep crack growth under static loading. More precisely, above a critical value of loading period, crack growth rates are proportional to the loading period, regardless of the waveshape, indicating that a time–dependent crack growth process takes place. This time-dependent crack growth process seems to be affected by environment. Indeed in vacuum it corresponds with CCG, so that a cumulative rule of creep damage and fatigue damage provides realistic predictions. In air however the time-dependent crack growth process exhibits a K-dependence different from that observed during creep crack growth and dependent on temperature. As a consequence the cumulative rule using creep crack growth and fatigue crack growth data cannot account for the observed behaviour. An alternative procedure, based on a superposition model, is proposed to predict creep-fatigue crack growth rates at very low frequencies on the basis of results obtained at higher frequencies. This methodology could be used in standard crack growth life prediction methods but it has to be assessed by comparing predictions with experimental data obtained under very low frequency loadings. Finally this methodology could be extended to applications where aluminium alloys would be fatigued at elevated temperature and at low frequencies.

6. Acknowledgements

This work was carried out within the framework of the French National Programme on Supersonic Aircraft and the financial support by the French Ministry of Research is gratefully acknowledged.

7. References

Bensussan, P., Jablonski, D. A. and Pelloux, R. M. (1984). A study of creep crack growth in 2219-T851 aluminum alloy using a computerized testing system. *Metallurgical and Materials Transactions a Physical Metallurgy and Materials Science,* Vol. 15A, No. January: 107-120.

Bensussan, P., Maas, E., Pelloux, R. and Pineau, A. (1988). Creep crack initiation and propagation: fracture mechanics and local approach. *Journal of Pressure Vessel Technology,* Vol. 110, No. 1: 42-50.

Ewing, D. J. F. (1978). Strip yield models of creep crack incubation and growth. *International Journal of Fracture,* Vol. 14, No. 1: 101-117.

Harter, J. A. (2006). AFGROW USERS GUIDE AND TECHNICAL MANUAL (http://www.siresearch.info). WRIGHT-PATTERSON AIR FORCE BASE OH 45433-7542

Hénaff, G., Marchal, K. and Petit, J. (1995). On fatigue crack propagation enhancement by a gaseous atmosphere: Experimental and theoretical aspects. *Acta Metall Mater,* Vol. 43, No. 8: 2931-2942.

Hénaff, G., Menan, F. and Odemer, G. (2010). Influence of corrosion and creep on intergranular fatigue crack path in 2XXX aluminium alloys. *Engineering Fracture Mechanics,* Vol. 77, No. 11: 1975-1988.

Hénaff, G., Odemer, G., Koffi, E., Benoit, G. and Journet, B. (2008). Prediction of creep fatigue crack growth rates in inert and active environments in an aluminium alloy, *Proceedings of International Conference on Fatigue Damage in Structural Materials VII*, Hyannis, MA, USA.

Hénaff, G., Odemer, G. and Tonneau-Morel, A. (2007). Environmentally-assisted fatigue crack growth mechanisms in advanced materials for aerospace applications. *International Journal of Fatigue,* Vol. 29, No. 9-11: 1927-1940.

Jata, K. V., Maxwell, D. and Nicholas, T. (1994). Influence of Environment and Creep on Fatigue-Crack Growth in a High-Temperature Aluminum-Alloy-8009. *Journal of Engineering Materials and Technology-Transactions of the Asme,* Vol. 116, No. 1: 45-53.

Kaufman, J. C., Bogardus, K. O., Mauney, D. A. and Malcolm, R. C. (1976). Creep Cracking in 2219-T851 Plate at Elevated Temperatures. In: *Mechancis of Crack Growth, ASTM STP 590*, 149-168. American Society for Testing and Materials.

Leng, Y. (1995). Study of creep crack growth in 2618 and 8009 aluminium alloys. *Metallurgical and Materials Transactions a Physical Metallurgy and Materials Science,* Vol. 26A, No.: 315-328.

Majimel, J., Molenat, G., Casanove, M. J., Schuster, D., Denquin, A. and Lapasset, G. (2002). Investigation of the evolution of hardening precipitates during thermal exposure or creep of a 2650 aluminium alloy. *Scripta Materialia,* Vol. 46, No. 2: 113-119.

Majimel, J., Molenat, G., Danoix, F., Blavette, D., Lapasset, G. and Casanove, M. J. (2002). A study of the hardening precipitation in a 2650 aluminium alloy for aeronautics. *Aluminum Alloys 2002: Their Physical and Mechanical Properties Pts 1-3,* Vol. 396-4, No.: 1025-1030.

Menan, F. and Hénaff, G. (2009). Influence of frequency and exposure to a saline solution on the corrosion fatigue crack growth behavior of the aluminum alloy 2024. *International Journal of Fatigue, Fatigue Damage of Structural Materials VII,* Vol. 31, No. 11-12: 1684-1695.

Menan, F. and Hénaff, G. (2009). Influence of frequency and waveform on corrosion fatigue crack propagation in the 2024-T351 aluminium alloy in the S-L orientation. *Materials Science and Engineering: A,* Vol. 519, No. 1-2: 70-76.

Odemer, G. (2005). Tolérance au dommage avec prise en compte des interactions fatigue-fluage de l'alliage 2650-T6. PhD Thesis, *ENSMA*, Poitiers: 283

Odemer, G., Hénaff, G. and Journet, B. (2006). Creep crack growth resistance of an age hardened aluminium alloy for supersonic applications. *Scripta Materialia,* Vol. 54, No. 1: 51-55.

Odemer, G., Hénaff, G., Journet, B. and Rémy, L. (2006). Creep-fatigue interactions during crack growth in a 2650 T6 aluminium alloy, *Proceedings of Fatigue'2006, 9th International Congress on Fatigue*, Atlanta, Georgia, USA, Elsevier.

Riedel, H. (1977). A Dugdale model for crack opening and crack growth under creep conditions. *Materials Science and Engineering,* Vol. 30, No. 3: 187-196.

Sadananda, K. (1978). A Theoretical Model for Creep Crack-Growth. *Metallurgical Transactions a-Physical Metallurgy and Materials Science,* Vol. 9, No. may: 635-641.

Vitek, V. (1977). A theory of the initiation of creep crack growth. *International Journal of Fracture (Historical Archive),* Vol. 13, No. 1: 39-50.

Vitek, V. (1978). A theory of diffusion controlled intergranular creep crack growth. *Acta Metallurgica,* Vol. 26, No. 9: 1345-1356.

Part 4

Microstructure Phenomena

14

New Approaches to Reaction Kinetics during Molten Aluminium Refining Using Electron Backscatter Diffraction (EBSD)

Alfredo Flores and Jesús Torres
Centro de Investigación y de Estudios Avanzados del IPN, Unidad Saltillo
México

1. Introduction

The use of aluminium scrap to produce different alloys has increased considerably at the start of the current century because of the low amount of energy required for its melting, in comparison to the energy required to produce aluminium from bauxite. However, contamination problems can arise if the different kinds of scrap with several chemical compositions are not separated using appropriate methods. In this way, contamination with elements such as Fe, Sb, Mg, Na, K, Pb, and Sn is quite common, so melt treatment practices have been recommended. Of these contaminants, antimony is considered to be among the most harmful because of its high potential toxicity, which is of special concern for products intended for handling of food and drink. Also, modification with sodium and/or strontium is not effective because of the formation of intermetallic compounds that remove these elements from solution, preventing any effect of this modification on the eutectic silicon phase.

The negative effects of antimony on the rate of modification of the silicon eutectic with sodium and/or strontium in casting Al-Si alloys have been broadly studied by (Wang & Gruzleski, 1990), (Wang & Gruzleski, 1992), (Garant et al., 1992), and (Tuttle et al., 1991). The general problem in mixing antimony with sodium and/or strontium is the formation of high melting temperature compounds that are difficult to remove. Moreover, it is possible to generate phases with harmful morphologies that affect the mechanical properties of this type of alloy. These compounds eliminate sodium and/or strontium from the solution, preventing the effect of sodium/strontium modification on the silicon eutectic phase. On the other hand, antimony has been shown to possess a great chemical affinity for calcium, forming stable compounds that can be removed through dross. However, to study the mechanism of reaction, it is first necessary to define the stoichiometry of the reaction. Different techniques have been proposed to hinder the effects of antimony, including dilution with pure aluminium, separation of polluted scrap, addition of an excess of the modifier agent, or removal by means of chemical agents, as described by (Castrejón, 1995). However, no effective method has yet been developed at the cast shop facility level. Antimony, among other elements, possesses great affinity for calcium, as demonstrated long ago by (Hardy, 1941), who established that Ca_3Sb_2 or AlSb phases could form when these elements are present in molten aluminium. Nevertheless, the mechanism of reaction outside of molten aluminium scrap has not been determined.

Another important application of aluminium scrap from cans is the production of automotive alloys such as AA380, AA319 and AA356. However, these alloys specify no more than 0.10 wt.% Mg to avoid the harmful effects of Mg on mechanical properties, as shown by (Caseres, 1999). Various techniques have been developed to remove Mg from molten aluminium, such as methods based on gaseous mixtures of Ar/Cl_2 or Ar/SF_6. Other techniques are based on the optimisation of solid reactive groups like Na_2SiF_6, AlF_3, $KAlF_4$ or SiO_2. Previous studies performed by (Martinez, 19998) on the removal of Mg from Al-Si-Cu alloys established that it is possible to remove Mg from 700 °C to 800 °C by injecting submerged SiO_2 powder. This author claims that Mg removal takes place through the formation of a complex $MgAl_2O_4$ compound. On the other hand, (Escobedo et al., 2003) studied the removal of Mg from molten aluminium by injecting submerged powders of SiO_2 particles with an irregular morphology, determining the reaction rate and the values of some kinetic parameters of technological interest. For some initial conditions, it was possible to remove almost 100% of the Mg in time periods on the order of 70 min. The reaction was found to stop once the formation of a complex layer of reaction products covered the SiO_2 particles. These authors suggested that the predominant reaction is transitory, indicating that contact time between the molten phase and the solid particles is quite rapid, occurring in fractions of a second. Therefore, the main disadvantage of this process is the entrapment of solid particles in the solidified alloy, called inclusions, as well as the excessive formation of slag rich in $MgAl_2O_4$ and agglomerates of Al_2O_3-SiO_2 particles.

To better understand the reactions involved in the injection of submerged powders of SiO_2 for Mg removal from molten aluminium, it is necessary to mention the elaboration of mullite refractories and metal-matrix composites. Al-Mg fibers surrounded by Al_2O_3 SiO_2 are taken as the products of the reaction of MgO and $MgAl_2O_4$. (Ghosh et al., 2003) studied the production of $MgAl_2O_4$ by direct reaction between MgO and Al_2O_3 at 1400 ^oC, represented by the next equation:

$$MgO(s) + Al_2O_3(s) = MgAl_2O_4(s) \quad (1)$$

$$\Delta G°_{973K} = -7{,}69 \text{ kcal/mol}$$

(Zhong et al., 1995) performed an extensive bibliographical investigation on interfacial reactions occurring during the production of aluminium-Al_2O_3 fibers lined with SiO_2 composites, with several initial Mg concentrations. They analysed experiments performed by other authors, who found that $MgAl_2O_4$ formed at the Al_2O_3 fiber interface contained an Al alloy with 4 wt. % Mg, at 800 ^oC. (Fishkis, 1991) also confirmed the formation of $MgAl_2O_4$ at the interface of Al_2O_3 fibers lined with SiO_2, embedded in an aluminium alloy containing 3 wt. % Mg. However, in similar experiments performed by (Pai & Ray, 1976) they found MgO as the main reaction product, although the alloys tested contained more than 4 wt.% Mg. The proposed reaction is:

$$3Mg_{(Al)} + Al_2O_3(s) = 3MgO(s) + 2Al(l) \quad (2)$$

$$\Delta G°_{973K} = -28{,}63 \text{ kcal/mol}$$

(Pfeifer et al., 1990) found similar results to those reported by Pai et al. They accept the formation of MgO via the reaction given by equation (2), indicating that MgO could also be formed by direct reaction between dissolved Mg and O_2 from the atmosphere, according to:

$$2Mg_{(Al)} + O_2 = 2MgO(s) \quad (3)$$

$$\Delta G°_{973K} = -237{,}38 \text{ kcal/mol}$$

Note the high Gibbs free energy of this reaction. However, O_2 is not soluble in molten aluminium, limiting the extent of such a reaction, as was established by (Campbell, 2003). (Lloyd et al., 1994) found that for Mg concentrations less than 3 wt. %, the following reaction takes place:

$$Mg_{(Al)} + 4/3Al_2O_3(s) = MgAl_2O_4(s) + 2/3 \text{ Al (l)} \quad (4)$$

$$\Delta G°_{973K} = -19{,}17 \text{ kcal/mol}$$

The reaction between the SiO_2 of the lining material and Mg is given by:

$$SiO_2(s) + 2Mg_{(Al)} = 2MgO(s) + Si_{(Al)} \quad (5)$$

$$\Delta G°_{973K} = -61{,}71 \text{ kcal/mol}$$

(Hallstedt et al., 1990) established the rate of diffusion of the Al^{+3} and Mg^{+2} cations through MgO and $MgAl_2O_4$, determining that diffusion through $MgAl_2O_4$ is up to ten orders of magnitude faster than through MgO. Moreover, they found that the interfacial reactions between dissolved Mg and SiO_2 stopped as the concentration of Mg increased, becoming negligible at Mg concentrations above 7 wt. %. (Molins et al., 1991) characterised the interface between Al_2O_3 fibers lined with SiO_2 and an alloy containing 3 wt. % Mg. They found not only MgO, but also $MgAl_2O_4$, formed through the following chemical reaction:

$$Mg_{(Al)} + 2Al(l) + 2SiO_2(s) = MgAl_2O_4(s) + 2Si_{(Al)} \quad (6)$$

$$\Delta G°_{973K} = -98{,}01 \text{ kcal/ mol}$$

After ageing the alloy at 500 °C for 6 h, dissolved Mg reacted with the SiO_2 of the Al_2O_3 fiber lining. Using transmission electron microscopy, these authors identified Al_2O_3, MgO and $MgAl_2O_4$ phases. Their results indicate that the chemical reactions in the solid state are slow enough to permit identification of the several oxides being formed. The results about the effect of initial Mg concentration on the nature of reaction products during the production of Al-Al_2O_3 composites have been corroborated by (McLeod & Gabryel, 1992), establishing that for a Mg concentration less than 3 wt. %, the main reaction product will be $MgAl_2O_4$. They constructed an equilibrium diagram representing different situations similar to the one shown in Figure 1, and the utility of this diagram will be discussed later.

2. Kinetic considerations for studying reaction mechanisms

The thermodynamics of molten aluminium solutions for refining purposes have been studied for many years. Most of the important systems behave as ideal solutions at temperatures above 973 K, so chemical refining methods can be used to remove elements such as Ca, K, Mg, Na, and Sr, as shown in the works of (DiRusso, 1960), (Gruzleski & Closset, 1990), (Gariepy & Dube, 1984), and (Moore, 1990). On the other hand, alloying can be performed taking advantage of the aluminothermic reduction of oxides such as CuO, MnO_2, FeO, and SiO_2. Nowadays, software can be used to determine parameters such as the

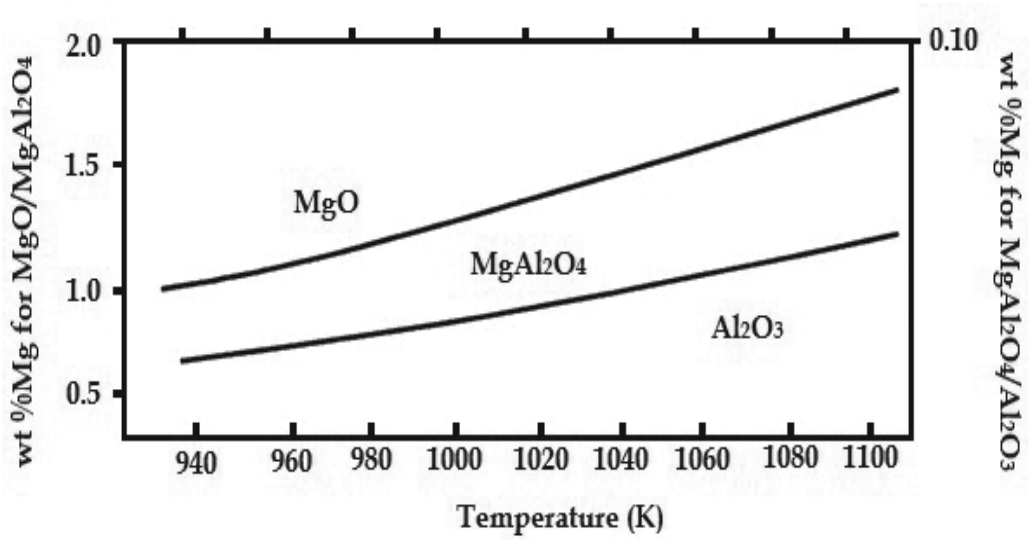

Fig. 1. Thermodynamic stability diagram of the oxides in molten Al-Mg alloys, (Mcleod & Gabryel, 1992).

Gibbs free energy of reaction, chemical potential values, and activity coefficients, helping to understand how a system will behave in a given set of conditions such as temperature, pressure, and initial chemical composition. Special software has even been developed for multicomponent systems, such as the programs used by (Kattner, 1997) and Gröbner et al., 2002). Therefore, the utility of thermodynamic software is its ability to determine the Gibbs free energy of reaction of, for example, the aluminothermic reactions given by equations (1) through (6). Also, the following chemical reaction from the work of (Moreno, 2005) can be considered:

$$2Sb_{(Al)} + 3Ca(s) = Ca_3Sb_2(s) \quad (7)$$

$$\Delta G°_{973K} = -157.28 \text{ kcal}$$

The formation of intermetallic phases once the reduced element dissolves first in the molten solution has been shown to lower the activity coefficient of Sb, thus increasing the negative value of the Gibbs free energy of reaction, as shown by (Rajagopalan et al., 1999). It must also be considered that the use of a flux to remove the chemical compounds formed as slag can increase their activity coefficients, therefore augmenting the negative value of the Gibbs free energy.

Using mechanically added powders and agitation, studies by (Langlais, 1991), (Muñis et al., 2008), (López, 2006), and (Ayala, 2010) have demonstrated the ability of aluminothermic reactions to produce Al-Sr and Al-Zr alloys with different chemical compositions. The molten aluminium solutions in these experiments contained above 1 wt.% Mg, as this amount was observed to increase bath reactivity. This effect has been well-documented by (Langlais, 1991), as Mg lowers the superficial tension of aluminium and also possesses a greater chemical affinity for any element other than aluminium. These investigations reveal that the diffusion of magnesium from the bulk to the boundary layer is the kinetic controlling step, so the reactions kinetics are determined by parameters including the initial

Mg concentration in the melt, temperature, powder size, particle residence time, and agitation speed.

Aluminothermic reduction reactions are analysed based on the following experimental observations described by (Levenspiel, 2002) and (Rosenquist, 1987):

a. The kinetics of heterogeneous chemical reactions are governed by one or more of the following kinetic steps:

1. Transport of the reactive species from the bulk to the boundary layer.
2. Chemical reaction at the interfaces between reactive molten metal particles.
3. Formation of reaction products.
4. Mass transfer through the layers of reaction products to the bulk.

b. Two different types of chemical reactions can occur during metallurgical refining processes: molten metal-gas and molten metal-solid reactions. Molten metal-solid reactions can occur during mechanical powder addition and agitation, and can consist of two different reactions:

1. Permanent contact reaction, which occurs at the interface of the reaction between the slag and the molten metal.
2. Transitory reaction, which occurs inside the molten metal between the particles discharged by the plume carrier gas-reactive powder and the molten metal.

The study of the interactions occurring between the reactive powders and the molten bath is quite complex. Nevertheless, some reaction zones have been determined, which are shown in Figure 1. The description of these zones comes from the work of (Macias & Flores, 1999).

- Jet zone, just at the exit of the injection lance.
- Bubbling zone, composed of the injected powder particles and the carrier gas bubbles merging from the lance.
- Broke-up zone, where the carrier gas bubbles reach the slag and pass into the atmosphere.
- Slag zone.
- Dispersion zone, where the carrier gas bubbles and slag particles are dispersed.
- Intermediate zone, where the fluid becomes stagnant.

For the chemical refining reactions that will be described in this work, the kinetic model that best fits the experimental results is termed the "decreasing nucleus model", which is also useful for determining the mechanisms of the reactions taking place. The following heterogeneous chemical reactions are likely to occur between molten metal and the injected SiO_2 particles:

$$aA(\text{fluid}) + bB(\text{solid}) = \text{fluid products}$$

$$aA(\text{fluid}) + bB(\text{solid}) = \text{solid products} \quad (8)$$

$$aA(\text{fluid}) + bB(\text{solid}) = \text{solid and fluid products}$$

When the reactive particles contain a significant amount of impurities, or if the reaction product is rigid enough, particles sizes do not decrease during reaction, yielding the name of this kinetic process. In this process, the chemical reaction is carried out first at the particle-molten metal interface, instantly forming a reaction product layer. Then, the reaction zone moves inside the particle, until reaching complete conversion. Because of the differences in atomic size between the participant chemical species, this reaction results in a significant amount of porosity, ensuring diffusion in both directions for the reduced and oxidised

species. Therefore, the complete chemical reaction occurs in the 4 different stages described above. These stages occur in series, so the slowest one governs the global reaction rate. In this way, 3 different reaction mechanisms could take place, as depicted numerically in Table I, which indicates the corresponding equations of conversion time versus particle radius and chemical composition at the boundary layer.

In this Table, τ is the value of total conversion time, t is actual time, r_c is the actual radius of the particle, R is the initial radius of the particle, and X_B is the mole fraction of the diffusive species B. Generally speaking, because of the high temperature at which most pyrometallurgical refining processes of molten metals are performed, the reaction rate at the liquid-solid interface is high and does not constitute a limiting step. Thus, the velocity at which chemical species diffuse through the layers of reaction products constitutes the rate-determining step. Each of the kinetic mechanisms described in Table I result in specific susceptibilities to the process variables such as temperature, powder size, stirring speed, initial chemical composition of the melt, residence time of the reactive particles inside the melt, etc., so a statistical analysis must be performed to determine the reaction mechanisms governing the reaction rate.

Even when refining is performed in a controlled atmosphere, it is not possible to avoid the dissolution in the melt of small amounts of nitrogen or oxygen. Therefore, some undesired chemical compounds can form mainly complex aluminates or nitrides, affecting the efficiency of the reaction.

Stage	t/τ ratio versus particle size and chemical composition
Diffusion from the bulk to the boundary layer	$\frac{t}{\tau} = 1 - \left(\frac{r_c}{R}\right)^3$
Diffusion through the layer of reaction products	$\frac{t}{\tau} = 1 - 3\left(\frac{r_c}{R}\right)^2 + 2\left(\frac{r_c}{R}\right)^3$
Chemical reaction at the interface	$\frac{t}{\tau} = 1 - \frac{r_c}{R} = 1 - (1 - X_B)^{1/3}$

Table I. Controlling stages for the decreasing nucleus model, and the equations indicating equivalent complete reaction time.

The kinetics of heterogeneous chemical reactions has been studied for more than 100 years. However, advanced analytical tools such as electron back scatter diffraction (EBSD) in scanning electron microscopes have only recently permitted a proper assessment of the stoichiometry of the chemical reactions taking place. It is worth mentioning that before EBSD analysis existed, electron diffraction in the transmission electron microscope (TEM) was the most accurate technique to determine the crystallographic structure of unknown phases in a sample. Therefore, phase identification by EBSD is complementary to TEM analysis. Nevertheless, it is important to mention the differences between phase identification and phase verification, as several definitions could exist. The main difference between these terms is the number of candidate phases that must be analysed to determine the right phase. In the case of phase verification, the operator knows quite well the phases that are present in the sample, usually analysing less than 5 possible phases. In phase identification, the right phase is sought from a database of crystallographic compounds with no operator assistance.

EBSD patterns contain a great amount of information on the crystalline structure of the sample, which can allow for the determination of the spatial group of a certain phase, such as the symmetry elements contained in the pattern. Therefore, the EBSD diffraction pattern is a fundamental vehicle for determining the phases present in a sample and for a deep analysis of reaction kinetics as described in the works of (Schwartz et al., 2009) and (Randle & Engler, 2000).

3. Electron backscatter diffraction in the scanning electron microscope.

When an electron beam hits a metallic sample in the scanning electron microscope, several dispersion and interaction phenomena occur, producing various signals as shown in Figure 2. Backscattered electrons are used to form an image, for chemical analysis, or for crystallographic analysis of the volume studied. Crystallographic analysis is performed by evaluating the diffraction pattern, which is generated when the primary electrons are diffracted by the lattice planes of the crystals. To obtain the best signal conditions for the EBSD analysis, the surface of the sample must form a small angle 2Θ with the electron beam. Figure 3 also shows the classic diffraction analysis from the lattice planes, as described in the work of (Randle and Engler, 2000). Moreover, it shows that the Θ angles for which diffraction occurs depend on the wavelength (λ) and the interplanar space of the dispersant phase, d.

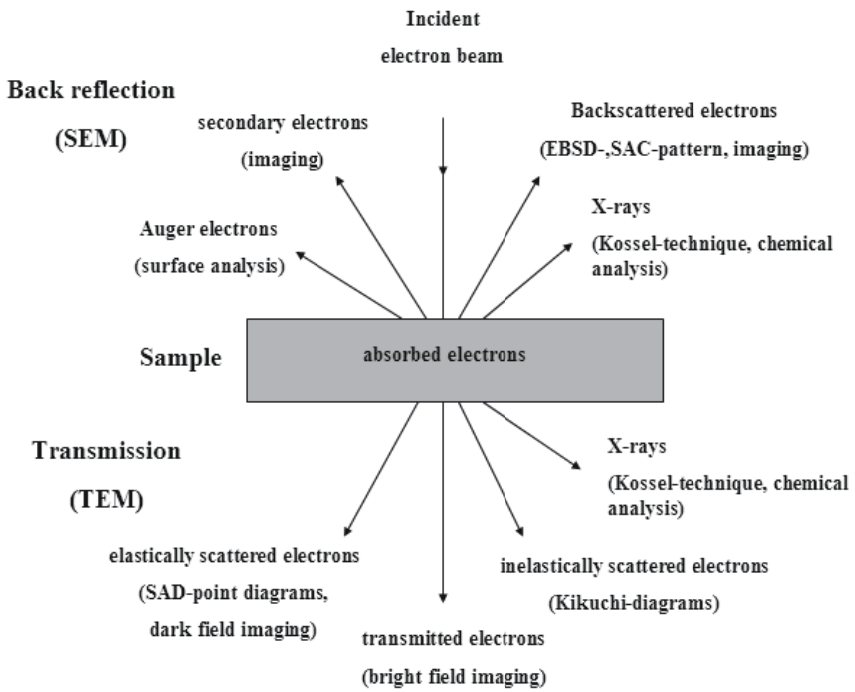

Fig. 2. Summary of the different signals generated due to the interaction of electrons with matter in a scanning electron microscope, as described in the work of (Randle & Engler, 2000).

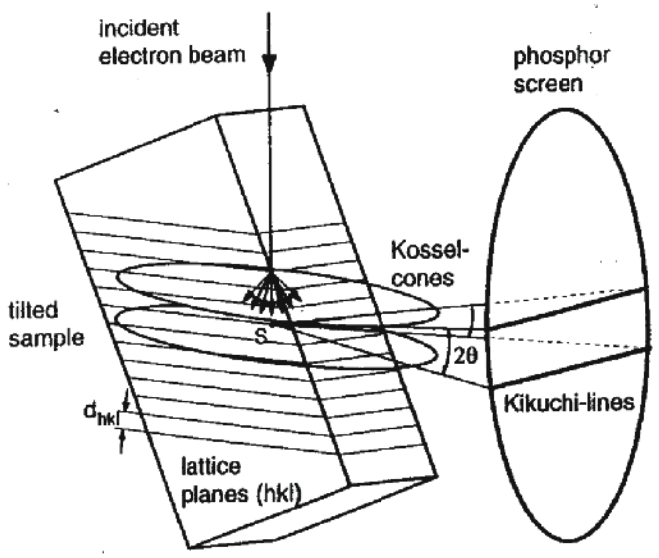

Fig. 3. Origin of Kikuchi lines from the perspective of EBSD, as described in the work of (Randle & Engler, 2000).

Because electron diffraction through the Bragg Θ angle occurs in all directions, the diffracted beam is in the form of the surface of a cone, extending approximately from the normal plane to the reflecting atomic planes with a medium apical angle of 90-Θ_B. In fact, considering that the source of electron dispersion lies between the lattice planes as shown in Figure 3, two cones of radiation are formed from each family of planes. Substituting the typical values of λ and the interplanar space of the lattice d into the Bragg equation, a Q of 0.5º is obtained. Therefore, the apical angle of a diffraction cone is approximately 180º, indicating that the cones are almost planar. When a phosphor screen of the camera in the EBSD analysis system is positioned such that it collects the diffraction cones, a pair of parallel conical sections are formed as a result, called Kikuchi lines. The sections are spaces at an angular $2\Theta_B$ distance, proportional to the interplanar spacing.

Having obtained a good EBSD pattern from a metallic sample, the next step is to determine the punctual chemical composition of a particle of interest. This is done in the scanning electron microscope using either energy dispersive spectroscopy (EDS) or wavelength dispersive spectroscopy (WDS) analysis, and is important to enable a search of the crystallographic phase databases. Then, the pairs of Kikuchi lines are identified using the Hough transformation to obtain points in a Hough space that can be located automatically. Moreover, the width of the lines can also be calculated. The width of a pair of Kikuchi lines is inversely proportional to the interplanar spacing of the atomic planes, and together the lines form a reduced volume of the unit cell. More than one volume element can be generated if more than three Kikuchi bands can be located. The unique property of the volume elements calculated in this way, starting from the EBSD pattern, is that when each volume element is multiplied by an enter, it reproduces the reduced volume of the lattice. Once the number of volume elements have been calculated, it is relatively simple to find the highest common multiple for the smaller volume elements. Then, it is necessary to search the available crystallographic charts. One of the most important crystallographic databases

is that of the (International Crystallographic Diffraction Data, 2009), containing more than 100,000 different inorganic compounds.

Before describing the experimental evidence studied in this work, it is worth mentioning that the work in itself deals with the reaction kinetics of molten aluminium refining using EBSD to identify and therefore propose the numerical reaction rates governing Mg and Sb removal by SiO_2 and Ca, respectively. Extensive work has been conducted to measure the reaction rates of thousands of chemical reactions, so the fundamentals of such reactions are well established and are reported in several classical books such as those by (Levenspiel, 2002), (Rosenquist, 1987), (Szekely et al., 1971), and (Poirier & Geiger, 1994). On the other hand, different analytical techniques continuously emerge, permitting a study of the phenomena occurring in deep molten metals. EBSD in an SEM has been useful not only for measuring reaction rates and determining the values of kinetic parameters, but also in determining the mechanism of reaction.

4. Reaction kinetics of important aluminium systems; experimental part

This part of the chapter will present the methodology used to assess the stoichiometry of the reaction occurring during the refining of Mg or Sb from molten aluminium by mechanically added powders and agitation of SiO_2 and Ca, respectively, using EBSD in an SEM as analytical techniques. To obtain samples for microscopic analysis, several experiments were conducted using an electrical resistance furnace with automatic temperature control as a melting unit, which contained a silicon carbide crucible and had a 4-kg molten aluminium capacity. A controlled velocity stirring device was coupled to the furnace to maintain SiO_2 or Ca particles inside the melt. An average of 2.5 kg of molten alloy was used with the following initial chemical composition in weight percent: 9.50 Si, 0.18 Fe, 3.50 Cu, 0.03 Mn, 1.18 Mg, 0.30 Zn, and 0.08 Ti. Once the alloy melted and the temperature of interest was reached, i.e., 750 °C, the stoichiometric amount of SiO_2 or Ca was added to the center of the vortex formed by the impeller of the agitation system. In the case of Sb removal by Ca, the initial chemical composition of the alloy was adjusted to 0.5 wt. % Sb. The morphology of the added particles was irregular spherical, with a variable diameter between 0.15 and 0.22 mm. Agitation velocity was fixed at 120 r.p.m., which was kept constant during each experiment. The quantities of reactants were calculated according to the stoichiometry of reactions given by equations (6) and (7) and the amount of molten alloy. Reaction temperatures of 700, 725, 750 and 775 ^{o}C were studied, with stirring maintained for 60 min. Samples from the melt were taken every minute during the first 10 min, and every 5 min thereafter. The solidified samples were chemically analysed using plasma emission spectroscopy to determine the Mg or Sb concentrations as a function of sampling time at constant temperature. Part of each sample was metallographically prepared for observation in the SEM using a complementary combination of micropuntual structural analysis techniques such as EDS and EBSD. EBSD analysis requires a sample surface in very good condition to obtain Kikuchi lines with a suitable resolution. To obtain suitable samples, a vibratory polishing machine was used at 7200 Hz without vertical movement. Then, the samples were polished for 2 hours with nylon clothing discs impregnated with a solution of diamond paste in distilled water, with 1 μm diamond particle sizes. Then, a third polishing step was applied for 2 hours using diamond paste with a 0.25 μm particle size. Final polishing was performed using macrocloth discs mounted over a static plate using colloidal silica as an abrasive at pH 9.8. This technique was very useful for the identification of

reaction products formed by the chemical reactions taking place and their main structural characteristics. Also, the width of the layers of reaction products was measured, and those values were used in the following analysis of the reaction kinetics. In these cases, confidence levels of EBSD analysis of 0.7 were chosen to ensure excellent identification.

4.1 Kinetics of antimony removal from molten aluminium by Ca addition

First, after the addition of calcium the antimony-containing aluminium alloy, a removal reaction occurs over time, as seen in Figure 4. As much as 85.2% of antimony was removed after 40 minutes of reaction. The morphology and size of antimony and calcium-rich particles are shown in the SEM micrograph of Figure 5, together with the corresponding EDS patterns.

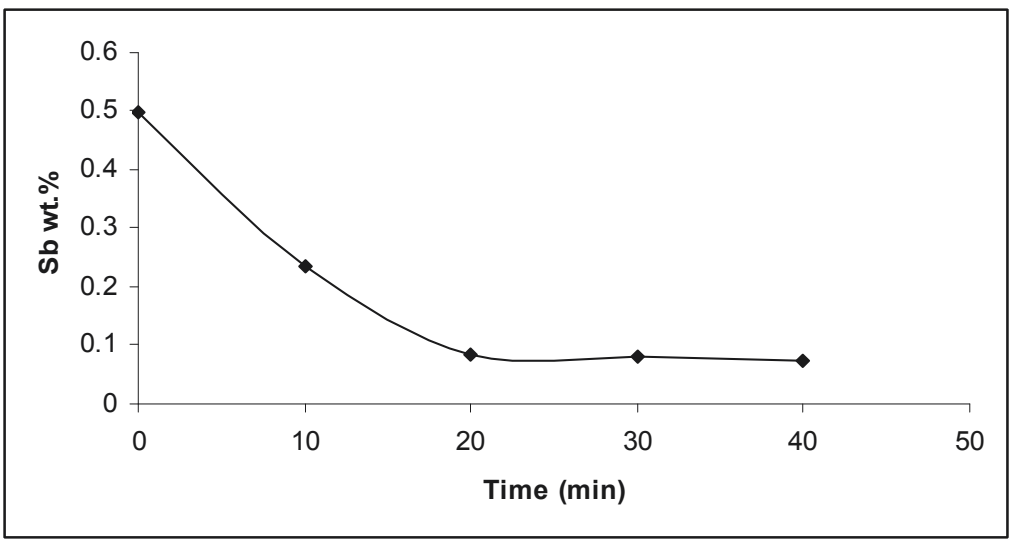

Fig. 4. Rate of antimony removal from molten aluminium after calcium addition, at 750 °C.

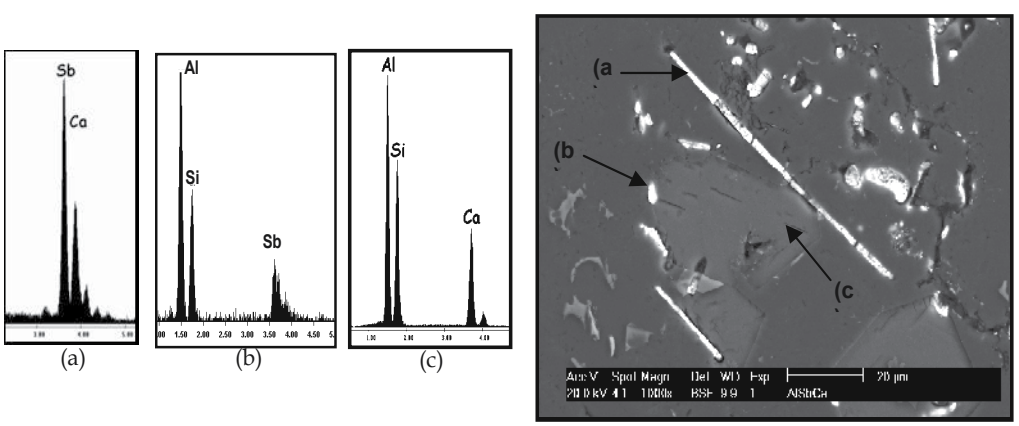

Fig. 5. EDS patterns of; a), Sb-Ca; b), Al-Si-Sb; and c), Al-Si-Ca rich particles, and SEM micrograph of the analyzed area.

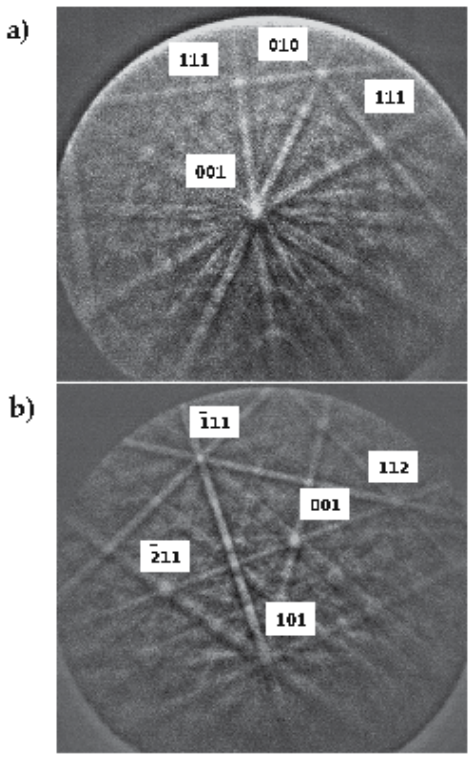

Fig. 6. EBSD patterns and their corresponding indexing for the (a), Ca_2Sb; and (b), AlSb phases.

However, when EBSD was used, the Ca_2Sb, and AlSb phases were identified, as shown in Figure 6. These results indicate that the antimony removal reaction is as follows:

$$Sb(Al) + 2Ca = Ca_2Sb(s) + Al \quad (9)$$

The SEM micrograph shown in Figure 7 demonstrates that the Ca_2Sb phase is of pre-dendritic nature, i.e., the particles are formed while the molten alloy is still at high temperature. Upon solidification, these particles grow over the aluminium grain boundaries, acquiring a needle-like morphology, reaching a maximum length of 50 μm. Although very small particles on the order of 5 μm were also observed, because of their density (3.72 g/ml) is higher than that of aluminium, the particles will tend to settle down in the molten metal. On the other hand, a close relationship has been observed between particles of Ca_2Sb and those containing Al, Ca, and Si, although it was not possible to determine the crystallographic characteristics of those particles by EBSD. Apart from the lack of availability of cards containing the crystallographic characteristics of ternary Al-Ca-Sb phases, no Al-Ca-Sb or Al-Si-Sb equilibrium diagrams are available.

Kinetics of the removal of magnesium from molten aluminium by the addition of SiO_2

Figure 8 shows a partially reacted SiO_2 particle that has been immersed in molten aluminium for 1 minute at 750 ^{o}C. The central part of this micrograph shows the corresponding EDS pattern. The EBSD patterns shown in the upper part of this micrograph are characteristic of the SiO_2 and $MgAl_2O_4$ phases.

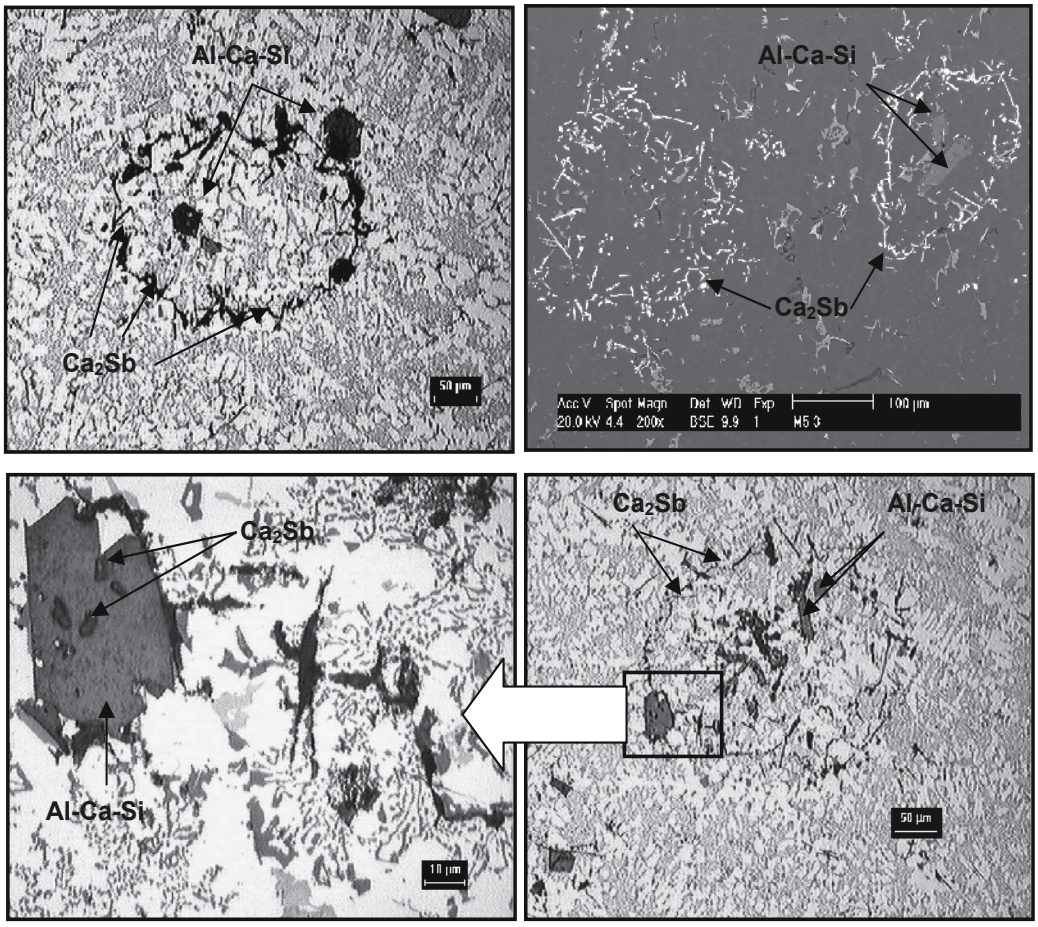

Fig. 7. Microstructural features of AlCaSi and CaSb particles after calcium addition to AlSb alloys.

A line scan analysis was performed in the SEM to obtain information about the distribution of elements at the interface solid (SiO_2)-melt phase, as well as over the layers of reaction products. At least 10 particles per sample were measured for this analysis. Figure 9 shows typical results for a particle analysed after it was immersed for 1 minute in molten aluminium at 750 ^oC. Similar analyses were performed for particles immersed for longer periods of time.

These results indicate that the SiO_2 reduction reactions occurring during Mg refining of molten aluminium leading to $MgAl_2O_4$ formation occur immediately once the particles come into contact with molten aluminium. Therefore, we conclude that the formation of $MgAl_2O_4$ occurs faster than the other phases because no evidence was found of the formation of MgO or Al_2O_3, as demonstrated by the Gibbs free energy:

$$2Al(l) + 3/2SiO_2(s) = Al_2O_3(s) + 3/2Si_{(Al)} \quad (10)$$

$$\Delta G°_{973K} = -63{,}86 \text{ kcal/ mol}$$

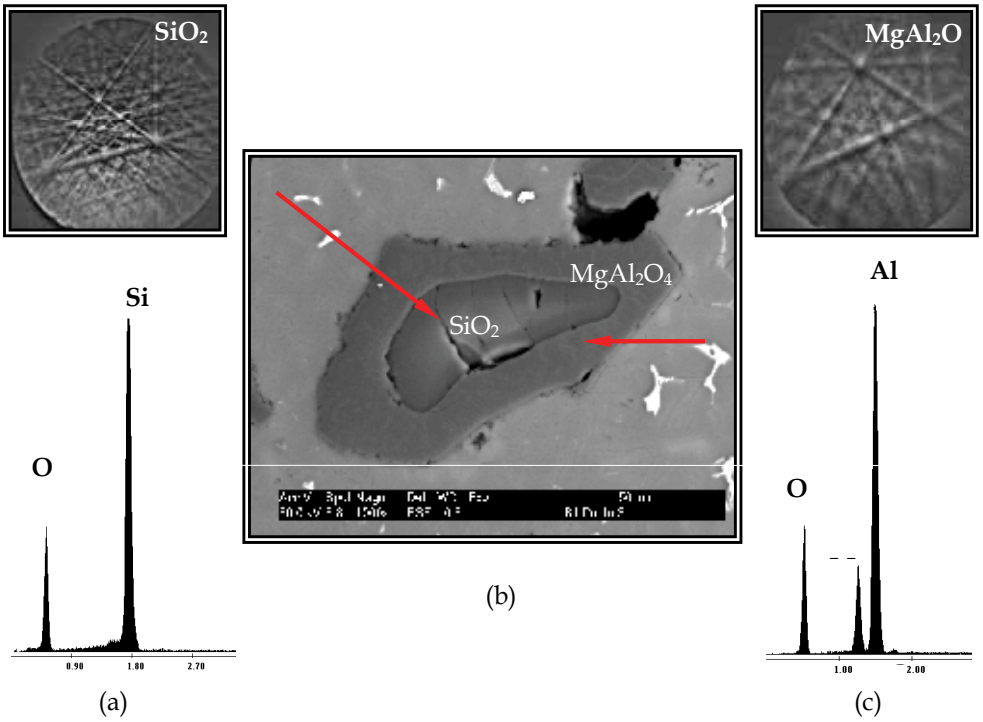

Fig. 8. (a), EDS and EBSD patterns of SiO_2 particles; (b), SEM micrograph of the particles, and (c), EDS and EBSD patterns of the $MgAl_2O_4$ layer of reaction products. The micrographs correspond to a particle that has been reacting in the molten bath for 1 minute at 750 °C.

Figure 10 shows the variation of Mg concentration as a function of time at 750 °C. This graph shows that Mg concentration diminishes continuously until reaching a constant value at constant temperature.

For reaction times less than 5 minutes, only Al_2O_3, $MgAl_2O_4$ and Si were formed as reaction products. However, SiO_2 nuclei still persist under these conditions. The micrograph in Figure 11a) shows the EDS and EBSD patterns of the nucleus of a SiO_2 particle that was immersed for 5 minutes in molten aluminium at 750 °C, where Fig. 11b) shows the partially reacted SiO_2 particle. Finally, Fig. 11c) shows the EDS and EBSD patterns of the $MgAl_2O_4$ in the layer of reaction products. According to (Zhong et al., 2003), the layers of reaction products will grow until the Mg^{+2} ions in the melt are depleted. Complete conversion of the SiO_2 nucleus into reacted products occurs after 60 min, and the conversion is closely related to Mg depletion as shown in Fig. 10.

Figure 12 shows the SiO_2-melt interface of a particle that was immersed for 10 minutes at 750 °C, where the SiO_2 nucleus still exists. A layer of Al_2O_3 adjacent to the nucleus and an external thin layer of $MgAl_2O_4$ are also observed. The increase in the amount of Al_2O_3 instead of $MgAl_2O_4$ can be explained in terms of the depletion of Mg from the melt and over the boundary layer, as Mg depletion also affects the amount of MgO that could be formed. On the contrary, as Al concentration is always constant at the boundary layer, it is always diffusing through the pores in the layers of reaction products. According to the stability of oxides in the Al-Mg-O_2 system (31) shown in Figure 1, below 0.49 wt. % Mg, the Al_2O_3 phase

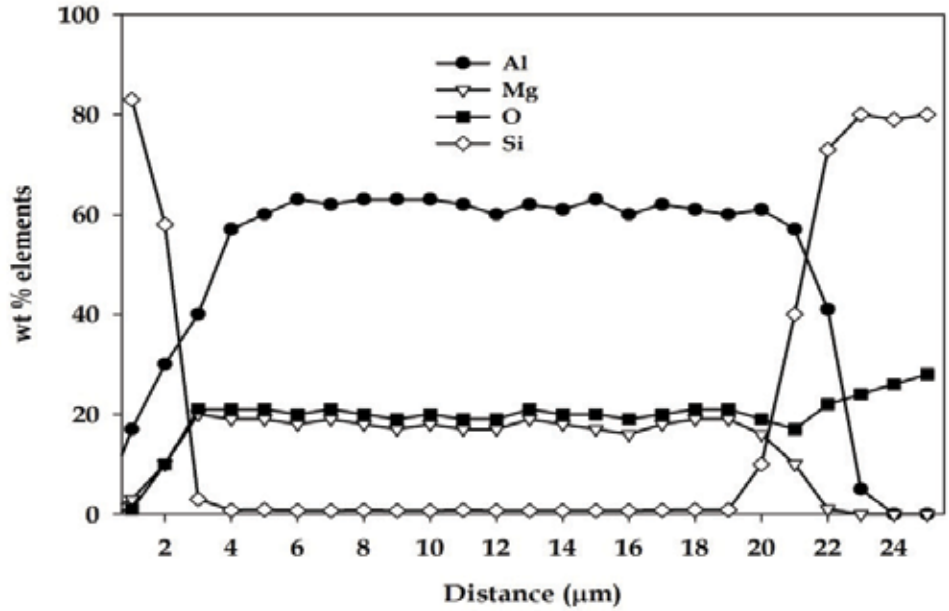

Fig. 9. Elemental distribution through the particle shown in Figure 8.

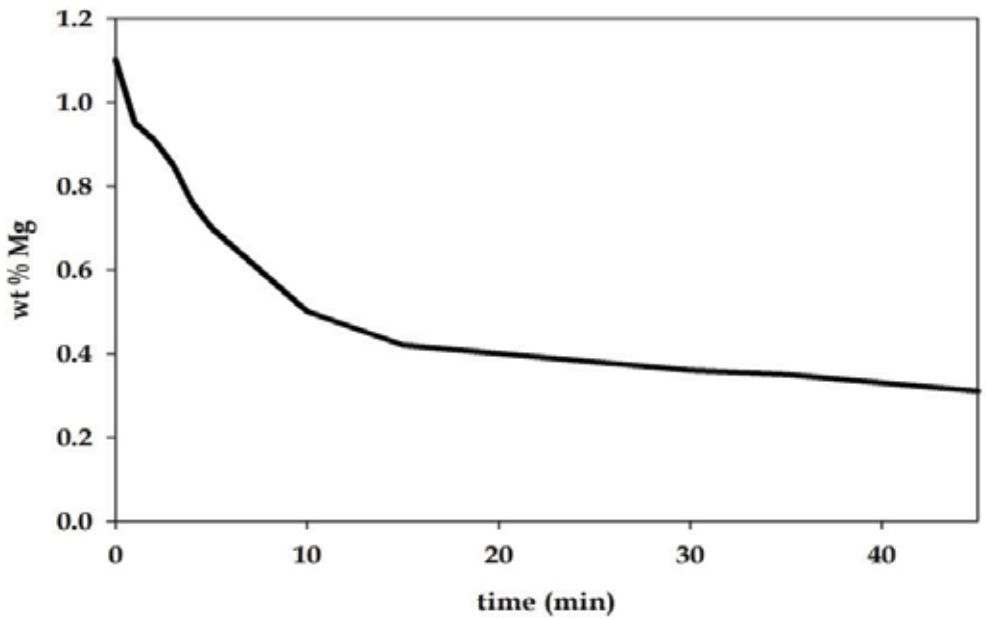

Fig. 10. Variation of Mg concentration as a function of time during SiO_2 particle addition with mechanical agitation at 750 °C.

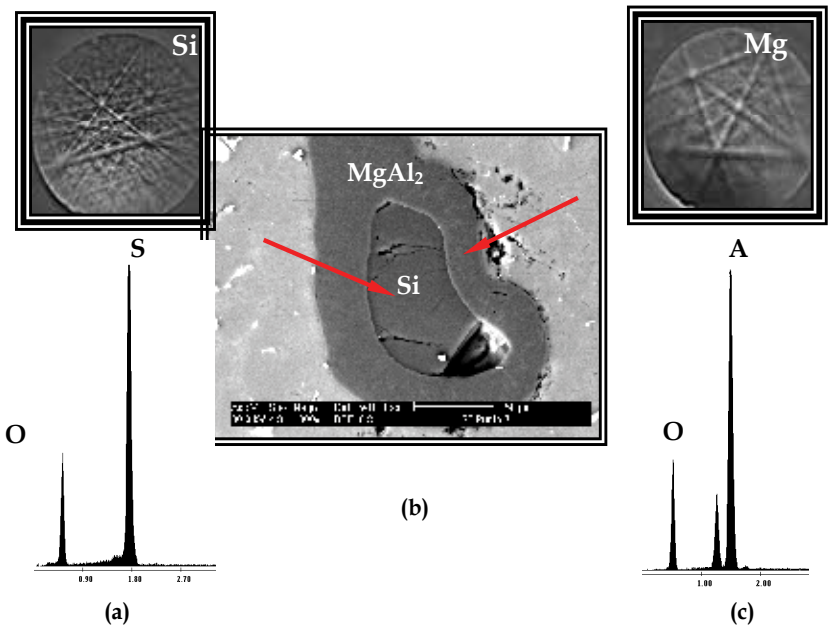

Fig. 11. (a), EDS and EBSD patterns of the nucleus of a SiO_2 particle reacted for 5 minutes at 750 °C in molten aluminium; (b), SEM micrograph of the particle; and (c), EDS and EBSD patterns of $MgAl_2O_4$ in the layers of reaction products.

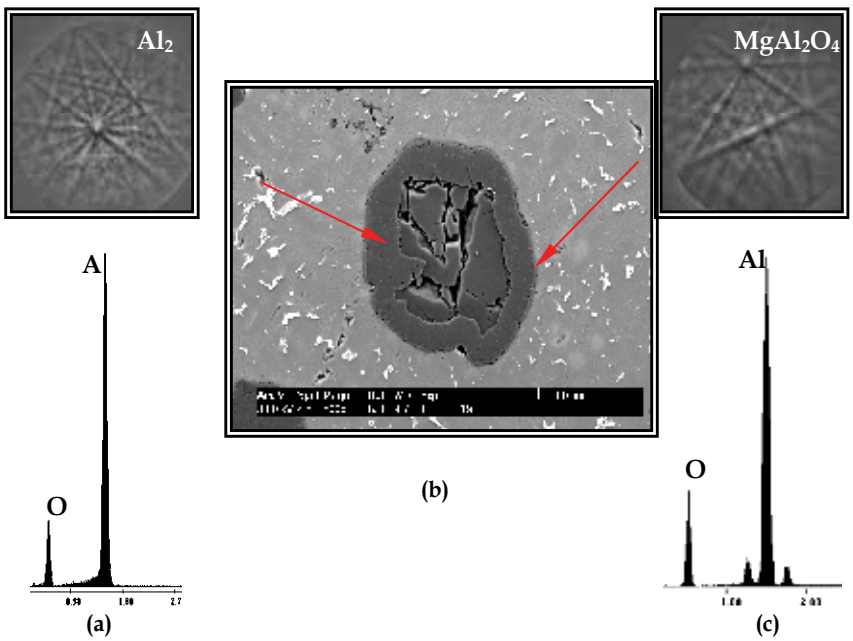

Fig. 12. (a), EDS and EBSD patterns of Al_2O_3 around the nucleus of a SiO_2 particle reacted for 10 minutes at 750 °C in molten aluminium; (b), SEM micrograph of the particle; and (c), EDS and EBSD patterns of $MgAl_2O_4$ in the outer layers of reaction products.

is stable over the complete range of temperatures studied here, indicating the dissolution of MgO. This demonstrates that reactions given by equations (5) and (10) occurred. Finally, particles that were immersed for more than 20 minutes at any temperature consisted basically of an Al_2O_3 nucleus surrounded by a thin layer of $MgAl_2O_4$ at the outer layer.
According to the results presented in the former analysis, the conversion rate of the SiO_2 particles into reaction products can be followed using the unreacted nucleus model, considering spherical particles of constant size. The control stage could be the diffusion of reactants through the layers of reaction products, or chemical reaction. The time at which the diameter of the nucleus becomes zero can be determined experimentally is calculated with the following equation:

$$\tau = \frac{a\rho_{slag}R_p^2}{24\rho_{Al}D_{efec}C_{Mg}} \tag{11}$$

where,
τ = total conversion time of a particle (sec).
a = stoichiometric factor depending on the chemical reaction considered.
ρ_{slag} = slag density ($kg.m^{-3}$).
R_p = average particle radius (m).
ρ_{Al} = aluminium density ($kg.m^{-3}$).
D_{efec} = effective diffusion coefficient of Mg through the layers of reaction products ($m^2.s^{-1}$).
C_{Mg} = actual Mg concentration at the solid SiO_2-melt interface ($mol.m^{-3}$).
Data extracted from Figure 9 can be used to calculate the values of the r_c/R and t/τ ratios. Furthermore, the dependence between these ratios can be determined to establish the kinetic control stage. Figure 13 shows this dependence at 750 °C. According to the shape of the curve of this figure, the controlling kinetic step is the diffusion of Mg and Al through the layers of reaction products. If the chemical reaction was the kinetic controlling step, the shape of the graph should be a straight line between the r_c/R = 1,0 and t/τ = 1,0 points.

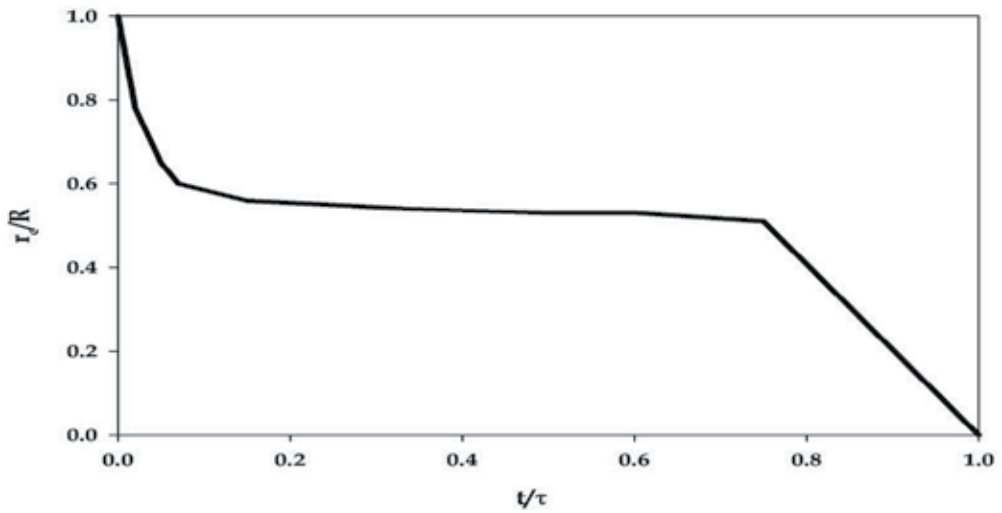

Fig. 13. Graphic representation of the dependence of r_c/R vs. t/τ for the conversion of an SiO_2 particle into reaction products at 750 °C.

Regarding the mechanisms of reaction in the SiO_2-melt system studied here, the most accurate explanation is that given by (Zhong et al. 2003), who states that the formation of $MgAl_2O_4$ is strongly dependent on the initial Mg concentration, as has been thermodynamically calculated and experimentally demonstrated in this work. Therefore, for initial Mg concentrations below 3 wt.%, the stable phase in the range of temperatures from 700 to 850 ^oC is $MgAl_2O_4$, a situation that can be corroborated by observing Figure 1. However, the reaction between SiO_2 particles and magnesium dissolved in molten aluminium will be the most favourable, as indicated by the global reaction given by equation (6). The presence of MgO was not confirmed in this work, and according to the literature cited, this phase could occur only for higher initial Mg concentrations, i.e., above 3.5 wt. %. Nevertheless, this concentration is easily attained at the solid SiO_2-melt interface, specifically at the early time points following particle addition, ensuring the formation of a significant amount of MgO. In turn, most MgO is consumed by the $MgAl_2O_4$ formation reaction.

Some studies have established that the reaction between dissolved Mg and SiO_2 particles takes places rapidly as it can be difficult to determine the nucleation stage of MgO particles. (Molins et al., 1991) studied the interfacial reaction between a molten Al_4Mg alloy and Al_2O_3 fibers, and showed that the MgO nucleus remain very small, forming thin layers of about 10 nanometers thickness. The diffusion of Mg^{2+} cations therefore occurs through the grain boundaries of MgO particles by an infiltration mechanism. The growth process of MgO layers continues until the grains around the interface matrix/reaction zone are large enough to close the intergranular spaces. Hence, the rate-determining step must be the diffusion of chemical species through the layers of reaction products.

The Gibbs free energy of reaction given by equation (10) indicates that the reduction of SiO_2 by Al also occurs, as the Al^{+3} cations can diffuse through the spaces left by the released Si. Silicon back-diffusion occurs through the grain boundaries of MgO and Al_2O_3, and Si dissolves in the molten aluminium phase. On solidification, Si is rejected from the solid solution, remaining as large crystals around foreign particles.

When the stoichiometric amounts of MgO and Al_2O_3 are reached and the equilibrium conditions indicated in Figure 1 are obeyed, the reaction given by equation (1) takes place. In this way, the formation of $MgAl_2O_4$ and the interdiffusion of Al^{+3}, Mg^{+2} and Si^{+4} cations occur simultaneously. Once the Mg concentration in the molten alloy falls below 0.30 wt. %, aluminium continues to react with the SiO_2 nucleus, forming more Al_2O_3 at a constant growth rate controlled by the diffusion of Al^{+3} cations through the layers of reaction products. In turn, the small amount of MgO that can be formed through the reaction of Mg^{+2} cations with SiO_2 is dissolved in the Al_2O_3 phase, as shown in Figure 1.

Reactions among molten aluminium and dissolved magnesium with solid SiO_2 require the diffusion of ions, although the diffusion of O^{-2} ions is negligible because of their larger ionic size. The relationship among ionic radii of Mg^{+2}, Al^{+3}, and Si^{+4} with respect to O^{-2} is 0.47, 0.34 and 0.28, respectively, as shown by (Zhong et al., 2003). Therefore, the interdiffusion of Mg^{+2} and Al^{+3} cations is kinetically possible through the lattice in the structure of SiO_2 of the O^{-2} anions, or through the Si^{+4} cations resulting from the SiO_2 decomposition. Such reactions are given by:

$$Mg^o - 2e- = Mg^{+2} \quad (12)$$

$$2(Al^o - 3e-) = 2Al^{+3} \quad (13)$$

$$2(Si^{+4} + 4e^{-}) = 2Si^{o} \quad (14)$$

When the Mg^{+2} cations occupy interstitial sites inside the SiO_2 lattice, the positions of O^{-2} anions must be adjusted to retain electrical neutrality and diminish the distortion energy of the lattice. The result is a change in crystal structure. The processes involved in this phenomenon are governed by the chemical potential values of the partial reactions, in this case, those given by reactions (5) or (10). As $MgAl_2O_4$ is the final reaction product, the reaction given by global equation (6) could be accepted, as this satisfies the described mechanism of reaction. However, to minimise interfacial energy, $MgAl_2O_4$ must form intermediate reaction products as follows. This situation can be represented in the stoichiometric form $xMgO\text{-}yAl_2O_3$, so when x=1 and y=13, the formula will be $MgAl_{26}O_{40}$; when x=1 and y=1, the formula will be $MgAl_2O_4$ (stoichiometric); when x=1 and y=0, the formula will be MgO. Moreover, the relationship x-y of $MgAl_2O_4$ ensures electrical neutrality in the oxide phase.

A kinetic condition necessary for diffusion of chemical species is continuous nanoporosity in the layers of reaction products. (Zhong et al., 2003) have determined that the formation of MgO over SiO_2 particles involves a volume contraction of 13.6 %, whereas the formation of $MgAl_2O_4$ over SiO_2 particles causes a volume contraction of 27 %. Because of these changes, the new phases formed break their unions with the original SiO_2 particles instantly, transforming into thousands of small crystals, producing the necessary voids required for the diffusion of chemical species. This breaking-up is continuous, occurring together with the nucleation and growth of new phases over the former phases. However, for the last stages of SiO_2 chemical reduction by Mg or Al, the mechanism of reaction abruptly changes, as the concentration of Mg at the reaction interface lies below 0.3 wt. %. At this time, the MgO that is formed dissolves in Al_2O_3. Then, these Al_2O_3 crystals grow continuously until reaching a micron size, closing the spaces for diffusion and thus stopping the chemical reaction underway.

The above explanations are important from the technological point of view, as unreacted SiO_2 particles can remain entrapped in the molten metal as inclusions. On the other hand, knowing the true nature of the reaction products and the way that the stoichiometry of reaction changes as a function of Mg concentration in the melt and at the reaction interface, could be useful for developing specific types of fluxes for removing these particles. Of course, reaction kinetics could be accelerated, diminishing the size of the nucleus of SiO_2 particles added for Mg refining from molten aluminium.

4.1 Kinetic study

According to classical kinetic theory (differential method), the rate of magnesium removal by SiO_2 particle addition could be calculated by the following formula:

$$-V\frac{dC_{Mg}}{dt} = K(C_{Mg} - C_{Mg(eq)})^{n} S_p \quad (15)$$

where:

C_{Mg} = actual concentration of Mg in the bath at constant temperature (wt. %)

$C_{Mg(eq)}$ = Mg concentration in the bath, at equilibrium, at constant temperature (wt. %)

K = reaction rate constant ($cm-(wt.\ \%)^{1-r}/s$)

t = time (s)

n = order of reaction

Sp = total area of reaction (cm^2)
V = volume of the bath (cm^3)
Equation (15) can be simplified considering that the value of $C_{Mg(eq)}$ is close to zero in the range of temperature under study. The value of K_p captures the effects of particle size and the volume of the bath, so equation (15) could be rewritten as follows:

$$-\frac{dC_{Mg}}{dt} = K_p (C_{Mg})^n \tag{16}$$

This equation can be transformed into a linear equation of the form:

$$-\ln\left[\frac{dC_{Mg}}{dt}\right] = n\ln(C_{Mg}) + \ln(-K_p) \tag{17}$$

The order of reaction n can be obtained from experimental results through a linear graph of ln (dC_{mg}/dt) vs. ln (C_{Mg}). The works conducted by (Flores et al., 1998) and (Escobedo et al., 2003) showed that the value of n is close to 1. The values of K_p for every temperature are directly obtained from the y-intercept of the straight line. In finding an analytical solution of equation (16), considering that the value of n is equal 1, the following expression is obtained:

$$C_{Mg} = C^{\circ}_{Mg} \exp\left[(-K_p)t\right] \tag{18}$$

The value of K_p can be used to obtain the activation energy of the process through the following Arrhenius-type expression:

$$K_p = Ae^{-Q/RT} \tag{19}$$

where:
A= Frequency factor
Q= activation energy (joule/mol)
R= universal gas constant (joule/mol-K)
T= temperature (K)
This expression must be transformed into a linear one, yielding the following equation:

$$K_p = lnA - Q/RT \tag{20}$$

The slope of a linear graph of ln(K_p) versus 1/RT is used to determine the value of activation energy, whereas the y-intercept of the straight line is the value of ln(A). (Macias & Flores, 1999) measured the activation energy of the Mg removal process using solid fluxes, reporting that this process requires 11540 cal/mol. This value is close to typical values obtained for diffusion-controlled metallurgical processes.

5. Conclusions

Antimony was removed from molten aluminium by adding powders of a master calcium-aluminium alloy, with as much as 85.2 wt. % of the initial Sb removed. The compounds formed after calcium addition were identified using electron backscattered diffraction in a scanning electron microscope, identifying phases such as the intermetallic compound Ca_2Sb.

The chemical reaction between magnesium dissolved in molten aluminium and SiO_2 particles reacts according to a mechanism where the diffusion of Al^{+3}, Mg^{+2}, and Si^{+4} ions through the porosity of the layers of reaction products determines the reaction kinetics. EBSD determined the true nature of the reaction products, demonstrating the formation of $MgAl_2O_4$ and Al_2O_3 over former SiO_2 nuclei.

Future work must focus on studying the effect of powder size, temperatures above 800 ^oC, and enhanced agitation conditions on the reaction rate in the systems studied. These findings are important for the commercial production of inclusion-free high-quality Al-Si-Cu alloys.

6. References

American Society for Metals (1988). *Metals Handbook Vol. 15: Casting, 9th Ed.* ISBN-0-87170-007-7. USA. pp. 55-60.

Ayala, Z. (2010). Análisis Cinético de la Obtención de Aleaciones Maestras Al-Zr, Mediante la reducción Aluminotérmica del ZrO_2. *Master´s Thesis*, CINVESTAV Saltillo, México.

Campbell, J. (2003). *Castings*. 2nd Ed. Butterwoth-Heinemann Linacre House. pp. 4-5. ISBN-0-7506-4790-6. Oxford, UK.

Caseres C.H. (1999). The Effect of Mg on the Microstructure and Mechanical Behavior of Al-Si-Mg Casting Alloys. *Metallurgical and Materials Transactions A.* pp. 2611-2618. ISSN-1073-5623.

Castrejón-Valdez, J. D. (1995). Estudio de la Remoción de Antimonio de Aluminio Líquido Mediante la Inyección de Polvos de Calcio-Silicio. *Master´s Thesis*, CINVESTAV Saltillo, México.

DiRusso, E. (1960). Reduction of the Calcium Content of Eutectic Aluminium-Silicon Alloys by Means of Controlled Addition of Phosphorous. *Alluminio,* Vol. 29, No.3. pp 121-127.

Escobedo, J.C., Hernández, J.F., Escobedo, S., Flores, A., and Cortés, D.A. (2003). Estudio cinético de la eliminación de magnesio en las aleaciones de aluminio mediante la inyección de polvos de sílice. *Revista de Metalurgia, Madrid*, Vol. 39. pp. 172-182. ISSN-0034-8570.

Fishkis, M. (1991). Interfaces and Fracture Surfaces in Saffil/Al-Mg-Cu Metal-Matrix Composites", *Journal of Matererials Science*. 26 . pp. 2.651-2.661. ISSN-0022-2461.

Flores A., Sukiennik M., Castillejos A. H., Acosta F. A., Escobedo J. C. (1998). A Kinetic Study on the Nucleation and Growth of $Al_8FeMnSi_2$ Intermetallic Compound for Aluminium Scrap Purification", *Intermetallics.* Vol. 6. pp. 217-227. ISSN-0966-9795.

Flores, A., Muñiz, R., Torres, J., Macías, E., and Rodríguez, N. (2008). Estudio del mecanismo de reacción durante la refinación de magnesio de aleaciones de aluminio líquidas usando partículas de SiO_2. *Revista de Metalurgia, Madrid.* Vol. 44 (2) Marzo-Abril. pp. 138-150. ISSN-0034-8570.

Garant, M., Laslaz, G., Jacob, S., Meyer, P., Gurerin, P.H., Adam, R. (1992). State of the Art use of Sb-Na and Modified Al-Si Casting Alloys. *Transactions of the American Foundrymen's Society (AFS), USA*. pp. 821-832. ISSN-0065-8375.

Gariepy B., and Dube, G. (1984). Treating Aluminium (Alloys) with Chlorine. *European Patent, EP181227A*.

Ghosh, A., Sarkar, R., Mukherjee, B., and Das, S.K. (2003). Effect of Spinel Content on the Properties of Magnesia–Spinel Composite Refractory. *Journal of the European Ceramamic Society*. Vol. 1. pp. 1-7. ISSN-0955-2219.

Gröbner, J., Kevorkov, D., Schmid-Fetzer, R. (2002). Thermodynamic modeling of Al-Ce-Mg phase equilibria coupled with key experiments. *Intermetallics*. Vol. 10. pp. 415-422. ISSN-0966-9795.

Gruzleski, J.E., Closset, B.M. (1990). *The Treatment of Liquid Aluminium-Silicon Alloys*. American Foundrymen´s Society Inc., Des Plaines, Illinois, USA. ISBN-087-4331218.

Hallstedt, B., Liu, Z.K., and Agren, J. (1990). Fiber-Matrix Interactions During Fabrication of Al_2O_3-Mg Metal Matrix Composites. *Materials Science and Engineering A. Vol.* 129. pp. 135–145. ISSN-0921-5093.

Hardy, C. (1941). Calcium to Purify Scrap Aluminium. *Metals Progress*, July. pp. 70-71. ISSN-0026-0665.

International Center for Diffraction Data ICDD (2009). 12 Campus Blvd. Newton Square, PA 19073-3273 USA; URL:www.icdd.com.

Kattner, U.R. (1997). The Thermodynamic Modeling of Multicomponent Phase Equilibria. *Journal of Minerals, Metalsand Materials*. Vol. 49, No. 12. pp. 14-19. ISSN-1047-4838.

Langlais, J. (1991). Strontium Extraction by Aluminothermic Reduction. *Canadian Metallurgical Quarterly*. Vol. 31, No.2. pp. 127-131. ISSN-0008-4433.

Levenspiel, O. (2002). *Ingeniería de las Reacciones Químicas*. Editorial Reverté 2a Edición. ISBN-9686-7082-94. España. pp. 406–415.

Lloyd, D.J., Jin, I., and Weatherly, G.C. (1994). Controlling the Interface Reaction in Alumina Reinforced Aluminium Composites. *Scripta Metallurgica*. Vol. 31. pp. 393–396. ISSN-1359-6462.

López-Saucedo F. (2006). Estudio Termodinámico y Cinético de la Reducción de $SrCO_3$ por Al(l) Bajo Condiciones de Vacío. *Master Thesis*. Cinvestav Unidad Saltillo, México.

Macias-Avila, E., Flores-Valdés, A. (1999). A Kinetic Model for Removal of Magnesium from Molten Aluminium by Submerged Na_2SiF_6 Powders Injection. *Aluminium Transactions*, Vol. 1, No. 1. pp. 79-92. ISSN-1521-0200.

Martínez C. (1998). Estudio de la Inyección de Sílice para la Eliminación de Mg en Aluminio. *Master´s Thesis*. CINVESTAV Saltillo, México.

Mcleod, A.D., and Gabryel, C.M. (1992). Kinetics of the Growth of Spinel, $MgAl_2O_4$, on Alumina Particulate in Aluminium-Alloys Containing Magnesium. *Metallurgical and Materials Transactions*. Vol. A. 23. pp. 1279-1283. ISSN-1073-5623.

Molins, R., Bartoute, J.D., and Bienbenu, A. (1991). Microstructural and Analytical Characterization of Al_2O_3-(Al-Mg) Composite Interfaces. *Matererials Science and Engineering A*. Vol. *A*135. pp. 111-117. ISSN-0921-5093.

Moore, J.J. (1990). *Chemical Metallurgy*, 2nd Edition. Butterworths. ISBN-04-0805-3690. UK. pp. 322-323.

Moreno, C. (2005). Estudio de la Remoción de Antimonio del Aluminio Líquido Mediante la Adición de Partículas de Calcio. *Master´s Thesis*. CINVESTAV Saltillo, México.

Muñiz, R., Flores, A., Torres, J. (2008). A Kinetic Study on Strontium Extraction by Metallothermic Reduction Using Submerged SrO Powders Injection. *Materials Letters* Vol. 62, Issues 4-5. pp. 637-640. ISSN-0167-577X.

Pai, B.C. and Ray, S. (1976). Fabrication of Aluminium-Alumina (Magnesia) Particulate Composites in Foundries Using Magnesium Additions to Melts. *Materials Science and Engineering A*. Vol. 24. pp. 31-45. ISSN-0921-5093.

Pfeifer, M., Rigsbee, J.M., and Chawla, K.K. (1990). The Interface Microstructure in Alumina (fp) Fiber Magnesium Alloy Composite. *Journal of Materials Science*. Vol. 25. pp. 1563-1567. ISSN-0022-2461.

Poirier, D.R. and Geiger, G.H. (1994). *Transport Phenomena in Materials Processing*. TMS Editors, Warrendale, PA, USA. pp. 535-537. ISBN-0873-3927-28.

Rajagopalan, P.K., Sharma, I.G., and Krishan, T.S. (1999). Production of Al-Zr Master Alloy Starting from ZrO_2. *Journal of Alloys and Compounds*. Vol. 285. pp. 212-215. ISSN-0925-8388

Randle, V., and Engler, O. (2000). *Introduction to Texture Analysis, Macrotexture, Microtexture and Orientation Mapping*. Gordon and Breach Science Publishers. ISBN: 9056992244. Netherlands.

Rosenquist, T. (1987). *Fundamentos de Metalurgia Extractiva*. LIMUSA. ISBN-9681-8214-40. España. pp. 127-139.

Schwartz, A.J., Kumar, M., and Adams, B.L. (2009). *Electron Backscatter Diffraction in Materials Science*. Kluwer Academic/Plenum Publishers. ISBN: 978-0-387-88135-5. USA.

Tuttle, B.L., Twarog, D., Daniels, E. (1991). The Effect of Trace Amounts of Antimony on Structure and Properties of Aluminium Alloys A356.2. Transactions of the American Foundrymen`s Society, USA. pp. 7-16. ISSN-0065-8375.

Szekely, J., Carlson, J.G., and Helle, L. (1971). *Rate Phenomena in Process Metallurgy*. Jhon Wiley and Sons, Inc., USA. pp. 369-371. ISBN-0471-8430-32.

Wang, W., Gruzleski, J.E. (1990). Interactive Effects During Sodium or Strontium Treatment of Antimony-Containing A356 Alloy. Transactions of the American Foundrymen`s Society. pp. 227-234.

Wang, W, Gruzleski, J.E. (1992). Modifier-Antimony- Interactions - The Problem, Mechanisms and Solution. Proceedings of *3rd international Conference on Molten Aluminium Processing*. November 9-10, 1992. Sheraton World Resort, Orlando Florida. pp. 93-124.

Zhong, W.M., Esperance, G.L., and Suery, M. (1995). Interfacial Reactions in Al-Mg (5083)/SICP Composites During Fabrication and Remelting. M*etallurgical and Materials Transactions. Vol. A*26. pp. 2625-2635. ISSN-1073-5623.

Zhong, W.M., Esperance, G.L., and Suery, M. (2003). Effect of Current Mg Concentration on Interfacial Reactions During Remelting of Al-Mg(5083)/Al_2O_3(p) Composites", *Materials Characterization.* Vol. 49. pp. 113-119. ISSN-1044-5803.

15

Modelling of Precipitation Hardening in Casting Aluminium Alloys

Linda Wu and W. George Ferguson
University of Auckland
New Zealand

1. Introduction

Precipitation hardening, because it involves the hardening of the material over a prolonged time, is also called age hardening, or ageing. By the appropriate heat treatment of precipitation hardening, the strength or hardness of some heat-treatable aluminium alloys can be enhanced by the formation of nano-meter sized second-phase precipitated particles within the original phase matrix. The fine precipitates in the alloy impede dislocation movement by forcing the dislocations to either cut through the precipitated particles or go around them. By restricting dislocation movement during deformation, the alloy is strengthened. Thus precipitation hardening is the most versatile and demanding heat treatment in aluminium alloys, either for wrought or casting alloys.

The precipitation-hardening process generally involves following three basic steps:

a. Solution heat treatment, or homogenization, is the first step where the alloy is heated between the solvus and solidus temperatures and soaked until all of the soluble phases are dissolved and a homogeneous solid-solution structure is produced.
b. Quenching is the second step where the solid solution is rapidly cooled to a lower temperature, usually room temperature. This forms the formulation of a supersaturated solid solution (SSSS) since the solubility of one or more alloying elements in aluminium decreases with decreasing temperature.
c. The final step in the precipitation hardening process is aging that allows controlled decomposition of the supersaturated solid solution (SSSS) and the formation of strengthening precipitates. It is the process where the supersaturated solution is heated below the solvus temperature to produce a finely dispersed precipitates. When ageing occurs at room temperature, it is called natural ageing. Ageing above room temperature is called artificial ageing.

With the age-hardening aluminium alloys having become the backbone of the automotive and aerospace industries, although a century has now elapsed since the phenomenon of age or precipitation hardening was discovered by the German metallurgist, Alfred Wilm (Wilm, 1911), new observations are still being made as the latest experimental techniques reveal more details of the actual atomic process involved. Precipitation hardening was hailed as the first nanotechnology (Polmear, 2006) and now it is possible to develop fine-scale microstructures in a much wider range of alloys through the use of novel processing methods. The optimization of material processing techniques has, however, for a long time,

been pursued by trial and error. As it involves working blind, this method is costly and wasteful of manpower. It is desirable for material scientists to conduct fewer experiments to attain a specified goal. Fortunately, this has become possible with the development of materials and computer science.

Since the precipitation of second phase particles is critical to the properties of many industrially important aluminium alloys, modelling of precipitation kinetics and strengthening in age hardening aluminium alloys has gained considerable interest among researchers. During the precipitation process, three major physical elementary mechanisms are involved: i.e. nucleation, growth and coarsening. Based on how these three processes are treated, modelling of the precipitation kinetics in aluminium alloys can be divided into two main approaches. One of approaches is based on the Shercliff-Ashby process model (Shercliff & Ashby, 1990a) in which only one average particle size is assumed and the three processes are considered in isolation with the implicit assumption that one process is essentially complete before the next one begins. Shercliff and Ashby first attempted to assemble a process model for the ageing of the simplest of the age-hardening aluminium alloys, by introducing a process model widely used in chemical engineering but relatively rare in processing of solid materials. Their process model draws together established knowledge of the kinetics of microstructure evolution with dislocation behavior, in order to determine the mechanical properties. This model gives a good description of some Al-Cu and Al-Mg-Si (Shercliff & Ashby, 1990b) , wrought as well as casting alloys (Rometsch & Schaffer, 2002) and also 8000 Al-Li aluminium alloys (Pandey, 1995).

In the other approach, which is more refined, Kampmann and Wagner have produced a numerical approach (KWN model) (Kampmann et al., 1987; Kampmann & Wagner, 1984) capable of describing the particle size distribution (PSD) in the time domain, while dealing with the nucleation-growth-coarsening phenomena within the same formulation. Hence in the KWN model, the particle size is assumed to be a continuous parameter. And then a strength model is used to evaluate the resulting change in hardness or yield strength at room temperature by taking into account contributions from lattice resistance, solid solution hardening and precipitation hardening. Though the KWN model has been developed for a few decades and successfully applied to a number of aluminium alloy systems, such as 2xxx, 6xxx and 7xxx (Myhr & Grong, 2000; Myhr *et al.*, 2001; Robson, 2004a; Robson, 2004b) , however, most of modelling work has been focused on the wrought aluminium alloys and none modelling work has been applied to the casting aluminium alloys. In the present work, the KWN model has been for the first time applied to the casting aluminium alloys A356 and A357.

2. Shercliff-Ashby process model

2.1 Components of the process model

The complete Shercliff-Ashby model for isothermal age hardening includes the following components or – best called sub-models:

1. The initial growth of a volume fraction of precipitate, and consequent changes in solute concentration;
2. The dependence of the equilibrium volume fraction of precipitate on ageing temperature;
3. Precipitate coarsening by competitive growth;
4. The contribution of solid solution strengthening to the yield strength;

5. The contribution of shearable precipitates to the strength; and
6. The contribution of non-shearable or bypassing precipitates to the strength (Orowan Strengthening).

The sub-models (1) ~ (3) belong to the microstructure evolution. And the contributions to the strength model consist of the sub-models (4) ~ (6).

2.1.1 Precipitation from supersaturated solid solution

After solution heat treatment and quenching, the non-equilibrium phase precipitates from the solid solution on ageing. During the early stages of precipitation, the initial precipitation kinetics are described by Shewmon (Shewmon, 1963): the mean solute concentration in the matrix $\bar{c}$ decays exponentially with time t, raised to a power close to unity:

$$\bar{c}(t) = c_e + (c_i - c_e)\exp(-t/\tau_1) \tag{1}$$

where c_i is the initial solute concentration, c_e is the solute concentration at equilibrium at the ageing temperature, and τ_1 is a temperature-dependent time constant.

The volume fraction f of precipitate is directly proportional to solute loss $c_i - \bar{c}(t)$, tending to a final equilibrium value, f_e, when $\bar{c} = c_e$, thus:

$$\frac{f(t)}{f_e} = \frac{c_i - \bar{c}(t)}{c_i - c_e} = 1 - \exp(-t/\tau_1) \tag{2}$$

2.1.2 The dependence of f_e on ageing temperature

The concentration of solute at the metastable solvus temperature c_s is described by (Swalin, 1962):

$$c_s = A_0 \exp(-Q_s / RT_s) \tag{3}$$

Where A_0 is a constant, and Q_s is the free energy of solution of the solute, T_s is solid solvus temperature.

The equilibrium concentration of solute c_e at a temperature $T < T_s$ is:

$$c_e = A_0 \exp(-Q_s / RT) \tag{4}$$

Dividing the above two equations gives the following equation:

$$c_e = c_s \exp\left[-Q_s\left(\frac{1}{T} - \frac{1}{T_s}\right)\right] \tag{5}$$

The equilibrium volume fraction of precipitate at temperature T is given by:

$$f_e = f_{\max}\left(\frac{c_s - c_e}{c_s}\right) \tag{6}$$

where $f_{\max}$ is the maximum possible volume fraction precipitated at absolute zero. Substituting from equation (5):

$$f_e = f_{\max}\left\{1-\exp\left[-\frac{Q_s}{R}\left(\frac{1}{T}-\frac{1}{T_s}\right)\right]\right\} \tag{7}$$

The above equation shows the dependence of f_e on how far the ageing temperature T lies below the (metastable) solid solvus temperature, T_s .

2.1.3 Particle coarsening

Since the coarsening of precipitates was first described by Ostwald (Ostwald, 1900), particle coarsening is often called Ostwald ripening. Most theories of Ostwald ripening are based on the classical works of Lifshitz and Slyozov (LS) (Lifshitz & Slyozov, 1961) and of Wagner (Wagner, 1961), commonly referred to as LSW theory. The LSW theory predicts a cube law relating the mean particle radius $\bar{r}$ at time t to that, $\bar{r}_0$, at time t = 0:

$$\bar{r}^3(t)-\bar{r}_0^3=\frac{c_1 t}{T}\exp(-\frac{Q_A}{RT}) \tag{8}$$

Where c_1 is a constant, Q_A is the activation energy for volume diffusion of atoms between particles, R the Universal gas constant (8.314 J/mol K) and T the aging temperature.

2.1.4 The contribution of the solid solution to the strength $\Delta\sigma_{ss}$

For this strengthening mechanism, solute atoms of one element are added to another, resulting in either substitutional or interstitial point defects in the crystal. The substitution of solute atoms for aluminium atoms distorts the crystal lattice, hinders dislocation mobility and hence strengthens the alloy. The glide resistance caused by a solute at a mean concentration $\bar{c}$, expressed as a contribution to the yield strength, $\Delta\sigma_{ss}$, is given by (Friedel, 1964; Nabarro, 1967; Cottrell, 1964; Nabarro *et al.*, 1979; Hospital, 1987; Hull & Bacon, 2001):

$$\Delta\sigma_{ss}=c_2\left[\bar{c}_j\right]^{2/3} \tag{9}$$

where c_2 is a constant related to the size, modulus and electronic mismatch of the solute including various resolution factors, and $\bar{c}_j$, the mean solute concentration of a specific alloying element in the matrix.

2.1.5 The contribution of shearable precipitates to the strength $\Delta\sigma_A$

When particles are small, the dislocations will shear the precipitates, which is sometimes called precipitate resistance (Cahn et al., 1996). For this cutting mechanism, the contribution of shearable precipitates to the yield strength can be represented by:

$$\Delta\sigma_A=c_3 f^m \bar{r}^n=c_3 f^{1/2}\bar{r}^{1/2} \tag{10}$$

where c_3 is an alloy constant that depends on the particular strengthening mechanism, i.e., coherency, surface, chemical, stacking fault, and/or modulus hardening. The exponents m and n are always positive, for most dislocation particle interactions, both m and n have the values 0.5 (Starke, 1977; Sanders, 1980).

2.1.6 The contribution of bypassing precipitates to the strength $\Delta\sigma_B$

When the precipitates grow during the precipitation the strength is increased and the dislocation can no longer cut the precipitates. The mechanism by which dislocations bypass precipitates was first proposed by Orowan (Orowan, 1948) and is referred to as the Orowan mechanism or dispersed particle strengthening. A simple (but adequate) form of the Orowan equation is:

$$\Delta\sigma_B = \frac{c'Gb}{l} \tag{11}$$

where c' is a constant, G the shear modulus, and b the Burgers vector. The particle spacing, l, in the slip plane of the dislocation is related to the volume fraction, f, and radius, r. Substituting $l = c''\frac{r}{f^{1/2}}$ (where c'' is a constant) into equation (11) gives:

$$\Delta\sigma_B = c_4\frac{f^{1/2}}{r} \tag{12}$$

where c_4 contains all the constants in equations (11) and c''.

2.2 Assembly of the process model

In real alloys where a number of different strengthening mechanisms are operative at room temperature (Hatch et al., 1984), it is reasonable to assume that the individual strength contributions can be added linearly. Considering age hardening aluminium alloys, the following contributions are of importance, i.e., with precipitation hardening due to shearing and bypassing of particles by dislocations and solid solution hardening effects. Therefore, the resulting expression for the overall macroscopic yield strength σ is:

$$\sigma = \sigma_i + \sigma_{ss} + \sigma_{ppt} \tag{13}$$

Where σ_i is the intrinsic yield strength, which remains constant during ageing. σ_{ss} is the solid solution strength and σ_{ppt} is the precipitation hardening strength due to shearing and bypassing of particles by dislocations.

The method of assembling the process model is to combine the microstructure evolution of sub-models into the different contributions to the yield strength (Kocks *et al.*, 1975; Martin, 1980), then identify the overall yield strength with the sum. Both mean solute concentration $\bar{c}$ and volume fraction f vary with time, reaching steady values before the peak of the ageing curve is reached.

In order to combine the equations of sub-models together to give a process model for ageing, Shercliff and Ashby proposed the *temperature corrected time, P*, which was defined by:

$$P = \frac{t}{T}\exp-\frac{Q_A}{RT} \tag{14}$$

This parameter, referred to as "kinetic strength" by Ion *et al.*(Ion et al., 1984), measures the number of kinetic jumps that have taken place in time *t*. Over most of the ageing curve, the initial radius r_0 <<r, hence we may re-write equation (8):

$$r(t) = C_1 P^{1/3} \tag{15}$$

In the Shercliff-Ashby modeling work, the net contribution of precipitation to the strength from the shearing and bypassing precipitates was defined by taking their harmonic mean:

$$\Delta\sigma_{ppt} = \left[\frac{1}{\Delta\sigma_A} + \frac{1}{\Delta\sigma_B} \right]^{-1} \tag{16}$$

If define the value of P corresponding to the peak strength as P_p and the volume fraction f reaches an equilibrium volume fraction f_e, then from the fact that the peak in the ageing curve lies very close to the point where the two contributions to peak strengthening are equal, $\Delta\sigma_A = \Delta\sigma_B$, and we can get $C_3 f_e^{1/2} P_P^{1/6} = C_4 f_e^{1/2} P_P^{-1/3}$, which gives the relationship:

$$C_4 = C_3 P_P^{1/2} \tag{17}$$

From the equation (17), we can conclude that the value of P required to reach the peak over a wide range of temperature is often roughly constant. Its value can be found from equation (14) by substituting values for the times t_p corresponding to the peaks of the ageing curves at several temperatures and taking the mean. Hence we use this value, P_p, to normalize the kinetic strength (noting that P/P_p =1 at the peak), equation (15) becomes:

$$r(t) = C_5 \left(\frac{P}{P_p} \right)^{1/3} \tag{18}$$

Then another parameter S_0, the "peak precipitation strength" is introduced into the model and defined by:

$$S_0 = \frac{C_3}{2} f_e^{1/2} P_p^{1/2} \tag{19}$$

Because P_p is constant, $S_0^2 \propto f_e$. Substituting r and S_0 into equations (10) and (12) and then taking the harmonic mean gives:

$$\Delta\sigma_{ppt} = \frac{2S_0 \left(P / P_p \right)^{1/6}}{1 + \left(P / P_p \right)^{1/2}} \tag{20}$$

Note that when $P = P_p$, $\Delta\sigma_p = S_0$, which defines the peak in the ageing curve.
Since $S_0^2 \propto f_e$ and according to equation $f(t) = f_e * \left[1 - \exp(-t / \tau_1) \right]$, by assuming the cubic coarsening law holds from the very beginning of precipitation even while the volume fraction is changing, and replacing f_e by $f(t)$, gives a corresponding variation in S^2:

$$S^2(t) = S_0^2 \left[1 - \exp(-t / \tau_1) \right] \tag{21}$$

From these equations it may deduced that when $t >> \tau_1$, $f(t)$ tends to f_e and $S(t)$ has reached the peak precipitate strength, S_0.

From equation (9), the initial solute concentration c_i can be expressed in terms of the initial solid solution strength $\Delta\sigma_{ssi}$, that is, $c_i = c_4\Delta\sigma_{ssi}^{3/2}$; and similary equilibrium solute concentration c_e can be expressed in terms of the final solid solution strength contribution $\Delta\sigma_{ss0}$, that is, $c_e = c_4\Delta\sigma_{ss0}^{3/2}$. Substituting these expressions into equation (1) gives:

$$\overline{c}(t) = c_4[\Delta\sigma_{ss0}^{3/2} + (\Delta\sigma_{ssi}^{3/2} - \Delta\sigma_{ss0}^{3/2}) \times \exp(-t/\tau_1)] \tag{22}$$

Substituting this value into equation (9), the evolution of the corresponding solid solution strength is then described by:

$$\Delta\sigma_{ss}(t) = \left[\Delta\sigma_{ss0}^{3/2} + (\Delta\sigma_{ssi}^{3/2} - \Delta\sigma_{ss0}^{3/2}) \times \exp(-t/\tau_1)\right]^{2/3} \tag{23}$$

Experiments have shown that the volume fraction and solute concentration reach their equilibrium values at a time which is a constant fraction of the time to reach peak strength (Anderson, 1959). Therefore, the time constant τ_1 in the equations can be scaled as t_p:

$$\tau_1 = K_1 t_p \tag{24}$$

where K_1 is a constant.
Or using the definition of P_p:

$$\tau_1 = K_1 P_p T \exp(Q_A/RT) \tag{25}$$

The peak precipitate strength S_0 depends on the ageing temperature because the volume fraction f_e does so. Combining this with equation (21) gives:

$$S_0^2(T) = (S_0)_{\max}^2 \left\{1 - \exp\left[-\frac{Q_s}{R}\left(\frac{1}{T} - \frac{1}{T_s}\right)\right]\right\} \tag{26}$$

Combining equation (7) and (26) gives:

$$S^2(t,T) = (S_0)_{\max}^2 \left\{1 - \exp\left[-\frac{Q_s}{R}\left(\frac{1}{T} - \frac{1}{T_s}\right)\right]\right\} \times \left[1 - \exp-(t/\tau_1)\right] \tag{27}$$

Similarly the solid solution contribution to the strength depends on the ageing temperature because it determines the amount of solute left in solution. The temperature-variation of the equilibrium solid solution component of the yield strength is:

$$\begin{aligned}(\Delta\sigma_{ss0})_T &= c_2(c_e)^{2/3} \\ &= (\Delta\sigma_{ss0})_{T_s} \exp\left[-\frac{2}{3}\frac{Q_s}{R}\left(\frac{1}{T} - \frac{1}{T_s}\right)\right]\end{aligned} \tag{28}$$

At $T = T_s$, the concentration of the matrix equals the alloy concentration, and there is no precipitate. In the as-quenched condition the alloy is a uniform solution of the full alloy content, hence the as-quenched strength, σ_q, is given by:

$$\sigma_q = \sigma_i + (\Delta\sigma_{ss0})_{T_s} \tag{29}$$

By combining equation (28) and (29) gives:

$$(\Delta\sigma_{ss0})_T = (\sigma_q - \sigma_i)\exp\left[-\frac{2}{3}\frac{Q_s}{R}\left(\frac{1}{T}-\frac{1}{T_s}\right)\right] \tag{30}$$

In the over-aged condition, the coarse precipitate contribute to the strength can be negligible, hence the over-aged strength σ_{oa} depends only on the matrix solute concentration. Thus σ_{oa} is the sum of the solid solution strength and the intrinsic strength of pure aluminium σ_i :

$$(\sigma_{oa})_T = \sigma_i + (\Delta\sigma_{ss0})_T \tag{31}$$

Combining equations (30) and (31) gives the variation of the over-aged strength with temperature:

$$(\Delta\sigma_{oa})_T = \sigma_i + (\sigma_q - \sigma_i)\exp\left[-\frac{2}{3}\frac{Q_s}{R}\left(\frac{1}{T}-\frac{1}{T_s}\right)\right] \tag{32}$$

Using known values of σ_i and σ_q, the over-aged strength can be calculated.

2.3 Calibration of the model

The most difficult aspect in application of the Shercliff-Ashby model is calibration of the constants used in the process model. There are six constants that need to be calibrated from ageing curves: activation energy for ageing Q_A (KJ mol-1), peak temperature-corrected time P_p (s K-1), metastable solvus temperature T_s (°C), solvus enthalpy Q_s (KJ mol-1), maximum strength parameter at absolute zero $(S_0)_{\max}$ (MPa), constant coefficient K_1 relating τ_1 to t_p. These constants do not change with temperature for the specific alloy.

2.3.1 Calibration Q_A and P_p

Q_A and P_p can be found by calibrating the data to the peaks of the ageing curves. The values of peak hardness σ_p and the time to peak t_p at various temperatures can be read from the ageing curves. By finding the time to peak t_p at various temperatures, P_p is evaluated directly.

From equation (14) it can be deduced that $P_p = \frac{t_p}{T}\exp\left(\frac{-Q_A}{RT}\right) = cons\tan t$, and taking natural logs it becomes:

$$\ln P_p = \ln(t_p / T) - (Q_A / RT) \tag{33}$$

By putting $x = 1/T$ and $y = \ln(t_p / T)$, an Arrhenius plot of y against x results in a straight line. The value of Q_A can be derived from the slope (Q_A / R). The value of P_p can be either calculated from $y_0 = \ln P_p$ when $x = 0$, or taken as the mean value of P_p at each temperature.

2.3.2 Calibration $(S_0)_{\max}$, Q_s and T_s

The temperature dependence of the equilibrium volume fraction is contained in the parameter S_0 since $S_0^2 \propto f_e$. From equation (26), by plotting S_0^2 against temperature enables

us to find values for $(S_0)_{\max}$ and T_s. From the graph, at the intersection of the extrapolated curve with the temperature axis, $S_0^2 = 0$, and from equation (26), it can be deduced that $T = T_s$; at the intersection with the S_0^2 axis, $T = 0$, it can be deduced that $S_0 = (S_0)_{\max}$. When $(S_0)_{\max}$ and T_s have been determined, the solvus enthalpy Q_s for each ageing temperature can be calculated using:

$$Q_s = \frac{-R}{(1/T - 1/T_s)} \ln\left[1 - \frac{S_0^2}{(S_0)_{\max}^2}\right] \tag{34}$$

The main problem is how to determine the value of S_0 from the ageing curves. At peak ageing, $(\Delta\sigma_{ppt})_p = S_0$. The peak precipitation strength contribution, $(\Delta\sigma_{ppt})_p$, is found by subtracting the other contributions (solid solution $\Delta\sigma_{ss}$ and intrinsic σ_i) from the measured peak strength σ_p.

$$(\Delta\sigma_{ppt})_p = S_0 = \sigma_p - (\Delta\sigma_{ss} + \sigma_i) \tag{35}$$

At peak hardness, the other contribution to $(\Delta\sigma_{ss} + \sigma_i)$ is the over-aged strength σ_{oa} since f has reached its equilibrium value f_e before the peak. The value of σ_{oa}, however, depends on the value of Q_s and T_s as described by equation (32), which are not known. Thus we have to use an iterative method. We first estimate the value of σ_{oa}: it must lie between the as quenched strength σ_q (when all the solute is in solution), and the intrinsic strength σ_i (when no solute is left in solution). Thus:

$$(\sigma_{oa})_{est} = (\Delta\sigma_{ss0} + \sigma_i)_p = \left(\sigma_i + \sigma_q\right)/2 \tag{36}$$

Thus, using equation (36) an initial estimated value of S_0 is obtained by:

$$(S_0)_{est} = \sigma_p - (\sigma_{oa})_{est} \tag{37}$$

For each ageing temperature, it is possible to get the value of $(S_0)_{est}$. A graph of $(S_0)_{est}^2$ against temperature T is then plotted. From the graph, the first estimated values of $(S_0)_{\max}$ and T_s are obtained and Q_s is calculated from equation (34).
From these values of Q_s and T_s, a better estimate of σ_{oa} and S_0 may now the obtained using equations (36) and (37). The whole procedure is repeated until the fit between theory and data is satisfactory.

2.3.3 Calibration of K_1

It remains to determine the time constant τ_1 which is related to the peak temperature corrected time by equation (25). The constant K_1 is adjusted to give the required decay. The decay of the solid solution component of the strength is then given by equation (23) with $\Delta\sigma_{ssi} = \sigma_q - \sigma_i$ and $\Delta\sigma_{ss0} = \sigma_{oa} - \sigma_i$.

2.4 Application of the model

The modelling method is applied to casting alloys A356 and A357. All the processes for calibration and constructing the predicted ageing curves are programmed under MATLAB

which is a large software package that has many advanced features built-in, and it has become a standard tool for many working in science or engineering disciplines.

2.4.1 Input data

The input data for each alloy includes its composition, as quenched strength σ_q and the strength of σ_i, which is defined as being the sum of the intrinsic strength of pure aluminium and solid solution strengthening contributions which remain constant during ageing, as well as the information of ageing curves which includes temperature T, time to peak yield strength t_p and the peak yield strength σ_p. All this information is used to calibrate the constants thus the predicted ageing curves for various temperatures can be constructed.

The most detailed data set available was from Rometsch, etc. (Rometsch & Schaffer, 2002) for the ageing of casting alloy A356 & A357 at various temperatures. The compositions (in wt.%) are to be Al-7.0 Si-0.40Mg-0.13Fe-0.03Sr for A356 and Al-7.0 Si-0.60Mg-0.13Fe-0.03Sr for A357. The equilibrium precipitates are Mg_2Si. σ_i is 43 MPa and as quenched strength σ_q = 75MPa for A356 and σ_q = 85MPa for A357. All above data with a data set for peak time and yield strength at various temperatures are listed in Table 1 & Table 2.

Nominal composition of Mg (wt%)	1.0		
σ_i (*MPa*)	43		
σ_q (*MPa*)	75		
Ageing data	Temperature T (°C)	Time to peak t_p (s)	Peak YS σ_p (MPa)
	250	268	207
	230	699	239
	210	1630	256
	190	5188	271
	170	39,156	268
	150	263,090	272

Table 1. Data used for calibration for A356

Nominal composition of Mg (wt%)	1.0		
σ_i (MPa)	43		
σ_q (MPa)	85		
Ageing data	Temperature T (°C)	Time to peak t_p (s)	Peak YS σ_p (MPa)
	250	191	258
	230	503	277
	210	979	294
	190	4354	297
	170	34,026	300
	150	267,881	303

Table 2. Data used for calibration for A357

2.4.2 Calibration results

The calibration results for the alloys A356 and A357 using the above input data are listed in Table 3.

Parameter	Symbol	A356	A357
Activation energy for ageing (KJ mol^{-1})	Q_A	130.38	137.66
Peak temperature-corrected time (s K^{-1})	P_p	3.58×10^{-14}	4.36×10^{-15}
Metastable solvus temperature (°C)	Ts	269.59	286.66
Solvus enthalpy (kJ mol^{-1})	Q_s	55.39	50.30
Maximum strength parameter at absolute zero (MPa)	$(S_0)_{\max}$	229.70	259.34
Constant relating τ_1 to t_P	K_1	0.0990	0.1009

Table 3. Calibration results for A356, A357

2.4.3 Modelling results

The contributions to the full ageing curve of the intrinsic strength, solid solution strength, and precipitation hardening due to shearable and non-shearable stresses for A356 at 175 °C are shown in Fig.1. The net contribution of precipitation to the strength from the shearing and bypassing precipitates was modelled by taking their harmonic mean.

After calibration, the ageing curves for different isothermal ageing temperatures for alloys A356 and A357 were modelled, as shown in Fig. 2 and Fig. 3 respectively. And the values of t_p and σ_p for the different Al-Mg-Si alloys are listed in Table 4.

Material		Ageing at 50°C	Ageing at 100°C	Ageing at 150°C	Ageing at 175°C	Ageing at 190°C	Ageing at 210°C
A356	t_p (hour)	10000*	2400	20.00	2.75	0.93	0.24
	σ_p (MPa)	100.26*	284.60	282.97	279.79	275.95	266.62
A357	t_p (hour)	10000*	3000	19.00	2.33	0.74	0.18
	σ_p (MPa)	104.22*	316.21	314.70	312.01	308.92	301.78

t_p is limited to 100000 hours, * means not to peak ageing yet.

Table 4. t_p and σ_p for ageing at different temperatures for A356, A357

From Fig. 2 and Fig. 3 and Table 4, we can see that:

a. The modelling results show that when ageing at a lower temperature, it takes a longer time to reach peak yield strength (or hardness), but the peak yield strength is higher, and vice versa. This is the basic ageing trend.

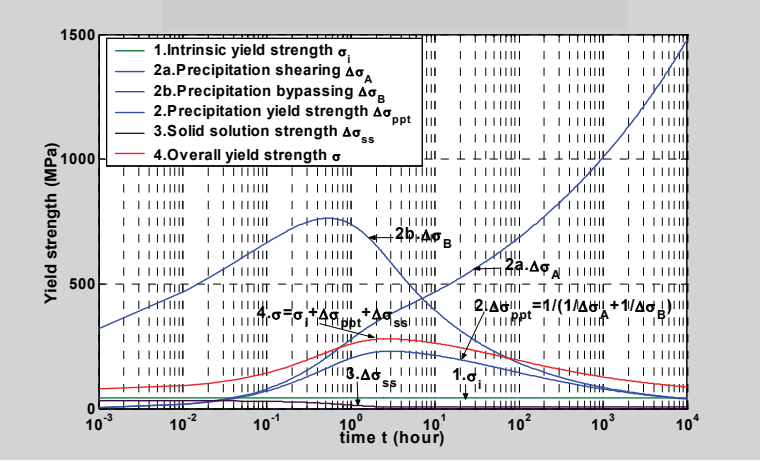

Fig. 1. Ageing curve of different contributions for A356 ageing at 175°C

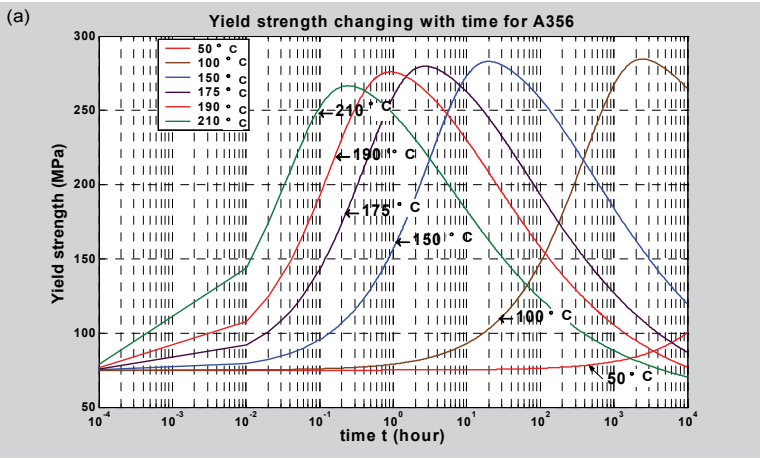

Fig. 2. Ageing at different temperatures for A356

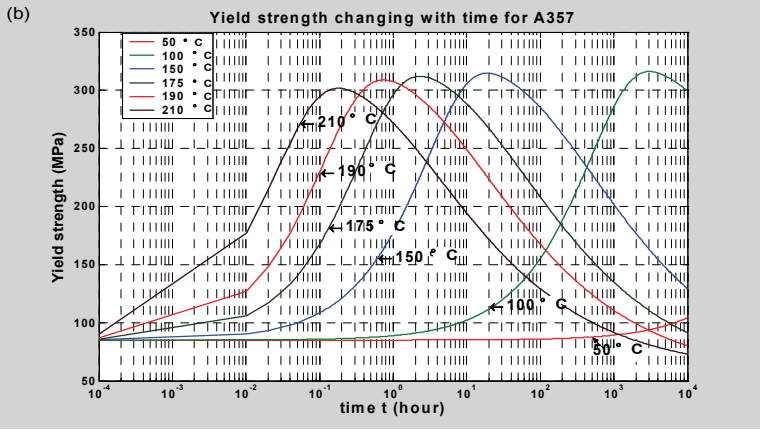

Fig. 3. Ageing at different temperatures for A357

b. Time to the peak yield strength t_p is very sensitive to the temperature; however, the peak yield strength σ_p doesn't change much as temperature changes.
c. At low temperature (such as 50°C), there is almost no yield strength or hardness gain for the initial of which means that the modeling results shows poor agreement with the experimental data at low temperatures.

2.4.4 Model validation

The modelling results are validated by ageing A356 at different temperatures, and recording hardness at different ageing times. The samples were cut from as cast A356 aluminium wheels, ground flat and the testing surfaces were finished with 1200 grit SiC paper.
The samples were solution treated in an unstirred salt bath at 540±3 °C for 75 minutes, then quenched in water to room temperature and aged without delay. Artificial ageing was carried out in an oil bath (for 150°C) and salt baths (for 175°C, 210°C) with a temperature variation of ±2 °C. At various times, a sample was removed from the bath then quenched in water to room temperature, and Rockwell hardness tests for Scale E and Scale K were done. For long ageing processes the samples were transferred to an air furnace after initial ageing in an oil or salt bath. Following heat treatment and before hardness testing, the artificial ageing samples were kept in a refrigerator, and natural ageing samples were kept at room temperature. The average value of at least five effective readings were used for each data point. The ageing curves for hardness are shown in Fig. 4.

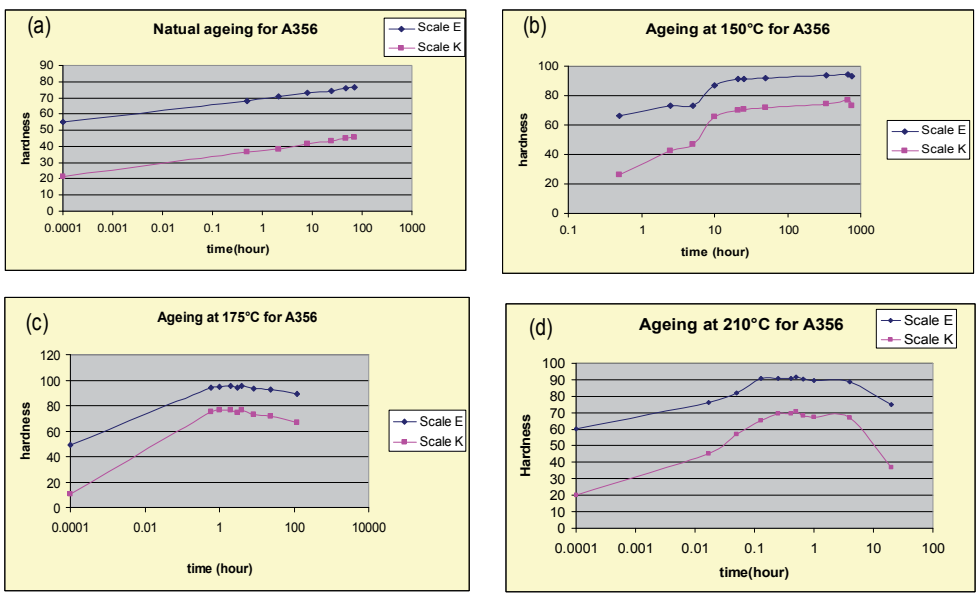

Fig. 4. Hardness changes with time for A356 at (a) Natural ageing; (b) 150°C; (c) 175°C; (d) 210°C

From the above ageing curves, we can see that the experimental data is in good agreement with the modelling results for artificial ageing. However, for natural ageing, the hardness (or yield strength) increases with time, whereas the modeling curve shows almost no change for the initial 100 hours. This means that at lower temperature, the modeling results for Schercliff–Ashby method were in poor agreement with the experimental data. This could be

due to two reasons: the first is that among the input data used for calibration there is no information for low temperatures; the other reason is that in the present model, the ageing curve is mainly controlled by particle coarsening, with negligible input from nucleation and growth. Because for low temperature, it may take a longer time to reach the process of particle coarsening, nucleation and growth can not be neglected. Therefore, for the present calibration of the Schercliff–Ashby modelling method it is recommended that it not be applied at low ageing temperature.

3. Kampmann and Wagner Numerical model (KWN model)

The KWN model consists of the following two distinct but integrated modules:

a. A microstructure model for prediction of the precipitation kinetics during ageing with coupled nucleation, growth and coarsening (and likewise dissolution) in dilute alloy systems, assuming spherical particles with uniform thermodynamic properties.
b. A strength model, which converts the relevant output parameters into an equivalent room temperature yield stress or hardness.

3.1 Precipitation kinetics model

Modelling Microstructure evolution is the first step of any integrated model for predicting the properties of a given material. The modelling of precipitation kinetics is based on the Kampmann and Wagner type numerical model (KWN model). It has a number of features that make it suitable for industrial process modelling.

The essential features of this model are summarized below (Robson et al., 2003; Robson, 2008; Robson, 2004b):

a. The continuous size distribution of the particles is subdivided into a large number of size classes $[R_j, R_{j+1}]$ containing N_j particles respectively.
b. The continuous time evolution of the particle distribution is split up into a sequence of discrete time steps.
c. At each time step, the number of newly nucleated particles with the size of slightly above the critical radius is calculated using classical nucleation theory and allocated to an appropriate size class.
d. The growth of existing particles is calculated by assuming growth is diffusion controlled and spherical growth morphology. The influence of the Gibbs–Thomson effect is used to calculate the modified interfacial compositions for each size class at each time step. Therefore, the existing ones grow or shrink depending on their size.
e. Coarsening arises naturally in the model, and no simplifying assumptions for the shape of the particle size distribution are predesigned.
f. The change in matrix solute level due to precipitate formation or dissolution is calculated at each time step using the mean field approximation.

3.1.1 Nucleation of new precipitates

According to classic nucleation theory, the nuclei form as a result of localised compositional fluctuations that occur statistically within the supersaturated matrix. Provided that the incubation period can be neglected at the same time as possible effects of elastic coherency strains around the nucleated particles are ignored, the nucleation rate j is conveniently expressed as (Myhr & Grong, 2000; Myhr et al., 1998; Myhr et al., 2004; Myhr et al., 2001; Myhr et al., 2002):

$$j = j_0 \exp\left[-\left(\frac{A_0}{RT}\right)^3\left(\frac{1}{in\left(\bar{C}/C_e\right)}\right)^2\right]\exp\left(-\frac{Q_d}{RT}\right) \tag{38}$$

where j_0 is a pre-exponential term, A_0 a parameter related to the potency of the heterogeneous nucleation sites in the parent material (J/mol), Q_d the activation energy for diffusion, $\bar{C}$ the mean solute content in the matrix, and C_e is the equilibrium solute content at the particle/matrix interface (given by the phase diagram), R universal gas constant (8.314 J/*Kmol*), T temperature (K).

3.1.2 Particle growth

When a spherical particle of radius r and solute concentration C_p is embedded in a super-saturated solid solution of a mean concentration $\bar{C}$, it will either dissolve or grow, depending on whether the particle/matrix interface concentration C_i exceeds $\bar{C}$ or not. According to the diffusion-controlled growth, under the mean field approximation, the growth rate of particles can be expressed as (Myhr & Grong, 2000; Myhr et al., 2001; Myhr et al., 2004; Wagner et al., 1991):

$$v = \frac{dr}{dt} = \frac{\bar{C} - C_i}{C_p - C_i}\frac{D}{r} \tag{39}$$

The diffusion coefficient D is calculated at a given temperature from:

$$D = D_0 \exp\left(\frac{-Q_d}{RT}\right) \tag{40}$$

The influence of interfaces on equilibrium (i.e. the interface curvature) has to be taken into account. This is the Gibbs–Thomson effect that modifies the solubility limits given by equilibrium thermodynamics (phase diagram). Through the Gibbs-Thomson equation (Madras & McCoy, 2003; Porter & Easterling, 1992; Miyazaki et al., 1996; Myhr et al., 2001):

$$C_i = C_e \exp\left(\frac{2\gamma V_m}{rRT}\right) \tag{41}$$

where γ is the particle–matrix interface energy, and V_m is the molar volume of the particle.
Based on the above equations, it is possible to obtain an explicit expression for the critical radius r^* of a particle that neither will grow nor dissolve (Langer & Schwartz, 1980):

$$r^* = \frac{2\sigma V_m}{RT}\left(\ln\left(\frac{\bar{C}}{C_e}\right)\right)^{-1} \tag{42}$$

The radii of particles which nucleate in each time interval are tracked separately. As the fraction of solute in the matrix decreases during precipitation, the driving force for nucleation and growth of the precipitate particles decreases and the critical particle radius increases, reducing the nucleation rate with time. Because r^* depends on the current value of C_e, the thermal stability of the precipitates is sensitive to changes in the temperature during heat treatment. It follows that reheating promotes particle dissolution, whereas cooling or

isothermal annealing favours nucleation, growth and coarsening in a successive manner. Thus in the KWN model, the applied thermal programme has a large influence on the evolution of the particle size distribution with time.

3.1.3 Coarsening

Coarsening arises naturally in the model when the average solute concentration in the matrix $\overline{C}$ becomes larger than the solute concentration at the precipitate/matrix interface Ci, thus resulting in the dissolution of the smaller precipitates. Therefore, those particles which have a radius $< r^*$ will have a negative growth rate according to equation (39) and will thus start to shrink. Particles with a radius $> r^*$ will retain a positive growth rate and will continue to increase in size. When the size of a group of particles reaches zero they are removed from the size distribution.

3.1.4 Mass balance

Once the volume fraction is computed, from the mass balance relating the amount of solute tied up in particles to the amount of the solute drained from the matrix, we can calculate the mean concentration in the matrix phase $\overline{C}$ as:

$$\overline{C} = \frac{(C_0 - C_p f)}{(1 - f)} \tag{43}$$

where $f = \int_0^\infty \frac{4}{3}\pi r^3 \phi dr$ (ϕ) is the size distribution function) is the volume fraction. The newly obtained matrix composition is employed as an input for the thermodynamic computations in the next time step.

3.2 Strength model

After predicting the microstructure evolution, the second step is to derive reliable microstructure/properties relationships. I will consider here the case of the yield stress or hardness. The strength model considering particle size distribution also includes precipitation hardening due to shearing and bypassing of particles by dislocations σ_p and solid solution hardening σ_{ss}.

3.2.1 Precipitation hardening

Pursuing the usual approach for determining the critical resolved shear stress (or yield strength) from the interaction of gliding dislocations with point obstacles (Ardell, 1985; Lloyd, 1985; Gerold, 1980), according to Deschamps and Brechet (Deschamps *et al.*, 1998; Deschamps & Brechet, 1998), the relationship between σ_{ppt} and $\overline{F}$ is given as:

$$\sigma_{ppt} = \frac{M\overline{F}}{bL} \tag{44}$$

Where $\overline{F}$ denotes the mean obstacle strength and σ_{ppt} the resulting increase in the overall macroscopic yield strength, M is the Taylor factor and b is the magnitude of the Burgers vector and L is the mean effective particle spacing in the slip plane along the curved dislocation. The microstructural variables $\overline{F}$ and L evolve with aging time and are themselves functions of other microstructural variables as well as aging temperature.

Moreover, assuming a mono-dispersive system of spheres, the effective particle spacing L in the slip plane can be expressed in terms of the mean particle size $\bar{r}$, the particle volume fraction f, and the mean obstacle strength $\bar{F}$ using the Friedel statistic (Friedel, 1964; Brown & Ham, 1971) which applies best for low obstacle strengths, and relies on the assumption of a steady-state for the number of precipitates along the dislocation line in motion. Thus, equation (44) becomes (Wagner et al., 1991; Deschamps & Brechet, 1998)：

$$\sigma_{ppt} = \frac{M}{b\bar{r}}\left(2\beta Gb^2\right)^{-1/2}\left(\frac{3f}{2\pi}\right)^{1/2}\bar{F}^{3/2} \tag{45}$$

where G is the shear modulus of the aluminium matrix and β is a constant close to 0.5.
In the general case, where the alloy contains a mixture of weak (shearable) and strong (non-shearable) particles, the mean obstacle strength is conveniently defined as:

$$\bar{F} = \frac{\sum_i N_i F_i}{\sum_i N_i} \tag{46}$$

where N_i is the number density of particles that belongs to a given size class r_i, and F_i is the corresponding obstacle strength.
The obstacle strength depends on the mechanism of overcoming.

- In the case of particle shearing (weak particles), the obstacle strength can have a number of different dependencies on the particle radius, depending on the main interaction mechanism between the shearable particle and the dislocation. It is a fair approximation to assume that F_i is proportional to the particle radius as long as r is smaller than the critical radius for shearing r_c

$$\bar{F}_i = 2\beta Gb^2\left(\frac{r_i}{r_c}\right) \tag{47}$$

- In the case of precipitate by-passing (strong particles, characterised by $r_i > r_c$), the obstacle strength is constant

$$\bar{F}_i = 2\beta Gb^2 \tag{48}$$

3.2.2 Solid solution hardening σ_{ss}

In age hardening, aluminium alloys elements, such as Mg, Si and Cu give rise to considerable solid solution strengthening. Provided that the contribution from each element is additive, the solid solution hardening potential of the alloy σ_{ss} can be expressed as:

$$\sigma_{ss} = \sum_j k_j C_j^{2/3} \tag{49}$$

where C_j is the concentration of a specific alloying element in solid solution and k_j is the corresponding scaling factor.

3.2.3 Overall yield strength and hardness

In alloys where several strengthening mechanisms are operative at room temperature, it is reasonable to assume that the individual strength contributions can be added linearly. Thus,

the resulting expression for the overall macroscopic yield strength σ is the same as the equation (13) used in Shercliff-Ashby model.
Conversion from yield strength (MPa) to hardness (VPN) can then be done through a simple regression formula (Grong, 1997):

$$H_v = 0.33\sigma_y + 16.0 \tag{50}$$

3.3 Application to the casting aluminium alloys

Although the KWN model has been successfully applied to different aluminium alloys (Myhr et al., 2001; Robson, 2004a), there are no reports of application to casting aluminium alloys. The present modelling work is the first time that KWN model has been applied to the casting aluminium alloys A356 and A357 for different ageing temperatures and compared with the experimental data.

3.3.1 Isothermal ageing

The modelling work is applied to the casting alloys A356 and A357 with chemical composition of Al–7.0Si–0.40Mg–0.13Fe–0.03Sr and Al–7.0Si–0.62Mg–0.13Fe–0.03Sr (Rometsch & Schaffer, 2002) by weight percentage respectively. The experimental data used to validate the model is obtained from the literature (Rometsch & Schaffer, 2002) and our experimental data. The yield strength is taken as approximately three times the Rockwell hardness scale E for A356.
The modelling results for ageing at various temperatures for A356 and A357 are shown in Fig. 5 and Fig. 6.
By choosing suitable parameters used in the microstructural and strength models, the modelled yield strength results for A356 (Fig. 5) and A357 (Fig. 6) are in very good agreement with the experimental data from the literature as well as own data. Because of greater Mg content, if ageing at the same temperature, the peak yield strength is higher and the time to peak ageing is shorter for A357 than for A356.

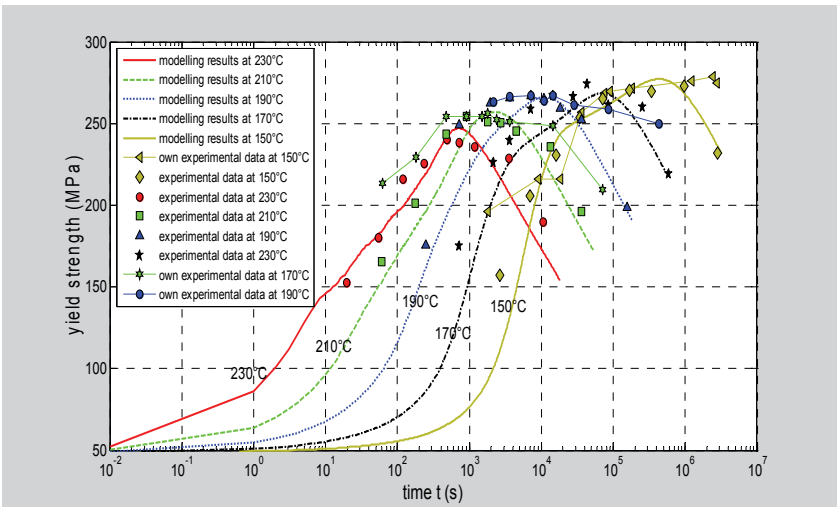

Fig. 5. Modelling results for ageing at various temperatures for A356

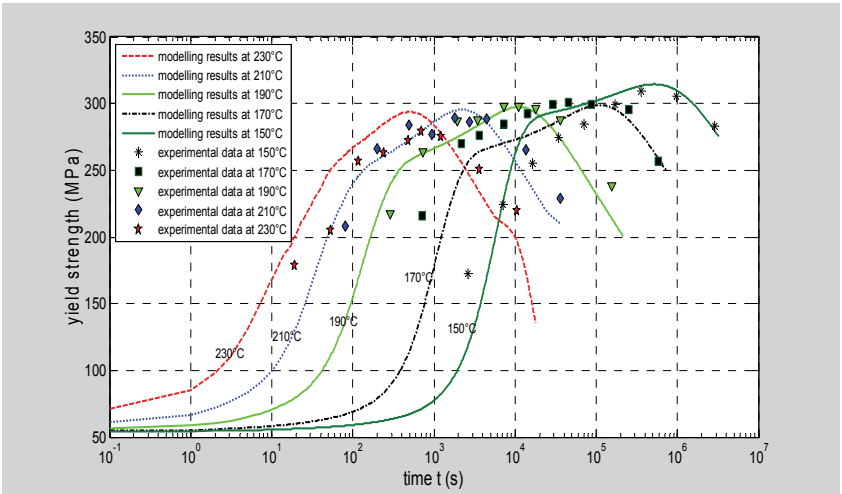

Fig. 6. Modelling results for ageing at various temperatures for A357

Fig. 7 gives the particle size distribution (PSD) after ageing at different temperatures for 3 hours for A356. For this time it is over-ageing for 210°C and 230°C, peak-ageing for 190°C and under-ageing for 170°C. The distribution broadens significantly in going from under ageing to over ageing. The evolution of PSD with time, as shown in Fig.8, indicates the particles gradually move to a larger size and therefore the broadness of the shape of distribution becomes greater with time evolution. Fig. 9 shows how the number of particles per unit volume changes with time at different temperatures.

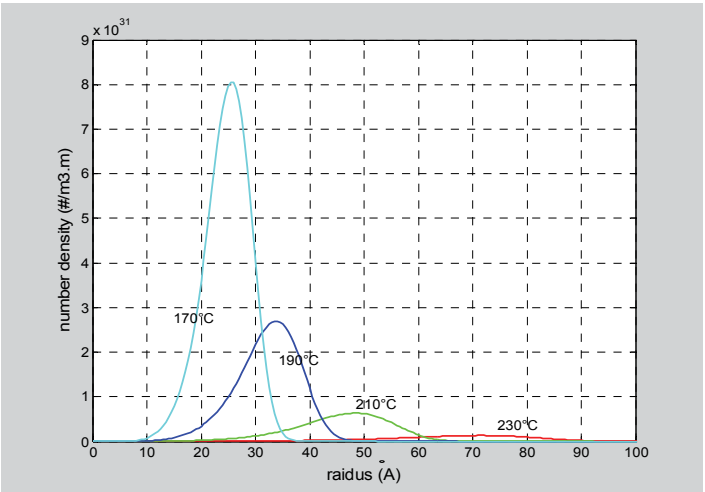

Fig. 7. Particle size distribution (PSD) after ageing: (a) 3 hours for different temperatures for A356

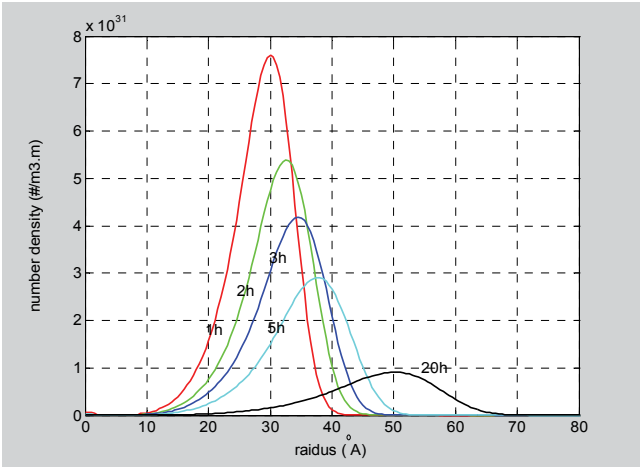

Fig. 8. Particle size distribution (PSD) after ageing different times at 190° C for A357

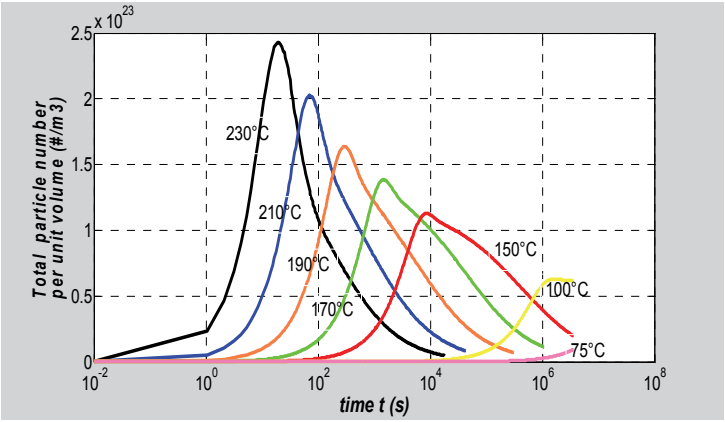

Fig. 9. Evolution of total number of particles per unit volume for ageing at different temperatures for A357

The total number of particles per unit volume increases to the peak value then decreases gradually. For higher temperature, it is faster to the peak value.

4. Comparing with Shercliff-Ashby methodology

Figures Fig.10 and Fig. 11 show the modelling results of yield strength under different ageing temperatures by the Schercliff-Ashby method and the KWN model for A356 and A357 respectively. The key for the figures is: '150-1' stands for modelling at 150°C by method 1- KWN model, '150-2' stands for modelling at 150°C by method 2- Schercliff-Ashby method, and '150-3' stands for experimental data for ageing at 150°C. Other symbols stand for the similar meanings. The experimental data is obtained from Rometsch & Schaffer's work (Rometsch & Schaffer, 2002).

From Fig. 10 and Fig. 11 we can see that most of the experimental data are located between the two modelling methods which means that the results simulated by both methods are in

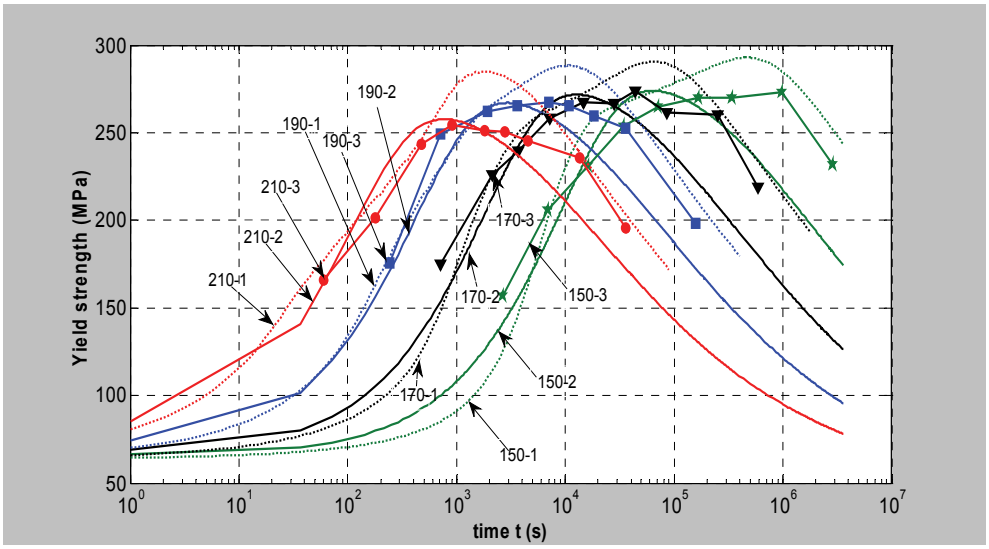

Fig. 10. Modelling of age hardening for A356 at ageing temperatures of 150°C, 170°C, 190°C and 210°C by Schercliff-Ashby method and KWN model, and comparasion with experimental data.

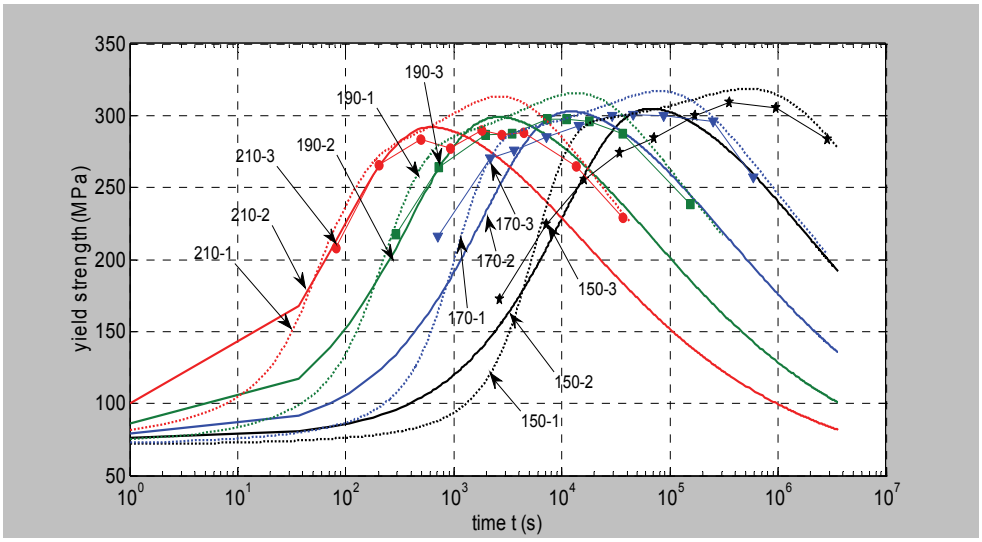

Fig. 11. Modelling of age hardening for A357 at ageing temperatures of 150°C, 170°C, 190°C and 210°C by Schercliff-Ashby method and KWN model, and comparasion with experimental data.

reasonable agreement with the experimental data. For the top part of the simulated ageing curve, the broadness is greater with the KWN model than the Schercliff-Ashby method. Therefore, the shape of ageing curves modelled by the KWN model are in closer agreement to the experimental data which means that the KWN model can give a better simulation of results. The reason for this is that the KWN model involves the whole precipitation process that is initiated by nucleation, then proceeds to particle growth and eventually ends with

Ostwald coarsening. These three processes significantly overlap. The existing particles may grow or shrink depending on their size. If the particle size is greater than the critical size, it will grow; otherwise, it will dissolve. Whereas in the Schercliff-Ashby method, the particle size is only controlled by the Ostwald coarsening, no nucleation is considered. However, in the KWN model, not only the time is discretized, but also the continuous size distribution is subdivided into a large number of size classes, which results in a large amount in calculation time. Therefore, the Schercliff-Ashby method is faster than the KWN model. Normally, the Shercliff-Ashby method can be completed in a few minutes, whereas for KWN model, may take about one day to finish the calculation. Moreover, since most constants used in the equations are calibrated from ageing data, the modelled peak yield strength is more accurate for the Schercliff-Ashby method than the KWN model. Furthermore, some constants determined by calibration in the Schercliff-Ashby method, such as activation energy Q_A, solvus enthalpy Q_s, solvus temperature T_s, can also be used in the KWN model. But only when there exist series ageing data, which means series peak yield strength - ageing time to peak yield strength can we use the Schercliff-Ashby method.

5. Conclusions

In the Shercliff-Ashby process model, the most important and difficult part is to calibrate the constants used in the equations from the systematic experimental data (ageing curves). Since lack of information at low temperature for calibration, the modeling results were in poor agreement with the experimental data at low temperatures.

The Kampmann and Wagner numerical (KWN) model can be applied to not only wrought aluminium alloys, but also the casting alloys, such as A356 and A357. By choosing suitable parameters used in the microstructural and strength model, the modelling results are in good agreement with the experimental data obtained from the literature as well as own experimental data. This is the first time that the KWN model has been applied to the casting aluminium alloys.

For the casting aluminium alloys A356 and A357, the modelling results simulated by the KWN model are in better agreement with the experimental data than that by the Schercliff-Ashby method. However, the Schercliff-Ashby method can provide more accurate peak yield strength values and some constants calibrated in the Schercliff-Ashby method can also be used in the KWN model. Therefore, these two modelling methods complement each other.

6. Reference

Anderson, W.A., (1959) Precipitation from solid solution, ASM, metals park, Ohio

Ardell, A. (1985) Precipitation hardening. *Metallurgical and Materials Transactions A,* 16, 2131.

Brown, L.M. & Ham, R.K. (1971) *Dislocation-Particle Interactions, in Strengthening methods in crystals, eds Kelly, A. and Nicholson, Robin*. Amsterdam, New York,: Elsevier Pub. Co.

Cahn, R.W. & Haasen, P. (1996) *Physical metallurgy*. Elsevier Science Publishers, North-Holland, Amsterdam ; New York.

Cottrell, A. (1964) *Theory of crystal dislocations*. New York: Gordon and Breach.

Deschamps, A. & Brechet, Y. (1998) Influence of predeformation and ageing of an Al-Zn-Mg alloy-- II. Modeling of precipitation kinetics and yield stress. *Acta Materialia,* 47, 293.

Friedel, J. (1964) *Dislocations,* Pergamon Press

Gerold, V. (1980) Precipitation Hardening ,*Dislocations in Solids,* 4, 219.
Grong, O. (1997) *Metallurgical Modeling of Welding*. The Institute of Materials, London, second ed.
Hatch, J.E. (1984) *Aluminum : properties and physical metallurgy*. Metals Park, Ohio: American Society for Metals.
Hospital, J.T. (1987) *Dislocations*. St. Lucia, Qld.: University of Queensland.
Hull, D. & Bacon, D.J. (2001) *Introduction to dislocations,* 4th edn. Oxford [Oxfordshire] ; Boston: Butterworth-Heinemann.
Ion, J.C.; Easterling, K.E. & Ashby, M.F. (1984) A second report on diagrams of microstructure and hardness for heat-affected zones in welds. *Acta Metallurgica,* 32, 1949.
Kampmann, R.; Eckerlebe, H. & Wagner, R., (1987) Precipitation Kinetics in Metastable Solid Solutions-Theoretical Considerations and Application to Cu-Ti Alloys. In: *Phase Transitions in Condensed Systems--Experiments and Theory*: 525. Boston, Massachusetts; USA; .
Kampmann, R. & Wagner, R., (1984) Kinetics of Precipitation in Metastable Binary Alloys-Theory and Application to Cu-1.9at% Ti and Ni-14at% Al. 91.
Kocks, U.F.; Argon, A.S. & Ashby, M.F. (1975) Thermodynamics and Kinetics of Slip. *Progress in Materials Science,* 19, 1.
Langer, J.S. & Schwartz, A.J. (1980) Kinetics of nucleation in near-critical fluids. *Physical Review A,* 21, 948.
Lifshitz, I.M. & Slyozov, V.V. (1961) The kinetics of precipitation from supersaturated solid solutions. *Journal of Physics and Chemistry of Solids,* 19, 35.
Lloyd, D.J. (1985) Precipitation Hardening. *Strength of Metals and Alloys (ICSMA 7),* 3, 1745.
Madras, G. & McCoy, B.J. (2003) Temperature effects for crystal growth: a distribution kinetics approach. *Acta Materialia,* 51, 2031.
Martin, J.W. (1980) *Micromechanisms in particle-hardened alloys*. Cambridge ; New York: Cambridge University Press.
Miyazaki, T.; Koyama, T. & Kobayashi, S. (1996) A new characterization method of the microstructure using the macroscopic composition gradient in alloys. *Metallurgical and Materials Transactions A,* 27, 945.
Myhr, O.R. & Grong, O. (2000) Modelling of non-isothermal transformations in alloys containing a particle distribution. *Acta Materialia,* 48, 1605.
Myhr, O.R.; Grong, O. & Andersen, S.J. (2001) Modelling of the age hardening behaviour of Al-Mg-Si alloys. *Acta Materialia,* 49, 65.
Myhr, O.R.; Grong, Ø.; Fjær, H.G. & Marioara, C.D. (2004) Modelling of the microstructure and strength evolution in Al-Mg-Si alloys during multistage thermal processing. *Acta Materialia,* 52, 4997.
Myhr, O.R.; Grong, Ø.; Klokkehaug, S. & Fjær, H.G., (2002) Mathematical Modelling of Weld Phenomena. Bhadeshia, H.K.D.H. (Ed.). London: Maney Publishing.
Myhr, O.R.; Kluken, A.O.; Klokkehaug, S.; Fjaer, H.G. & Grong, O. (1998) Modeling of microstructure evolution, residual stresses and distortions in 6082-T6 aluminum weldments. *Welding Journal ; VOL. 77 ; ISSUE: 7 ; PBD: Jul 1998*, pp. 286.s.
Nabarro, F.R.N. (1967) *Theory of crystal dislocations*. Oxford,: Clarendon P.
Nabarro, F.R.N.; Duesbery, M.S. & Hirth, J.P. (1979) *Dislocations in solids*. Amsterdam ; New York: North-Holland Pub. Co.

Orowan, E. (1948) *Symposium on Internal Stresses in Metals and Alloys, Session III discussion*.

Ostwald, W. (1900) Über die Vermeintliche Isomeric des Roten und Gelben Quecksilberoxyds und die Oberflächenspannung Fester Körper. *Z. Phys. Chem.,* 34, 495.

Pandey, A.D., (1995) A process model for age-hardening in aluminum-lithium alloy AA8090. The University of Regina (Canada), Canada.

Polmear, I.J. (2006) *Light alloys : from traditional alloys to nanocrystals,* 4th edn. Amsterdam ;: London : Elsevier Butterworth-Heinemann.

Porter, D.A. & Easterling, K.E. (1992) *Phase transformations in metals and alloys,* 2nd edn. London ; New York: Chapman & Hall.

Robson, J.D. (2004a) Microstructural evolution in aluminium alloy 7050 during processing. *Materials Science and Engineering A,* 382, 112.

Robson, J.D. (2004b) Modelling the overlap of nucleation, growth and coarsening during precipitation. *Acta Materialia,* 52, 4669.

Robson, J.D. (2008) Modelling precipitation in zirconium niobium alloys. *Journal of Nuclear Materials,* 377, 415.

Robson, J.D.; Jones, M.J. & Prangnell, P.B. (2003) Extension of the N-model to predict competing homogeneous and heterogeneous precipitation in Al-Sc alloys. *Acta Materialia,* 51, 1453.

Rometsch, P.A. & Schaffer, G.B. (2002) An age hardening model for Al-7Si-Mg casting alloys. *Materials Science and Engineering A,* 325, 424.

Sanders, T.H., 1980, *Stone Mountain, Ga*.

Shercliff, H.R. & Ashby, M.F. (1990a) A process model for age hardening of aluminium alloys--I. The model. *Acta Metallurgica et Materialia,* 38, 1789.

Shercliff, H.R. & Ashby, M.F. (1990b) A process model for age hardening of aluminium alloys--II. Applications of the model. *Acta Metallurgica et Materialia,* 38, 1803.

Shewmon, P.G. (1963) *Diffusion in solids*. New York,: McGraw-Hill.

Starke, E.A. (1977) Aluminium alloys of the 70's: Scientific solutions to engineering problems. An invited review. *Materials Science and Engineering,* 29, 99.

Swalin, R.A., (1962) *Thermodynamics of Solids*. Wiley, New York

Wagner, C. (1961) Theorie der alterung von niederschlägen durch unlösen. *Z. Elektrochem,* 65, 581.

Wagner, R.; Kampmann, R. & voorhees, P.W., (1991) Homogeneous second-phase precipitation. In: *Materials science and technology : a comprehensive treatment*. Cahn, R.W.;Haasen, P. & Kramer, E.J. (Eds.). Wiley-VCH, Weinheim.

Wilm, A. (1911) Physikalisch-metallurgische untersuchungen über magnesiumhaltige aluminiumlegier ungen. *Metallurgie,* 8, 225.

16

Metallographic Etching of Aluminium and Its Alloys for Restoration of Obliterated Marks in Forensic Science Practice and Investigations

R. Kuppuswamy
Forensic Science Programme, School of Health Sciences, Universiti Sains Malaysia Malaysia

1. Introduction

1.1 The problem

A problem of common occurrence in forensic science is the restoration of obliterated serial numbers on the chassis and engine of stolen motor vehicles, firearms, jewellery, valuable tools, and machinery (Nickols, 1956; Wolfer & Lee, 1960; Jackson, 1962; Cunliffe & Piazaa, 1980; De Forest & Gaensslen, 1983; Schaefer, 1987; O'Hara & O'Hara, 1994; Moenssens *et al* (1995); Heard, 1997; Petterd, 2000; Lyle, 2004; Katterwe, 2006; Seigel, 2007; Mozayani & Noziglia, 2006; Jackson *et al* (2008); Levin, 2010). Serial numbers or other markings, which are unique to that particular item, are usually marked on the above metal surfaces during the manufacturing process. Criminals alter or obliterate these identification marks during thefts or other illegal uses in order to prevent their identity. On many occasions a fraudulent number would be introduced after removing the original one. In abandoned vehicles all serial numbers are verified in order to detect alterations in the identity of the vehicle (Svensson *et al*, 1981). Sometimes the serial numbers on firearms are removed more professionally making it hard to distinguish whether the numbers are original or not (Shoshani *et al*, 2001). Restoration of the original obliterated numbers provides important forensic evidence in order to return the items to the owner and also to follow up the criminal proceedings against the perpetrator. In cases involving firearms the recovered numbers provide an important investigative lead. The history and the ownership of the firearm can be obtained only from the serial number. In forensic practice a few experimental techniques are being used successfully to restore the obliterated serial numbers on the above surfaces. The methods include: *chemical etching, heat treatment, magnetic particle, ultrasonic cavitation and relief polishing* (Nickols, 1956; Polk & Giessen, 1989; Maxwell, 1993; Heard, 1997; Hogan *et al*, 2006; Katterwe, 2006). Nondestructive methods such as hardness testing, magnetic imaging, x-ray imaging, eddy current, infrared imaging, scanning acoustic microscopy, electron channeling contrast and thermal wave imaging are also proposed (Hogan *et al*, 2005; Katterwe, 2006; Klees, 2009). However, chemical etching is most popular because it is sensitive, easy to apply on any size and also kind of object and reproducible. Etching can be applied on all metal surfaces including precious ones (Crowe & Smith, 2005).

This chapter presents background information on serial number restoration and etching techniques applied to recover the obliterated markings on aluminium and especially two of

its important alloys, Al-Zn-Mg-Cu and Al-Si. The etching results arising from some of these surfaces are illustrated. For the sake of completeness, some brief notes on the classical recovery of obliterated marks on iron and steel surfaces and use of methods other than chemical etching are also added.

1.2 Serial number marking methods

The common methods of marking objects include: *stamping, pin stamping, type wheel marking, engraving, laser etching* and *embossing* (Collins, 1999; Petterd, 2000; Katterwe, 2006). The serial numbering on motor vehicles and firearms is generally performed by *stamping*. In this process the steel die bearing the digit is struck with a single stroke manually or using a pressing machine. This causes an indented character. The amount of pressure applied per character to achieve a certain depth depends on the hardness of the metal surface. In *pin stamping* small pins are used to form individual dots on the substrate. Like in stamping, metal is being compressed beyond its elastic limit and a permanent impression is created. The impact pin is made of tungsten carbide and is driven rapidly toward the surface to be marked. Pin stamping is applied to mark vehicle identification number (VIN). *Type wheel markings* are made in a hydraulic press with type wheels controlled by computers. This type of marking is used by some automobile manufacturers with VIN. *Engraving* is a chip cutting operation where the substrate is cut away by a tiny spinning head leaving the marks. *Laser etching* uses an intense laser beam operated by a computer controlled system. Quality, depth and precision of laser marking are controlled by laser frequency, scan speed and Q-switching. Automobile components and modern firearms are currently being marked by laser. The characters are usually shallow and they are visible to the eye only because the heat of the laser changes the appearance of the metal inside each character (Collins, 1999). *Embossing* is similar to die stamping, but used on thin plates. The die is pushed onto the plate from behind producing a raised appearance of the marks.

1.3 Stress and deformation on the metal

Metallurgical aspects of serial number recovery are described in (Turley, 1987; Polk & Giessen, 1989; Collins, 1999; Petterd, 2000; Katterwe, 2006; Hogan *et al*, 2006). The atoms within metals of interest have a three dimensionally periodic crystalline arrangement within local regions. These regions are called grains. Between the grains are interlocking regions known as grain boundaries. The strength of these boundaries relates directly to the strength of the metal surface and its ability to resist stress. When a number is stamped onto a metal surface using sufficient pressure, the metal is unable to resist it and a permanent change in shape takes place. The grains around and beneath the indented characters are deformed and the alignment of the crystal structure is altered. This deformation known as cold work will not only be confined to the crystals immediately below the character, but will extend to a considerable region below the impression. The deformation is carried deeper than the depth of the marking themselves. This can be referred to as zone of plastic strain. Thus, the stamping operation produces a visible indentation of the mark and a plastically deformed region underneath it extending to a considerable depth. Significantly, an imprint of the mark is latent below the visible indentation in the form of plastically deformed regions. In other words, the region of plastic strain carries information of the stamped number and it is crucial to number restoration in forensic investigations. Depth of this strain is dependent on the metal, the size and shape of the die and the force used to produce the indentation.

Experiments have demonstrated that in case of zinc the zone may run to depths of at least 20 times the depth of the deepest character (Kehl, 1949), while in steel the affected region may be six times as deep as the stamped mark (Thornton & Cashman, 1976). In cases of engraved marks on steel and aluminium surfaces the depths of recoverable deformations varied between 2 and 3 times the depths of engraving (Azlan *et al*, 2007; Izhar *et al* 2008; Bong & Kuppuswamy, 2010; Uli *et al*, 2010).
In cases of marks produced by pin stamping and engraving the depth of plastic deformation or strain is not as great as in stamping. Pin stamped and engraved characters, if obliterated, can be recovered but are more sensitive to the depth of erasure (Collins, 1999). Laser etching on the other hand has no deformation but produces heat affected zone (HAZ). The depth of this zone will depend on the intensity of the laser and scan speed.
The properties of the metals are known to change because of the altered crystalline structure of the metal during marking a number (Thornton & Cashman, 1976; Polk & Giessen, 1989; Hogan *et al*, 2006). The cold worked or deformed region has physical and chemical properties different from that of nondeformed metal. Important property changes are an increase in hardness and decrease in ductility and yield stress. In addition changes occur in the electrical resistivity, the magnetization behaviour of ferromagnetic alloys, the electronic work function and the chemical potential among others. Every one of these property changes is used advantageously to detecting the plastically deformed regions that are residually present after the visible indentations of serial numbers have been removed. For example, hardness differences are exploited in chemical etching, ultrasonic cavitation and relief polishing, while differences in magnetic properties are utilized in magnetic particle method. Heat treatment applicable to cast iron substrates relies on the residual stresses present below the stamped region (Kehl, 1949; Maxwell, 1988; Katterwe, 2006).

1.4 Methods used for the removal of the markings

Criminals have used the following methods for the removal of the serial numbers: *filing or grinding, peening, welding and drilling* (Cook, 1989; Heard, 1997; Petterd, 2000; Katterwe, 2006). During grinding or filing the marks are usually removed till the base of metal so that the number would no longer be visible. If the erasure of the serial number does not go deep enough to remove the underlying plastic zone, the obliterated marks may be restored by suitable methods. But, if the metal removal extends entirely into the plastic region, the numbers cannot be recovered. Sometimes the perpetrator after grinding the area will polish it and substitute a false number. This process introduces a new deformation overlying the original deformation.
Occasionally, there will be no removal of metal by grinding but the marks will be defaced by peening so that they will not be discernible. This alteration involves hammering the mark using centre punch or cold chisel. The degree of deformation caused by peening can vary. If the deformation caused by peening operation is localized or superficial recovery may be possible.
Drilling and welding of the area bearing numbers are also encountered. With drilling, the outline of the numbers may sometimes become visible by careful polishing of the area and examining it using a stereomicroscope under oblique lighting conditions. However, when the numbers are fused by welding, the recovery is almost impossible. Here the plastic strain carrying the original number would be relieved due to heating.
Markings may also be converted using dies of similar size and style. For example, the digit 6 can be changed into 8. A careful examination under magnification will reveal in such cases

discontinuity of the outlines, unevenness of stamping and additional marks (Massiah, 1976; Kuppuswamy & Senthilkumar, 2004).

2. Etching of metal surfaces for restoration of obliterated marks

Macroetching techniques are probably the most informative and widely used for quality control, failure analysis and in research studies in material science (Vander Voort, 1984). The mechanical inhomogeneity in a metal caused by stamping or other marking process will be determined by macroetching the obliterated surface and examining the marks revealed with the unaided eye or with the aid of a hand magnifier.

A wide variety of chemical etching reagents for iron and steel and common nonferrous metals and alloys are available in literature (Kehl, 1949; Nickols, 1959; Metallographic reagents for iron and steel, 1974; Massiah, 1976; Petzow, 1976; Vander Voort, 1984). Detailed etching procedures and time of etching are also compiled therein. Composition of the alloy will strongly influence the choice of a particular etchant.

Before the etching process begins, the item should be photographed showing details of the obliterated area. If necessary, the area may be dusted with fingerprint powder and lifted with tape. The area should be degreased using alcohol/acetone before any surface preparation.

2.1 Mechanism of etching

Etching is basically a controlled corrosion process resulting from electrolytic action between surface areas of different potential (Kehl, 1949; Vander Voort, 1984; Polk & Giessen, 1989). The etching solution does not act in a uniform manner on different faces of the crystals, or on different areas of the grain. The cold worked regions are known to be chemically more reactive, as the position of the deformed metal in the electromotive series is raised. Hence they will dissolve in an acid at a more rapid rate than the surrounding unaffected regions (regions not affected by stamping). The desired result is a local change in reflectivity of light that reveals the obliterated marks (Polk & Giessen, 1989; Thornton & Cashman, 1976). Thus the etching technique relies on the difference in the etching behaviour between the deformed and undeformed regions in order to produce the desired image contrast.

2.2 Surface preparation

Metallurgical literature devotes considerable attention to specimen preparation before etching (Kehl, 1949; Vander Voort, 1984; Vander Voort, 1986). The steps mainly include grinding (using coarse abrasives) and subsequent polishing of the metal surface (using fine abrasives) in order to study the microscopic structural characteristics. However in forensic practice the area of the engine/chassis number of a car, for example, may contain a lot of scratches and gouges caused during the obliteration of the number. A careful microscopic examination with illumination from low angle will sometimes reveal traces of the numbers against the scratches prior to any surface preparation (Matthews, 1962; Srinivasan & Thirunavukkarasu, 1996). The presence of the cutting marks, however, may interfere with the interpretation of the recovered marks during etching. Hence the obliterated surface should be made smoother by use of emery papers of different grades starting from coarser grades and finishing with finer ones (Polk & Giessen, 1989; Katterwe, 2006). Careful polishing producing smooth finish free from all grinding scratches is to be preferred. This is important as such scratches may affect the contrast of the recovered number. However care should be taken that more metal that includes the residual deformation zone is not removed during preparation stage.

Sometimes the obliterated serial number plate of a firearm has to be removed and examined from its back to reveal the negative impression caused by the stamping of the front side of the plate (Cooper, 2002).

2.3 Etching technique

Chemical etchants are used at room temperature either by swabbing the sample or immersing and gently agitating it (Kehl, 1949; Nickols, 1959; Massiah, 1976; Petzow, 1976; Vander Voort, 1984; Katterwe, 2006). The surface is swabbed by use of cotton-tipped applicator. The cotton should be dipped regularly in fresh etchant and applied until the desired contrast is obtained. The swab is moved slowly back and forth across the surface with gentle pressure. The surface is observed closely for the appearance of any marks. Swabbing is mostly preferred in number restoration, as it provides control over etching technique. Immersion is preferred in cases where restoration is slow to developing. In such situations a small surround of plasticine is built around the obliterated area and the reagent is filled within (Nichols, 1959; Petterd, 2000). The reagent is removed at intervals and replenished. Control of the etching time is important as the obliterated numbers would appear and disappear during the etching. While some restorations appear within minutes of reagent application, others would take about an hour or more. Under-etching fails to reveal the obliterated marks, while over-etching destroys the recovered marks. As etching time and temperature are closely related, it is desirable to do etching at room temperature.

2.4 Photography of the recovered marks

Photography is the best method for permanent record of the restored marks. Photographic methods are similar to those used for recording latent fingerprints and also documents dealing with obliterations. Recovered marks are inherently very faint and the contrast with the background would be usually poor. They can further be seen only at certain angles of illumination. The examiner should be familiar with close-up and macrophotographic techniques. In cases of firearms where the specimen is relatively small, macrophotography of the marks can be carried out in the photo-copying stand using appropriate illumination. However, when dealing with engine and chassis of cars the camera has to be set up on an adjustable tripod. Several exposures are to be made by shifting the light source so that it illuminates the surface from different directions. Black and white photography using high contrast film may also help to bring out the faint outlines of the number. Light reflected by a mirror may be advantageously used to record the faintly recovered digits. A combination of flash and available light sources is also recommended (Katterwe, 2006). Current digital photographic techniques provide greater advantage offering contrast enhancement software procedures. Sometimes the area carrying the recovered marks was dusted with fluorescence finger printing powders (Lightning Redwop and Lightning Greenwop) and a piece of clean cellophane tape was used to lift the marks. The lifted tape, when viewed through a 550 nm barrier filter using an alternate light source at 450 nm bandwidth, produced excellent contrast of the marks (Nalini & Hemalatha, 2003).

2.5 Specimen storage after etching experiments

When the etching examination is completed the area of the chassis, engine or frame of firearm should be thoroughly washed in a stream of distilled water and acid neutralized using ammonia (Nicholls, 1956; Massiah, 1976). The surface should be dried and the area is covered with grease or shellac to prevent oxidation or further etching. When cars and

firearms are to be stored for long periods of time during criminal proceedings, they must be protected from atmospheric corrosion.

3. Macroetchants for revealing strain patterns in steel

In metallurgical investigations visualization of macrostructure is carried out by macroetching (Kehl, 1949; Petzow, 1976; Vander Voort, 1984). For study of steels strong acids were used initially for "deep" etching. Later copper-containing macroetchants were used for studying primary structure. These procedures were quite unsuitable to develop the plastically deformed regions in order to reveal the obliterated marks. It was Fry in 1921 who published macroetchants for revealing strain patterns on iron and steel (Vander Voort, 1984). His reagent is very popular even today and has many variations. The most popular composition is cupric chloride 90 g, hydrochloric acid (conc.) 120 ml and water 100 ml, which is used exclusively to restore marks on the chassis and engine of motor vehicles and frames of firearms. This solution contains considerable HCl that keeps the free copper from depositing on the sample during etching (Vander Voort, 1984). Applying this reagent many successful recoveries are reported in literature (Nickolls, 1956; Matthews, 1962; Wilson, 1979; Heard, 1997; Kuppuswamy & Senthilkumar, 2004; Warlow, 2004; Wightman & Matthew, 2008; Siaw & Kuppuswamy, 2009). (Turley, 1987) used this reagent to study the relationship between the depth of the stamp mark and the depth to which stamp marks could be recovered on plain carbon steels ranging in carbon content from 0.04 to 0.52% C. He noted that the depth of restoration increased with increased depth of stamp mark. However, the increase was nonlinear. He also found that etching with this reagent was superior to magnetic techniques for old stamp marks and also to recover the marks obliterated by overpunching. More recently (Azlan *et al*, 2007) found one variation of Fry's reagent with composition of 5 g $CuSO_4$, 60 ml water, 30 ml conc. ammonium hydroxide and 60 ml water to be most sensitive to low carbon steel surfaces, while (Siaw & Kuppuswamy, 2009) noted that the most popular one (90 g $CuCl_2$, 120 ml HCl (conc.) and 100 ml H_2O) to be quite effective on medium carbon steel surfaces used in the chassis of cars. Recently (Wightman & Matthew, 2008) reported that even though Fry's reagent was an effective etch for recovering erased marks in steel, ageing of the reagent gave a decrease in performance and took longer time to etch. The same authors (Wightman & Matthew, 2008a) have proposed thixotropic etching paste of Fry's reagent using alumina which provided more controlled chemical attack with obliterated surfaces and found that the recovery was better. Thus Fry's composition is contributing enormously to the success of serial number restoration for steel surfaces for many decades. (Heard, 1997) remarked that although Fry's reagent is the best for steel, it can also be used, with care, on any other material. (Massiah, 1976) also reported that usual reagents for aluminium when used along with Fry's reagent would be more effective.

4. Restoration techniques for aluminium and its alloys

Etching techniques for obliterated stamped marks for iron and steel using Fry's reagent have been described in detail in forensic literature more than any other metal because of the greater use of these in automotive engines and chassis and also firearms. There has been frequent tampering of serial numbers on these items. An important development which is of concern to forensic examiners is in the use of aluminium alloys in motor vehicle components and more especially in frames of firearms. Aluminium is a relatively weak material. For

applications requiring greater mechanical strength it is alloyed with metals such as copper, magnesium, manganese and zinc, usually in combination with two or more of these elements together with iron and silicon (King, 1987). Aluminium alloys are widely utilized in various structures and components because of their good strength and low density. In addition many automobile parts have been manufactured with Al alloys instead of steel materials to reduce the weight of the car (Okayasu *et al*, 2008). In addition many firearms like Ruger pistol, Czechoslavakian P-01 pistol, S & W Special Airweight Airlite revolver and Brazilian pistols use aluminum alloy frames. Ergal, a hard aluminium alloy (AA 7075) is also used for manufacturing firearms (Bond, 2008).

4.1 Recovery of stamped marks by chemical etching

Many etching reagents are recommended in metallurgical literature for aluminium alloys (Mondolfo, 1943; Kehl, 1949; Nickols, 1956; Massiah, 1976; Petzow, 1976; Vander Voort, 1984). Among them sodium hydroxide is one of the reagents most commonly employed in a variety of concentrations. All these reagents are mainly useful in material science investigations for the identification of the constituents of the alloy or the crystals themselves. However, only a few etchants among them will be able to reveal the plastic deformation zones carrying original markings. Recovery of marks on aluminium surfaces unlike steel is difficult. There has been no popular reagent to etch aluminium surfaces as we find in Fry's composition for steel. The standard reagents used in etching on iron and other metal surfaces provide too vigorous reaction with aluminium resulting in pitted metal and blurred results (Chisum, 1966). There have been a few attempts in the past to identify suitable etchants. These works are summed up below.

(Nickolls, 1956) recommended the use of Villela's solution comprising 2 parts HF, 1 part HNO_3 and 3 to 4 parts glycerin, as it responded to treatment to all aluminium alloys. For castings made with high silicon alloys he suggested to give a quick rub with Hume-Rothery's reagent: 200 g $CuCl_2$, 5 ml HCl, and 1 l H_2O. He also illustrated successful restoration on an aluminium crank case developed with this procedure. Villela's reagent should not be stored in glass bottles. (Masssiah, 1976) compiled a list of etchants for different metal surfaces and his work is a useful reference for number restoration procedures. He advocated use of the reagent comprising 200 ml (conc.) HCl and 200 ml distilled water. This mixture was saturated with cupric ammonium chloride. He also suggested diluting the above reagent for optimal results on different aluminium alloys. (Chisum, 1966) used the following reagents: (i) 1N NaOH and (ii) 0.1M $HgCl_2$ in 0.1N HCl after polishing by sanding. A preliminary wash of the surface with 1N NaOH gave more even coating of Hg. After removing this wash, a solution of 0.1M $HgCl_2$ was applied with a cotton swab. The numbers appeared after the aluminium oxide mass was blown off. The mercury coating catalyzed the oxidation of aluminium and the number became visible because plastically deformed regions oxidized faster than the surrounding metal (Polk & Giessen, 1989). The working time excluding of polishing was 20 min. Brown (2001) noted that the Ruger P-Series aluminium alloy framed pistol was found to be most difficult to restore erased serial numbers. He used acidic ferric chloride chemical reagent (25 g $FeCl_3$, 25 ml HCl, and 100 ml H_2O) after polishing the metal surface using water and 600-grit sand paper. He used a modified application of the etchant. The reagent was added drop wise using saturated cotton tipped swab and the tip of the swab was lightly pressed directly to the frame and removed. No wiping of the swab across the frame was performed. The reagent effervesced for 1 to 2 min and was removed by spraying with distilled water. After a few

applications of the above procedure for 10 min the number appeared as darker "ghostly" lettering. The contrast however was extremely poor and ring lighting and oblique lighting did not improve it. (Klees, 2002) reported a case in which the serial number and barcode of a Smith & Wesson pistol was obliterated by abrading. The serial number area of the pistol consisted of nonferrous metal pad surrounded by a polymer skin. This metal pad was laser etched with 3/32"alphanumeric characters. He used a chemical etching reagent with a low corrosive rate with the nonferrous metallic media to fully restore the serial number and partially restored barcode. He however did not mention the composition of the reagent he used. Importantly, he described procedures on how to decrypt manually the partially recovered barcode. (Peeler *et al*, 2008) developed stamped marks on Al motor cycle frames that involved the swabbing of 60% HCl for about 1 h or until "drag" was felt on the swab, then flushing with water to remove all etchant and continuing etching with 40% NaOH until no further darkening of the surface was observed. The cycle was repeated if necessary. The etching took as nearly as 6 h for acid swabbing followed by alkali swabbing for about 1 h. The time varied according to the substrate. The materials they tested were Al-Si and Al-Mg alloys. They reported that many numbers were able to be recovered without the use of the alkali; however the use of the alkali after acid swabbing enhanced the contrast between stamped and unstamped areas. They also successfully used the above method for restoration of 9 motorcycle frames involved in criminal cases.

It is known that the strain patterns in most metals can be revealed by annealing the specimen after deformation so as to obtain recrystallization. In the region that receives critical amount of strain, generally 5 to 8%, grain growth is more rapid (Vander Voort, 1984). This area is visualized more clearly on etching. (Okayasu *et al,* 2008) used this principle to reveal the plastic deformation zone in aluminium alloys such as 2017 duralumin. A severe plastic deformation was imposed by applying a compressive force of 5 kN at a rate 1 mm/min onto the specimen. The deformed samples were heated to 673 K for 3 h. The surface was polished to mirror finish and etched for 1 min using Dix-Keller reagent consisting of 4 ml HF, 6 ml HCl, 8 ml HNO_3, 80 ml H_2O and 50 ml ethyl alcohol. After etching the plastic deformation zone was darkly etched, but the undeformed zone lightly etched. The deformation zone was in agreement with the microhardness measurements.

Although the etching methods described above are the most important and widely used procedures for revealing the obliterated marks on aluminium surfaces, it is sometimes possible to restore the obliterated numbers by methods other than etching.

4.2 Recovery of embossed marks using x-ray radiography

X-ray radiograph is known to detect internal variations and defects in metals and it provides permanent records in the form of photographic films and image files (Jeon *et al,* 2009). The use of X-rays to recover obliterated marks has not been successful to visualize the minute damaged areas left after the removal of the number (Petterd, 2000; Katterwe, 2006). However, the method has been successfully used to locate serial numbers that have been hidden with paint or by welding another piece of metal on top of the original (Nickolls, 1956; Petterd, 2000; Katterwe, 2006). (Jeon *et al,* 2009) investigated the forged embossed numbers on car license plates of 1-mm thick and 335x170 mm aluminium sheet. In this case the criminals had obliterated the original number by painting the plate and flattened it by hammering. They then embossed a new number over the flattened one and painted it. However, when the plate was exposed to x-rays with 30 kV/mm and 20 mA for 2 min and

the resultant radiographs were treated with image processing programme the original numbers appeared quite distinctly.

4.3 Recovery of laser etched marks—alternate approaches

4.3.1 Relief polishing

Relief polishing works successfully where it is known that an alloy is composed of relatively hard and soft structural constituents. By hand polishing it is possible to abrade the softer constituent at a greater rate than the harder one, thus leaving the harder phase in bold relief at the end of the polishing operation. When such polished specimen is examined microscopically using oblique illumination difference between structural details will be seen (Kehl, 1949; Katterwe, 2006). Following this principle (da Silva & dos Santos, 2008) restored the partially obliterated laser engraved serial number on aluminium-alloy frames of Brazilian pistols. It is known that laser engraving creates heat affected zone of 2-25 μm which has greater hardness than the rest of the metal. The obliterated area was polished using abrasive papers 600, 1200 and water. The images were captured in a stereomicroscope while the polishing was on. The scratches caused during obliteration of the number were removed at a faster rate than the original marks produced by the laser and the original numbers became visible. This was due to the difference of hardness in the regions where the number was written by laser and the remaining region of the frame. The difference in removal rates allowed the original digits or fragments of them to appear. However, these authors noted that relief polishing cannot be applied to frames which are damaged or carrying deep scratches. Such polishing removed both the digits and the scratches.

4.3.2 Adobe Photoshop

(Klees, 2009) recently used Adobe Photoshop in one real forensic investigation. Here, the laser-etched bar code and serial numbers of a Smith & Wesson pistol were partially obliterated. A digital photograph of the obliterated area was produced and enhanced for brightness and contrast using Adobe Photoshop. This procedure increased the visibility of the partial characters and bars. Using the magnifier and Line tool, the obliterated portion of the bars were redrawn and scanned with a barcode reader to detect the original marks.

4.4 Restoration of obliterated mechanically engraved marks—recent findings

The present author along with Izhar and Rahman (Izhar *et al*, 2008), Bong (Bong & Kuppuswamy, 2010), and Norjaidi and Firdaus (Uli *et al*, 2010) reviewed the sensitivity and efficacy of some common etchants on Al (99% purity), Al-Zn-Mg-Cu and Al-Si alloys. High strength Al-Zn-Mg-Cu alloy finds applications in automobile components and frames of firearms, while Al-Si alloy is used as motor vehicle engines. The chemical composition of the aluminium specimens they investigated is given in **Table 1.**

Specimen	Cu	Mg	Si	Fe	Mn	Zn	Pb	Ni	Zr
Al (99% purity)	0.05	0.51	0.360	0.250	0.017	0.008	--	--	--
Al-Zn-Mg-Cu alloy	1.6	2.4	< 0.12 (Si+Fe)		--	6.3	--	--	0.14
Al-Si alloy	2.18	0.20	10.76	0.84	0.18	0.75	0.054	0.076	--

Table 1. Chemical composition of the aluminium specimens in % weight.

The experimental details and the results are summed up below.
Every one of the aluminium specimens (refer **Table 1**) was cut into small plates and marked with some characters by use of a computer controlled engraving machine "Gravograph". The machine made reproducible marks. The depths of engravings were between 0.02 to 0.03 mm (the difference in thickness before and after erasure of the marks). Engraved marks on the specimen plates were obliterated by grinding the marks (using sand papers of different grades - P80, P150 and finished with fine grade P320) to different depth levels upto and (0.01, 0.02, 0.03, 0.04 mm etc) below the bottom of the engraving depth. Several of such plates erased to different depth levels were prepared.
Further, engraved marks on some plates were obliterated by (i) peening, using centre punch till the marks were no longer discernible, and (ii) grinding the original marks and engraving a new mark over the erased area. The obliteration methods were comparable to those encountered in real forensic cases.
Eight metallographic etchants of which some contained NaOH in different concentrations alone or together with an acid were used. The reagent composition and the references are given in **Table 2.**

Serial number	Reagent Composition	Reference(s)
1	1. Hydrochloric acid 60% 2. Sodium hydroxide 40%	(Peeler *et al*, 2008) (Izhar *et al*, 2008)
2	10% aq. phosphoric acid	Mondolfo, 1943 Petzow, 1976 Vander Voort, 1984
3	1. 10% Sodium hydroxide 2. 10% Nitric acid	Petterd, 2000
4	1. Sodium hydroxide 10 g 2. Water 90 ml	Mondolfo, 1943 Kehl, 1949 Petzow, 1976 Vander Voort, 1984 Petterd, 2000 (Dong *et al*, 2005) Katterwe, 2006
5	Acid ferric chloride 1. Ferric chloride 25 g 2. Hydrochloric acid 25 ml 3. Water 100 ml	(De Forest *et al*, 1983) Brown, 2001
6	1. 1N sodium hydroxide (1 mol/l) 2. 0.1M mercuric chloride aq. (0. 1 mol /l) in 0.1N Hydrochloric acid (0.1 mol/l)	Chisum, 1966 (Polk & Giessen, 1989) Rowe, 2003
7	Hume -Rothery reagent 1. Cupric chloride 15 g in 100 ml of water 2. 50% HNO_3	Mondolfo, 1943 Vander Voort, 1984
8	Nital* 1. 1 part Nitric acid 2. 9 parts Ethanol	(Cunliffe & Piazza, 1980)

Table 2. Etching reagents used to restore erased engraved marks on aluminium and its alloy surfaces.

*Nital solution is a highly flammable liquid and concentrations greater than 5% should never be stored, as at 10 % it is comparable to rocket fuel in its volatility (Vander Voort, 1984).

No additional polishing was carried out before etching as the surfaces were previously smoothed during the erasure of the marks. Further polishing had the danger of removing the plastic zone which was of the order of micrometers in cases of engraving.

The specimen surfaces erased to different depths by grinding were etched with every one of the reagents given in **Table 2**. The reagents were applied either by swabbing or immersion (10% aq. phosphoric acid reagent only) and the recovery was closely monitored. The most efficacious reagent was determined to be the one which restored the marks on the plate erased to maximum depth and also that provided good contrast of the recovered marks with the background.

The selected reagent was then tested to recover marks on plates obliterated by peening and overengraving.

Among the eight common metallographic reagents tested, reagents 4 to 8 (in **Table 2**) did not give the desired contrast and sensitivity (see for details Izhar *et al*, 2008; Bong & Kuppuswamy, 2010; & Uli *et al*, 2010) and hence were not suitable. The reagents 1 to 3 produced superior results both in terms of contrast and sensitivity for etching specific aluminium surfaces.

The reagent 1, 60% HCl and 40% NaOH on alternate application on *aluminium (99% purity)* (Izhar *et al*, 2008) and *Al-Zn-Mg-Cu alloy* surfaces (Bong & Kuppuswamy, 2010) were quite successful for recovering the marks obliterated by erasure, overengraving and peening. These are seen in Figs. 1 to 6. The success of alternate application of acid and alkali to

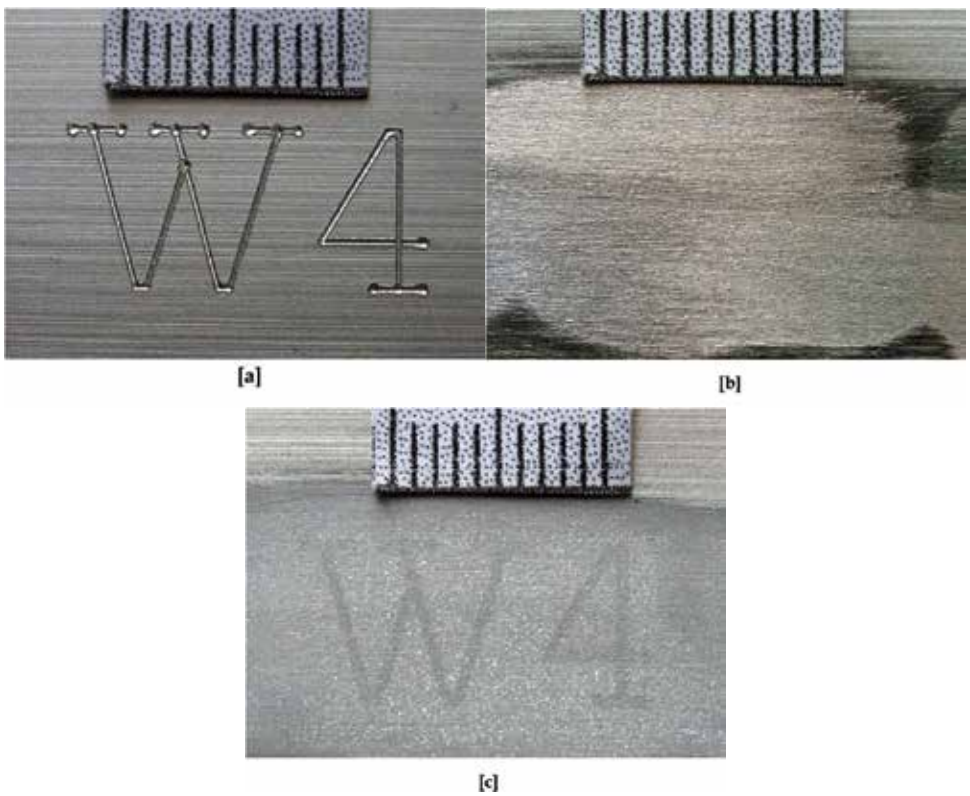

Fig. 1. a) The original engraved marks "W4" on Al (99% purity). b) Surface after grinding of the marks up to the depth of engraving (0.02 mm). c) The recovered number "W4" after etching process. Etching reagent: Alternating swabbing of 60% HCl and 40% NaOH. Etching time: 28 min.

Fig. 2. a) Original engraved marks MO3 on Al (99% purity) surface were erased (hence not seen) and a new marks W98 were engraved over the erased area. b) The original marks MO3 were restored in the presence of the new marks W98. Note partial overlapping of the original digits "0" and "3" respectively with the new ones "9" and "8". Etching reagent: Alternating swabbing of 60% HCl and 40% NaOH. Etching time: 20 min.

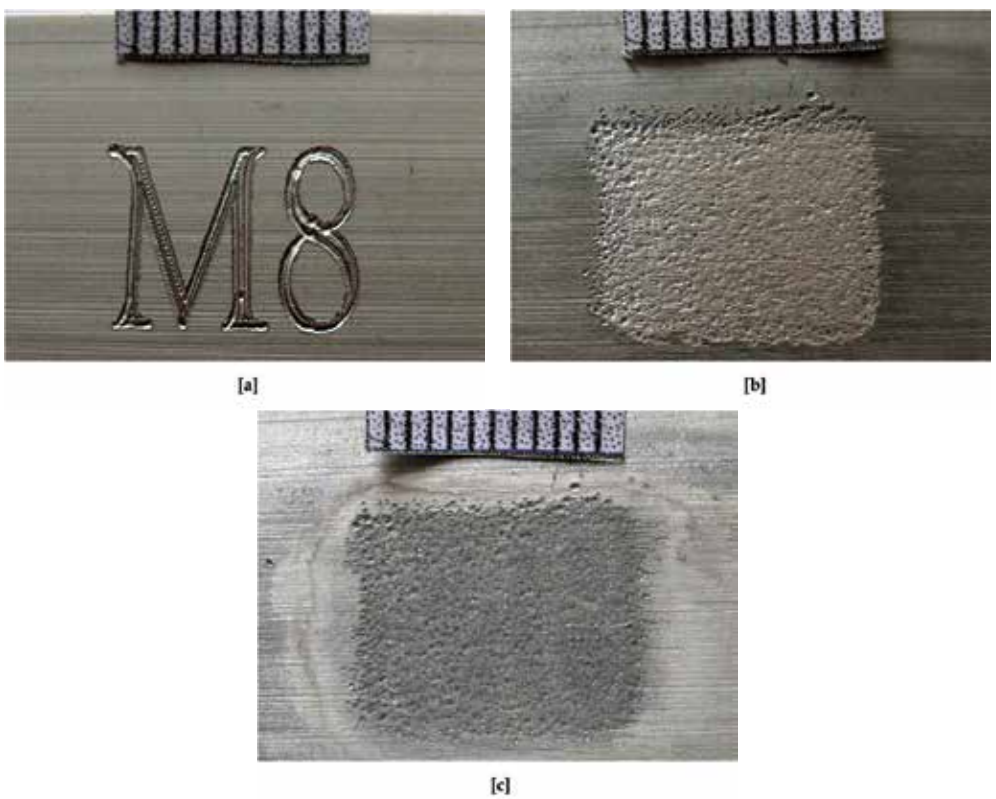

Fig. 3. a) The original engraved marks M8 on Al (99% purity). b) The marks were obliterated by peening using centre punch. c) See the outline of the recovered marks M8. Etching reagent: Alternating swabbing of 60% HCl and 40% NaOH. Etching time: 20 min.

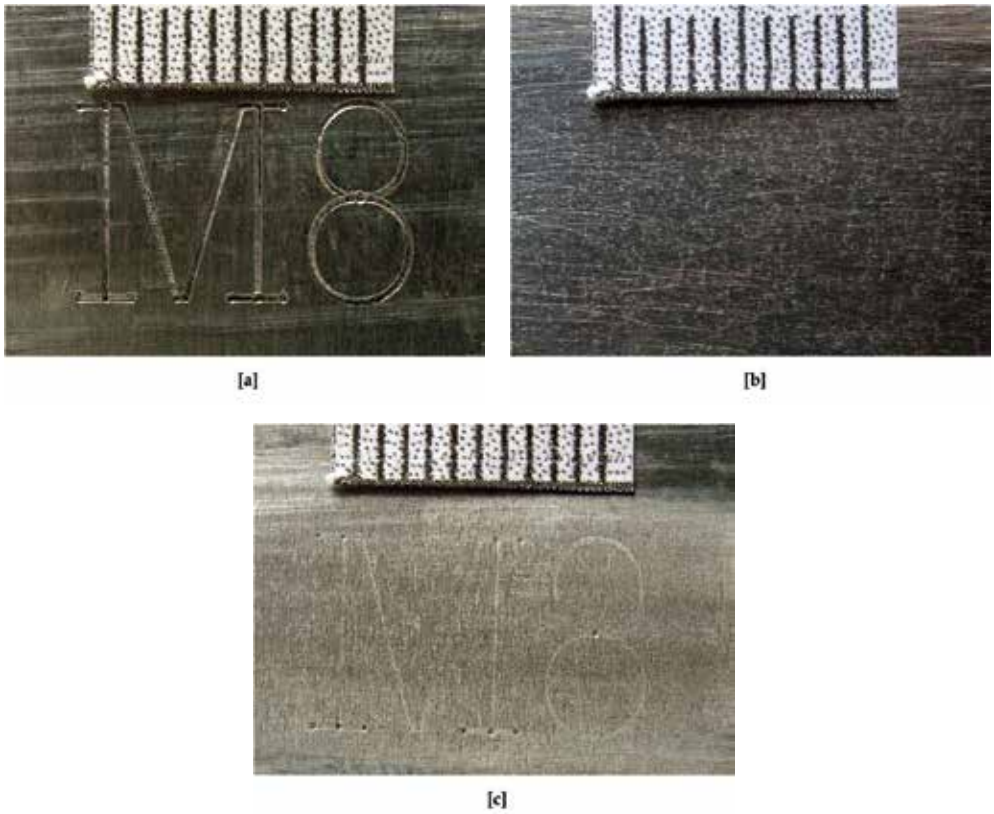

Fig. 4. a) The original engraved marks "M8" on Al-Zn-Mg-Cu alloy surface. b) Surface after grinding of the marks up to the depth of engraving (0.02 mm). c) The recovered number "M8" after etching process. Etching reagent: Alternating swabbing of 60% HCl and 40% NaOH. Etching time: 16 min.

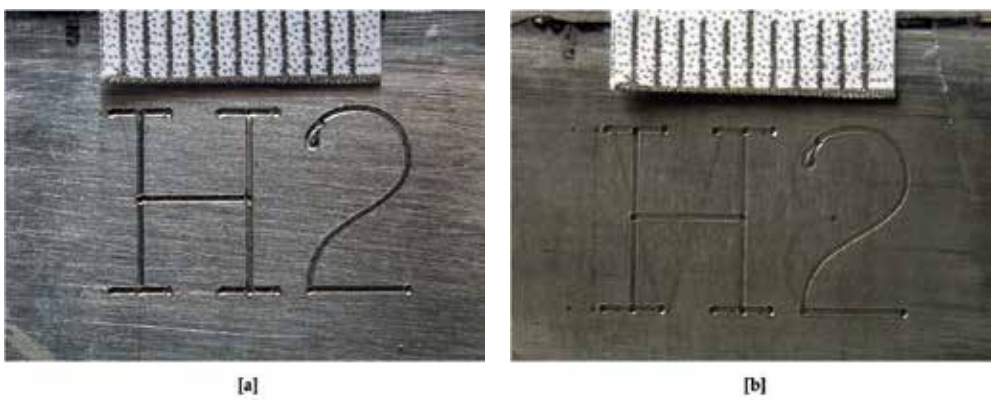

Fig. 5. a) Original engraved marks "M8" on Al-Zn-Mg-Cu alloy surface were erased (hence not seen) and in their place a new marks "H2" were engraved. (b) The original marks "M8" were restored faintly in the presence of "H2". Etching reagent: Alternating swabbing of 60% HCl and 40% NaOH. Etching time: 32 min.

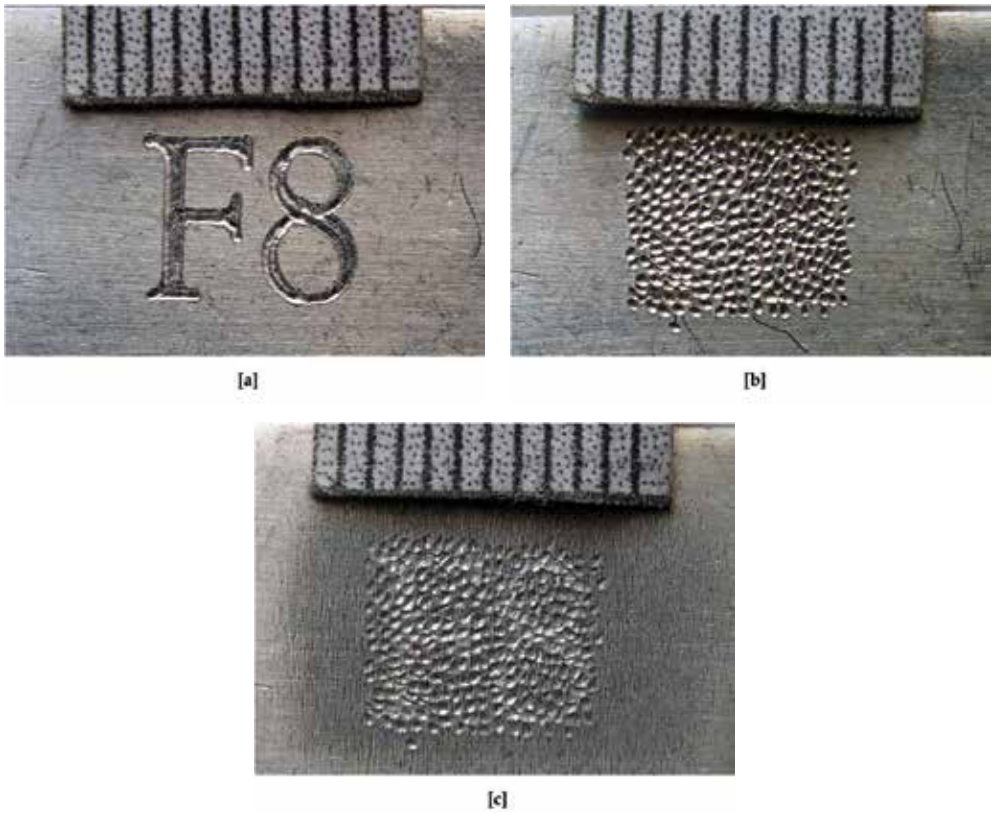

Fig. 6. a) The original engraved marks "F8"on Al-Zn-Mg-Cu alloy surface. b) The marks were obliterated by peening using centre punch. c) The outline of the obliterated marks "F8" were recovered quite distinctly with good contrast. Etching reagent: Alternating swabbing of 60% HCl and 40% NaOH. Etching time: 12 min.

restoring the marks was attributed to the amphoteric nature of aluminium (Massiah, 1976; Dong *et al*, 2005). Aluminium could be etched both with acid and alkali. A specific percentage of each of these on alternate swabbing produced the desired results.

For *Al-Zn-Mg-Cu alloys* (Bong & Kuppuswamy, 2010) another application, 10 % aq. phosphoric acid by immersion for extended hours recovered the marks with excellent contrast. The results provided by this reagent are shown in Figs. 7 to 9. Phosphoric acid worked well on Al-Zn-Mg-Cu alloy because the reagent provided good etching on Mg_5Al_8. Further it was reported that this reagent showed strain in Al-Mg base alloys (Petzow, 1976; Vander Voort, 1984).

Comparing the etching response of phosphoric acid with that of alternating 60% HCl and 40% NaOH, it was noted that the former was able to provide better contrast and sensitivity, although the erased surface was to be immersed for long hours. It is recommended that when using this reagent the obliterated surface is immersed at least for 1 h and a closer watch is followed thereafter; otherwise the marks disappeared when the immersion was prolonged. More work is needed to utilize completely the potentiality of this etchant for high strength aluminium alloys.

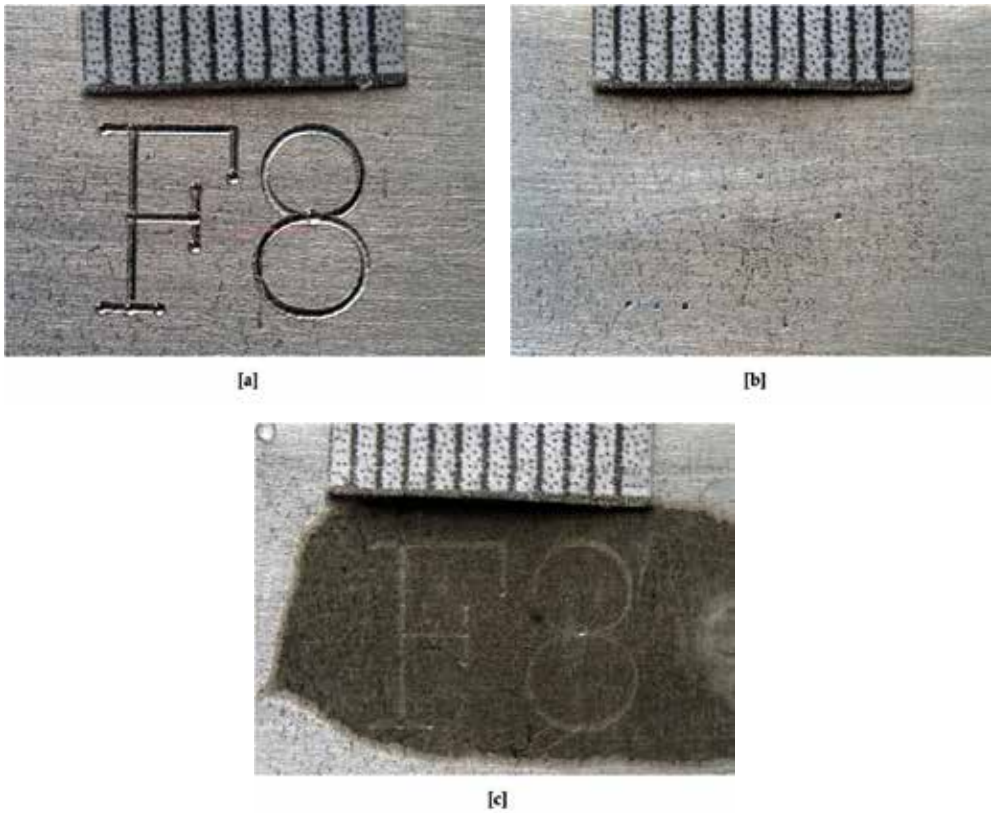

Fig. 7. a) The original engraved marks "F8" on Al-Zn-Mg-Cu alloy surface. b) Surface after grinding of the marks up to the depth of engraving (0.02 mm). c) The recovered number "F8" after etching process. Etching reagent: 10% aq. phosphoric acid by immersion. Etching time: 6 h.

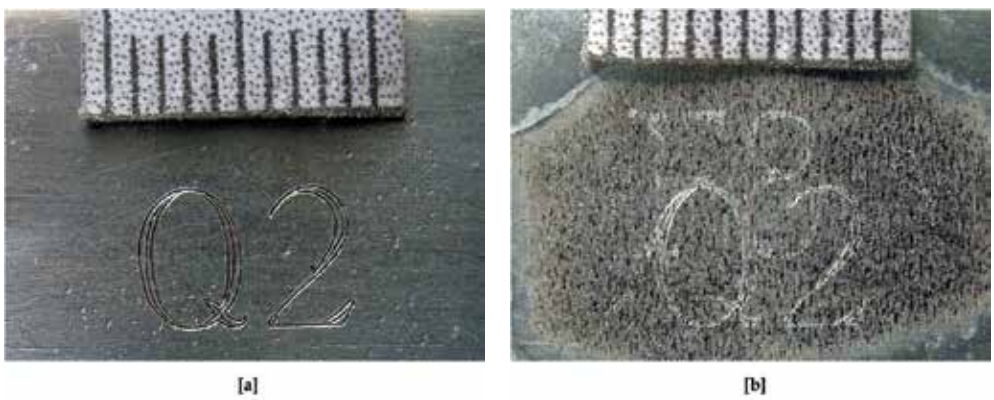

Fig. 8. a) Original engraved marks "F8" were erased on Al-Zn-Mg-Cu alloy surface (hence not seen) and in their place a new marks "Q2" were engraved. (b) The original marks "F8" were restored in the presence of "Q2". Etching reagent: 10% aq. phosphoric acid by immersion. Etching time: 8 h.

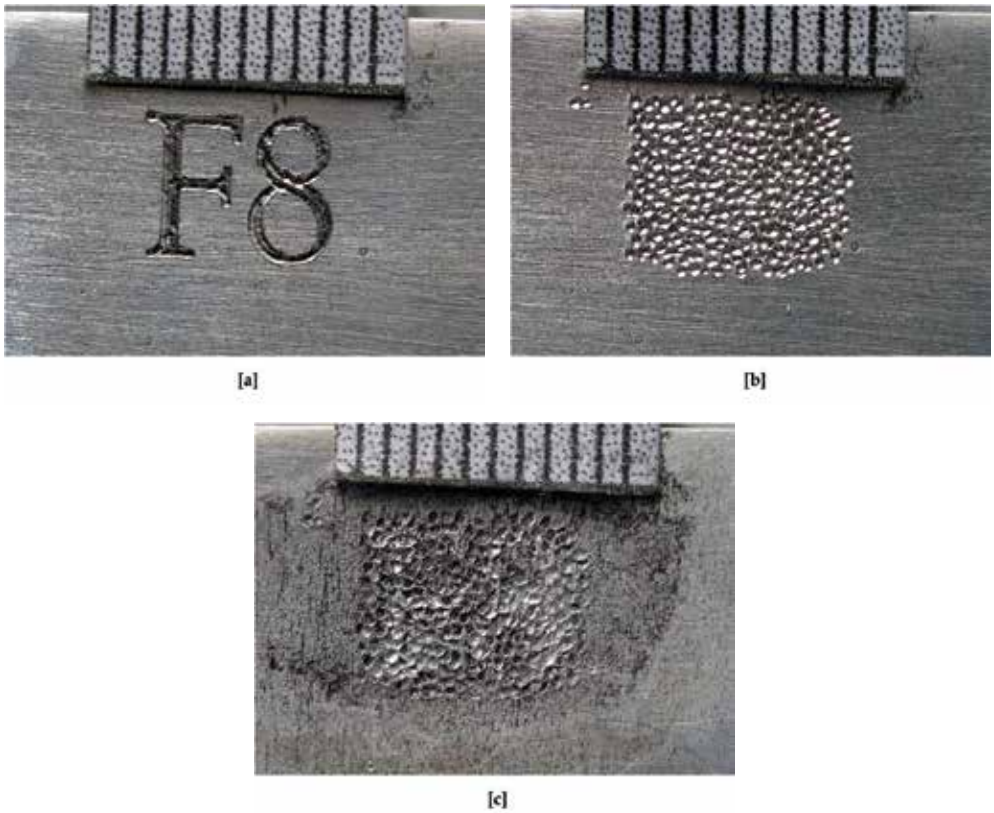

Fig. 9. a) The original engraved marks "F8" on Al-Zn-Mg-Cu alloy surface. b) The marks were obliterated by peening using centre punch. The obliterated marks "F8" were recovered distinctly with good contrast. Etching reagent: 10% aq. phosphoric acid by immersion. Etching time: 5 h.

The obliterated marks on *Al-Si alloy* surfaces responded effectively to the swabbing of 10% NaOH followed by 10% HNO_3. While NaOH etching restored the marks, the rinsing with HNO_3 removed the black deposit (Mondolfo, 1943; Petzow, 1976) caused by NaOH swabbing thereby increasing contrast. (For details see Uli *et al*, 2010). Interestingly, Hume-Rothery reagent recommended for etching Al-Si alloy surfaces in metallurgical literature (Mondolfo, 1943; Vander Voort, 1984) could not restore the obliterated marks.

Table 3 gives the reagents recommended for etching Al, Al-Zn-Mg-Cu and Al-Si alloys together with the application methods employed and also the characteristics of the recovered marks. The etchants described therein were sensitive enough to revealing the obliterated engraved marks where the deformation zones were shallow. Hence they could be applicable to recover other kinds of markings—*stamping, pin stamping and type wheel marking*— where the depths of serial numbers and the cold worked metal left behind would be considerable (Katterewe, 2006).

The experiments had also shown that alternate application of 60% HCl and 40% NaOH suitable for etching both Al (99% purity) and Al-Zn-Mg-Cu alloy was not effective on Al-Si alloy. Further 10% aq. phosphoric acid produced good contrast on Al-Zn-Mg-Cu alloy alone. Significantly, 10% NaOH swabbing followed by 10% HNO_3 used for the etching of

Material	Etchant composition	Comments
Al (99% purity)	1. Hydrochloric acid 60% 2. Sodium hydroxide 40%	The two reagents were applied alternately, 3 min for each solution until the erased marks were retrieved. Between the applications the surface was wiped with a cotton wool and cleaned with acetone. For the engraved plates erased only upto the depth of erasure (0.02 mm) the obliterated marks appeared after about 7 min. For deeper obliterations the time of recovery increased upto 60 min. The procedure gave good contrast and sensitivity of the marks.
Al-Zn-Mg-Cu alloy	1. Hydrochloric acid 60% 2. Sodium hydroxide 40%	The two reagents were applied alternately, first with HCl for 3 min followed by NaOH for a similar period till the numbers became visible. Between the applications the surface was wiped with a cotton wool and cleaned with acetone. For engraved plates erased only upto the depth of erasure (0.02 mm) the number started to appear in about 2 min after application of 60% HCl. NaOH swabbing was followed that darkened the surface and further swabbing by HCl removed all the dark deposition showing the numbers clearly. When erasures were deeply produced the time of recovery increased upto 20 min. The procedure gave good contrast and sensitivity of the marks.
	10% aq. phosphoric acid	The obliterated area was surrounded by modelling clay. 0.5 ml of the reagent was filled inside the clay. The reagent was renewed every one hour. The dark discoloration was gently removed periodically using cotton applicator. The marks showed as faint outlines after a few minutes. After an hour or more the marks appeared white in colour. Immersion time: 1-16 h, dependent on the depth of erasure of the marks. The time needed to recover marks was varying and not consistent when the experiments were repeated. Constant monitoring was required, as immersion for longer time destroyed the marks. Recovered marks were good in contrast and sensitivity.
Al-Si alloy	1. 10% Sodium hydroxide, 2. 10% Nitric acid	The two solutions were applied alternately by swabbing the obliterated surface, first, with the NaOH for 3 min and then HNO_3 for 1 min. The surface was wiped with a cotton wool and cleaned with acetone in between the applications. For engraved plates erased only upto the depth of engraving (0.02 mm) faint marks started to show after 3rd min of the reagent application and clearer marks appeared during the 25th min of application. For deeper obliterations the time of recovery increased upto 40 min. The procedure produced marks with good contrast and sensitivity.

Table 3. Reagents for etching Al (99% purity), Al-Zn-Mg-Cu and Al-Si alloys for restoration of obliterated marks. The reagents were sensitive enough to recover the marks on the engraved plates erased down 0.02 to 0.04 mm below the engraving depth. The marks produced by the reagents were also reproducible.

Al-Si alloy did not produce desirable results for Al (99% purity) and Al-Zn-Mg-Cu alloy. It was thus significant that some etchants which worked rather well for some Al alloys had no effect on others. Hence in forensic restorations an evaluation of the composition of the alloy should be made before selecting the reagent.

The researchers have also demonstrated that the depths of recovery of obliterated marks decreased when a new number was overengraved after erasing the original number. For example in the case of Al (99% purity) surfaces the recoverable depth was 0.04 mm when the numbers were erased by grinding. However, when the marks were erased by grinding and a new number was engraved in their place, the recoverable depth decreased to 0.02 mm (Izhar *et al*, 2008). Similar effects were observed with the other two Al alloys (Bong & Kuppuswamy, 2010; Uli *et al*, 2010) and also with steel surfaces (Azlan *et al*, 2007). The results only indicated that the deformation zone from the original engraving was not affected by the new overengraving up to certain levels, but beyond this depth the original deformation was lost. Though not definite, it appears that some overlapping of the new zone with the original deformation did occur at a certain depth. The practical significance of this observation in real cases is that the sensitivity of the etching technique is lowered where a new number is overstamped after removing the original marks.

The marks obliterated by centre punching were recoverable only when the depths of punches were not deep enough. During our experiments many centre punched marks could not be recovered. The centre punching produced a series of holes which were closely spaced on the original marks. It was found that when the holes were within the limits of depths of original engraving the recoveries were successful.

5. Problems for future research

There have been constant efforts to identify effective etchants to reveal marks on aluminium surfaces which are finding increasing engineering applications. The problem encountered is one of poor contrast between the recovered numbers and background metal surface. The work on engraved marks has identified some sensitive and contrast producing reagents for etching Al (99% purity), Al-Zn-Mg-Cu and Al-Si alloys. However, the reagents restored those marks that were erased only upto a few micrometres depth. Further when new deformation was introduced over the original engraving, the contrast of the marks became poorer. Hence further refinements are to be considered in order to optimize the sensitivity and efficacy of the current methods. In recent years different aluminium alloys are being introduced in the firearms and motor vehicle industry. There is a need to carry out experiments to identify appropriate etchants for these surfaces. It is also desirable to conduct independent researches on restoration of stamping, pin stamping, engraving and type wheel marks in order to assess the recoverable erasure depths, as no work has been directed in this direction so far. Similar works however are available for steel surfaces (Turley, 1987; Wightman & Matthew, 2008).

Modern pistols and motor vehicles use laser engraved serial numbers and barcodes. Laser engraving of valuable jewellery may also be encountered in practice. These laser etched marks are difficult to be restored until the present time, as the process removes the metal by vaporization from intense heat produced by the laser during engraving. There will be no plastic deformation zone caused by such effect as in the case of stamping or engraving a number. The heat affected zone produced has different hardness than the rest of the metal. A more recent study (Klees, 2009) to determine the obliterated laser engraved markings on

ferrous frames of firearms using scanning electron microscopy and x-ray mapping proved quite ineffective. When the heat affected zone was removed, only some ghost remnants were restored in backscattered imaging. The method could not provide surface analysis to contrast the roughness differences produced during laser etching. Relief polishing, as noted earlier was also not effective for deep obliterations. Hence newer methods to exploit the hardness differences between heat affected and unaffected area should be addressed in the near future.

It is known that if a new serial number is directly stamped onto the smoothed/erased area of the old one, the recovery is impossible because of overlap of the two (old and new) deformation zones (Polk & Giessen, 1989). The present author experienced during his experimental work that when fresh engraved marks were made over the original ones some characters accidentally overlapped; such overlapped *original* characters could not be recovered. However, when the newer overengraved marks were slightly displaced from the previous number, recovery was full/partial dependent on the degree of overlap [Figs. 2. b), 5. b) & 8. b)]. It is worthwhile that this problem is addressed by material scientists for a good solution that will have far reaching implications in serial number restoration in forensic science practice.

6. Conclusions

This chapter has presented information on serial number restoration in forensic science investigations and also etching and other techniques pertaining to the visualization of obliterated marks on aluminium surfaces. Appropriate etchants from the many that are recommended for aluminium surfaces were identified. Some were sensitive enough to develop obliterated engraved marks, where the deformation zones were minimal of the order of tens of micrometers. They presented the marks with good contrast. Their etching responses on different aluminium surfaces are illustrated. Etching techniques are simple to employ and extremely useful in serial number restoration. They have revealed plastic deformation zones with great sensitivity and reproducibility.

Development of more sensitive etching methods for different kinds of aluminium alloys used in modern automotive components and firearms should be undertaken in the future. Also work remains to be done to find suitable techniques to raise obliterated laser etched marks. Further quantitative information is needed to establish the relationship between the depths of engraved/pin stamped/laser engraved marks and the respective depths upto which these marks can be restored.

Restoration of obliterated marks by chemical etching is both an art and a science. High quality surface preparation, selection of appropriate etchants, dexterity, alertness and care exercised during etching of the specimen, good observational skills to interpret the faintly recovered marks and mastery over closeup/macrophotographic techniques are all fundamental to the successful restoration of obliterated marks in forensic science practice and investigations.

7. Acknowledgements

The financial support provided by Universiti Sains Malaysia, (USM) Penang, Malaysia (Short Term Research Grant 304/PPSK/6139069) is gratefully acknowledged. The author would like to thank Professor Subodhkumar for graciously supplying the Al-Zn-Mg-Cu

alloy sample and for discussions; Professor R. Jagannathan for his comments on the manuscript and advice. Thanks are also due to Professor Syed Waliullah Shah, Mr. S. Panneerchelvam, Dr. Gnandev Phutane, Dr. Mohamad Hadzri Yaacob, Dr. Noor Izani Noor Jamil, Mr. S. Karthikeyan and Mrs. Vatsala Padmanabhan for their encouragement of this work. The author greatly appreciates and is grateful to the assistance given by his graduate student Mr. Mohd Firdaus bin Che Amran for conducting etching experiments for this review and Miss Sharifah Mastura Bt Syed Mohd Daud for her assistance. Thanks are also due to Mr. Wan Mohd Sahnusi, Mrs. Rosniah Yusoff, and Mr. Muhamad Zulkhari Othman for laboratory assistance; Mr. John Jeyasekar deserves special mention for library assistance. The author also wishes to acknowledge the use of library facilities of JRD TATA Memorial Library, Indian Institute of Science, Bangalore, India.

8. References

"Metallographic reagents for iron and steel", (1974). *Metal Progress*, 106 (1): pp. 201-209.

Azlan, M.Z.M., Kuppuswamy, R., & Harun, H. (2007). Restoration of engraved marks on steel surfaces by etching technique, *Forensic Sci. Int.* 171(1): pp. 27-32.

Bond, J.W. (2008). Visualization of latent fingerprint corrosion of metallic surfaces, *J. Forensic Sci.* 53(4): p. 812.

Bong, Y.U. & Kuppuswamy, R. (2010). Revealing obliterated engraved marks on high strength aluminium alloy (AA7010) surfaces by etching technique, *Forensic Sci. Int*. 195(1-3): pp. 86-92.

Brown, E.W. (2001). Serial number restoration on Ruger P Series aluminium alloy frames, *AFTE Journal,* 33(1): p. 57.

Chisum, W.J. (1966). A catalytic process for restoration of serial numbers on aluminium, *J. Forensic Sci. Soc*., 6(2): p. 89.

Collins, M. (1999). Modern marking and serial numbering methods, *AFTE Journa*l, 31(3) pp. 309-317.

Cook, C.W. (1989). Obliterated serial numbers, *AFTE Journal*, 21(2): pp. 166-167.

Cooper, M. (2002). Serial number "restoration" on a Colt All American Model 2000, *AFTE Journal*, 34(1): p. 48.

Crowe, G. & Smith, R.M. (2005). Restoration of a jeweller's mark in gold jewellery, *AFTE Journal*, 37(4): pp. 379-381.

Cunliffe, F. & Piazza, P.B. (1980). *Criminalistic and Scientific Investigation,* Prentice Hall, New Jersey.

da Silva, L., & doss Santos, P.A.M. (2008). Recovering obliterated laser engraved serial numbers in firearms, *Forensic Sci. Int.* 179(2): pp. e63-e66.

De Forest, P.R., Gaensslen, R.E. & Lee, H.C. (1983). *Forensic Science, An Introduction to Criminalistics*, McGraw-Hill Book Company, New York.

Dong, S., Liao, Y. & Tian, Q. (2005). Sensing of corrosion on aluminium surfaces by use of metallic optical fibre, *Applied Optics*, 44(30): pp. 6334-6337.

Heard, B.J. (1997). *Handbook of Firearms and Ballistics: Examining and Interpreting Forensic Evidence*, John Wiley, New Jersey.

Hogan, B.E, Smith, D.R. & Hall, B.R. (2006). MAPP gas: An alternative to oxyacetylene, *J. Forensic Identi*, 56(2): pp. 232-241.

Izhar, M.B.M., Kuppuswamy, R. & Rahman, A.A. (2008). Recovering obliterated engraved marks on aluminium surfaces by etching technique, *Forensic Sci. Int.* 177(2-3): pp. 221-227.

Jackson, R.L. (1962). *Gross's Criminal Investigation: A practical Textbook for Magistrates, Police Officers and Lawyers*, Sweet and Maxwell, London.

Jackson, A.R.W., Jackson J.M. & Mountain, H. (2008). Forensic Science (2nd Ed.), Pearson, Prentice Hall, London

Jeon, O.–Y., Kim, S.-H., Lee, J., Park J.-T., Kim, T.-H., Park, H.-S, Huh, I.-K. & Kang, H.-T. (2009). Nondestructive imaging of hidden figures on license plates by x-ray radiograph, *Forensic Sci. Int.* 188(1-3): pp. e11-e13.

Katterwe, H. (2006). Restoration of serial numbers, in: Stauffer, E. & Bonfonti M.S. (Eds.). *Forensic Investigation of Stolen-Recovered and Other Crime-Related Vehicles*, Academic Press, Amsterdam, pp. 177-205.

Kehl, G. L. (1949). *The Principles of Metallographic Laboratory Practice*, McGraw Hill Book, New York.

King, F. (1987). Aluminium and Its Alloys, Ellis Horwood Ltd, Chichester.

Klees, G.S. (2002). The restoration of obliterated laser-etched firearm identifiers by conventional and alternative decryption methods, *AFTE Journal*, 34(3): pp. 264-267.

Klees, G.S. (2009). The restoration or detection of obliterated laser-etched firearm markings by scanning electron microscopy and x-ray mapping, *AFTE Journal*, 41(2): pp. 184-187.

Kuppuswamy, R. & Senthilkumar, M. (2004). Restoration of vehicle identification numbers, *J. Forensic Identi*. 54(1): pp. 13-21.

Levin, N. (2010). The forensic examination of marks, A review: 2007-2010, Interpol 16th IFSS, Lyon, France: pp. 30-43.

Lyle, D.P. (2004). *Forensics For Dummies*, Wiley Publishing, Inc., Indianapolis, Indiana.

Malikowski, S.G. (2004). The restoration of an obliterated serial number and barcode using digital photography and Adobe Photoshop, *AFTE Journal*, 36(2): p. 237.

Massiah, E. (1976). A compilation of techniques and chemical formulae used in the restoration of obliterated markings, *AFTE Journal*. 8(2): pp. 26-62.

Matthews, J.H. (1962). Firearms Identification Part 1, University of Wisconsin Press, USA.

Maxwell, S.L. (1993). The application of heat treatment for the restoration of vehicle identification numbers, National Institute of Forensic Science Workshop, Canberra, pp. 1-16.

Moenssens, A.A., Starrs, J.E., Henderson, C.E. & Inbau, F.E. (1995). *Scientific Evidence in Civil and Criminal Cases* (4th Ed.), The Foundation Press, Inc, Westbury, New York.

Mozayani, A. & Noziglia, C. (Eds.) (2006). The Forensic Laboratory Handbook, Procedures and Practice, Human Press, N.J.

Mondolfo, L.F. (1943). *Metallography of Aluminum Alloys*, John Wiley & Sons, Inc. New York, Chapman & Hall limited.

Nalini, N. & Hemalatha, M. (2003). Glowing numbers, *Journal of Forensic Identi*, 53(4): pp. 421-423.

Nickolls, L.C. (1956). *The Scientific Investigation of Crime*, Butterworth & Co., London.

O'Hara, C.E. & O'Hara, G.L. (1994). Fundamentals of Criminal Investigation, Charles Thomas, U.S.A.

Okayasu, M., Sato, K. & Mizuno, M. (2008). A new etching technique for revealing the plastic deformation zone in an Al-Cu-Mg alloy, *J. Mater Sci*, 43: pp. 2792-2798.

Peeler, G., Gutowski, S., Wrobel, H. & Dower, G. (2008). The restoration of impressed characters on aluminium alloy motorcycle frames, *J. Forensic Identi*, 58(1): pp. 27-32.

Petterd, C. (2000). Serial number, *in*: Siegel, J.A., Saukko, P.J. & Knupfer, G.C. (Eds.), *Encyclopedia of Forensic Sciences*, Academic Press, San Diego, pp. 1205-1210.

Petzow, G. (1976). *Metallographic Etching*, American Society for Metals, Metals Park, Ohio.

Polk, D.E. & Giessen, B.C. (1989). Metallurgical aspects of serial number recovery, *AFTE Journal,* 21(2): pp. 174-181.

Rowe, W. (2009). Firearm and Tool Mark Examinations, *in*: James, S.H. & Nordby, J.J. (Eds.), *Forensic Science, An Introduction to Scientific and Investigative Techniques*, CRC Press, London, pp. 422-423.

Schaefer, J. (1987). Serial number restoration observation, *AFTE Journal*, 19(3): pp. 276-277.

Siaw, H.Y. & Kuppuswamy, R. (2009). On the sensitivity of some common metallographic reagents to restoring obliterated marks on medium carbon (0.31% C) steel surfaces, *Forensic Sci. Int.*, 183(1-3): pp. 50-53.

Siegel, J.A. (2007). *Forensic Science, the basics*, Taylor & Francis, London.

Shoshani, E., Klain, A. & Argaman, U. (2001). Altering a serial number, *AFTE Journal*, 33(2): pp. 133-135.

Srinivasan, G.J. & Thirunavukkarasu, G. (1996). Decipherment of an obliterated vehicle identification number, *J. Forensic Sci.* 41(1): pp. 163-165.

Svensson, A., Wendel, O. & Fisher, B.A.J. (1981). *Techniques of Crime Scene Investigation* (3rd ed.), Elsevier, New York.

Thornton, J.I. & Cashman, P.J. (1976). The mechanism of the restoration of obliterated serial numbers by acid etching, *J. Forensic Sci. Soc.*, 16(1): 69-71.

Turley, D.M. (1987). Restoration of stamp marks on steel components by etching and magnetic techniques, *J. of Forensic Sci.*, 32(3): pp. 640-649.

Uli, N., Kuppuswamy, R. & Firdaus, M.A.C. (2010). A survey of some metallographic etching reagents for restoration of obliterated engraved marks on aluminium–silicon alloy surfaces, *Forensic Sci. Int.*: doi:10.1016/j.forsciint.2010.11.005

Vander Voort, G.F. (1984). *Metallography, Principles and Practice,* McGraw Hill Book Company, New York.

Vander Voort, G.F. (1986). *Applied Metallography,* Van Nostrand Reinhold Company, New York.

Warlow, T. (2004). *Firearms, The Law, and Forensic Ballistics*, CRC Press, Washington D.C.

Wightman, G. & Matthew, J. (2008). Restoration of stamp marks on steel components. *Forensic Science International*, 180(1): pp. 32-36.

Wightman, G. & Matthew, J. (2008a). Development of an etching paste, *Forensic Science International*, 180(1): pp. 54-57.

Wilson, P.B. (1979). The restoration of erased serial identification marks, *Police Journal*, 52 (Jul-Sep): pp. 233-242.

Wolfer, D.A. & Lee, W.J. (1960). Application of magnetic principles to the restoration of serial numbers, *J. of Criminal Law, Criminology and Police Science,* 50(5) pp. 519-520.

Part 5

Machining and Machinability

17

Performance Optimization in Machining of Aluminium Alloys for Moulds Production: HSM and EDM

Andrea Gatto[1], Elena Bassoli[1] and Luca Iuliano[2]
[1]*University of Modena and Reggio Emilia*
[2]*Politecnico di Torino*
Italy

1. Introduction

In order to face the demands of today's competition, i.e. short time-to-market for customized products in small batches, in the field of moulds construction a growing interest is seen for materials that combine high mechanical properties with the possibility of a quicker and easier machining (Klocke, 1998). Aluminium alloys offer many machining advantages such as excellent machinability and finish degree with high cutting speed, low cutting forces, outstanding tool life (Kishawy et al., 2005; Schultz & Moriwaki, 1992). Elevated thermal exchange and weight reduction, which means easier handling, compared to steels are additional characteristics that lead to increasing applications in the automotive and aerospace industry and in the field of mould production (Amorim & Weingaertner, 2002; Ozcelik et al., 2010). The use of Aluminium moulds, whose thermal conductivity is up to 5 times higher than of traditional steel moulds, ensures an impressive reduction of cooling time at closed mould, which is the longest step in polymers injection moulding cycle. Moreover, high thermal exchange promotes a better workpiece accuracy, lower risk of warpage and sink marks, lower molded-in stresses (Erstling, 1998). Good corrosion resistance of Aluminium is an additional advantage in processing molten polymers. Relatively recent Aluminium alloys derived by aeronautical uses offer high tensile strength and hardness: the gap with steels is thus reduced or even reversed in terms of specific properties (Amorim & Weingaertner, 2002; Starke & Staley, 1996). Wrought heat-treatable alloys develop high specific strength thanks to age-hardening and have been widely used for airframes. Above all Al-Cu alloys (2xxx series) and Al-Zn alloys (7xxx series) are recognized for best damage tolerance and strength, respectively (Starke & Staley, 1996). The addition of transition elements, i.e. Cr, Mn or Zr, leads to dispersions capable of controlling the grain structure. Two examples of such alloys are Al 2219 and Al 7050, which are good candidates for injection moulds applications.
If the first examples of Aluminium moulds for plastic injection were limited to preproduction, the properties of these new alloys match the requirements of medium production volumes (up to 10000 parts/year), which today are also the main market demand (Miller & Guha, 1998; Erstling, 1998; Klocke, 1998; Amorim & Weingaertner, 2002; Pecas et al., 2009).

Two machining operations are typically required in the tooling phase: milling, to produce the overall mould cavity and functional features, and Electro Discharge Machining (EDM), to obtain specific surface textures or complex geometrical details (Klocke, 1998; Lopez De Lacalle et al., 2002).

As to milling operation, several studies prove that Aluminium alloys allow the advantageous adoption of high cutting speed, in the field of High Speed Machining (HSM), which ensures time and cost savings together with excellent surface finish and dimensional accuracy with low tool wear and reduced bur formation (Chamberlain, 1979; Schultz & Moriwaki, 1992). In the case of Aluminium alloys, cutting speed can be increased up to one order of magnitude above the current practice, leading to important industrial profits.

Due to the combination of increased productivity and high quality, HSM has obviously become one of the most promising manufacturing technologies in recent decades, and has been applied in a lot of fields, such as aeronautics and astronautics, automobile, die, and mould industries (Bassoli et al., 2010; Kishawy et al., 2005). Besides the above improvements, HSM can even broaden the production capabilities foe example of thin webs, since it involves peculiar cutting conditions, characterized by low cutting forces and low surface temperatures (Kishawy et al., 2005). At high cutting speed, feed and depth of cut can be reduced without cutbacks on material removal rate or machining time: cutting stress is thus decreased. Moreover, high-speed cutting of Al alloys has almost no detrimental effect on tool wear. Even if high chip temperature is obtained, even near to the melting point, this is not enough to activate diffusion wear on most of today's tool materials. Hence only mechanically-activated wear mechanisms occur, in the form of flank wear (Kishawy et al., 2005; Yoshikawa & Nishiyawa, 1999). Schultz and Moriwaky (1992) outline that the material-specific cutting mechanisms in HSM influence the whole cutting process, including cutting parameters as well as tool, machine components and strategies. Many authors agree that the high-speed field is difficult to be defined and is relative to the work piece material. Some researchers believe that HSM can be identified as the domain where shear-localization develops almost completely in the primary shear zone (Kishawy et al., 2005), but for others this phenomenon can be ascribed only to hard alloys giving segmental chip. High thermal conductivity and low hardness of Aluminium alloys are responsible for continuous chip formation even under high speed cutting, unless the alloy is in the overaged state (Schultz & Moriwaki, 1992). Anyway, a limited secondary shear zone is certainly characteristic of high speed cutting.

For Aluminium alloys, values of cutting speed that are considered typical of HSM are in the range 1000 to 10000m/min, but optimum results were obtained for 3500-4500m/min with feed rates between 5000 and 10000mm/min (Schultz, 1984). Lower surface roughness can be obtained than for conventional machining. Despite the described potential, many issues still need to be addressed before the full industrial exploitation of HSM. Traditional laws between cutting parameters do not apply to the field of high-speed machining and the mechanisms of chip removal still need investigation (Kishawy et al., 2005).

EDM is used for the machining of complex shapes and textures typical of plastic injection moulds. EDM is one of the most widespread non-conventional material removal processes (Ho & Newman, 2003). The material removal mechanism is based on spark erosion: electrical energy is turned into thermal energy through a series of discrete electrical discharges occurring between the electrode and workpiece immersed in a dielectric fluid (Tsai et al., 2003). A plasma channel is generated between cathode and anode (Shobert, 1983) at a temperature in the range of 8000 to 12000°C (Diver et al., 2004) or as high as 20000°C (Pham et al 2004). A volume at the surface of each pole is heated and molten. When the

pulsating direct current supply, occurring at the rate of approximately 20000–30000Hz (Liu et al., 2005), is turned off, the plasma channel breaks down. The temperature suddenly drops and the plasma channel implodes due to the circulating dielectric: the molten material is flushed from the pole surfaces in the form of microscopic debris (Ho and Newman, 2003). The described mechanisms produces a variety of micro-features on the EDMed surface. In addition to overlapping craters and resolidified material, in the form of globules or splashes, cracks and a thermally affected layer can be present (Lee & Tai, 2003). The heat-affected layer is quite different from the original material and, although it can be beneficial in terms of enhanced abrasion and erosion resistance, it introduces a variation in the mechanical properties that should be carefully controlled. The process does not involve any contact between the tool and the workpiece. Thereby, machining forces are negligible and electrically conductive materials can be machined regardless of their strength and hardness (Lee & Tai, 2003; Kuppan et al., 2008; Tan and Yeo, 2008). Distinctive advantages can be obtained in the production of complex geometrical features and small details, i.e. in the manufacture of moulds, dies, automotive, aerospace and surgical components. In die-sinking EDM the electrode feeds into the workpiece removing material by spark erosion until its geometry is mirrored in the part (Simao et al., 2003; Guu et al., 2003). The main process parameters are peak current during current supply, its duration or pulse-on-time and the delay interval before next peak, or pulse-off-time, and the average voltage between electrode and workpiece through the gap. Pulse power and energy are detemnined by the pulse intensity and duration, while the flushing and cooling efficacy depend on the duty factor, ratio between the pulse-on-time and the overall cycle duration. Machining accuracy depends on the electrode tolerances, on the gap between the electrode and the workpiece, which varies with the machining parameters and the local geometry, and on wear. In particular, wear of the electrode along the feed direction can be compensated, but wear along the cross-section turns into part inaccuracy (Khan, 2008). EDM is a complex process influenced by a number of variables and subject to many error sources. Thermal, chemical and electrical phenomena interact in the sparking process, which has a stochastic nature (Pham et al 2004). The occurrence of discharges is a probabilistic phenomenon whose distribution is not random but chaotic, which means that even if the system develops in every moment following deterministic rules, the final outcome can not be predicted and its time evolution appears random, because the initial condition of the system affects the subsequent events dramatically (Han and Kunieda, 2001). Hence, modelling and predicting the process performances is a challenging problem and process set-up is often based on experimental data (Pham et al 2004).

As regards EDM of Aluminium alloys, literature studies concerning the machining performances are quite rare. Amorim and Weingaertner (2002) identify process parameters for highest material removal rate, finding that duty factor higher than 0,8 promotes instability with short-circuit pulses. Khan (2008) evaluates electrode wear in EDMing of Aluminium and mild steel. It is claimed that higher thermal conductivity of Aluminium leads to comparatively higher energy dissipation into the workpiece than in the electrode, which turns into lower tool wear. As to the EDMed surface morphology, Miller and Guha (1998) report that the heat affected layer in Aluminium alloys is not harder than the base material and is not susceptible to cracking, unlike what is observed for steel. Some researchers dealt with surface modification through EDM, using specific electrodes and fluids to obtain hard layers with increased wear- and corrosion resistance (Lin et al., 2001; Mohri et al., 2008). Much is still to be studied as to machining accuracy and its link to electrode wear and EDMed surface morphology.

Aim of this research is to verify the HS- and ED Machinability of three Aluminium alloys: Al2219 and Al7050, derived from aeronautical applications, in addition to Al7075, which is more common for pre-series moulds, to provide control data. For both technologies the machining performance is evaluated in specific tests through a multiscale approach: measurements of the macroscopic process outputs are merged with the investigation of mechanisms at a microscopic level. The methodology enhances optimization chances with respect to traditional practice.

2. Materials and methods

The three alloys Al2219 (Al-Cu), Al7050 and Al7075 (Al-Zn) are provided as laminated and T6 heat treated. Composition, physical and mechanical characteristics of the three alloys are shown in Table 1.

		Al2219 – T6	**Al7050 – T6**	**Al7075 – T6**
Chemical composition (wt. %)	Cu	6.345	1.804	1.528
	Mn	0.279	0.004	0.078
	Zr	0.1211	0.115	0.008
	Fe	0.111	0.080	0.290
	Si	0.053	0.040	0.159
	Ti	0.038	0.029	0.029
	Zn	0.028	6.260	5.800
	Mo	0.01	2.296	2.635
	Pb	0.008	0.003	0.003
	Ni	0.005	0.008	0.005
	Cr	0.001	0.003	0.192
	Al	bal.	bal.	bal.
Brinell Hardness		115	147	150
Young Modulus [GPa]		72	72	72
Ultimate Tensile Strength [MPa]		452	579	432
Yield stress [MPa]		348	515	316
Elongation at break [%]		7.60	7.60	9.80
Thermal conductivity [W/mK]		120	153	130
Melting Temperature [°C]		543	524	532

Table 1. Composition, physical and mechanical characteristics of the studied alloys

2.1 HSM tests

High speed face milling tests are performed using a 100mm diameter mill with 7 uncoated carbide inserts (ISO grade K) having a rake angle of 30°. Inserts' geometry is shown in Figure 1. Cutting speed (V) is ranged from 600 to 2200m/min and feed per tooth (f_z) between 0.075 and 0.18mm/tooth·rev, corresponding to values of table speed between 1000 and 7000mm/min. A full 4^2 factorial plan is adopted, with the levels in geometric progression as shown in Table 2. The tests are performed across the lowest limit of HSM, to investigate the variations in chip formation mechanisms when the high speed cutting regime is initiated. Axial depth of cut is kept constant at 2mm. The operations are performed

on a CNC milling machine with 3 controlled axes with maximum spindle speed of 8000rpm. Preliminary tests proved that the set of parameters V=220m/min; f_Z=0.18mm/tooth·rev exceeds the maximum machine power. For this specific test feed per tooth is thus reduced to 0.14mm/tooth·rev. Each test was stopped after a machined volume of 150cm^3.

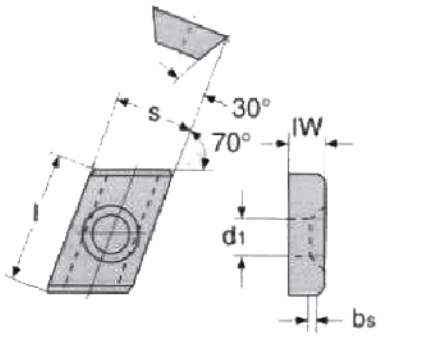

Dimensions [mm]				
l	s	d_1	IW	b_s
12,77	10,0	4,1	3,5	0,9

Fig. 1. Geometry of the inserts

V [m/min]	600 – 925 – 1426 - 2200
f_z [mm/tooth·rev]	0.075 – 0.1 – 0.13 - 0.18

Table 2. Levels of cutting speed and feed per tooth used in the HSM tests

The effect of cutting parameters on surface roughness, tool wear and chip formation mechanisms are studied with the aid of SEM observation and EDX semi-quantitative analysis, as well as through multiple regression analysis.

Average roughness (R_a) is measured on the milled surfaces with a stylus meter (Hommel T1000), using a sampling length of 15 mm. Five measurements are performed on each specimen. Tool inserts are observed through optical- and scanning electron microscope (OM, SEM) to evaluate wear mechanisms and entity. On chip produced during the milling tests a wider and more complex analysis is carried out. Chip dimensions and morphology are analyzed through OM, then SEM observation is adopted on both convex and concave chip surfaces to investigate tool-chip interaction and chip formation mechanisms. Moreover, chip samples are embedded in epoxy resin and sectioned perpendicularly to the cutting edge. The sections are polished through SiC papers and diamond sprays up to 1μm. Etching is carried out to study grain shape and dimensions, as well as deformation. Keller's reagent is used (Table 3) for 5÷30 s.

HF (48% soln.)	1
HCl (conc.)	1.5
HNO_3 (conc.)	2.5
H_2O	95

Table 3. Composition of Keller's reagent (vol. %)

2.2 EDM tests

As to EDM, in addition to surface roughness and erosion mechanisms, dimensional accuracy is also addressed. Hence a specific benchmark geometry is defined for the electrode, shown in Figure 2. It allows pointing out the typical problems of moulds machining: different geometrical features are present to outline dimensional accuracy, eroded surface morphology and electrode wear both parallel and orthogonal to the feed direction, as well as on concave and convex edges.

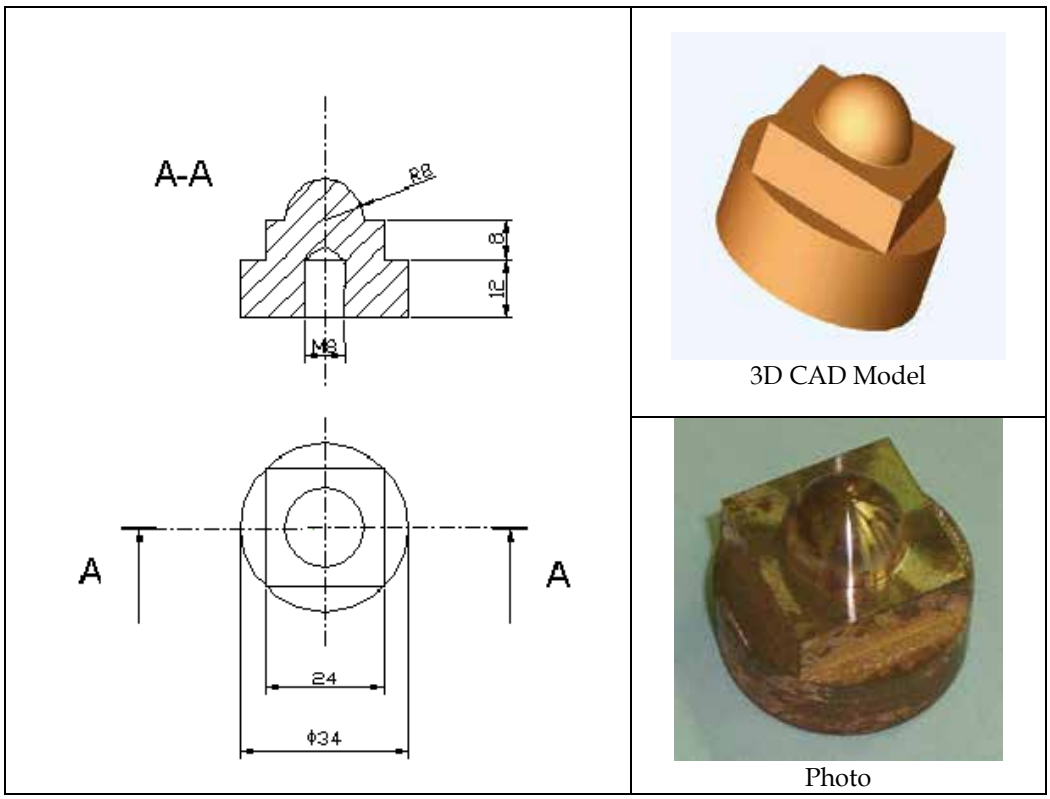

Fig. 2. Geometry of the electrodes employed in the tests

Electrolytic copper electrodes are produced and used to machine the three Aluminium alloys through three steps: roughing, semifinishing and finishing. Process parameters suggested by the machine producer are adopted in each phase, as listed in Table 4. It is important to notice that these parameters refer generically to Aluminium to be processed with Copper electrodes, whereas no specification is available for the single alloy. Machining is performed with a vertical movement in the Z direction of the electrode holder. Roughing operations are performed leaving 2mm stock, reduced to 0.5 mm after the semifinishing step. The total machined depth of the finished specimens is 20mm.

A commercial dielectric fluid specific for EDM is adopted (ELECTROFLUX DF – ATIUR). Every test is repeated three times, with the same procedure and process parameters on each alloy. Figure 3 shows a machining step.

Specimens are obtained separately for the three machining steps: after roughing, after roughing and semifinishing, and after the complete cycle up to finishing. A new electrode is employed to produce each sample.

	Roughing	Semifinishing	Finishing
Supply voltage [V]	31	48	not specified
Peak current [A]	35	25	7,3
Gap [mm]	0,250-0,375	0,135-0,210	0,020-0,043
Electrode polarity	+	+	+

Table 4. EDM parameters used in the tests

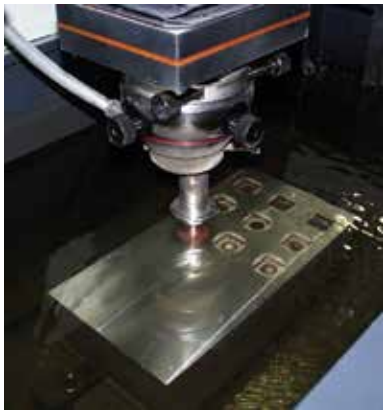

Fig. 3. Machining phase

For each specimen, the following measurements are carried out:
- dimensional measurements on the electrodes in order to study wear in relation to the type of operation and alloy;
- dimensional measurements on the workpieces, to evaluate machining tolerance relative to the type of operation and alloy;
- roughness measurements on the workpieces.

Dimensional measurements are performed with a coordinate measuring machine (CMM), evaluating the geometrical features shown in Figure 4. Roughness measurements are obtained with a contact stylus meter with a sampling length of 4.8mm.

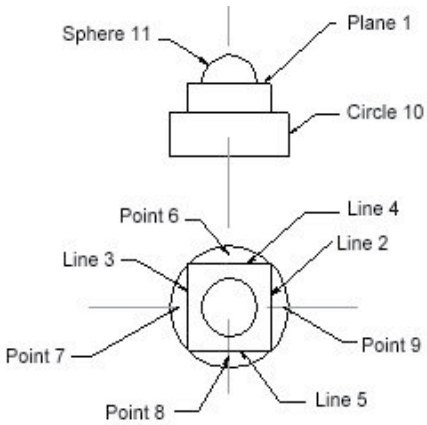

Fig. 4. Geometrical elements measured on workpieces and electrodes

Both the electrodes and the workpieces are sectioned by micro-cutting: a cut containing the benchmark axis is obtained and 5mm thick slices are then produced (Figure 5). Axial sections are polished up to 1μm diamond paste and chemical etched, using potassium dichromate on copper and fluoro-hydrochloric reactant on the Al alloys. OM observation is performed to evaluate wear entity and shape accuracy, taking into account also eventual variations for the different local geometry and orientation. The presence of outer heat-affected or molten and re-solidified layer is also investigated.

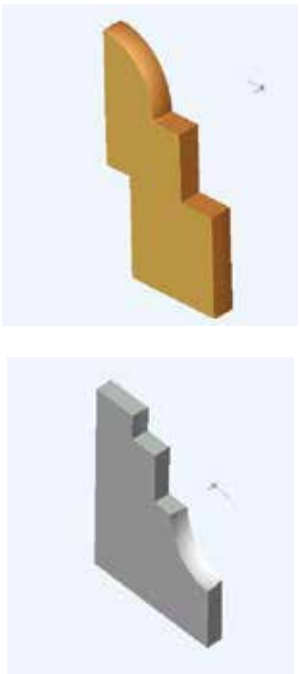

Fig. 5. Electrode and workpiece sections (5 mm)

SEM observation is carried out to verify the presence and composition of deposits on the worn electrode surfaces, as well as the eroded surfaces morphology on the workpieces.

3. Results and discussion

3.1 HSM tests

All the inserts show uniform wear: notches, breaks or craters are not observed. For each parameter combination flank wear (V_B) is measured through OM and surface roughness (R_a) by the stylus meter; all the results are summarized in Table 5. V_B and R_a are analyzed through statistical tools. Multiple regression models are evaluated including as independent variables: feed per tooth and cutting speed, their product and their squares. The significance of models and of regression parameters is checked by variance analysis.

Tool wear

Tool wear is very low for all the tests, observation of the inserts prove that abrasive effects causing the backward motion of the cutting edge are minimal. The volume machined for every test is very far from the tool life limit.

		Al 7075		Al 7050		Al 2219	
V [m/min]	**f_Z [mm/tooth rev]**	**V_B [mm]**	**R_a [µm]**	**V_B [mm]**	**R_a [µm]**	**V_B [mm]**	**R_a [µm]**
600	0.075	0.12	0.39	0.14	0.16	0.08	0.37
600	0.100	0.13	0.41	0.27	0.28	0.11	0.41
600	0.130	0.14	0.45	0.25	0.39	0.12	0.41
600	0.180	0.21	1.90	0.30	0.53	0.14	0.63
925	0.075	0.10	0.31	0.19	0.21	0.09	0.36
925	0.100	0.11	0.32	0.22	0.18	0.11	0.50
925	0.130	0.17	0.53	0.22	0.74	0.11	0.25
925	0.180	0.21	1.07	0.31	1.06	0.12	0.73
1426	0.075	0.10	0.17	0.17	0.15	0.14	0.40
1426	0.100	0.15	0.33	0.20	0.20	0.14	0.31
1426	0.130	0.18	0.39	0.21	0.34	0.17	0.44
1426	0.180	0.17	0.88	0.26	0.36	0.14	1.08
2199	0.075	0.15	0.23	0.15	0.10	0.16	0.24
2199	0.100	0.13	0.27	0.18	0.23	0.21	0.43
2199	0.130	0.12	0.44	0.20	0.29	0.19	0.69
2199	0.140*	0.16	0.40	0.21	0.21	0.19	0.44

* Due to maximum power limits of the CNC machine

Table 5. Results for flank wear and surface roughness for the three alloys

Figures 6, 7 and 8 show plots of the regression models developed for the three alloys within the experimental domain. Experimental figures are superimposed as asterisks to the contour lines.

For the alloy 7075 the main affecting factors are cutting speed and feed per tooth according to the model described in equation (1), for which $R^2_{adj} = 0.70$.

$$V_B = -0.016 + 0.000065\ V + 1.4\ f_Z - 0.00058\ V \cdot f_Z \quad (1)$$

If the plot in Figure 6 is observed, it can be remarked that wear is minimum for low values of cutting speed and feed per tooth; it increases for high values of feed per tooth in the field of low cutting speed or for high values of cutting speed if feed per tooth is quite low. Amongst the last two unfavourable cases, the first condition (low cutting speed and high feed per tooth) gives the worst results and should be carefully avoided for this alloy.

Further considerations can be made by dividing the diagram into three areas:

- middle values of feed per tooth: wear is almost unaffected by increasing cutting speed;
- high values of feed per tooth: wear decreases when cutting speed increases;
- low values of feed per tooth: wear increases with cutting speed.

For alloy 7050 the best fit of experimental data is obtained with the model in equation (2), which involves only feed per tooth and the product of feed per tooth and cutting speed. The model describes a big fraction of the total variance ($R^2_{adj} = 0.81$).

$$V_B = 0.1016 + 1.35\ f_Z - 0.00031\ V \cdot f_Z \quad (2)$$

Figure 7 outlines that the highest tool wear is obtained for high values of feed per tooth, in the same area as observed for alloy 7075. By increasing cutting speed, tool wear improves at any value of feed per tooth: the best result is obtained with high values of cutting speed and low values of feed per tooth.
For alloy 2219, the model includes not only cutting speed, feed per tooth and their product, but also square feed per tooth. The model, described by equation (3), provides a very good fit of experimental data ($R^2_{adj} = 0.86$).

$$V_B = -0.086 + 0.00004\ V + 2.46\ f_Z - 7.43^*\ f_Z^2 - 0.00023\ V \cdot f_Z \quad (3)$$

It is evident in Figure 8 that highest wear is produced by intermediate values of feed per tooth and middle-high cutting speed. In the area of high cutting speed, both low and high values of feed per tooth yield to similar limited wear.

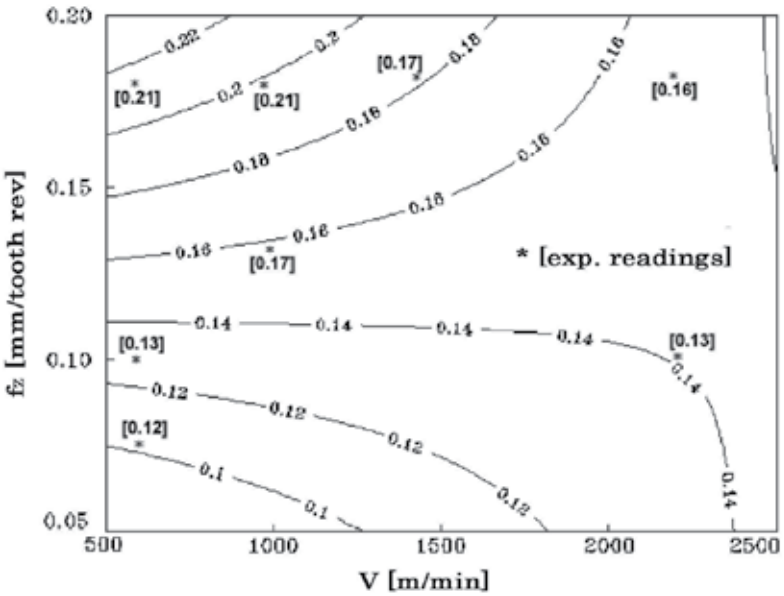

Fig. 6. Flank wear V_B [mm] versus cutting speed and feed per tooth for the alloy 7075

Surface roughness and chip formation mechanisms

Surface finish is generally very good for all the tests. Multiple regression analysis on the measurements of surface roughness leads to models that are not completely satisfactory for any of the three alloys, hence they are not proposed. Figure 9 shows a scatterplot of surface roughness values in the experimental domain, where the results for the three alloys can be compared. It can be observed that for all the alloys surface roughness shows strong increases with increasing feed per tooth in the range of low-medium cutting speed. If high cutting speed is adopted, instead, smoother surfaces are obtained even for high values of feed. Better results are in general obtained for alloy 7050 than for 7075, in particular as to the maximum values. The observed trend suggests that the mechanisms of chip removal are positively affected by the use of high cutting speed in the considered experimental domain, with some disparities even for alloys that are very similar in composition. These aspects are further studied though the observation of chip morphology.

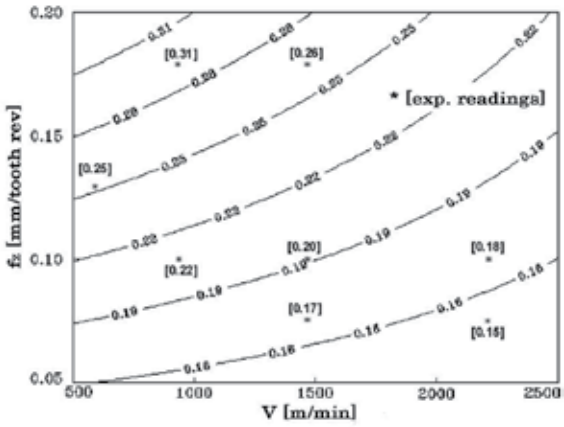

Fig. 7. Flank wear V_B [mm] versus cutting speed and feed per tooth for the alloy 7050

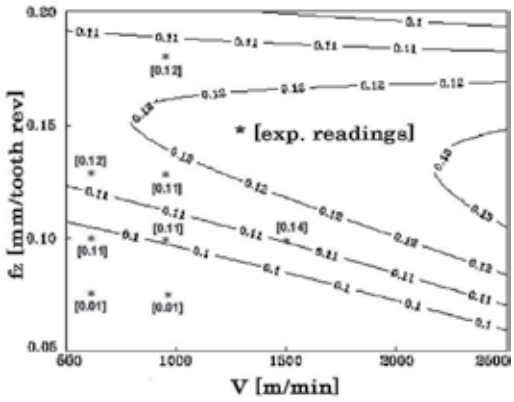

Fig. 8. Flank wear V_B [mm] versus cutting speed and feed per tooth for the alloy 2219

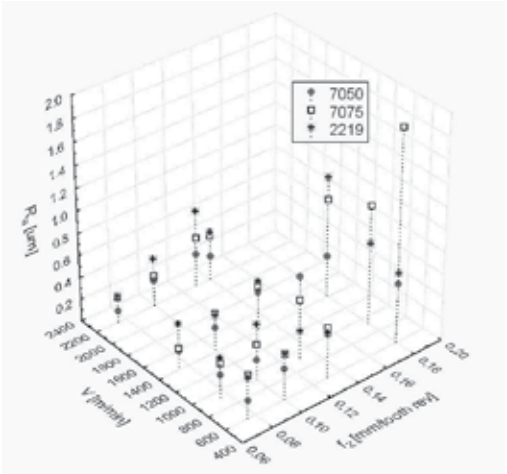

Fig. 9. Scatterplot of R_a versus cutting speed and feed per tooth for the three alloys

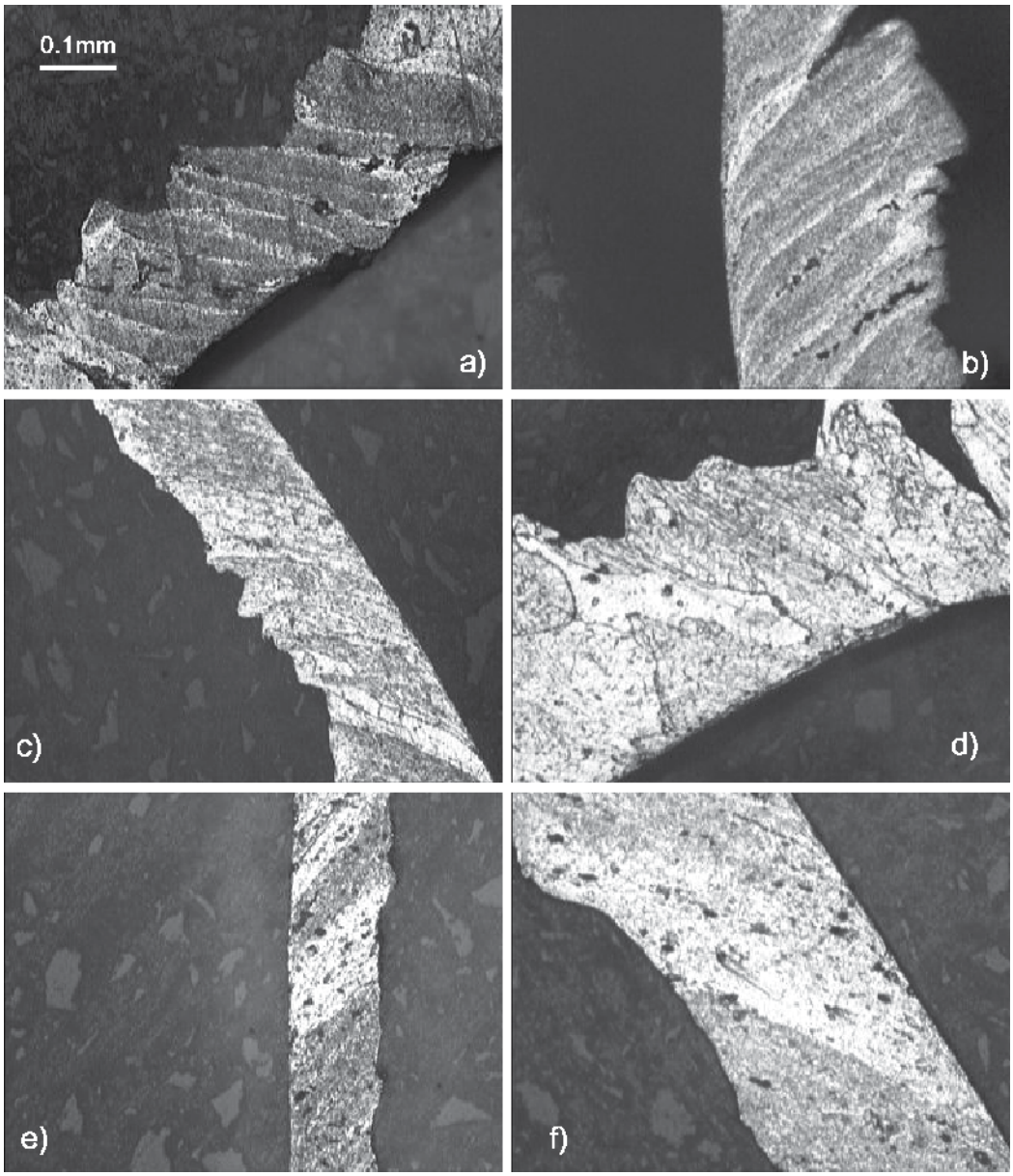

Fig. 10. Optical micrographies of chip sections after etching corresponding to the minimum (a,c,e) and maximum (b,d,f) roughness of the machined surface. Alloy 7075: a) V=1426m/min, f_Z=0.075 mm/tooth rev and b) V=600m/min, f_Z=0.18mm/tooth rev. Alloy 7050: c) V=2199m/min, f_Z=0.075 mm/tooth rev and d) V=925m/min, f_Z=0.18mm/tooth rev. Alloy 2219: e) V=2199m/min, f_Z=0.075 mm/tooth rev and f) V=1426m/min, f_Z=0.18mm/tooth rev

Figure 10 shows longitudinal sections after chemical etching of chip corresponding to the minimum and maximum roughness value of the machined surface for the three alloys. Chip formation is well consistent with Pijspanen's model. Shear planes and non-homogeneous grain distribution can be observed. For Al 7050 and 7075 the secondary shear zone is evident only for low cutting speeds, whereas for alloy 2219 it occurs at any speed, even if it becomes less pronounced if cutting speed is high. This behaviour is consistent with HSM mechanisms reported in literature. Feed does not show a clear effect on secondary shear deformation.
Convex chip surface, i.e. the one interested by the contact with the tool face, is shown in Figure 11 for the three alloys. Chip are obtained with V=2199m/min and f_Z=0.075 mm/tooth rev, which yield to roughness values that are minimum for two alloys and very near to the minimum for the other. The smoother surface is observed for Al 7050, free from micro-groves and tears that are present for alloy 2219 and, to a very high extent, for 7075. These observations account for a smoother tool-chip interaction, lower friction, lower adhesion and more regular mechanisms of chip formation for alloy 7050 in comparison to the others. Alloy 7075, in particular, provides the worst results. This outcome is consistent with the differences in surface roughness obtained on the workpieces. It is remarkable to conclude that the two alloys of the 7xxx series, even if very similar in composition and mechanical characteristics, provide significantly different results by HSM. Better surface finish of Al7050 could be ascribed to the higher weight percentage of Zr, that controls grains dimension and distribution.

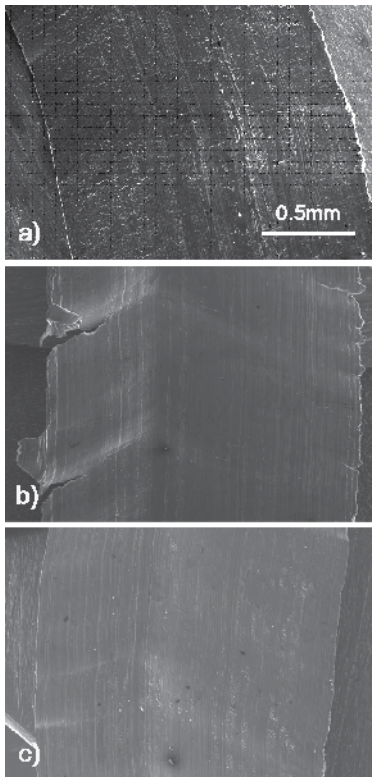

Fig. 11. SEM images of convex chip surface corresponding to V=2199m/min, f_Z=0.075 mm/tooth rev: a) Al7075; b) Al7050; c) Al2219

3.2 EDM tests

Dimensional accuracy

Figure 12 shows some workpieces after the three steps of the EDMing cycle, ready for the CMM measurements.

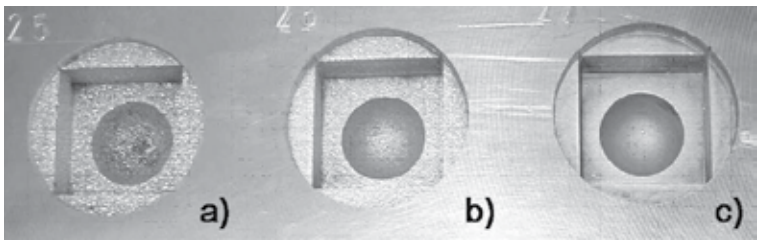

Fig. 12. Workpieces obtained after the operations of roughing (a), semifinishing (b), finishing (c)

All the geometric elements in Figure 4 are measured on the new electrode, on the worn one after operation and on the workpiece. Measurements are compared to the nominal values to obtain the dimensional deviation. An example of the measurements relative to the sphere diameter (nominal value=8mm) is shown in Table 6, referring to the semifinishing step on Al2219.

The percent dimensional deviation between the workpieces and the electrodes before machining is then calculated for each of the three alloys and three EDM steps. Since not all the distributions of percent deviations are Gaussian, averaging the obtained values is not acceptable to estimate the dimensional accuracy of each operation. Thus, the deviation range corresponding to the 95^{th} percentile of observed data is chosen to assess the process dimensional performances (Table 7). For alloys 2219 and 7050 the deviation percentage decreases when the peak current is reduced from roughing to finishing.

Percent deviations are also calculated between the dimensions of the new and worn electrodes, to estimate wear entity. The results are summarized in Figure 13.

	New electrode before semifinishing	Worn electrode after semifinishing	Workpiece after semifinishing
Measured diameter of sphere 11 [mm]	8.17	8.22	8.25
Deviation from nominal value [mm]	-0.17	-0.22	-0.25

Table 6. Example of dimensional measurements after an EDM step

Surface roughness and erosion mechanisms

Table 8 shows the results for roughness measured with the portable stylus after the different operations. Obviously, for all the three alloys surface roughness decreases as current intensity is reduced from roughing to finishing. The erosion mechanisms and the consequent surface morphology are deepened though OM and SEM observation.

Figures 14 and 15 show OM images of workpieces' etched sections, after roughing and finishing, for the three alloys. For an easier interpretation of the results, the vertical direction

Alloy	Operation	Estimated Deviation Range (95% of observ.)
7075	Roughing	2,6 - 2,7 %
	Semifinishing	1,1 - 1,2 %
	Finishing	1,9 - 2,0 %
7050	Roughing	2,3 - 2,4 %
	Semifinishing	1,9 - 2,0 %
	Finishing	1,8 - 1,9 %
2219	Roughing	2,4 - 2,5 %
	Semifinishing	2,1 - 2,2 %
	Finishing	1,9 - 2,0%

Table 7. Percent dimensional deviation ranges calculated for the EDM operations

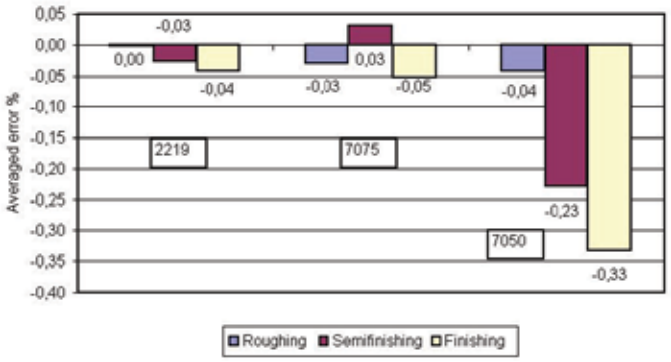

Fig. 13. Diagram of the dimensional deviation between new and worn electrodes

Alloy	Operation	Ra [µm]
7075	Roughing	9.0
	Semifinishing	4.5
	Finishing	1.1
7050	Roughing	12.5
	Semifinishing	4.5
	Finishing	1.6
2219	Roughing	9.0
	Semifinishing	6.3
	Finishing	2.2

Table 8. Roughness measured on the EDMed surfaces

of all the images coincides with the feed direction during the operations. The images refer to the areas A on the top of sphere 11 and D on plane 1. The radius in the spherical A zone is big enough to exclude a significant effect on the gap geometry during the operations, with respect to the planar area D. The two areas can thus be considered geometrically equivalent, whereas they strongly differ as to the machining time, which is roughly two times higher in the A zone. No significant disparities can be appreciated in the morphology of the two

areas, proving that machining depth and progressive electrode wear does not affect the erosion mechanisms and the obtained surface, which depends for each alloy only on the process parameters.
If the three alloys are compared, different morphologies are observed, suggesting different erosion mechanisms. The entity of the superficial molten and resolidified layer and of the thermally affected zone below decreases from Al 2219 to Al 7050, with middle results for Al 7075.
Figure 16 shows, as an example, the etched sections of electrodes used for roughing and finishing operation on alloy 2219. Observations on the worn electrodes appear very similar for the three alloys: all the operations produce craters on the electrode surface. The roughing step also yields to a large amount of deposits.
In Figures 17 and 18 SEM observations of workpieces and electrodes after roughing are shown. The morphology of EDMed surfaces, with craters surrounded by molten and re-solidified material, appears more regular for alloy 7050 compared to Al 7075, Al 2219 shows an intermediate behavior. The alloy 7075 shows evident surface cracks, not present in Al 2219 and 7050, the latter being also more uniform, with less re-solidified material.

7. Conclusion

The performance of HSM and EDM on aeronautical Aluminium alloys 7050, 7075 and 2219 are studied, with the aim to provide technological know-how for moulds production. In both cases the machining performance is evaluated in specific tests through a multiscale approach: measurements of the macroscopic process outputs are merged with the investigation of mechanisms at a microscopic level. The methodology enhances optimization chances with respect to traditional practice.
As to HSM, tool wear and surface roughness are investigated versus cutting parameters. Chip formation is also deepened to support macroscopic results. The best surface finish is obtained for Al 7050 with high cutting speed and low feed. Minimal tool wear is observed in the considered conditions. Microscope observation of tools and chip proves that surface finish is ruled by tool-chip adhesion and that alloys having almost the same chemical composition can provide substantially different results due to grain dimension and distribution.
EDM performances are evaluated in terms of surface finish, dimensional and geometrical accuracy of the workpieces and wear mechanisms of the electrodes. Moreover, SEM observation is performed to investigate the presence and composition of deposits on the electrode surfaces, as well morphology of EDMed surfaces. The chosen benchmark allows to evaluate machining quality in various geometrical configurations, which can influence the erosive mechanisms and are representative of the industrial operative conditions. No remarkable differences can be identified as to dimensional tolerances between the three alloys: results are satisfactory for all of them. A slight trend to give lower roughness values can be noticed for the alloy 7050. The results are coherent with the regular morphology observed on the machined surfaces of this alloy. The observation of the erosion mechanisms allows to affirm that, for the same process parameters and very similar finishing results, the morphology of the machined surface can be considerably different, for example as to cracks density.
The above considerations, together with the higher mechanical properties of Al 7050 with respect to 2219 and 7075, suggest its profitable use for moulds production.

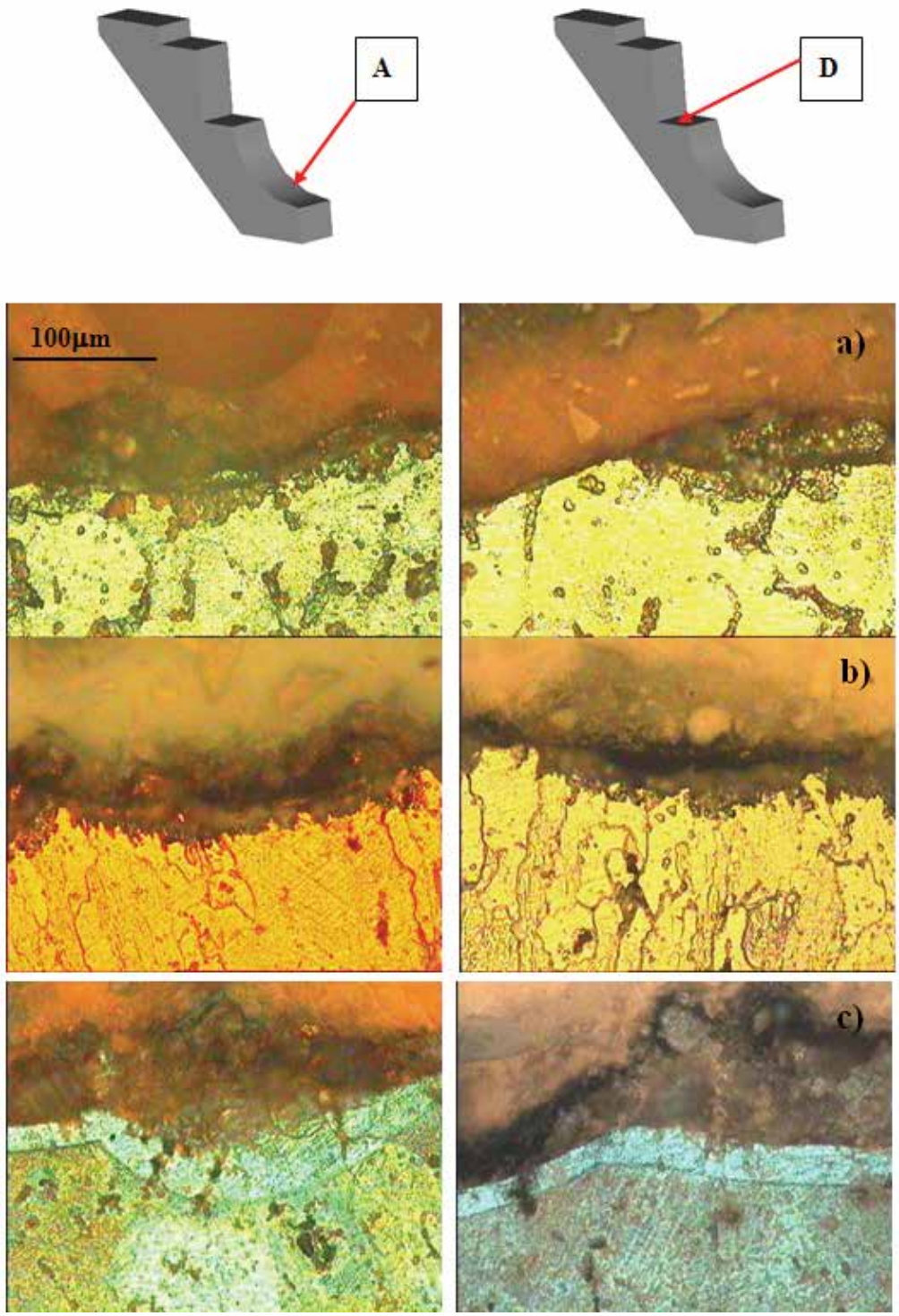

Fig. 14. Etched sections of roughed workpieces: a) Al 7075, b) Al 7050, c)Al 2219

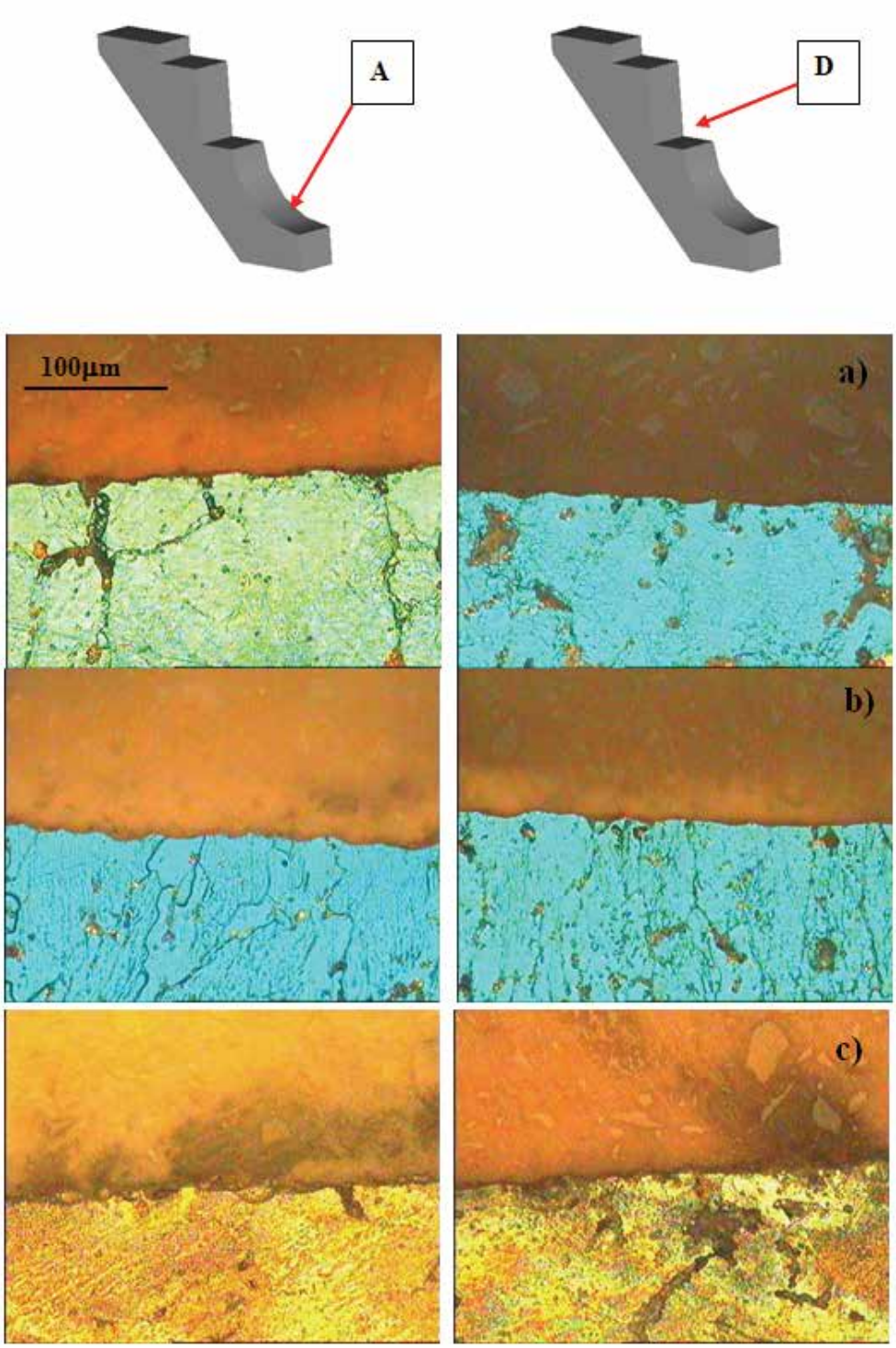

Fig. 15. Etched sections of finished workpieces: a) Al 7075, b) Al 7050, c)Al 2219

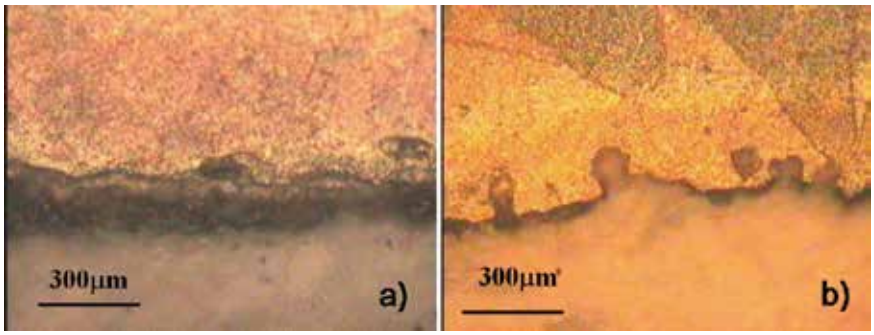

Fig. 16. Etched section of the electrode use for roughing (a) and finishing (b) on Al2219

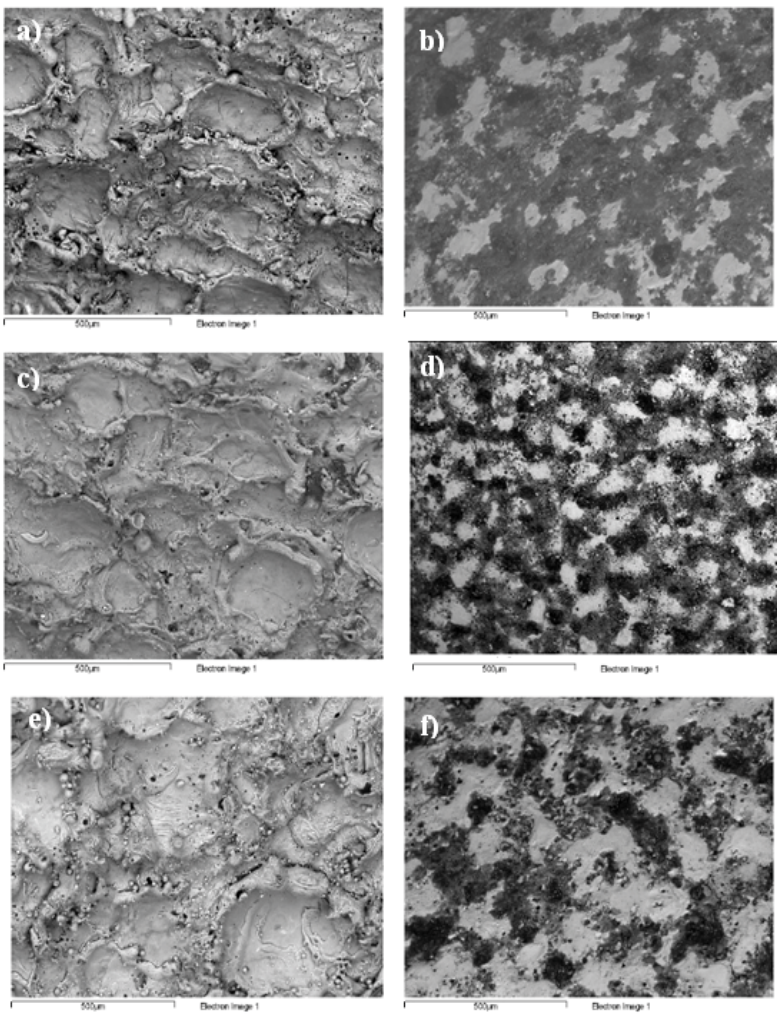

Fig. 17. Surfaces of the workpieces: a)Al 7075, c) Al7050, e)Al 2219 after roughing; and of the electrodes: b) Al 7075, d) Al7050, f)Al 2219; after roughing (A zone)

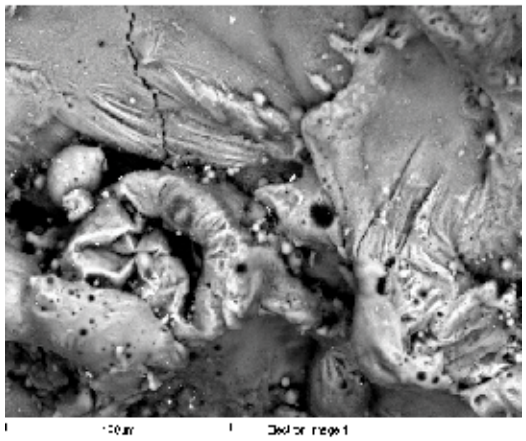

Fig. 18. Detail of Al7075 after roughing

8. References

Amorim, F.L. & Weingaertner, W.L. (2002). Influence of duty factor on the die-sinking Electrical Discharge Machining of high-strength aluminum alloy under rough machining, *J. Braz. Soc. Mech. Sci.*, 24, 3, ISSN 0100-7386

Bassoli, E.; Iuliano, L. & Salmi, A. (2010). Deep drilling of Aluminium die-cast parts: surface roughness, dimensional tolerance, and tool-chip interaction, *Mat. and Manuf. Proc.*, 25, 6, 442 – 449, ISSN 1042-6914.

Chamberlain, B. (1979). Machinability of Aluminium Alloys, In: *Metals Handbook, Vol. 2 – Properties and Selection: Nonferrous Alloys and Pure Metals - 9th Edition*, 187–190, ASM Intl., ISBN 0871700085.

Diver, C.; Atkinson, J.; Helml, H.J. & Li, L. (2004). Micro-EDM drilling of tapered holes for industrial applications, *J. Mater. Process. Technol.*, 149, 296–303

Erstling, A. (1998). Aluminium - Ein Werkstoff Inspiriert - Designer -Blasform, *Der Stahlformenbauer*,.6, 70-80.

Gatto, A. & Iuliano, L. (1994). Chip formation analysis in high speed machining of a nickel base superalloy with silicon carbide whisker-reinforced alumina, *Int. J. Mach. Tool. Manu.*, 34, 8, 1147-1161, ISSN 0890-6955.

Gatto, A.; Iuliano, L. & Settineri, L. (1998). High-speed turning experiments on metal matrix composites, *Composites Part A*, 29, 12, 1501-1509, ISSN 1359-835X.

Gatto, A.; Iuliano, L.; Bassoli, E. & Violante, M.G. (2002). High speed milling of light alloys: tool performance and chip formation analysis, *Proceedings of ESDA 2002*, July 8-11 2002, Istanbul, Turkey.

Guu, Y.H.; Hocheng, H.; Chou, C.Y. & Deng, C.S. (2003). Effect of electrical discharge machining on surface characteristics and machining damage of AISI D2 tool steel, *Mat. Sci. and Eng. A*, 358, 1-2, 37-43

Han F., Kunieda, M. (2001). Chaos Found in Distribution of EDM Spark, *Proc. of ISEM XIII*, pp. 185–192.

Ho, K.H. & Newman, S.T., (2003). State of the art electrical discharge machining (EDM), *International Journal of Machine Tools and Manufacture*, 43,13, 1287-1300.

Iuliano, L.; Violante, M.G.; Gatto, A. & Bassoli, E. (2008). Study of the EDM process effects on Aluminum alloys, *Int. J. Manufacturing Technology and Management, Special Issue on "Innovative approaches in Technology and Manufacturing Management"*, 14, 3-4, 326-341.

Khan, A.A. (2008). Electrode wear and material removal rate during EDM of aluminum and mild steel using copper and brass electrodes, *Int J Adv Manuf Technol,* 39, 482–487

Kishawy, H.A.; Dumitrescu, M.; Ng, E.-G. & Elbestawi, M.A. (2005). Effect of coolant strategy on tool performance, chip morphology and surface quality during high-speed machining of A356 aluminum alloy, *Int. J. Mach. Tool. Manu.*, 45, 2, 219-227, ISSN 0890-6955

Klocke, F. (1998). The process sequence in tool and diemaking, *Proc. of the Int. Symposium for Electromachining*, pp. 65-97, Germany, May 11-13 1998, Vol. 1.

Kuppan, P.; Rajadurai, A. & Narayanan, S. (2008). Influence of EDM process parameters in deep hole drilling of Inconel 718, *Int J Adv Manuf Technol*, 38,74–84.

Lee, H.T. & Tai, T.Y. (2003). Relationship between EDM parameters and surface crack formation, *J. Mater. Process. Technol.*, 142, 3, 676-683

Lin, Y.C.; Yan, B.H. & Huang, F.Y. (2001). Surface modification of Al-Zn-Mg aluminum alloy using the combined process of EDM with USM, *J. Mater. Process. Technol.*, 115, 3, 359-366, ISSN 0924-0136

Liu, H.-S.; Yan, B.-H.; Huang, F.-Y. & Qiu, K.-H. (2005). A study on the characterization of high nickel alloy micro-holes using micro-EDM and their applications, *J. Mater. Process. Technol.*, 169, 418–426

Lopez De Lacalle, L.N.; Lamikiz, A.; Salgado, M.A.; Herranz, S. & Rivero, A. (2002). Process planning for reliable high-speed machining of moulds, *Int. J. of Production Res.*, 40, 12, 2789 – 2809.

Miller, P. & Guha, A. (1998). Effects of Electrical Discharge Machining on the surface characteristics of mold materials, The J. of injection molding technology, 2, 3, 128-135, ISSN 533-905X.

Mohri, N.; Saito, N.; Tsunekawa, Y. & Kinoshita, N. (1993) Metal Surface Modification by Electrical Discharge Machining with Composite Electrode, *CIRP Annals - Manufacturing Technology*, 42, 1, 219-222, ISSN 0007-8506.

Müller, C. & Blümke, R. (2001). Influence of heat treatment and cutting speed on chip segmentation of age hardenable aluminium alloy, *Mat. Sci. and Tech.*, 17, 6, 651-654.

Pecas, P.; Ribeiro, I.; Folgado, R. & Henriques, E. (2009). A Life Cycle Engineering model for technology selection: a case study on plastic injection moulds for low production volumes, *J. of Cleaner Production*, 17, 9, 846-856, ISSN 0959-6526

Pham, D. T.; Ivanov, A.; Bigot, S.; Popov, K. & Dimov, S. (2007). An investigation of tube and rod electrode wear in micro EDM drilling, *Int J Adv. Manuf. Technol.*, 33, 103–109.

Ozcelik, B.; Ozbay, A. & Demirbas, E. (2010). Influence of injection parameters and mold materials on mechanical properties of ABS in plastic injection molding, *Int. Comm. in Heat and Mass Transfer*, In Press, ISSN 0735-1933

Schultz, H. (1984). High speed milling of aluminium alloys, High SpeedMachining, ASME, New York.

Schultz, H. & Moriwaki, T. (1992). High-speed machining. *Annals of the CIRP*, 41, 2, 637–643.

Shobert, E.I. (1983). What happens in EDM, In: *Electrical Discharge Machining: Tooling, Methods and applications*, E.C. Jameson (Ed.), 3-4, Society of Manufacturing Engineers, Dearborn, Michigan.

Simao, J.; Lee, H.G.; Aspinwall, D.K.; Dewes R.C. & Aspinwall, E.M. (2003). Workpiece surface modification using electrical discharge machining, *Int. J. Mach. Tool. Manu.*, 43, 2, 121-128.

Starke E.A. Jr. & Staley, J.T. (1996). Application of modern aluminum alloys to aircraft, *Progress in Aerospace Sciences*, 32, 2-3, 131-172, ISSN 0376-0421.

Tan, P.C. & Yeo, S. H. (2008). Modelling of overlapping craters in micro-electrical discharge machining, *J. Phys. D: Appl. Phys.*, 41, 205302 (12 pp)

Tsai, H.C.; Yan, B.H. & Huang, F.Y. (2003). EDM performance of Cr/Cu based composite electrodes, *Int. J. Mach. Tool. Manu.*, 43, 3, 245–252

Yoshikawa, H. & Nishiyawa, A. (1999). CVD diamond coated inserts for machining high silicon aluminum alloys, *Diamond and RelatedMaterials*, 8, 1527–1530.

18

Machining and Machinability of Aluminum Alloys

V. Songmene, R. Khettabi, I. Zaghbani, J. Kouam, and A. Djebara
École de technologie supérieure (ÉTS), Department of Mechanical Engineering,
1100 Notre-Dame Street West, Montreal Quebec H3C 1K3
Canada

1. Introduction

The use of materials with low specific weight is an effective way of reducing the weight of structures. Aluminum alloys are among the most commonly used lightweight metallic materials as they offer a number of different interesting mechanical and thermal properties. In addition, they are relatively easy to shape metals, especially in material removal processes, such as machining. In fact, aluminum alloys as a class are considered as the family of materials offering the highest levels of machinability, as compared to other families of lightweight metals such as titanium and magnesium alloys. This machinability quantifies the machining performance, and may be defined for a specific application by various criteria, such as tool life, surface finish, chip evacuation, material removal rate and machine-tool power. It has been shown that chemical composition, structural defects and alloying elements significantly influence machinability [W Konig et al., 1983]. Thus, with similar chemical compositions, the machinability of alloys can be improved by different treatments. Heat treatments, which increase hardness, will reduce the built-up edge (BUE) tendency during machining [M. Tash et al., 2006]. In the case of dry machining, the major problems encountered are the BUE at low cutting speeds and sticking at high cutting speeds, hence the need for special tool geometries [P. Roy et al., 2008]. It has been shown that high levels of Magnesium (Mg) increase the cutting forces at the same level of hardness [M. Tash et al., 2006], while a low percentage of Copper (Cu) in aluminum alloy 319 decreases the cutting force. Similarly, it has been found that heat treatment of 6061, especially aging, influences the forces only at low cutting speeds, while at high speeds, the influence is negligible because of the low temperature rise seen in the cutting zone [Demir H et al., 2008]. Cutting force is just one among several parameters to be considered for a full assessment of the machinability of metallic alloys, with the others being the tool life, the surface finish, the cutting energy and the chip formation mode.

Aluminum alloys are classified under two classes: cast alloys and wrought alloys. Furthermore, they can be classified according to the specification of the alloying elements involved, such as strain-hardenable alloys and heat-treatable alloys. Most wrought aluminum alloys have excellent machinability. While cast alloys containing copper, magnesium or zinc as the main alloying elements can cause some machining difficulties, the use of small tool rake angles can however improve machinability. Alloys having silicon as the main alloying element involve larger tool rake angles, lower speeds and feeds, making

them more cost-effective to machine. Aluminum alloys, which are not sensitive to heat treatments, can be hardened by cold work that can improve their machinability when sharp tools are used. Following (ASM Handbook, Volume 16) the machinability of different aluminum alloys has been treated in general manner with a classification (A, B, C, D and E) according to the alloy state. Traditionally, the machinability of materials involve tool life, cutting forces, productivity or chip form, with less attention paid to particle emission. In this work, the authors address the machinability of aluminum alloys from several points of view, including cutting forces, chip forms and segmentation, and metallic particle emission. The following section addresses machinability, while section 3 focuses on metallic particle emission during the machining of aluminum and the effect of materials, cutting conditions and lubrication mode.

2. Machinability of aluminum alloys

2.1 Cutting force during machining of aluminum alloys

While the cutting forces during the machining of aluminum alloys are relatively low, they can nevertheless provide a good indicator for a comparison of different alloys under the same machining conditions (Zaghbani and Songmene, 2009). A typical cutting force signal acting on the cutter in the axial direction (thrust force Fz) during drilling is presented in Figure 1. Portion a-b of the graph (Fig. 1a) corresponds to the drill point engagement into the workpiece while the portion b-c corresponds to the real cutting. Portion b-c is usually employed to estimate the cutting force or the energy required to shape metals. Using an enlarged graph (Fig. 1b), it is possible to identify the action of each flute of the cutter during the cutting process.

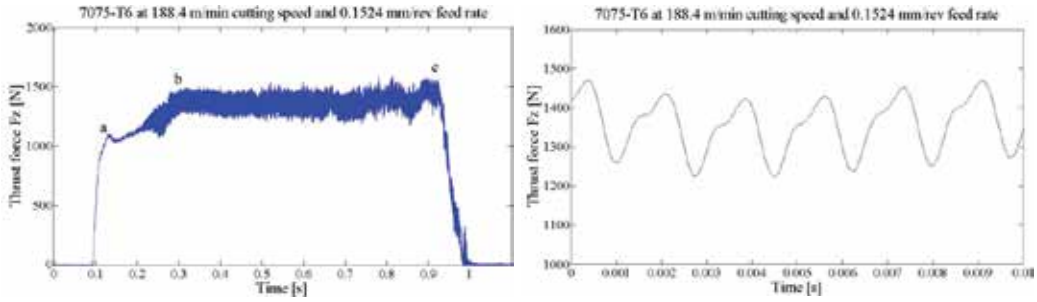

(a) (b)

Fig. 1. Typical instantaneous cutting forces during drilling of 7075-T6 aluminum alloys

The average thrust force (portion b-c of Fig. 1a) for different cutting speeds when drilling four different aluminum alloys (6061-T6, 7075-T6, A356-T0, A319-T0) is presented in Figure 2 (Kouam et al, 2010). It can be seen that only the 7075-T6 is sensitive to variations of the cutting speed, and exhibits a decrease in the average thrust force, which is probably due to the softening effect observed at relatively high speeds. The three other alloys exhibit a low sensitivity to variations of cutting speed.

The cutting forces are more sensitive to the variations of the feed. In fact, the feed determines the chip thickness, which is the major factor governing the cutting forces. Different drilling tests were performed using a High Speed Steel drill with a 10 mm diameter and a point angle of 118° in order to determine the effect of feed and alloys on

cutting forces. The results obtained are presented in Figure 3. As expected, the thrust force increases with the feed rate at different cutting speeds for all tested materials. These results (Fig. 3) confirm the previous works of different authors (M.C. Shaw, 1989; E. J A. Armarego, 1984; Subramnian et al., 1977 and Balout et al., 2002). The thrust force (F_z) increases as the feed rate increases for the cast and wrought materials.

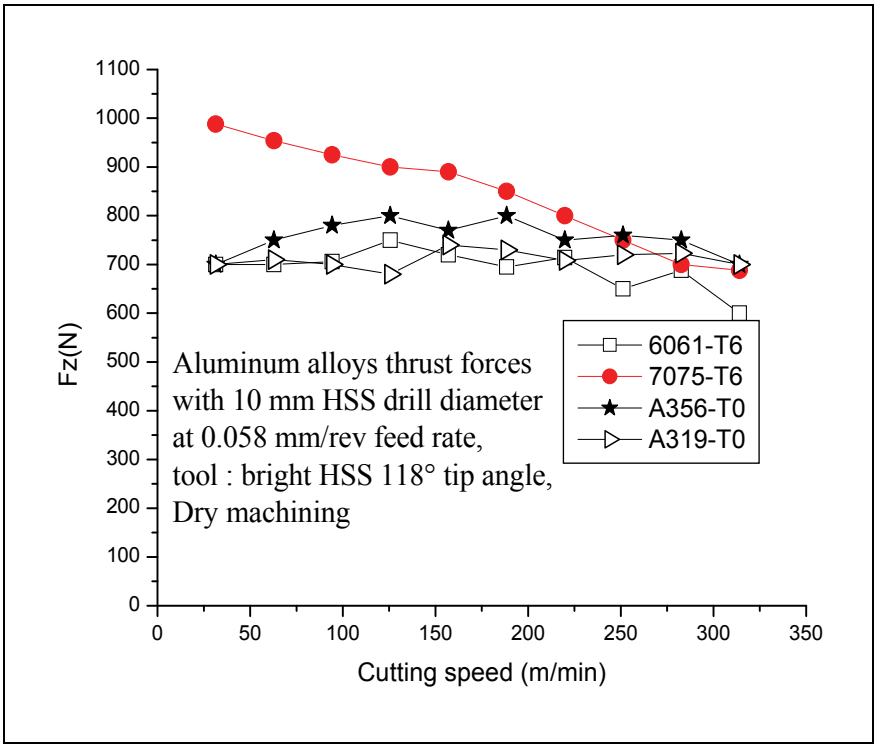

Fig. 2. Thrust force Fz at different cutting speeds for 6061-T6 material, 7075-T6 material, A356-T0 material and A319-T0 material

2.2 Chip formation and chip segmentation

The chip shape and microstructure constitute a good indicator of the deformation having occurred during the machining process. The chip formation mode depends on the workpiece material, the tool geometry and the cutting conditions. A small and segmented chip is preferable when cutting metals. Several research works have analyzed chip formation in order to identify the optimal conditions for improving machining and machinability. Xie et al. (1996) developed a coefficient identifying chip segmentation, called the flow localization parameter β. Several tests were carried out in the laboratory in order to characterize the chip shape during the machining of aluminum alloys. Figure 4 presents the chip morphology obtained from scanning electronic microscopy (SEM) as a function of cutting speed and alloys when drilling different aluminum alloys at a feed rate of 0.15 mm/rev. It can be observed that even brittle materials, such as A356-T0 and A319-T0, can produce continuous and long chips at low cutting speeds. Similarly, more ductile materials, such as 6061-T6 and 7075-T6, can also produce discontinuous chips (in this case, at moderate speeds).

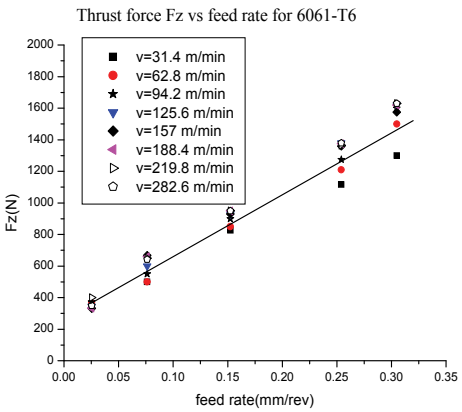

6061-T6

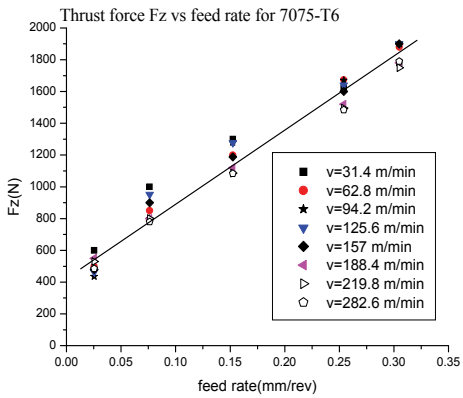

b) 7075-T6

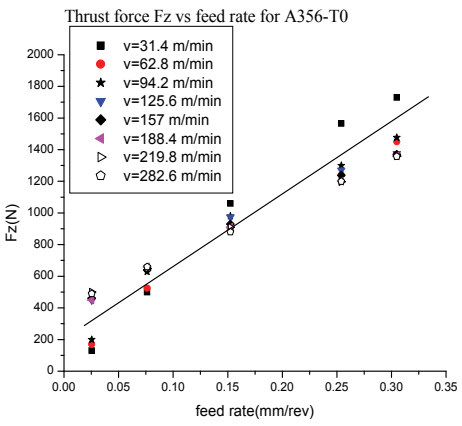

c) A356-T0

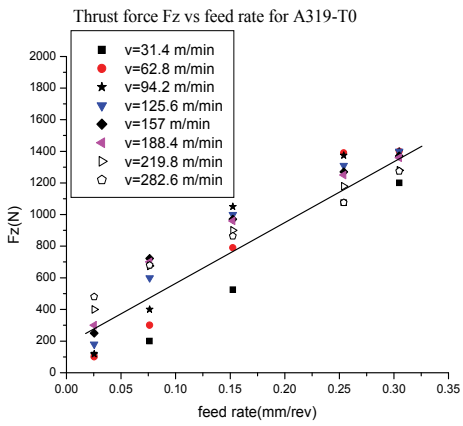

d) A319-T0

Fig. 3. Thrust force Fz at different feed rates; a- 6061-T6 material, b- 7075-T6 material, c- A356-T0 material and d- A319-T0 material.

Materials	Chip form at 31.4 m/min	Chip form at 94.2 m/min	Chip form at 188.4 m/min
6061-T6	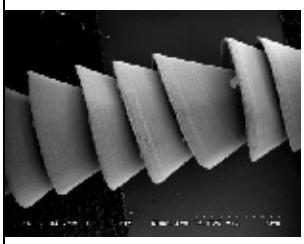	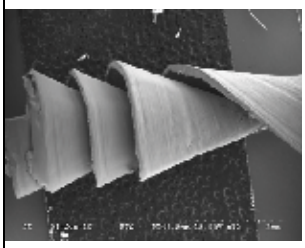	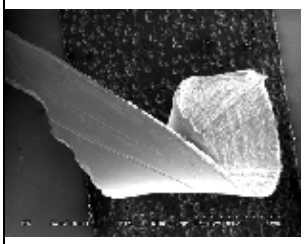
7075-T6	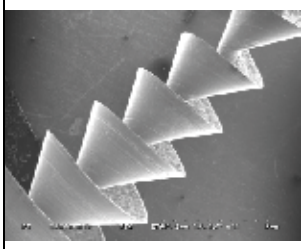	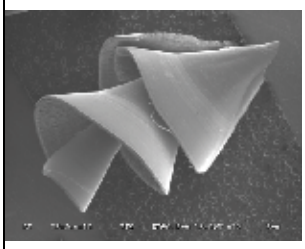	
A356-T0	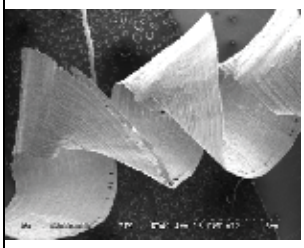	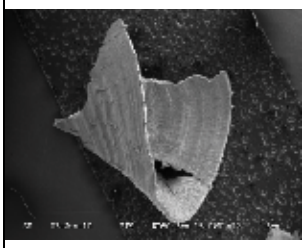	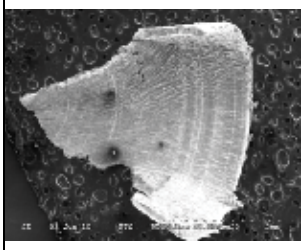
A319-T0	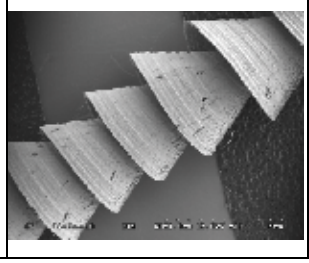	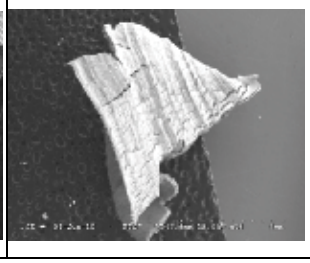	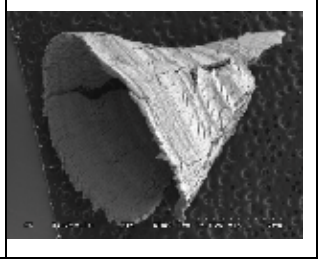

Fig. 4. SEM images of chip obtained during the drilling of aluminum alloys at 0.15 mm/rev feed rate and at different cutting speeds

Figure 5 presents different chip forms and lengths (small, middle and long chip), and is representative for the others materials. In this graph (Fig. 5), the limit zone between continuous and discontinuous chips is delimited. Such limits have made it possible to obtain experimentally Figure 6 delimitating continuous chip form zone to discontinuous chip form zone for each material tested. Determining these limits can help in selecting cutting conditions that will lead to the desired discontinuous chip. The production of discontinuous chips is recommended, especially for automated production, where easy-to-manage chip will not stop production.

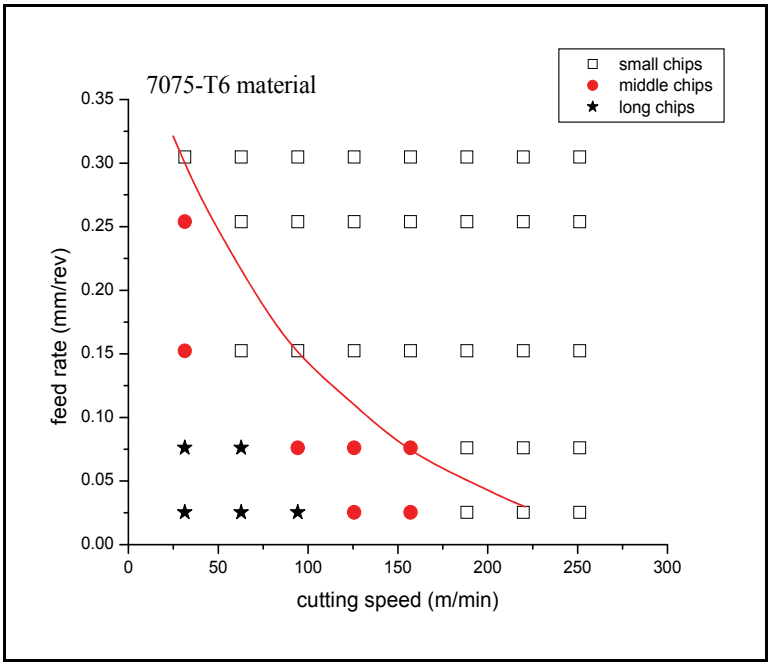

Fig. 5. Experimental chip form map for 7075-T6

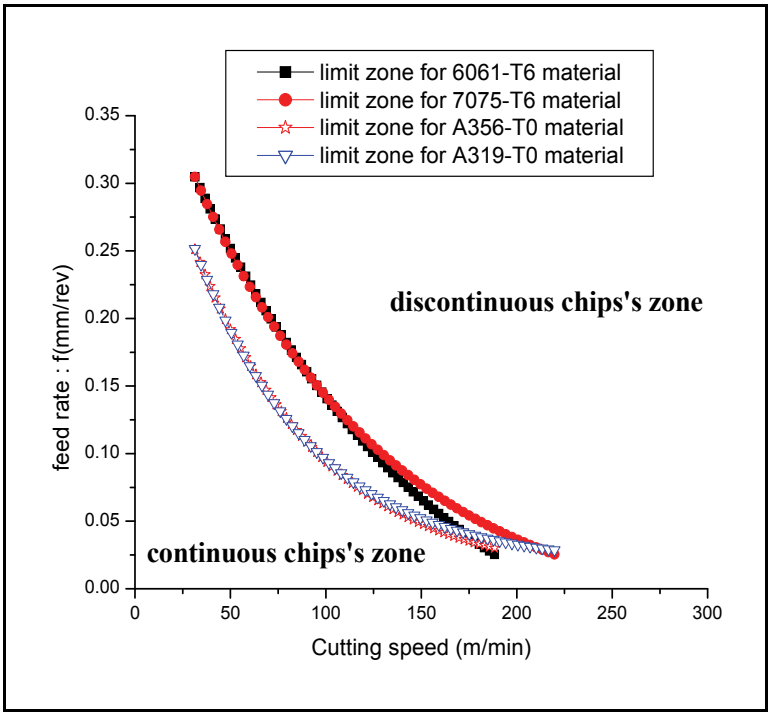

Fig. 6. Experimental chip form transition limits of different materials

It is observed in Figure 6 that at low cutting speeds, the chip is generally continuous for different materials. For 6061-T6 and 7075-T6 materials, the chip length decreases as the cutting speed increases, and it is the same for A319-T0 and A356-T0. This decrease in the length of the chip depends not only on the cutting speed, but also on the feed rate. Figure 6 suggests that the chip length depends not only on the material properties (ductility and brittleness for example) but also on the cutting conditions. Equation (1) can allow the prediction of the chip form, depending on the cutting parameters and the material used. Chip breakability is one of the major issues faced in machining aluminum alloys; in fact, long chips can cause damage to the machined surface, to the cutter and to the machine evacuation system. Chip segmentation is one of the practical tools used to compare the chip breakability of different alloys. From Figure 6, the general trend equation delimiting different chip form zones for the tested aluminum alloys can be expressed as follows:

$$f = f_0 + Ae^{-(\frac{v}{B})} \tag{1}$$

where f is the feed rate, v is the cutting speed, A and B are constants, depending on the workpiece material used. The constants of equation (1) are given as follows in Table 1:

Material	f_0(mm/rev)	A	B
6061-T6	0.00021	0.5	130.62
7075-T6	0.00033	0.45	100.48
A356-T0	0.01	0.4	65.84
A319-T0	0.02	0.4	62.80

Table 1. Constant values for different materials used in the equation (1)

The chip segmentation is schematized in Figure 8 for an orthogonal cutting process. Xie et al. (1996) found that there are some critical values of the product of the cutting speed and feed rate for which chip segmentation begins. The segmentation can also be defined by the segmentation band density. According to the formulation of Becze and Elbestawi (2002), the chip segmentation density η_s can be also estimated by the following equation:

$$\eta_S^{-1} = \left(A + B\exp(CV)\right) * \left(1 + D\left(\frac{f - f_0}{f_0}\right)\right) \tag{2}$$

where f is the feed rate, V is the cutting speed, and A, B, and C are empirical constants. Khettabi et al. (2009) developed a simple method for determining the chip segmentation density using the distance (l) corresponding to 10 segmentation bands (Eq. 3).

$$\eta_s = \frac{1}{l_b} = \frac{10}{l} \tag{3}$$

where l_b is the band width (see Fig. 7).

The chip compression ratio, the chip thickness and the tendency for segmentation during machining of 6061-T6 are presented in Table 2. The gray cells represent a continuous chip formation zone, while the white cells represent conditions at which the formation of segmented chip occurred. The chip compression ratio C_h can be calculated using Eq. 4 or estimated using Eq. 5:

$$C_h = \frac{\sin\phi}{\cos(\phi - \alpha)} \tag{4}$$

where a is the tool rake angle and ϕ is the shear angle,

$$C_h = \frac{h}{h_c} \tag{5}$$

where h is the undeformed chip thickness and h_C is the chip thickness (Fig. 8).
For the cutting of aluminum alloy 6061-T6 with a -7 rake angle, the segmentation is observable at speeds starting at 200 m/min, while for the null rake angle, observable chip segmentation starts at about 250 m/min, and for a rake angle of +7°, there is no noticeable segmentation. In the absence of a noticeable chip segmentation, the chip is continuous, while the chip is partially or completely segmented when segments are visible.

Rake angle (°)	100 m/min	150 m/min	200 m/min	250 m/min	300 m/min
-7	0.1876	0.1925	0.2081	0.2199	0.2320
0	0.2147	0.2027	0.2299	0.2330	0.2387
+7	0.2587	0.2744	0.2593	0.2806	0.2894
← Thick chip /Thin chip →					

Table 2. Chip ratio (6061-T6 Aluminum)

In Table 2, the chip compression ratio is geometrically measured for the aluminum alloy 6061-T6. When the cutting speed increases, so does the chip compression ratio, and the chip becomes thin and brittle. It has been observed that when the chip becomes brittle, dust emission decreases significantly (Balout et al., 2007; Khettabi et al., 2008).
While aluminum alloys are considered easy to machine, they can generate harmful metallic particles during the machining process. There is a correlation between chip morphology, cutting parameters, machinability and dust emission. Segmented chips produce less dust, a good finish and allow better machinability than continuous chips, while an increase in the segmentation density increases dust emissions. The following section will focus on the metallic particle generation during the machining of aluminum alloys.

3. Metallic particle emission

3.1 Dust emission problem

In addition of chips, the shaping of metallic alloys, including the machining of aluminum alloys, produce metallic particles of different sizes that can be harmful to the machine tool operator. Diseases caused by exposure to dust range from simple respiratory irritation to bronchitis, asthma and cancer. Consequently, the regulatory health and safety agencies overseeing machining are requiring that more and more manufacturers reduce dust generated from manufacturing processes. A risk prevention and control committee of the World Health Organization working group held in Switzerland in 1999 (EHO, 1999) called for research into dust production process parameters, which should help assess the reliability and costs of changing systems in order to improve dust control. The United States' Environmental Protection Agency (EPA) has found that even low concentrations of certain metals can cause acute pulmonary effects.

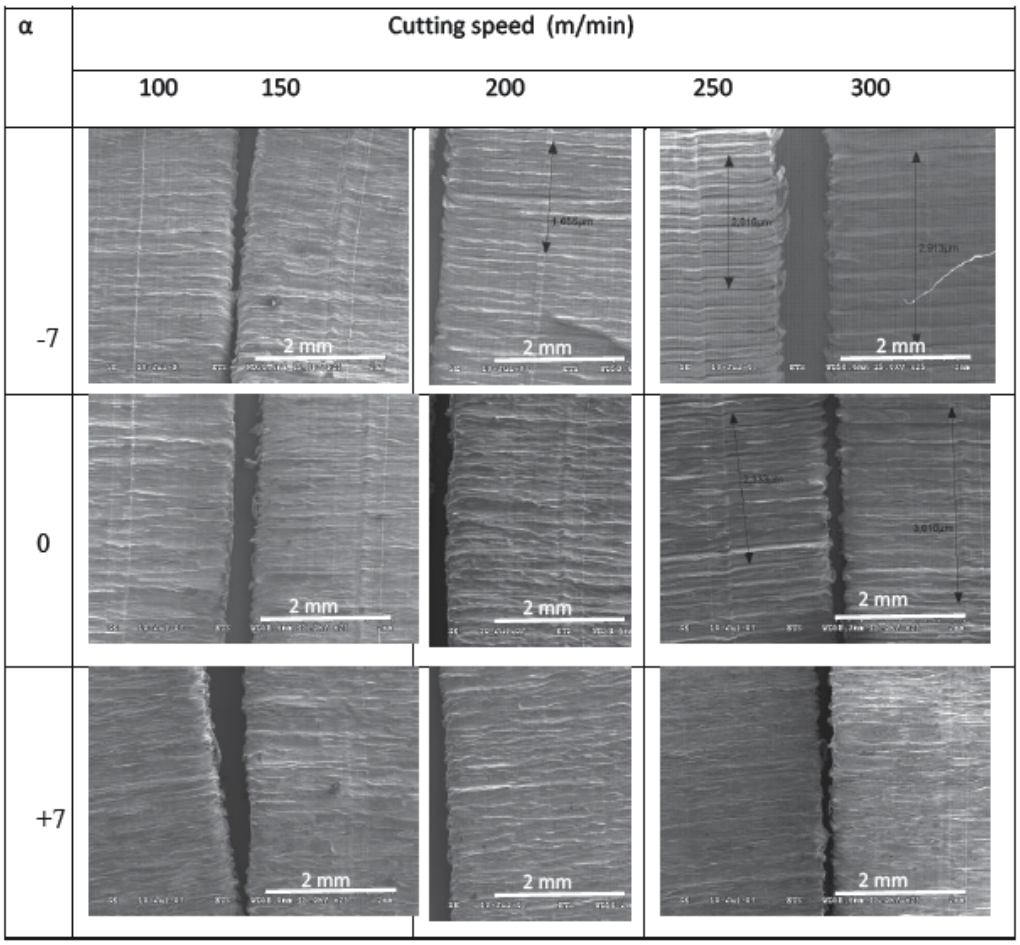

Fig. 7. Aluminum 6061-T6 chip segmentation as a function of cutting speed and tool rake angle when turning 6061-T6

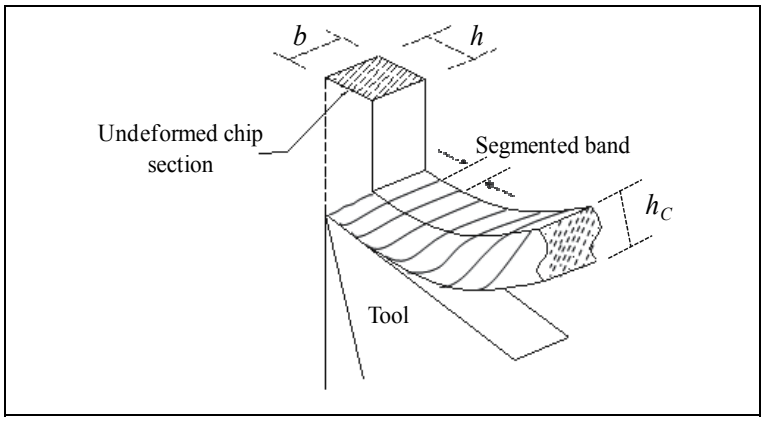

Fig. 8. Orthogonal cutting (uncut chip cross-section)

In situations where the main polluters are gases, air quality control in the industrial environment is usually carried out in free air by sampling particulate matter smaller than 2.5µm (PM 2.5) or by gas receptors. An evaluation of process emissivity must be done using high sensitivity methods. While carrying out measurements in free air (far from the cutting zone) is the usual method for air quality control, it is however not appropriate for determining the emissivity of operations and of materials. Free air measurement involves large sampling volumes, and thus considerably increases the testing time and reduces dust concentration. To identify the emission capacity of each operation in the laboratory, the system must be isolated in order to ensure that the measurements involve only the dust produced by the operation under study. For different cutting processes (Fig. 9) several sampling devices, such as laser photometers (DustTrack), APS (Aerodynamic Particle Sizer Spectrometer), MOUDI (Micro-Orifice, Uniform-Deposit Impactor), ELPI or SMPS (Scanning Mobility Particle Sizer), can be used to measure the particles produced. The measurement device could be connected to the dust recovery enclosure by a suction pipe, and a computer equipped with a data acquisition and analysis system is also connected to the measuring device. For the SMPS system, it can be possible to connect the Nanometer Aerosol Sampler (NAS) at the exit of the DMA of the SMPS in order to collect particles with specially prepared substrates allowing for microscopy analysis of generated particles. For the ELPI or the MOUDI systems, particles can be collected directly on the substrate. Figure 10 shows experimental evidence of fine and ultrafine particles generated during machining carried out in the laboratory. The AFM can show the particles in 3D (Fig. 10a) while with the SEM, it is only in 2D (Fig. 10b).

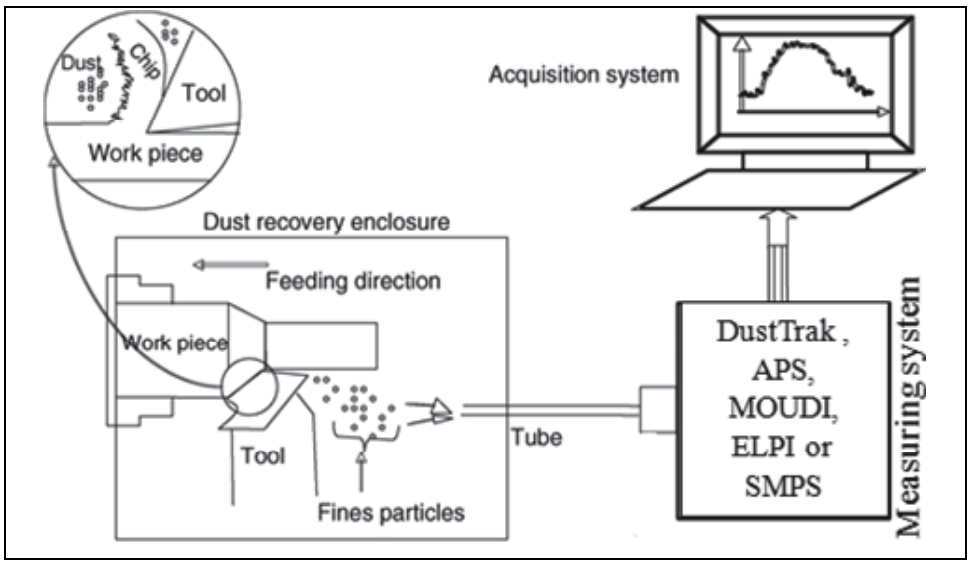

Fig. 9. Experimental set-up used for metallic particle emission test

3.2 Effects of cutting conditions and alloys

Arumugan et al. (2002) studied dust mass concentration during machining and found that the cutting speed is the most influential factor among all cutting parameters (the others being feed and depth of cut). The concentration decreased as the speed was increased in a

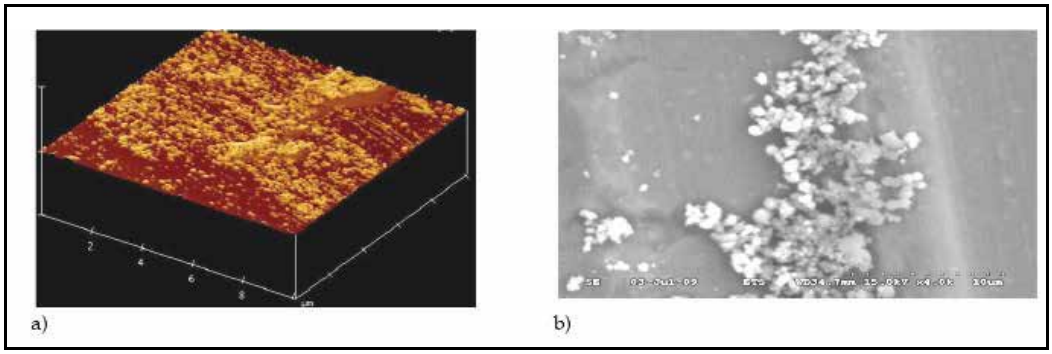

Fig. 10. Particle shape visualization by a) AFM in 3D and b) SEM

specific feed zone. Songmene et al. (2007, 2008) found two different zones (I and III) corresponding to low and high cutting ranges, respectively, in which the dust emission is low. Between the two zones was the zone II in which the dust emission increases with the cutting speed and reached a maximum. Machining in zone I (low cutting speeds) is not recommended because productivity would be reduced. In zone III (high cutting speeds), which is the recommended zone, the dust emission decreases while the productivity and the part quality are improved. Therefore, high speed machining is not only good for improving productivity and lowering the cutting forces and energy consumption, but also for protecting the environment and worker health.

Khettabi et al. (2009) found the same link between dust emission and cutting speed during the turning of aluminum alloys and steels. The result was also confirmed during the dry machining of aluminum alloys and steel materials (Figure 11).

The concentration of particle emissions was found to be higher for wet machining than for dry machining for sub-micron size particles (Zaghbani et al., 2009b). For this size range, the particle mass concentration is 5 to 30 times greater for wet than for dry milling. However, for micronic particles, the mass concentration of particles generated in wet milling is lower than the particle mass concentration in dry milling. Consequently, the cutting fluid allows the generation of more sub-micron wet and dry particles (Fig. 12).

3.3 Understanding and modeling particle emissions

The formation of fine and ultrafine particles during machining is attributable to different phenomena, such as: macroscopic and microscopic friction, plastic deformation and chip formation mode. The friction of the chip micro-segments between themselves produces micrometric and nanometric sized particles. Similarly, the friction at the tool rake face with the chip also produces particles. Figure 13 can give an illustration of the dust emission mechanisms by friction of the chip on the tool rake face.

Particle formation by friction proceeds through two main steps, depending on the workpiece material: step 1 occurs during the material separation while step 2 takes place when the chip slides on the tool rake face. In the case of brittle materials, the chip is formed by brittle fracture, with the chip contact length being very small. In this situation, the contact between the tool material and the irregular chip surface can break up particles from the internal chip surface. If the workpiece material is ductile, the chip will be formed by micro-segments that undergo a local work hardening due to the action of some asperities of the tool rake face. Then, the hardened small part is separated by a local brittle fracture. This

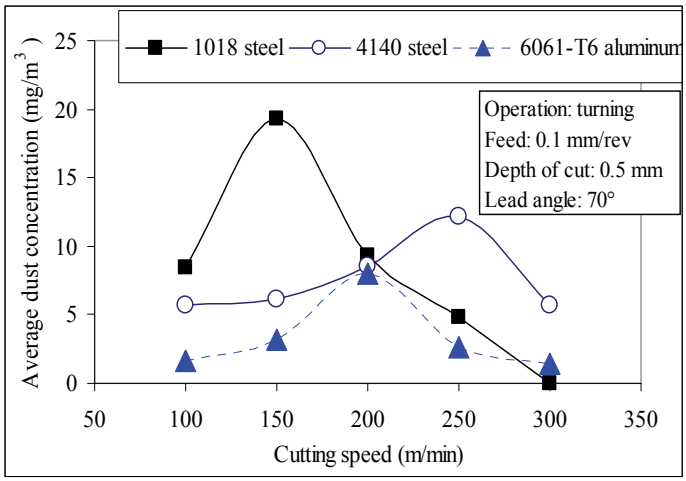

a)

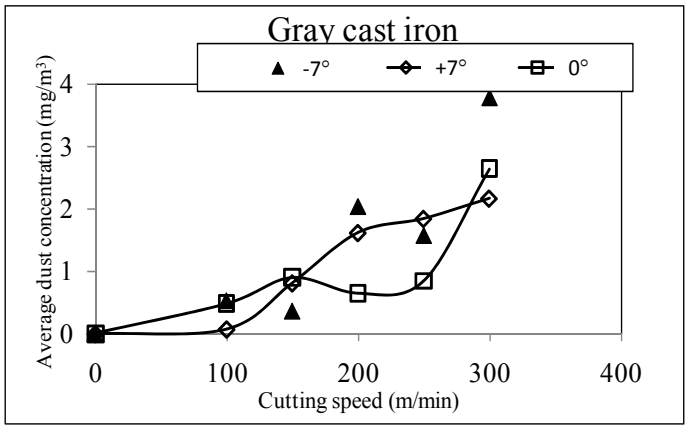

b)

Fig. 11. Average dust concentration (PM2.5) as a function of cutting speed when turning a) steels and 6061-T6 aluminum and b) gray cast iron.

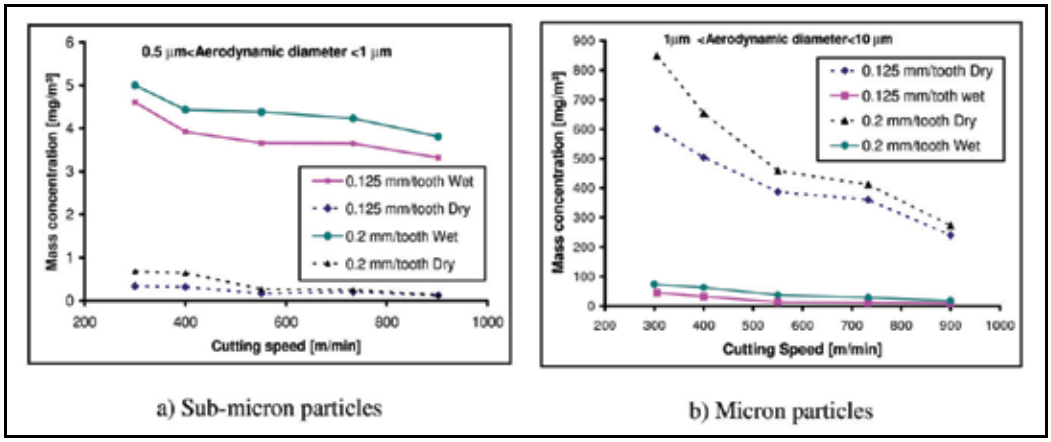

Fig. 12. Influence of the cutting speed on mass concentration for different particle sizes

mechanism describes how friction or micro-friction can produce small particles during machining. The size of the particles separated depends on the tool rake face roughness, the cutting conditions, and the workpiece material.

The dust generation mechanism is not caused purely by the mechanical effect, as the temperature of the chip formation zone also plays a big role in this mechanism. The temperature involved in the cutting process alters the mechanical properties of the material, and modifies the chip formation mode and the particle emission. The temperature and the plastic deformation effects are integrated into the deformation energy that will subsequently be used in modeling.

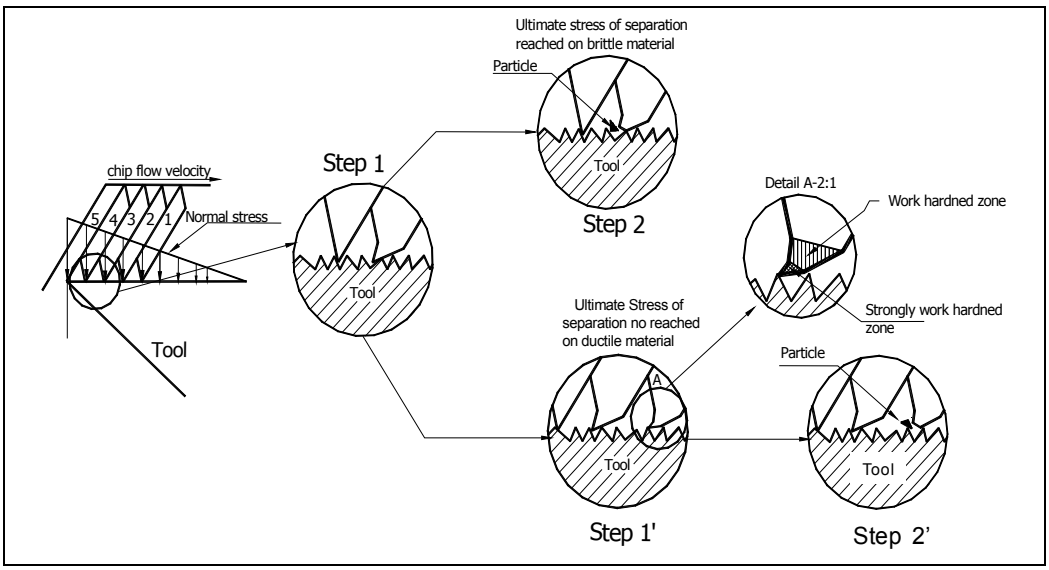

Fig. 13. Schematic illustration of mechanisms of dust emission at the chip-tool

The measurement system generates different types of information concerning the sampled dust, including the aerodynamic diameter, the stocks size, the electrical mobility etc. However, some transformations should be done to evaluate the mass, the volume or the

number of particles when the concentration and the flow rate are known. It presents the dust particle concentration versus the acquisition time. Khettabi et al. (2007) propose a new more representative dimensionless index, which has a physical meaning, and allows a large-scale comparison. This new index is the ratio of the dust mass to the mass of chip removed from the workpiece material:

$$Du = \frac{m_{Dust}}{m_{Chip}} \tag{6}$$

where m_{Dust} (g) is the mass of total dust generated and m_{Chip} (g) is the mass of the chip produced.

The mass of the chip m_{chip} (g) is evaluated by multiplying the volume of material removed by the density.

Khettabi et al. (2010a) developed a hybrid model of particle emission during machining processes which was based on the energy approach, combined with macroscopic friction (tool-chip), microfriction, and plastic deformation of materials:

$$D_u = A \times \frac{\beta_{max} - \beta}{\beta_c} \times R_a \times \eta_S \cdot \left(\frac{V_0}{V}\right)^{\delta} \exp\left(\frac{-E_A}{\tan\phi(1 - C_h \sin\alpha) V_c \frac{F_{sh}}{bf}}\right) \tag{7}$$

where A is the factor of proportionality and δ is a material parameter introduced to characterize the capacity of the material to produce metallic dust. For each material, a constant δ is attributed. The parameter δ is experimentally determined to obey the following criteria (Eq. 8).

$$\delta \equiv \begin{cases} \delta \geq 1 \rightarrow Ductile \quad materials. \\ 0.5 < \delta < 1 \rightarrow semi - ductile \quad materials \\ 0 < \delta \leq 0.5 \rightarrow Brittle \quad materials \end{cases} \tag{8}$$

Aluminum alloys are generally considered to be ductile materials. For cast aluminum alloys: $0.5 \leq \delta \leq 1.0$ and for wrought aluminum alloys: $1.5 \leq \delta$ (6061-T6:δ=1.5)

All parameters in equation 7, such as the rake angle α, the shear angle ϕ, the cutting speed V, the feed f, the roughness Ra, βmax, and βc, can be known or easily determined. The shearing force and temperature can be measured directly or estimated, although measurements will be difficult in the case of some processes. Estimation is possible using the Needelman-Lemonds constitutive equations.

The predictive dust emission model (Eq. 7) is found to be in agreement with experimental results (Figs. 14, 15, 19, 20). An algorithm was programmed and used to simulate dust emissions during the dry machining of aluminum and steel alloy. Carbide tools with different geometries were used for different tests.

Brittle materials, such as cast aluminum alloy or gray cast iron, present a special behavior (Fig 15). In this case, zone III has disappeared, and dust emission is continuously increased

with the cutting speed. The decrease in dust emission at high speed (Fig.14, zone III) is attributed to the softening effect of the ductile materials, which is not the case for brittle materials such as cast aluminum alloy or gray cast iron (Fig. 15).

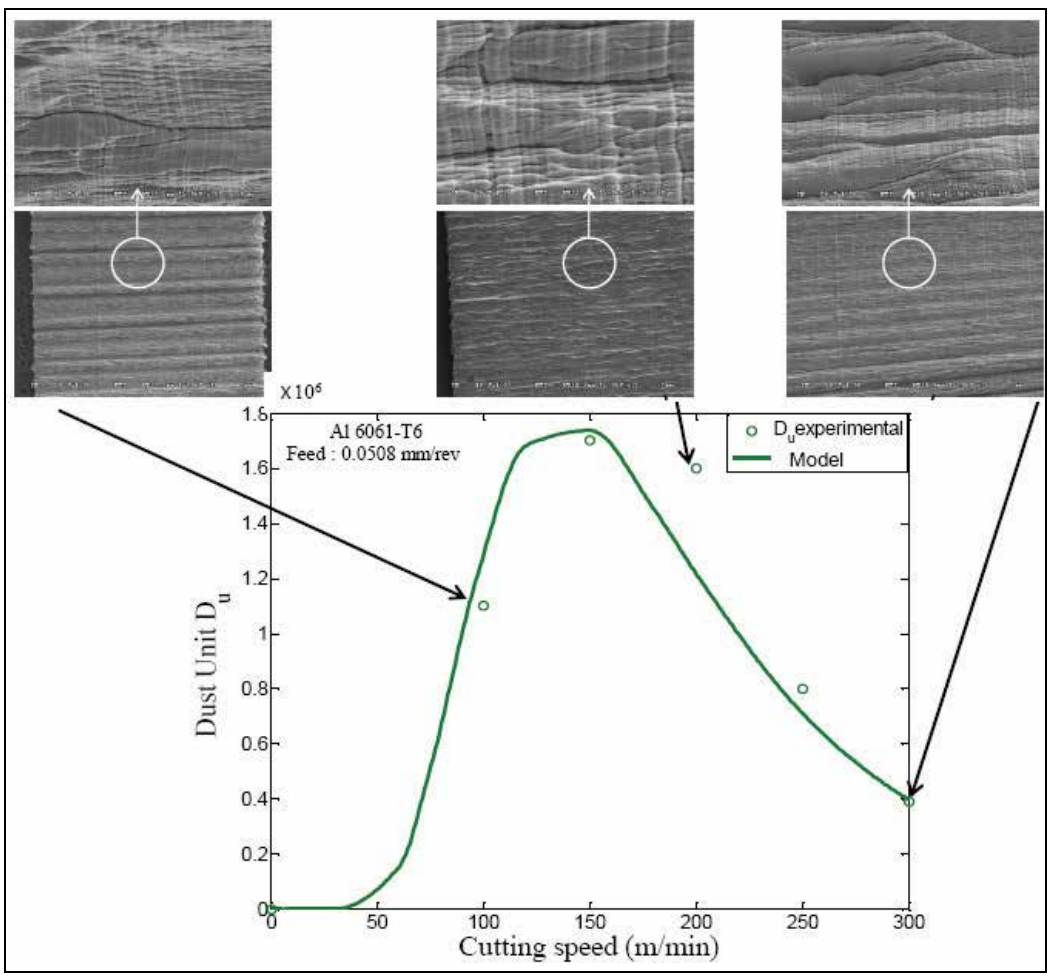

Fig. 14. Simulation results and experimental results for dust emission when dry machining Al 6061-T6

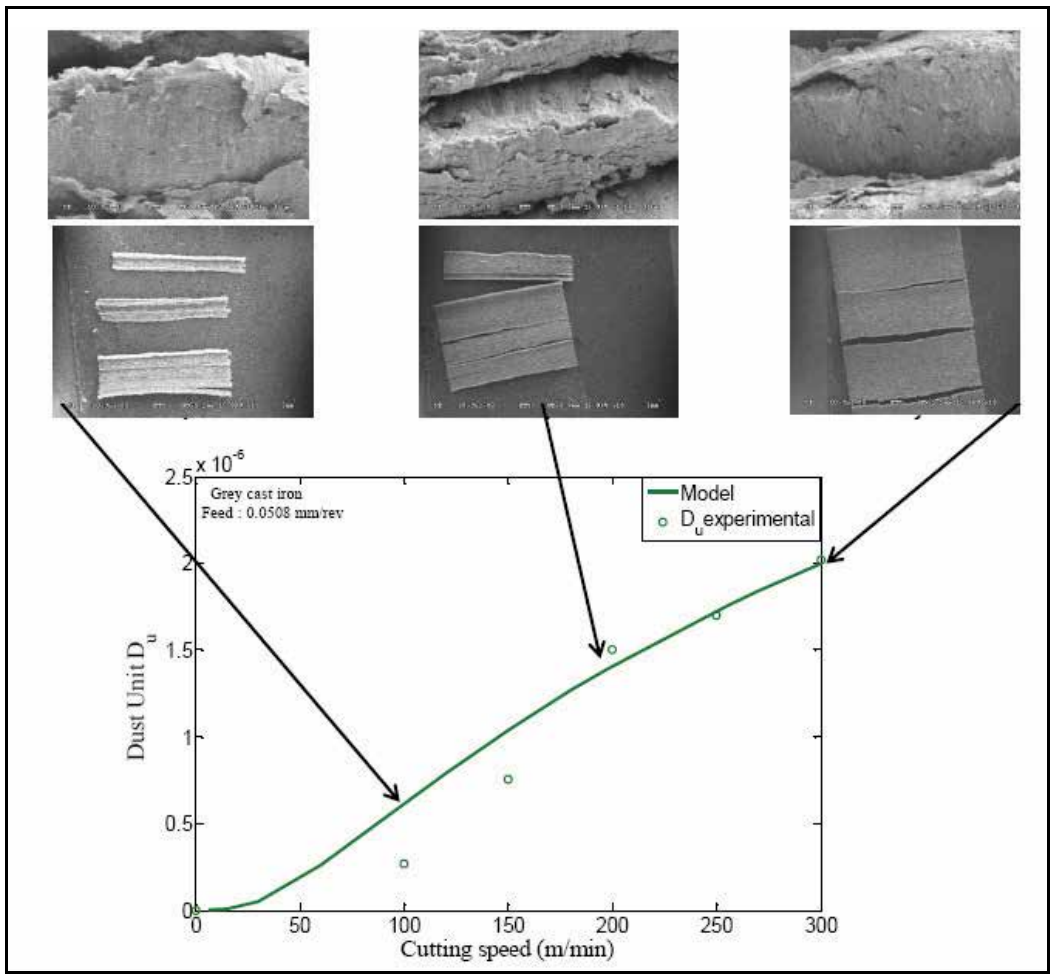

Fig. 15. Simulation results and experimental results for dust emission when dry machining gray cast iron

In the intermediate cutting speed range (zone II, between 100 and 150 m/min, Fig. 14), the particles emission is higher compared to the other ranges. The highest value of the particles emission corresponds to the critical value of the cutting speed that should be avoided. The critical cutting speed appears to be widely influenced by the workpiece material, and not by the machining processes (Khettabi et al., 2010b). It seems that the critical cutting speed depends significantly only on the workpiece material, and not on the machining processes, the tool geometry or the heat treatment. For the 6061-T6 aluminum alloy, the critical cutting speed is around 150 m/min during drilling, milling and turning (Figs. 16-18). It also observed that the critical cutting speed is still invariable for different rake angles and different lead angles.

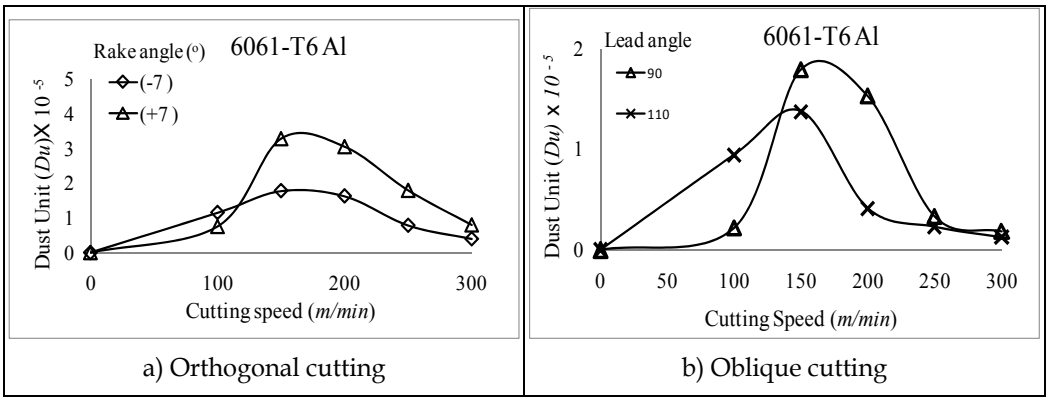

a) Orthogonal cutting b) Oblique cutting

Fig. 16. Particle emission as a function of cutting speed and tool geometry during oblique and orthogonal cutting of 6061-T6 aluminum alloy

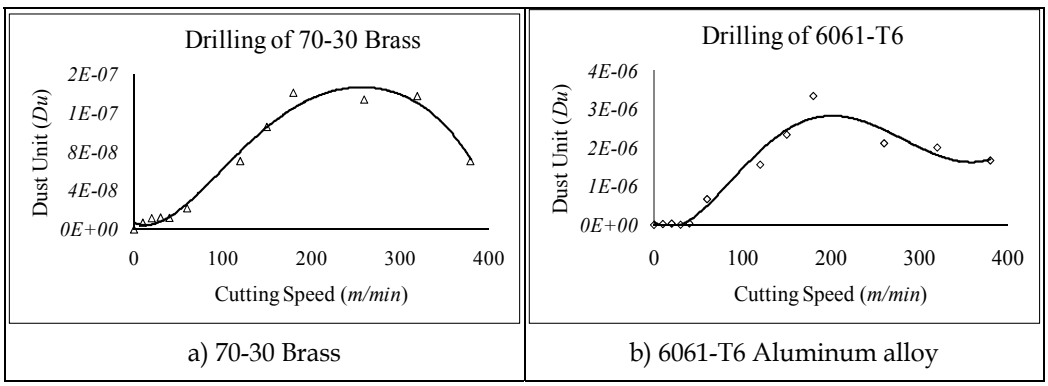

a) 70-30 Brass b) 6061-T6 Aluminum alloy

Fig. 17. Particle emission during drilling of a) 6061-T6 aluminum alloy, and b) 70-30 Brass

Heat treatment influences the mechanical properties, and consequently, the quantity of particles emitted (Fig. 18). It was found that the critical value of the cutting speed, at which particle emission is at a maximum, depends on the material, and not significantly on the heat treatment. However the quantity of particles emitted at that critical speed depends on workpiece materials conditions (Fig. 18).

Figure 19 presents the simulation results (Eq. 7) for dust emission as a function of the feed and cutting speeds for dry machining of aluminum alloy 6061-T6. It was found that the

generated dust decreases with chip thickness, a result which is consistent with the experimental findings of Akarca et al. (2005) and Fang (2007). Therefore, an increase in the feed rate could reduce the amount of dust generated during machining. When the feed rate and cutting speeds both increase, the chip becomes more segmented, and consequently, the dust emission decreases.

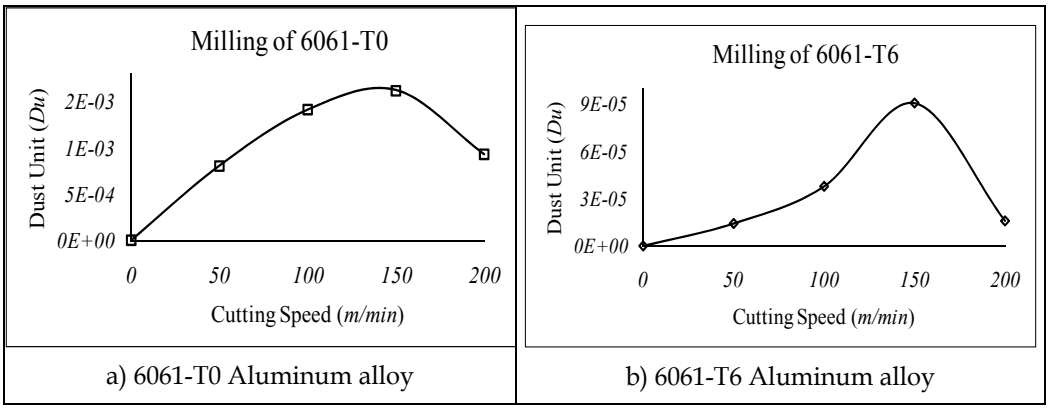

a) 6061-T0 Aluminum alloy b) 6061-T6 Aluminum alloy

Fig. 18. Experimental (Du) during milling of aluminum alloy 6061-T6 and T0

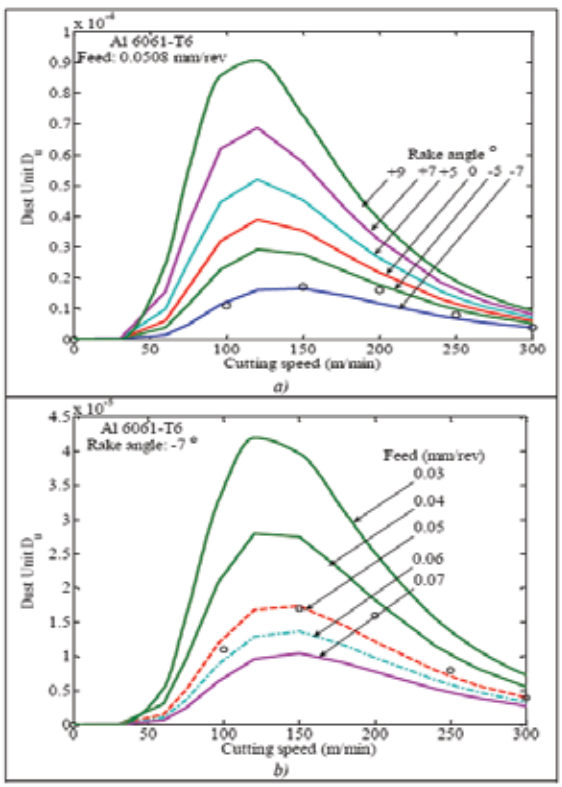

Fig. 19. Simulation results for particles emission during dry machining of Al 6061-T6 varying with cutting speed and: a) rake angle and b) feed

Figure 20 presents the simulation results (Eq. 7) for dust emission as a function of the tool rake angles and the cutting speeds for aluminum alloys, steels and cast iron. These results show good agreement with experimental data and the proposed model results (Figure 20). Even nanoparticle emission results during machining confirm the rake angle effect (Tönshoff et al, 1997). When the tool rake angle increases, the dust emission also increases.

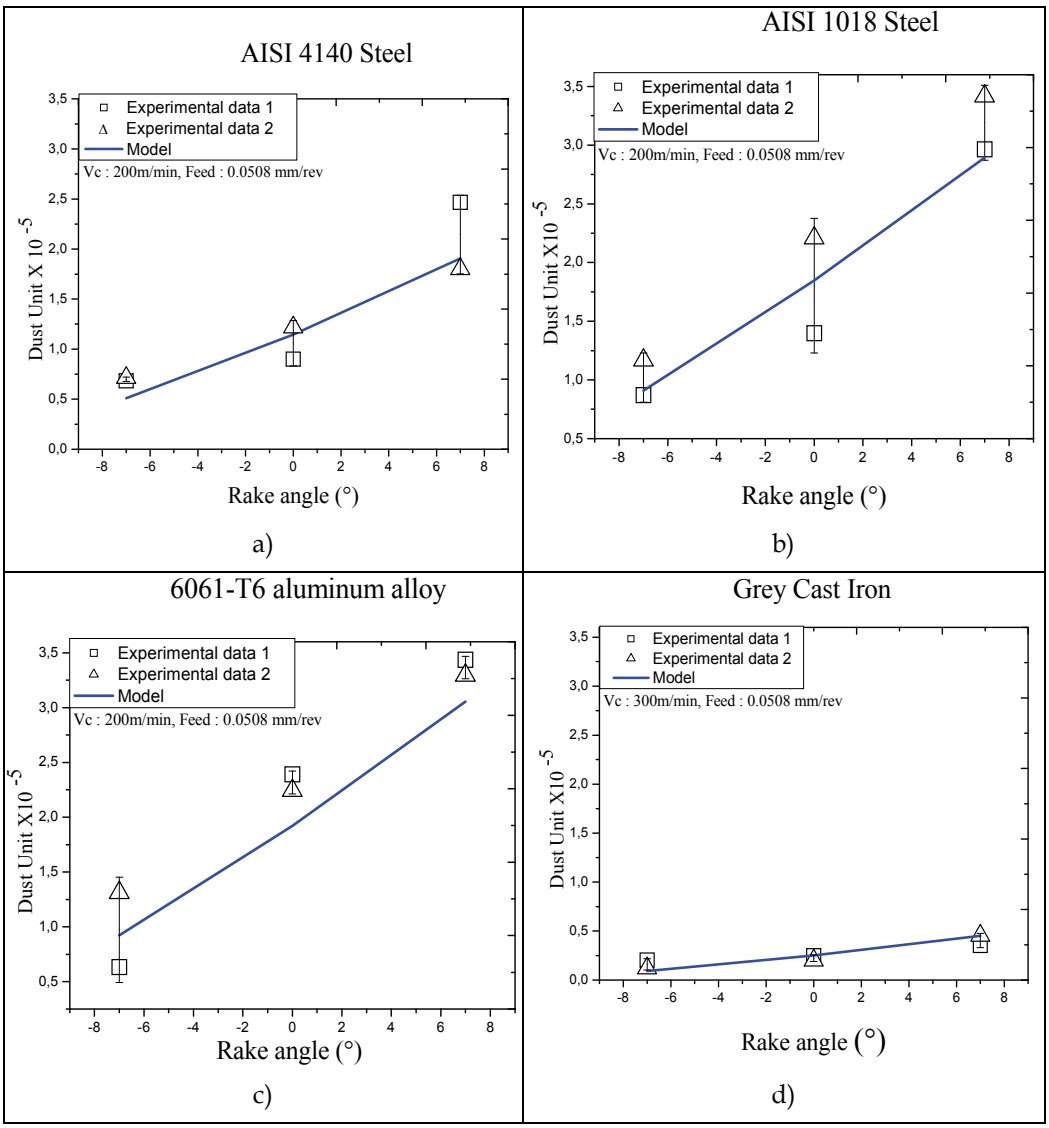

Fig. 20. Predicted dust emission data as given by equation 7 (line) compared to two experimental data of AISI 1018, AISI 4140 steels, gray cast iron and 6061-T6 aluminum alloy

3.4 Metallic particle size distribution

Size distribution as a function of the different concentrations shows a decrease in particles emission when cutting speed is increased (Figs. 21-22). A comparison for different aluminum alloys illustrate that particles emissions can decrease when the material toughness decreases (Figs. 21-22). Small-sized metallic particles, such as ultrafine particles, are known to be potentially more dangerous.

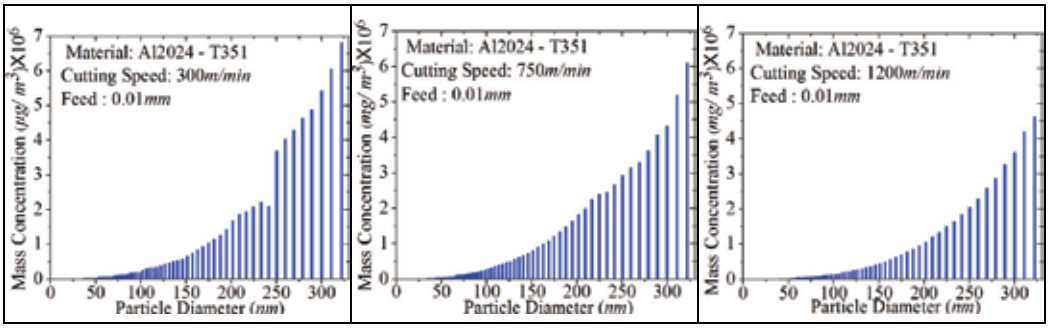

Fig. 21. Mass concentration as a function of size distribution for the 2024-T351 aluminum alloy

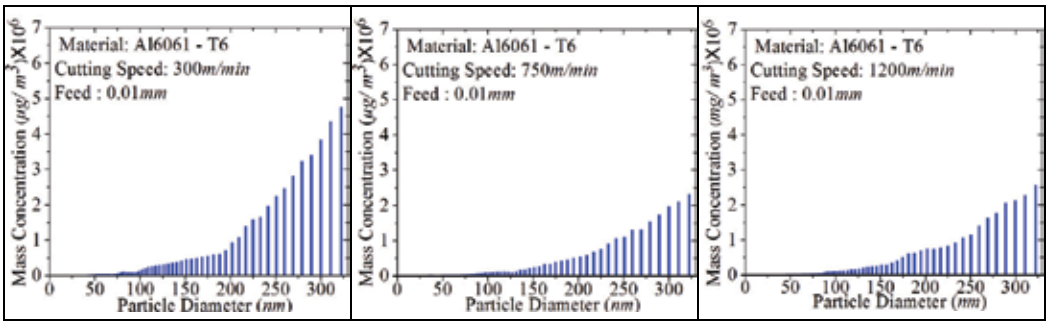

Fig. 22. Mass concentration as a function of size distribution for the 6061-T6 aluminum alloy

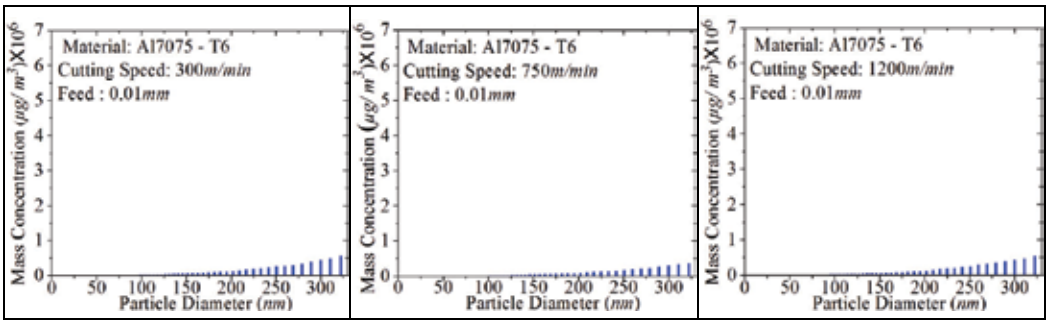

Fig. 23. Mass concentration as a function of size distribution for the 7075-T6 aluminum alloy

The combined influence of the cutting speed and the feed on the particle size depends on the workpiece material. During the milling process, the experiment shows that there is no homogenous influence of the cutting speed and the feed on the particle size for the materials tested (Fig. 23).
For purpose of analysis, it is very difficult to consider all particle size distributions, and for that reason, the mean size is considered as the particle size parameter. The mean particle size can be obtained by the following equation (Eq. 9):

$$Dm = \frac{\sum_{l}^{u} nD_p}{N} \tag{9}$$

where (N) is the total number of particles; (n) is the number (weighted) of particles per channel; (Dp) is the particle diameter (channel midpoint); (l) is the lower channel boundary, and (u) is the upper channel boundary.
For aluminum alloy 2024-T351, increasing the feed rate or cutting the speed enhances the mean particle size (Dm) until a certain value is reached, and then stagnation is observed (Fig. 24). The relatively low value of the mean particle size (Dm) was (23.4 nm) obtained for low feeds and speeds (0.01 mm/rev and 300 m/min).
For aluminum alloy 6061-T6, the influence of the cutting speed on the mean particle size (Dm) remains quite similar to what is seen in alloy 2024-T351, except that the influence of the feed rate for 6061-T6 is at a maximum at the intermediate value of feed. For low cutting speeds and low feed rates, it can be seen that there is a tendency for the mean particle size (Dm) to decrease (Fig. 24). Generally, it can further be seen as well that an increase in the feed rate can contribute to a decrease in the mean particle size (Dm) (Fig. 24). For aluminum alloy 7075-T6, the influence seems to be similar to the behavior of the aluminum alloys 2024-T351, with some variations. When both the cutting speed and the feed rate decrease, the value of the mean particle size (Dm) decreases (Fig. 24). The influences of the cutting speed and of the feed rate on the mean particle size (Dm) seem to trend in the same direction, but the variation in Dm is not very wide, especially for the aluminum alloys 6061-T6 and 7075-T6. For 6061-T6, the value of Dm is located between 131 nm and 173 nm nominal size, except for the smallest value, of about 50.2 nm. However, for the 7075-T6, the value of Dm is located between 125 nm and 146 nm.

4. Conclusion

The development of aluminum alloys is often conditioned by aeronautical requirements, but aluminum is very interesting for several applications in other sectors. Depending on the nuances, the composition, the treatments and the cutting conditions of these alloys, the material can be classified according to its machinability, recyclability, energy consumption and particle emission.
The machining of aluminum alloys is relatively easy as the cutting forces involved are low and the tool life is relatively high if there is no built-up edge or material adhesion problem. However, some problems may arise with the chip form and particle emissions. It is shown that long, continuous and spiral chips can indeed be prevented by selecting appropriate machining feeds and speeds.

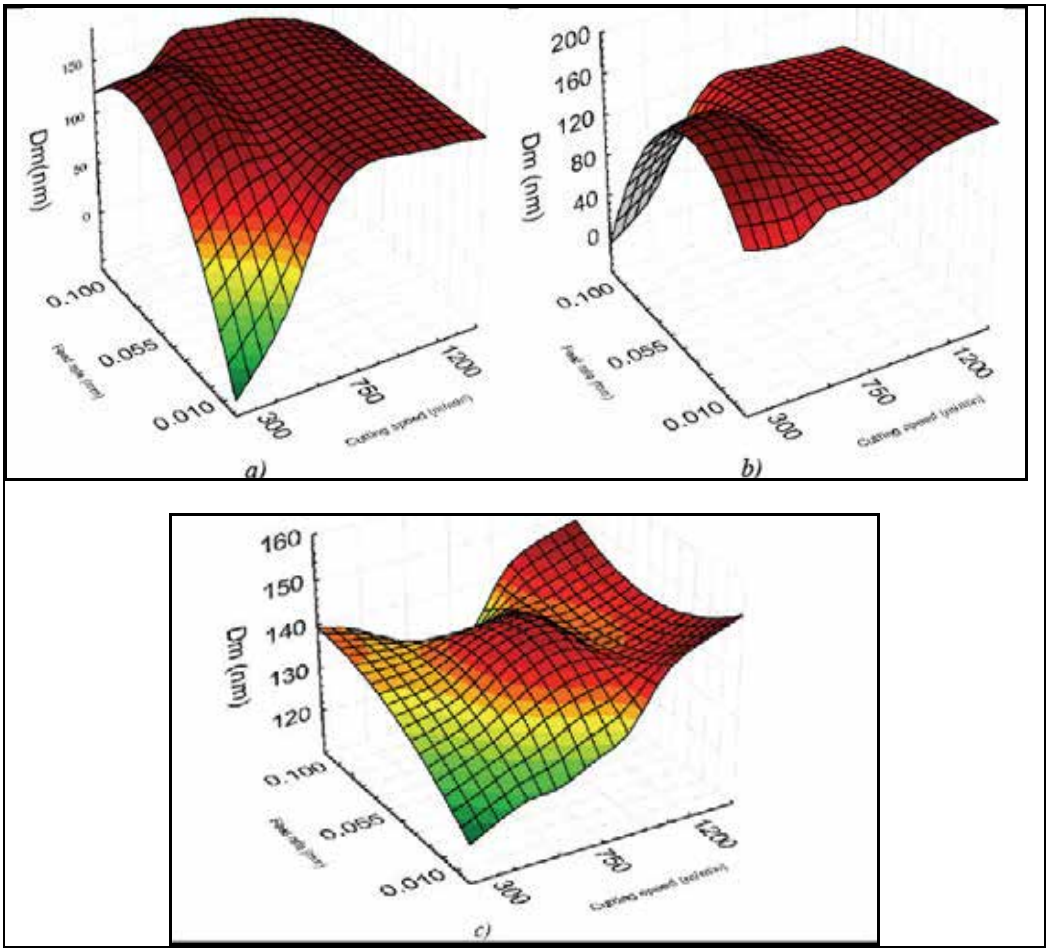

Fig. 24. Influence of the cutting speed and the feed rate on the mean particle size of the aluminum alloy: a) 2024-T351, b) 6061-T6, and c) 7075-T6

The machining of aluminum alloys generates fine and ultrafine particles, which have a relatively high sedimentation time and remain airborne for a long time, and could jeopardize the health of the worker. The machining of aluminum alloys using a special tool material and geometry during dry cutting at high speeds can be advantageous and sustainable.

5. References

Akarca, S.S. Altenhof, W.J. & Alpas, A.T. (2005). Characterization and Modeling of Subsurface Damage in a 356 Aluminum Alloy Subjected to Multiple Asperity Sliding Contacts, Minerals, *Metals and Materials Society*, Warrendale, PA, USA, 2005, p 107–120

Armarego, E. J. A. (1984). Predictive Models for Drilling Thrust and Torque- a comparison of three Flank Configurations. *Annals of the CIRP*, Vol. 33, No. 1, pp. 5-10.

Arumugam, P. U., Malshe, A. P., and Batzer, S. A., Bhat, D. G., 2002. Study of airborne dust emission and process performance during dry machining of aluminum-silicon alloy with PCD and CVD diamond coated tools NAMRC, *ID. Society of Manufacturing Engineers. MR02-153*, pp 1-8, May 21-24 2002 West Lafayette.

ASM Handbook, *Volume 16 – Machining*, Ninth edition, Joseph R. Davis senior Editor, page numbers (761-766), ISBN 978-0-87170-022-3, Metal Park, OH 44073

Balout, B., Songmene, V., Masounave, J. (2002). Usinabilité des alliages de magnésium et d'aluminium Partie I: Forces de coupe. proc. of the international symposium on enabling technologies for light metal and composite materials and their end-products, *41th conf. of metallurgists of CIM,* 2002 Vancouver, BC, Canada , pp. 223-242.

Balout, B, Songmene, V., Masounave, J. (2007). An experimental study of dust generation during dry drilling of pre-cooled and pre-heated workpiece material. *Journal of Manufacturing Processes*. Vol. 9, No. 1, pp. 23-34.

Becze and Elbestawi (2002). A chip formation based analytic force model for oblique cutting. *Int. Journal of Machine Tools and Manufacture*, Vol. 42. No. 4, pp. 529-538.

Demir H, Gündüz S. (2008). The effects of aging on machinability of 6061 aluminium alloy, *Journal of Material and Design*, doi:10.1016/j.matdes.2008.08.007

Fang, H.-W. (2007). Characteristic Modeling of the Wear Particle Formation Process from a Tribological Testing of Polyethylene with Controlled Surface Asperities, *J. Appl. Polym. Sci.*,Vol. 103, pp 587–594.

Konig, W, Erinski D., 1983, Machining and Machinability of Aluminium Cast Alloys, *Annals of the ClRP*, Vol 32, N 2

Khettabi, R., Songmene, V and Masounave, J., (2007), Effect of tool lead angle and chip formation mode on dust emission in dry cutting, *Materials Processing Technology* 194 (1-3), pp.100-109.

Khettabi R., Songmene V., Zaghbani I. and Masounave J (2010a), Modeling of fine and ultrafine particle emission during orthogonal cutting, *Journal of Materials Engineering and Performance*, JMEPEG 19, pp. 776–789.

Khettabi, R., Songmene, V. and Masounave J. (2010 b). Influence of machining processes on particles emission, *49th Annual Conference of Metallurgists of CIM*, 4-6 Oct. 2010, Vancouver, BC, Canada, pp. 277-288.

Kouam J., Masounave J. and Songmene V. (2010). Pre-holes Effect on Cutting Forces and Particle Emission During Dry Drilling, *49th Annual Conference of Metallurgists of CIM*, 4-6 Oct. 2010, Vancouver, BC, Canada, pp. 253-263.

Mackerer, C. R., (1989). Health Effects of Oil Mists: A Brief Review, *Toxicology & Industrial Health*, Vol. 5, pp. 429-440.

Ostiguy C, Roberge B, Ménard L, Endo C.A. (2008). Guide de bonnes pratiques favorisant la gestion des risques reliés aux nanoparticules de synthèse, *Guide technique R-586*, Études et recherches, IRSST, Montréal, Canada, 2008, pp. 73

Roy P. Sarangi S.K; Ghosh. A.; Chattopadhyay A.K., (2008), Machinability study of pure aluminium and Al–12% Si alloys against uncoated and coated carbide inserts, *Int. Journal of Refractory Metals & Hard Materials*. In press

Shaw, M.C. (2005). Metal Cutting Principles, 2nd edition, Oxford, New York, chap 9, pp. 183.

Songmene V., Masounave J., & Khettabi R. (2007). Safe, environmentally-friendly and cost effective machining. Safety, Health and Environmental World Congress, Santos, Brasil, July 22-25, 2007, pp. 44-48

Songmene V., Balout B., & Masounave J. (2008). Clean Machining: Experimental Investigation on Particle Formation, Part II: Influence of Machining Strategies and Drill Condition, *Int. J. Environmental Conscious Design & Manufacturing, (ECDM)*, 2008, Vol. 14, No. 1, pp. 17–33

Subramanian, K., and Cook, N., H. (1977). Sensing of Drill Wear and Prediction of Drill Life. *J. of Engineering for Industry*, Trans of ASME, Vol. 99, Serie B, pp. 295-301.

Tönshoff, B. Karpuschewski, & T. Glatzel, (1997). Particle Emission and Emission in Dry Grinding, *Annals of the CIRP*, Vol. 46, No. 2, pp. 693–695.

Xie, J.Q., Bayoumi, A.E. & Zbib, H.M. (1996). Study on shear banding in chip formation of orthogonal machining. *Int. J. Machine Tools & Manufacture*, Vol. 36, No. 7, pp. 835-847.

Tash M., Samuel F.H., Mucciardi F., Doty H.W., Valtierra S., (2006), Effect of metallurgical parameters on the machinability of heat-treated 356 and 319 aluminum alloys, J. *Materials Science and Engineering*, Vol. 434, pp. 207–217

Zaghbani I. and Songmene V. (2009a) A force-temperature model including a constitutive law for Dry High Speed Milling of aluminium alloys, *Materials Processing Technology,* 2 0 9 (2 0 0 9) pp 2532–2544.

Zaghbani, I., Songmene, V. and Khettabi, R., (2009b), Fine and Ultra fine particle characterisation and Modeling In High Speed Milling of 6061-T6 Aluminium Alloy; *Journal of Materials Engineering and Performance*, Vol.18, Issue 1 (2009), pp 38-49.

Edited by Tibor Kvackaj

The present book enhances in detail the scope and objective of various developmental activities of the aluminium alloys. A lot of research on aluminium alloys has been performed. Currently, the research efforts are connected to the relatively new methods and processes. We hope that people new to the aluminium alloys investigation will find this book to be of assistance for the industry and university fields enabling them to keep up-to-date with the latest developments in aluminium alloys research.

ISBN 978-953-51-5974-2

Photo by Rost-9D / iStock

IntechOpen